AD-A253 132

REPORT DO

Form Approved
OMB No. 0704-0188

Public reporting burden for this collection of info... gathering and maintaining the data needed, and ... collection of information, including suggestions f... Davis Highway, Suite 1204, Arlington, VA 22202-4302, and to the Office of Management ... for reviewing instructions, searching existing data sources, ... regarding this burden estimate or any other aspect of this ... te for Information Operations and Reports, 1215 Jefferson ... n Project (0704-0188), Washington, DC 20503.

1. AGENCY USE ONLY (Leave blank)	2. REPORT DATE	3. REPORT TYPE AND DATES COVERED
	May 26, 1992	Final 01 FEB 91 to 31 JAN 92

4. TITLE AND SUBTITLE

Optoelectronics Research Center

5. FUNDING NUMBERS

DTIC
ELECTE
JUL 27 1992
S D
C

6. AUTHOR(S)

S.R.J. Brueck

49620-89-C-0028

7. PERFORMING ORGANIZATION NAME(S) AND ADDRESS(ES)

Center for High Technology Materials
UNM, EECE Building, Room 125
Albuquerque, NM 87131-6081

8. PERFORMING ORGANIZATION REPORT NUMBER

AFOSR-TR- 92 0072

9. SPONSORING/MONITORING AGENCY NAME(S) AND ADDRESS(ES)

Dr. Howard Schlossberg
Department of the Air Force
Air Force Office of Scientific Research
Bolling AFB, DC 20332-6448

NE

10. SPONSORING/MONITORING AGENCY REPORT NUMBER

2301/AS

11. SUPPLEMENTARY NOTES

12a. DISTRIBUTION/AVAILABILITY STATEMENT

unlimited

12b. DISTRIBUTION CODE

13. ABSTRACT (Maximum 200 words)

The AFOSR Optoelectronics Research Center (OERC) at the Center for High Technology Materials of the University of New Mexico has become a leading university optoelectronics program. Novel InGaAs and AlGaAs device structures have been pioneered. Exciting recent results include demonstration of large second-order nonlinearities in SiO_2 and extensive development of PLZT. Processing advances include investigation of III-V regrowth over patterned wafers and the extension of interferometric lithography techniques. External cavity operation of diode lasers has provided a wealth of information about internal device physics and the fundamental limits of laser spectral and temporal characteristics. Single element and array geometries modeling has led to greater understanding and device performance. The AFOSR OERC has pioneered development of surface-emitting lasers. Since the first demonstration of the resonant-periodic gain concept was reported several years ago, advances have been made in device and mirror design, optical pumping with record output powers, in ultrafast gain switched operation, in record low series resistance, and overall and slope efficiencies for electrical operation. A recent advance in integrated structures is the coupling of phototransistors with surface-emitting lasers to make "smart pixels" that can operate in parallel on an array of optical signals.

14. SUBJECT TERMS	15. NUMBER OF PAGES
Optoelectronics, device structures, PZLT, III-V materials growth, diode lasers	437
	16. PRICE CODE

17. SECURITY CLASSIFICATION OF REPORT	18. SECURITY CLASSIFICATION OF THIS PAGE	19. SECURITY CLASSIFICATION OF ABSTRACT	20. LIMITATION OF ABSTRACT
unclassified	unclassified	unclassified	unclassified

Report AFOSR-F4960-89-C-0028

OPTOELECTRONICS RESEARCH CENTER

S.R.J. Brueck
Center for High Technology Materials
University of New Mexico
EECE Building, Room 125
Albuquerque, NM 87131-6081

May 8, 1992

Final Report for
Period 1 February 1991 - 31 January 1992

Prepared for:

Air Force Office for Scientific Research
Building 410
Bolling AFB, DC 20332-6448

Office of Naval Research
Bandelier West
University of New Mexico
Albuquerque, NM 87131

92-19909

92 7 22

EXECUTIVE SUMMARY

The AFOSR Optoelectronics Research Center (OERC) at the Center for High Technology Materials of the University of New Mexico has become a leading university optoelectronics program with substantial impact on the development of the field. Novel InGaAs and AlGaAs device structures such as resonant-periodic gain surface-emitting lasers and leaky-mode diode laser arrays have been pioneered. An exciting recent result is the demonstration of large second-order nonlinearities in SiO_2, both in macroscopic plates and in thin films grown on Si substrates. PLZT is another electrooptic material that has been extensively developed. Processing advances have included careful investigation of III-V regrowth over patterned wafers that allow unique device structures such as leaky-mode laser arrays, and the extension of interferometric lithography techniques that have led to the definition of isolated and passivated quantum wire and dot structures in Si and related materials. External cavity operation of diode lasers has provided a wealth of information on internal device physics and on the fundamental limits of laser spectral and temporal characteristics. Modeling of both single-element and array geometries has led to improved understanding and device performance. The AFOSR OERC has been a pioneer in the development of surface-emitting lasers. The first demonstration of the resonant-periodic gain concept was reported several years ago. Since then, advances have been made in device growth (MOCVD), in device and mirror design, in optical pumping with record output powers (> 50kW) for any semiconductor device, in ultrafast gain switched operation, in record low series resistance, overall and slope efficiencies for electrical operation. A major advance in integrated structures is the coupling of phototransistors with surface-emitting lasers to make "smart pixels" that can operate in parallel on an array of optical signals. This opens the possibility of an entirely new class of optical information processing.

A major feature of the AFOSR OERC has been interactions with the Air Force Phillips Laboratory and with other Air Force laboratories including the Rome Laboratory.

DTIC QUALITY INSPECTED 4

Accession For
NTIS GRA&I
DTIC TAB
Unannounced
Justification
By
Distribution/
Availability Codes
Dist | Avail and/or Special
A-1

TABLE OF CONTENTS

EXECUTIVE SUMMARY ..... *i*
TABLE OF CONTENTS ..... *ii*
I. INTRODUCTION 1
II. CURRENT ACCOMPLISHMENTS 3
II.1 MATERIALS: 3
II.1.1 MOCVD Materials Growth and Applications 3
Crystal Growth Facility 3
Research with the Air Force 4
Materials Supplier for Other Major Laboratories 4
MOCVD Research 5
Current Programs 5
II.1.2 Nonlinear and Electrooptic Materials 6
Semiconductor Quantum Well Materials 6
PLZT and related Materials 10
Nonlinearities in SiO_2 11
II.2 PROCESSING AND FABRICATION 17
II.2.1 MOCVD Regrowth 17
II.2.2 Interferometric Lithography Fabrication of Quantum Wire and Dot Structures 17
II.3 DEVICES 21
II.3.1 Semiconductor Lasers 21
External cavity transverse mode filtering of high-power lasers and laser arrays 21
Antiguiding wide stripe lasers 22
Bow-tie waveguide laser structures 22
Modal characteristics of broad-area lasers 23
Side-Mode Injection Locking of Semiconductor Lasers 23
VERTICAL-CAVITY SURFACE-EMITTING LASERS 24
Optical pumping of low-threshold VCSELs 24
High-power, large-area optical pumping of VCSELs 25

Distributed-feedback Resonant-Periodic-Gain Surface-Emitting Lasers 25

Thermal properties of etched-well surface-emitting diode lasers 26

Thermal waveguiding in etched-well surface-emitting diode lasers 58

DIODE LASER ARRAYS 59

Measurements and interpretation of near-field phase fronts by shearing interferometry 59

Coupling of multistripe arrays to external resonators with spatial filters 59

Theory of diffraction-coupled arrays 59

Broad-area mode-coupling model for carrier-guided diode laser arrays 60

Thermal focusing effects in carrier-guided diode laser arrays 61

Theory of nonabsorbing-mirror diode laser arrays 61

OPTICAL SWITCHING 62

VCSEL-based bistable optical switches 62

Mode switching and beam scanning in twin-stripe lasers and laser amplifiers 62

Mode switching in grating-coupled surface-emitters 62

NONLINEAR DYNAMICS OF SEMICONDUCTOR LASERS 63

Multi-gigahertz modulation of semiconductor lasers and laser amplifiers 63

Dynamics of external cavity semiconductor lasers and laser arrays 63

EXTERNAL CAVITY SEMICONDUCTOR LASERS: STABILIZATION, METROLOGY 64

Longitudinal mode stabilization, linewidth narrowing 64

High power, tunable external cavity lasers 64

Double external cavity laser studies 64

Doppler velocimetry using laser diodes 65

II.4 DEVICE INTEGRATION 65

Vertical-Injection Surface-Emitting Lasers: 65
Optical Switches And Logic Gates Based On VCSELs: 66
Optical Logic Gates Based On HPT/VCSEL Switches: 69
Transverse-injection Multi-Quantum-Well Resonant-Periodic-Gain (MQW-RPG) VCSELs 69
II.5 SPECTROSCOPY 73
GaAs/AlGaAs laser facet passivation for elevated catastrophic optical damage thresholds 73
Photoacoustic Spectroscopy of Weak Absorptions 73
Spatially Resolved Confocal-Photoluminescence Spectroscopy 73
III. REFERENCES 75
APPENDIX A: PUBLICATIONS
APPENDIX B: PRESENTATIONS

I. INTRODUCTION

The *Optoelectronics Research Center* (OERC) at the University of New Mexico that was begun in FY87 under the auspices of the Air Force Office of Scientific Research. The OERC has functioned in conjunction with the *Center for High Technology Materials* (CHTM), which is also supported by the State and University of New Mexico, with the *Optoelectronic Materials Center*, which is being funded by DARPA, and with the SRC/SEMATECH University Center of Excellence in *Metrology and On-Line Analysis for Semiconductor Manufacturing*. CHTM is an interdisciplinary research organization with faculty and research representation from four departments: Electrical Engineering, Physics, Chemistry and Chemical Engineering.

Since its inception, the AFOSR OERC has become a leading university optoelectronics program with substantial impact on the development of the field. Just one evidence is the 1991 DOD Critical Technologies Plan, recently submitted to Congress, which highlights the strong University of New Mexico programs in the areas of III-V lasers and laser arrays.

The program of the AFOSR OERC has been primarily experimental with theoretical work in support of our experimental efforts. Emphasis has been on the invention, demonstration, and study of novel optoelectronic structures and devices, which have unique capabilities of interest to the Air Force and national requirements in general. In addition, we have trained Air Force personnel and civilian students in the fabrication, characterization, and utilization of optoelectronic devices to satisfy needs at the Air Force laboratories as well as at other federal laboratories and commercial organizations.

The goal of the AFOSR OERC is to be at the forefront of advances in optoelectronics. We strongly believe that the coupling and increasing merger of optics and electronics has already had important consequences, but that the major advances which will occur over the next decade will dwarf those seen to date. These will result from advances in linear and nonlinear materials, in device processing, in device design, and in device integration. Examples of materials and structures are quantum wells, superlattices, strained-layer semiconductors, and new nonlinear materials. Processing developments relate to smaller dimensions and improved techniques for the selective deposition, modification and removal of materials. Improved devices result also from increased understanding of the underlying device and material physics and from innovative approaches to device design and synthesis. Integration of multiple optical functions and between optical and electronic functions will have a increasing impact.

The AFOSR OERC has produced significant results in all of these areas. Details are provided below. In III-V materials and structures, novel InGaAs and AlGaAs device structures such as resonant-periodic gain surface-emitting lasers have been pioneered. An exciting recent result is the demonstration of large

second-order nonlinearities in SiO_2, both in macroscopic plates and in thin films grown on Si substrates. PLZT is another electrooptic material that has been extensively developed. Processing advances have included careful investigation of III-V regrowth over patterned wafers that allow unique device structures such as leaky-mode laser arrays, and the extension of interferometric lithography techniques that have led to the definition of isolated and passivated quantum wire and dot structures in Si and related materials. External cavity operation of diode lasers has provided a wealth of information on internal device physics and on the fundamental limits of laser spectral and temporal ch. ..teristics. Modeling of both single-element and array geometries has led to improved understanding and device performance. A major advance in integrated structures is the coupling of phototransistors with surface-emitting lasers to make "smart pixels" that can operate in parallel on an array of optical signals.

An important driver for the success of the AFOSR OERC program is the vertical integration of capabilities within CHTM. These extend from semiconductor and nonlinear materials growth and characterization, through fabrication and processing, to device synthesis, characterization and integration. The juxtaposition of these resources within a common research setting provides an important cross-fertilization that is crucial for rapid progress in this multidisciplinary area.

Interaction with Air Force personnel and research and development programs and needs is a major aspect of this AFOSR OERC. Particularly close relations are maintained with the Air Force's Phillips Laboratory programs in diode lasers and nonlinear optics. Strong ties are also maintained with the Rome Laboratory programs in photonics.

A recent addition to these interactions is the formation of the Alliance for Photonic Technology (APT). APT is a cooperative technology transfer initiative between CHTM, the Phillips Laboratory, Sandia National Laboratories, and Los Alamos National Laboratory to provide a common, and user-friendly, interface between these diverse laboratories and industry. The Rome Laboratory has also expressed interest in joining this cooperation.

II. CURRENT ACCOMPLISHMENTS

As noted above, the AFOSR OERC has generated a substantial body of results since its inception in FY-87. Recent highlights are presented here. As was noted above, an important feature of the OERC is its broad range of capabilities and talents. Any division into the areas of materials, fabrication, devices and integration such as is attempted here is necessarily arbitrary. Materials are grown for devices, not simply to study the materials and growth physics. The ultimate tests of the materials are in their performance in device applications. Thus, descriptions of laser performance appear under the materials section. This and other similar sorting anomalies are inevitably found in the following.

II.1 MATERIALS:

II.1.1 MOCVD Materials Growth and Applications

Establishment of CHTM's MOCVD growth facility was realized in 1987 with the support of the State of New Mexico and AFOSR. Major advancements have been made in very high efficiency AlGaAs GRIN-SCH QW laser technology, including strained GaAlInAs alloys for improved threshold, power and reliability over a wavelength range from 680 nm to 1000 nm. Perhaps the most demanding and exciting application for the MOCVD materials has been in the development of vertical-cavity surface-emitting lasers (VCSEL). In concert with advances in fabrication and processing, the MOCVD material has demonstrated unsurpassed AlGaAs VCSEL performance and, combined with low-defect MOCVD regrowth of optical transistors and thyristors, the first monolithic optical computing logic elements based on VCSELs have been produced. In addition to the above laser materials growth, studies have been conducted on HEMT and HBT device materials, heterostructures for green light emission from GaAs and Leaky-Mode phased array lasers, just to name a few. Experiments with zinc, tellurium, and carbon doping, and regrowth on patterned substrates of GaAs and AlGaAs have also been instrumental in realizing device goals.

A brief outline of accomplishments over the past 3 years follows.

Crystal Growth Facility

Fully functional in early 1987, the existing Crystal Growth Facility has been a consistent asset to the Center with nearly 1000 epitaxial growths to date. The custom designed reactor, which was configured with a high vacuum residual gas analysis provided through AFOSR funding, has provided consistently high quality material for CHTM, the Air Force and other laboratories. The facility has proven to be an excellent training ground for students with an overriding emphasis on safety of operations.

Research with the Air Force

A primary objective of the MOCVD capability at CHTM has been to support the programs of direct interest to the Air Force. This has been effected by joint research with personnel of the Air Force's Phillips Laboratory.

High Efficiency AlGaAs GRIN-SCH Lasers

Our MOCVD materials have been utilized in a number experiments involving the Phillips Laboratory including Broad Area Devices for External Cavities, Broad Area Unstable Resonators utilizing Etched Facets, Buried Lenslets, and, in the near future, Buried Continuously Graded Refractive Index Structures. Unstable resonator structures investigated have produced several hundred milliwatts of power in a single mode from apertures as wide as 170 μm.

Strained Quantum Well (SQW) GaAlInAs Lasers

Higher efficiency and power, lower threshold and better reliability are all motives for using SQW lasers. An additional advantage is that GaAs substrates are transparent to the laser radiation. SQW structures are now routinely used in the majority of laser diode work at the AFOSR OERC.

Leaky-Mode Laser Arrays

A new process was developed for fabrication of Leaky-Mode Laser Arrays. This process, now being utilized by TRW as well, has proven to be very simple and relies on a high quality epitaxial regrowth interface. Powers up to 750 mW in a stable supermode have been observed.

Materials for Phillips Laboratory contractors

The CHTM MOCVD materials have been utilized by a number of Phillips Laboratory contractors in order to enhance their research activities. The list includes David Sarnoff Research Center, Hughes Research Labs, TRW Research Center, Sandia National Laboratory and Spectra Diode Laboratories.

Materials Supplier for Other Major Laboratories

Materials grown by MOCVD have been used by a number of major research laboratories. In some cases only the epitaxial material has been provided and in others, processing of the material has also been included. This list of laboratories includes:

Army Night Vision and Electrooptics Laboratory
Sandia National Laboratories

Lawrence Livermore Laboratory
Spectra Diode Laboratories
Hughes Research Laboratories
TRW research Center
Rockwell Science Center
David Sarnoff Research Laboratories
Crystal Specialties Corporation
CVD Metalorganics Division of Morton Thiokol
Optic Electronic Corporation
Fermionics Corporation
Oregon State University
University of California Los Angeles

MOCVD Research

A number of experiments have been conducted under AFOSR funding which have had broad application in a number different projects. It is of fundamental importance to do experimental growths aimed at producing enough data to generate empirical constants needed for predicting material growth rates, composition and doping. We find that our reactor has a stability of about 1% variation in thickness over the period of one week. The uniformity was also analyzed demonstrating a total variation of 3.8% over a 2" diameter wafer. The aluminum composition varies by less than 0.1% in AlGaAs. Detailed studies of carbon, zinc and tellurium doping have been carried out. The advantage of carbon doping over zinc is its extremely low diffusion coefficient. Regrowth on GaAs and AlGaAs is very important for a number of new optoelectronic devices and detailed studies have been carried out on different surface treatments prior to growth and these have been analyzed using photoluminescence, C-V, and DLTS profiling. Laser diodes with regrown active region interfaces have also been measured and it has been shown that minimal degradation of performance can bee achieved by using ammonium sulfide and *in-situ* HCl etching prior to regrowth. Finally, 680-nm laser diodes with power outputs of nearly 500 mW have been fabricated by incorporating strained GaAlInAs quantum wells in an AlGaAs large-optical-cavity laser structure.

Current Programs

The following is a summary of projects currently active in the MOCVD materials growth:

1. **Si and SiGe Growth on Si at Low Temperature by Conventional MOCVD.** Preliminary studies show that this very important material system can be grown very easily by MOCVD if the system has very low moisture and oxygen levels. Precursors of silane and tetramethyl germanium are used in hydrogen. Excellent material quality is observed at growth temperatures as low as 650°C. Doping is

accomplished using arsine and trimethyl indium. Detailed materials characterization is underway.

2. **Vertical Cavity Surface Emitting Lasers and Optical Logic Elements.** Further development of the VCSELs and pnpn switching elements is underway. Efforts to minimize surface defect density and improve device-to-device uniformity are underway. Epitaxial regrowth is an attractive way of testing laser and switch devices independently as well as monolithically. This is done by including GaAs substrates in the pnpn regrowth runs on VCSEL substrate structures.

3. **Establishing MOCVD Growth of AlGaInP Visible Diode Laser Materials for 633-nm CW Operation.** Utilizing funds secured under contracts from DARPA for a new MOCVD reactor, the University of New Mexico for building expansion, and the New Mexico research and Development Institute (NMRDI) for facilitization and operations, the Crystal Growth Facility will double its capability and diversify into the AlGaInP materials with the aim of producing high efficiency 633-nm laser diodes. Engineering is complete, ground breaking is underway and a detailed request for proposal for the new reactor has been issued. This RFP includes a option to bid on a new multi-wafer radial reactor concept for which a patent application has been filed. This increased III-V epitaxial growth capability will directly benefit the programs of the AFOSR OERC.

II.1.2 Nonlinear and Electrooptic Materials

Semiconductor Quantum Well Materials

Most quantum well optoelectronic devices rely on externally applied electrical fields to control the optical properties. Approaches to investigating the properties of any quantum well design under electric field are necessary, especially as evidence is mounting that nonrectangular quantum wells have significant advantages over rectangular wells. The configuration we studied is shown in Fig. II-1.

We use Airy Functions as general solutions of Schrödinger equation for a quantum well with an electric field. Since Airy functions are the eigenfunctions for these situations, the benefits of this approach include accuracy and simple formulations. Previous attempts, however, were only able to apply Airy Function solutions to electric fields higher than 100 kV/cm as the solution becomes numerically unstable for lower fields. These fields are larger than the typical fields used for actual devices. Furthermore, it was also difficult to handle the Airy functions for an asymmetric triangular quantum well in an electric field. In Fig. II.1, we can see that when the electric field exceeds 62 kV/cm in one direction, the holes lose confinement, while 94 kV/cm in the other direction eliminates electron confinement in the asymmetric triangular quantum well. We were successfully

able to calculate the bound states for fields less than ±100 kV/cm. These results are shown in Fig. II-2. This work was done in collaboration with Guernot Pomrenke's program at Emory University with Prof. K. Bajaj. A short article is in preparation.

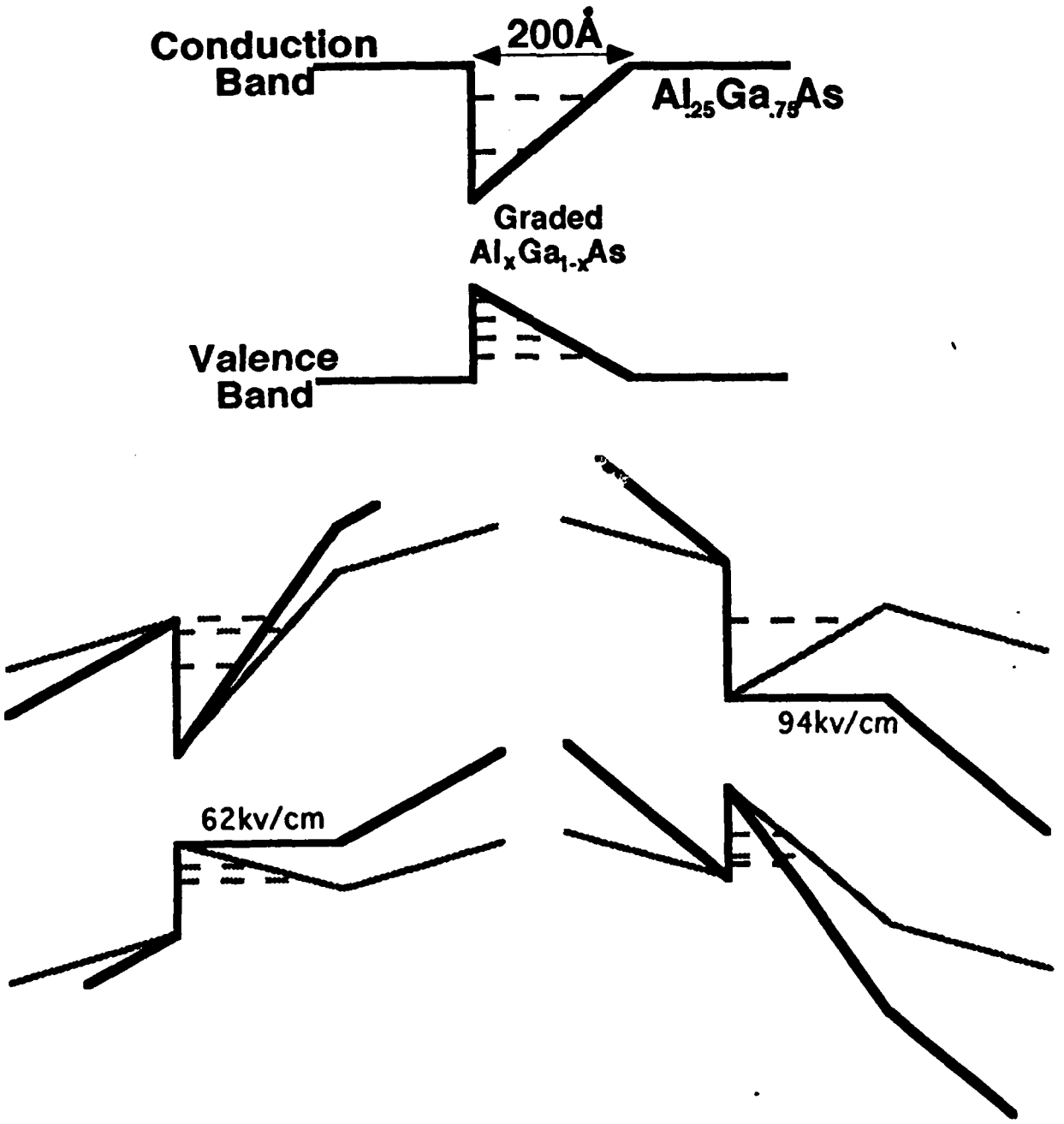

Figure II-1. The asymmetric triangular quantum well studied (top), showing the applied fields necessary to eliminate confinement in the valence band (left) and conduction band (lower right).

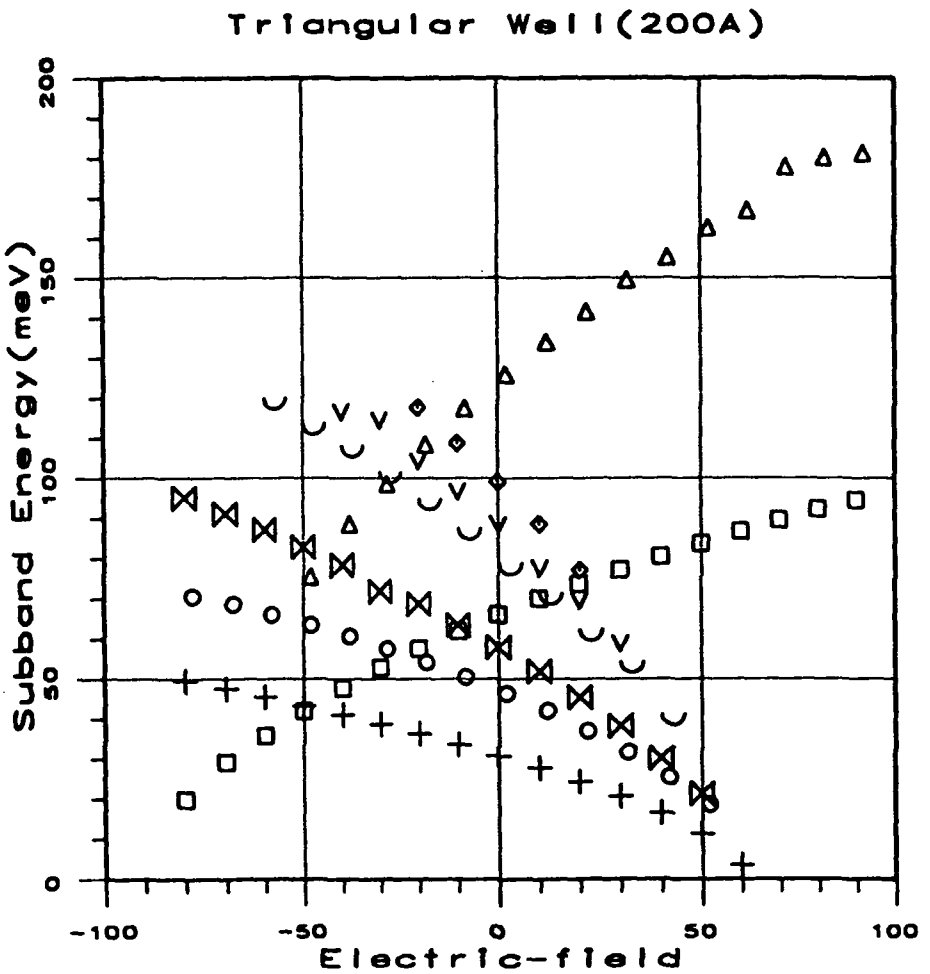

Figure II-2. Results of the Airy Function calculation for the asymmetric triangular quantum well in Fig. II.1. Notice the bound states for electrons and holes disappear as anticipated.

Many device concepts make use of transitions between energy levels in semiconductor structures. Given that a real device will usually have to operate over some temperature range, understanding of the temperature dependence of the energy levels is key to furthering the technology of such a device. While the temperature dependences of band gaps are well known, only recently have the temperature dependences of the band offsets that play a crucial role in quantum

well and other heterostructure devices been investigated. We have elaborated on our previous studies by including the role thermal expansion effects play in the temperature dependences of band offsets.

Using a thermodynamic approach, we examined the role thermal expansion plays in determining the temperature dependence of band gaps and band offsets. Because of the large variation in the standard volume of electrons (or, equivalently, variation in conduction band deformation potential) with symmetry of the conduction band, most of the band gap temperature variation can be ascribed to the valence band for the X gap, while the variation is more evenly divided between the conduction and valence band for the Γ band gap. The particulars of the AlAs/GaAs system have been examined in detail, we find evidence that X electrons have a larger electron-phonon entropy than Γ electrons, and that the lowest conduction band offset exhibits considerable temperature variation. Results are summarized in Fig. II.3:

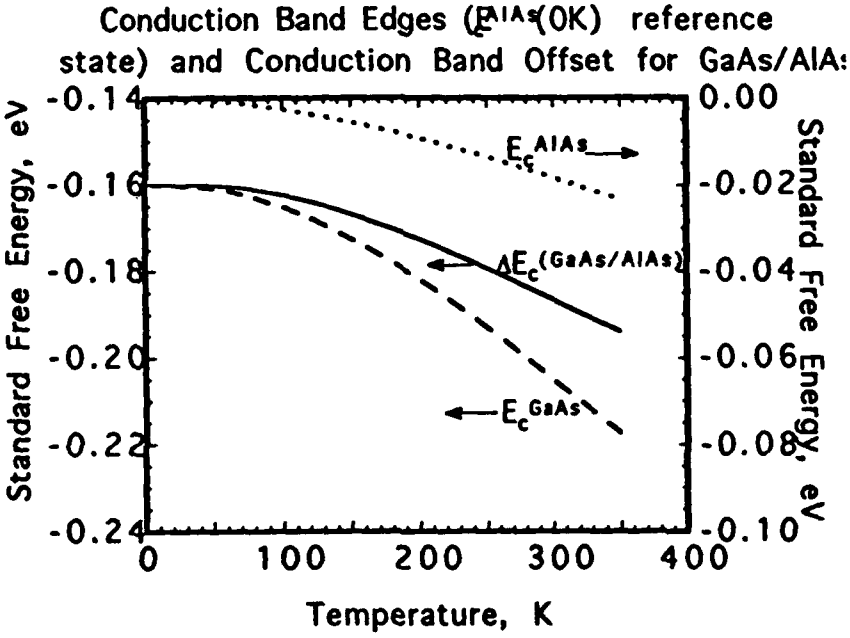

Figure II-3. Predicted conduction band offset temperature dependence of the AlAs/GaAs system. Notice that the magnitude of the offset variation is close to the magnitude of the band gap variations.

This also was a collaborative effort with another AFOSR Grant at Oregon State University.

PLZT and related Materials

Lead-lanthanum zirconate-titanate (PLZT) is a promising material for thin film electrooptic and nonlinear optical applications. In various regions of its phase diagram, PLZT exhibits rhombohedral, tetragonal or cubic crystal structures, with corresponding variations in the second-order nonlinearity. At room temperature, the composition with 28% lanthanum and 0% zirconium, PLZT 28/0/100, is on the border between the cubic and tetragonal phases. This composition exhibits a large quadratic electrooptic effect, as well as a large transparency range (0.3 - 6 μm). We have concentrated on the properties of thin films of PLZT of this composition. We have also investigated a number of compositions such as 15/0/100 and 7/0/100 which are fully in the tetragonal regime. Deposition has been by rf-sputtering, by ion-assisted ion-beam sputtering, and by laser ablation. Substrates include fused silica and sapphire as well as Si and GaAs. These later hold out the promise of monolithic integration with semiconductor-based sources and detectors.

Highly oriented PLZT films have been deposited with <001> or <100> crystallographic directions normal to the film surface. Figure II-4 shows X-ray diffraction scans of 0.4-μm thick films deposited on a variety of substrates by rf-sputtering. Note the strong <100> and <200> diffraction peaks and the relative absence of other orientations. In contrast, a bulk ceramic sample (bottom of figure) shows a number of diffraction peaks corresponding to the varied crystallite orientations.

The spatially resolved electrooptic properties of these films have been extensively explored using a confocal scanning polarization microscopy configuration. Planar interdigitated electrodes (Cr:Au) were deposited with an electrode gap of 8 μm. An image of the electrooptic response of a 28/0/100 film, obtained with ~ 0.4 μm resolution is shown in Fig. II-5. The nonuniformity seen in the figure provides information on compositional and orientational effects in the films. This characterization capability has allowed us to dramatically improve the uniformity of the deposited films. These films exhibit hysteresis in the electrooptic response due to domain formation. For the paraelectric composition 28/0/100, we have observed, for the first time, a saturation of the electrooptic effect at high fields as shown in Fig. II-6. Switching speeds to 3 ns, instrumentation limited, have been measured in PLZT 28/0/100 films. In addition, extensive measurements of the second harmonic generation properties of these films have been carried out. A field-on/field-off contrast ratio of 900:1 has been observed. Photorefractive effects, leading to screening of the field and a decrease in the second harmonic output on a time scale of ms, have been observed and phenomenologically modeled.

Nonlinearities in SiO_2

Fused silica is ubiquitous in modern technology. Its extremely low linear optical losses have enabled the fiber optics industry. SiO_2 also plays a dominant role in microelectronics technology where the unique properties of the SiO_2-Si

interface are largely responsible for the behavior of metal-oxide-semiconductor (MOS) devices underlying advances in computer hardware.

Unlike its related quartz crystalline phase, fused silica is amorphous with a macroscopic inversion symmetry that forbids second-order nonlinear processes. Thus, the discovery by Österberg et. al. [1986] of efficient second harmonic generation (SHG) in a variety of Si-Ge glass fibers upon "training" with optical fields has generated considerable interest in the physics and applications of this unexpected phenomenon. Stolen and Tom [1987] proposed a mechanism based on electric-field-induced nonlinearities where the field arises from a third-order optical rectification process. Bergot *et al.* [1988] have observed an enhancement of the nonlinearity with the application of a transverse electric field. Recently, Anderson *et al.*[1991] have proposed a photovoltaic effect based on interference between the fundamental and harmonic fields that phenomenologically accounts for the observed strength of this field [Kamal, 1990] which is about four orders of magnitude larger than the field expected from optical rectification. This field interacts with the material third-order nonlinearity, $\chi^{(3)}$, to provide an effective $\chi^{(2)} = \chi^{(3)}E_{dc}$. Similar field-induced nonlinearities have been observed in a variety of material systems, e.g. paraelectric PLZT [Mukherjee, 1990].

We have observed, for the first time, a permanent second-order nonlinearity in the near surface region of bulk fused SiO_2 induced by a temperature / static electric field poling process. The induced $\chi^{(2)}$s achieved are three to four orders of magnitude larger than found in the fiber experiments and approach that of traditional nonlinear optical materials such as $LiNbO_3$.

The preparation process for generating the $\chi^{(2)}$ nonlinearity in a sample involves heating it to 250°-325°C in a laboratory ambient while applying a dc bias of 3 to 5 kV across the nominally 1.6-mm thick samples. After ~15 minutes of poling the heater is turned off and the sample is cooled to room temperature. Once cooled, the electric field is removed and a stable $\chi^{(2)}$ nonlinearity is observed. For most experiments, electrodes (stainless steel and Si) were simply physically contacted to the sample. Samples have been maintained at room temperature without special precautions for several months without any noticeable degradation of the nonlinearity. Application of heat alone, above ~ 250°C, removes the nonlinearity. The necessary voltage did not scale with the sample thickness. Attempts to pole commercial fused silica coverslips (180-μm thick) with a linearly scaled voltage were unsuccessful. However, large nonlinearities were observed when these same samples were placed atop a 1.6-mm thick sample and the larger voltage was applied across both samples.

The SHG signal from these poled samples was obtained with 10-ns pulses at 1.06 μm from a 1-mm diameter Q-Switched Nd-YAG laser beam operating at 10 Hz at an intensity of 10 MW/cm^2. The SHG signals were recorded with a photomultiplier tube (maximum signal / noise ~500:1).

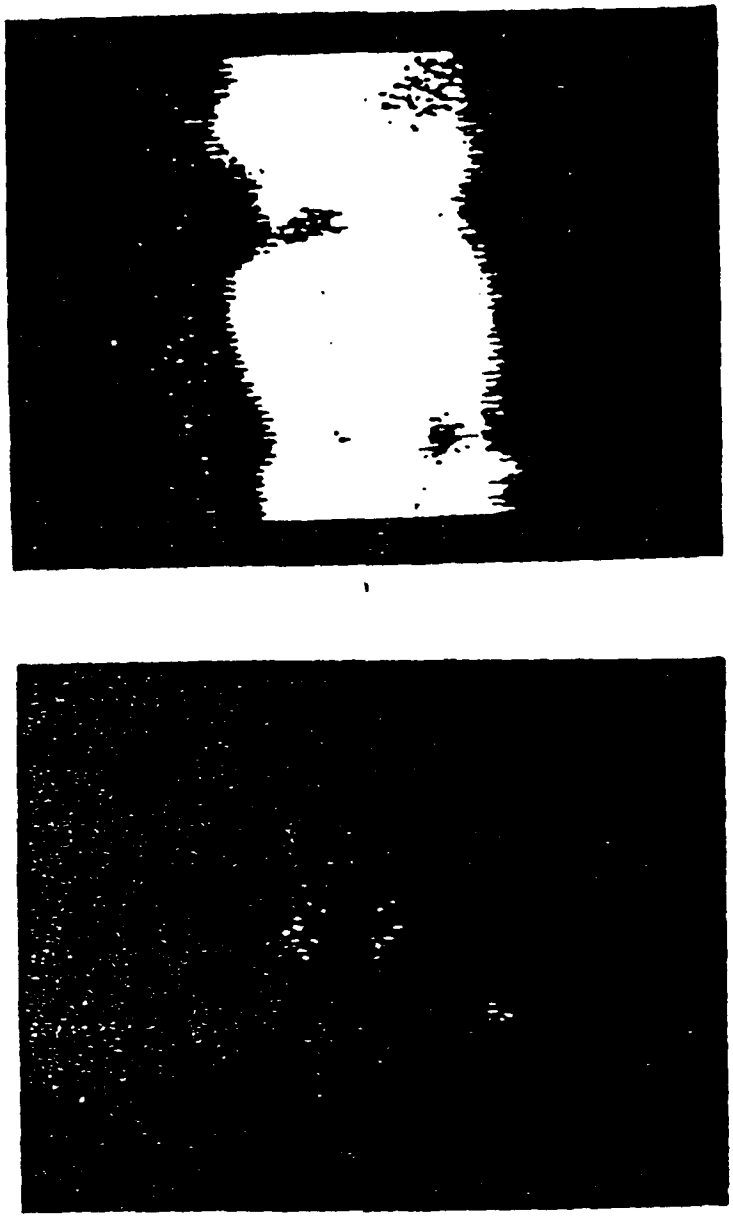

Figure II-5: Confocal microscopy images of the induced birefringce in PLZT thin films at E=20 kV/mm (top) and E=0 kV/mm (bottom). The distance between the electrodes is 8 μm; the spatial resolution is ~0.4 μm.

We used several commercial grades of amorphous silica including Optosil, Homosil, Infrasil, and Suprasil. The strength of SHG signal was approximately the same for all samples (within a factor of two variation) except for Suprasil which showed a signal only ~10% as large. Suprasil, manufactured by a synthetic process, has a level of metal impurities only 10% that of the other grades.

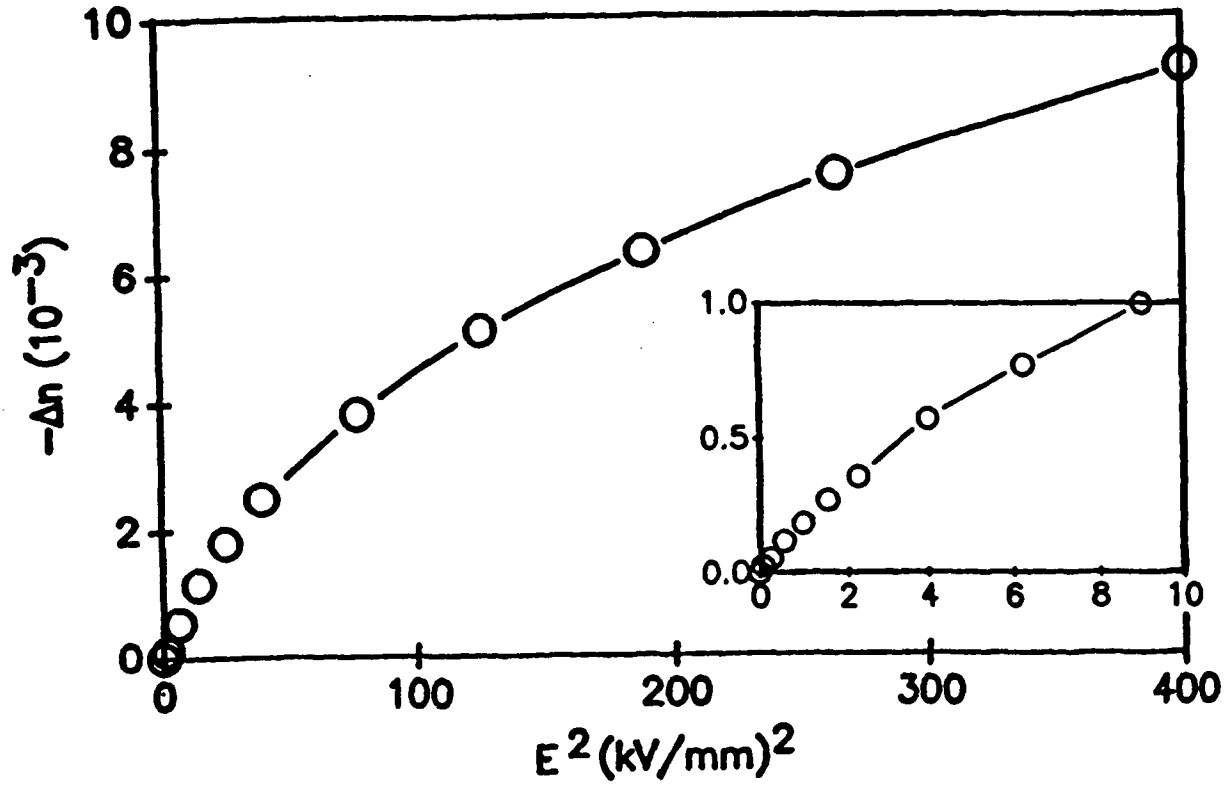

Figure II-6: Saturation of the quadratic electrooptic effect in PLZT 28/0/100 films at high applied electric fields.

This large difference in SHG signals suggests that impurities play a role in the generation of the large observed nonlinearity. Typically, the dominant metal impurity in Optosil and related materials is Al with a concentration of 20-50 ppm. Al is known to substitute for Si in as-grown fused silica samples. Brower [1979] has investigated the formation of paramagnetic impurity centers associated with these Al impurities including $AlO_{3/2}^{-}$ and $AlO_{3/2}^{-}$-Na^{+} complexes formed under ionizing radiation. The temperature induced destabilization of these complexes is similar to the observed dependence of the SHG signal on poling temperature. Indeed, almost all trapping centers observed in SiO_2 films have shown thermal discharge temperatures in the range from 100-400°C [DiMaria, 1978].

Perhaps similar charge compensated molecular complexes are formed and oriented during the poling process and induce a macroscopic $\chi^{(2)}$. If such localized moieties are indeed present then the individual hyperpolarizability β can be estimated from the measured $\chi^{(2)}$. Assuming an impurity density of 50 ppm, β is estimated to be 10^{-37} m^4/V, many orders of magnitude larger than that of Urea or MNA. This casts significant doubt on a localized impurity model for the nonlinearity.

Another possibility for the nonlinearity is a field-induced third-order process similar to that proposed for the fiber experiments. Using the known fused silica $\chi^{(3)} \sim 10^{-22}$ m^2/V^2, the dc field required to generate the observed $\chi^{(2)}$ is ~ 10^7 V/cm. This large field might be generated in the fused silica by charge separation at high temperature followed by trapping as the temperature is lowered with the field applied. The major charge carriers in fused silica (9-eV bandgap) in this temperature range are likely to be cations such as Na^+. Under the applied temperature and bias, these cations will drift to the cathode leaving a space-charge region with a fixed concentration of trapped negative charge very similar to that in Schottky barriers. Under these conditions, the major part of the externally applied potential is dropped over a depletion region of only several micrometers enhancing the field strength. Assuming an impurity density of 50 ppm (the nominal total impurity concentration) and a poling voltage of 5 kV, a space charge width of 5-6 μm and a maximum field strength of 10^7 V/cm is estimated across the depletion region, comparable with the experimental observations. Additionally, this mechanism is consistent with the experimental observation of a fixed voltage rather than a fixed field requirement on thickness scaling. This model provides for regions of high field at each end of the sample. Experimentally, the nonlinearity is only observed on the anode side. This may be due to inequivalent charge distributions leading to varying field strengths and effective lengths, or to charge injection due to tunneling (which seems unlikely with the poor contacts used) or to hot carriers from plasma breakdown near sharp protrusions on the electrodes.

We have generated a very large second-order nonlinearity in the near surface regions of bulk fused silica. The $\chi^{(2)}$ coefficient of 1×10^{-12} m/V is of the same order as crystal quartz and is three orders of magnitude larger than that reported for fibers. A possibility for the microscopic mechanism of this nonlinearity involves the creation and orientation of nonlinear complexes during the poling process. However, this model leads to questionably large values for the hyperpolarizability. Another possibility is the generation of a large dc field (10^7 V/cm) by charge separation and trapping during the poling process, which induces the large $\chi^{(2)}$ by a field-induced third-order process. Because of the ready manufacturability of silica optical materials and their integration with semiconductor optoelectronics, this nonlinearity may have important applications in waveguide and other optoelectronic devices.

In a recent development, we have extended the observation of these large nonlinearities to thin films of SiO_2 grown on Si substrates. This was accomplished by growing a thin film of silicon nitride above the SiO_2. The Si_3N_4/SiO_2 interface is known to be highly defected and provide a large number of deep traps for charge storage. This is the underlying principle behind one type of nonvolatile memory element used in microelectronics. This result is particularly significant since the nitride layer also provides a high-quality waveguide as well as integration with semiconductor structures.

II.2 PROCESSING AND FABRICATION

II.2.1 MOCVD Regrowth

With advances in fabrication and growth technologies, these two areas are becoming inextricably intertwined. Efforts in regrowth on GaAs epilayers following fabrication for both leaky-mode diode laser arrays and integrated HPT-VCSEL switches are discussed in the materials and integration sections.

II.2.2 Interferometric Lithography Fabrication of Quantum Wire and Dot Structures

The use of optical interference effects to form grating structures with a period comparable to the optical wavelength is well established [Anderson 1983]. It is quite simple to fabricate gratings to periods of approximately 0.25 μm using an Ar-ion laser source. Adjusting the exposure and development conditions, it is possible to generate line-space ratios that deviate substantially from unity and hence to generate very small structures that are of interest for quantum confinement effects. Interest in this topic, and application to Si structures, has been rekindled by the observation of efficient visible photoluminescence from electro-porous Si [Canham, 1990; Halimaoui, 1991]. This luminescence has been attributed to quantum size effects which both shift the spectral peak to shorter visible wavelengths and, because of the strong localization, enhance the luminescence efficiency.

By optimizing the interferometric lithography process, we have been successful in generating photoresist mask structures to only 40 nm. Working with <110> oriented Si, we have used the highly anisotropic KOH wet etching characteristics to transfer these patterns into the Si. Figure II-7 shows an electron micrograph of a series of 40-nm wide, 0.7-μm deep Si lines on a 1-μm pitch. The Si width can be further reduced by simple oxidation processes. Figure II.8 shows a micrograph of a similar structure (initially 150-nm wide) that has been thermally oxidized to a depth of approximately 60 nm. The remaining Si is shown by the slightly darker lines in the center of each structure. Finally, Figure II.9 shows the result of stripping off the SiO_2 with a HF solution. At the waist, these structures are only 10 nm wide! We have further optimized this process to leave very small (10-40 nm diameter) isolated Si wires surrounded by SiO_2. These are very interesting structures that will provide an important test of the mechanism for the observed photoluminescence.

Further refinements on the lithography process allow parallel connections of many similar wires and offer the possibility of electrical excitation and observation of quantum transport effects. This is illustrated in Figure II-10 which shows a top view of 12-μm long, 50-nm wide Si wires connected to ~1-μm wide "bussbars" running at right angles. This structure was fabricated using a double exposure, moiré technique.

Figure II-7: Electron micrographs of 40-nm wide Si structures, 0.7-µm deep on a 0.5 µm pitch formed by interferometric lithography and KOH etching of <110> Si. The vertical walls are Si <111> planes.

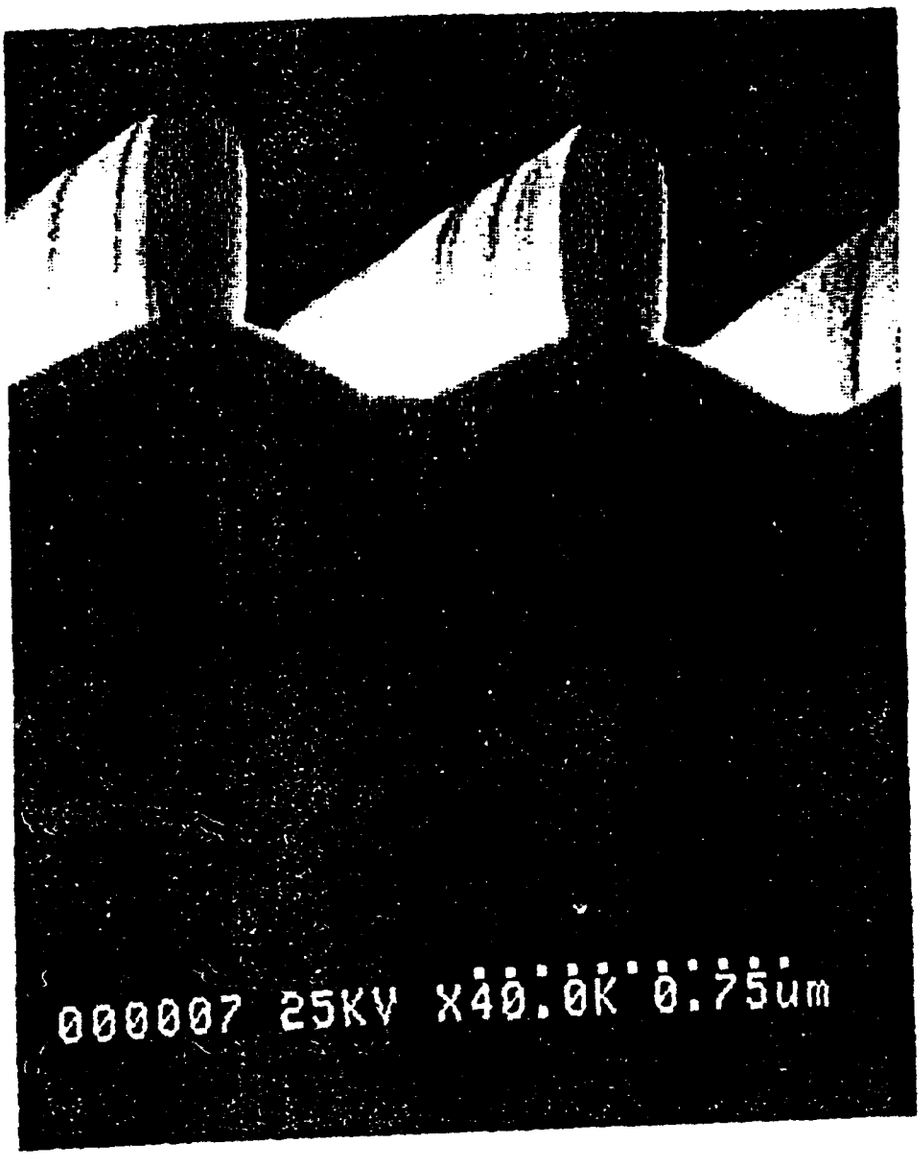

Figure II-8: Electron micrographs of 150-nm wide Si lines that have been thermally oxidized to a depth of ~70 nm. Note the darker Si structure in the center of each oxidized line.

This interferometric lithography process shows great promise for a number of important applications. Conventional imaging lithography is now being used for ~0.5-μm critical dimension (CD) structures in advanced development laboratories. Using phase-shift mask techniques, estimates are that 0.2-μm CDs will be achieved on a manufacturing scale within the decade. The present results demonstrate 0.01-μm CDs - and further extension to shorter wavelength optical sources is straightforward. It will be important to increase the flexibility of this process to more complex structures if it is to have a significant range of application.

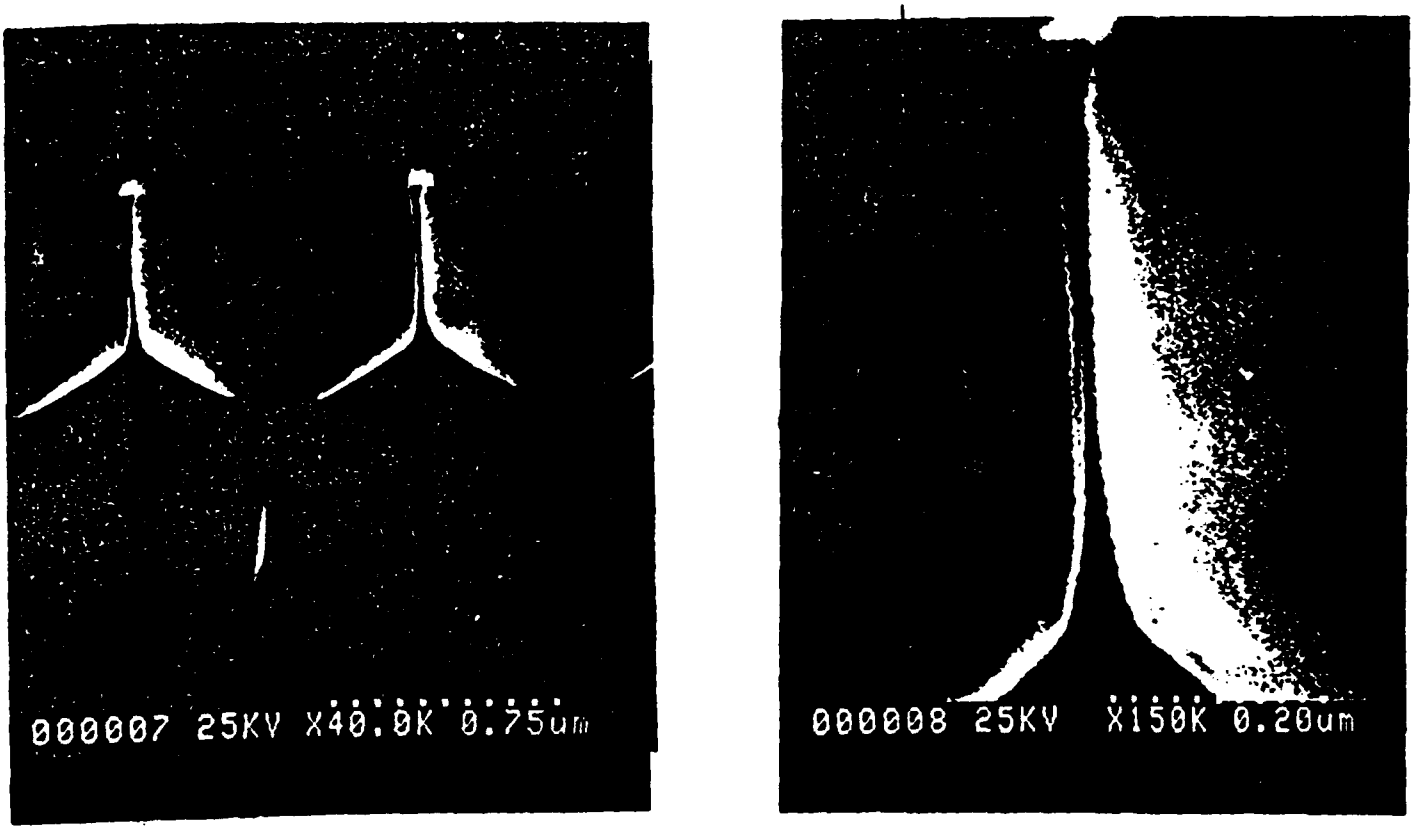

Figure II-9: Electron micrographs of the sample of Fig. II-8 after chemical removal of the SiO_2. The minimum dimension of the Si is only 10 nm!

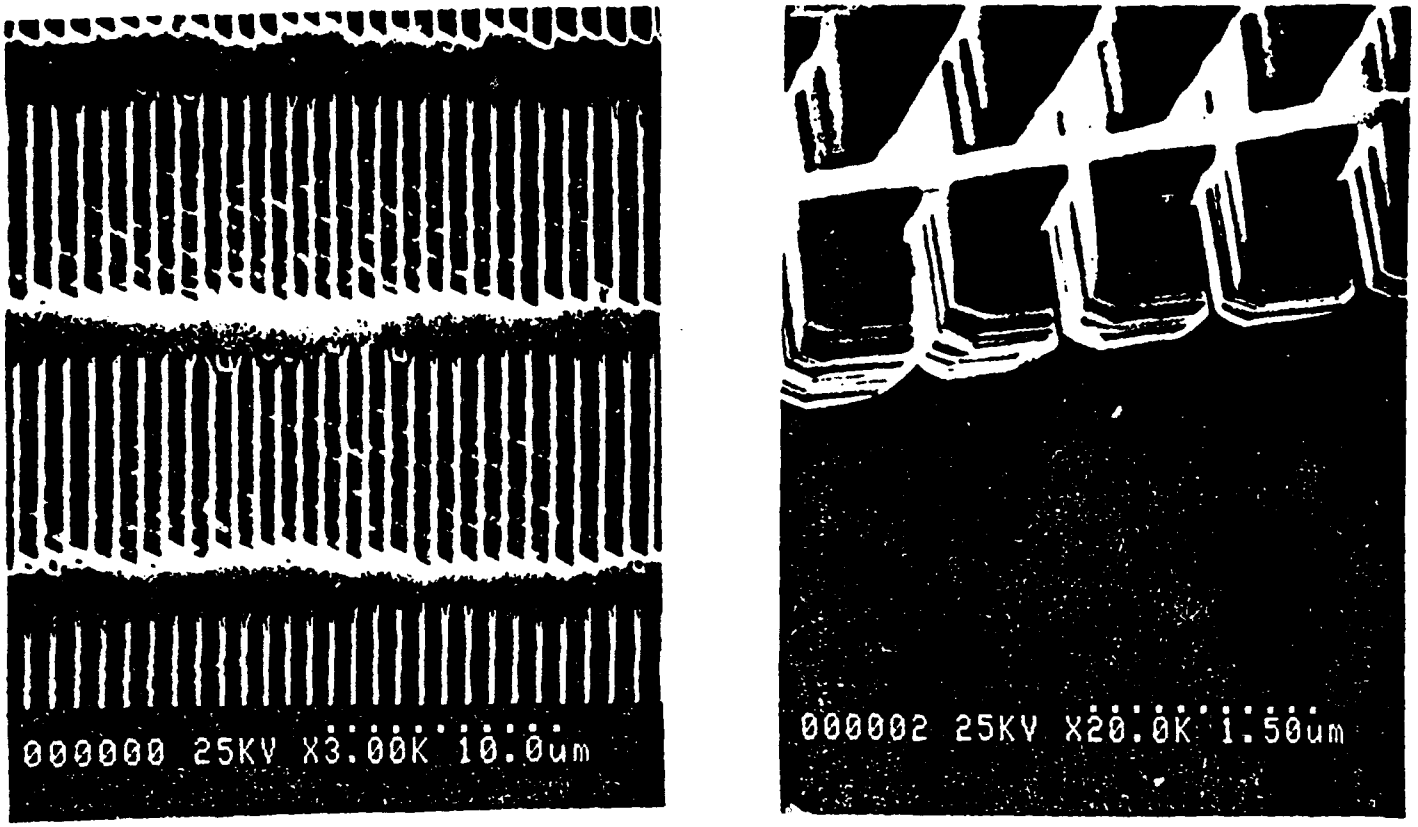

Figure II-10: Electron micrographs of a pattern with 50-nm wide lines etched into <110> Si connected in parallel to ~ 1-μm "bussbars" every 12 μm. This pattern was the result of a moiré double exposure.

II.3 DEVICES

II.3.1 Semiconductor Lasers

External cavity transverse mode filtering of high-power lasers and laser arrays

Since Sept. 1989, CHTM personnel have grown GaAs/AlGaAs and InGaAs/GaAlAs GRIN-SCH SQW laser wafers and fabricated several wide stripe laser designs emitting from 740 to 980 nm. Typical performance: J_{th} ~300 A cm^{-2}, η_{int} close to unity, power output better than 1 W/facet pulsed (1 μs, 1% duty cycle), multiple transverse mode with strong tendency to filamentation characteristic of wide stripe lasers.

Initial experiments (conducted jointly with PILOT personnel during 1990-91) on transverse mode filtering have been very successful: an anamorphic external cavity has been designed which is stable in the vertical direction and unstable in the horizontal (epitaxial) plane. With an AR-coated internal facet this allows

nearly diffraction-limited output powers of ~300 mW (without an HR-coated back facet) at up to $3I_{th}$.

This work is being carried out in collaboration with Chuck Moeller of the Phillips Laboratory and Greg Dente of GCD Associates.

Antiguiding wide stripe lasers

The success with external cavity transverse mode filtering has led to the theoretical analysis and design of wide stripe lasers with built-in index antiguides: these effectively comprise distributed unstable resonators on the laser chips. Two designs have been investigated: the buried-lenslet (BL) and buried continuous grade (BCG) structures.

The *buried lenslet device* embeds diverging lenticular pieces of low-index material close to the active stripe, creating a negative effective index profile in the lateral direction. Theoretical work is underway in collaboration with Dr. Alan H. Paxton of Mission Research Corp., Albuquerque. Several samples have been fabricated and tested, and the initial results are encouraging: the better (magnification ~4) devices showed single transverse mode, nearly diffraction limited outputs to $2I_{th}$ and 100 mW. Two-point transverse coherence sampling measurements have been performed at the Phillips Laboratory, showing ~90% coherence over more than 50 μm. A second set of samples is in process, covering higher magnifications (2-5). We are also studying the trade-off between magnification and laser threshold.

The *buried continuous grade device* also produces a negative effective index profile, this time by etching an appropriate continuous lateral profile in GaAs close to the active stripe, then overgrowing with AlGaAs. We have begun characterizing laser-assisted chemical etching processes for producing these continuous profiles: several sample wafers have been etched and studied by optical microscopy and surface profilometry. Fabrication of complete devices will proceed when this process has been adequately characterized.

This work is being carried out in close collaboration with Mike Allen and Craig Largent of the Phillips Laboratory, with Greg Dente and Mike Tilton of GCD Associates, and with Al Paxton of Mission Research Corporation.

Bow-tie waveguide laser structures

Another technique for producing mode discrimination is by differential radiation losses at some feature such as a diffraction coupling section or a cinched waveguide section. We are studying an Ortel structure and a new "bow-tie" structure. Wafers have been grown and design calculations are underway to make the first devices for testing at CHTM.

This work is being carried out as part of his research program by Karl Dahlhauser, a student at UNM as well as an officer at the Phillips Laboratory, in collaboration with Greg Dente and Mike Tilton of GCD Associates.

Modal characteristics of broad-area lasers

Recent progress in broad-area semiconductor lasers, with nearly 5 W of reported cw output power, demonstrates that they represent an attractive alternative to diode laser arrays for high-power applications. Understanding the lateral mode structure of these devices becomes therefore increasingly important. We have investigated experimentally SONY carrier-guided broad-area lasers with thin GaAs/AlGaAs double-heterostructure active regions. These devices are known to operate in a superposition of many lateral modes with complicated near-field patterns and broad double-lobe far fields. However, our observations of near- and far-field patterns indicate that much simpler modal configurations can exist near threshold. For a 50-μm wide device at room temperature (threshold current I_{th} = 119 mA), the near field evolves from three peaks at 121 mA, four at 131 mA, and so on, which corresponds to excitation of a combination of first three, four, *etc.* lateral modes. Combination of two lowest-order modes was observed at 5°C for pumping level of 120 mA (I_{th} = 107 mA). Because of the very small modal gain differences, no single lateral mode can be observed alone. Similar measurements performed on a 200-μm wide device revealed four stable peaks from very low current level (< 5 mA) up to the threshold. We have interpreted these measurements assuming weighted combinations of individual modes, yielding a basis of unperturbed broad-area modes important for studies of perturbed systems, such as thermal effects and spatial redistribution of carriers in high-power broad-area lasers and carrier-guided arrays.

Side-Mode Injection Locking of Semiconductor Lasers

There has been a growing interest recently in application of injection-locking techniques to semiconductor lasers. A primary motivation for these studies is the prospect for application of injection-locked lasers in coherent optical communication systems. The performance of such systems is greatly influenced by noise characteristics of the light source. We have conducted the first multimode numerical studies of field-noise spectra in injection-locked semiconductor lasers. Field-noise spectra are important since they carry direct information about linewidth and lineshape. In the simulations, we consider InGaAsP/InP index-guided master and slave lasers emitting at ~1.54 μm. The master oscillator wavelength is adjusted to match various modes of the slave laser. First, stationary solutions of the multimode rate equations without any noise terms are found for both the master and slave oscillators. These solutions are then used as initial conditions in simulations of temporal evolution with Langevin noise terms included. The temporal behavior of the master laser is found first to provide an injected signal with a noise component. In addition to the spontaneous emission noise and

electron population fluctuations, the injected signal also contains partition noise. The multimode stochastic rate equations with external injection terms are then solved for the slave laser. This allows us to investigate side-mode injection locking and the competition between the target mode and the dominant free-running mode. The field-noise spectra are obtained from the time-dependent solution using a fast Fourier transform algorithm. The stable locking range is predicted to increase with the detuning from the gain peak. This implies that better locking and eased operational tolerances can be expected with side-mode injection. This prediction is confirmed by numerical simulation of noise spectra with different target modes. While the noise spectra for the peak-mode injection indicate poor locking of the free-running dominant mode, the field-noise spectrum of the slave laser is almost a replica of the master oscillator when mode +3 (short-wavelength side of the gain spectrum) is chosen. Thus, by proper choice of the injected mode, it is possible to achieve nearly perfect locking. The results are consistent with our earlier calculations of frequency-noise spectra.

VERTICAL-CAVITY SURFACE-EMITTING LASERS

Optical pumping of low-threshold VCSELs

During the last three years, enormous strides have been made in VCSEL science and technology. Our invention and refinement of the resonant periodic gain (RPG) medium has been critical, enabling CW operation for the first time. We have also been innovative in applying a now-standard VCSEL technology: high-reflectivity (>99%) epitaxial mirror growth and design. Our optical pumping studies have produced single transverse mode operation up to ~15 mW from a 8-μm diameter spot, with a threshold of ~10 mW of absorbed power at 750 nm. Because of these modest power requirements, VCSELs pumped by conventional edge-emitting diode lasers have been developed, with pump-limited power outputs up to 100 mW quasi-CW; VCSEL outputs are single mode at low powers (<10 mW) with spectral widths of ~0.02 nm. The diode-pumped VCSELs have been modulated at gigahertz rates by applying the modulating waveform directly to the pump laser.

Picosecond optical pulses from VCSELs have been generated and characterized by optical pumping with picosecond dye-laser pulses. The output pulseshape was obtained from the cross-correlation of pump and signal sources. The dependence of VCSEL laser pulsewidth and pump-signal delay are in good agreement with a simple rate equation model of the pulse formation. A cavity lifetime of 8.3 ps, compared with a gain medium transit time of ~0.1 ps is found for these very high-Q cavities. These measurements have been extended to double-pulse excitation to investigate the potential of these devices for very high data-rate communications applications. The output pulses are resolvable for input delays as short as 15 ps.

High-power, large-area optical pumping of VCSELs

Using high-power dye lasers, we have investigated power scaling properties of the optically pumped RPG-VCSEL, investigating the results of pumping spots from 10 μm to several mm in diameter. Generally, the threshold power per unit area did not increase, but there were large variations in this threshold power density and in the external quantum efficiency due to variations over the wafer surfaces. Using a single-shot flash-pumped dye laser, we pumped areas up to 1 cm^2, achieving pulse energies greater than 20 mJ for 500 ns (duration limited by pump laser), for peak powers in excess of 40 kW. The spectral output was very broad (envelope widths ~1 nm) and the optical power conversion efficiency was in the range 20-35%. Future efforts will emphasize medium-power (multi-watt) diode-pumped compact VCSELs and transverse mode filtering for best spatial coherence. We will apply the techniques (external cavities, antiguides) learned using edge-emitters to enhance the coherence properties of these high-power VCSELs.

This work is being carried out in collaboration with Cheryl White and Al Paxton of Mission Research Corporation.

Distributed-feedback Resonant-Periodic-Gain Surface-Emitting Lasers

The dramatic progress in vertical-cavity surface-emitting lasers over the last two years has resulted in a variety of novel device structures. Recent development efforts have concentrated on reducing the lasing threshold and/or increasing the maximum output power. A significant new concept, allowing to achieve gain enhancement in the vertical direction, was replacement of the bulk active region with narrow (single- or multiple-quantum-well) layers in a carefully designed Bragg resonator such that the positions of the active layers coincide with antinodes of the laser radiation at a designed wavelength of operation. VCSELs with a single active region satisfying this resonant condition are often called microlasers. A simple extension of the microlaser concept leads to introduction of distributed-Bragg-reflector resonant-periodic-gain (DBR-RPG) lasers, in which multiple active regions are separated by half-wave spacers. The most recent advance in RPG laser structures, proposed and demonstraed at UNM, is a distributed-feedback resonant-periodic-gain (DFB-RPG) VCSEL, where an RPG active region is intercalated with the multilayer high reflectors (MHRs). This design, shown schematically in Figure II-11, eliminates the need for end reflectors and reduces the total thickness of the device, while retaining all of the characteristic features of the RPG medium. Our first DFB-RPG VCSEL GaAs/AlGaAs/AlAs laser has been fabricated by MOCVD. The device consists of a stack of 10-nm thick GaAs single quantum wells separated by half-wave AlAs/$Al_{0.15}Ga_{0.85}As$ spacers. The whole structure contains 42.5 periods, of which 24 are at the GaAs substrate side and 18.5 at the top. The output light is collected through the top reflector. The total thickness of the DFB-RPG structure is ~5.5 μm. For the sake of comparison, a DBR-RPG laser with the same cumulative active medium thickness and MHR reflectivities would be almost two

times thicker (~10.5 μm). A direct consequence of shorter cavity length is increased longitudinal mode spacing. Compared to an equivalent DBR-RPG device, a remarkable difference between the two structures is the absence of any side modes within the entire high-reflectivity band of the DFB-RPG laser. The as-grown wafers were optically pumped using the 740-nm output of an Ar-ion-pumped dye laser, with the pumping beam diameter of 10 μm. The cw output power of 7 mW (without heat sinking), see Figure II-12, is considerably higher than that obtainable from single-quantum-well microlasers and is comparable to that of DBR-RPG devices. The output power density was 4.5 MW/cm^2, the highest ever reported for any semiconductor laser.

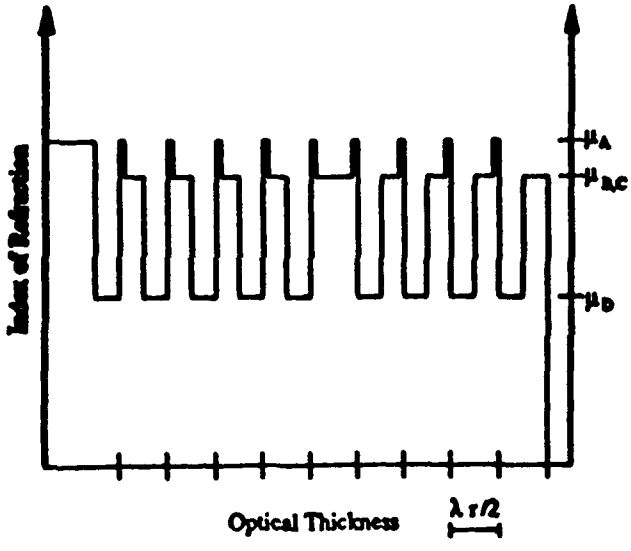

Figure II-11: Refractive index profile of DFB-RPG structure showing GaAs quantum well gain regions intercalated with the λ/4 reflector stack. The number of periods is reduced for clarity.

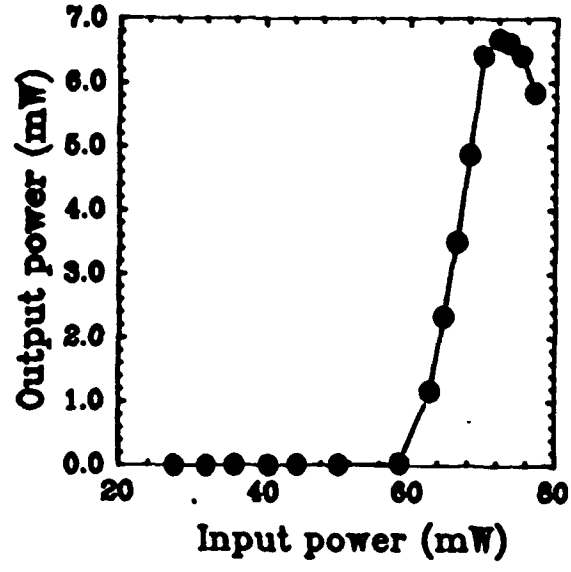

Figure II-12: Typical input/output curve for room temperature cw optical pumping at 740 nm.

Thermal properties of etched-well surface-emitting diode lasers

Vertical-cavity surface-emitting lasers are generating considerable interest due to their potential for integration into 2-D arrays. Efficient heat dissipation, along with ultra-low threshold, is critical for applications such as optical interconnects where massive integration is required. Yet, thermal effects in VCSELs received very little attention so far. The only published analysis is based

on assumptions of homogeneous heat generation in the active region and one-dimensional vertical heat flow between the active region and a heat sink. These approximations lead to overestimated heating effects. In our approach, we use analytical solutions for current spreading derived for Burrus-type LEDs. The heat spreading problem is solved analytically using an equivalent electrical circuit technique. Thermal-electrical self-consistency is achieved by an iterative process. Our model provides a useful tool for the design of devices operating cw at room-temperature.

Thermal waveguiding in etched-well surface-emitting diode lasers

Inherent single-longitudinal-mode behavior and narrow non-astigmatic output beams are among attractive features of vertical-cavity surface-emitting lasers. It is, however, more difficult to control their transverse mode structure, which can involve many high-order modes. Transverse-mode behavior of VCSELs is very poorly understood, mainly because little is known about transverse profiles of complex permittivity in these devices. We have carried out the first comprehensive study of factors that determine the waveguiding properties of VCSELs. The analysis has been performed using a new self-consistent thermal-electrical model of VCSELs, featuring a realistic distribution of heat sources and two-dimensional current- and heat-flux spreading. The device under consideration is a typical double-heterojunction GaAs/AlGaAs etched-well VCSEL with bulk active region. The laser is assumed to have a 2.5-μm thick active region, 5.5-μm long cavity, and a circular window of 10-μm diameter etched through the substrate. We have examined distributions of injected current density and temperature profiles, which in turn determine the active-region permittivity profile. Strong nonuniformity of current density indicates that etched-well VCSELs may suffer from poor matching between the optical field of fundamental transverse mode, which has an intensity peak at $r = 0$, and the optical gain, which with improper design may be maximum at the edges of the active region. Inhomogeneity of current density can be softened by increasing the donor concentration in the *N*-AlGaAs cladding layer. This is due to reduction of *N*-AlGaAs sheet resistance resulting in deeper penetration of carriers towards the device axis. In the limit of zero sheet resistance, a perfectly uniform distribution would be obtained for the entire active region. Hence, inhomogeneity of carrier-induced refractive index perturbation can be controlled by selecting proper *N*-AlGaAs doping level. Current density distribution also influences temperature profiles via Joule heating. While the average active-region temperature remains nearly constant with varying *N*-AlGaAs doping level, the actual temperature profiles do change, offering means to control the nature of thermal waveguiding from antiguiding to thermal focusing. Depending on specific application, either of these effects may be of interest. The ability to engineer thermal waveguiding in etched-well VCSELs by rather simple technological process is a unique feature of these devices.

DIODE LASER ARRAYS

See also the work on leaky-mode diode laser arrays reported in the MOCVD section.

Measurements and interpretation of near-field phase fronts by shearing interferometry

We have proposed and demonstrated a reliable technique for measuring near-field phase fronts of phased-array semiconductor lasers. Laterally sheared interferograms are generated in a Sagnac-type ring interferometer with zero optical path difference between two beams, eliminating problems due to equal optical path requirements in other systems. A Fourier transform method is used to extract phase difference information from the nonuniformly illuminated interferograms; phase discontinuities between adjacent stripes of carrier-guided laser arrays are observed. The technique is suitable for high-power diode lasers with their short-coherence lengths. Reconstructed lateral phase fronts provide information about the modal composition of the array and agree well with measured far-field patterns.

Coupling of multistripe arrays to external resonators with spatial filters

A high-power (68 mW with output facet reflectivity of 90% which corresponds to estimated 266 mW with output facet reflectivity of 30%), on-axis, single-lobe far field with nearly diffraction-limited (0.64°) full width at half maximum has been achieved from a ten-stripe carrier-guided anti-reflection-coated laser array by coupling to an external cavity with a spatial filter. The in-phase operation has been verified by wavefront measurements using shearing interferometry. The power penalty for inserting a spatial filter in external cavity is less than ~20%. This technique provides a very attractive approach to achieving inexpensive high-power fundamental-transverse-mode laser sources.

Theory of diffraction-coupled arrays

Diffraction-coupled arrays, where in addition to usual evanescent coupling of individual waveguide modes further interaction is provided by diffraction in a laterally unguided section, were proposed for operating in a stable, single far-field lobe. The performance of these arrays is, however, very sensitive to the device design, since phase relations between adjacent waveguides are critical for supermode selection. We have developed a new model of diffraction-coupled arrays based on coupled-mode theory. The eigenmodes of the waveguide section (supermodes) are calculated using the improved coupled-mode theory which takes into account nonorthogonality of the basis of unperturbed waveguide modes and allows for coupling between all of these modes. The eigenmodes of the system are determined by mixing of the supermodes in the diffraction region. The supermode mixing coefficients are obtained by evaluating the reflected image at the interface between the guided and unguided sections of the device using the Huygens-Fresnel

diffraction integral. We have applied the new model to 10-stripe GaAs/AlGaAs laser arrays with fixed center-to-center spacing of 10-μm and various stripe widths ranging from 6 μm to 3 μm. A simple-minded approach, in which beam-optics considerations are used to phase-match the nearest neighbors, starts to fail when the length of the unguided section is increased beyond 30 μm. This is mainly due to an increasing role of diffraction from further neighbors. In addition, the supermode mixing coefficients are very sensitive to details of the waveguiding channel design. For example, changing the channel width from 6 to 4 μm results in significant side-lobes in the far-field pattern. Also, the unguided section length of ~10 μm has to be controlled to within a fraction of micrometer in order to achieve single-lobed far fields. Our results show that the improved coupled-mode theory, with accurate treatment of diffraction in the unguided section, provides a valuable insight into the mechanisms governing the performance of diffraction-coupled arrays and allows an understanding of the complex interplay of evanescent coupling, diffraction coupling, and beam optics imaging occurring in these devices.

Broad-area mode-coupling model for carrier-guided diode laser arrays

The supermode theory often adopted to explain modal behavior of phased array lasers is suitable only for index-guided arrays, since it requires a basis of individual waveguide modes. For carrier-guided arrays, with no built-in lateral variation of refractive index, such approach fails to predict correctly the number of system modes and their relative gains. It is more appropriate to treat the carrier-guided array as a perturbed broad-area laser, since the number of lateral modes is not limited in this case by the number of array elements. Recently, a simple model of carrier-guided arrays was proposed by Verdiell and Frey [19xx], based on the standard perturbation theory. It assumes an infinite loss outside the active region and ignores differences between modal gains of all the unperturbed (broad area) modes, claiming that these simplifications would not affect the results significantly. We have shown that either of these assumptions has important consequences on the calculated modal gains for the array modes. Rather than using the perturbation theory, we have followed the coupled mode formulation, but with a basis of broad-area modes instead of individual waveguide modes. An active broad-area waveguide is considered, with the gain-index coupling as well as spatially averaged temperature effects included. The perturbation due to array structure is assumed in form a raised sinusoidal modulation of permittivity, with gain maxima at stripe centers. A smooth half-period cosine profile of temperature is also included in the perturbation. A comparison of the present theory with earlier simplified perturbation analysis corresponding to a limit of very high loss and constant reveals that the previous treatment is unreliable in predicting the modal gains of high-order array modes (mode number larger than the number of emitters). It should be emphasized that these high-order modes usually dominate in carrier-guided arrays, hence precise knowledge of their modal gains is very important in considerations of mode ordering and mode suppression schemes. Our results reveal

that earlier agreement between the simplified model and experimental observations was fortuitous. On the other hand, broad-area coupled-mode theory can contribute to improved understanding of array laser behavior and constitutes an important design and interpretation tool.

Thermal focusing effects in carrier-guided diode laser arrays

We have examined in detail the role of active region heating in carrier-guided diode laser arrays, showing that thermal effects are important for the array mode selection. The specific device type considered was a uniform 10-stripe GaAs/AlGaAs carrier-guided array. The array is regarded as a perturbed broad-area laser whose modes are coupled via complex-permittivity perturbations induced by heating and injected carriers. Array modes are determined using the coupled-mode theory. The thermal perturbation is taken as a half-period cosine with center value of ΔT, vanishing at the lateral claddings. When heating-induced waveguide nonuniformity is small, the dominant array mode is $m = 10$. Calculated temperature dependence of modal gain spectra reveals that with raising temperature, the highest-gain mode shifts gradually from $m = 10$ to $m = 13$. Thus, thermal focusing results in sequential excitation of high-order modes with increasing pumping current. Calculated near- and far-field patterns for $\Delta T = 4°C$ are in excellent agreement with injection-seeding experiments, while numerical simulations with $\Delta T = 10°C$ give somewhat narrower near fields for $m > 10$. This indicates that the active-region heating may not be as severe as previously thought. Sensitivity of the high-order modes to thermal focusing can be used to establish the actual temperature increase with good accuracy.

Theory of nonabsorbing-mirror diode laser arrays

Nonabsorbing mirror (NAM) GaAs/AlGaAs arrays have been demonstrated by Spectra-Diode researchers to deliver thermally limited cw output powers as high as 2.4 W from a 100-μm aperture. Typically, these devices operate in high-order array modes with a double-lobed far field. We have shown that with careful design, the NAM section can be utilized to favor single far-field lobe operation. We treat the NAM array as a composite cavity consisting of a waveguide region in which parallel single-mode waveguides are coupled through evanescent fields of guided modes, and a uniform NAM section which provides further coupling between individual waveguide modes via diffraction. The eigenmodes of the waveguide section (supermodes) are calculated using the improved coupled-mode theory. The supermode mixing coefficients, determining the eigenmodes of the composite cavity, are obtained by evaluating the reflected image at the interface between the waveguiding and uniform sections of the device using three-dimensional diffraction integral. If the phase difference between light returning from the NAM section and injected back into any particular waveguide and its nearest neighbor is an integer multiple of 2π, the in-phase supermode is reinforced. On the other hand, small variation in the NAM-section length and/or the waveguide spacing is sufficient to

change the far-field dramatically. The performance of NAM arrays is, therefore, very sensitive to details of the waveguide structure.

OPTICAL SWITCHING

VCSEL-based bistable optical switches

Theoretical studies have indicated that VCSEL-like structures will permit absorptive bistable optical switching at thresholds a factor of four lower than conventional MQW etalons. The proposed mechanism is saturation (by carrier screening) of the excitonic absorption, and the nonlinear absorption will be optimized in the same way as the gain in a RPG-VCSEL, by maximizing the spatial overlap of the antinodes of the optical field within the etalon with the quantum wells. Experiments have been performed to determine the excitonic resonance wavelengths, and these data togther with a model for the quantum well absorption spectrum have been used to design a wafer for MBE growth.

In future studies of this phenomenon, arrays of bistable switches will be grown and characterized, and applied to problems requiring fast (GHz) threshold or pulse coincidence detection. A prime example of such a problem is time-division demultiplexing of data or sensor channels.

Mode switching and beam scanning in twin-stripe lasers and laser amplifiers

The overall concept of mode switching is to allow the laser output to be modified (switched, scanned or modulated) without having to switch the laser on or off, requiring modulation of the carrier density. This is a significant advantage, because changes in carrier density are limited dynamically by the carrier lifetime, which is typically a few nanoseconds.

In the twin stripe laser, theory shows that linear beam position scanning or bistable mode switching is possible, by adjusting the injection currents into the stripes, by increasing the intensity of a beam coupled into one stripe, or by injecting an optical trigger pulse. An initial batch of twin stripe lasers has been fabricated and is undergoing initial testing.

Mode switching in grating-coupled surface-emitters

Theoretical studies have shown the existence of spatially bistable and separable modes from grating-coupled surface-emitting (GSE) lasers. These modes offer the prospect of fast switching transitions in these devices, which are extremely difficult to modulate or switch by conventional means owing to their very long photon lifetimes. Future studies will concentrate on designing and testing GSE structures which will oscillate preferentially in such asymmetric modes as opposed to the more usual symmetric spatial output patterns.

NONLINEAR DYNAMICS OF SEMICONDUCTOR LASERS

Multi-gigahertz modulation of semiconductor lasers and laser amplifiers

Theoretical and experimental studies of semiconductor lasers modulated at depths approaching 100% at gigahertz rates have been carried out, showing a tendency to chaotic oscillations via period doubling. It was determined that these tendencies are most pronounced at specific irrational ratios between the modulation and relaxation oscillation frequencies, but this effect should not be a problem in conventional optical communication and sensing systems which use lower modulation depths.

This work is in collaboration with Sylvia Mancha and Dave Gallant of the Phillips Laboratory and Greg Dente of GCD Associates.

Dynamics of external cavity semiconductor lasers and laser arrays

Extensive theoretical and experimental research has been done on the dynamics of external cavity lasers at feedback levels ranging from -80 to -10 dB of the emitted power. The problem of coherence collapse, the catastrophic spectral broadening within a single diode mode which can be deleterious for communication or sensing systems, has been investigated in detail, demonstrating a quasiperiodic route to deterministic chaos in most circumstances and a period doubling route in certain special cases. In each case, there are clear self-pulsing precursors due to feedback-induced undamping of the relaxation oscillations in the laser diode.

At higher feedback levels, mode mixing effects in external cavity lasers with small tilt misalignments, or in double external cavity lasers, have been studied experimentally and theoretically. Several novel phenomena have been observed and explained, including low-frequency self-pulsations, spectral mode splitting, subharmonic bifurcations leading to chaos, and sudden-onset transitions to chaotic or multimode states. Apart from the fundamental significance of these studies to the science of nonlinear dynamics, there are also practical implications for designing laser-based systems in which optical feedback is often inevitable. Studies of this kind are especially important where high analog fidelity or low digital error rates are required, such as precision control, analog high-speed transmission or data transmission within and between computers.

Dave Gallant and Dave Bossert of the Phillips Laboratory and Greg Dente of GCD Associates have collaborated on this work.

EXTERNAL CAVITY SEMICONDUCTOR LASERS: STABILIZATION, METROLOGY

Longitudinal mode stabilization, linewidth narrowing

The slow phase diffusion processes which determine the laser linewidth can be filtered effectively by a combination of drive current and temperature stabilization in concert with external optical feedback from either a simple external reflector (mirror or grating) or a composite high-Q external resonator (etalon or cell containing a resonant medium). Using various combinations of these procedures, we have obtained ~10 kHz linewidths from semiconductor lasers at milliwatt power levels, with tuning ranges of ~10 nm centered at the gain peak. These external cavity lasers are potentially useful for coherent optical communication, spectroscopy or precision Doppler velocimetry (see below).

High power, tunable external cavity lasers

By careful AR coating and placement of a wide stripe laser diode in a dispersive external cavity (e.g. one containing a diffraction grating), we have obtained pulsed power outputs of up to 600 mW (1 μs, 10 kHz) in a single longitudinal diode mode whose width has been tentatively measured at 0.05 nm (instrument-limited). The tuning range was better than 30 nm, and the device was extremely stable with respect to changes in the drive current and ambient temperature.

Double external cavity laser studies

Double external cavity lasers have been studied experimentally and theoretically for a variety of purposes: (1) to determine the stability conditions for a single external cavity laser with respect to additional optical feedback, (2) to investigate the feasibility of using compact external cavity arrangements for effective mode stabilization and linewidth narrowing, and (3) to understand their nonlinear dynamical properties.

(1) External cavity lasers have feedback sensitivities comparable to those of isolated lasers, but it is possible to minimize this sensitivity by careful choice of the mirror reflectivity, internal facet reflectivity and cavity length. This information will be useful in designing stable external cavity lasers for real systems in which feedback is unavoidable.

(2) A compact double external cavity laser was designed, constructed and successfully tested. While a short external cavity provides effective longitudinal mode selection, it does not provide effective linewidth narrowing; on the other hand, a long external cavity will narrow the linewidth of a single mode but will not select that mode very strongly. As an alternative to the grating external cavity (whose coupling strength is much less than a mirror cavity), we first built a combination

short (<1 mm)-long (10 cm) cavity which provided ~100 kHz linewidth in a single longitudinal mode. To make this structure more compact, we used a combination of two short (millimeter) cavities with a small phase offset; the vernier principle of combined external cavities made this equivalent to a short-long combination, the long external cavity length being the least common integer multiple of the two actual cavity lengths.

Doppler velocimetry using laser diodes

Using diffuse reflections from a moving object (a piece of paper on a turntable), Doppler backscatter modulation of a laser diode has been demonstrated theoretically and experimentally. The resulting noise satellite peak has been detected using a spectrum analyzer, and velocities of ~1-10 m s^{-1} have been measured. Data have been read out using both an external detector to monitor the laser output, and using direct monitoring of the voltage across the laser diode itself. A compact screened housing has been built for the laser Doppler velocimeter, and sensitivity measurements indicate that effective reflections as small as -65 dB can be detected. A compact readout system using a dedicated mixer (instead of the bulky spectrum analyzer) has been designed and is under construction, and we are planning experiments to use the device for measuring airflow velocities.

II.4 DEVICE INTEGRATION

Again, the difficulty in separating materials growth and processing, device synthesis and integration is apparent in this section. Much of the work on electrical pumping of VCSEL lasers as well as on their integration with phototransistors and photothyristors is collected here with an emphasis on use in optical switching and interconnection applications.

Vertical-Injection Surface-Emitting Lasers:

Vertical-cavity surface-emitting lasers (VCSELs) are the building blocks of multi-stage, two-dimensional optical networks, with potential applications in photonic switching, optical computing, and optical interconnection architectures. Not only are they useful as individually-addressable source arrays, they are also the major component in many optical switches and logic modules. To perform their multifarious optical functions, the VCSEL-based components must be cascadable, integrable, and be capable of direct parallel access. Their integrability into dense, two-dimensional functional arrays is essential to the realization of compact optical networks, provided that the thermal dissipation can be reduced to a tractable level. This presupposes the availability of high-performance VCSELs with low operating voltage and current, low series resistance, and high overall power efficiency. Most of the previous achievements in VCSEL technology are deficient in these areas, due in large measure to their high series resistance. We have made significant

improvements by using a new VCSEL structure, which has set new benchmarks in electrical performance characteristics.

The series resistance of a VCSEL derives principally from: the contact resistance, the spreading resistance, and the impedance of the heterobarriers (mirror layer interfaces) to carrier transport. We have successfully reduced all three with a novel VCSEL design. Our ability to continuously grade all the heterointerfaces by MOCVD growth, and thus minimize carrier trapping and scattering, was particularly instrumental in reducing the series resistance of the VCSEL to a heretofore unheard of 20-Ω level. The threshold voltage was also reduced to the 2.5-3.0-V range, which is close to the values required for conventional 5 V laser drivers. VCSELs with a threshold density as low as 770 A/cm^2 have been demonstrated, again close to the lowest value ever achieved by any type of surface-emitting laser. The cw, room-temperature lasing characteristics are comparable to those of state-of-the-art MBE results, with optical outputs up to 2 mW, differential quantum efficiency as high as 80%, and power dissipation as low as 12 mW per VCSEL. The epilayer structure and the VCSEL device characteristics are summarized in Figure II-13.

Since the VCSELs are processed as a two-dimensional array, their individual addressability is readily demonstrable. Their packing density, however, has yet to be determined. The uniformity of the MOCVD-grown VCSELs is presently not optimal, with thickness variations of ±2% across a 2-inch wafer producing a comparable lasing wavelength dispersion (±20 nm). On the one hand, this is a shortcoming; but on the other hand, it is also a useful characteristic that can be exploited to good purpose in an integrated, polychromatic source array for wavelength-division-multiplexing system applications.

Optical Switches And Logic Gates Based On VCSELs:

VCSEL strengths (compared to surface-emitting LEDs, for example) include their superior power efficiency, low beam divergence, good modal characteristics, high optical contrast (between lasing and spontaneous emission levels), high output power, and inherent thresholding behavior. These qualities are well-suited for a two-dimensional array of cascadable, optical threshold switches. An efficient optical switch should exhibit high optical gain and low switching energy. Thus low input optical power is used to switch on a more powerful laser source without any electronic intermediary. The integration of a heterojunction phototransistor (HPT) with a VCSEL satisfies all of these requirements. A high gain HPT (β=500) can amplify the photocurrent induced by a relatively low input optical power (< 50 μW) to provide a collector current of several mA, which is sufficient to drive a well-designed VCSEL above its lasing threshold. Thus, with the VCSEL and HPT biased in series, a low optical input to the HPT can switch on the VCSEL from its quiescent (dark) state, characterized by weak spontaneous emission, to a large output power lasing state, thus achieving a significant optical gain. The lasing

threshold of the VCSEL provides a threshold for the optical switching characteristic.

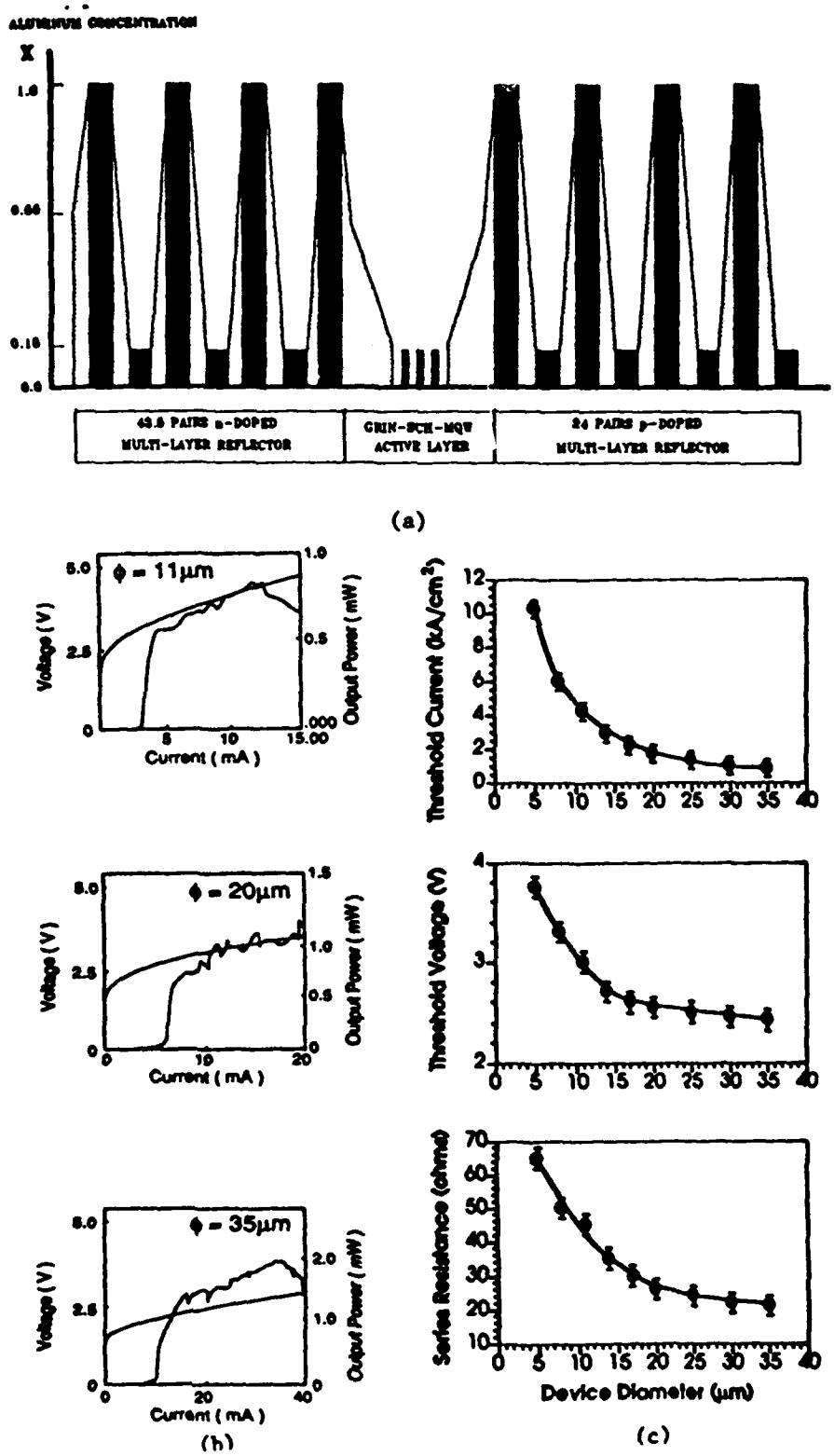

Figure II-13: Epilayer structure of graded-interface VCSEL. The LI and VI curves are shown for several device diameters. (c) summarizes the device performance as the active diameter is varied.

We have demonstrated optical switching (Figure II.14) with a HPT/VCSEL switch. The optical transfer characteristic shows an optical threshold of 120 μW and a maximum differential gain of 200. Since the cw output is 2.5 mW, an overall optical gain of 20 was achieved. The optical contrast is as high as 32 dB. The energy required to effect switching is about 5 pJ. These are by far the best VCSEL-based optical switching results ever reported.

Optical Logic Gates Based On HPT/VCSEL Switches:

These optical switches have also been used to successfully demonstrate various optical logic functions, such as AND, OR, and XOR (Figure II.15). The last gate is particularly important (and also the most difficult to achieve), since the XOR and AND gates are central to binary arithmetic operations. All the logic gates consist of simple combinations of HPTs as input channels and one VCSEL output port (2 for the XOR gate). In each case, the optical input levels determine whether they are individually or collectively sufficient to switch on the VCSEL in the case of AND and OR, and to switch off the VCSEL in the case of NAND or NOR. For the XOR gate, one of the two VCSEL outputs are turned on if and only if only one input is present. These have all been demonstrated experimentally, with good gain and contrast, as illustrated in Figure II.15. The gates are readily integrable into two-dimensional optical logic arrays providing the parallel processing of many different input optical channels. These results are the best experimental data on VCSEL-based optical logic operation to date. We have recently improved upon these results even further using monolithic integrated logic gates. Plans for a much higher level of functional integration have also been laid down in the form of a compact binary adder, which utilizes the XOR-gate and the AND-gate to simulate a multi-channel chip-level binary arithmetic logic unit.

Transverse-injection Multi-Quantum-Well Resonant-Periodic-Gain (MQW-RPG) VCSELs

The MQW-RPG VCSEL has demonstrated excellent lasing characteristics under optical pumping conditions. Although much of the early work on VCSELs had been on transverse-injection devices, efficient cw lasing at room temperature has been an elusive goal for these structures. Transverse-injection is appealing since it is particularly well-suited to the monolithic integration of VCSELs into arrays and other hybrid integrated circuits. The enhanced gain and high efficiency of an optically-pumped RPG laser suggest that an electrically-pump analog would be highly desirable. However, the large separation between quantum wells makes transverse injection imperative for these structures. Our efforts to demonstrate a transverse-injection RPG VCSEL has centered on two approaches, one based on the shallow diffusion of ohmic contacts into an etched-mesa sidewall, and the other based on ion-implantation of the contacts. Material-selective diffusion of the source material in the layers of the heterostructure at high temperatures has been a formidable obstacle to the formation of a p-n junction without incurring shunt

current paths. The latter significantly increased the threshold current for lasing and exacerbated the self-heating problem, thus making room-temperature operation difficult. Despite these difficulties, we were successful in demonstrating for the first time the pulsed operation of a five-quantum-well RPG-VCSEL at room-temperature (Fig. II-16). The threshold current is 45 mA (9 mA per well), which contains a large contribution from shunt currents. Further research is required to eliminate the shunt current paths in order to achieve cw operation.

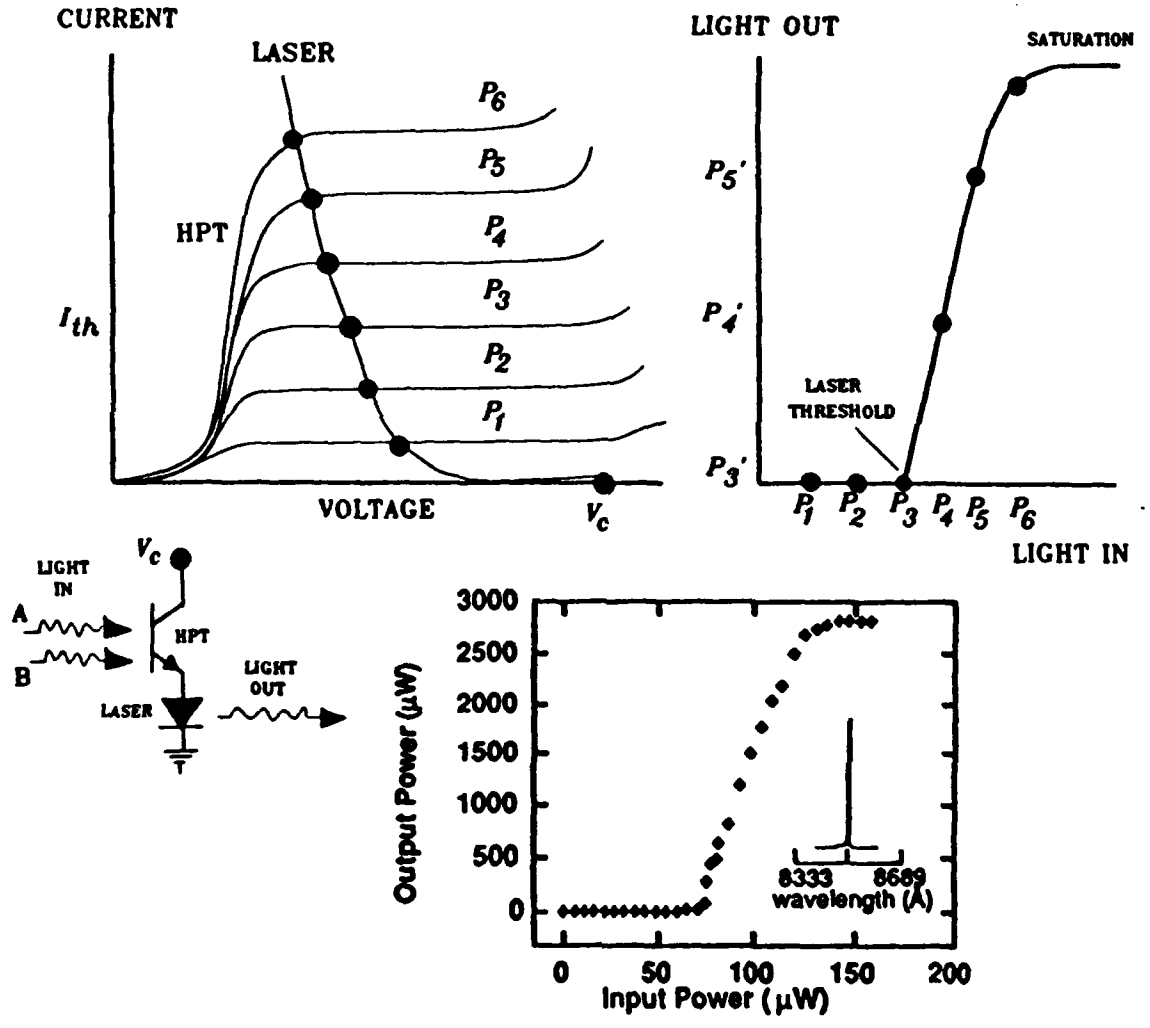

Figure II-14: Light-light characteristics of a HPT/VCSEL showing an optical gain of more than 20.

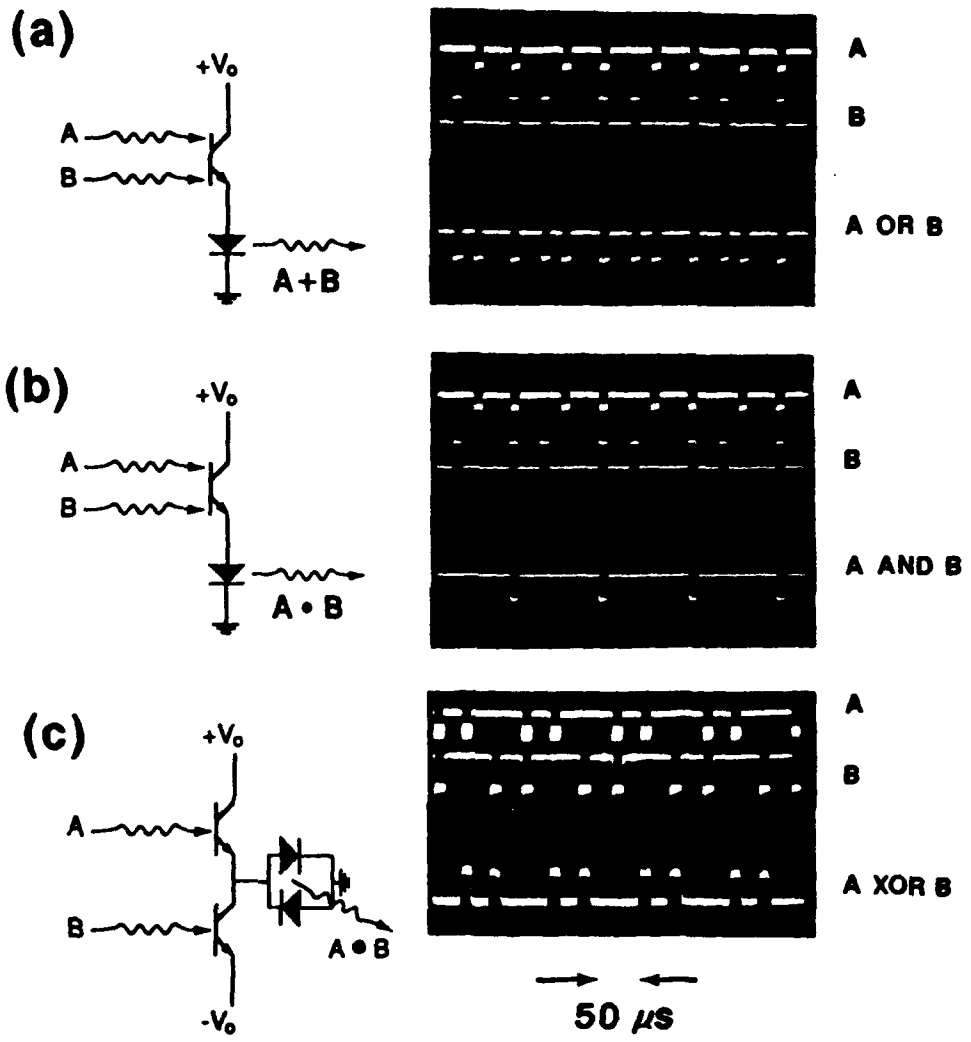

Figure II-15: Demonstration of logic functions with HPT/VCSEL circuits.

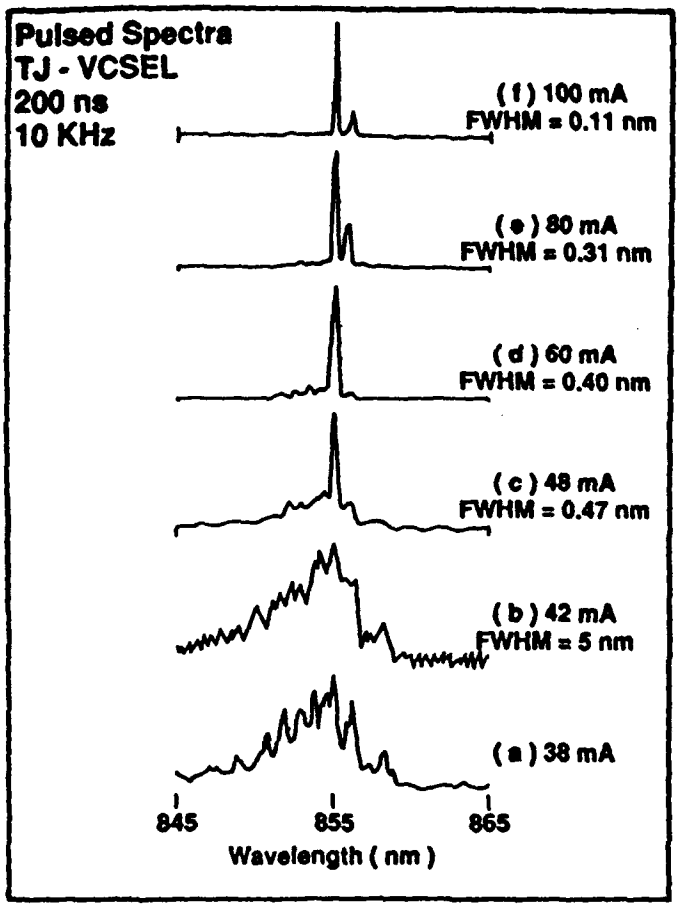

Pulsed Light - Current Characteristics of
Lateral Injection Vertical Cavity Surface - Emitting Lasers

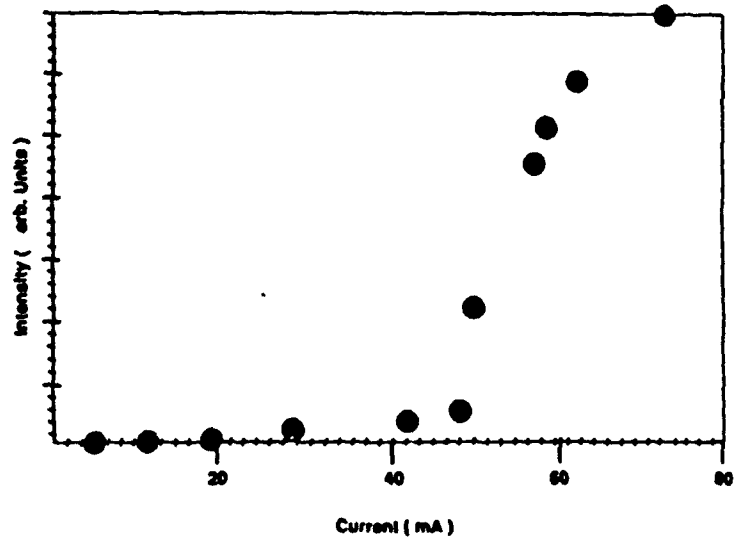

II.5 SPECTROSCOPY

A number of spectroscopic efforts in support of the materials, processing, device and integration goals of the AFOSR OERC are reviewed here.

GaAs/AlGaAs laser facet passivation for elevated catastrophic optical damage thresholds

In collaboration with the Phillips Laboratory's PILOT Program, we have treated and tested over 50 lasers grown at CHTM for catastrophic optical damage in pulsed (1 μs) operation. The passivation treatment consists simply of dipping the laser chips into an aqueous solution of a suitable sulfide (sodium or ammonium salts have been used) for a few minutes. Typically the damage threshold has increased by a factor of two, but there have been large variations between devices. The passivation is seen to wear off after 2-4 hours. Future studies will investigate the passivated surface chemistry and will involve vacuum overcoating with an impermeable dielectric film for longevity. In particular, facet etchback techniques and surface Raman spectroscopy will be employed. Previous Raman and photoluminescence studies carried out at CHTM have demonstrated a spectral signature, tentatively identified as amporphous-As, associated with the passivation.

Rob Racicot of the Phillips Laboratory is collaborating on this project.

Photoacoustic Spectroscopy of Weak Absorptions

The sensitivity of surface-photoacoustic-wave detection has been extended by several orders of magnitude to a surface specific absorbance of $\alpha l \sim 10^{-9}$ using narrow bandwidth interdigitated surface-acoustic wave detection and an optical irradiation pattern that provides a matched signal. Major advantages include narrow-bandwidth detection and an increased irradiated area that permits more optical energy on the sample. A rapid, nondestructive, reproducible liquid-bonding technique has been developed to permit extension of these measurements to a wide variety of substrates. This represents the highest sensitivity yet achieved for surface absorption measurements.

Spatially Resolved Confocal-Photoluminescence Spectroscopy

It is commonly thought that the spatial resolution of photoluminescence (PL) in semiconductors is limited by carrier diffusion lengths, and is thus less than that of a technique such as Raman scattering which is limited only by diffraction to lengths on the order of an optical wavelength. However, using confocal microscopy this need not be true. In confocal photoluminescence spectroscopy, the PL is imaged through a pinhole matched to the input pinhole that defines the laser optical pumping geometry. Only PL that originates within the illuminated volume

is allowed to reach the spectrometer and detector. By translating the detection pinhole, PL originating from sample volumes excited by diffusion can be observed. Figure II-16 shows the peak PL intensity observed from a single GaAs quantum well contrasted with the reflected/scattered 514.5-nm pump light. The much broader spatial scale of the PL directly displays the effects of transverse diffusion in the quantum well. These measurements are being extended to ultrafast time scales to directly measure carrier diffusion constants.

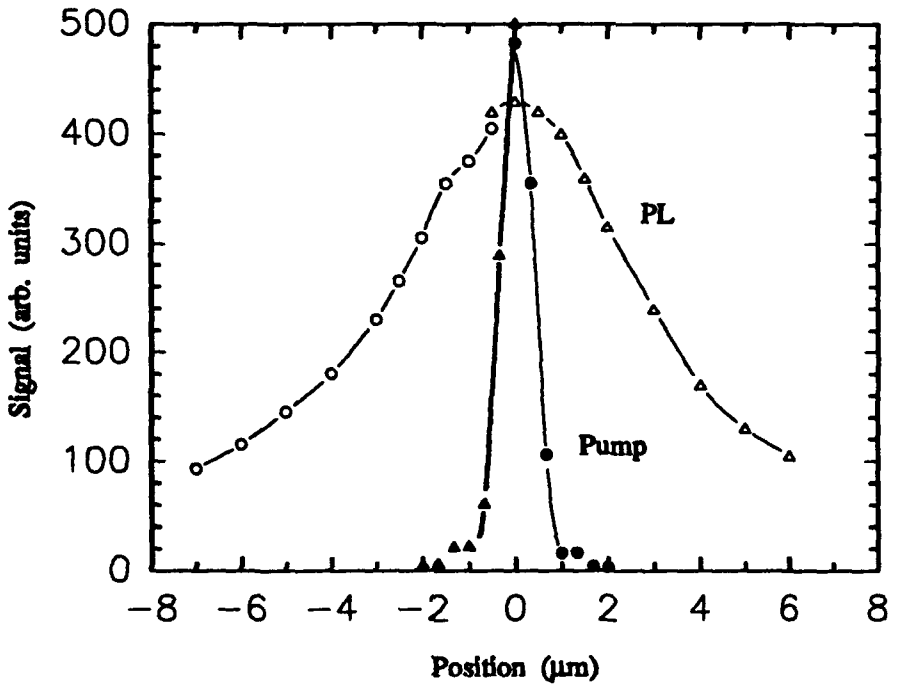

Fig. II-16: Spatial resolved photoluminescence (PL) from a GaAs quantum well structure obtained in a confocal microscopy arrangement. The x-axis is the position along the sample with the input pump light, obtained by scanning the confocal aperture in the collection optics, centered at x=0 with a width of ~ 1.5 μm. The PL trace clearly shows a much wider emission area as a result of carrier diffusion.

III. REFERENCES

D. Z. Anderson, V. Mizrahi and J. E. Sipe, Opt. Lett. **16**, 796 (1991).

E. H. Anderson, C. M. Hurwitz and H. I. Smith, *Holographic Lithography with Thick Photoresist*, Appl. Phys. Lett. **43**, 874-875 (1983).

M.-V. Bergot, M. C. Farries, L. Li, L. J. Poyntz-Wright, P. St. J. Russell, and A. Smithson, Opt. Lett. **13**, 592 (1988).

K. L. Brower, Phys. Rev. **B20**, 1799 (1979).

L. T. Canham, *Silicon Quantum Wire Array Fabrication by Electrochemical and Chemical Dissolution of Wafers*, Appl. Phys. Lett. **57**, 1046-1048 (1990).

S. W. Corzine, R. S. Geels, J. W. Scott, R.-H. Yan, and L. A. Coldren, *Design of Fabry-Perot Surface-Emitting Lasers with a Periodic Gain Structure*, IEEE J. Quantum Electron., **QE-25**, 1513-1524, (1989).

D. J. DiMaria in The Physics of SiO_2 and its Interfaces: Proceedings of the International Topical Conference, Yorktown Heights, NY March 1978, S. T. Pantelides, ed. (Pergamon Press, NY, 1978).

I. N. Duling, Electron. Lett. **27**, 544 (1991).

M. E. Ferman et. al., Opt. Lett. **15**, 752 (1990).

R. Geels, R. H. Yan, J. W. Scott, S. W. Corzine, R. J. Simes, and L. A. Coldren, *Analysis and Design of a Novel Parallel-Driven MQW-DBR Surface-Emitting Diode Laser*, Techn. Digest, CLEO '88 Conf. on Lasers and Electro-Optics, Anaheim, California, 25-29 April 1988, Paper WM1, pp. 206-207.

A. Halimaoui, C. Oules, G. Bromchil, A. Bsiesy, F. Gaspard, R. Herino, M. Ligeon, and F. Muller, *Electrouminescence in the Visible Range during Anodic Oxidation of Porous Silicon Films*, Appl. Phys. Lett. **59**, 304-306 (1991).

H. Haus and K. Bergman, Opt. Lett. 16, 663 (1991).

D. Herriott, H. Kogelnik, and R. Kompfner, *Off-Axis Paths in Spherical Mirror Interferometers*, Appl. Opt. **3**, 523-526 (1963).

D. R. Herriott and H. J. Schulte, *Folded Optical Delay Lines*, Appl. Opt. **4**, 883-889 (1965).

M. Hofer et. al. Opt. Lett. 16, 502 (1991).

R. K. Jain, ed. Characterization of Very High-Speed Semiconductor Devices and Integrated Circuits, Proc. SPIE 795 (1987).

J. L. Jewell, A. Scherer, Y. H. Lee, S. L. McCall, J. P. Harbison, L. T. Florez, R. S. Tucker, C. A. Burrus, C. J. Sandroff, and N. A. Olsson, *Vertical Cavity Surface Emitting Microlasers*, LEOS'90 Conf. Proc., LEOS 1990 Annual Meeting, Boston, MA, Nov. 4-9, 1990, Paper SDL1.2/MKK2, p. 378.

A. Kamal, M. L. Stock, A. Szpak, C. H. Thomas, D. A. Weinberger, M. Frankel, J. Nees, K. Ozaki, and J. Valdmains, in Digest of the Optical Society of America Annual Meeting (Opt. Soc. Amer. Washington, D.C., 1991) paper JTuA3.

F. Koyama, S. Kinoshita, and K. Iga, *Room-Temperature Continuous Wave Lasing Characteristics of a GaAs Vertical Cavity Surface-Emitting Laser*, Appl. Phys. Lett., **55**, 221-222, (1989).

M. Mahbobzadeh and M. Osinski, *Novel Distributed-Feedback Resonant-Periodic-Gain Structure for Vertical-Cavity Surface-Emitting Semiconductor Lasers*, Electron. Lett. **26**, 1716-1718 (1990).

M.-H. Meynadier, R.E. Nahory, J.M. Worlock, M.C. Tamargo, J.L de Miguel, and M.D. Sturge, Phys. Rev. Lett. **60**, 1338 (1988).

A. Mukherjee, S. R. J. Brueck, and A. Y. Wu, *Electric-Field Induced Second-Harmonic Generation in PLZT*, Opt. Commun. **76**, 220-224 (1990).

W. Nakwaski, *Dynamical Thermal Properties of Stripe-Geometry Laser Diodes*, IEE Proc. Pt. I (Solid-State & Electron Dev.), **131**, 94-102, (1984).

W. Nakwaski and M. Osinski, *Temperature Profiles in Etched-Well Surface-Emitting Semiconductor Lasers*, Jpn. J. Appl. Phys. (Lett.) **30**, L596-L598 (1991).

W. Nakwaski and M. Osinski, *Thermal Properties of Etched-Well Surface-Emitting Semiconductor Lasers*, IEEE J. Quantum Electron. QE-27, 1391-1401 (1991).

W. Nakwaski and M. Osinski, *Thermal analysis of etched-well surface-emitting diode lasers*, to be published in *Microwave & Opt. Techn. Lett.*, vol. 4, November 1991.

U. Österberg and W. Margulis, Opt. Lett. **11**, 516 (1986).

M. Poelker and R. K. Jain, to be published.

M. Y. A. Raja, S. R. J. Brueck, M. Osinski, C. F. Schaus, J. G. McInerney, T. M. Brennan, and B. E. Hammons, "*Wavelength-Resonant Enhanced Gain/Absorption Structure for Optoelectronic Devices*, in Post-Deadline Papers, XVI Int. Conf. on Quantum Electron. IQEC'88, Tokyo, Japan, 18-21 July 1988, Paper PD-23, pp. 52-53.

M. Y. A. Raja, S. R. J. Brueck, M. Osinski, C. F. Schaus, J. G. McInerney, T. M. Brennan, and B. E. Hammons, "*Resonant Periodic Gain Surface-Emitting Semiconductor Lasers*", IEEE J. Quantum Electron., **QE-25**, 1500-1512 (1989).

D. J. Richardson et. al., Electron. Lett. **27**, 730 (1991).

R. G. Smart and D. C. Hanna, Postdeadline paper, CLEO'91, Baltimore, Md. (May, 1991).

T.W. Steiner, D.J. Wolford, T.F. Kuech, and M. Jaros, Superlattices and Microstructures, 4, 227 (1988).

R. H. Stolen and H. W. K. Tom, Opt. Lett. **12**, 587 (1987).

B. Tell, Y. H. Lee, K. F. Brown-Goebeler, J. L. Jewell, R. E. Leibenguth, M. T. Asom, G. Livescu, L. Luther, and V. D. Mattera, *High-Power CW Vertical-Cavity Top Surface-Emitting GaAs Quantum Well Lasers*, Appl. Phys. Lett. **57**, 1855-1857 (1990)

W. R. Trutna and R. L. Byer, *Multiple-Pass Raman Gain Cell*, Appl. Opt. **19**, 301-312 (1980).

B.A. Wilson, IEEE J. Quantum Electron. QE-24, 1763 (1988).

B.A. Wilson, C.E. Bonner, R.C. Spitzer, P.Dawson, K.J. Moore, and C.T. Foxon, J. Vac. Sci. Technol. B6, 1156 (1988).

A. Yariv, **Introduction to Optical Electronics**, pp 18-24 (Holt, Rinehart and Winston, New York, 1971)

APPENDIX A: PUBLICATIONS

An inclusive publication list from the initiation of this grant (2/1/89) is included. Publications originating within this incremental reporting period are highlighted in **bold**, and copies are included.

E. A. Armour, S. Z. Sun, K. Zheng, D. P. Kopchik and C. F. Schaus, "AlGaAs Regrown on AlGaAs by MOCVD," paper presented at IEEE Summer Topical Meetings, Newport Beach, CA (1991).

L.L. Boyer, A.Y. Wu, G.W. Metzger, and J.R. McNeil, *Properties of Ion Beam Deposited PLZT*, J. Vac. Sci. Tech. A7 (3) 1199, 1989.

S.R.J. Brueck, M.Y.A. Raja, M. Osinski, C.F. Schaus, M. Mahbobzadeh, J.G. McInerney, and K.J. Dahlhauser, "Optical Cavity Design for Wavelength-Resonant Surface-Emitting Semiconductor Lasers," SPIE Proc. 1043, 111, 1989.

R.P. Bryan, G.R. Olbright, and J. Cheng, "Cascadable Surface-Emitting Laser Logic: Demonstration of Boolean Logic," Electronics Letters, Vol. 27, No. 11, pp 893-894, May 23, 1991.

E. A. Callan, J.G. McInerney, and H. Li, "Measurements of Velocities by Backscatter Modulation in Semiconductor Injection Lasers," Proc. 13th IEEE Conf. on Ideas in Science and Engineering (ISE '91), Albuquerque, NM, May 1991.

J. Cheng, G.R. Olbright, and R. Bryan, "Binary Arithmetic Using Optical Symbolic Substitution and Cascadable Surface-Emitting Laser Logic Devices," Proceedings of the 1991 Topical Meeting on Optical Computing and Photonic Switching, Salt Lake City, Utah, p. 10/MA3, March 3, 1991.

J. Cheng, "Parallel Optical Architecture for Binary Arithmetic Using Integrated Arrays of Phototransistor-Surface Emitting Laser Logic Gates," Optical Computing and Processing. Vol. 1, no. 3, pp189-197, April 1991.

J. Cheng, G. Olbright, R. Bryan, "Binary Arithmetic Using Optical Symbolic Substitution and Integrated Phototransistor Surface-Emitting Laser Logic," Applied Optics, Vol. 30, No. 30, pp. 4284-4287, Nov. 1991.

C.-P. Cherng and M. Osinski, "Lateral wavefront measurements of high-power semiconductor lasers using a three-mirror cyclic interferometer", SPIE Proceedings Vol. 1319 - 15th Congress of the International Commission for Optics "Optics in Complex Systems" (F. Lanzl, H.-J. Preuss, G. Weigelt, Eds.), Garmisch-Partenkirchen, Germany, August 5-10, 1990, pp. 40-41.

C.-P. Cherng and M. Osinski, "Coupled Broad-Area Mode Theory of Gain-Guided Laser Arrays," Journal of Applied Physics 70, pp. 4617-4619 (October 1991).

C.-P. Cherng and M. Osinski, "Fundamental Array Mode Operation of Semiconductor Laser Arrays Using External Spatial Filtering," SPIE Proceedings Vol. 1418 - Laser Diode Technology and Applications III (D. Renner, Ed.), SPIE Symposium on High Power Lasers, OE/LASE'91, Los Angeles, California, January 20-25, 1991, pp. 372-385.

C.-P. Cherng, T. C. Salvi, M. Osinski, and J. G. McInerney, "Near-Field Wavefront Measurements of Semiconductor Laser Arrays by Shearing Interferometry", Applied Optics 29, pp. 2701-2706 (June 1990).

C-P. Cherng, T.C. Salvi, M. Osinski, and J.G. McInerney, "Lateral Near-Field Wavefront Measurements of Semiconductor Laser Arrays," Appl. Opt. (submitted).

K. H. Chung, J. G. McInerney, and M. Osinski, "*Measurement of semiconductor laser linewidth enhancement factor using coherent optical feedback*", SPIE Proceedings Vol. 1043 - Laser Diode Technology and Applications (L. Figueroa, Ed.), SPIE Symposium on Lasers and Optics OE/LASE'89, Los Angeles, California, January 18-20, 1989, pp. 175-183.

K. H. Chung, J. G. McInerney, and M. Osinski, "*Coherent feedback effects in short-external-cavity semiconductor lasers (invited paper)*", Proceedings of the 2nd ASEAN Science and Technology Week, Manila, Philippines, January 30 - February 4, 1989, pp. 525-547.

R. C. Dye, R. E. Muenchausen, N. S. Nogar, A. Mukherjee and S. R. J. Brueck, "Laser-Writing of Superconducting Patterns on $YBa_2Cu_3O_{7-\delta}$ Films," Appl. Phys. Lett., Vol 57, June 1990.

Y.-C. Fong and S.R.J. Brueck, "Confocal Photoluminescence: A Direct Measurement of Semiconductor Carrier Transport Parameters," submitted to Appl. Phys. Lett.

P. L. Gourley, L. R. Dawson, T. M. Brennan, B. E. Hammons, J. C. Stover, C. F. Schaus, and S. Sun, "Optical Scatter in Epitaxial Semiconductor Multiconductor Multilayers," Appl. Phys. Lett. 58:1360 (1991).

P.L. Gourley, S.K. Lyo, T.M. Brennan, B.E. Hammons, C.F. Schaus and S.Sun, *Lasing Threshold in Quantum Well Surface-Emitting Lasers: Many-Body Effects and Temperature Dependence*, Appl. Phys. Lett. **55**, 2698-2700, 1989.

J. P. Hohimer, G. R. Hadley, D. C. Craft, T. H. Shiau, S. Sun, and C. F. Schaus, "Stable-mode operation of leaky-mode diode laser arrays at high pulsed and cw currents," Appl. Phys. Lett. 58:452 (1991).

W.H. Hong, H.H. So, H.K. Park, and J.G. McInerney, *Circuit Models for Frequencey Modulation Response of Semiconductor Lasers*, Electron Lett. **25**, 591, 1989.

Y.-S.Kuo, Y.-C. Fong, C. wu, J.G. McInerney, and J.K. McIver, "Single Cell Brillouin Enhanced Four-Wave Mixing with Focusing Geometry," submitted to Optics Letters.

Y. Li, C.-K. Wu, M.B. Snipes, Jr., and J.G. McInerney, "Widely Tunable, High-Power External Cavity Semiconductor Lasers," Proc. ann. Meeting of Opt. Soc. of Am. (OSA '91), San Jose, CA, Nov. 1991.

H-F. Liu, M. Osinski and T. Kamiya, *Optical Chaos in Modulated Multi-Terminal Semiconductor Lasers* in Solitons and Chaos in Optical Systems, H.C. Morris and D.M. Heffernan, eds., Plenum Press, New York, 1990.

J.-M. Luo and M. Osinski, "Stable-Locking Bandwidth in Sidemode Injection Locked Semiconductor Lasers," Electronics Letters 27, pp. 1737-1739 (September 1991).

J.-M. Luo and M. Osinski, "Multimode Small-Signal Analysis of Side-Mode Injection-Locked Semiconductor Lasers," submitted to Japanese Journal of Applied Physics (Letters).

J.-M. Luo, M. Osinski, and J.G. McInerney, "Side-Mode Injection Locking of Semiconductor Lasers," IEEE Proceedings Pt J - Optoelectronics 136, 33-37, 1989.

J.-M. Luo and M. Osinski, *"Side-mode injection locking characteristics of semiconductor lasers: Multimode analysis,"* Proceedings of the First International Workshop on Photonic Networks, Components and Applications (J. Chrostowski and J. Terry, Eds.), Montebello, Quebec, Canada, October 11-13, 1990, Series in Optics and Photonics Vol. 2, World Scientific, Singapore 1991, pp. 195-199.

J.-M. Luo, M. Osinski, and J. G. McInerney, *"Theory of side-mode injection-locked semiconductor lasers," (invited paper)* Proceedings of the 2nd ASEAN Science and Technology Week, Manila, Philippines, January 30 - February 4, 1989, pp. 621-653.

M. Mahbobzadeh and M. Osinski, "Novel Distributed-Feedback Structure for Surface-Emitting Semiconductor Lasers," SPIE Proceedings Vol. 1418 - Laser Diode Technology and Applications III (D. Renner, Ed.), SPIE Symposium on High Power Lasers, OE/LASE'91, Los Angeles, California, January 20-25, 1991, pp. 25-31.

M. Mahbobzadeh,E. Gandjbakhch, and M. Osinski, "High-Power Operation of Distributed-Feedback Resonant-Periodic-Gain Surface-Emitting Lasers," SPIE Proceedings Vol. 1582 - Integrated Optoelectronics for Communication and Processing (C.-S. Hong, Ed.), SPIE Symposium on Optical Fiber Materials and Devices, OE/Fibers'91, Boston, Massachusetts, September 3-6, 1991, pp. 121-131.

M. Mahbobzadeh, E. Gandjbakhch, E. A. Armour, K. Zheng, S.-Z. Sun, C. F. Schaus, and M. Osinski, "Distributed-Feedback Vertical-Cavity Surface-Emitting Laser with Resonant-Periodic-Gain Active Region," to be published in SPIE Proceedings Vol. 1634 - Laser Diode Technology and Applications IV (D. Renner, Ed.), SPIE Laser and Sensor Engineering Symposium, OE/LASE'92, Los Angeles, California, January 19-24, 1992, Paper 1634-49.

M. Mahbobzadeh and M. Osinski, "Resonant-Periodic-Gain Distributed-Feedback Surface-Emitting Semiconductor Laser", United States Patent serial number 07/526,083, filed on May 18, 1990, awarded on January 2, 1991.

M. Mahbobzadeh and M. Osinski, "Novel Distributed-Feedback Resonant-Periodic-Gain Structure for Vertical-Cavity Surface-Emitting Semiconductor Lasers," Electron. Lett., Vol. 26, pp. 1716-1718, 27 Sept. 1990.

M. Mahbobzadeh, M.Y. Raja, J.G. McInerney, C.F. Schaus, and S.R.J. Brueck, *Mode Stability of Resonant Periodic Gain Surface-Emitting Semiconductor Lasers*, Proc. SPIE Vol 1219 264-276, 1990.

K. J. Malloy and J. A. Van Vechten, "Thermal Expansion to Band Gap and Band Offset Temperature Dependences," Jour. Vac. Sci. Technol., B9, 2212, 1991.

L.D. Marin, D-S. Seo, and J.G. McInerney, "Double External Cavity Semiconductor Lasers," IEEE, ISE '90

D. L. McDaniel, Jr., J. G. McInerney, M.Y.A. Raja, C. F. Schaus and S. R. J. Brueck, "Vertical Cavity Surface-Emitting Semiconductor Laser with CW Injection Laser Pumping," Photonics Tech. Lett. 3, 156-158, March 1990.

D.L. McDaniel, Jr., J.G. McInerney, C.F. Schaus, and S.R.J. Brueck, "Injection Laser Pumped Resonant-Periodic-Gain Vertical Cavity Semiconductor Lasers," Proc. ISE '90, Alb., NM, May 1990, pp. 242-250

J.G. McInerney, J.-D. Park, S.-S. Seo, H. Li, and J. Ye, "Nonlinear Dynamics of Double External Cavity Semiconductor Lasers," submitted to CLEO '92

J.G. McInerney, D.S. Seo, and J.D. Park, "External Cavity Semiconductor Lasers," Proc. XIII IEEE Conf. on Ideas in Science and Electronics (ISE 90), Alb., NM, May 1990, (Invited paper), pp. 212-222

J.G. McInerney, "Low-Frequency Intensity Noise in External Cavity Semiconductor Lasers," Proc. SPIE, Vol. 1376 (Special Issue on Laser Noise), paper #16.

J.G. McInerney, J-D Park, D-S Seo and M. Osinski, *Nonlinear Dynamics of Asymmetric External Cavity Semiconductor Lasers* in Solitons and Chaos in Optical Systems, H.C. Morris and D.M. Heffernan, eds., Plenum Press, New York, 1990.

A. Mukherjee, S. R. J. Brueck and A. Y. Wu, "Electro-Optic Effects in Thin-Film Lanthanum-Doped Lead Zirconate Titanate," Opt. Lett. 15, 151-153 Feb. (1990).

A. Mukherjee, S. R. J. Brueck and A. Y. Wu, "Electric Field Induced Second Harmonic Generation in PLZT," Opt. Commun. 76, (3,4) 220-222 May (1990).

A. Mukherjee, M. Mahbobzadeh, C. F. Schaus, S. R. J. Brueck, "Ultrafast operation of optically pumped resonant periodic gain GaAs surface emitting lasers," IEEE Photon. Tech. Lett. 2:857 (1990).

B.W. Mullins, S.F. Soares K. A. McArdle, C.M. Wilson, and S.R.J. Brueck, "A Simple High-Speed Si Schottky Photodiode," IEEE Photon. Tech. Lett., Vol. 3, No. 4, pp 360-363, April 1991.

R.F. Murison, S.R. Lee, N. Holehouse, A.H. Moore, K.M. Dzenko, A. Righettti, G. Grasso, F. Fontana, C.F. Schaus, S.Z. Sun, N.A. Dinkel, J.C. Connelly, "High Power 980 nm Ridge Waveguide Laser in Single Mode Fiber Coupled Package,

R. Myers, N. Mukherjee, and S.R.J. Brueck, "Large Second-Order Nonlinearity in Poled Fused Silica," Optics Letters, Vol 16, No. 22, pp.1732-1734, Nov. 15, 1991.

M. Osinski, "Vertical-Cavity Surface-Emitting Semiconductor Lasers for Optical Interconnections," Invited Paper, Proceedings of the First International Workshop on Photonic Networks, Components & Applications, Montebello, Quebec, Canada, October 11-13, 1990, Series in Optics and Photonics - Vol. 2 (J. Terry and J. Chrostowski, Eds.), World Scientific, Singapore 1991, pp. 70-80.

M. Osinski, "Vertical-Cavity Surface-Emitting Semiconductor Lasers: Present Status and Future Prospects," Invited Paper, Laser Diode Technology and Applications III (D. Renner, Ed.), SPIE Symposium on High Power Lasers, OE/LASE'91, Los Angeles, California, January 20-25, 1991, pp. 2-24.

M. Osinski, *Effective Mass of Holes in Quaternary InGaAsP Alloys Lattice-Matched to InP.*, CRC Critical Rev. in Solid State and Matr. Sci. 15, 327-343, 1989.

J.D. Park, D.S. Seo, W.A. Moeur, and J.G. McInerney, "Nonlinear Dynamics and Chaos in Asymmetric External Cavity Semiconductor Lasers," Proc. ISE '90, Alb., NM, May 1990.

J.D. Park, D.S. Seo, and J.G. McInerney, "Self-Pulsations in Strongly Coupled Asymmetric External Cavity Semiconductor Lasers," IEEE J. Quantum Electron., Vol. 26, pp. 1353-1362, Aug. 1990.

J.D. Park, D.S. Seo, J.G. McInerney, G.C. Dente, and M. Osinski, *Low-Frequency Self-Pulsations in Asymmetric External-Cavity Semiconductor Lasers Due to Multiple Feedback Effects*, Opt. Lett 14, 1054-1056, Oct. 1989.

M. R. Poor, A. M. Hurd, C. B. Fleddermann, and A. Y. Wu, "PLTZ Thin Film Etching using Plsma Techniques," in the Seventh International Symposium on the Applications of Ferroelectrics, University of Illinois, Urbana, Illinois (1990). (in press)

M. R. Poor, A.M. Hurd, C.B. Fleddermann, and A.Y. Wu, "Plasma Etching of PLTZ and PLT using Chlorine Baseed Gases, in the Symposium on Ferroelectric Thin Films," Spring Meeting, Materials Research Society, San Francisco, CA, April 1990.

M.Y.A. Raja, S.R.J. Brueck, M.O. Scully, and C. Lee, "Resonant Periodic-Gain Surface-Emitting Semiconductor Lasers and Correlated Emission in a Ring Cavity," Physical Review, Vol 44, No. 7, pp 4459-4607, Oct. 1991.

M.Y.A. Raja, S.R.J. Brueck, M. Osinski, C.F. Schaus, J.G. McInerney, T.M. Brennan, and B.E. Hammons, *Resonant Periodic Gain Surface-Emitting Semiconductor Lasers*, IEEE Jour. Quantum Electron. QE-25, 1500-1512, June 1989.

M.Y.A. Raja, S. Sun, M. Mahbobzadeh, C.F. Schaus, and S.R.J. Brueck, *High-Efficiency CW Lasing in Photopumped InGaAs/AlGaAs Resonant Periodic Gain Structures at Room-Temperature*, Appl. Phys. Lett (submitted).

M.Y.A. Raja, S.R.J. Brueck, M. Osinski, C.F. Schaus, J.G. McInerney, T.M. Brennan and B.E. Hammons, *Wavelength-resonant Periodic Gain Surface-Emitting Semiconductor Lasers*, IEEE J. Quantum Electron. 25, 1500 (Special Issue on Semiconductor Lasers), June 1989.

C.F. Schaus, A. Torres, J. Cheng, C. Hains, Z. Sun, K. Zheng, E. Armour, "Transverse-Junction Vertical-Cavity Surface-Emitting Lasers," Applied Physics Letters 58, 1736, (1991).

C.F. Schaus, M.Y.A. Raja, J.G. McInerney, H.E. Schaus, S. Sun, M. Mahbobzadeh, and S.R.J. Brueck, *High-Efficiency CW Operation of MOCVD-Grown GaAs/AlGaAs Vertical-Cavity Lasers with Resonant Periodic Gain*, Electron. Lett. 25, 637-638, May 1989.

C.F. Schaus, H.E. Schaus, S. Sun, M.Y.A. Raja, and S.R.J. Brueck, *MOCVD Growth of GaAS/AlGaAs Wavelength Resonant Periodic Gain Vertical Cavity Surface-Emitting Laser*, Electron. Lett. 25, 538-539, April 1989.

H.E. Schaus, C.F. Schaus, S. Sun, M.Y.A. Raja, A. Jacome-Torres and J.G. McInerney, *Growth of High-Efficiency Resonant-Periodic-Gain Vertical Cavity Surface-Emitting Lasers*, Proc. 16th Int. Symp. on GaAs Related Compounds (Inst. of Phys. Conf. Ser. 1990), Jan. 1990.

D.S. Seo, L.D. Marin, and J.G. McInerney, "Double External Cavity Semiconductor Lasers," Proc. ISE '90, May 1990, pp. 223-230.

D-S. Seo, J-D. Park, J.G. McInerney and M. Osinski, *Compound Cavity Modes in Semiconductor Lasers with Asymmetric Optical Feedback*, Appl. Phys. Lett. 54, 990-992, March 1989.

D-S. Seo, J-D. Park, J.G. McInerney and M. Osinski, *Multiple Feeback Effects in Asymmetric External Cavity Semiconductor Lasers*, IEEE Jour. Quantum Electron. QE-25, 2229-2238, Nov. 1989.

T. H. Shiau, S. Sun, C. F. Schaus, K. Zheng, and G. R. Hadley, "Highly Stable Strained Layer Leaky-Mode Diode Laser Arrays," IEEE Photon. Tech. Lett. 2:534 (1990).

M.B. Snipes, Jr. and J.G. McInerney, "High Power, Diffraction Limited, Wide Stripe Injection Lasers, Using an External Resonator for Transverse Mode Filtering," Proc. 13th IEEE Conf. on Ideas in Science and Engineering (ISE '91), Albuquerque, NM, May 1991.

S. Z. Sun, E. A. Armour, K. Zheng, and C. F. Schaus, "Zinc and Tellurium Doping in GaAs and AlGaAs Grown by MOCVD," Journal of Crystal Growth, 113:103 (1991)

S. Z. Sun, E. A. Armour, D. P. Kopchik, K. Zheng, P. Zhou, Julian Cheng, and C. F. Schaus, "MOCVD Growth of Vertical Cavity Surface-Emitting Lasers with Graded-Composition Mirrors," presented at GaAs and Related Materials, Seattle, WA (1991), to be published.

W. E. Thompson and M. Osinski, "Longitudinal Behavior in Semiconductor Laser Diodes", Technical Digest, OSA 1990 Annual Meeting, Boston, Massachusetts, November 4-9, 1990, Technical Digest Series 1990 Vol. 15, Paper MK11, p. 16.

F. Wang, C.-B. Juang, C. Bustamante, and A. Y. Wu, "Electro-Optic Properties of (Pb,La)(Zr,Ti)O_3, (Sr,Ba)Nb_2O_6 and $Ba_2NaNb_5O_{15}$ Thin Films by a Confocal Scanning Defferential Polarization Microscope," in the 4th International SAMPE Electronics Conference, Volume 4, Electronic Materials-Our Future, pp. 712-721, ed. R. E. Allred, R. J. Martinez, and K. B. Wischmann, (Society for the Advancement of Material and Process Engineering) 1990.

Feiling Wang and A.Y. Wu, "An Analytical Model for the Quadratic Electrooptic Effect on Perovskites," Submitted to Physical Review Letters.

A.B. Wegner, S.R.J. Brueck, and A.Y. Wu, "Integrated PLZT Thin Film Waveguide Modulators, in the Second Symposium on Integrated Ferroelectrics," Naval Postgraduate School Monterey, CA. March 6-8, 1990

D. F. Welch, W. Streifer, C. F. Schaus, S. Sun, P. L. Gourley, "Gain characteristics of strained quantum well lasers," Appl. Phys. Lett. 56:10 (1990).

D.F. Welch, W. Streifer, C.F. Schaus, S. Sun and P.L. Gourley, *Gain Characteristics of Strained Quantum Well Lasers*, Appl. Phys. Lett. 56, 10-12, Jan 1990.

A. Y. Wu, Deposition of (Pb,La)(Zr,Ti)O_3, (Sr, Ba)Nb_2O_6, $Ba_2NaNb_5O_{15}$, $KTiOPO_4$, and beta-BaB_2O_4 Thin Films," in the 4th International SAMPE Electronics Conference, Volume 4, Electronic Materials-Our Future, pp. 722-733, ed R. E. Allred, R. J. Martinez, and K. B. Wischmann, (Society for the Advancement of Material and Process Engineering) 1990.

A. Y. Wu, F. Wang, C.-B. Juang, and C. Bustamante, "2-D High Definition and High Resolution PLZT Thin Film Spatial Light Modulators, in the Seventh International Symposium on the Applications of Ferroelectrics, University of Illinois, Urbana, Illinois (1990).

A. Y. Wu, F. Wang, C.-B. Juang, and C. Bustamante, "Electro-optic and Non-Linear Optical Coefficients of (Pb,La)(Zr,Ti)O_3, $BaTiO_3$, (Sr,Ba)Nb_2O_6, and $Ba_2NaNb_5O_{15}$ Thin Films," in the Symposium on Ferroelectric Thin Films, Spring Meeting, Materials Research Society, San Francisco, California (1990).

C.-K. Wu, J.G. McInerney, and B.W. Liby, "Phase-Locking of Semiconductor Diode Lasers by Phase Conjugate Injection," submitted to Optical Letters

C.-K. Wu, Y. Li, M.B. Snipes, Jr. and J.G. McInerney, "High-Power Widely Tunable Line-Narrowed External Cavity Semiconductor Lasers," Proc. 13th IEEE Conf. on Ideas in Science and Engineering (ISE '91), Albuquerque, NM, May 1991.

J. Ye, H. Li, and J.G. McInerney, "Period-Doubling Route to Chaos in a Semiconductor Laser with Weak Optical Feedback," submitted to PRL, Oct. 1991.

J. Ye, H. Li, and J.G. McInerney, "Dynamic Analysis of Coherence Collapse in the External Cavity Semiconductor Laser," Proc. 13th IEEE Conf. on Ideas in Science and Engineering (ISE '91), Albuquerque, NM, May 1991.

S.H. Zaidi, M. Yousaf, and S.R.J. Brueck, "Grating Coupling to Surface Plasma Waves I. First-Order Coupling," J. Opt. Soc. Am., Vol. 8, No. 4, pp. 770-779, April 1991.

S.H. Zaidi, M. Yousaf, and S.R.J. Brueck, "Grating Coupling to Surface Plasma Waves II. Interactions Between First- and Second-Order Coupling," J. Opt. Soc. Am., Vol. 8, No. 6, pp. 1348-1359, June 1991.

S.H. Zaidi, D.W. Reicher, B. Draper, J.R. McNeil, and S.R.J. Brueck, "Characterization of Thin Al films Using Grating Coupling to Surface Plasma Waves," submitted to Journ of Appl. Phys., Nov. 1991.

P. Zhou, Julian Cheng, C. F. Schaus, S. Z. Sun, K. Zheng, E. Armour, C. Hains, Wei Hsin, D. R. Meyers, and G. A. Vawter, "Low Series Resistance High-Efficiency GaAs/AlGaAs Vertical-Cavity Surface-Emitting Lasers with Continuously Graded Mirrors Grown By MOCVD," IEEE Photon. Tech. Lett. Vol. 3, p. 591, (1991).

P. Zhou, J. Cheng, C.F. Schaus, S.Z. Sun, C. Hains, K. Zheng, E. Armour, W. Hsin, D.R. Myers, and G.A. Vawter, "Cascadable, Latching Photonic Switch with High Optical Gain by the Monolithic Integration of a Vertical-Cavity Surface-Emitting Laser and a PNPN Photothyristor," IEEE Photonics Technol. Lett., Vol. 3, pp. 1009-1012, Nov. 1991.

CASCADABLE SURFACE-EMITTING LASER LOGIC: DEMONSTRATION OF BOOLEAN LOGIC

Indexing terms: Logic devices, Optical logic

We demonstrate cascadable optical logic (AND-, OR- and exclusive OR-gates) implemented with heterojunction phototransistors and vertical-cavity surface-emitting lasers. We also discuss an architecture for implementing binary arithmetic using cascadable surface-emitting laser logic devices and optical symbolic substitution.

We describe cascadable optical logic gates (AND, OR and XOR) based on heterojunction phototransistors wire-bonded to vertical-cavity surface-emitting laser (VCSEL) structures.[1] These surfaCe-Emitting Laser Logic (CELL) devices have high optical gain (>20 overall, >200 differential), high on/off contrast (>34 dB), and low switching energy. We are able to realise optical logic functions such as inversion, AND, NAND, OR, NOR, and XOR, etc., using only simple combinations of phototransistors and VCSELs. Using these optical logic devices, we describe an architecture for implementing parallel binary arithmetic based on optical symbol substitution.[2]

The optical Boolean logic operations are demonstrated using simple combinations of high-gain AlGaAs/GaAs *npn* phototransistors and low threshold AlGaAs/GaAs VCSELs.[1] The details of the epitaxial growth are described in Reference 1. We electrically isolated the VCSELs[3] and phototransistors using proton implantations. A bilayer (Au-photoresist) implantation mask is also used as a liftoff mask to form self-aligned electrical contacts. The input (output) apertures of the phototransistors (VCSELs) are circular with 15 μm diameters.

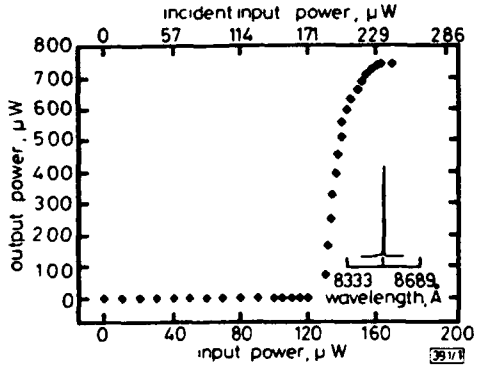

Fig. 1 *Light output against light input of discretely integrated CELL at $V_0 = 8{\cdot}0$ V*

Insert: typical lasing spectrum

In Fig. 1 we show the light output against light input characteristic of the CELL device. The principle of operation of the devices is as follows. When illuminated, the phototransistors are switched from a high collector–emitter voltage, low collector current 'off' state to a low voltage, high current 'on' state. In the 'on' state, sufficient current is available that the VCSEL is driven to lasing. At greater than 160 μW absorbed (230 μW incident; sample is not antireflection coated) input optical power, the current saturates and thus the output power from the VCSEL also saturates. This saturation behaviour is desirable for digital optical logic so that the 'on' state is represented by a single power level (binary) rather than by a range of output powers. Furthermore, the CELL pair has very high on/off contrast[1] (>34 dB) due to the threshold behaviour of the VCSEL.

In Fig. 2 we show the circuit configuration and the optical input and output signals from the CELL circuit for AND- and XOR-gate operation. For the optical OR- and AND-gate operations, a single CELL is used to realise the Boolean function (see Fig. 2). To operate as an AND gate, the intensity of the optical inputs A and B into the phototransistor must be such that they can collectively, but not individually, produce enough current gain to switch on the VCSEL. In the OR-gate configuration, each optical input is of sufficient intensity to produce enough current gain to saturate the VCSEL output power. Consequently, the OR gate can be achieved, using the same engineered structure as the AND gate, simply by adjusting the power levels of the inputs. This situation is possible because the incident power level which produces enough current gain to drive the VCSEL to threshold (~130 μW absorbed/186 μW incident) is more than one half the power level at which the device saturates (~160 μW absorbed/230 μW incident).

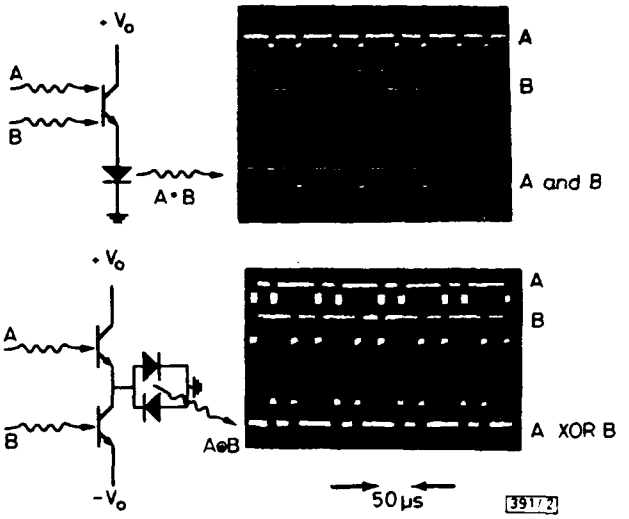

Fig. 2 *Digital optical circuit configurations and logic operations for optical AND- and XOR-gate*

Input beams to gates are labelled A and B

By configuring two phototransistors and two VCSELs as shown in Fig. 1*b*, we have also demonstrated an optical XOR gate. For this circuit configuration, when the optical inputs A and B are present or absent, the potential between the phototransistors is 0 V and therefore no current flows through the VCSELs (this represents the OFF state). However, if only optical input A (input B) is present, then the potential between the phototransistors is approximately $+V_0(-V_0)$ and current flows only through the forward biased VCSEL diode (thus representing the ON state). Therefore, for this circuit configuration, we obtain an optical XOR as shown in Fig. 2. Optical inverters, NOR- and NAND-gates using combinations of VCSELs and phototransistors can also be realised. The optical logic functions (AND, OR, and XOR) were operated up to 2 MHz. The speed of the CELL devices, which depends upon the operating voltage, photocurrent, device geometry, and the transient properties of the VCSELs, is beyond the scope of this Letter.

Because the wide absorption band of the phototransistor overlaps the emission wavelength of the VCSEL, the CELL devices are cascadable. It is therefore possible to implement digital optical computing architecture using arrays of CELLs. For this application, the outputs of a set of CELLs are used as the inputs for another set of CELLs and thus the multiple levels of gate operations required for optical computing can be performed. For example, in Fig. 3 we show a schematic diagram of the circuit for an AND–OR-gate sequence using three CELLs. Structures in which the emitter emission wavelength does not overlap the absorption band of the photodetector (e.g. an InGaAs VCSEL integrated with an AlGaAs/GaAs phototransistor) are not cascadable and therefore these devices cannot be used in optical computing architectures.

As an example of an optical computing system, we describe how cascadable combinations of phototransistors and VCSELs are well suited to implement binary arithmetic. The addition can be implemented using combinations of only AND and OR gates, but this would require complementary optical logic inputs. It is much simpler to implement binary

addition using the XOR and AND gates, which will directly perform the SUM and CARRY operations required for the realisation of a half adder in a single logic step. For binary addition, the inputs consist of two N-bit words (two linear arrays) arranged as parallel rows of N-bit optical data. The optical signals from the linear arrays are incident on a $1 \times N$ linear array of phototransistors and VCSELs configured to produce the required logic gates (XOR and AND) for the binary addition. In this configuration, multiple binary optical words could be added simultaneously in a two-dimensional array. An N-bit binary half adder requires sequencing the optical data through the AND/XOR logic array N times. The optical outputs of each logic array provide the inputs for the next sequential logic array, which is repeated N times until all the CARRY bits have been shifted from the least significant bit to the most significant bit, at which point the optical addition of the input words is complete. The required spatial shift of the CARRY bit by one digit with respect to the SUM bit can be accomplished with digital optical logic arrays consisting of alternating columns of phototransistors (at the input plane of the array) and VCSELs (at the output plane). The optical outputs from the logic gates are from adjacent VCSEL columns thereby producing the required spatial shift. These spatial transformations, called optical symbolic substitution, provide a flexible architecture for shifting digital data that is central to binary arithmetic.[2] Properly designed, optical symbolic substitution also allows binary addition to take place by recycling the output optical data through a single logic array N times, resulting in a highly compact system and very significant reduction of hardware.[4]

In summary, we have demonstrated cascadable Boolean optical logic operations (AND, OR, and XOR) based on optical circuits of phototransistors and VCSELs. With the proper circuit configurations, a complete set of optical logic functions can be realised. Although we used discrete components for these demonstrations, the phototransistor and VCSEL devices are designed to be fully integrable into a monolithic structure to be described in a future publication. We have also discussed a scheme for implementing optical binary addition using symbolic substitution and the cascadable CELL devices. The half adder described above is simple, compact, and has a relatively low component count. The laser-logic based processors have distinct advantages over spatial-light modulator based processors (such as those based on S-SEEDs)[5] for digital optical computing applications because laser-logic based processors do not require the hundreds of bias beams and the associated optical engineering complexities necessary to implement spatial-light modulator based processors.

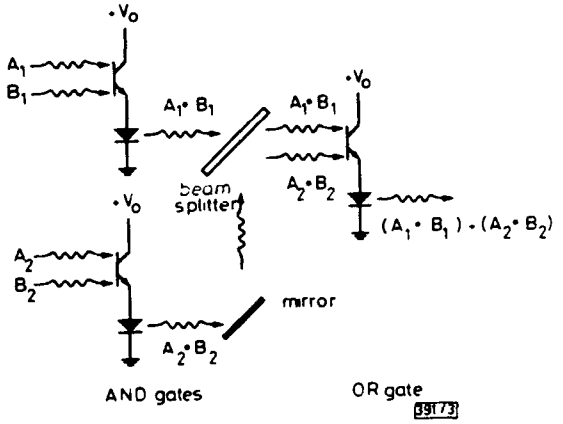

Fig. 3 *Digital optical circuit configuration showing how AND–OR-gate sequence can be implemented by cascading CELL gates*

Acknowledgments: The authors gratefully acknowledge technical discussions and assistance from K. Lear, T. Brennan, S. Samora and B. E. Hammons. Sandia National Laboratories research is supported by DOE contract No. DE-ACO4-76DP00789. University of New Mexico research is supported in part by AFOSR and DARPA.

R. P. BRYAN
G. R. OLBRIGHT
Sandia National Laboratories
Albuquerque, NM 87185, USA

J. CHENG
University of New Mexico
Center for High Technology Materials
Albuquerque, NM 87131, USA

18th March 1991

References

1 OLBRIGHT, G. R., BRYAN, R. P., LEAR, K. L., BRENNAN, T. M., POIRIER, G., LEE, Y. H., and JEWELL, J. L.: 'Cascadable laser logic devices: discrete integration of phototransistors with surface-emitting laser diodes', *Electron. Lett.*, 1991, **27**, (3), pp. 216–217

2 HUANG, A.: 'Parallel algorithms for optical digital computers'. Tech. Dig. IEEE Tenth Int. Optical Computing Conf., 1983, pp. 13–17

3 LEE, Y. H., TELL, B., BROWN-GOEBELER, K., JEWELL, J. L., LEIBENGUTH, R. E., ASOM, M. T., LIVESCU, G., LUTHER, L., and MATTERA, V. D.: 'High efficiency (1·2 mW/mA) top-surface-emitting GaAs quantum well lasers', *Electron. Lett.*, 1990, **26**, pp. 1308–1309

4 CHENG, J., OLBRIGHT, G. R., and BRYAN, R. P.: 'Binary arithmetic using optical substitution and phototransistor-surface emitting laser logic'. Topical Meeting on Optical Computing, Optical Society of America, Salt Lake City, March 1991

5 PRISE, M. E., CRAFT, N. C., LAMARCHE, R. E., DOWNS, M. M., WALKER, S. J., D'ASARO, L. A., and CHIROVSKY, M. F.: 'Module for optical logic circuits using symmetric self electro-optic effect devices', *Appl. Opt.*, 1987, **29**, p. 2164

PROC. ALB, NM 5/91 ISE '91

Measurements of Velocities by Backscatter Modulation in Semiconductor Injection Lasers

Elizabeth A. Callan, John G. McInerney, and Hua Li
Optoelectronic Device Physics Group
Center for High Technology and Materials
University of New Mexico
Albuquerque, NM 87131

Abstract

Backscatter-modulation, also known as self-mixing, involves coherent mixing of the frequency-shifted backscatter light from a target with the source light to produce an intensity modulation. Measuring the Doppler shift allows determination of the velocity of the target, thus producing a velocimeter. The use of semiconductor lasers (laser diodes) as the light source leads to reduced costs of the system, as well as reduced size, increased ruggedness, and high efficiency. The theory of backscatter-modulation and velocimetry using laser diodes as the light source is presented in this paper. An experimental setup is discussed as well as presentation of the results.

Introduction

The extensive use in industry, aerospace and robotics for optical velocimetry has encouraged the exploration of a variety of system strategies. One of these strategies involves coherent detection, in which the Doppler shifted and backscattered light from a target is coherently mixed with the source light to produce a beat-frequency intensity modulation.

Most coherent detection systems involve some variation of unequal-path interferometry and are characterized by complicated precision optics and sensitive alignment. Local heterodyne interferometry based on semiconductor lasers has been demonstrated, making a wide range of low-cost applications possible, including velocimetry with fiber-optic coupling [1] and directional anemometry [2]. However, the problems of complexity and sensitive alignment involved with interferometers are still present in most laser velocimetry systems.

To eliminate the complexity and the need for precise alignment, a self-referencing system has been introduced that involves backscatter-modulation. For backscatter-modulation, a beat signal is created by introducing a portion of the light scattered from a target back into the source laser. Measuring the Doppler shift allows direct determination of the velocity of the target, thus producing a velocimeter. This approach has been studied using He-Ne lasers [3], CO_2 lasers [4,5], and laser diodes [6-9]. The backscatter-modulation method requires only one lens to collimate the beam and is self-aligning due to the non-directionality of the backscatter. Therefore, it presents significant advantages over interferometric approaches.

Using a semiconductor laser (laser diode) as the source reduces the size of the system. There is also a strong coupling between the phase and amplitude of the optical field that results in even minute (-80 dB or more) amounts of coherent external optical feedback causing noticeable changes in the gain and oscillating frequency of the laser. Furthermore, laser diodes are rugged, efficient, reliable and inexpensive.

In order to understand velocimetry, it is first necessary to understand the characteristics of laser diodes. Then, the change in the laser characteristics when feedback, such as backscatter, is introduced into the laser diode, must be understood. Each of these will be addressed

in detail, then applied to velocimetry by laser diode backscatter modulation.

Semiconductor lasers

Laser diodes are forward-biased p-n junction diode structures grown epitaxially in direct-gap semiconductors. By means of lattice-matched semiconductor heterostructures [10,11], built-in confinement of injected charge carriers and generated photons results, with the injected carriers recombining across the energy gap of the semiconductor. Optical gain can be produced by stimulated emission, once the drive current is sufficient to raise the system above the lasing threshold, where the gain equals the loss. Coherent external feedback reduces the threshold condition, which results in nearly simultaneous changes in the amplitude and phase of the optical electric field.

Static Properties

The semiconductor laser may be considered as a single cavity with a gain medium the length of the diode, L_d. While the optical beam is propagating it will experience an exponential gain g per unit length from stimulated emission and an exponential loss α_{in} per unit length due to scattering from defects and free carrier absorption. Choosing the cavity axis to be in the positive z-direction, the optical electric field obeys

$$E(z) = E(0)\exp[j\beta z + (g - \alpha_{in})z/2] \quad (1)$$

where β is the longitudinal propagation constant of the lasing mode.

As with most laser systems, the oscillating field must be replicated after exactly one round trip. Applying the appropriate boundary conditions to ensure round trip replication, the oscillating condition for the laser is

$$r_1 r_2 \exp[(g - \alpha_{in})L_d]\exp(j\omega\tau_d) = 1 \quad (2)$$

where r_1 and r_2 are the field reflectivities at the ends of the laser cavity, and $\tau_d = 2L_d/v_g$ is the optical round trip delay in the laser diode cavity, neglecting spontaneous emission. If spontaneous emission were included, the left side of equation 2 is slightly less than unity when the laser is operating. The real part of the lasing equation (2) defines the solitary laser threshold gain, g_{th}, while the imaginary part defines the oscillating frequency, ω as follows

$$g - g_{th} = \alpha_{in} - \frac{1}{L_d}\ln(r_1 r_2) \quad (3)$$

$$\omega\tau = 2m\pi \quad (4)$$

for some integer m. The two equations must be satisfied simultaneously.

Dynamic Properties

The dynamic properties of the semiconductor laser are described by the rate equations for the optical electric field E(t) and the injected electron density N(t) and for a single lasing mode are:

$$\frac{dE}{dt} = j(\omega - \Omega)E + \frac{v_g}{2}(g - \alpha_t)(1 - j\alpha)E \quad (5)$$

$$\frac{dN}{dt} = \frac{J}{ed} - \frac{N}{\tau_s} - v_g g \mid E^2 \mid \quad (6)$$

where ω is the lasing angular frequency, Ω is the cavity mode frequency, v_g is the group velocity of light in the laser medium, α_t is the total loss coefficient (including the laser output), α is the ratio of the carrier-induced changes in the real and imaginary parts of the electric susceptibility in the laser medium (laser linewidth enhancement factor), J is the injected current density, e is the electronic charge, d is the thickness of the active layer, and τ_s is the spontaneous electron lifetime. Equation 5 can be separated into its real and imaginary parts, representing the field amplitude and phase respectively. Noting

that the photon density $S(t)$ is proportional to the square of the field amplitude, $S(t)$ and the field phase $\phi(t)$ are obtained:

$$\frac{dS}{dt} = v_g(g - \alpha_t)S + v_g g n_{sp} \quad (7)$$

$$\frac{d\phi}{dt} = (\omega - \Omega) + \frac{v_g \alpha}{2}(g - \alpha_t) \quad (8)$$

where n_{sp} is the spontaneous emission factor which depends on the degree of excitation in the laser medium. The laser linewidth enhancement factor α quantitatively measures the amount of phase-amplitude coupling. This phenomenon leads to many of the unique dispersive and dynamic properties of semiconductor lasers.

Lasers with weak to moderate coherent backscatter

Static Properties

When coherent feedback is introduced back into the laser diode, an external cavity is created as illustrated in Figure 1. The cavity considered for the laser diode may be extended to include the entire cavity by replacing the reflectivity at one end r_2 with an effective reflectivity r_{eff}. The laser oscillation condition (equation 2) then becomes

$$r_1 r_{eff} \exp[(g - \alpha_{in})L_d] \exp(j\omega\tau) = 1 \quad (9)$$

If the external feedback is weak enough that multiple round trip coupling may be neglected, i.e. $| r_{ext} r_2 | << 1$, then

$$r_{eff} = r_2 + (1 - | r_2 |^2) r_{ext} \exp(j\omega\tau_{ext}) \quad (10)$$

where r_{ext} is the field reflectivity of the external reflector with coupling losses and $\tau_{ext} = 2L_{ext}/c$ the optical round trip delay through the external cavity of length L_{ext}. The term $(1 - | r_2 |^2)$ accounts for the light transmission throught the laser facet.

With weak feedback, $| r_{ext} | << | r_2 |$, the reflection coefficients r_2 and r_{ext} may be considered to be real and positive. The amplitude and phase of r_{eff} may be written as

$$| r_{eff} | = r_2[1 + \kappa_{ext} \cos(\omega\tau_{ext})] \quad (11)$$

$$\phi_r = -\kappa_{ext} \sin(\omega\tau_{ext}) \quad (12)$$

where the coupling coefficient to the external cavity κ_{ext} is defined by

$$\kappa_{ext} = \frac{r_{ext}}{r_2}(1 - | r_2 |^2). \quad (13)$$

The external feedback changes the lasing frequency as well as the threshold gain. The change in the optical field phase during one round trip is

$$\Delta\phi_L = -\alpha\Delta g L_d + (2L_d/v_g)\Delta\omega - \phi_r, \quad (14)$$

where $\Delta\omega = \omega - \Omega$ is the change in the lasing frequency and Δg is the change in the threshold gain due to the external feedback,

$$\Delta g = g - g_{th} = -(\kappa_{ext}/L_d)\cos(\omega\tau_{ext}). \quad (15)$$

Possible emission frequencies, where the phase condition is satisfied, are characterized by $\Delta\phi_L = 0$. From equations (14) and (15), the frequency shift created by the feedback can be calculated

$$\begin{aligned} \Delta\omega &= \omega - \Omega \\ &= (\kappa_{ext}/\tau_d)\sqrt{(1 + \alpha^2)} \\ &\quad \sin[\omega\tau_{ext} + arctan(\alpha)] \end{aligned} \quad (16)$$

The gain and frequency equations (15, 16) are the most important equations for determining the static properties of external laser cavity semiconductor lasers. They both have a strong dependence on $\omega\tau_{ext}$, the feedback phase, which indicates that both are sensitive to the cavity length L_{ext}.

Dynamic properties

To determine the dynamic properties of laser diodes with an external cavity, the rate ewuation for the time-dependent electric field is modified to include the time delayed feedback

$$\begin{aligned}\frac{dE}{dt} &= j(\omega-\Omega)E(t) \\ &\quad + (\frac{v_g}{2})(g-\alpha_t)(1-j\alpha)E(t) \\ &\quad + \kappa E(t-\tau_{ext})\exp(j\omega\tau_{ext})\end{aligned} \tag{17}$$

with $\kappa = \kappa_{ext}/\tau_d = \tau_{ext}(1-\mid r_2 \mid^2)/\tau_d r_2$. The rate equation for the carrier density $N(t)$ remains unchanged:

$$\frac{dN}{dt} = \frac{J}{ed} - \frac{N}{\tau_e} - v_g g \mid E^2 \mid . \tag{5}$$

Again, the field equation can be separated into the photon density and the optical phase:

$$\begin{aligned}\frac{dS}{dt} &= v_g(g-\alpha_t)S(t) + v_g g n_{sp} \\ &\quad + 2\kappa\sqrt{[S(t)S(t-\tau_{ext})]} \\ &\quad \cos(j\omega\tau_{ext}+\delta\phi)\end{aligned} \tag{18}$$

$$\begin{aligned}\frac{d\phi}{dt} &= (\omega-\Omega) + \frac{v_g\alpha}{2}(g-\alpha_t) \\ &\quad - \kappa\sqrt{[S(t-\tau_{ext})/S(t)]} \\ &\quad \sin(\omega\tau_{ext}+\delta\phi)\end{aligned} \tag{19}$$

with $\delta\phi = \phi(t) - \phi(t-\tau_{ext})$.

In principle the modulation characteristics of external-cavity lasers may be described by studying equations 5, 18 and 19. Steady state solutions of these rate equations are determined by setting all the derivatives equal to zero. The resultant expressions define the feedback-induced gain and frequency changes and are identical to those obtained using the effective reflectivity model (equations 15 and 16). Since the system of equations is highly nonlinear, the dynamical properties of the external cavity laser are best evaluated numerically. The description of modulation characteristics is much more difficult than for the solitary laser since the frequency or phase modulation of $\phi(t)$ directly affects the intensity modulation. Therefore, any modulation of the injection current yields a simultaneous modulation of the optical intensity and frequency which are strongly inter-related.

Velocimetry by laser diode backscatter modulation

Theory

Now suppose that the external reflector is moving at a velocity v, assumed non-relativistic, measured along the laser axis. The external cavity length is then given by

$$L_{ext}(t) = L_{ext}(0) + vt \tag{20}$$

where v is positive when the reflector is receding from the laser. The frequency of the backscatter modulation is found by differentiating the phase equation (19) and is given by

$$f_v = \frac{2v}{\lambda} \tag{21}$$

where the subscript v indicates the functional dependence on the velocity and λ is the free-space wavelength of the external cavity laser emission. For very weak feedback coupling coefficients, as applicable in realistic velocimetry, λ is indistinguishable from the free-space wavelength λ_0 of the free-running laser diode. Therefore, the velocity of the external reflector can be determined by observing the intensity noise spectrum of the laser, or an equivalent quantity. The modulation depth in the laser power can be approxi-

mated by

$$m_v = (1 + a/P)\kappa_{ext} \qquad (22)$$

where a is the constant of proportionality between the laser power P and the normalized excess drive current $(I - I_{th})/I_{th}$ above threshold. The phase-amplitude coupling in the semiconductor gain medium should generate significant modulation, which is the primary reason semiconductor lasers as very suited to velocimetry applications.

Experiments

The experimental arrangement used to perform velocimetry measurements at the University of New Mexico is illustrated in Figure 2. A lens is placed after the laser diode (Hitachi HLP-1400) to collimate the beam. The rotating target has a diffusely reflecting surface (plain white paper) and is angled so that there is a velocity component parallel to the incident beam. The Doppler signal is observed by placing a 30/70 beam splitter in the external cavity and monitoring the beam fluctuations with a photodiode connected to a 30-dB RF amplifier and displayed on a RF spectrum analyzer. The length of the cavity was 25 cm, which produced coherent feedback.

The velocity component involved in the modulation is given by

$$\omega r \sin\theta \qquad (23)$$

where ω is the angular velocity, r is the distance of the beam-incidence point from the axis of rotation, and θ is the angle of the target rotation axis with respect to the beam axis. In this experimental configuration, the modulation velocity is varied by changing the target's angular velocity or the angle of tilt with respect to the beam.

Figure 3 displays the output of the spectrum analyzer with a target velocity component of 2.93 m/s along the laser axis. The large peak on the left is the frequency of the local oscillator and is considered to be the reference (zero) frequency. The measured frequency shift is obtained by subtracting the frequency of the Doppler peak observed from the analyzer's local oscillator. Figure 4 shows a comparison of the calculated and observed frequency shifts, as the angular velocity of the rotating target was varied. The observed frequency shifts are identical to the expected shifts.

The velocity component that modulates the laser is dependent on the angle of the target with the incident beam, as shown in equation 21. Maintaining a constant rotation speed, the target angle was varied and the results are displayed in Figure 5. At angles less than 10° (the target surface nearly perpendicular to the incident beam), the signal was no longer distinguishable from the system noise, due to the decreasing magnitude of the velocity component modulating the laser.

Future Work

Two other methods for detecting the Doppler signal are being investigated: placing the photodiode at the back facet of the laser diode, if the packaging permits transmission in that direction, and directly monitoring the variation of the laser diode voltage. Each data extraction system will be evaluated to determine its limitations and sensitivity. Efforts will also be directed toward exploring the incorporation of ranging measurements into the system and replacing the spectrum analyzer with less expensive and more compact electronics.

References

1. K. Kyuma, S. Tai, M. Numoshita, and T. Hakayama, "Fiberoptic Laser Doppler Velocimeter Using an Ex-

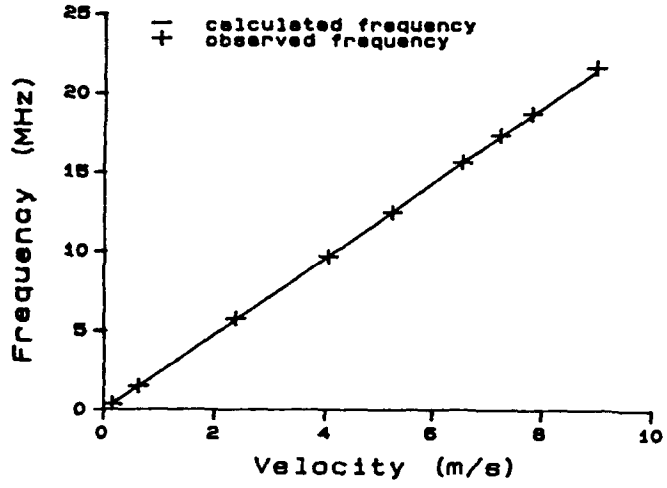

Figure 4. Comparison of the calculated and observed frequency shifts when the velocity is changed by varying the target's angular velocity

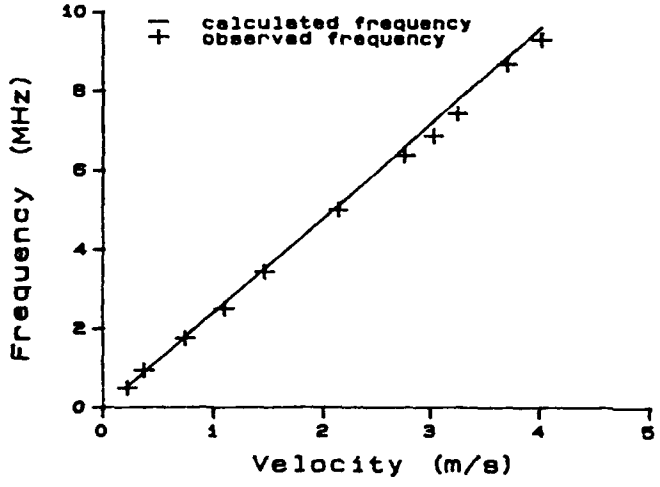

Figure 5. Comparison of the calculated and observed frequency shifts when the velocity is changed by varying the angle of the target with respect to the laser axis

ternal Cavity Semiconductor Laser", Appl. Phys. Lett. 45, 1005 (1984).

2. J. D. C. Jones, M. Corke, A. D. Kersey, and D. A. Jackson, "Miniature Solid-State Directional Laser Doppler Velocimeter,", Electron. Lett. 22, 967 (1982).
3. M. J. Rudd, "A Laser Doppler Velocimeter Employing the Laser as a Mixer-Oscillator," J. Phys. E 1, 723 (1968).
4. J. H. Churnside, "Laser Doppler Velocimetry by Modulating a CO2 Laser with Backscattered Light," Appl. Opt. 23, 61 (1984).
5. J. H. Churnside, "Signal-to-Noise in a Backscatter-Modulated Doppler Velocimeter," Appl. Opt. 23, 2097 (1984).
6. S. Shinohara, A. Mochizuki, H. Yoshida, and M. Sumi, "Laser Doppler Velocimeter Using the Self-Mixing Effect of a Semiconductor Laser Diode," Appl. Opt. 25, 1417 (1986).
7. P. J. deGroot, G. M. Gallatin, and S. M Macomber, "Ranging and Velocimetry Signal Generation in a Backscatter-Modulated Laser Diode," Appl. Opt. 27, 4475 (1988).
8. P.J. deGroot and G. M. Gallatin, "Backscatter-Modulation Velocimetry with an External-cavity Laser Diode," Opt. Lett. 14, 165 (1989).
9. H. W. Jentink, F. F. M. deMul, H. E. Suichies, J.G. Aarnoudse, and J. Greve, "Small Laser Doppler Velocimeter Based on the Self-mixing Effect in a Diode Laser," Appl. Opt. 27, 279 (1988).
10. G. H. B. Thompson, "Physics of Semiconductor Laser Devices", Wiley, 1980.
11. G. P. Agrawal and N.K. Dutta, "Long Wavelength Semiconductor Lasers", Van Nostrand Reinhold, 1986.

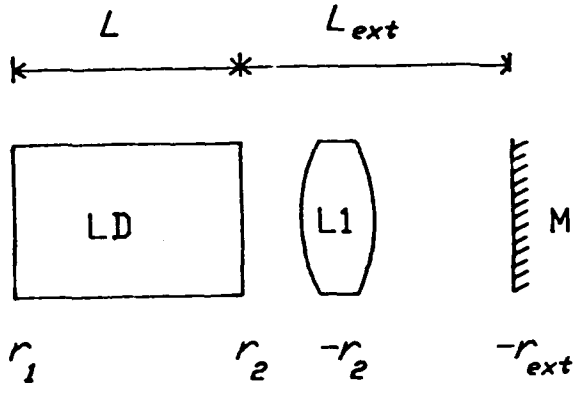

Figure 1. External cavity laser

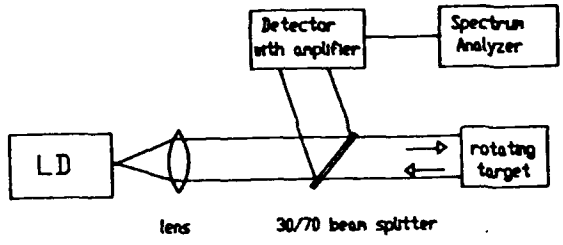

Figure 2. Experimental arrangement for velocity measurements

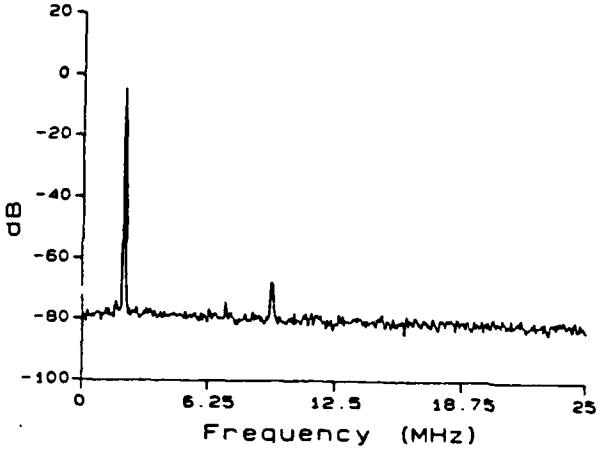

Figure 3. Spectrum analyzer output for a velocity of 2.93 m/s

1991 OSA DIGEST ON OPTICAL COMPUTING

Binary Arithmetic Using Optical Symbolic Substitution and Cascadable Surface-Emitting Laser Logic Devices

Julian Cheng

University of New Mexico[†], *Center for High Technology Materials, Albuquerque, NM 87131*
Voice: (505) 277-5605, FAX: (505) 277-6433

G. R. Olbright and R. P. Bryan

Sandia National Laboratories[††], *Albuquerque, NM 87185*

In this paper, we describe the design and operation of optical logic gates based on heterojunction phototransistor (HPT) and vertical-cavity surface-emitting laser (VCSEL) structures. We call the HPT/VCSEL structure a surface-emitting laser logic device. These structures will find use in optical communication systems as well as in parallel optical computing architectures. We illustrate complete sets of optical logic functions, upon which arithmetical logic units (ALU) are based, and provide specific examples of binary arithmetic operations based on optical symbolic substitution.

Two-dimensional surface-normal optical switching architectures represent potentially very compact, high throughput, parallel processors that are free from the effects of electromagnetic interference. These systems require the development of high speed photonic switches that are compatible with a surface-normal architecture, and which can provide high optical gain and contrast, and operate with low optical input energies. Direct optical addressing is particularly desirable since the electrical addressing of large matrices of active devices necessarily entails the added complexity of matrix-scanning and time-multiplexing. The switching elements should not be excessively sensitive to temperature variations, external optical feedback, or polarization diversity. Optical switches based on the integration of a HPT or pnpn devices with a VCSEL meet many of these requirements. Here, a single device provides electronic amplification, optical gain, switching, control and logic with little or no electronic intermediary. It eliminates the need for an additional external optical source or an optical bias beam. By varying the degree of positive optical or electrical feedback between the VCSEL and HPT, these structures can function alternatively as an optical amplifier, an optical switch, or a bistable logic or memory device.

Photothyristor-controlled switching of electroluminescence has been demonstrated by NEC[1] and Mitsubishi,[2] using arrays of integrated AlGaAs/GaAs p-n-p-n HPT/LED structures called the VSTEP (vertical to surface transmission electrophotonic array), which demonstrated optical switching of LED-like power levels at data rates in excess of 100 MB/s. However, LED-based structures are inefficient devices with high drive current, low optical output, and little or no optical gain. Moreover, the LED electroluminescence is not collimated but Lambertian, which gives rise to serious optical crosstalk problems that become intractable for a densely-packed array in a free-space optical system. A VCSEL, on the other hand, has very low beam divergence, much higher radiative efficiency, and is capable of providing high optical gain and contrast[3]. VCSELs exhibiting low-threshold current and high differential quantum efficiency have been demonstrated[4], using proton-implant current isolation and planar vertical-injection device structures.

Complete optical logic functions such as inversion, AND, NAND, OR, NOR, and exclusive XOR, etc., can be realized using simple combinations of phototransistors or photothyristors and lasers. The principle of operation of the optical OR and AND gates are shown in Fig. 1, while actual demonstrations of these logic operations are shown in Fig. 2, which displays the input and output optical pulse sequences. In the dark, the phototransistors are in the OFF-state, which exhibits a high bias voltage and low collector current. When the optical input is sufficiently strong, and the HPT gain is sufficiently high, the collector current exceeds the threshold of the VCSEL. The HPT goes into a low bias voltage, high conductance ON-state and switches on the VCSEL. If multiple optical inputs, each of sufficient intensity to switch on the VCSEL, are incident on the HPT, then an

Optical Computing and Processing, 1991, volume 1, number 3, pages 189–197

Parallel optical architecture for binary arithmetic using integrated arrays of phototransistor–surface emitting laser logic gates

JULIAN CHENG†

We outline a simple, compact, parallel optical architecture for performing binary addition using optical symbolic substitution and an integrated array of multi-function optical logic gates based on heterojunction phototransistors (HPTs) and vertical-cavity surface-emitting lasers (VCSELs). An adder design leveraging on opto-electronic integration is presented, in which the component count, the optical packaging, the number of optical alignments and free space propagation have all been simplified or reduced to a minimum. Cascadable optical logic functions AND, OR and XOR are demonstrated using HPT/VCSEL logic gates, as are latching logic functions using pnpn/VCSEL structures.

1. Introduction

Two-dimensional surface-normal optical switching architectures represent potentially very compact, very high information throughput, parallel processors that are free from the effects of electromagnetic interference. By allowing direct parallel optical access via the third dimension, large arrays can be addressed in real time, rather than time-multiplexed, thus relaxing the input–output bottleneck. These processor arrays may serve as the building blocks for a more general optical network, e.g. as parts of a parallel pipeline in which successive processors are cascaded and optically interconnected. To provide for multiple fanout, optical gain at each stage is highly desirable. Each processor array thus consists of high speed, surface-normal photonic switches that operate with low input optical energies, and provide high optical gain and contrast. To be practical, they should also be integrable, cascadable, optically-addressable, and their outputs reconfigurable. Direct optical addressing is particularly important since the electrical addressing of large matrices of active devices necessarily entails the added complexity of matrix-scanning and time-multiplexing, with the resultant loss of real-time parallelism. Moreover, the switching elements must not be excessively sensitive to temperature variations, external optical feedback, or polarization variations.

Optical switches based on the integration of heterojunction phototransistors (HPTs) or p–n–p–n devices with a vertical cavity surface-emitting laser (VCSEL) meet many of these requirements [1, 2]. Here, a single device provides electronic amplification as well as optical gain, switching, control and logic without an electronic intermediary. Such devices eliminate the need for an additional external optical source or an optical bias beam, as is necessary for devices based on spatial light modulators (SLMs). By varying the degree of positive optical or electrical feedback between the VCSEL and HPT, these structures can function alternatively as an optical amplifier, an optical switch, or a bistable logic or memory device [1–3], which will find use in optical communication systems as well as in parallel optical computing architectures.

Phytothyristor-controlled switching of electroluminescence has been demonstrated at data rates in excess of $100\,\mathrm{MB\,s^{-1}}$ using arrays of integrated AlGaAs/GaAs p–n–p–n HPT/LED structures called the VSTEP [4, 5]. These LED-based structures are inefficient devices with high drive current, low optical output, and little or no optical gain [6]. Moreover, the

Received 29 April 1991.

Author's address: University of New Mexico, Center for High Technology Materials, Albuquerque, NM 87131, USA.

† Work supported in part by AFOSR and DARPA.

optical OR gate is obtained. To operate as an AND-gate, the intensity of each optical input must be such that they can collectively, but not individually, produce enough current gain to switch on the VCSEL. The AND and OR gates are sufficient to carry out binary addition, but all the other logic functions, including the exclusive OR (XOR), can be implemented using only a single logic level without cascading. Each logic gate contains a single phototransistor and a single VCSEL, except for the exclusive-OR gate, which is based on a symmetrical differential drive configuration.

Boolean logic recognizes a combination of input bits and outputs one bit. Symbolic substitution,[5] which is based on optical pattern transformations, recognizes not only a combination of bits but also their relative spatial configuration. Thus it recognizes an input symbol, i.e. an optical pattern of bits, and outputs another symbol, i.e. a new optical pattern of bits. Because of the added degree of freedom represented by the configurational information, it is well suited for the high speed, massively parallel processing of optical data. Not only are multiple patterns processed in parallel, the logical functions can sometimes be repeatedly sequenced in parallel. We will illustrate this with the example of a two-dimensional binary half-adder, using a two-dimensional array of phototransistor/VCSEL or photothyristor/VCSEL logic gates.

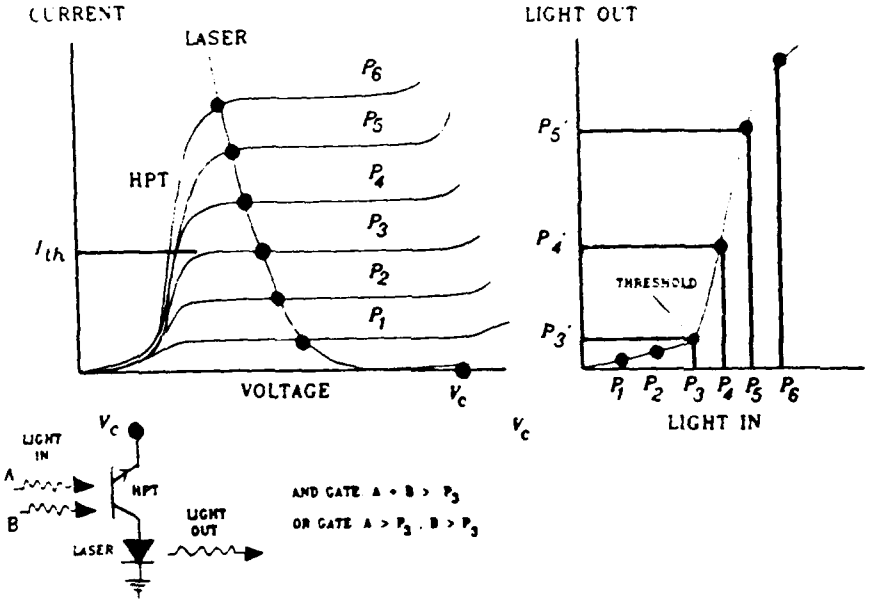

Fig. 1. Non-latching optical AND (a) and OR (b) logic gates based on a phototransistor and a vertical-cavity surface-emitting laser, and their operating principles.

Binary addition involves the SUM and CARRY operations and can be simulated using only AND- and OR-gates (but this would require complementary optical inputs). It is simpler to simulate these optically using the exclusive OR (XOR) logic function. The SUM is implemented with an XOR-gate, and the CARRY with an AND-gate. Using symbolic substitution, the states 0 and 1 are represented by symbols, i.e. by a VCSEL in the ON-state or OFF-state. To implement binary addition, the inputs consist of two N-bit words, i.e. two linear arrays of N symbols (optical inputs A and B) arranged as parallel rows of optical bits (Fig. 3). The addition algorithm consists of a set of rules, which prescribe the pattern shifts and transformations that similate the SUM (XOR) and CARRY (AND) operations (see Fig. 4). The result of adding bits A and B is to produce new symbols, in which the top half contains a left-shifted symbol representing the CARRY-bit, while the bottom contains a right-shifted symbol representing the SUM-bit. The SUM bit is 1 only if A or B is 1 (i.e. A XOR B), while the CARRY-bit is 1 only if A and B are both 1 (i.e. A AND B).

The optical "HALF-ADDER" hardware contains a two-dimensional array of optical switches enabled by an array of input optical signals incident on columns of photodetectors, which in turn are interleaved with columns of VCSELs that generate the optical output pattern. Each position in the array consists of two optical-logic gates, AND and XOR, each of which contains one or more

HBTs and VCSELs. The schematic layout for each element (bit) in a row of this N-bit ADDER is depicted in Fig. 3, which also illustrates the lateral spatial shift in the symbolic substitution scheme. The switched VCSEL outputs are shifted diagonally as shown to simulate the symbolic substitution.

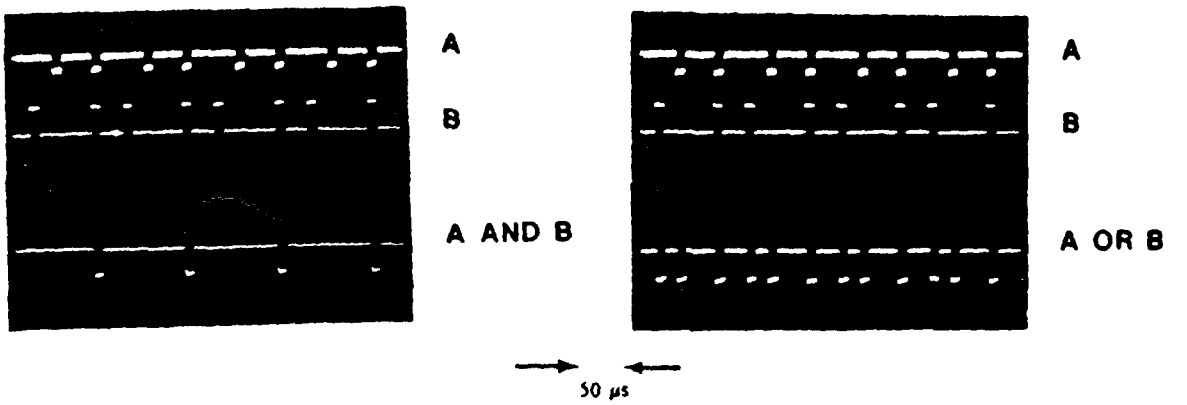

Fig. 2. Optical input and output pulse sequences for an optical AND- and an OR-gate. The VCSEL used in this experiment has an overall optical gain of > 20 and an on/off contrast of 34 dB.

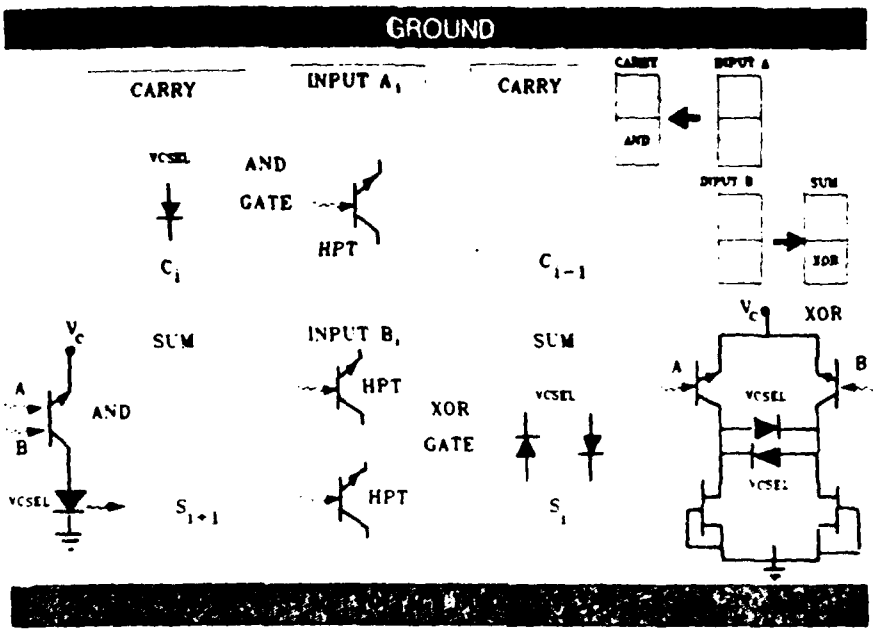

Fig. 3. The binary half-adder based on optical symbolic substitution and its implementation using HPT/VCSEL logic. The rows represent bits in a N-bit binary word. Each bit position contains an AND gate and an XOR gate, with two diagonally-staggered optical output VCSELs (SUM and CARRY).

We illustrate binary addition in Fig. 4. Each bit in the sum of A + B is replaced by the corresponding left and right-shifted CARRY and SUM bits (VCSEL outputs), thus replacing the original rows of A and B with new, spatially-shifted symbols representing rows of CARRY and SUM bits. These are fed into the next logic array to undergo another symbolic substitution cycle, thereby producing a new row of CARRY and SUM bits. These steps are repeated until there are no 1 bits left in the CARRY row.

The N-step symbolic substitution procedure can be achieved by cascading N HPT/VCSEL logic arrays, but it can also be done by cycling the output through the the logic array N times during a

complete arithmetic operation. The cycling of the 2-D optical signals is achieved with the optical scheme depicted in Fig. 4. However, this requires that the logic array be reset after each pass through the half-adder, while preserving the previously generated optical outputs as the inputs for the next pass. This sequence requires a latching pnpn/VCSEL array and an optical memory buffer array (see Fig. 4). The latter consists of a simple array of latching identity switches, i.e., photodetector/laser switches, in which optical input logic level of 1 (light on) switches the photodetectors and thus the VCSELs on. The outputs of the optical logic processor (S1) trigger the memory buffer array (S2), whose latched optical outputs "store" the switched optical data from the previous pass. Switching the bias voltage on and off clocks the logic unit, and initiates new passes through the processor, while S2 is then erased (reset) to store the next set of outputs from S1. A maximum of N passes are needed to complete an N-bit binary addition. Thus, using a 128 x 128 array cycling at a 10 ns clock rate, 128 pairs of 64-bit words can be added in parallel in less than 640 ns.

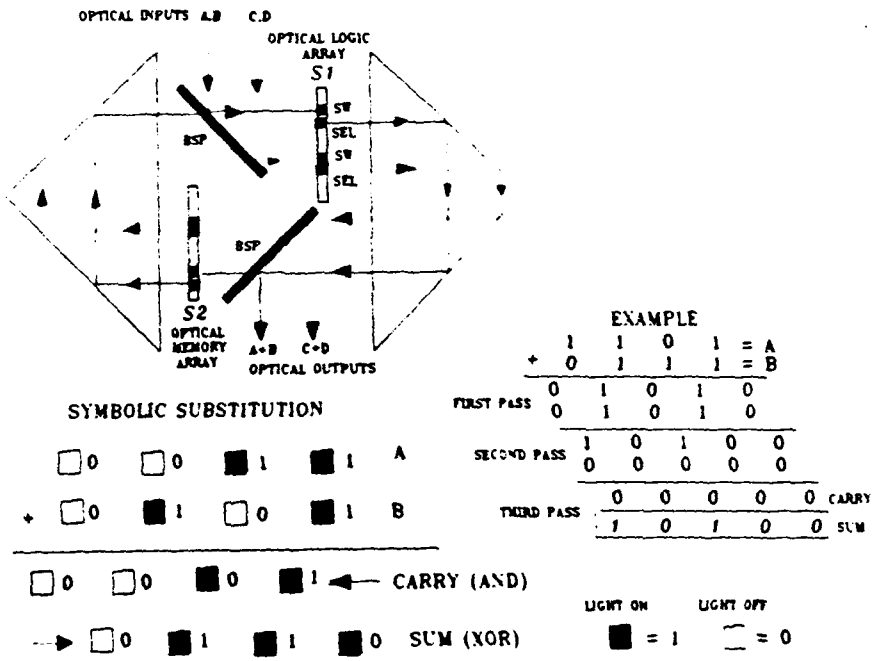

Fig. 4. The optical ALU hardware for a multi-pass binary half-adder, which includes a logic array and a memory array. Also shown are the rules for addition using symbolic substitution and an example of binary addition using the half-adder.

Here we have described binary addition using symbolic substitution and surface-emitting laser logic devices. The half-adder described above is simple, compact, and has a relatively low component count. Full adders, which would simultaneously take into account all CARRY operations, would speed up the ALU process time by a factor of N, (a single pass or clock period is required).

† UNM research is supported by AFOSR contract No. F49620-89-C-0028.

†† SNL research is supported by DOE contract No. DE-AC04-76DP00789.

1. Y. Tashiro, K. Kasahara, H. Hamao, M. Sugimoto, T. Yanase, Jpn. J. Appl. Phys. 26, L1014 (1987).
2. K. Hara, K. Mitsunaga, K. Kyuma, IEEE Photonic Technol. Letters 1, 370 (1989).
3. G. R. Olbright, K. Lear, J. L. Jewell and P. Esherick, Invention disclosure filed with Sandia Corporation, SD-4896, S-71 738 (Jan. 1990).
4. Y. H. Lee, B. Tell, K. Brown-Goebeler, J. L. Jewell, R. E. Leibenguth, M. T. Asom, G. Livescu, L. Luther, V. D. Materra, Electron. Lett. 26, 1308 (1990).

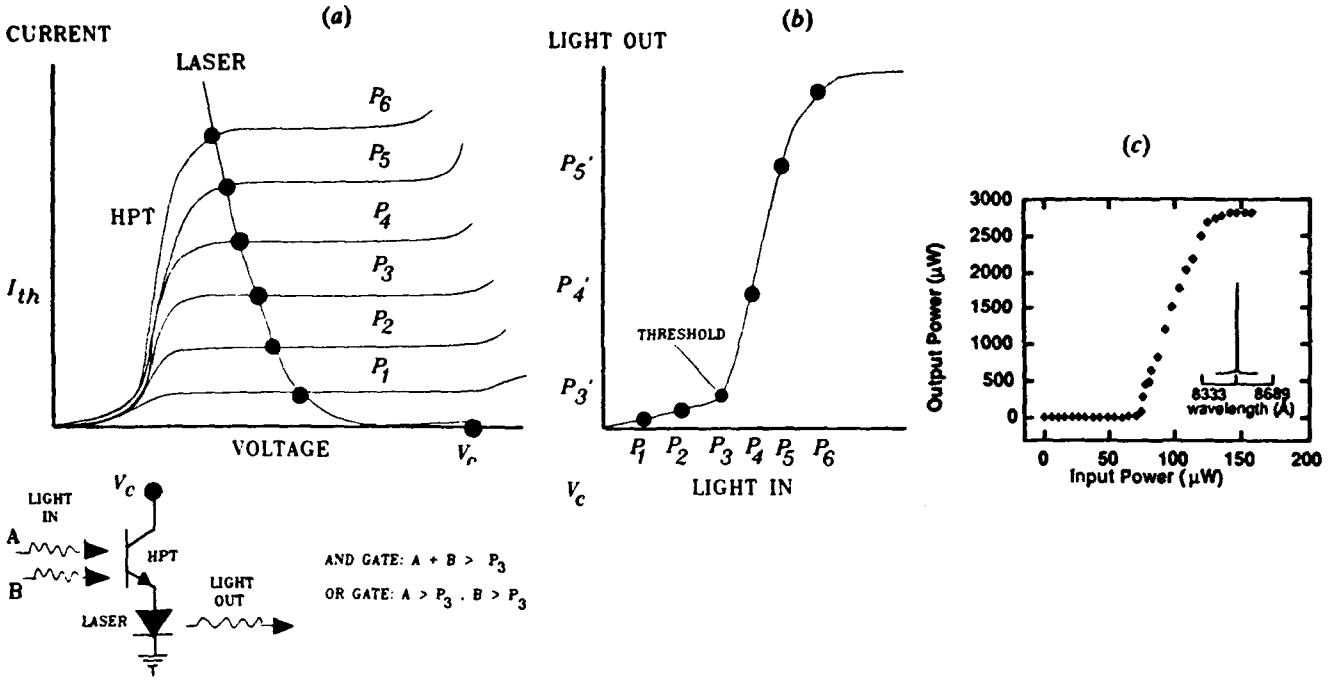

Figure 1. *(a)* **The operating principles of a thresholding optical switch based on the series combination of a heterojunction phototransistor and a vertical-cavity surface-emitting laser. *(b)* and *(c)* show the schematic and experimental thresholding optical transfer characteristics, respectively.**

Lambertian angular distribution of the LED electroluminescence gives rise to serious optical crosstalk that becomes intractable for a densely-packed array in a free-space optical system. A VCSEL, on the other hand, has very low beam divergence (gaussian far-field width of 8°) [7], much higher radiative efficiency (>1.5 mW c.w. output) [8], and when integrated with a HPT is capable of providing high optical gain (>20) and contrast (>34 dB) [2]. VCSELs exhibiting low-threshold current and high differential quantum efficiency have been fabricated [8], using proton-implant current isolation and planar, vertical-injection device structures.

In this paper, we outline a new parallel optical processing architecture based on the HBT/VCSEL optical switching technology. We will demonstrate the operation of optical logic functions, upon which optical arithmetic logic units (ALUs) are based. Specifically, we discuss the horizontal integration of multiple logic functions on a single chip to form a monolithic ALU, and demonstrate the logic gate designs that facilitate this integration. Based upon this, we will provide a specific example of an optical computing architecture for performing binary arithmetic using optical symbolic substitution [9].

Our objectives for the optical system design are to achieve compactness, minimize the optical and opto-electronic component count, reduce the complexity of bulk optical implementation, and maximize subsystem integration whenever feasible. The excessive dependence on complicated optical packaging [10] and on critical optical alignment are anathema to the design of practical and reliable switching systems. Free-space propagation should be reduced to a minimum to avoid the problems with timing skew, beam divergence and optical crosstalk. To achieve these goals, we discard the conventional approach of cascading sequential single-function logic arrays, taking advantage instead on the integrability of optoelectronics, i.e. by the horizontal integration of multiple logic functions on a single chip. Drastic reduction in hardware, along with the added benefits of simplified packaging and reduced optical alignment, can be achieved in repetitive operations by recycling the output data through a single processor. We will illustrate the embodiment of each of these goals below by the design of a compact binary adder.

2. *Optical logic and symbolic substitution*

The operating principles of a HPT/VCSEL optical logic switch are illustrated in figure 1, which shows the electrical characteristics of the two-terminal HPT and the VCSEL (figure 1 (*a*)). These devices are electrically connected in series, with the VCSEL serving as the load for the HPT. An optical input impinging on the HPT generates an optically-injected base current,

which is amplified by a high-gain HPT to provide a current source for the VCSEL. When the collector current exceeds the threshold of the VCSEL, the laser is switched on. The optical switching threshold is thus set by the current threshold of the laser, which determines the threshold-switching behaviour in the optical transfer characteristic (figure 1 *b*)). The design of the logic gates is described in [2] and the experimental results are shown in figure 1 (*c*).The achievable optical contrast, i.e. the difference between the spontaneous emission level below threshold and the high optical output at saturation, is quite high (34 dB). The overall gain achieved in the linear amplification region, i.e. between threshold and saturation, is greater than 20 (the maximum differential gain is 200), which allows a significant optical fan-out capability.

Complete optical logic functions such as inversion, AND, NAND, OR, NOR, and exclusive-OR (XOR), etc. can be realized using simple combinations of HPTs or photothyristors and lasers [2]. The designs of the AND, OR, and XOR logic gates, as well as the actual experimental demonstrations of their operation, are shown in figure 2, (figure 2 displays the input and output optical pulse sequences). In the dark, the phototransistors are in the OFF-state, which exhibits a high collector–emitter voltage and low collector current. When the optical input is sufficiently strong, the HPT exhibits a low collector–emitter voltage and a high collector current that exceeds the threshold of the VCSEL. If multiple optical inputs, each sufficiently intense to switch on the VCSEL, are incident on the HPT, then an optical OR-gate is obtained. To operate as an AND-gate, the intensity of each optical input must be such that they can collectively, but not individually, produce enough current gain to swtich on the VCSEL. Each logic gate, except for the XOR, contains a single phototransistor and a single VCSEL, and all the gates can be implemented as a single stage of optical logic without cascading.

The XOR gate, which produces an optical output (logic state 1) when an optical input is incident on only one of the two HPTs, requires a symmetrical configuration, which is shown in figure 2(*c*). The differential format allows the voltage at the point connecting the two HPTs, and thus the bias voltage across the two VCSELs, to go to nearly zero when both HPTs are in the ON-state (1,1) or the OFF-state (0,0), thus producing no optical output (logic 0). When only one HPT is optically switched on, i.e. in the (1,0) or (0,1) state, this voltage is shifted sufficiently in either the positive or negative direction to bias one of the two VCSELs above threshold, while reverse-biasing the other.

The HPT/VCSEL logic gates are non-latching in the absence of positive feedback. By providing optical or electrical feedback, it is possible to achieve latchable optical switching. This can be done, for example, by replacing the HPT with a pnpn photothyristor structure [3], which has built-in latching characteristics. The design and switching characteristics of a latchable pnpn/VCSEL switch are described in detail in [3]. Figure 3 (*a*) and (*b*) illustrate its switching and optical transfer characteristics, respectively, which show that an optical pulse of sufficient intensity can switch the photothyristor from its resistive-state into its conducting state, which then supplies enough current to drive the VCSEL above its lasing threshold. The VCSEL remains turned-on after the optical switching pulse has subsided, provided that a holding voltage remains to bias the VCSEL above its lasing threshold. Latching logic gates similar in design to the non-latching HPT/VCSEL gates have been made, two of which (AND or OR) are shown in figure 3 (*c*) and (*d*). As we will shown below, the complement of latching and non-latching optical logic gates greatly simplify the design of an optical binary adder.

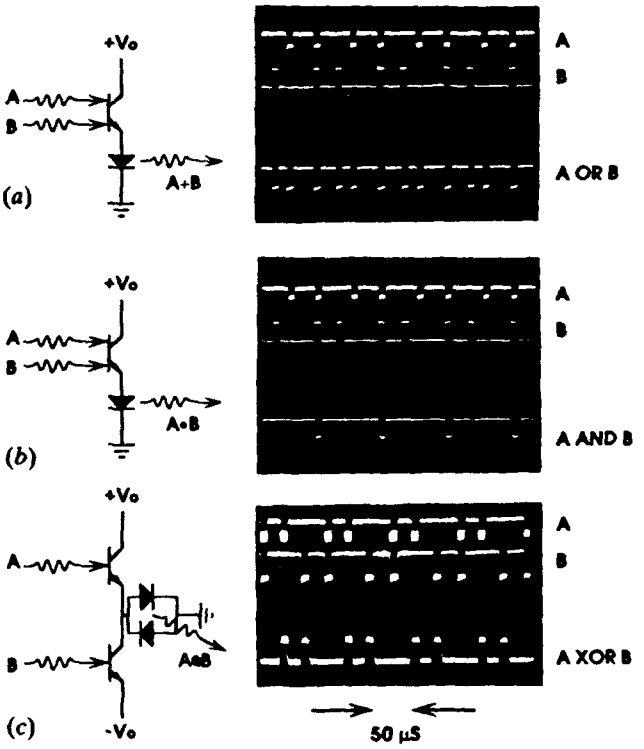

Figure 2. The structure and experimental demonstration of optical-logic gates (*a*) AND, (*b*) OR, and (*c*) XOR, based on HPT/VCSEL optical switches. The photographs illustrate the input and output optical pulses. Note that the baseline corresponds to the logic-0 state, while the 15 μs wide pulses (which appear inverted in some of the traces) correspond to the logic-1 state.

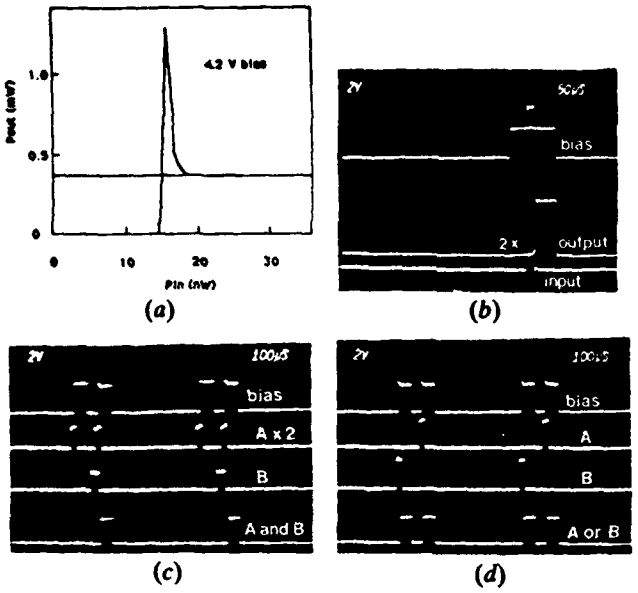

Figure 3. **(*a*) Optical transfer characteristic of a latching pnpn/VCSEL optical switch [3], showing threshold switching and latching. A constant optical output intensity is maintained without any holding power. (*b*) An input optical pulse switches on the VCSEL, which is latched until the bias voltage is reduced below a holding voltage. Optical AND gate (*c*) and NOR gate (*d*) operation are shown, with latching output characteristics.**

Optical logic operations can only be practical if there is a sufficient input signal dynamic range, so that moderate variations in input intensity can be tolerated. In general, the input optical signals can be pre-processed (digitized) by an array of simple optical switches, whose switching thresholds can provide binary input signal discrimination while regenerating more-or-less uniform optical signal outputs. Still, there remains a problem for those logic gates with additive inputs, such as AND and NAND, which is not applicable to those with non-additive inputs, such as OR, NOR, XOR, or INVERT. The optical switching threshold must be readjusted for these gates, which can be achieved by tuning the bias voltage to accommodate the desired range of input intensities. The abrupt optical transitions of latching optical switches at threshold also improve the input dynamic range.

3. Optical binary adder using symbolic substitution

In binary addition, the SUM and CARRY operations can be implemented using only the AND-gate and OR-gate, although this would necessitate the use of complementary optical inputs as well as cascaded multi-stage single-function logic chips. The use of cascaded multi-stage logic implies increased optical hardware and alignment, which can present formidable practical problems. These complications can be avoided by the monolithic integration of the AND and XOR logic functions on a single optoelectronic chip.

Traditional Boolean logic, such as AND and NOR, recognizes a combination of input bits and outputs one bit. Symbolic substitution recognizes not only a combination of bits but also their relative spatial configuration, and transforms the latter into a new pattern of bits. These spatial optical pattern transformations provide a flexible architecture for the shifting of digital data that is central to binary arithmetic. The optical output of each stage must convey not only the logic information, but the two-dimensional configurational information as well, which has been transformed by the rules of optical symbolic substitution into a format suitable for direct input (cascade) into the next logic array. Properly designed, these spatial transformations allow binary addition to take place by recycling the output optical data through a single logic array N times, resulting in a highly compact optical system with very significant reduction in hardware. We will illustrate this later with the example of a two-dimensional binary half-adder, using a two-dimensional array of HPT/VCSEL optical logic gates as described above [2].

In the symbolic substitution scheme, the states 0 and 1 are represented by optical symbols, i.e. by a VCSEL operating above threshold (ON-state) and below threshold (OFF-state), respectively. The inputs consist of two N-bit words, i.e. two linear arrays of N symbols (optical inputs A and B) arranged as parallel rows of optical bits. The addition algorithm consists of a set of rules (figure 4(a)), which prescribe the pattern shifts and transformations that implement the SUM (XOR) and CARRY (AND) operations. The result of adding bits of A and B is to produce new symbols, in which the top half contains a left-shifted symbol representing the CARRY-bit, while the bottom contains a right-shifted symbol representing the SUM-bit. The SUM bit is 1 only if A or B is 1 (i.e. A XOR B), while the CARRY-bit is 1 only if both A and B are 1 (i.e. A AND B). The shifting of both the SUM and CARRY bits is necessary because of the logic circuit design (figure 5), which requires the HPTs and VCSELs to be laterally displaced on the logic chip.

The optical 'ADDER' hardware contains a two-dimensional, integrated array of HPT/VCSEL optical switches (figure 5) enabled by two rows of input optical signals that are incident on columns of photodetectors (HPTs). The columns of HPTs are interleaved with columns of VCSELs that generate the optical outputs. Each position in the array consists of two of the optical-logic gates, AND and XOR, each of which contains two HPTs and one or more VCSELs (see figure 2). The

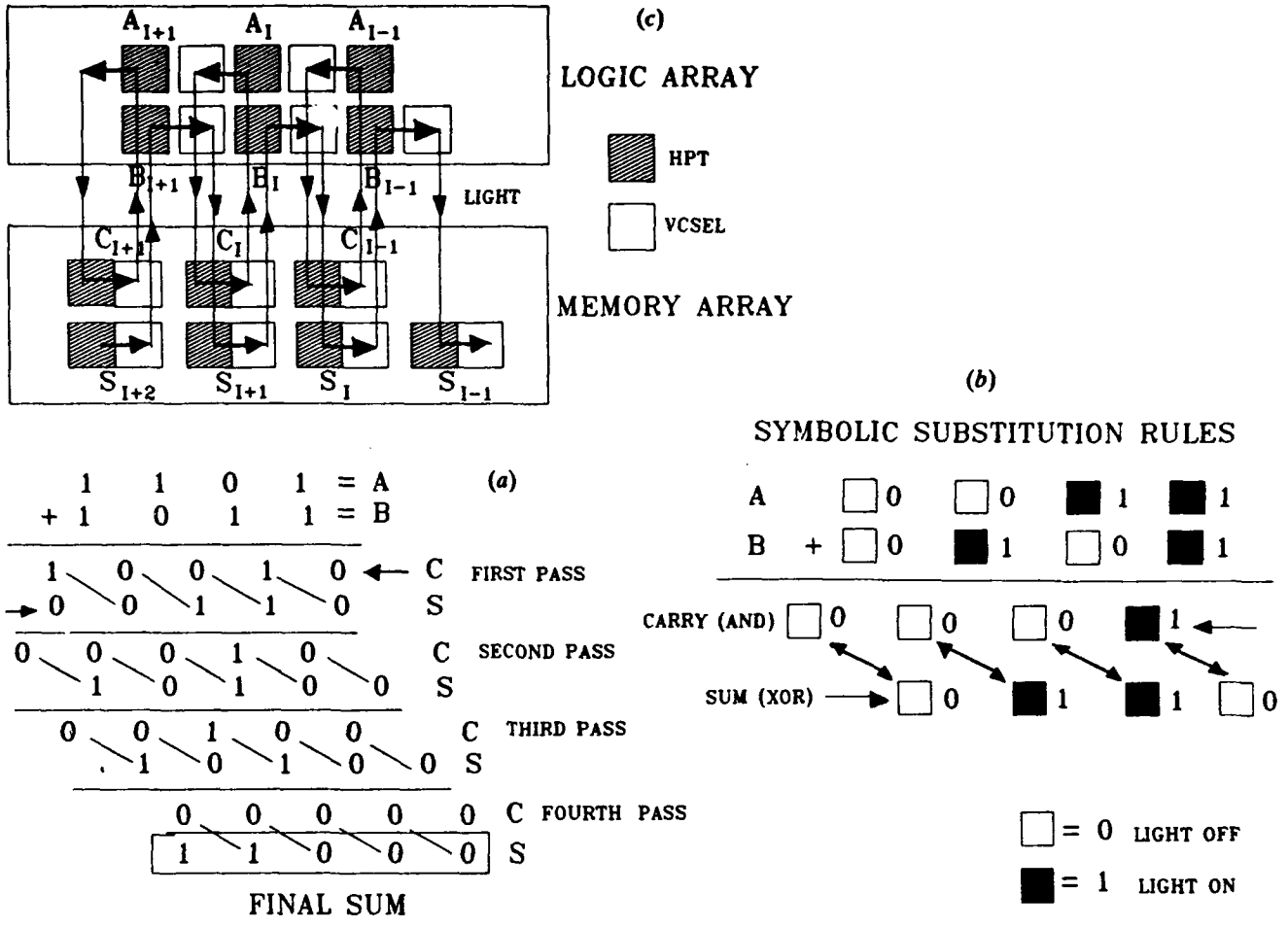

Figure 4. **(*a*) The rules of optical symbolic substitution for binary addition, illustrating the lateral spatial shifting of the CARRY and SUM bits, (*b*) example of the binary addition of two 4-bit words using a half-adder and symbolic substitution, which requires 4 cycles, and (*c*) schematic illustration of the bit configurations and their spatial transformations in the logic and memory arrays that enable the outputs to be optically folded (cascaded). The arrows describe the spatial shifts within the logic and memory arrays. The solid lines indicate the optical propagation paths of the CARRY and SUM bits between these two arrays.**

schematic layout for each element (bit) in a row of this *N*-bit ADDER is depicted in figure 5, which also illustrates the lateral spatial shifts of the CARRY bit with respect to the SUM bit by one significant digit in the symbolic substitution scheme. The *N*-bit optical inputs impinge on the HPTs on two adjacent rows of the array, whose elements are vertically aligned. The corresponding logically-switched laser outputs are shifted diagonally as shown to implement the symbolic substitution.

The binary addition of two 4-bit words using symbolic substitution is illustrated in figure 4 (*b*). Each bit in the sum of A and B is replaced by slightly left-shifted and right-shifted CARRY and SUM bits (VCSEL outputs). Thus after the first pass, the original inputs (A and B) are replaced by new, spatially-shifted symbols representing rows of CARRY and SUM bits. The addition of the *i*th bits of inputs A and B produce the *i*th output CARRY-bit, which is left-shifted to lie above the $(i+1)$th SUM-bit, while the *i*th SUM-bit is right-shifted to lie beneath the $(i-1)$th CARRY-bit (figure 4 (c) and figure 5). This ends one pass through the logic array. In principle, the two new rows of optical CARRY and SUM bits (VCSEL outputs) are then transmitted (cascaded) to another identical, space-invariant logic array to undergo the next symbolic substitution cycle, thereby producing new rows of CARRY and SUM bits. These steps are repeated *N* times until all the CARRY bits have been shifted from the least significant bit to the most significant bit, at which point the addition is complete. The sequential operation of the half-addition cycles is regulated by clock pulses, which enable successive logic arrays in the cascade after suitable turn-on delays that take into

account the various electronic turn-on and optical propagation delays, which could be less than a clock period.

4. Optically-folded implementation of the binary adder

Since the cascaded logic arrays are identical, great simplification can be achieved if the two-dimensional output optical signals are recirculated as inputs for the same logic array. This can be achieved with the simple optical scheme depicted in figure 6, which uses two 90° prism reflectors, plus two beamsplitters for optical input and output. It is necessary to resect the logic array after each pass through the half adder, while preserving the previously generated optical outputs as the inputs for the next pass. The array is reset by toggling the bias voltage on and off during each clock period. To preserve the previous data while providing enough of a propagation delay to accommodate the finite (reset) rise and fall times of the switches, an optical buffer memory array is required. The latter consists of two simple arrays of latching switches (i.e. latching photothyristor/VCSEL switches or latching HPT/VCSEL switches), in which an optical input logic level of 1 switches the HPT and thus the VCSEL to the ON-state. Two memory buffers are needed, one to provide optical inputs for the new passage through the adder, while the other is reset to accept the new optical output data. Different clock pulses alternately enable the memory buffers to accept and store data, or to reset them in preparation for new data. Alternatively, a latching photothyristor/VCSEL array can replace the HPT/VCSEL array, and only one memory buffer would be required. In this case, the outputs of the optical logic processor triggers the buffer memory array, whose latched optical outputs 'store' the switched optical data from the previous pass. Switching the bias voltage on and off clocks the logic unit, and initiates new passes through the processor, while the buffer is then erased (reset) to store the next set of outputs from the logic unit. The HPT/VCSEL devices can be operated in this latching configuration by allowing optical feedback between the VCSEL and HPT [10].

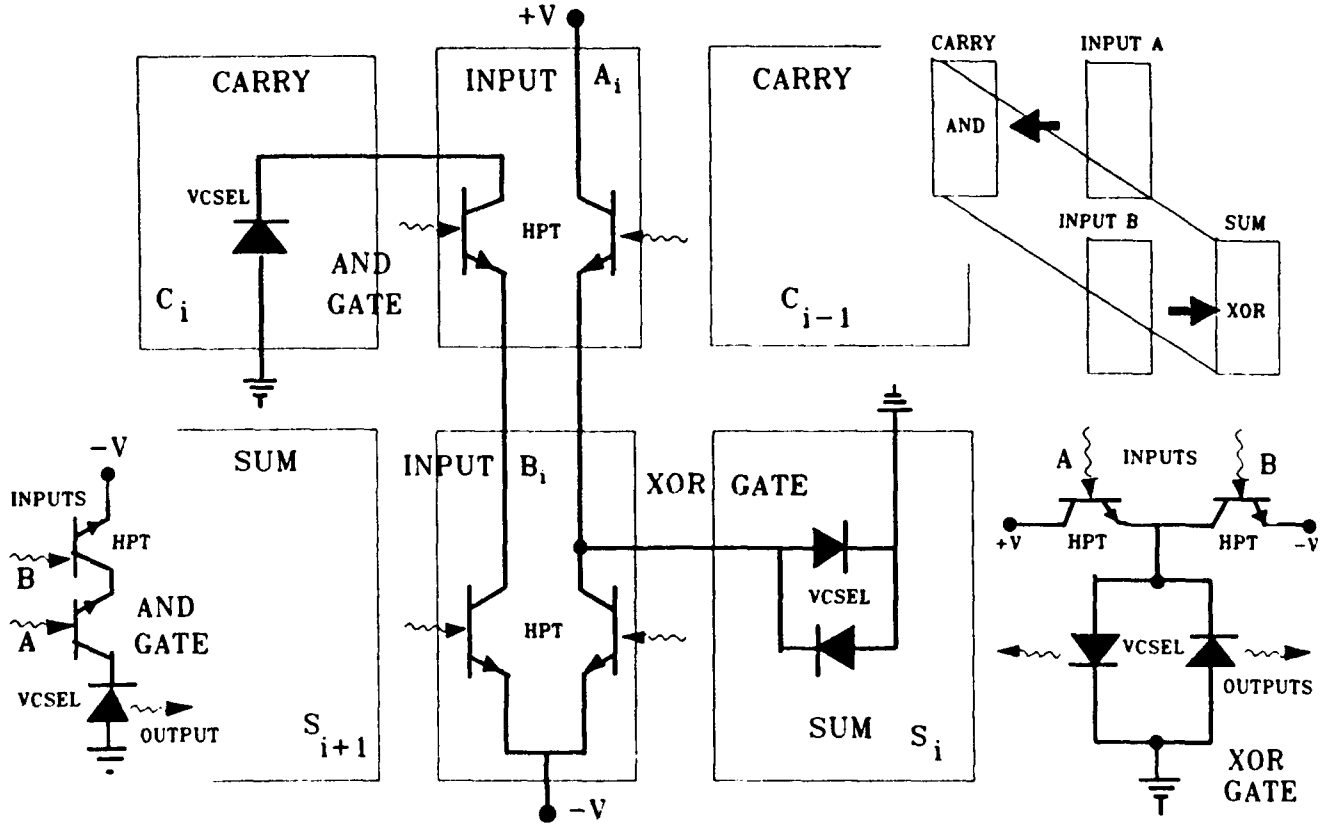

Figure 5. Schematic layout of a HPT/VCSEL logic array designed for binary addition using the symbolic substitution architecture. Each bit (column) consists of a single AND-gate (CARRY) and a single XOR-gate (SUM). The positions of the HPTs and VCSELs illustrate the implementation of the input-to-output configuration transformations.

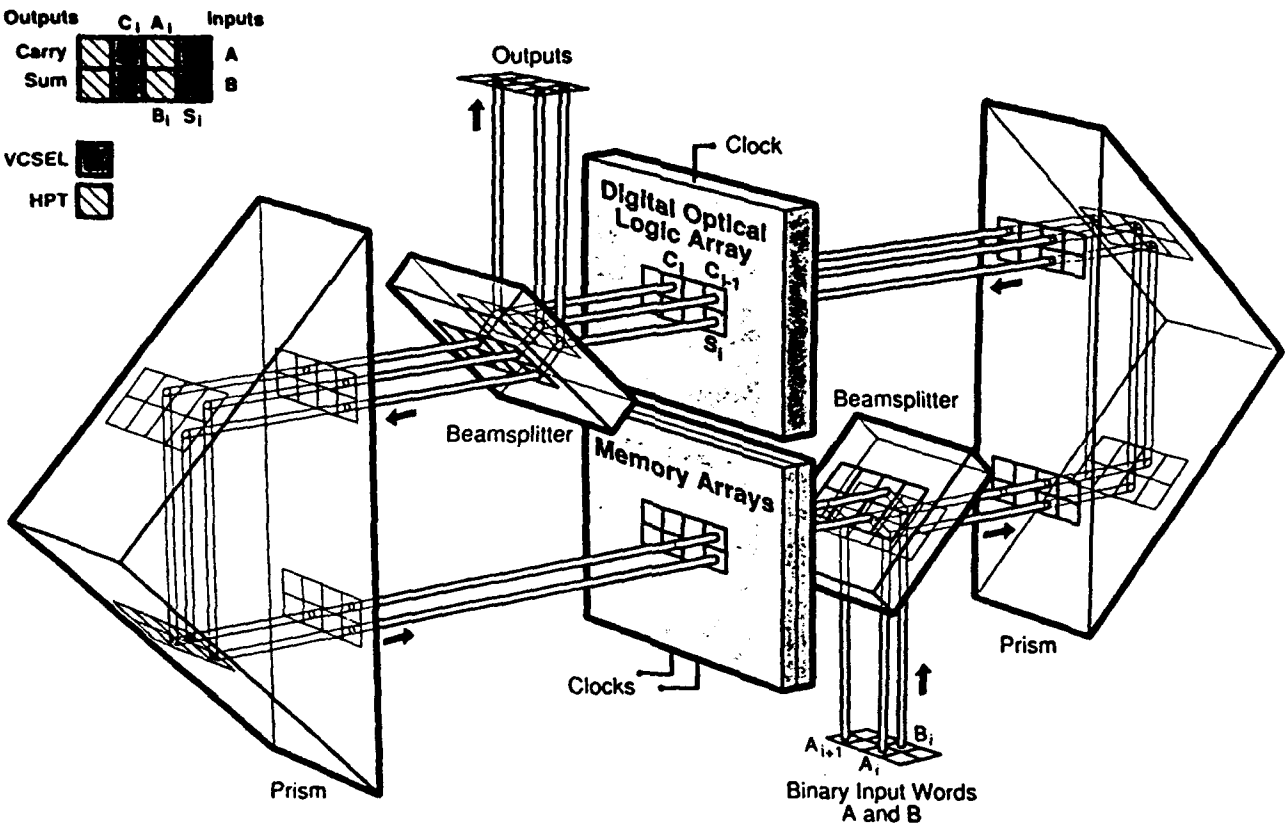

Figure 6. A three-dimensional view of the recirculating binary half-adder showing the optical pattern transformations that allow the previous optical output data to be folded back (recirculated) as the inputs of a single logic array. Optical memory buffers are used to store the previous data. Clock pulses regulate the generation, transfer, and storage of data during successive cycles.

Figure 6 illustrates the manner in which optical symbolic substitution reconfigures the logic outputs to permit the SUM and CARRY (VCSEL) outputs to optically fold back and impinge upon the proper columns of HPTs in the logic array. This is shown more succinctly in the alignment diagram in figure 4(c), which illustrates the bit alignments and the spatial reconfigurations that take place within the logic and memory arrays. The arrows indicate the spatial displacements of the optical outputs (VCSELs) relative to the optical inputs (HPTs) within the logic array, while the lines indicate the propagation paths of light between the logic processor and memory units. The shifts in the memory array compensate the shifts in the logic array to enable the optical folding.

5. A compact optically-integrated binary adder

This optical-folding scheme can be further integrated and simplified into a highly compact form, using a single beamsplitter, an optical logic chip and an optical memory chip, as shown in figure 7. Each of these chips is mounted on a heat sink, and all the optical inputs and outputs are located at the front (epi) surface. The chips are placed on two opposing facets of a beamsplitter cube. A two-dimensional array of encoded, polarized optical input beams are incident on the cube from an orthogonal direction, and are deflected towards the logic chip, where they impinge upon columns of HPTs to provide optical inputs for the first pass of the binary addition process. This chip executes the optical logic functions and the symbolic substitution shifts. The optical outputs provided by the VCSELs then propagate across the cube towards the appropriate HPT inputs on the memory chip, which contains an array of latching, VCSEL-based optical switches. The latched optical switches preserve the output data as inputs for the next cycle, while the logic chip is reset (power disabled) for the next pass, thus competing the first cycle in the binary addition process.

When the logic chip is empowered once again, the outputs of the VCSELs on the memory chip initiate the next round of logic/shift operations. However, the

memory chip must now undergo a similar reset operation (power disabled) in preparation for the reception of new output data from the logic array. This can only occur if the logic array itself is latching, or at least that it possesses sufficient persistence to preserve the newly-switched optical outputs while the memory array is reset. The latching, or persistence, can be achieved by the use of p–n–p–n photothyristor logic gates [10]. Thus successive stages of the N-bit binary addition are regulated by clock signals that alternately disable and then re-enable the power to each chip, with a suitably-chosen temporal delay that permits each chip to be reset after each stage while preserving the output data from the previous cycle. The optical data 'toggles' back and forth between the two chips in response to these clock pulses. The polarizing beamsplitter cube splits off a part of the optical output beam power, which emerges from the facet opposite to the input port. This provides real-time optical signals that represent the output data during each stage of the N-pass binary addition process.

The propagation distance of the optical signals is limited to the width of the beamsplitter cube, and is not cumulative since the signals are regenerated during each pass. For high density arrays, a microlens array may be needed to avoid optical crosstalk due to a small but finite beam divergence. The advantages of this scheme are the high degree of compactness, the drastic reduction of both optical and electronic hardware, and the minimization of free-space propagation and optical alignment. Architectural simplicity has been achieved at the expense of chip complexity, which is a much more tractable problem.

6. Summary

In conclusion, we have described the parallel execution of binary arithmetic in real-time using HPT/VCSEL optical-logic gates and an architecture based on optical symbolic substitution. The implementation of this technology has been illustrated by the example of a highly-compact binary half-adder. Experimental demonstration of the latching and non-latching optical logic functions have been achieved, and thus all the basic building blocks of this parallel optical architecture have been realized. Monolithic integration of these logic gate arrays and the proposed binary adder is in progress.

In the compact binary adder design, optoelectronic component count (2 chips with microlens arrays), optical component count (1 beamsplitter), optical alignment (a single alignment of the two chips), and free space propagation (one pass) have all been reduced to a minimum. More importantly, the real-time parallelism and compactness of optics have been exploited to good advantage. In this simplified architecture, we have utilized optics only at its strengths (parallelism and compactness), while leveraging the rest on optoelectronic integration with almost no electronic

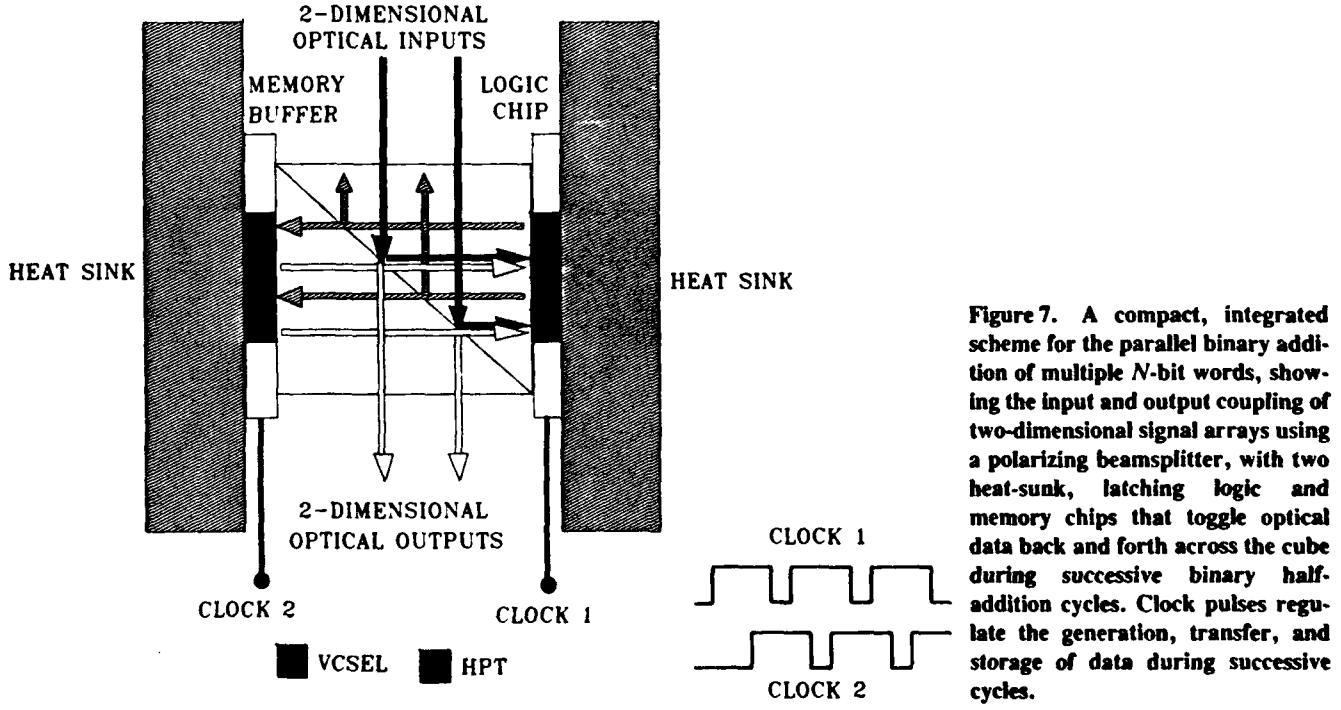

Figure 7. A compact, integrated scheme for the parallel binary addition of multiple N-bit words, showing the input and output coupling of two-dimensional signal arrays using a polarizing beamsplitter, with two heat-sunk, latching logic and memory chips that toggle optical data back and forth across the cube during successive binary half-addition cycles. Clock pulses regulate the generation, transfer, and storage of data during successive cycles.

intermediary. With a spatial period of 100 μm, a single 128 × 128 logic array (0·5" × 0·5") cycling at a 5 ns clock rate can add 128 pairs of 64-bit words in parallel within 320 ns (384 million fixed point operations per second). With larger chips (1 sq. in.) and smaller components, 1–2 billion operations per second should be feasible. Using the present-generation switches operating at 10 V, 2 mA and 50% duty cycle, or 10 mW per switch, a manageable thermal flux of 10^2 W cm^{-2} will be generated. The clock rate is presently limited by the unlatching time requirement of the buffer memory arrays.

References

[1] Olbright, G. R., Bryan, R. P., Lear, K. L., Brennan, T. M., Lee, Y. H., and Jewell, J. L., 1991, *Electron. Lett.*, **27**, 216.

[2] Bryan, R. P., Olbright, G. R., and Cheng, J., 1991, *Electron. Lett.* **27**, 893.

[3] Zhou, P., Cheng, J., Schaus, C. F., Sun, S. Z., Hains, C., Zheng, K., Myers, D. R., and Vawter, G. A., *IEEE Photonics Technol. Lett.* **3**(11) (to appear).

[4] Tashiro, Y., Kasahara, K., Hamao, H., Sugimoto, M., Yanase, T., 1987, *Jpn. J. Appl. Phys.*, **26**, L1014.

[5] Hara, K., Mitsunaga, K., and Kyuma, K., 1989, *IEEE Photonic Technol. Lett.*, **1**, 370.

[6] Ogura, I., Tashiro, Y., Kawai, S., Yamada, K., Sugimoto, M., Kubota, K., and Kasahara, K., 1990, *Appl. Phys. Lett.*, **57**, 540.

[7] Tai, K., Hasnain, G., Wynn, J. D., Fischer, R. J., Wang, Y. H., Weir, B., Gamelin, J., and Cho, A. Y., 1990, *Electron. Lett.*, **26**, 1628.

[8] Lee, Y. H., Tell, B., Brown-Goebeler, K., Jewell, J. L., Leibenguth, R. E., Asom, M. T., Livescu, G., Luther, L., and Materra, V. D., 1990, *Electron. Lett.*, **26**, 1308.

[9] Huang, A., 1983, in *Technical Digest, IEEE Tenth International Optical Computing Conference*, pp. 13–17.

[10] Cloonan, T., Herron, M. J., Tooley, F. A. C. P., Richard, G. W., McCormick, F. B., Kerbis, E., Brubaker, J. L., and Lentine, A. L., 1990, *IEEE Photonics Technol. Lett.*, **2**, 438.

Binary arithmetic using optical symbolic substitution and integrated phototransistor surface-emitting laser logic

Julian Cheng, G. R. Olbright, and R. P. Bryan

J. Cheng is with the Center for High Technology, University of New Mexico, Albuquerque, New Mexico 87131. G. R. Olbright and R. P. Bryan are with the Sandia National Laboratories, Albuquerque, New Mexico 87185.

Received 14 January 1991.
0003-6935/91/250001-03$05.00/0.

© 1991 Optical Society of America.

We outline an architecture for performing binary addition by using optical symbolic substitution and optical logic gates based on heterojunction phototransistors and vertical-cavity surface-emitting lasers.

Two-dimensional optical switching architectures represent potentially compact, high-information-throughput, parallel processors that will be found useful in optical communication and optical computing systems. These systems require the development of high-speed photonic switches that are compatible with a surface-normal architecture, provide high optical gain and contrast, and operate with low input optical energies. Direct optical addressing is particularly important because the electrical addressing of large matrices of active devices entails the added complexity of matrix scanning and time multiplexing. Moreover, the switching elements must not be excessively sensitive to external optical feedback or to temperature and polarization variations. Optical switches based on the integration of heterojunction phototransistors (HPT's) or p-n-p-n devices with a vertical-cavity surface-emitting laser (VCSEL) meet many of these requirements.[1] Here, a single device provides electronic amplification as well as optical gain, switching, control, and logic without an electronic intermediary. Such devices eliminate the need for an additional external optical source or an optical bias beam, as is necessary for light-modulator-based devices. In this paper we describe the design and demonstration of HPT/VCSEL optical logic gates and outline the horizontal integration of multiple logic functions on a single chip to form a monolithic arithmetic logic unit. Based on this, we provide a specific example of an optical computing architecture for performing binary arithmetic by using optical symbolic substitution.[2]

Photothyristor-controlled switching of electroluminescence has been demonstrated at data rates in excess of 100 MB/s by using arrays of integrated AlGaAs/GaAs p-n-p-n HPT/light-emitting diode (LED) structures called the VSTEP.[3,4] These LED-based structures are inefficient devices with high drive current, low optical output, and little or no optical gain.[5] Moreover, the LED electroluminescence is not collimated but is Lambertian, which gives rise to serious optical cross talk that becomes intractable for a densely packed array in a free-space optical system. A VCSEL on the other hand has low beam divergence [Gaussian far-field width of 8°, (Ref. 6)] and a much higher radiative efficiency (> 1.5 mW cw output),[7] and, when integrated with a HPT, is capable of providing high optical gain (> 20) and contrast (> 34 dB).[8] VCSEL's exhibiting low-threshold current and high-differential quantum efficiency have been fabricated[9] by using proton-implant current isolation and planar, vertical-injection device structures.

Complete optical logic functions, such as inversion, AND, NAND, OR, NOR, and exclusive-OR (XOR), can be realized by using simple combinations of HPT's or photothyristors and lasers. The designs of the AND, OR, and XOR logic gates, as well as the actual experimental demonstrations of their operations, are shown in Fig. 1. In the dark, the HPT's are in the off state, which exhibits a high collector–emitter voltage and low collector current. When the optical input is sufficiently strong, the HPT exhibits a low collector–emitter voltage and a high collector current that exceeds the threshold of the VCSEL. If multiple optical inputs, each sufficiently intense to switch on the VCSEL, are incident upon the HPT, then an optical OR gate is obtained. For AND gate operation, the intensity of each optical input must be such that the inputs can collectively, but not individually, produce enough current gain to switch on the VCSEL. Each logic gate, except the XOR, contains a single HPT and a single VCSEL, and all the gates can be implemented as a single stage of optical logic without cascading.

Binary addition can be implemented by using only the AND and OR gates, although this would necessitate the use of complementary optical inputs and cascaded multistage single-function logic chips, with the attendant problems of increased optical hardware and alignment These complications are avoided by the monolithic integration of AND and XOR logic functions on a single wafer. The XOR gate (Fig. 1), which produces an optical output (logic state 1) when an optical input is incident upon only one of the two HPT's, requires a symmetrical configuration, which is shown in Fig. 1(c). The differential format allows the voltage at the point connecting the two HPT's, and thus the bias voltage across the two VCSEL's, to go to nearly zero when both HPT's are in the ON-state (1, 1) or the off state (0, 0), thus producing no optical output (logic 0). When only one HPT is optically switched on, that is, in the (1, 0) or the (0, 1) state, this voltage is shifted sufficiently in either the positive or the negative direction to bias one of the two VCSEL's above threshold, while reverse biasing the other.

Traditional Boolean logic recognizes a combination of input bits and outputs one bit. Symbolic substitution recognizes not only a combination of bits but also their relative spatial configuration and transforms the latter into a new pattern of output bits. These spatial transformations provide a flexible architecture for the shifting of digital data, which is central to binary arithmetic. The optical outputs of each stage convey logic as well as configurational information, which has been transformed by the rules of optical symbolic substitution into a format suitable for direct input into the next logic array. Properly designed these spatial transformations enable binary addition to occur by recycling the output optical data through a single logic array N times, resulting in a highly compact optical system with significant reduction in hardware. We illustrate this with the example of a binary half-adder, using a two-dimensional array of HPT/VCSEL optical logic gates as described above.[2]

The logic states 0 and 1 are represented by a VCSEL operating above threshold (on-state) and below threshold (off-state), respectively. The inputs are two N-bit words (A and B) arranged as parallel rows of optical bits that impinge upon the HPT's at two adjacent rows of the array, whose elements are vertically aligned in a column. These are in turn interleaved with columns of VCSEL's that generate the optical outputs (Fig. 2). Each position in the array consists of two optical logic gates, AND and XOR, each of which contains two HPT's and one or more VCSEL's (see Fig. 1). The addition algorithm consists of a set of rules [Fig. 3(A)], which prescribe the pattern shifts that implement the SUM (XOR) and CARRY (AND) operations. The result

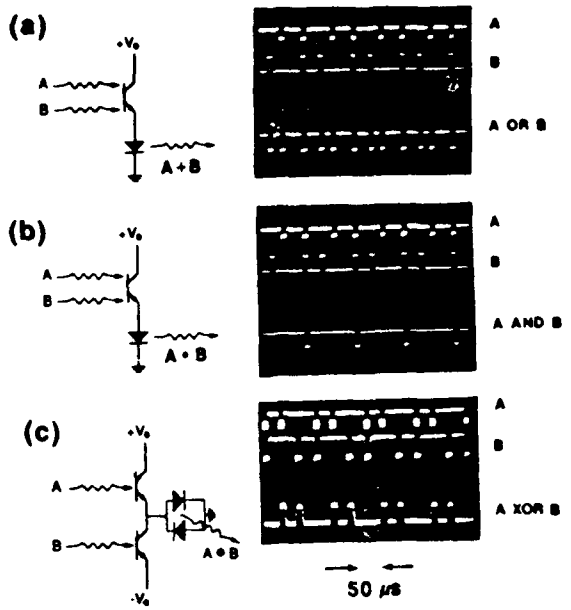

Fig. 1. Optical logic gates (a) AND, (b) OR, and (c) XOR, based on HPT/VCSEL optical switches. The photographs illustrate the input and output optical pulses.

of adding each bit of A and B is to produce new symbols, in which the top half contains a left-shifted symbol representing the CARRY bit, whereas the bottom contains a right-shifted symbol representing SUM bit. The addition of the ith bits of inputs A and B produces the ith output CARRY bit, which is left-shifted to lie above the $(i+1)$th SUM bit, whereas the ith SUM bit is right shifted to lie beneath the $(i-1)$th CARRY bit [Figs. 2-3(C)]. The SUM bit is 1 only if A or B is 1 (i.e., A XOR B), whereas the CARRY bit is 1 only if both A and B are 1 (i.e., A AND B). The shifting of each of the SUM and CARRY bits by one significant digit is an essential part of the binary addition process.

The binary addition of two 4-bit words with symbolic substitution is illustrated in Fig. 3(B). Each bit in the sum oa A and B is replaced by slightly left- and right-shifted

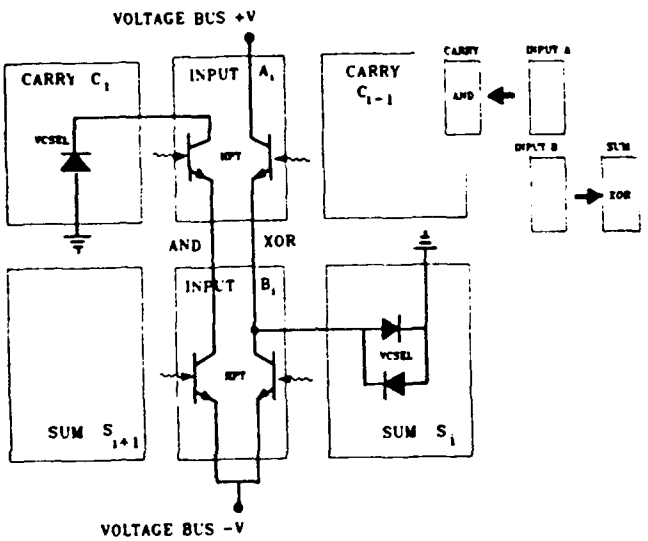

Fig. 2. Layout of a HPT/VCSEL logic array for binary addition by using symbolic substitution, illustrating the input-to-output configuration transformations.

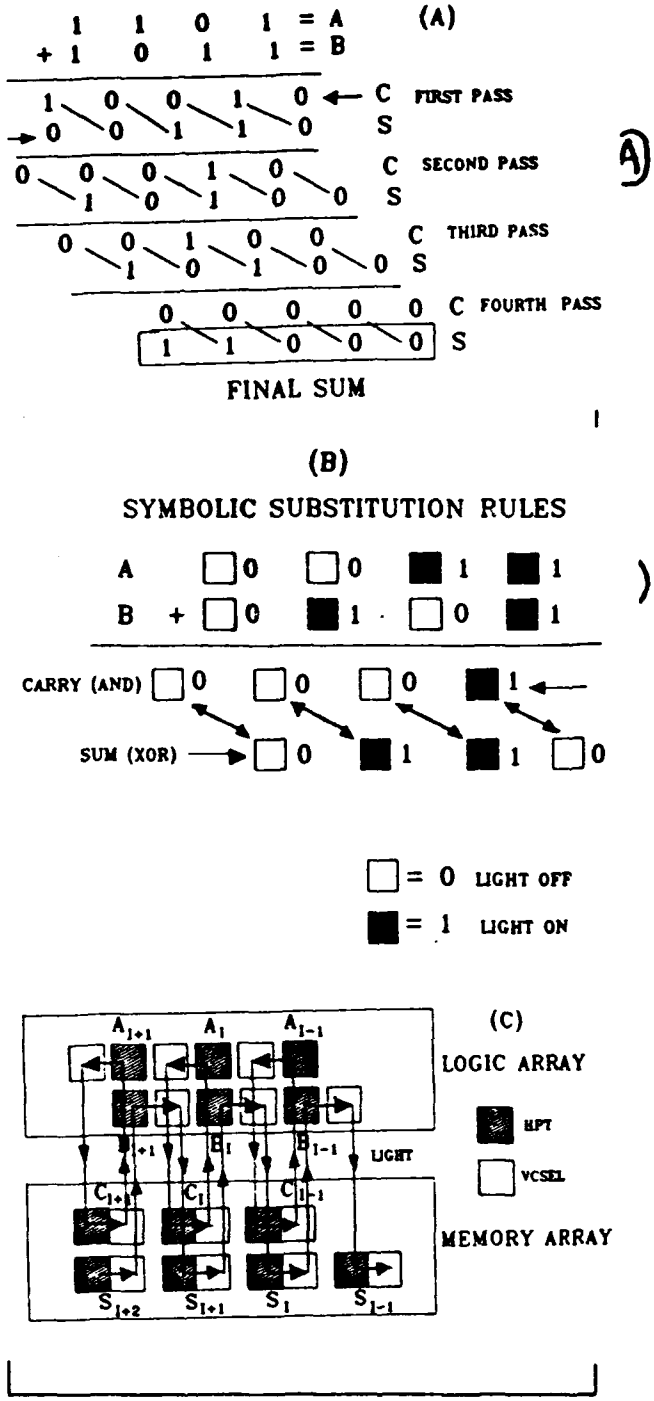

Fig. 3. (A) The rules of optical symbolic substitution, (B) binary addition of two 4-bit words using a half-adder, and (C) spatial transformations of the bit configurations in the logic and memory arrays that enable the outputs to be folded optically.

CARRY and SUM bits (VCSEL outputs). After each pass, the original inputs (A and B) are replaced by spatially shifted symbols representing new rows of CARRY and SUM bits, which are transmitted to the next (identical) logic array as inputs for the next pass. These steps are repeated N times until all the CARRY bits have been shifted to the most significant bit, at which point the addition is complete. The sequential operation of the half-addition cycles is regulated by clock pulses, which permit successive logic arrays in the cascade after suitable turn-on delays that take into account the various electronic turn-on and optical propagation delays, which could be less than a clock period.

Because the cascaded logic arrays are identical, great simplification can be achieved if the 2-dimensional output

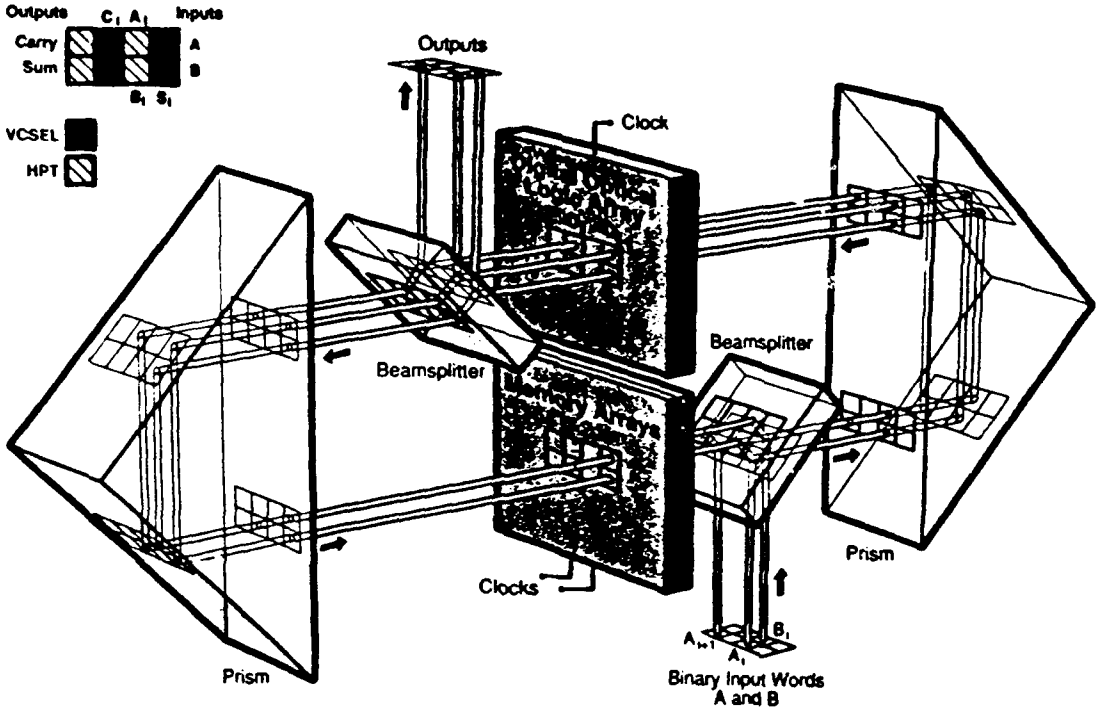

Fig. 4. Binary addition: Symbolic substitutions. A three-dimensional view of the recirculating binary half-adder.

optical signals are recirculated as new inputs for the same logic array. Figure 4 illustrates a simple scheme in which optical symbolic substitution reconfigures the logic outputs to permit the SUM and CARRY (VCSEL) outputs to fold back optically and impinge upon the proper columns of HPT's in a single logic array. Figure 3(C) shows more succinctly the bit alignments and spatial reconfigurations that take place within the logic and memory arrays. The arrows indicate the spatial displacements of the optical outputs (VCSEL's) relative to the optical inputs (HPT's) within the logic array, whereas the lines indicate the propagation paths of light between the logic processor and memory units. The shifts in the memory array compensate the shifts in the logic array to permit the optical folding.

This recycling scheme uses two 90° prism reflectors, plus two beam splitters for optical input and output. It is necessary to reset the logic array after each pass through the half-adder, while preserving the previously generated optical outputs as the inputs for the next pass. The logic array is reset by toggling the bias voltage on and off during each clock period. Preserving the previous data while providing enough of a propagation delay to accommodate the finite (reset) rise and fall times of the switches requires an optical buffer memory array. This consists of two simple arrays of latching HPT/VCSEL or p-n-p-n/VCSEL switches, in which an optical input logic level of 1 switches the HPT, and thus the VCSEL, to the on state. Two memory buffers are needed, one to provide optical inputs for the new passage through the adder while the other is reset to accept the new optical output data. Different clock pulses alternately enable the memory buffers to accept and store data or to reset them in preparation for new data. The outputs of the logic processor trigger the buffer memory array, whose latched optical outputs store the switched optical data from the previous pass. Switching the bias voltage on and off clocks the logic unit and initiates new passes through the latching photothyristor/VCSEL logic array can replace the HPT/VCSEL array, and then only one memory buffer would be required. This two-chip arrangement permits a much more compact scheme requiring only a single polarizing beam splitter to be used, in which the optical data toggles back and forth between the two chips in response to properly timed clock pulses.

In conclusion, we have described binary arithmetic using HPT/VCSEL optical logic gates and an architecture based on optical symbolic substitution. The implementation of this technology has been illustrated by the example of a highly compact binary half-adder.

The research at the University of New Mexico is supported by the Defense Advanced Research Projects Agency and the U.S. Air Force Office of Scientific Research, and that at Sandia National Laboratory is supported by the U.S. Department of Energy under Contract DE-AC04-76DP00789.

References

1. G. R. Olbright, R. P. Bryan, K. L. Lear, T. M. Brennan, Y. H. Lee, and J. L. Jewell, "Title," Electron. Lett. 27, 216–xxx (1991).
2. A. Huang, "Title," in *Technical Digest, IEEE Tenth International Optical Computing Conference* (Institute of Electrical and Electronics Engineers, New York, 1983), pp. 13–17.
3. ~~Y. Tashiro, K. Kasahara, H. Hamao, M. Sugimoto, T. Yamase, "Title," Jpn. J. Appl. Phys. 26, L1014–xxx (1988).~~ See next page
4. K. Hara, K. Mitsunaga, K. Kyuma, "Title," IEEE Photon. Technol. Lett. 1, 370–xxx (1989).
5. I. Ogura, Y. Tashiro, S. Kawai, K. Yamada, M. Sugimoto, K. Kubota, K. Kasahara, "Title," Appl. Phys. Lett. 57, 540–xxx (1990).
6. K. Tai, G. Hasnain, J. D. Wynn, R.J. Fischer, Y. H. Wang, B. Weir, J. Gamelin, A. Y. Cho, "Title," Electron. Lett. 26,

Leibenguth, M. T. Asom, G. Livescu, L. Luther, V. D. Materra, "Title," Electron. Lett. 26, 1308-xxxx (1990).

8. R. P. Bryan, G. R. Olbright, and J. Cheng, "Title," submitted to Elec. Lett.

1. Title, "Cascadable laser logic devices: discrete integration of phototransistors with surface-emitting laser diodes", pp. 216-217.

2. Title, "Parallel algorithms for optical digital computers",

3. Y. Tashiro, N. Hamao, M. Sugimoto, N. Takado, K. Kasahara, and T. Yamase, "Vertical to surface transmission electrophotonic device with selectable output light channel", App. Phys. Lett. 54, 329-331 (1989).

4. Title, "Differential optical switching at subnanowatt input power", pp. 370-372.

5. Title: "Reconfigurable optical interconnection using a two-dimensional vertical to surface transmission electrophotonic device array", pp. 540-542.

6. Title: "90% coupling of top-surface-emitting GaAs/AlGaAs quantum well laser output into 8μm diameter core silica fibre", pp. 1628-1629.

7. Title: "High efficiency (1.2mW/mA) top-surface emitting GaAs quantum well lasers", pp. 1308-1309.

8. Title: "Cascadable surface-emitting laser logic: demonstration of Boolean logic", Electron. Lett. 27, 893-894 (1991).

Coupled broad-area mode theory of gain-guided laser arrays

Chung-Pin Cherng[a] and Marek Osiński[a),b)
Center for High Technology Materials, University of New Mexico, Albuquerque, New Mexico 87131-6081

(Received 22 October 1990; accepted for publication 11 July 1991)

Multiple-stripe semiconductor laser arrays are analyzed using a broad-area mode coupling approach. Rather than considering coupling between individual waveguide modes as in the conventional supermode theory, a basis of broad-area modes is chosen. These modes are coupled through a perturbation of refractive index and gain profiles caused by nonuniform carrier injection, thermal effects, and/or built-in weakly guiding or antiguiding profiles. Present theory reveals that earlier simplified analysis involving broad-area mode-coupling may lead to significant errors in modal gains of high-order array modes.

High-power gain-guided diode laser arrays are very promising for applications in which optical power is of major concern, such as solid-state laser pumps. cw output power as high as 8 W has been reported.[1] These devices usually operate multimode, with a rather low degree of coherence. Many applications, for example free-space satellite and fiber communications, require a highly coherent light source, preferably emitting in a single lobe. It is therefore very important to reach a good understanding of lateral mode properties in gain-guided arrays.

Measurements of the near- and far-field patterns of gain-guided laser arrays using spectrally resolved techniques,[2-4] injection seeding,[5] and external cavity coupling,[6,7] all revealed significant contribution from high-order modes ($v > N$, where N is the number of array elements) which could not be related to any supermode results.[8-10] In order to obtain those high-order mode solutions, it was necessary to resort to complicated numerical models,[11,12] with which it was difficult to gain insight into the origin of those modes. Recently, an analytical treatment using a perturbation theory and involving broad-area modes has been proposed.[4] The problem was, however, oversimplified and rather unrealistic assumptions were made. Specifically, the active region was assumed to be laterally bound by infinitely lossy layers, and any differences between the gains of unperturbed broad-area modes were neglected, since they were presumed to have a negligible effect on calculated modal gains of the array modes.

In this letter, we show that approximations invoked in Ref. 4 may lead to significant errors. We adopt an analytical coupled-mode approach involving, as previously, broad-area modes coupled by perturbations of gain and refractive index along the lateral direction. Compared to the supermode theory valid for index-guided arrays,[8-10] the formulation is greatly simplified by the fact that the field overlap integral of any two broad-area modes vanishes due to their orthogonality. As a consequence of the large number of broad-area modes, the array also supports modes of the order v higher than the number of individual emitters N. These high-order modes agree well with those found from both self-consistent numerical modeling[12] and experimental observations,[3,4] but their modal gains differ significantly from the results obtained using the simplified perturbation theory.[4]

The theoretical formulation begins by deriving the coupled-mode equations using broad-area modes as expansion basis. Perturbation of complex permittivity is defined by

$$\Delta\epsilon^{(\mathrm{per})}(x)=\epsilon^{(\mathrm{array})}(x)-\epsilon^{(\mathrm{BA})}(x), \tag{1}$$

where $\epsilon^{(\mathrm{BA})}(x)$ is the unperturbed permittivity profile of the broad-area laser and $\epsilon^{(\mathrm{array})}(x)$ is the permittivity profile of the array, taking account of nonuniform carrier injection, thermal effects, and/or any built-in waveguide/antiguide profile. Following the general framework of coupled-mode theory,[10] we obtain the coupled-mode equations for multiple-stripe laser arrays:

$$\sum_{q=1}^{M}\frac{da_q(z)}{dz}=i\sum_{q=1}^{M}(\beta_p+\kappa_{pq})a_q(z), \tag{2}$$

where a_q is the expansion coefficient for qth array mode propagating in the $+z$ direction, M is the total number of broad-area modes included in the calculations, and β_p is the propagation constant of broad-area mode p. κ_{pq} is the coupling coefficient between any two broad-area modes p and q and is defined by

$$\kappa_{pq}=\omega\int\int_{-\infty}^{\infty}\Delta\epsilon^{(\mathrm{per})}\mathbf{E}_{tp}\cdot\mathbf{E}_{tq}dxdy - \int\int_{-\infty}^{\infty}\left(\frac{\Delta\epsilon^{(\mathrm{per})}\epsilon^{(\mathrm{BA})}}{\epsilon^{(\mathrm{BA})}+\Delta\epsilon^{(\mathrm{per})}}\right)E_{zp}E_{zq}dxdy, \tag{3}$$

with ω the lasing angular frequency, and $\mathbf{E}_{tp}$, E_{zp} the transverse and longitudinal components of mode p, respectively. Equation (2) can also be written in a matrix form

[a)] Also with the Department of Electrical and Computer Engineering, University of New Mexico.
[b)] Also with the Department of Physics and Astronomy, University of New Mexico.

 0021-8979/91/084617-03$03.00 © 1991 American Institute of Physics

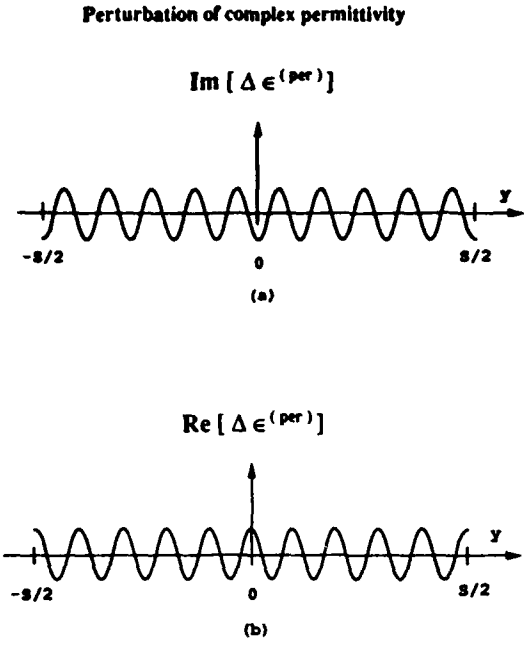

FIG. 1. Periodic perturbation profiles due to injected carriers in a uniform ten-stripe gain-guided array. (a) Periodic gain (imaginary part of $\Delta\epsilon^{(per)}$) and (b) periodic index antiguiding (real part of $\Delta\epsilon^{(per)}$).

$$\frac{dA}{dz}=i(B+K)A, \tag{4}$$

where B is a diagonal $M\times M$ matrix of propagation constants β_p and the elements of A and K are denoted as a_q and κ_{pq}, respectively. We seek the array mode solutions with the eigenvalues in the form $e^{j\sigma_\nu z}$, where σ_ν is the complex propagation constant of the array mode ν.

Figure 1 illustrates schematically the imaginary (gain) and real (index-antiguiding) parts of the perturbed permittivity $\Delta\epsilon^{(per)}$. The profiles shown represent periodic perturbations due to nonuniform carrier injection in a uniform gain-guided laser array with no built-in lateral waveguiding mechanism.

Consider a typical ten-stripe GaAs/AlGaAs gain-guided laser array with 6-μm-wide stripes situated on 10 μm centers. The analysis starts by finding guided broad-area modes for a 100-μm-wide rectangular waveguide with gain of 140 cm^{-1} and loss of 150 cm^{-1} inside and outside the active region, respectively. The carrier-induced antiguiding is included via the antiguiding factor of 2. The transverse confinement factor of 0.3 is assumed. The coupling coefficients are calculated according to Eq. (3), taking the modal gain modulation amplitude of 10 cm^{-1}. The eigenvalues σ_ν and the corresponding eigenvectors are then obtained from Eq. (4).

Figure 2 shows a comparison of the present theory with earlier simplified perturbation analysis[4] corresponding to a limit of very high loss and constant broad-area modal gain. While the real part of the propagation constant σ_ν is not affected by these approximations, the previous treatment is unreliable in predicting the modal gains of high-order array modes $\nu>10$. It should be emphasized

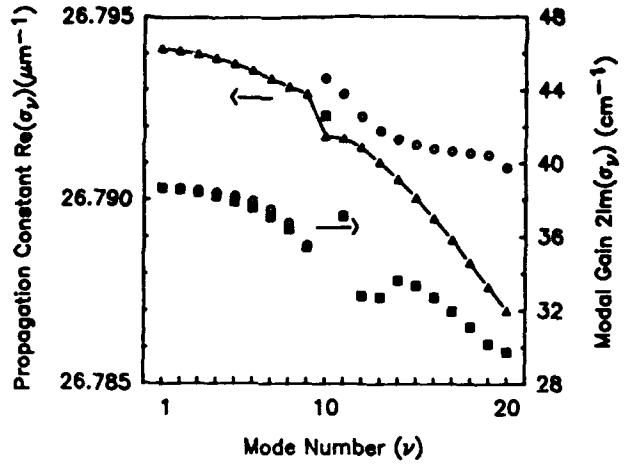

FIG. 2. Calculated propagation constants (triangles) and array modal gains for the first 20 array modes of a ten-stripe gain-guided array. Full squares represent modal gain results of the present theory, while open circles correspond to approximate analysis in which all broad-area modes have equal gains and the lateral cladding loss is infinite.

that these high-order modes usually dominate in gain-guided arrays, hence precise knowledge of their modal gains is very important in considerations of mode ordering and mode suppression schemes.

The large modal gain difference between array modes 9 and 10 also reflects on the corresponding propagation constants. An abrupt shift of the propagation constant between $\nu=9$ and $\nu=10$ array modes agrees well with a self-consistent numerical model.[12] This shift becomes larger when index-antiguiding is stronger, and vanishes when the index-antiguiding reduces to zero.

Figure 3 shows the calculated near- and far-field intensity patterns for the low-gain eigenmode $\nu=9$ and the

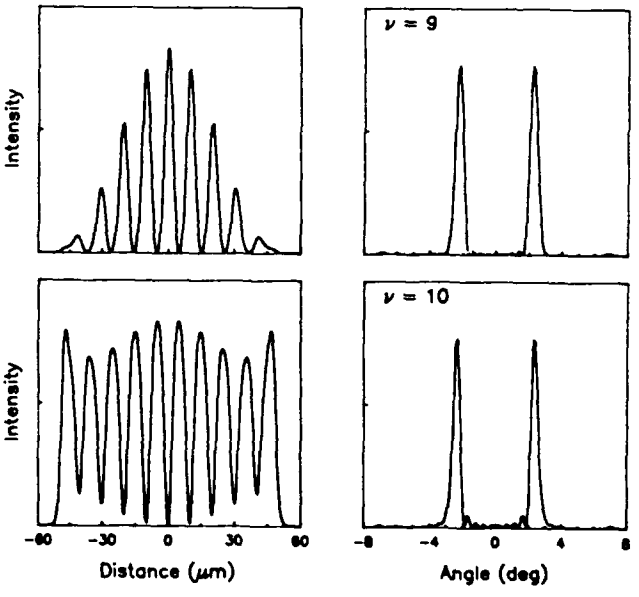

FIG. 3. Near- and far-field intensity patterns of the array modes $\nu=9$ and $\nu=10$.

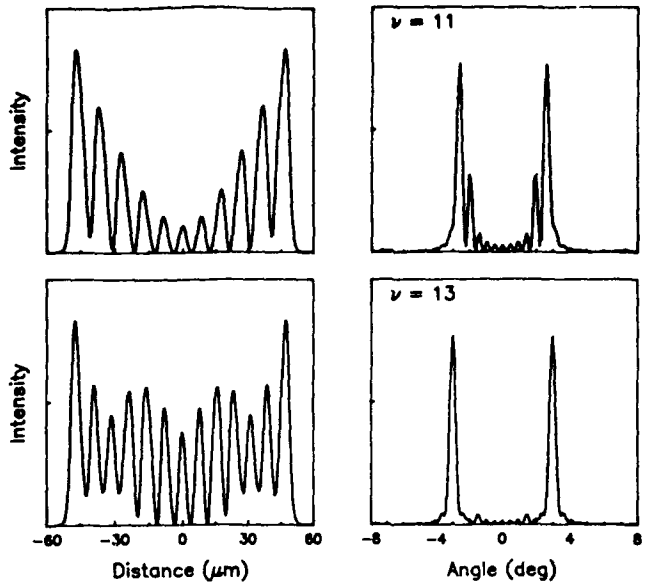

FIG. 4. Near- and far-field intensity patterns of the array modes $\nu = 11$ and $\nu = 13$.

highest gain eigenmode $\nu = 10$. We note that the array modes are labeled according to increasing frequency of oscillation (decreasing real part of propagation constant), and their order can in principle be identified in an array that is operating in a pure eigenmode by observing the number of primary maxima in the intensity distribution. The $\nu = 9$ array mode has 9 maxima located at the interspaces between the stripes where the gain is minimum, which explains why that array mode has a very low modal gain. The near- and far-field intensity patterns of the $\nu = 10$ array are not only very similar to those obtained from the supermode theory and numerical modeling, but also to the patterns observed experimentally.[3,4,5,12] Not surprisingly, the calculated near and far fields do not differ much from those obtained using the simplified perturbation theory,[4] since the real parts of σ_ν are almost unaffected by simplifications involved in the earlier approach.

As an example of high-order array modes resulting from the broad-area mode coupling, the near- and far-field intensity patterns for $\nu = 11$ and $\nu = 13$ array modes are shown in Fig. 4. As reported earlier,[4] the high-order modes are characterized by far-field intensity patterns having two major lobes as a slightly increasing angle compared to the $\nu = 10$ array mode. Array modes of the order as high as 20 have been reported in ten-stripe gain-guided arrays[3] and the present theory can describe all these array modes correctly.

In conclusion, we have adopted an analytical coupled-mode approach to describe the lateral mode structure of multistripe laser arrays with no built-in lateral waveguides. The devices are treated as broad-area lasers with gain- and index-antiguiding perturbations. We demonstrate that earlier formulation of broad-area perturbation theory leads to significant errors in calculated modal gains for array modes of order higher than the number of gain-guided array elements.

The authors wish to thank J. M. Verdiell and G. R. Hadley for helpful discussions. Financial support from the U.S. Air Force Office of Scientific Research is gratefully acknowledged.

[1] D. F. Welch, B. Chan, W. Streifer, and D. R. Scifres, Electron. Lett. **24**, 113 (1988).
[2] J. R. Andrews, T. L. Paoli, W. Streifer, and R. D. Burnham, Appl. Phys. Lett. **58**, 2777 (1985).
[3] J. M. Verdiell, H. Rajbenbach, and J. P. Huignard, J. Appl. Phys. **66**, 1466 (1989).
[4] J. M. Verdiell and R. Frey, IEEE J. Quantum Electron. **QE-26**, 270 (1990).
[5] G. R. Hadley, J. P. Hohimer, and A. Owyoung, Appl. Phys. Lett. **49**, 684 (1986).
[6] J. E. Epler, N. Holonyak, Jr., R. D. Burnham, T. L. Paoli, R. L. Thornton, and M. M. Blouke, Appl. Phys. Lett. **47**, 7 (1985).
[7] J. E. Epler, N. Holonyak, Jr., R. D. Burnham, T. L. Paoli, and W. Streifer, Appl. Phys. Lett. **47**, 1489 (1985).
[8] J. K. Butler, D. E. Ackley, and D. Botez, Appl. Phys. Lett. **44**, 293 (1984).
[9] E. Kapon, J. Katz, and A. Yariv, Opt. Lett. **9**, 25 (1984).
[10] A. Hardy and W. Streifer, J. Lightwave Technol. **LT-4**, 90 (1986).
[11] Y. Twu, A. Dienes, S. Wang, and J. R. Whinnery, Appl. Phys. Lett. **45**, 709 (1984).
[12] G. R. Hadley, J. P. Hohimer, and A. Owyoung, IEEE J. Quantum Electron. **QE-23**, 765 (1987).

PROCEEDINGS REPRINT

SPIE–The International Society for Optical Engineering

Reprinted from

Laser Diode Technology and Applications III

23–25 January 1991
Los Angeles, California

Volume 1418

©1991 by the Society of Photo-Optical Instrumentation Engineers
Box 10, Bellingham, Washington 98227 USA. Telephone 206/676-3290.

Fundamental array mode operation of semiconductor laser arrays using external spatial filtering

Chung-Pin Cherng and Marek Osiński

Center for High Technology Materials, University of New Mexico, Albuquerque, New Mexico 87131-6081

ABSTRACT

Detailed broad-area coupled-mode analysis of in-phase mode selection in carrier-guided arrays coupled to external cavities with spatial filters is presented and compared with experimental results. A high-power (68 mW with output facet reflectivity of 90% which corresponds to estimated 266 mW with output facet reflectivity of 30%), on-axis, single-lobe far field with nearly diffraction-limited (0.64°) full width at half maximum is achieved from a ten-stripe carrier-guided anti-reflection-coated laser array by coupling to an external cavity with a spatial filter. The in-phase operation is verified by wavefront measurements using shearing interferometry.

1. INTRODUCTION

Double-lobe far-field pattern is a persisting problem in high-power carrier-guided (often termed gain-guided) semiconductor laser arrays[1-6]. Typically, these devices operate in high order modes which better utilize an inhomogeneous gain profile of a uniform array. Double-lobe emission renders it very difficult to design and fabricate miniature optics that would collect most of the emitted light. Therefore, a highly stable single-lobe emission pattern, with most of the light in the central lobe, is strongly preferable for many applications, such as coupling to an optical fiber, laser printing, and free-space satellite-to-satellite communication.

Various configurations of spatial filters in external cavities have been used to achieve single lateral mode operation in carrier-guided arrays. Yaeli *et al.*[7] utilized a narrow, adjustable slit combined with a partially reflecting flat mirror to select the lowest-order array mode. Chang-Hasnain *et al.*[8] used an apertured graded-index lens external cavity, achieving clean fundamental array mode operation up to 102 mW and predominantly single-lobe output up to 500 mW, all under pulsed operation. A similar arrangement, but with a narrow-stripe mirror placed at a far-field side-lobe position, was applied[9-11] to obtain stable off-center emission in a high-order array mode with output power reaching 950 mW[11]. This technique relies on the fact that the array far fields are well resolved spatially and can be addressed individually by a proper spatial filter. In addition, this mode selection method can be applied to other high-power diode lasers, such as broad-area lasers.

In this paper, we report on theoretical and experimental studies of carrier-guided diode laser arrays coupled to spherical-mirror external cavities with spatial filters inserted with the goal of suppressing the high-order modes and obtaining a single-lobe output. Coupled-mode theory with broad-area mode basis is used to find the free-running array modes. The feedback facet of the array is assumed to be perfectly anti-reflection (AR) coated, in order to increase the coupling efficiency of the external feedback. Cavity modes of the array/spatial filter/external mirror system are then found by analyzing array mode mixing in the external cavity. Array mode selection is investigated for various configurations of the spatial filter. Experimentally, in addition to direct observation of the near and far fields, we measure lateral wavefronts by shearing interferometry to determine phase relations between adjacent emitters. Our results confirm that external spatial filtering represents a simple, and yet effective, technique for obtaining the diffraction-limited single-lobed output beam from a uniform carrier-guided laser array.

0-8194-0508-6/91/$4.00

2. COUPLED-MODE THEORY OF CARRIER-GUIDED ARRAYS WITH SPATIALLY SELECTIVE EXTERNAL FEEDBACK

Modal properties of phased-array diode lasers can be described using the improved coupled-mode theory[12-14], in which the array is regarded as a system of interacting single-mode waveguides. Such approach describes well the behavior of index-guided arrays, but is inadequate when carrier-guided arrays are considered. In the latter case, it is more appropriate to treat the array as a perturbed broad-area laser. Details of broad-area coupled-mode theory of free-running carrier-guided arrays are given elsewhere[15].

Using the array modes derived from coupled broad-area modes, we proceed with the analysis of external-cavity system illustrated in Fig. 1. A spherical mirror with radius R_m is placed at a distance d_m away from a perfectly AR-coated feedback facet which is located at $z = L$. In general, R_m and d_m are not assumed to coincide, but can differ slightly. A small defocusing distance Δd, such that $|\Delta d| << R_m$, is defined by $\Delta d = R_m - d_m$. A spatial filter with field transmission function $t(y)$ is located near the mirror surface. Although $t(y)$ may be arbitrary, we will limit our attention to filters that can efficiently discriminate against the higher-order array modes (the mode order $\nu > 1$). The system is analyzed by requesting that cavity modes must reproduce themselves after each completed roundtrip, similarly to earlier work on index-guided arrays with spatially filtered feedback[16].

Each cavity mode $E(y,z)$ is represented as a linear combination of the array modes $E^{(\nu)}(y)$, $\nu = 1, 2, 3, \ldots, N$, where N is the number of array modes included in the calculations. It should be noted that, in contrast to index-guided arrays, N for carrier-guided arrays is usually significantly greater than the number of active stripes in the array. For waves traveling along $-z$ and $+z$ directions, we employ expansion coefficients a and $\hat{a}$, respectively. For a cavity mode traveling in the $-z$ direction, we have

$$E(y,z) = \sum_{\nu=1}^{N} a_\nu(z) E^{(\nu)}(y) . \tag{1}$$

Thus, at the output facet ($z = 0$), $E(y,0)$ is specified by a column matrix $\mathbf{A}(0)$ constructed from the coefficients $a_\nu(0)$ in Eq. (1). Inside the laser, propagation of each array mode $E^{(\nu)}(y)$ is described by $\exp(i\sigma_\nu z)$, with a complex propagation constant σ_ν accounting for modal gain or loss in the laser. We assume that each array mode experiences an identical field reflectivity at the output facet, hence, no coupling between the array modes occurs as a result of reflection from the planar facet. According to these assumptions, the column matrix $\hat{\mathbf{A}}(L)$ constructed from the expansion coefficients $\hat{a}_\nu(L)$ and describing the system mode propagating in the $+z$ direction at the AR-coated feedback facet is given by

$$\hat{\mathbf{A}}(L) = \mathbf{GRA}(0) , \tag{2}$$

where $\mathbf{G} = \mathrm{diag}[\exp(i\sigma_\nu L)]$ and $\mathbf{R} = r\mathbf{I}$, with facet reflectivity $r = -.55$ and $\mathbf{I}$ the identity matrix.

In order to eliminate $\hat{\mathbf{A}}(L)$ in Eq. (2), we need to consider wave propagation inside the external cavity incorporating the spatial filter. We introduce a feedback matrix $\mathbf{C}_e$ which satisfies

$$\mathbf{A}(L) = \mathbf{C}_e \hat{\mathbf{A}}(L) . \tag{3}$$

$\mathbf{C}_e$ represents the cumulative effect of free-space propagation from the feedback facet up to the spatial filter, passing through the filter, reflection at the external mirror, repeated filtering, and repeated free-space propagation followed by coupling back into the array modes at $z = L$. Combination of all these steps leads to a following impulse response function for radiation emitted by a point source located at y_o and returning to an image point y_i [16,17]:

$$h(y_i;y_o) = -\frac{\exp(2ik_o d_m)}{\lambda d_m} \exp\left[\frac{k_o}{2d_m}\left(y_o^2 + y_i^2\right)\right]$$
$$\times \int_{-\infty}^{\infty} t^2(y) \exp\left[ik_o\left(\frac{1}{d_m} - \frac{1}{R_m}\right)y^2\right] \exp\left[-i\frac{k_o}{d_m}(y_o + y_i)y\right] dy . \tag{4}$$

Since the system is linear, any field distribution $U(y_o)$ at the feedback facet gives rise to a reflected image field $V(y_i)$ at the same plane described by the superposition integral[17]

$$V(y_i) = \int_{-\infty}^{\infty} h(y_i;y_o)U(y_o)dy_o \ . \tag{5}$$

For maximum optical coupling between array modes, we require $R_m = d_m$, or $\Delta d = 0$, which yields the following result for the reflected field $V(y_i)$

$$V(y_i) = -exp(2ik_o d_m)\int_{-\infty}^{\infty} U(y_o)\exp\left[i\frac{k_o}{2d_m}(y_o^2+y_i^2)\right]T(y_o+y_i)dy_o \ , \tag{6}$$

where $T(y_i+y_o)$ is the Fourier transform of the spatial filter field transmission function $t(y)$, defined as

$$T(y) = \frac{1}{\lambda d_m}\int_{-\infty}^{\infty} t^2(y')\exp\left[-i\frac{k_o}{d_m}yy'\right]dy' \ . \tag{7}$$

In the limit of a very wide spatial filter [$t(y)$ approaching unity], such that most of the diffracted light can pass through unobstructed, $T(y)$ becomes a delta function $\delta(y)$.

The existence of the quadratic phase term in Eq. (6) is the source of perturbation that leads to array mode mixing even when no spatial filter is inserted. In the framework of the coupled-mode theory, conversion of the array mode μ into the array mode ν as a result of a round trip in the external cavity is described by the coupling coefficient $C_e^{\mu\nu}$. Setting the source field $U(y_o) = E^{(\mu)}(y_o)$ in Eq. (6), multiplying the image field $V(y_i)$ by the array mode ν, and integrating over the image point coordinates yields

$$C_e^{\mu\nu} = -\exp(2ik_o d_m)\int_{-\infty}^{\infty}\int_{-\infty}^{\infty} T(y_o+y_i)\exp\left[i\frac{k_o}{2d_m}(y_o^2+y_i^2)\right]E^{(\mu)}(y_o)E^{(\nu)}(y_i)dy_o dy_i \ . \tag{8}$$

For $\mu = \nu$, Eq. (8) gives the effective reflection coefficient for the array mode ν. The off-diagonal elements of the matrix C_e ($C_e^{\mu\nu} = C_e^{\nu\mu}$, $\mu \neq \nu$) represent mutual coupling between array modes μ and ν. Taking into account Eq. (3) and requesting that the field patterns (cavity modes) reproduce themselves in a roundtrip inside the composite cavity, we obtain the following matrix equation

$$\mathbf{GC}_e\mathbf{GRA}(0) = \gamma_{ext}\mathbf{A}(0) \ , \tag{9}$$

where γ_{ext} denotes an eigenvalue. Therefore, the cavity modes are determined by the solutions of Eq. (9). For a chosen value of angular frequency ω, Eq. (9) is first solved for complex eigenvalues $\gamma_{ext}^{(\zeta)}$ ($\zeta = 1, 2, 3, ..., N$) and the corresponding eigenvectors, and then near- and far-field distributions can be calculated. The frequency ω used in coupled-mode solutions is not automatically a resonant frequency of the composite cavity. For resonant frequencies, additional round-trip phase condition must be satisfied:

$$arg[\gamma_{ext}^{(\zeta)}] = 2\pi M \ , \tag{10}$$

where M is an integer. The amplitude part of $\gamma_{ext}^{(\zeta)}$ determines the sequence in which cavity modes are excited when the modal gain is increased. The dominant cavity mode has the largest value of $|\gamma_{ext}^{(\zeta)}|$.

Since the matrices G and R are diagonal, only the off-diagonal elements of C_e may contribute to cross-coupling between the array modes. The quadratic phase term in Eq. (8) should not be neglected as long as the lateral dimension of the laser array is not very small compared to the radius of curvature of the feedback mirror. The function $T(y_o+y_i)$ may have a complicated form, depending on the specifications of the spatial filter. In the absence of any spatial filter [$T(y_o+y_i) = \delta(y_o+y_i)$], the coupling coefficient $C_e^{\mu\nu}$ is simply an overlap integral of the two array modes with a quadratic phase term iky_o^2/d_m. The image field returning to the feedback facet is reversed with respect to the object field, *i.e.* $E^{(\nu)}(y_i) \rightarrow E^{(\nu)}(-y_o)$. Because of the symmetry in the array mode field distributions, this field reversal causes the coupling between the array modes of different parity to almost vanish. For the same reason, coupling between even parity array modes is stronger than that between odd parity modes.

In order to enhance single-lobe operation of the array, the spatial filter should be selected in form of a slit of width $2W$ such that only the central lobe of the fundamental array mode would be allowed to pass through, *i.e.*

$$t(y) = \begin{cases} 1 & |y| \le W \\ 0 & |y| > W \end{cases} \tag{11}$$

It is easy to show that in this case $T(y_o + y_i)$ reduces to a sinc function:

$$T(y) = \frac{\sin\left[W k_o y / d_m\right]}{\pi y}. \tag{12}$$

Upon substitution of Eq. (12) into Eq. (8), the effect of spatial filtering on array mode mixing coefficients $C_e^{\mu\nu}$ can be evaluated exactly as long as the array mode distributions are specified. With proper choice of slit width $2W$, the effective reflectivity (self-coupling coefficient) C_e^{11} of the fundamental array mode will be strongly enhanced and all coupling coefficients $C_e^{\mu\nu}$, $\mu, \nu \neq 1$ involving high-order modes will be reduced dramatically, practically approaching zero.

3. IN-PHASE MODE SELECTION BY EXTERNAL SPATIAL FILTERING: THEORY

Consider a ten-stripe carrier-guided laser array with 6-μm wide stripes and 10-μm center-to-center spacing, placed in a 1-cm long external cavity with a perfectly reflecting spherical mirror. The device parameters used in calculations are shown in Table 1. Any variation of these parameters with pumping current is neglected. The external cavity length of 1 cm was chosen to enable comparison with earlier calculations of Ref. 16. In calculating the coupling coefficients $C_e^{\mu\nu}$, integration is extended over a 110-μm wide region.

For a solitary array, our broad-area coupled-mode theory[15] predicts that the dominant array mode is $\nu = 10$, with double-lobed far-field pattern featuring two narrow maxima separated by 4.8°. In the same instance, calculated FWHM of the single-lobed far field for the fundamental array mode ($\nu = 1$) is 0.58°. This value is slightly larger than the diffraction-limited beam width of 0.46° computed for a 100-μm wide uniform source, which we attribute to combination of a non-zero antiguiding factor b and a nonuniform near-field distribution of the array mode.

With perfect AR coating applied to one of the facets, external feedback is necessary for any array mode to have a finite threshold gain. Selective feedback can therefore be very effective in suppressing undesirable modes that may have high gains in a solitary array. Computation of system eigenmodes for the laser array in an external cavity with spatial filter start by evaluating the coupling coefficients $C_e^{\mu\nu}$ for a particular width of the spatial filter, which should be chosen to allow only the $\nu = 1$ array mode to pass freely and to block off all higher-order modes. We expect that the slit width should be close to the full width of the diffraction-limited central lobe, which, according to Ref. 18, gives $2W = 164$ μm for a 100 μm wide uniformly illuminated aperture. A 2-D numerical integration algorithm is used to evaluate the matrix elements $C_e^{\mu\nu}$ given in Eq. (8). Fig. 2 displays the self-coupling coefficients (effective reflectivity $C_e^{\nu\nu}$, $\nu = 1,2,...,20$) for three different filter widths: $2W = 160$, 164, and 172 μm, respectively. As expected, the fundamental array mode $\nu = 1$ has the largest reflection coefficient. $\nu = 2$ array mode has the second largest reflection coefficient because a small portion of its field can still pass through the spatial filter. Self-coupling coefficients for all the other high-order modes ($\nu > 2$) are practically approaching zero. A trend for increasing high-order mode reflectivity can be noticed for the filter width of 172 μm, larger than the optimal value of 164 μm.

Fig. 3 shows the cross-coupling coefficients ($C_e^{1\nu}$, $\nu = 2,3,...,20$) between the fundamental array mode and high-order modes, again for three different slit widths. Except for small cross-coupling between array modes 1 and 3, there is almost no coupling with any of the remaining array modes. As expected, cross-coupling between the fundamental array mode and odd-parity even-order modes is orders of magnitude weaker than for modes of the same parity. While both mode conversion and mode reflection coefficients for the high-order modes can be further reduced by making the spatial filter width smaller than 160 μm, it would be

counterproductive since it would also diminish the amount of feedback for the fundamental array mode.

The high value of effective reflectivity for the fundamental array mode suggests that it is likely to be the main contributor to a dominant system (cavity) mode $\zeta = 1$. In order to establish the order of cavity modes, we need to examine magnitudes of all the eigenvalues γ_{ext} of Eq. (9). Calculated normalized magnitudes of γ_{ext} are displayed in Fig. 4 for a slit width $2W = 164$ μm. Large difference between the values of γ_{ext} for $\zeta = 1$ cavity mode and the remaining modes indicates that high-order modes are strongly suppressed. Cavity mode discrimination deteriorates for wider slit opening in the spatial filter ($2W = 172$ μm, not shown in Fig. 4), since in this case all modes receive more feedback from the external cavity. On the other hand, suppression of high-order cavity modes is even more effective for a smaller slit width ($2W = 160$ μm), but at the expense of increasing lasing threshold.

By definition, the fundamental cavity mode $\zeta = 1$ has the lowest threshold gain. However, since with a proper choice of spatial filter width the effective reflection coefficient is highest for the fundamental array mode, and since the threshold gain is proportional to logarithm of inverse facet reflectivity, we expect that the $\nu = 1$ array mode will be a dominant component of the fundamental cavity mode. By the same token, we expect that the $\zeta = 1$ cavity mode should have a single-lobed far-field. Fig. 5 shows amplitude and phase parts of complex components of normalized eigenvector $A_1(0)$ representing the fundamental cavity mode for a slit width $2W = 164$ μm. The cavity mode contains contributions from even-parity modes, with phase relations between them determined by the eigenvalue equation (9). It is clear that the $\nu = 1$ array mode is the main contributor to the fundamental cavity mode. The only other non-negligible contribution comes from the array mode $\nu = 3$, which is consistent with that mode having the second largest self-coupling coefficient (*cf.* Fig. 2) and the second largest coefficient for mixing with mode $\nu = 1$ (*cf.* Fig. 3). The absence of opposite-parity mode mixing evident in Fig. 5 is a direct consequence of negligible cross-coupling coefficients for different-parity array modes. For smaller or larger slit widths, the corresponding eigenvectors $A_1(0)$ are similar except that contributions from $\nu > 1$ array modes are becoming relatively weaker or stronger, respectively.

The importance of spatial filtering can be appreciated if we compare the results of Fig. 5 with a corresponding supermode mixing-amplitude spectra in an external cavity without any spatial filter shown in Fig. 3, Ref. 16, calculated for a 10-stripe index-guided array. Without spatial filter, the external cavity introduces severe supermode mixing with poor mode discrimination. The cavity mode which most resembles the $\nu = 1$ supermode (with single-lobed far field) contains almost equal contributions of all five even-parity supermodes. This contrasts with almost complete elimination of array mode mixing achieved by selecting a proper spatial filter. One can therefore expect that the resulting far field of the $\zeta = 1$ cavity mode should bear a close resemblance to the $\nu = 1$ array mode. Indeed, as shown in Fig. 6, under the selective feedback imposed by the spatial filter and a spherical mirror, the system mode exhibits a single-lobed far-field pattern. With the FWHM of 0.58°, no further broadening of the central lobe is introduced by the array mode mixing compared to the beam width of the $\nu = 1$ array mode. however, the array mode mixing does show up in the appearance of side shoulders in the central lobe and in additional small peaks on both sides of the far-field pattern (Fig. 6). By inspecting the amplitude mixing spectrum of Fig. 5, we see that the shoulders are primarily due to the array mode $\nu = 3$, with their height consistent with the contribution of that mode to the fundamental cavity mode.

4. EXPERIMENTAL ARRANGEMENT

Configuration of experiments on far-field control in diode laser arrays by coupling to an external cavity with spatial filter is shown schematically in Fig. 7. The device under examination is a commercial carrier-guided ten-stripe uniform laser array (Spectra Diode Laboratories SDL-2410C) with front facet reflectivity of 30% and back facet reflectivity of 90%. Because of difficulties with access to the back facet, the AR-coating for enhanced optical feedback is performed on the front facet and the output light is collected from the back facet. The external cavity is formed by a spherical mirror having a 2.54 cm (1 inch) focal length and a variable-width slit as a spatial filter. The mirror is mounted on an $X-Y-Z$ linear translation stage. In order to obtain optimal optical coupling, the feedback mirror is placed at 5.08 cm (2 inches) away from the AR-

coated facet for a 1:1 ratio between the object and reflected image fields. Spatial control of feedback is achieved by adjusting the opening of the slit located just in front of the mirror. Due to the limited size of the mirror (1 inch diameter in the transverse direction) and the reflectivity of the Al-coated external mirror, it is estimated that less than one-sixth of light is actually imaged back onto the laser array. A charge-coupled-device (CCD) camera is placed in front of the uncoated facet of the laser array to measure the far-field patterns. The images picked up by the CCD camera are transmitted to a video analyzer to be displayed on a monitor, recorded by an $X-Y$ scanning recorder, and then stored by a digitizer and microcomputer.

The operation of the system starts by aligning the laser array with respect to the spherical mirror. Without applying any current, a low-power visible red He-Ne laser light is shone onto the facet of the laser array for rough alignment. Accordingly, the feedback mirror is adjusted to capture the reflected image of the laser light in the center of the mirror. Subsequently, a fine tuning is performed by maximizing the output power from operating diode laser array. Stable single-lobed far-field can be obtained by choosing a proper opening of the variable slit. No temperature control was attempted during the experiments, neither any attempt was made to resolve spectrally measured near- and far-fields.

Initial experiments were performed on an uncoated device. Subsequently, the feedback facet of the laser array was AR coated by using ion-beam assisted deposition. A single quarter-wave layer of HfO_2 was deposited. The power reflection at the AR coated facet, as inferred from measurements of threshold current before and after AR coating, is estimated not to exceed 1%.

5. IN-PHASE MODE SELECTION BY EXTERNAL SPATIAL FILTERING: EXPERIMENT

We began by measuring characteristics of the solitary laser array, without any feedback and before AR coating. The laser array had a threshold current of 237 mA. The near- and far-field patterns of the array with injection current ranging from 245 to 265 mA are shown in Figs. 8 and 9. Apparently, the $\nu = 10$ array mode is the dominant lasing mode, with 4.8° between its two lobes (I = 245mA). The measured separation between the two lobes agrees very well with calculated value of 4.8° obtained from our broad-area coupled-mode theory of carrier-guided arrays[15]. Separation between the two lobes becomes larger and the FWHM of each lobe becomes broader as the injection current increases. This indicates multi-longitudinal and/or multi-lateral modes lasing simultaneously. This is also consistent with our coupled-mode calculations as well as other models[6,19] which predict the highest modal gain of $\nu = 10$ array mode followed by modes $\nu = 11, \nu = 12$, and so on. With increasing mode order, separation between the far-field lobes also increases[6,15,19,20]. The broadening of the each lobe with increasing injection current is a consequence of progressively multimode operation.

The uncoated array was then placed in an external cavity to investigate competition between optical feedback and non-zero feedback-facet reflectivity. By adjusting the opening of the variable-slit spatial filter to ~ 0.83 mm, so that only the main lobe of the in-phase mode could pass through freely and all higher-order array modes were discriminated against, we achieved single-lobed far-field output. Note that the slit width is larger than discussed in Section 3 by roughly a factor of 5, proportionally to increased cavity length (from 1 cm to 5.08 cm). Due to additional feedback from the external cavity, the lasing threshold was reduced to 210 mA. As shown in Fig. 10, the FWHM of a single-lobed output beam at 230 mA was > 1.2°, which is over 2 times wider than the theoretical limit of 0.58°. This broadening may be due to multi-longitudinal operation in the lowest-order array mode, or to excitation of several lateral modes, or both. Driving the device at slightly higher pump level resulted in destruction of the single-lobed operation. Higher-order modes started to appear and the system displayed multi-lobed patterns. This indicates that predominant influence of external feedback gave way to Fabry-Perot mode selection inside the laser cavity, due to strong feedback-facet reflections. This result also underscores the importance of high-quality AR coating of the feedback facet in order to achieve high-power single-lobed operation.

After AR coating, the external-cavity laser array started lasing at 223 mA and 225 mA without and with the spatial filter, respectively. Without the spatial filter, the system operated with slightly higher efficiency, but displayed complicated multi-lobed patterns at all current levels. With optimal opening in the spatial filter, single-lobed far-field pattern was achieved at the pumping levels up to 530 mA. Fig. 11 illustrates the light emitted through the output facet, which has reflectivity $R_f = 0.9$, as a function of injection current ($L-I$ characteristic) of the external cavity laser array without (broken line) and with (solid line) the spatial filter. The output power penalty for inserting the spatial filter grows from ~ 15% at intermediate currents (< 350 mA) to ~ 20% at high current levels (> 500 mA). These power losses are due to reduced feedback caused by insertion of the spatial filter. Fig. 12 displays the far-field patterns at four different current levels (260 mA to 530 mA) corresponding to four points *a*, *b*, *c*, and *d* marked in the $L-I$ curve in Fig. 11. Since the AR coating eliminates the competition between the facet reflections and selective external feedback, the composite cavity is acting as a single resonant cavity for $v = 1$ array mode, but with the laser diode array as a gain medium. At moderate pumping levels (≤ 350 mA), the system outputs a stable single-lobed beam. Fig. 12(b) shows the far-field pattern for pumping current of 300 mA, with 0.8° FWHM and 12 mW output power. This lasing condition is maintained up to 2.35 times threshold current (530 mA) with 0.64° FWHM and total output power of 68 mW, as shown in Fig. 12(d). Above this current level, the residual facet reflectivity starts to intervene by weakly supporting some high-order array modes, modifying the lasing characteristics of the composite cavity and leading to multi-lobed far-field patterns. The FWHM of the single-lobed output beam is found to decrease with the output power down to 0.64°. This result is in a very good agreement with our broad-area coupled-mode prediction of diffraction-limited value of 0.58° obtained in Section 3. Also shown in Fig. 11 (dotted line) is the output power that would be emitted through an uncoated front facet with reflectivity $R_f = 0.3$, estimated by calculating the threshold current and differential efficiency for the external cavity configuration with the spatial filter. The internal quantum efficiency is assumed to be constant. The effective reflectivity of the feedback facet is 0.525, as estimated from variation of threshold current with and without external feedback. Because of the lower reflectivity (0.3 vs. 0.9), the threshold current is increased to 248 mA with simultaneous increase of external efficiency. The calculated output power at four current levels corresponding to points a, b, c, d, is 11.3, 49, 196 and 266 mW, respectively.

A small deviation of the spherical mirror from its optimal position of focal plane coinciding with the feedback facet changes the far-field characteristic dramatically. Displacing the mirror away from laser facet by ~ 8 μm destroys the single-lobed output completely. When bringing the mirror closer toward the laser facet, the tolerance is ~ 15 μm, *i.e.* two times larger. This difference in tolerances can be understood by noting that a converging beam forms an image inside the laser array which helps to confine the reflected field better. Very small lateral shift of feedback mirror (< 5 μm) causes a lateral shift of image position at the laser facet, thus promoting excitation of other array modes and resulting in a multi-lobed output beam.

An attempt to obtain a single-lobed far field with the spatial filter width smaller than 0.8 mm was only partially successful. A single-lobed output was achieved only at low injection currents (≤ 250 mA). This is believed to be due to 1) insufficient feedback level and severely distorted image field when the opening of spatial filter becomes too smaller, 2) strong competition of the residual facet reflectivity (~ 1%) with weak feedback, and 3) diffraction and/or scattering at the sharp edges of narrow slit opening, causing severe aberrations of the reflected field. For wider spatial filter widths (> 0.85 mm), the laser system always displayed multi-lobed output patterns regardless of the injection current levels.

We have also examined single-lobed external-cavity array operation under modulation conditions. Both sinusoidal (100 kHz, 70 mA peak-to-peak) and low-duty-cycle pulse (1.66 MHz, 100 ns pulse width, 80 mA pulse amplitude) modulation experiments were performed, with the modulated current superimposed on 220 mA DC bias. Without AR coating, sinusoidal modulation resulted in a substantial broadening of single-lobed far field (3.4 times the theoretical limit of 0.58°, and 1.7 times the CW width). A significantly better performance was obtained with pulse modulation, with FWHM of 1.3° slightly broadened compared to CW operation. In addition, a broad low-intensity floor, superimposed on the central lobe, developed when the uncoated array was modulated. After AR coating, the pulse modulation had no observable effect on single-lobed external-cavity operation. This improvement is due to stabilizing influence of external cavity combined with

After AR coating, the external-cavity laser array started lasing at 223 mA and 225 mA without and with the spatial filter, respectively. Without the spatial filter, the system operated with slightly higher efficiency, but displayed complicated multi-lobed patterns at all current levels. With optimal opening in the spatial filter, single-lobed far-field pattern was achieved at the pumping levels up to 530 mA. Fig. 11 illustrates the light emitted through the output facet, which has reflectivity $R_f = 0.9$, as a function of injection current ($L-I$ characteristic) of the external cavity laser array without (broken line) and with (solid line) the spatial filter. The output power penalty for inserting the spatial filter grows from ~ 15% at intermediate currents (< 350 mA) to ~ 20% at high current levels (> 500 mA). These power losses are due to reduced feedback caused by insertion of the spatial filter. Fig. 12 displays the far-field patterns at four different current levels (260 mA to 530 mA) corresponding to four points *a*, *b*, *c*, and *d* marked in the $L-I$ curve in Fig. 11. Since the AR coating eliminates the competition between the facet reflections and selective external feedback, the composite cavity is acting as a single resonant cavity for $v = 1$ array mode, but with the laser diode array as a gain medium. At moderate pumping levels (≤ 350 mA), the system outputs a stable single-lobed beam. Fig. 12(b) shows the far-field pattern for pumping current of 300 mA, with 0.8° FWHM and 12 mW output power. This lasing condition is maintained up to 2.35 times threshold current (530 mA) with 0.64° FWHM and total output power of 68 mW, as shown in Fig. 12(d). Above this current level, the residual facet reflectivity starts to intervene by weakly supporting some high-order array modes, modifying the lasing characteristics of the composite cavity and leading to multi-lobed far-field patterns. The FWHM of the single-lobed output beam is found to decrease with the output power down to 0.64°. This result is in a very good agreement with our broad-area coupled-mode prediction of diffraction-limited value of 0.58° obtained in Section 3. Also shown in Fig. 11 (dotted line) is the output power that would be emitted through an uncoated front facet with reflectivity $R_f = 0.3$, estimated by calculating the threshold current and differential efficiency for the external cavity configuration with the spatial filter. The internal quantum efficiency is assumed to be constant. The effective reflectivity of the feedback facet is 0.525, as estimated from variation of threshold current with and without external feedback. Because of the lower reflectivity (0.3 vs. 0.9), the threshold current is increased to 248 mA with simultaneous increase of external efficiency. The calculated output power at four current levels corresponding to points a, b, c, d, is 11.3, 49, 196 and 266 mW, respectively.

A small deviation of the spherical mirror from its optimal position of focal plane coinciding with the feedback facet changes the far-field characteristic dramatically. Displacing the mirror away from laser facet by ~ 8 μm destroys the single-lobed output completely. When bringing the mirror closer toward the laser facet, the tolerance is ~ 15 μm, *i.e.* two times larger. This difference in tolerances can be understood by noting that a converging beam forms an image inside the laser array which helps to confine the reflected field better. Very small lateral shift of feedback mirror (< 5 μm) causes a lateral shift of image position at the laser facet, thus promoting excitation of other array modes and resulting in a multi-lobed output beam.

An attempt to obtain a single-lobed far field with the spatial filter width smaller than 0.8 mm was only partially successful. A single-lobed output was achieved only at low injection currents (≤ 250 mA). This is believed to be due to 1) insufficient feedback level and severely distorted image field when the opening of spatial filter becomes too smaller, 2) strong competition of the residual facet reflectivity (~ 1%) with weak feedback, and 3) diffraction and/or scattering at the sharp edges of narrow slit opening, causing severe aberrations of the reflected field. For wider spatial filter widths (> 0.85 mm), the laser system always displayed multi-lobed output patterns regardless of the injection current levels.

We have also examined single-lobed external-cavity array operation under modulation conditions. Both sinusoidal (100 kHz, 70 mA peak-to-peak) and low-duty-cycle pulse (1.66 MHz, 100 ns pulse width, 80 mA pulse amplitude) modulation experiments were performed, with the modulated current superimposed on 270 mA DC bias. Without AR coating, sinusoidal modulation resulted in a substantial broadening of single-lobed far field (3.4 times the theoretical limit of 0.58°, and 1.7 times the CW width). A significantly better performance was obtained with pulse modulation, with FWHM of 1.3° slightly broadened compared to CW operation. In addition, a broad low-intensity floor, superimposed on the central lobe, developed when the uncoated array was modulated. After AR coating, the pulse modulation had no observable effect on single-lobed external-cavity operation. This improvement is due to stabilizing influence of external cavity combined with

suppression of internal resonances in AR-coated array.

6. PHASEFRONT MEASUREMENTS OF SINGLE-LOBED EXTERNAL-CAVITY LASER ARRAY

Different array modes have their own distinct phasefront distributions which uniquely determine their far-field diffraction patterns. A novel scheme for diode laser phasefront measurements presented in Ref. 21 and involving a lateral shearing cyclic interferometer is recalled here to confirm our identification of the dominant array mode in single-lobed laser array with spatially filtered feedback. Fig. 13 shows a somewhat more complicated set-up for phasefront reconstruction, in which special care has been taken to avoid any distortion in the near-field image. An almost collimated near-field image is obtained by the first objective lens system with 0.45 numerical aperture. This near-field is divided into two parts by an 80%T - 20%R beam splitter. The reflected part is directed into a ring interferometer for phasefront measurements[21]. The transmitted near-field is Fourier transformed by a second lens system and then magnified by a third lens so that the far-field diffraction patterns can be spatially resolved at the surface of the spherical mirror. During the measurements, relative shears of ~ 5, 10, and 20 μm are used to generate fringe patterns and a Fourier transform algorithm is used to retrieve the phase front[21].

With the optimum tuning, the array starts to lase with a single-lobed beam at ~ 285 mA and with a multi-lobed output above 320 mA. The high threshold and much smaller operating range for single-lobed output are mainly due to aberrations, multiple absorption, and reflections in the complex lens system inserted inside the external cavity. To ensure a single-lobed output, the operating current is kept at 316 mA during the phasefront measurements. Due to the arrangement of apparatus, only about 7 stripes (~ 70 μm) of the near-field are used in generating the fringe patterns[21]

Fig. 14 shows three fringe patterns recorded at the output of ring interferometer with three different shears (~ 5, 10, and 20 μm) between two interfering beams. Corresponding phase difference profiles extracted by a Fourier transform technique[21] are shown in Fig. 15. All of the retrieved phasefronts are almost flat across the entire range of measurements, which demonstrates quantitatively that all adjacent stripes are in-phase (0° phase shift between adjacent stripes) when single-lobed output is obtained in the far field. The 0° phase difference is inferred from our previous measurements[21] of free-running carrier-guided arrays with double-lobed far-field output. In that case, a half stripe-spacing lateral shear (~ 5 μm) was introduced between the two interfering beams so that adjacent stripes could partially overlap. This arrangement allowed us to detect phase discontinuities between two adjacent stripes. The resulting phase difference profile (Fig. 6, Ref. 21) clearly showed that in regions of overlap between two adjacent stripes there was a 180° phase jump.

In our present case, no phase difference is revealed in regions where the adjacent stripes overlap with each other. Thus, in conjunction with the single-lobed far-field output, we may conclude that indeed the array operates predominantly in the lowest-order (v = 1) array mode which has the same phase at lasing element. The phase difference plots for one-stripe (10 μm) and two-stripe (20 μm) relative shears also display 0° phase difference all across the junction. This again is different from our free-running results[21], where 180° phase difference was obtained for 10 μm shear and 0° phase difference was detected for 20 μm shear (*cf.* Figs. 9 and 10 in Ref. 21). A slightly inclined slope of the retrieved phase difference for shears of 5 and 10 μm is due to an imperfect zero frequency shift correction in processing of raw interferometer data. Other small features along the retrieved wavefronts indicate that the wavefront over a stripe was not perfectly flat but had a small curvature due to the gain-guided effect or small contributions from adjacent low-order array modes. Small phase jumps at the edges of the recovered wavefronts imply that the phase may not have been locked exactly at 0° at the array edges.

7. CONCLUSIONS

In conclusion, we present a thorough theoretical and experimental study of uniform carrier-guided diode laser arrays coupled to external cavities with spatial filtering. Theoretical analysis is based on a new broad-area

coupled-mode theory. Experimentally, a single-lobed, on-axis, high-power (68 mW with $R_f = 0.9$), nearly diffraction-limited (0.64° FWHM) beam is achieved in very good agreement with predictions of our analysis (0.58° FWHM). The corresponding output power of 266 mW with $R_f = 0.3$ is estimated for the same configuration and the same operating conditions. Single-lobed high-quality output beam is maintained up to $2.35I_{th}$ in CW operation. Measurements of corresponding near-field phasefronts confirm that the fundamental array mode is the major contributing mode.

8. ACKNOWLEDGMENTS

Financial support from the U.S. Air Force Office of Scientific Research and the Air Force Weapons Laboratory is gratefully acknowledged.

9. REFERENCES

1. D. E. Ackley, "Single Longitudinal Mode Operation of High Power Multiple-Stripe Injection Lasers", *Appl. Phys. Lett.*, vol. 42, pp. 152-154, 15 Jan. 1983.
2. D. R. Scifres, C. Lindstrom, R. D. Burnham, W. Streifer, and T. L. Paoli, "Phase-Locked (GaAl)As Laser Diode Emitting 2.6 W CW from a Single Mirror", *Electron. Lett.*, vol. 19, pp. 169-171, 3 March 1983.
3. P. Gavrilovic, K. Meehan, J. E. Epler, N. Holonyak, Jr., R. D. Burnham, R. L. Thornton, and W. Streifer, "Impurity Disordered, Coupled-Stripe $Al_xGa_{1-x}As$-GaAs Quantum Well Laser", *Appl. Phys. Lett.*, vol. 46, pp. 857-859, 1 May 1985.
4. F. Kappeler, "Monolithic Phase-Locked GaAlAs Laser Arrays", *Siemens Forsch.- u. Entwickl.-Ber.*, vol. 14, pp. 289-294, 1985.
5. J. Yaeli, "Phase Measurement of Laser Diode Array Radiation", *Appl. Phys. Lett.*, vol. 49, pp. 427-429, 25 Aug. 1986.
6. G. R. Hadley, J. P. Hohimer, and A. Owyoung, "Free-Running Modes for Gain-Guided Diode Laser Arrays", *IEEE J. Quantum Electron.*, vol. QE-23, pp. 765-773, June 1987.
7. J. Yaeli, W. Streifer, D. R. Scifres, P. S. Cross, R. L. Thornton, and R. D. Burnham, "Array Mode Selection Utilizing an External Cavity Configuration", *Appl. Phys. Lett.*, vol. 47, pp. 89-91, 15 July 1985.
8. C. Chang-Hasnain, D. F. Welch, D. R. Scifres, J. R. Whinnery, A. Dienes, and R. D. Burnham, "Diffraction-Limited Emission from a Diode Laser Array in an Apertured Graded-Index Lens External Cavity", *Appl. Phys. Lett.*, vol. 49, pp. 614-616, 15 Sept. 1986.
9. C. J. Chang-Hasnain, J. Berger, D. R. Scifres, W. Streifer, J. R. Whinnery, and A. Dienes, "High Power with High Efficiency in a Narrow Single-Lobed Beam from a Diode Laser Array in an External Cavity", *Appl. Phys. Lett.*, vol. 50, pp. 1465-1467, 25 May 1987.
10. C. J. Chang-Hasnain, A. Dienes, J. R. Whinnery, W. Streifer, and D. R. Scifres, "Characteristics of the Off-Centered Apertured Mirror External Cavity Laser Array", *Appl. Phys. Lett.*, vol. 54, pp. 484-486, 6 Feb. 1989.
11. R. G. Waarts, D. Mehuys, D. F. Welch, and W. Streifer, "675 mW Diffraction Limited Operation and Thermal Characteristics of Laser Diode Arrays in an External Cavity", *Electron. Lett.*, vol. 26, pp. 1586-1588, 13 Sept. 1990.
12. A. Hardy and W. Streifer, "Analysis of Phased-Array Diode Lasers", *Opt. Lett.*, vol. 10, pp. 335-337, July 1985.
13. A. Hardy and W. Streifer, "Coupled Modes of Multiwaveguide Systems and Phased Arrays", *J. Lightwave Technol.*, vol. LT-4, pp. 90-99, Jan. 1986.
14. W. Streifer, M. Osiński, and A. Hardy, "Reformulation of the Coupled-Mode Theory of Multiwaveguide Systems", *J. Lightwave Technol.*, vol. LT-5, pp. 1-4, Jan. 1987.

15. C.-P. Cherng and M. Osiński, "Coupled Broad-Area Mode Theory of Multiple-Stripe Laser Arrays", to be published in IEEE J. Quantum Electron., 1991.

16. A. Hardy, W. Streifer, and M. Osiński, "Influence of External Mirror on Antireflection-Coated Phased-Array Semiconductor Lasers", *Appl. Phys. Lett.*, vol. 49, pp. 185-187, 28 July 1986.

17. J. W. Goodman, "*Introduction to Fourier Optics*", McGraw-Hill, San Francisco, 1968, Chap. 5, pp. 90-92.

18. J. W. Goodman, "*Introduction to Fourier Optics*", McGraw-Hill, San Francisco, 1968, Chap. 4, pp. 62-65.

19. J.-M. Verdiell and R. Frey, "A Broad-Area Mode-Coupling Model for Multiple-Stripe Semiconductor Lasers", *IEEE J. Quantum Electron.*, vol. 26, pp. 270-279, Feb. 1990.

20. J. M. Verdiell, H. Rajbenbach, and J. P. Huignard, "Array Modes of Multiple-Stripe Diode Lasers: A Broad-Area Mode Coupling Approach", *J. Appl. Phys.*, vol. 66, pp. 1466-1468, 1 Aug. 1989.

21. C.-P. Cherng, T. C. Salvi, M. Osiński, and J. G. McInerney, "Near Field Wavefront Measurements of Semiconductor Laser Arrays by Shearing Interferometry", *Appl. Opt.*, vol. 29, pp. 2701-2706, 2 June, 1990.

Table 1: Carrier-Guided Array Parameters

Parameter	Value
Wavelength	0.82 μm
Array width	100 μm
Number of array elements	10
Stripe width	6 μm
Inter-stripe spacing	4 μm
Active layer thickness	0.2 μm
Al contents in cladding layer	20 %
Al contents in active layer	0.04 %
Antiguiding factor	2
Amplitude of gain modulation	1 cm^{-1}
Effective broad-area gain	40 cm^{-1}
Loss in unpumped region	50 cm^{-1}

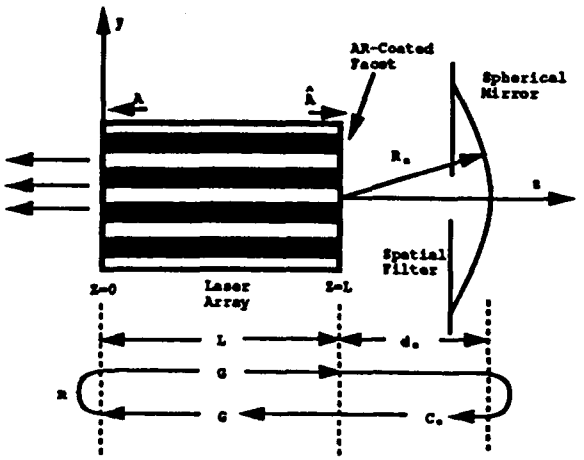

Fig. 1 Geometry of laser array coupled to an external cavity with spatial filter.

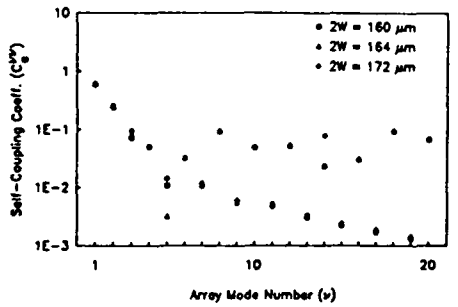

Fig. 2 Self-coupling coefficients for the first 20 array modes.

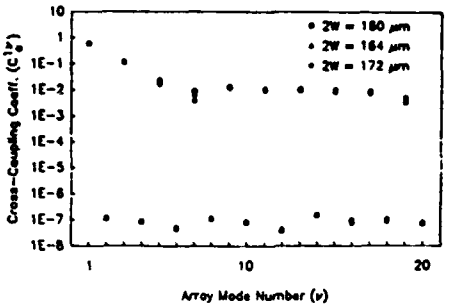

Fig. 3 Cross-coupling coefficients between ν = 1 and other array modes.

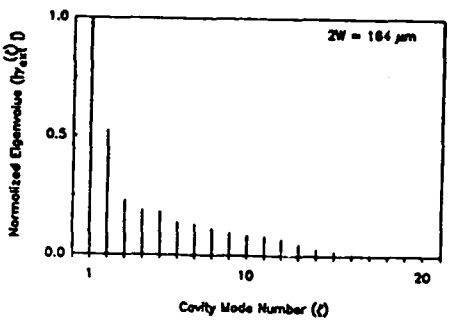

Fig. 4 Relative gain for cavity modes in a spatially filtered feedback configuration.

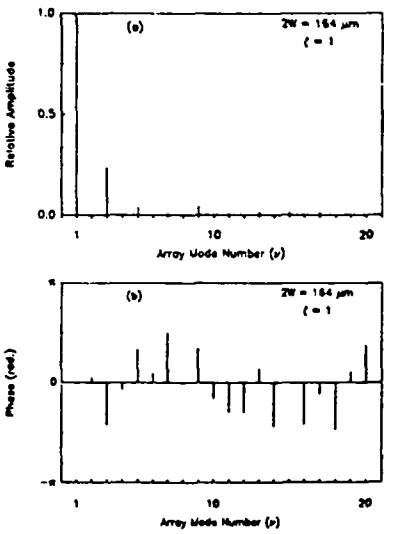

Fig. 5 Amplitude and phase parts of complex array-mode mixing coefficients for ζ = 1 cavity mode.

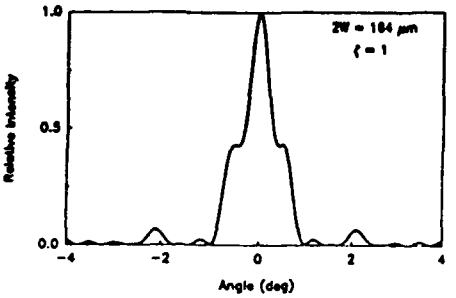

Fig. 6 Far-field radiation pattern for $\zeta = 1$ cavity mode.

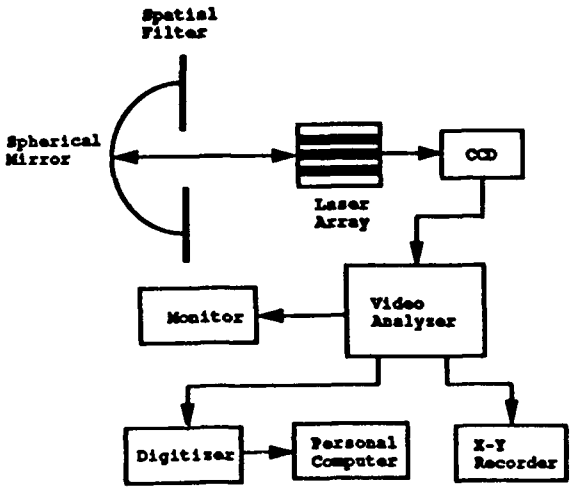

Fig. 7 Experimental set-up for studies of laser arrays in external cavity with spatial filter.

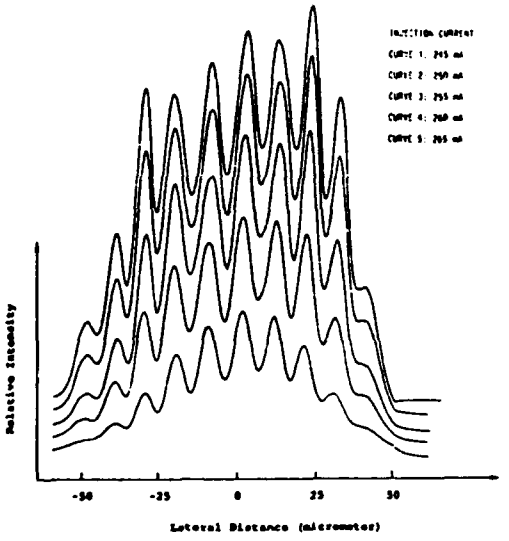

Fig. 8 Near-field patterns of a solitary ten-stripe carrier-guided array for various pumping currents.

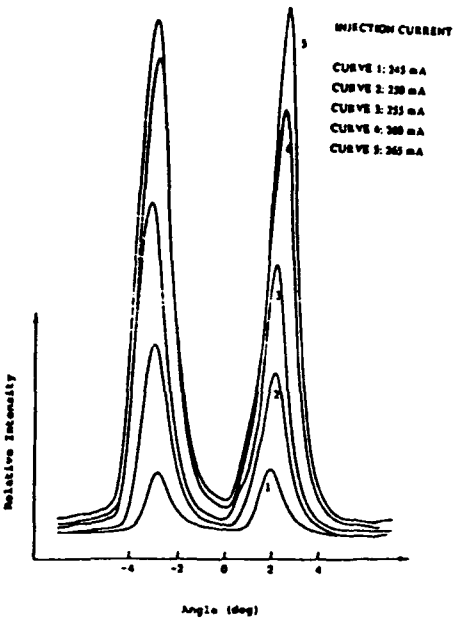

Fig. 9 Far-field patterns of a solitary ten-stripe carrier-guided array for various pumping currents..

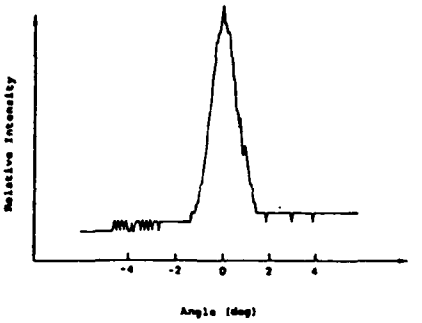

Fig. 10 Single-lobed far field pattern from an uncoated laser array coupled to an external cavity with spatial filter. Pumping current I = 230 mA.

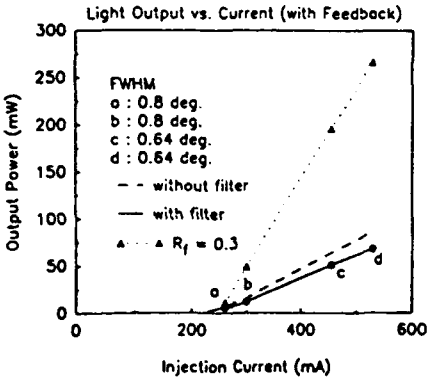

Fig. 11 The $L-I$ characteristics of external-cavity laser array without and with spatial filter.

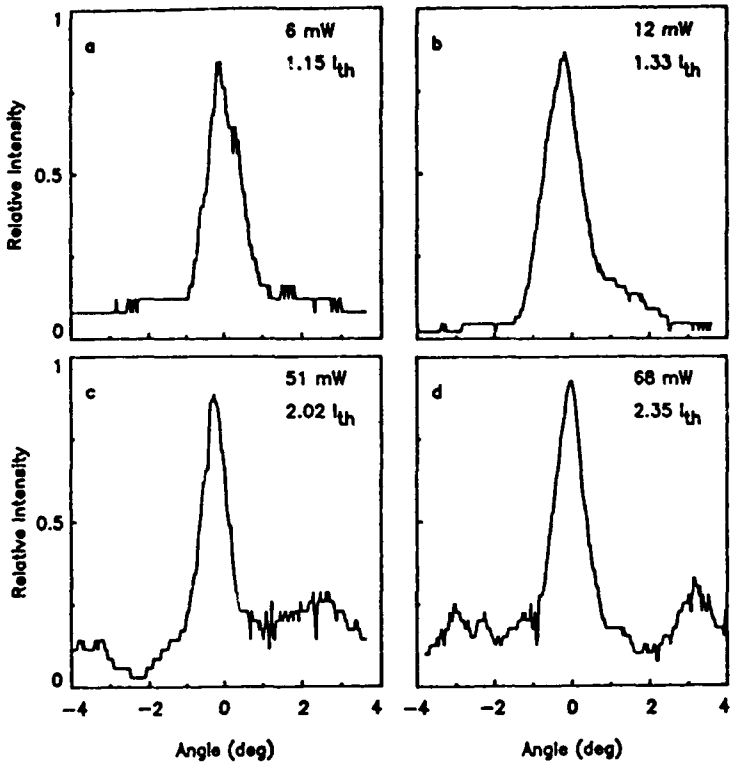

Fig. 12 Single-lobed far-field pattern from an AR-coated laser array coupled to spatial-filter external cavity and driven at four levels of pumping currents, corresponding to points $a-d$ in Fig. 11.

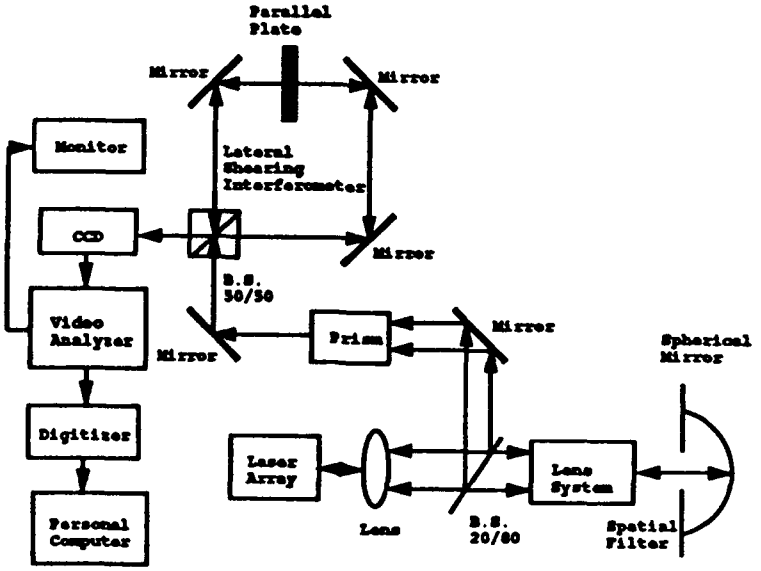

Fig. 13 Experimental set-up for phasefront measurements of single-lobed external-cavity laser array.

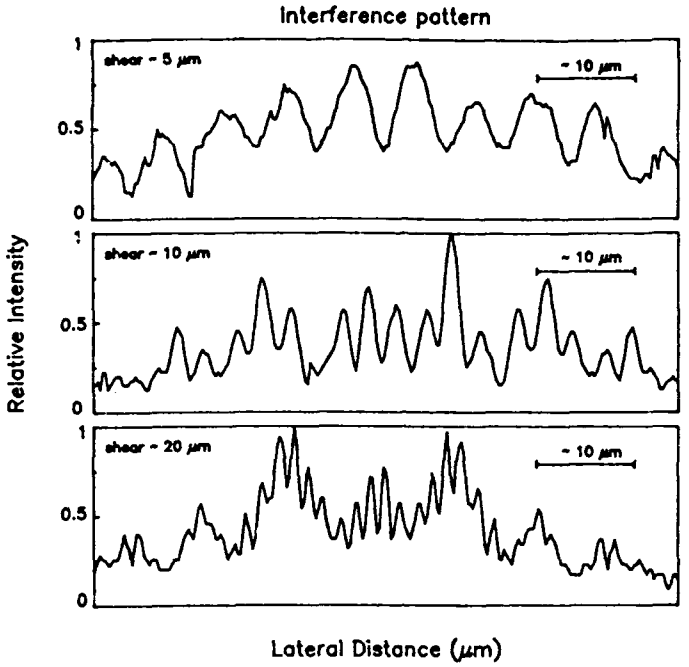

Fig. 14 Interference patterns for three shears (5, 10, 20 μm) at the output of ring interferometer.

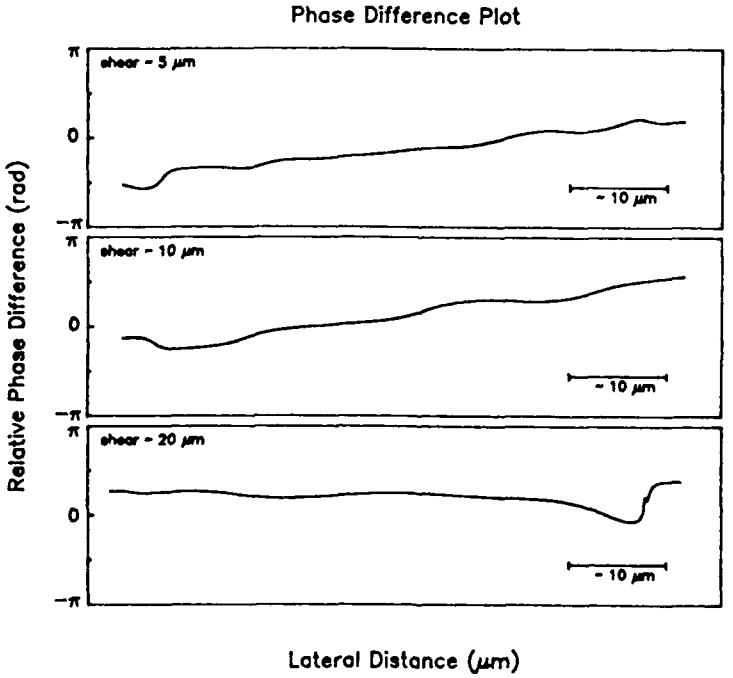

Fig. 15 Phasefront difference profiles retrieved from three interferences shown in Fig. 14.

Confocal Photoluminescence: A Direct Measurement of Semiconductor Carrier Transport Parameters

Yu-Chue Fong[a] and S. R. J. Brueck[a,b]

Center for High Technology Materials

University of New Mexico, Albuquerque, NM 87131

ABSTRACT

Using confocal microscopy a direct measurement of the minority carrier diffusion length of 5 μm is obtained for a 3-nm thick AlGaAs/GaAs graded-index separate confinement heterostructure. A photoluminescence spatial resolution of < 1 μm is obtained by translating the collection aperture of the confocal microscopy arrangement. This technique provides a method for obtaining spatial resolution in photoluminescence from semiconductor structures that is limited only by the optics rather than by carrier transport effects. This resolution is illustrated by monitoring enhanced carrier transport for a transversely graded thickness quantum well formed by MOCVD growth over a cleaved sample edge.

---

[a] Also Department of Electrical and Computer Engineering

[b] Also Department of Physics and Astronomy

Photoluminescence (PL) provides a powerful, noncontact diagnostic of semiconductor properties that is routinely applied to monitor composition, carrier concentration and dynamics, impurity species and concentrations, etc.[1] In semiconductor PL, electron-hole pairs are excited optically and their recombination following interaction with the lattice and with impurities, etc. provides the spectral information. In contrast to Raman scattering measurements, where the spatial resolution is determined solely by the optical arrangement, the spatial resolution of PL measurements is often limited by carrier drift and diffusion before recombination. Very high spatial resolution is attainable in the excitation step using electron-beams (cathodoluminescence) or by related techniques such as scanning tunneling microscopy[2]. However, excited carrier transport still determines the achievable resolution. Near-field optical microscopy [3,4] can image extreme sub-wavelength features defined by large dielectric discontinuities, but cannot provide spatial resolution for fine structure.

Confocal microscopy has advantages of enhanced spatial resolution, of optical sectioning or depth profiling, and of relative insensitivity to scattered light[5]. Much work has been done on confocal fluorescence in chemical and biological samples; instruments have also been developed specifically for use in semiconductor manufacturing inspection and metrology [6]. In its simplest form, confocal microscopy uses matched illumination and collection optics and back-focal-plane apertures to monitor the reflection (or transmission) of only a single focal spot on the sample. An image is formed either by translating the sample under this spot or by translating the optical train across the sample. When applied to PL, confocal microscopy clearly avoids the carrier transport issue by rejecting any luminescence that originates from carriers that have moved outside of the directly illuminated area. By translating the collection optics aperture to collect the luminescence as a

function of position, a simple and direct measurement of carrier transport parameters is immediately available. Similar experiments with lower resolution have recently been reported [7,8]. These experiments were focused on long-range carrier transport in "surface-free" samples and did not explore the resolution limits of confocal PL microscopy.

Here, we report initial results on confocal photoluminescence for a GaAs/AlGaAs graded-index separate confinement heterostructure (GRIN-SCH) quantum well semiconductor sample, similar to that used in many semiconductor laser structures. This structure was grown on a 1.2-mm wide, cleaved GaAs sample placed onto a 2"-diameter wafer. This results in significant variations in the quantum well thickness near the sample edges which are explored using confocal PL microscopy.

Effects observed include: direct measurement of carrier diffusion length (~5 μm at room temperature) in the quantum well; variation of PL peak frequency across entire sample with dramatic effects near the sample edges; a similar variation of PL quantum efficiency across sample; and evidence for carrier drift in the plane of the quantum well towards a wider quantum well.

The optical arrangement of the confocal PL microscope is shown in Figure 1. The excitation is provided by an Ar^+-ion laser beam at 514.5 nm which is imaged onto the sample using a 50-μm aperture in the back-focal-plane of the final objective, a beamsplitter, and a 60X microscope objective (N.A. = 0.85) to illuminate a ~0.75-μm diameter spot. The focal spot diameter was calibrated using a knife-edge technique. Total power was varied from 58 μW to 380 μW (~1-7 kW/cm^2) without any change in spatial or spectral characteristics. The PL was collected with the same microscope objective and imaged onto a matched 50-μm aperture in the back-focal-plane and further relayed to a spectrometer for spectral analysis. The

spectrometer slitwidths were large compared with the aperture to avoid any spurious spatial filtering. This collection aperture could be translated to allow direct measurement of carrier transport effects. Because of the 60X magnification, translation was readily accomplished with a simple micrometer stage.

The illuminated area on the sample is given by the Gaussian laser focal spot. The luminescence $L(\vec{r}_{GaAs})$ originates from a larger area as a result of carrier transport by diffusion and drift away from the excitation region. $L(\vec{r}_{GaAs})$ is imaged onto the plane of the collection aperture by the microscope objective, that is

$$I(\vec{r}_{aper}/M) = \int |h(\vec{r}_{aper}/M - \vec{r}_{GaAs})|^2 L(\vec{r}_{GaAs}) d\vec{r}_{GaAs}. \quad (1)$$

Here, M is the magnification and $h(\vec{r}) = 2J_1(\upsilon)/\upsilon$ with $\upsilon = 2\pi r \sin\alpha/\lambda_{lum}$ is the point spread function of the microscope objective at the luminescence wavelength with $\sin\alpha$ the numerical aperture. The spatial resolution of the collection is given by this point spread function convolved with the aperture function. For a sufficiently small aperture, the achievable resolution is just given by the Airy pattern associated with the lens and is ~0.8-μm diameter at the sample at the $1/e^2$ points at 800 nm. Typically, apertures of ~1/2 the diameter of the point spread function, referenced to the aperture plane, are required to achieve this resolution [5]; the 50-μm diameter aperture used in these experiments is slightly larger and somewhat degrades the achieved resolution.

The sample was prepared by MOCVD at a growth temperature of 725°C. The growth profile of the GRIN-SCH structure is shown as the inset to Fig. 1. The background n-type doping of the as-grown quantum well is equivalent to a bulk density of ~5×10^{16} cm^{-3}. The starting material was cleaved in a narrow stripe, 1.2 x 20 mm^2. This sample was mounted atop a 2" diameter wafer with the long

dimension perpendicular to the gas flow. The inhomogeneity in the gas flow introduced by the sample edges results in a variation in the growth rates, and in the final quantum well width, near the edges of the sample. Growth on patterned substrates is a important developing field within optoelectronic devices[9]. Regrowth over patterned areas is also increasingly important for device isolation and other novel functions that cannot be achieved with uniform growth. A detailed understanding of the growth process over steps and other topology is necessary for full exploitation of these possibilities.

Figure 2 shows the result of scanning the sample in a conventional confocal fluorescence microscopy arrangement with the collection aperture conjugate with the input aperture so that the PL of the excited region is monitored. Both the peak PL wavelength and the PL intensity at this wavelength show systematic shifts across the sample (0 is the middle of the 1.2-mm wide sample) with larger effects near the edge. The change in luminescence wavelength suggests that the quantum well width is increased near the sample edge. The PL was relatively broad, halfwidth of 23 nm, which suggests that sample inhomogeneities, impurity incorporation and interface roughness significantly affect the carrier transport. Previous studies of minority carrier lifetimes have shown that minority carrier recombination in narrow quantum well structures such as these is typically dominated by nonradiative interface effects and AlGaAs quality that depend sensitively on growth temperature and other parameters of the growth process [10].

The resolution of confocal PL is demonstrated in Fig. 3. The bottom panel shows the results of three images formed by translating the collection aperture. The narrowest scan is the coherent, bright-field confocal reflection image of the excitation beam with a HWHM of 0.38 μm. The enhanced spatial resolution of coherent confocal microscopy (proportional to h^4) and the shorter excitation

wavelength result in this high spatial resolution. The intermediate trace (HWHM ~ 0.9 μm) for PL from a thin dye film (LDS-821) sandwiched between glass slides provides a measure of the system resolution, which is lower for luminescence than for bright-field reflection. The widest trace is the sample PL taken at the center of the sample away from the variations in quantum well width.

At the excitation wavelength (514.5 nm) the $Al_{0.6}Ga_{0.4}As$ absorption length is about 0.2 μm so that the incident photons are absorbed into cladding and reach the quantum well by diffusion processes. Once in the quantum well, the diffusion process is two-dimensional. The Green's function in two dimensions is $K_o(\rho/L_D)$ where K_o is a modified Bessel function, ρ is the polar radius and $L_D^2 = D\tau$ with D the diffusion coefficient and τ the minority carrier lifetime. The minority carrier distribution is given by the convolution of the source distribution with this impulse response. For an excitation area small compared with the diffusion length, this simply gives a minority carrier spatial dependence that scales as K_o with an asymptotic dependence of $(\rho)^{-1/2}\exp(-\rho)$ where $\rho = \rho/L_D$. The solid curves in the figure give the best fit to this Bessel function with L_D=5.3 μm.

The middle panel of Fig. 3 shows the spatially resolved PL, obtained for a fixed excitation spot by translating the collection aperture, for an excitation spot approximately 15 μm from the sample edge in the region of rapid variation of the well thickness with distance. The gradient of the well width in this region results in an additional force on the carriers drifting them towards the thicker regions of the quantum well. This is responsible for the asymmetry and increased intensity on the right-hand side of the figure. An additional compensating influence on the spatial profiles is the rapidly decreasing local nonradiative decay rates as the carriers drift towards the sample edge. The solid curves in the figure give the best fit to the simple Bessel function diffusion calculation. The enhanced effective diffusion

length in the direction towards the surface is suggestive of carrier drift towards the wider portion of the quantum well. The top trace shows the measured PL peak frequency for the data of the middle panel. The shift in frequency clearly demonstrates that the PL is originating from carriers that are equilibrated with the local band structure. The three points marked with triangles were taken in a conventional confocal geometry, (Fig. 2) moving the sample with the two apertures in conjugate positions. There is good agreement between the frequency shifts in the two experiments.

In summary, a confocal microscopy technique providing high spatial resolution for PL experiments has been demonstrated. A spatial resolution of $< 1\ \mu m$ is achieved. The capabilities of this technique have been demonstrated by monitoring the spatial dependence of the PL for a transversely graded GRIN-SCH structure obtained by MOCVD growth on a patterned substrate. Future experiments will extend these measurements to more conventional patterned substrates including regrown laser arrays and unstable resonators. Additionally, measurements are planned adding ultrafast time resolution to this spatial resolution to obtain a more complete picture of the carrier dynamics.

Acknowledgements: We thank Prof. C. F. Schaus and Dr. S. Z. Sun for growth of the sample and for helpful discussions. Useful discussions with Prof. S. D. Hersee are gratefully acknowledged. Partial support for this work was provided by the Air Force Office of Scientific Research.

References:

1. M. Voos, R. F. Leheny, and J. Shah in Optical Properties of Semiconductors, M. Balkanski, ed. Volume 2 of **Semiconductor Handbook**, T. S. Moss, Series ed. (North-Holland, 1980).
2. D. L. Abraham, A. Veider, Ch. Schoenenberger, H. P. Meier, D. J. Arendt, and S. F. Alvarado, Appl. Phys. Lett. **56**, 1564 (1990).
3. E. Betzig, J. K. Trautman, T. D. Harris, J. S. Weiner and R. L. Kostelak, Science **251** 1468 (1991).
4. T. L. Ferrell, J. P. Goundonnet, R. C. Reddick, S. L. Sharp, and R. J. Warmack, J. Vac. Sci. Technol. **B9**, 525 (1991).
5. T. Wilson, in Confocal Microscopy, T. Wilson, ed. (Academic Press, London, 1990).
6. R. W. Wijnaendts-van-Resandt, "Semiconductor Metrology", in Confocal Microscopy, T. Wilson, ed. (Academic Press, London, 1990), Chap. 13, pp. 339-360.
7. L. M. Smith, D. J. Wolford, J. Martinsen, R. Venkatasubramian and S. K. Ghandi, J. Vac. Sci. Technol. **B8**, 787 (1990).
8. G. D. Gilliland, D. J. Wolford, T. F. Kuech, and J. A. Bradley, Appl. Phys. Lett. **59**, 216 (1991).
9. E. Kapon, S. Simhony, R. Bhat, and D. M. Hwang, Appl. Phys. Lett. **55**, 2715 (1989)
10. A. Hariz, P. D. Dapkus, H. C. Lee, E. P. Menu, and S. P. DenBaars, Appl. Phys. Lett. **54**, 635 (1989).

Figure Captions:

Fig. 1: Experimental arrangement for confocal photoluminescence. The inset shows the epitaxial growth structure.

Fig. 2: Peak wavelength of PL and relative signal intensity across the sample. Data is shown from the center to an edge of the 1.2-mm wide sample. The MOCVD gas flow was normal to this dimension. Note the rapid changes in PL wavelength and intensity near the sample edge.

Fig. 3: Spatially resolved PL taken by scanning the collection aperture with a fixed excitation spot. The narrowest scan in the bottom panel is the bright-field confocal reflectivity of the laser source (width ~ 0.76 μm), the next scan is the PL from a thin dye film (LDS-821) that provides a measure of the experimental resolution of ~1.8 μm at the luminescence wavelength. The final scan is the PL from the central position of the sample. The middle panel shows a similar scan from a position 15 μm from the sample edge. The asymmetry towards the right results from carrier drift because of the quantum well thickness gradient. The top panel shows the peak PL wavelength for this data. The points marked with a Δ were obtained in a conventional confocal arrangement (e. g. Fig. 2).

EXPERIMENTAL ARRANGEMENT FOR CONFOCAL PHOTOLUMINESCENCE MICROSCOPY

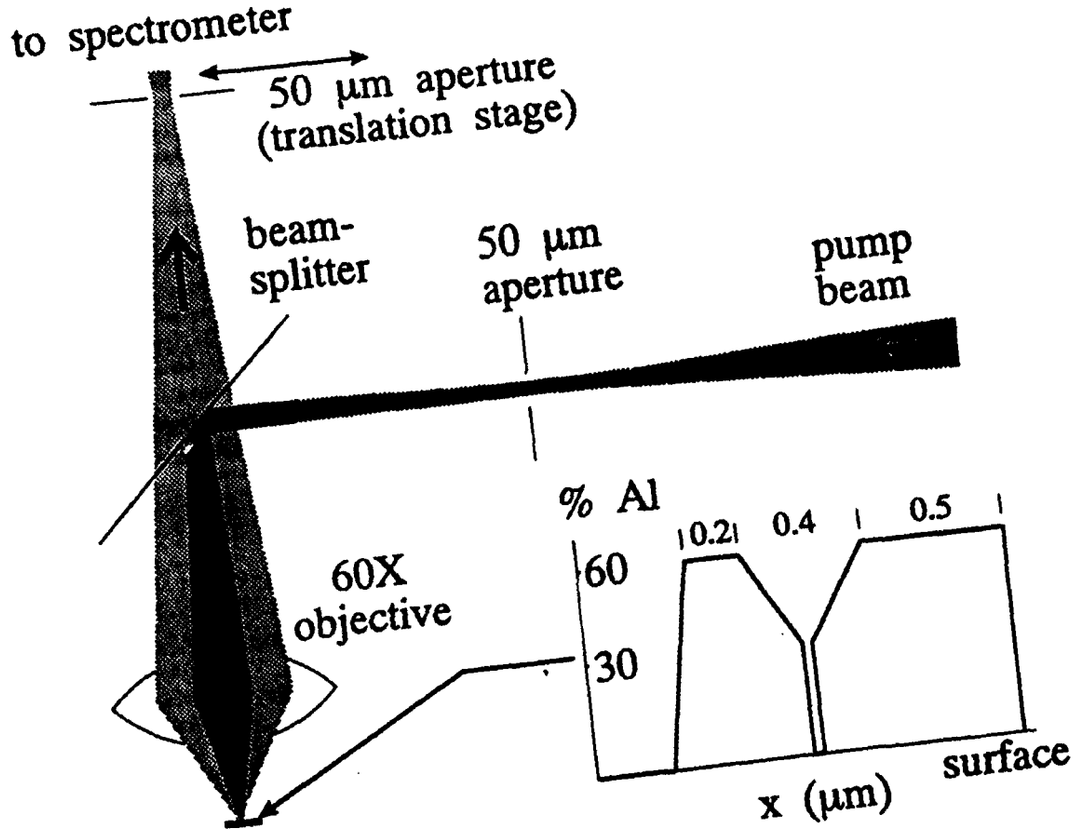

Fong and Brueck Fig. 1

PL VARIATION ACROSS GROWTH EDGE

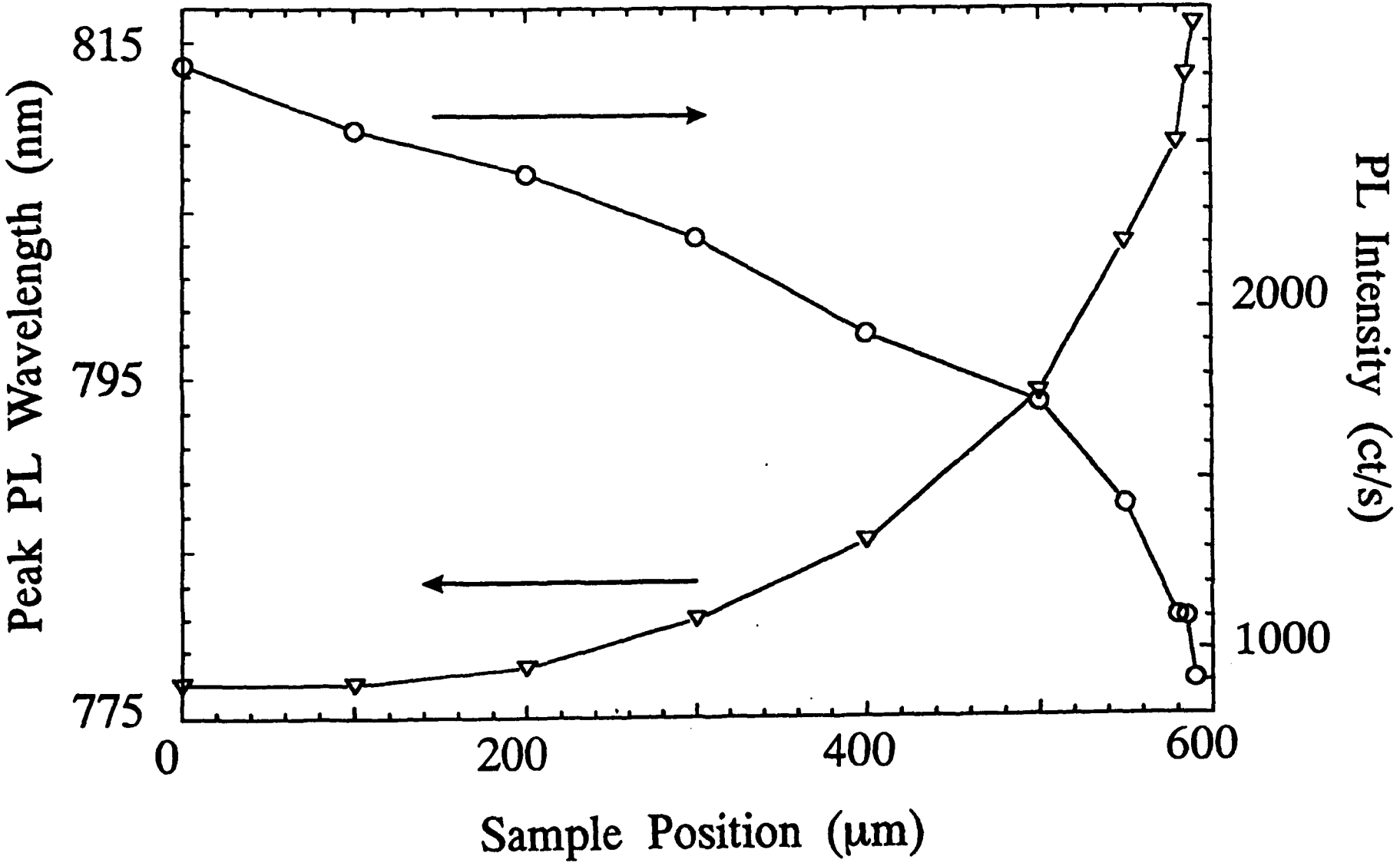

DIRECT MEASUREMENT OF CARRIER DIFFUSION IN GaAs QW

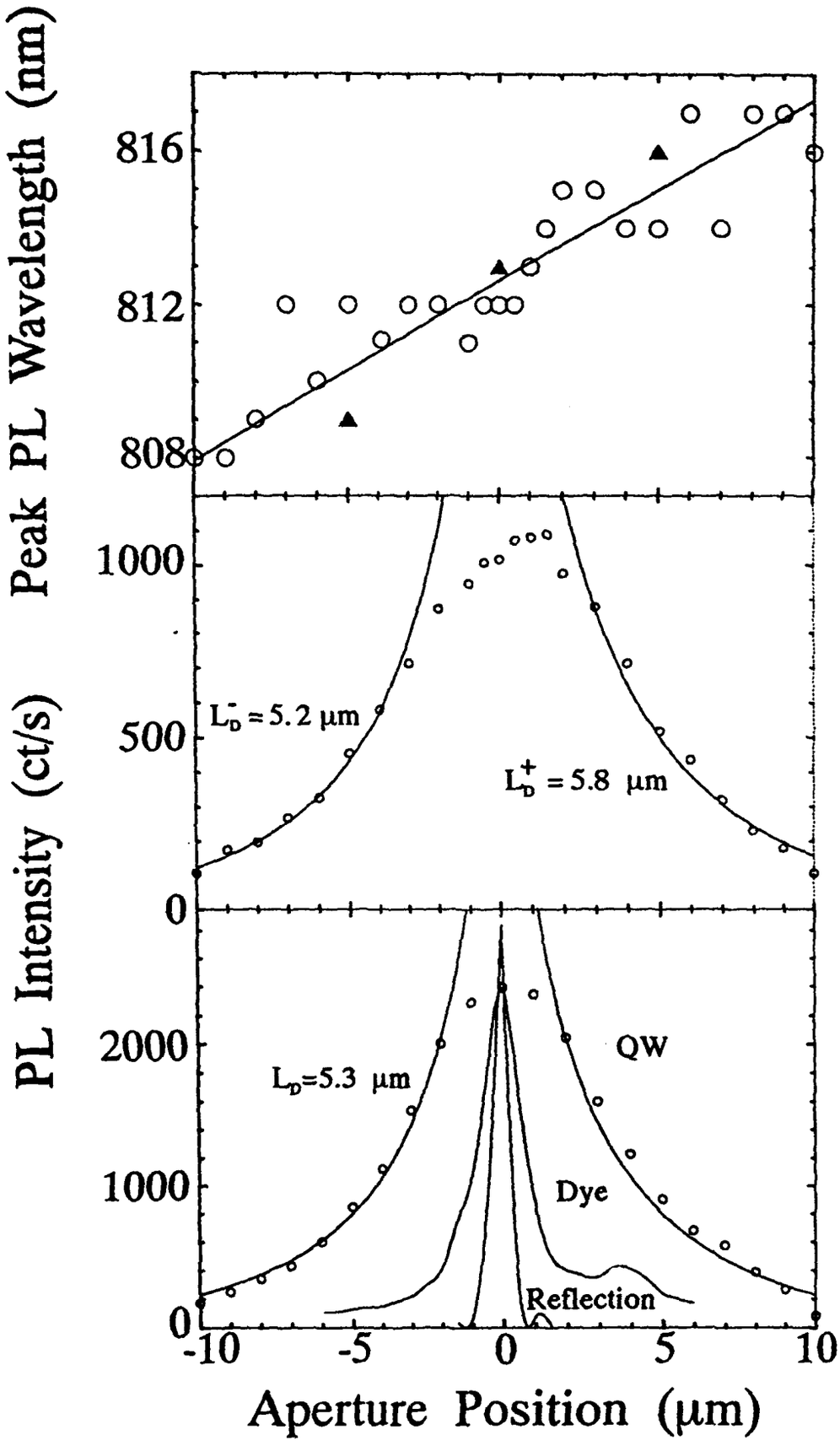

~~To be submitted~~
Accepted to APL
to be published 4/1/91

OPTICAL SCATTER IN EPITAXIAL SEMICONDUCTOR MULTILAYERS

P. L. Gourley, L. R. Dawson, T. M. Brennan, and B. E. Hammons
Sandia National Laboratories
Albuquerque, NM 87185

J. C. Stover
TMA Technologies, Inc.
Bozeman, MT 59715

C. F. Schaus and S. Sun
Center for High Technology Materials and
Department of Electrical and Computing Engineering
University of New Mexico
Albuquerque, NM 87131

ABSTRACT

We report the first measurements of optical scatter in epitaxial semiconductor multilayer structures. The structures comprise quarter-wave layers of $Al_{0.2}GaAs$/AlAs and GaAs/AlAs grown by molecular beam epitaxy and $Al_{0.2}GaAs$/AlAs grown by metal-organic chemical vapor deposition to assess differences due to growth technique and layer composition. The bidirectional reflective distribution function (BRDF) is measured at wavelength of 835 nm. This wavelength corresponds closely to the Bragg reflection condition of the multilayer which was determined by separate micro-reflectance spectroscopy. The BRDF measurement yields values for the total integrated scatter and and effective surface roughness. The former is in the range 7×10^{-4} to 5×10^{-3} while the latter is in the range 3 to 16Å. We suspect that the scattering loss is determined by the quality of the substrate material and not by artifacts produced in the growth process itself. Both growth techniques yield comparable scatter loss on average, but there are significant differences in microscopic surface morphology, uniformity of scatter across the wafer, and lower limits of scatter. The measurements have significant implications for applications such as surface emitting laser technology.

Semiconductor surfaces are routinely examined for structural defects by eye or under the microscope. Such examination usually occurs after polishing the wafer or after growth of an epitaxial layer. However, the optical scatter which reveals these defects to the eye is seldom measured quantitatively. This is in spite of the fact that optical scattering is a very powerful tool which yields information about the microstructure of the surface on an angstrom scale.[1] The importance of measuring optical scatter from microstructure of semiconductor surfaces and interfaces has arisen recently through the development of epitaxial semiconductor optics.[2] These structures comprise quarter-wave multilayers of semiconductors with applications including surface-emitting lasers, bistable optical devices, optical modulators and detectors. Multilayers used as mirrors feature narrow band reflectance which can exceed 99 percent. Spectral characteristics of multilayers grown by both molecular beam epitaxy[3] and chemical vapor deposition[4] have been reported. The ultimate reflectance which can be attained is limited by absorption and scattering. Elastic optical scattering is primarily determined by the crystalline imperfection of the mirror layers and interfaces. Defects such as interface roughness, surface defects (hillocks and oval defects), dislocations, and compositional uniformity will all contribute to optical scatter. Despite these defects, epitaxial mirrors are expected to exhibit less optical scatter than conventional multilayer mirrors prepared by vacuum deposition. The latter mirrors exhibit a columnar, polycrystalline morphology which limits the perfection of the layers.[5] This limitation is not present in single crystal semiconductor mirrors which are grown epitaxially on semiconductor substrates such that atomic registration is preserved from layer to layer. The substrate material can influence the perfection of the grown layers. It is the purpose of the present letter to report the optical scatter of semiconductor mirrors grown on commonly available GaAs substrates.

In this letter we report measurements of optical scattering from three different structures comprising epitaxial semiconductor multilayers

grown by molecular beam epitaxy (MBE) or metal-organic chemical vapor deposition (MOCVD). Two of the structures BI071 and UNM150 comprise $Al_{0.2}Ga_{0.8}As$/AlAs (710/640 Å) multilayers and are grown by MBE (Riber) and MOCVD, respectively. The third structure VR867 comprises an AlAs/GaAs (850/670 Å) multilayer grown by MBE (Vacuum Generators). All three of the mulilayers were designed as quarter-wave high reflectors for the wavelength range 800-900 nm as part of a surface-emitting laser. Each multilayer showed a reflectance peak in this wavelength range when the surface normal reflectance spectrum was measured (data not shown here). All of the structures lased continuously with high efficiency at room temperature when optically pumped with 7525 Å light.

The optical scatter from each structure was determined by measuring the bidirectional reflective distribution function (BRDF) as described previously.[6] In this measurement, collimated light at 835 nm was directed near normal incidence (4° off) onto the sample. This wavelength was chosen because it is near the design wavelength of the high reflectance zone of the mirrors. Consequently, only the top surface and first few mirror layers are sampled. Light scattered in the plane of incidence was measured as a function of angle from the normal with a small area (2.5 mm diameter) photodetector located 60 cm from the sample. The BRDF is defined as

$$\mathrm{BRDF} = \frac{1}{P_i/A}\,\frac{dP_s/d\omega_s}{A\cos\theta_s} \qquad (1)$$

where P_i is the incident power, A the irradiated area, and dP_s the differential power scattered into differential solid angle ω_s at angle θ_s from the normal in the plane of incidence. The units of BRDF are inverse steradians. In addition, the background scatter was measured with the sample removed from the light beam. This allowed us to isolate the effects of the instrumentation from the scattering measurements.

The BRDF measurement was performed separately for two different spot sizes of 2mm and 0.4mm. The larger spot size allows us to extend the range

of the BRDF measurement to small scattering angles. The smaller spot size allows us to decrease the scattering from pits on the wafers. Typically, we observed pits that were a few microns in size and spaced hundreds of microns apart. The BRDF measured with the smaller spot size is probably influenced by scattering from these pits which are associated with the substrate. With the smaller spot size, the scatter light was measured at a fixed angle (9° from normal which is sensitive to large rms roughness) while the wafer was raster scanned with respect to the fixed incident beam. This yielded a 2-dimensional map of the scattering from the wafer surface. With this map, regions of lowest possible scatter could be identified and full BRDF measurement made. From these maps we made histograms of the frequency of occurence of scattered intensity across the wafer, shown in Fig. 1. These data show average scattered intensities that vary from $5x10^{-3}$ for DK151, $8x10^{-4}$ for UNM150, and $5x10^{-4}$ for VR867. This latter wafer had the least average scatter and the scatter was most uniform across the wafer as 80% of the samples occured in the range $2x10^{-4}$ to $2x10^{-5}$. The lowest possible scatter $3x10^{-5}$ occured in a few selected positions on wafer UNM150. Wafer DK151 shows considerable more scatter and less uniformity than the other two wafers.

The BRDF measurements for low scatter regions on the three wafers are shown in Fig. 2a. As well, the instrumental background measurement is shown by the dashed line. Each scatter curve shows a pronounced peak at 0° corresponding to specular reflectance. There is a break in the data from -4° to -10° where the photodetector blocks the incident beam. Away from 0° the curves fall off by factors of 10^{8} to 10^{11} depending on sample. The shape of the BRDF is similar for the two MBE-grown structures. Although scattering from DK151 is about 10 times greater than VR867, both curves are relatively flat for angles larger than 15°. In contrast, the BRDF for the MOCVD-grown structure continues to decrease for angles up to 30°. Beyond 30° this curve is relatively flat, exhibiting 10 to 100 times less scatter than the MBE grown wafers.

The total scatter from each wafer can be computed from the BRDF measurement by assuming isotropic scattering. The calculated total integrated scatter (CTIS) is given by $CTIS = P_s^{tot}/P_{spec}$ where

$$P_s^{tot} = \int_0^{2\pi} d\phi \int_0^{\theta_{max}} P_s(\theta)\, d\theta \qquad (2)$$

where θ is the scattering angle and ϕ the angle out of the scattering plane. The CTIS calculated from the BRDF measurements of Fig. 2a are 1.3×10^{-5} for UNM150, 1.4×10^{-4} for VR867, and 3.2×10^{-4} for DK151. Thus for data of Fig. 2a, the reduced large angle scattering for the MOCVD-grown structure yields the lowest total scatter for all wafers.

The power spectral density (PSD) is a useful surface statistic which can be calculated directly from the BRDF measurements.[7-9] The method for obtaining the PSD from the scattering measurement has been previously discussed for the case of smooth surfaces.[10] The PSD can be interpreted as the roughness power per unit spatial frequency and is shown in Fig. 2b for the three different structures. All three curves show that the roughness power for scattering is maximum at low spatial frequencies and decreases almost monotonically to the upper limit of the spatial frequencies studied. This general behavior is characteristic of most optical surfaces. The curves for the two MBE grown structures are similar over most the spatial frequency range. The curve for the MOCVD grown structure is distinctly lower, especially at the higher spatial frequencies near 1 μm^{-1}. An effective root mean square roughness over the 1 to 30 μm range can be determined from the PSD curves by integrating over the range of spatial frequencies. The results give 2.7, 8.5, and 16 Å for UNM150, VR867, and DK151, respectively. The root mean square roughness statistic is more appropriate for single optical surfaces and care must be exercised in its interpretation for

multilayers. It represents the equivalent roughness of a hypothetical single optical surface with equivalent reflectivity.

The data of Fig. 2 correspond to wafer regions of lowest possible scatter in the histograms of Fig. 1. Scattering data shown in Fig. 3 were also obtained from wafer regions corresponding to the highest frequency of occurence in the histograms. In these measurements the BRDF was recorded with a larger spot size of 2mm. As a consequence, the scatter could be measured to much smaller angles than those in Fig. 2a. The scattering curves for VR867 and UNM150 shown in Fig. 3a are more sharply peaked about 0° scattering angle. Both curves are relatively flat beyond 15° and have similar magnitude. The calculated total integrated scatter is 8×10^{-4} for both curves. The PSD calculated from these curves are shown in Fig. 3b. The PSD decreases monotonically over the extended range 10^{-3} to 1 μm^{-1} corresponding to 1000 to 1 μm sizes. At low spatial frequency the PSD exhibits 3 major peaks. At high spatial frequency the PSD is nearly featureless but exhibits a minimum near 0.5 μm^{-1}.

As a separate part of this study, we examined the surfaces of the wafers by Normarski differential interference contrast microscopy. for sample VR867, under low magnification 50x the surface appears very smooth. Under high magnification 400x, the surface exhibits a very high density (about 10^6 cm^{-2}) of small ~1 μm pits, barely visible to the eye. The other two samples UNM150 and BI071 appeared very smooth under high magnification. Under low magnification, all of the samples featured pits ranging in size from a few to tens of microns. The pit density was in the range 10^4 to 10^5 cm^{-2}. These pits are likely due to inperfections in the substrate materials which are reproduced in the epitaxial layers. We note that the scattering measurements of Fig. 2 (Fig. 3) are made with a 0.4 mm (2mm) spot on the wafer. Thus, tens to hundreds of pits are sampled. We anticipate that these pits contribute significantly to the BRDF scatter measurements. Thus the measurements reported here may not represent the lower limit of intrinsic scatter by the grown-in roughness of the semiconductor surface/layer

interfaces. If smaller sampling areas (10 μm or less) could be used, the scattering contribution due to the pits could be eliminated completely.

In summary, optical scattering measurements of surface/interface roughness were made for semiconductor quarter-wave multilayers grown by both MBE and MOCVD. The results showed that most uniform low scatter across the wafer was achieved with the MBE technique. The MOCVD technique yielded the lowest possible total scatter 10^{-5} at selected wafer points, which compares favorably to state-of-the-art ring laser gyro optics.[11] More typically, the total scatter from such multilayers is about $1x10^{-3}$ and is probably limited by the quality of the substrate. Applications such as GaAs-based surface-emitting lasers[12] (especially single quantum well lasers) should benefit by improvements in multilayers which reduce optical scatter.

We thank G. Valliant and A. E. McDonald for technical assistance. This work is supported by the U. S. Department of Energy under contract number DE-AC04-76DP00789.

References

1. H. E. Bennett and J. O. Porteus, J. Opt. Soc. Am. 51 123 (1961).

2. see the review by P. L. Gourley, R. M. Biefeld, T. J. Drummond, and T. E. Zipperian, SPIE 792 178 (1987).

3. J. P. Van der Ziel and M. Illegems, Appl. Opt. 14 2627 (1975), 15 1256 (1976).

4. R. L. Thorton, R. D. Burnham, and W. Striefer, Appl. Phys. Lett. 45 1028 (1984).

5. K. H. Guenther, Appl. Opt. 15 2992 (1976).

6. J. C. Stover, S. A. Serati, and C. H. Gillespie, Opt. Engr. 23, 406 (1984).

7. J. M. Elson, J. P. Rahn, and J. M. Bennett, Appl. Opt. 19 669 (1980).

8. J. M. Elson and J. M. Bennett, J. Opt. Soc. Am. 69 31 (1979).

9. P. Beckmann in Progress in Optics, vol. 6, chap. 2, Pergammon Press, xxx.

10. E. L. Church and J. M. Zavada, Appl. Opt. 14 1788 (1975).

11. ref to ring laser gyro measurements.

12. see for example, P. L. Gourley, T. M. Brennan, B. E. Hammons, S. W. Corzine, R. S. Geels, R. H. Yan, J. W. Scott, and L. A. Coldren, Appl. Phys. Lett. 54 1209 (1989).

Figure Captions

1. Histograms showing the occurence of a given scattered intensity across the wafer for three different epitaxial semiconductor mirror structures. The incident and scattering angles are 4° and 9° from the surface normal, respectively. The spot size is 0.4 mm and the light wavelength is 835 nm.

2. (a) Bidirectional reflective distribution function (BRDF) measured for the three different wafers. The measurements were made with a 0.4mm spot size at selected positions on the wafer corresponding to low scatter. Upper curve: wafer DK151 grown by MBE, middle curve: wafer VR867 grown by MBE, bottom curve: wafer UNM150 grown by MOCVD.

(b) Power spectral density for the three wafers. The curves were computed from the bireflective distribution function shown in (a).

3. (a) Bidirectional reflective distribution function (BRDF) measured for samples VR867 and UNM150 with a 2 mm spot size at positions on the wafer corresponding to the average scatter.

(b) Power spectral density computed from the bireflective distribution function shown in (a).

DISTRIBUTION OF SCATTERED INTENSITIES ACROSS WAFER AT $\theta = 9°$

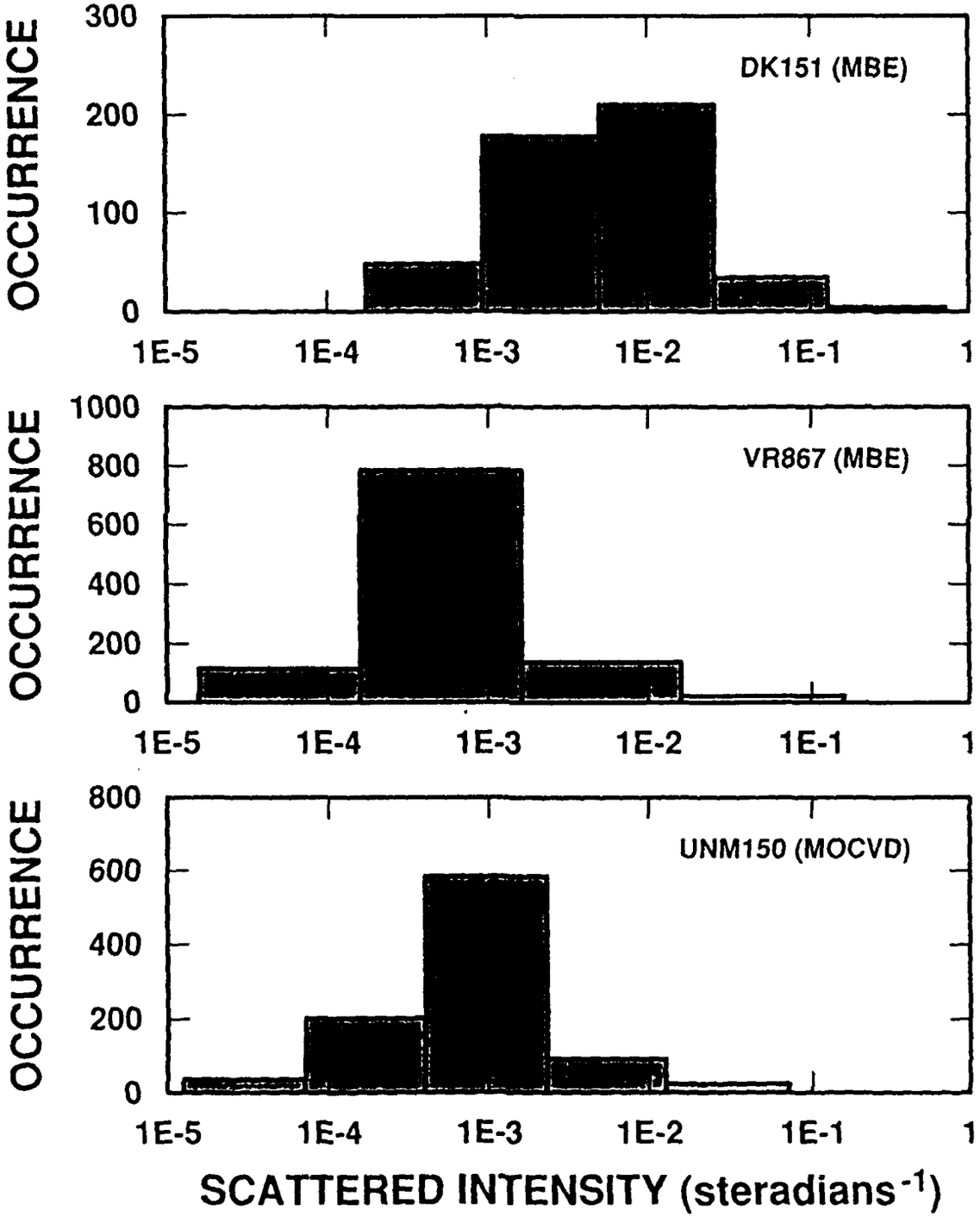

TA0206 01.03

Fig. 1

(a)

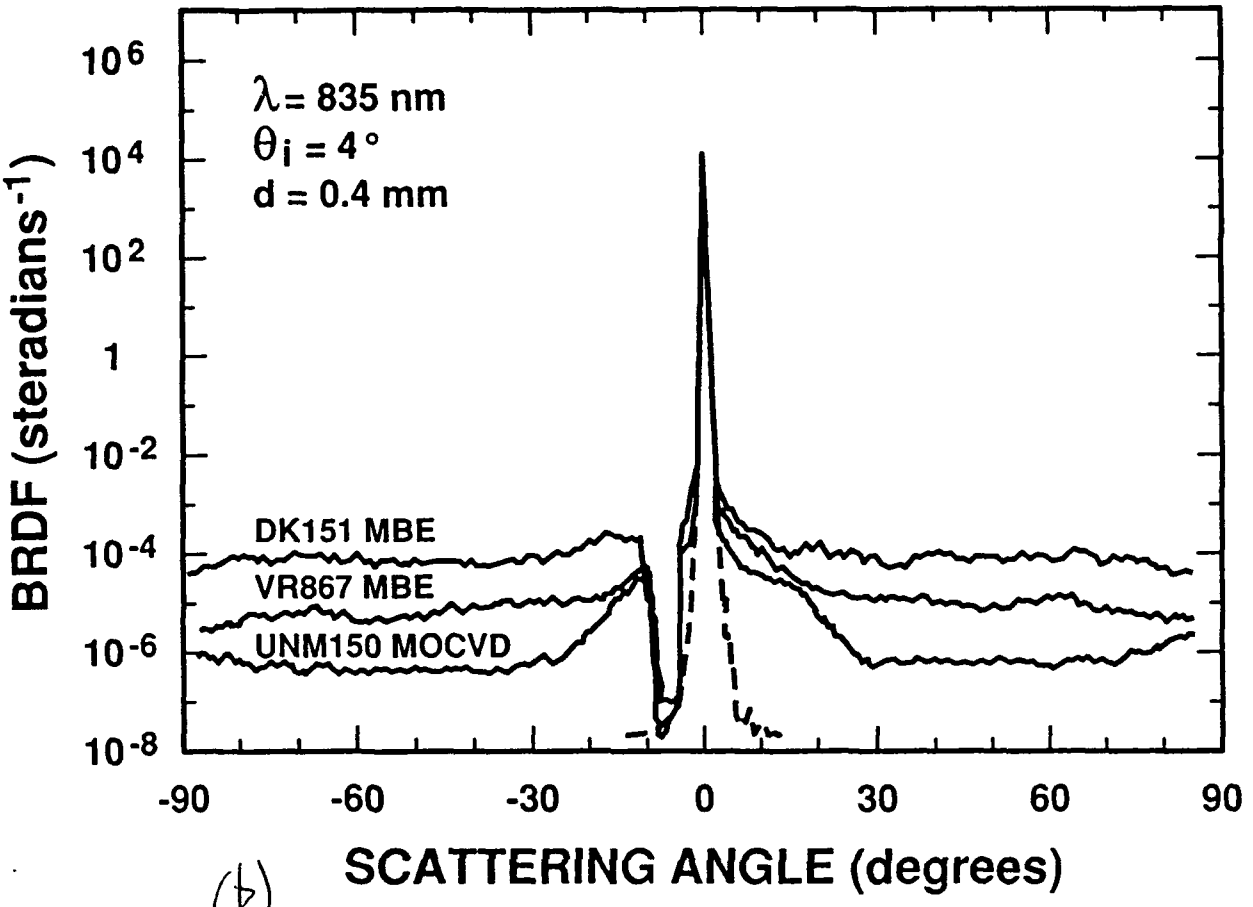

(b)

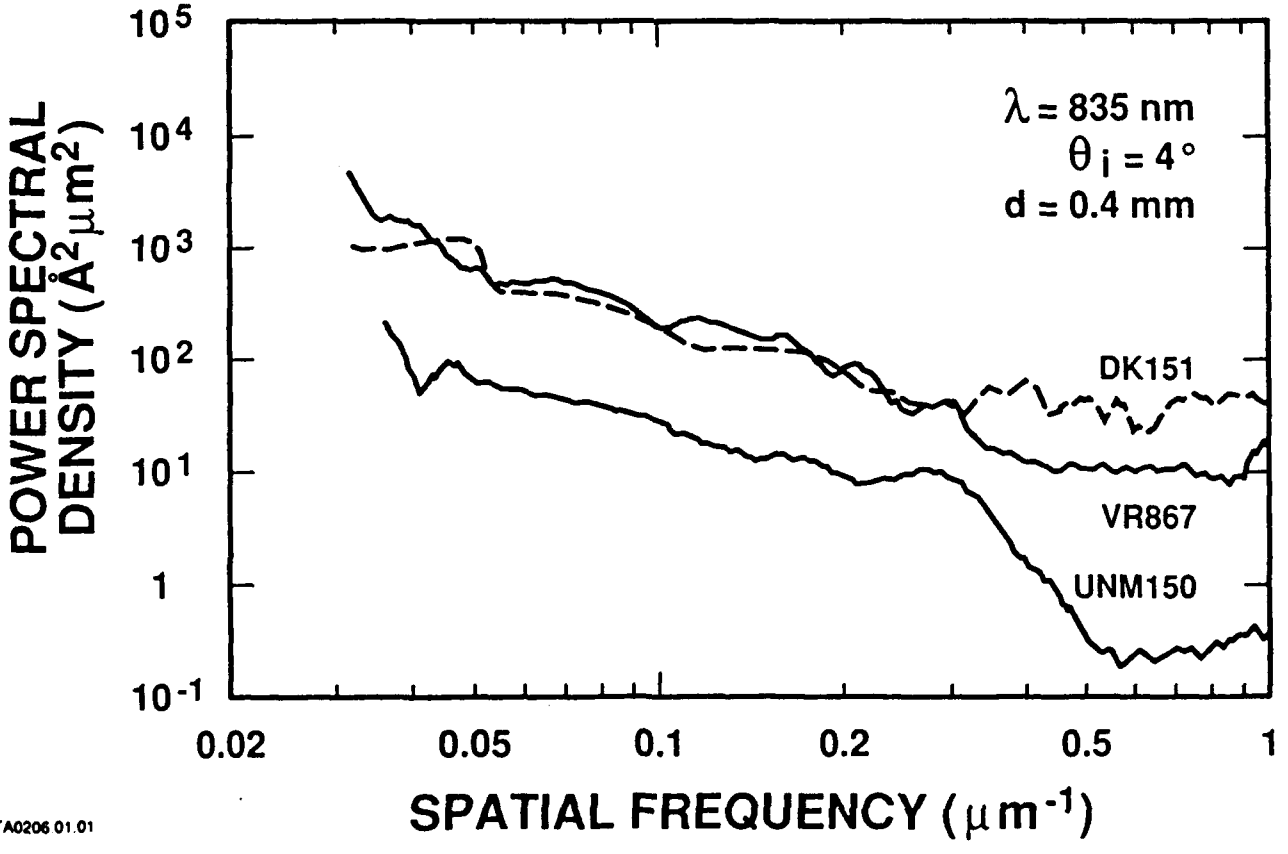

TA0206 01.01

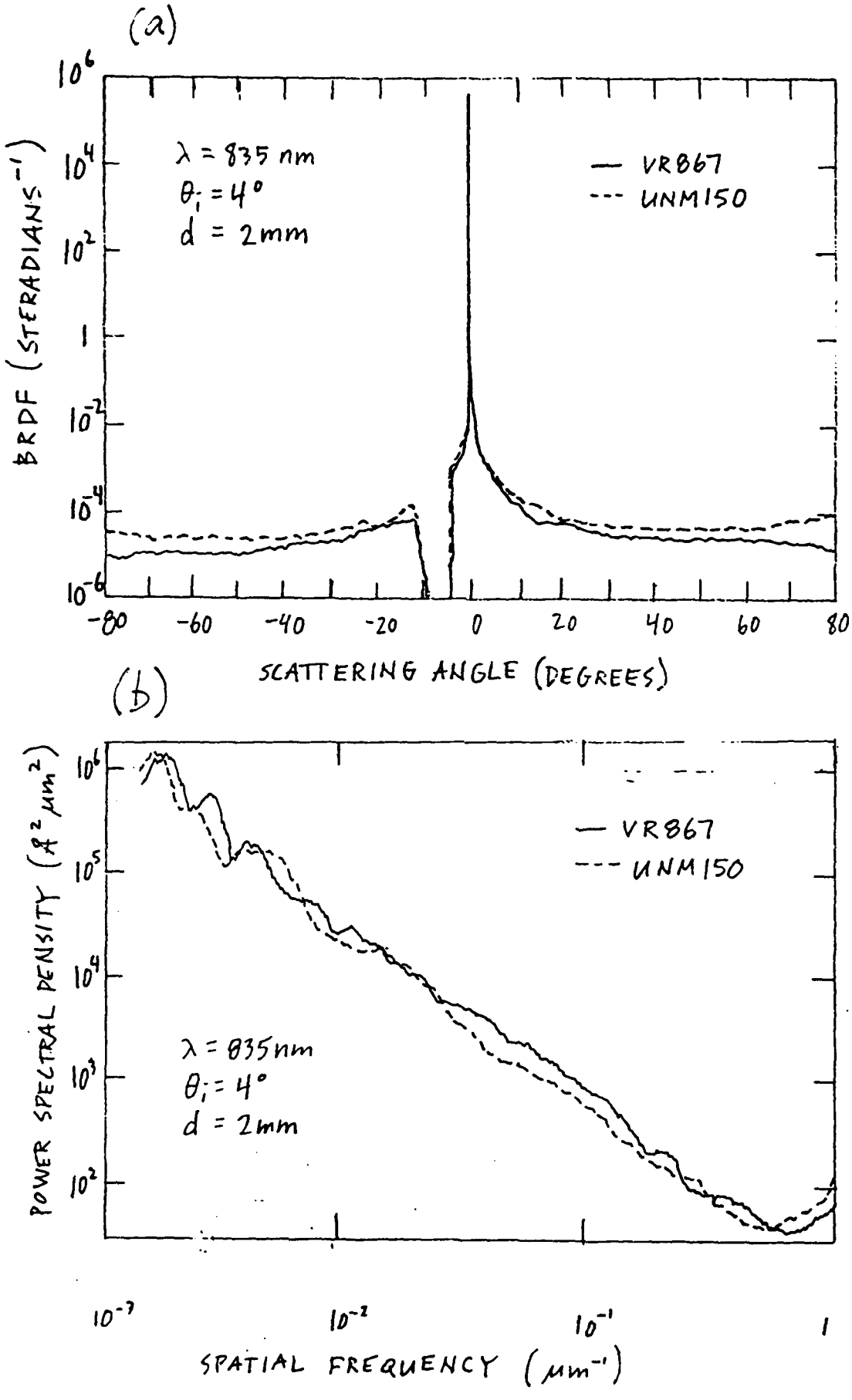
(a)
BRDF (STERADIANS^{-1})
10^6
10^4
10^2
1
10^{-2}
10^{-4}
10^{-6}
λ = 835 nm
θ_i = 4°
d = 2mm
— VR867
--- UNM150
-80 -60 -40 -20 0 20 40 60 80
SCATTERING ANGLE (DEGREES)
(b)
POWER SPECTRAL DENSITY (Å^2 µm^2)
10^6
10^5
10^4
10^3
10^2
— VR867
--- UNM150
λ = 835nm
θ_i = 4°
d = 2mm
10^{-3} 10^{-2} 10^{-1} 1
SPATIAL FREQUENCY (µm^{-1})

Fig 3

Opt. Lett.

Single cell Brillouin Enhanced Four-Wave Mixing with Focusing Geometry

Yung-Sheng Kuo, Yu-Chue Fong, Cunkai Wu,
John G. McInerney, and John K. McIver

Department of Physics and Astronomy
and
Center for High Technology Materials
University of New Mexico, Albuquerque, NM 87131, USA

Abstract

We report the generation of phase conjugated signal by single cell Brillouin enhanced four-wave mixing with a focusing geometry. A single cell containing the optical nonlinear medium is used simultaneously for conventional stimulated Brillouin scattering and for four-wave mixing. Experiments were performed using either CS_2 or $TiCl_4$ as the nonlinear medium. These materials have large Brillouin gain but differ greatly in their nonlinear index of refraction, thus the mechanism for four-wave mixing is shown to be Brillouin nonlinearity. An important advantage of this geometry is that the frequency of the phase conjugate signal is not shifted from the pump frequency.

Optical phase conjugation has received considerable attention recently because of its many potential applications. Since the first report by Zel'dovich et al[1], phase conjugation has become an important subfield of nonlinear optics. The most common ways of generating phase conjugation are stimulated Brillouin scattering (SBS) and degenerate four-wave mixing (DFWM)[2]. SBS is generated by directing an intense light beam into a nonlinear medium. If the input intensity reaches the SBS threshold, a Stokes wave which is the counterpropagating phase conjugate of the incident wave is generated. In the DFWM case two strong counterpropagating pump beams and a weak probe beam (at a small angle with respect to the pump beams) are mixed inside the nonlinear medium, resulting in the generation of a fourth (signal) wave which is the phase conjugate of the probe beam.

Both of the above methods have advantages and disadvantages. For instance, SBS does not occur until the incident pump intensity reaches a certain threshold, and the reflectivity never exceeds unity. Also, the Stokes wave frequency (ω_S) is slightly shifted from the input beam frequency (ω_L) by the acoustic frequency (Ω) of the nonlinear medium ($\Omega/\omega_L \approx 10^{-5}$ to 10^{-6})[3]. The advantages of SBS are the ease of optical alignment and the noncritical dependence on the optical quality of the input beam. On the other hand, four-wave mixing (FWM) requires that the two strong pump beams have a high degree of spatial coherence, and is sensitive to the optical alignment. One of the advantages of FWM is that the reflectivity of the probe beam can be larger than unity.

Brillouin enhanced four-wave mixing (BEFWM)[4] is a judicious combination of

the above processes. In fact, BEFWM is a nearly degenerate four-wave mixing configuration, in which the two strong counterpropagate pump beams and the weak probe beam (at a small angle with respect to one of the pump beams) overlap inside the nonlinear medium. In BEFWM the frequency of the probe beam is Brillouin-shifted (Stokes or anti-Stokes shift) with respect to one of the pump beams. These two waves interfere inside the active medium. This interference pattern drives an acoustic grating moving at a speed close to the acoustic speed in the medium. This acoustic grating scatters the other pump beam to form the phase conjugate beam. It has been demonstrated that the frequency of the phase conjugate beam can be upshifted[5], downshifted[6,7] or held fixed[8] with respect to the probe beam frequency by various combinations of the pump and probe beam frequencies.

BEFWM has been used to obtain phase conjugate reflectivities up to 10^6 with very weak probe intensities[9]. These high reflectivities are possible because the phase conjugate intensity grows exponentially in time until the pump beams are depleted and the gain is saturated. Recently, Ackerman et al[10], used a sophisticated double injection-seeded laser experimental arrangement with continuous tuning of the pump and probe frequencies to obtain a phase conjugate reflectivity of 3×10^7 with input energy ≈ 10 pJ.

In this letter, we report single cell BEFWM in a single cell containing a nonlinear medium which is simultaneously used for both conventional SBS and FWM. Scott et al[11,12] have reported experiments using a similar geometry with different combinations of the pump and probe frequencies and in a waveguide configuration.

Our experimental arrangement is schematically shown in Fig. 1. The pump beam E_1 with frequency ω is generated by a pulsed Nd:YAG laser. It consists of a single longitudinal mode with a pulse duration of 40 nsec and a beam diameter of 4 mm. This pump beam E_1 is initially P-polarized (polarization parallel to the plane of the paper), and is left circularly polarized in the nonlinear medium after it passes through the $\lambda/4$ plate and the focusing lens (f = 15 cm). In our initial experiment, the nonlinear medium was CS_2 because of its large Brillouin gain (0.04 cm/MW)[13]. The CS_2 cell was a long (18 cm) stainless steel tube with both end windows AR coated. Since the SBS process is not polarization conserving, i.e., the SBS mirror reflects light like a conventional mirror, the reflected wave E_2 is right circularly polarized. After a second pass through the $\lambda/4$ plate, E_2 becomes S-polarized (polarization normal to the plane of the paper), and is coupled out by the cube polarizer. It has a frequency $\omega - \Omega$, where Ω is the acoustic phonon frequency associated with the SBS process (in our case Ω = 3.75 GHz). E_2 is guided through the $\lambda/4$ plate to the other end of the nonlinear cell and enters at a small angle $\theta = 3.3^0$ with respect to E_1. It is now the probe beam E_3 in the FWM process. The resulting single cell BEFWM process is shown in Fig. 2. In this experimental configuration, E_1 and E_3 interfere to generate an acoustic grating which moves from left to right as shown in Fig. 2. This grating scatters E_2 to form the left circularly beam E_4 which is the phase conjugate of E_3. From energy conservation,

$$\omega_4 = \omega_1 + \omega_2 - \omega_3, \tag{1}$$

and in this experiment $\omega_1 = \omega$, $\omega_2 = \omega - \Omega = \omega_3$, so that $\omega_4 = \omega$. The phase matching

condition is

$$\Delta \mathbf{k} = -\mathbf{k}_1 - \mathbf{k}_2 + \mathbf{k}_3 + \mathbf{k}_4, \qquad (2)$$

where $|\mathbf{k}_i| = n\omega_i/c$. In our configuration, $\cos\theta \simeq 1$, $\Delta k \simeq 0$, and hence the phase matching condition is nearly satisfied.

Since E_1 is focused into the nonlinear medium, another focusing lens (f = 100 cm) is used to reduce the diameter of beam E_3. The two focal points are adjusted to maximize the phase conjugate signal which occurs when the two beams overlap i.e., the focal point of f_2 is to the left of f_1 and their separation is 4.5 cm in the nonlinear cell. The phase conjugate beam E_4 is detected by an energy meter behind the partially transmitting (50%) mirror M_3. When the input beam E_3 reaches the SBS threshold, a second SBS process occurs. In order to prevent the second SBS process occurring, the intensity of the beam E_3 must be less than SBS threshold of the medium. An identical CS_2 cell next to the FWM cell is used to measure the threshold under the same conditions. The measured SBS threshold is about 1.2 mJ. In our experiments the energy of the beam E_3 is always kept below one–half of the threshold energy. Thus the phase conjugate signal observed is derived only from the BEFWM process.

In this experiment, the energy of the input beam E_1 was kept at 23 mJ, while beam E_2 (which is the SBS version of E_1) was 17.5 mJ. Typical experimental results are shown in Fig. 3. The highest reflectivity in our case is about 60% with a pulse

duration of 16 nsec. Much higher reflectivities can be obtained using BEFWM. Watkins et al[14] measured the threshold of instability at phase mismatched condition and show that it exhibits minima as a function of phase mismatch, and that the minima occur at a significant phase mismatch. In our case, the phase match condition is satisfied, so the threshold of instability is even higher than 10. In this experiment, $gI_1L = 0.55$ (with $L = 3$ cm, I_1 is the pump intensity assumed to be undepleted in passing through the nonlinear medium, and g is the brillouin gain) which is well below the high reflectivity threshold, explaining why the reflectivity is only 60%.

In our first experiments, $\omega_2 = \omega_3 = \omega - \Omega$ so that the interference between beams E_2 and E_3 can also produce an index grating. In this case E_1 can be scattered by the index grating and a signal wave with $\omega_4 = \omega$ can be generated from a simple four-wave mixing process, i.e., from the contribution of $\chi^{(3)}$. CS_2 not only has a large Brillouin gain but also has a large $\chi^{(3)}$. In order to determine whether the signal comes from BEFWM or simple FWM, another series of experiments using the nonlinear medium $TiCl_4$ was performed. $TiCl_4$ has a Brillouin gair g_B which is 21% that of CS_2 but a $\chi^{(3)}$ value which is very small compared to that of CS_2[12,15]. Our experimental results show that when $TiCl_4$ is used at the small probe (E_3) regime, the reflectivity is about one-fifth as large as when CS_2 is the nonlinear medium. Figure 3 shows that the reflectivity decreases as the probe energy increases, a likely explanation of this behavior is total saturation[16]. This result confirms that the dominant process is BEFWM and is not due to $\chi^{(3)}$. In addition, the reflectivity in conventional DFWM is given by $(k\Delta nL)^2$ for small reflectivity where $\Delta n = n_2|E|^2$ and k is the wavevector and n_2 is the nonlinear index of refraction. For the conditions of our focusing

geometry the reflectivity due to FWM is calculated about 1.4% (with CS_2 as the nonlinear medium). This is much smaller than the measured reflectivity, so we can conclude that BEFWM is the dominant process. Because the interference between E_1 and E_3 plays an important role in the generation of phase conjugate signal in the BEFWM process, the rotation of the $\lambda/4$ plate should reduce the phase conjugate signal to zero as E_3 approaches a state of left circular polarization. This is confirmed by the experimental observation.

In conclusion, we have shown that phase conjugation can be generated by single cell BEFWM with a focusing geometry. With a relatively large probe energy the reflectivity reached 60%. The frequency of the phase conjugate beam is not shifted from the pump frequency, and with focusing geometry the optical alignment is easier than those using a waveguide configuration. In comparison with the conventional BEFWM configuration in which two nonlinear cells are used, our configuration is more compact.

References

1. B. Ya. Zel'dovich, V. I. Popovichev, V. V. Ragul'skii and F. S. Faizullov, JETP Lett. **15**, 109 (1972).

2. R. A. Fisher (ed), Optical Phase Conjugation (Academic Press, New York, 1983).

3. B. Ya. Zel'dovich, N. F. Pilipetsky, and V. V. Shkunov, Principles of Phase Conjugation (Springer-Verlag, Berlin, Heidelberg, 1985).

4. A. M. Scott and K. D. Ridley, IEEE J. Quantum Electron. **25**, 438 (1989).

5. M. J. Damzen, M. H. R. Hutchison, and W. A. Schroeder, Opt. Lett. **12**, 45 (1987).

6. A. M. Scott, Opt. Commun. **45**, 127 (1983).

7. N. G. Basov, I. G. Zubarev, A. V. Kotov, S. I. Mikhailov, and M. G. Smimov, Sov. J. Quantum Electron. **9**, 237 (1979).

8. M. D. Skeldon, P. Narum, and R. W. Boyd, Opt. Lett. **12**, 343 (1987).

9. N. F. Andreev, V. I. Bespalov, A. M. Kiselev, A. Z. Matveev, G. A. Passmanik, and A. A. Shilov, Sov. Phys. JETP Lett. **32**, 625 (1980).

10. J. R. Ackerman, and P. S. Lebow, J. Opt. Soc. Am. B **8**, 1028 (1991).

11. A. M. Scott, and P. Waggott, Opt. Lett. **12**, 835 (1987).

12. D. E. Watkins, K. D. Ridley, and A. M. Scott, J. Opt. Soc. Am. B **6**, 1693 (1989).

13. V. F. Efimkov, I. G. Zubarev, A. V. Kotov, A. B. Moronov and S. I. Mikhailov, Sov. J. Quantum Electron. **9**, 533 (1979).

14. D. E. Watkins, A. M. Scott and K. D. Ridley, IEEE J. Quantum Electron. **26**, 2130 (1990).

15. A. I. Erokhin, V. I. Kovalev, and F. S. Faizullov, Sov. J. Quantum Electron. **16**, 872 (1986).

16. A. I. Sokolovskaya, G. L. Brekhovskikh, and A. D. Kudryavtseva, IEEE J.

Quantum Electron. **QE-23**, 1332(1987).

Figure captions

Fig. 1. Experimental setup of the self-pumped BEFWM scheme. PBS, polarized beam splitter; $\lambda/4$, quarter wave plate; f_1, f_2 focal lenses with focal length 15 and 100 cm; M_1 and M_2 are total reflection mirrors; M_3, 50%R mirror; D, detector.

Fig. 2. Schematic diagram of the frequency and polarization relationship use in self pumped BEFWM. L(R): left (right) circular polarization; Ω is the acoustic frequency of the medium.

Fig. 3. Dependence of the phase conjugate reflectivity on the probe beam energy for a fixed pump energy 23 mJ. (O): CS_2 is the nonlinear medium; (●): $TiCl_4$ is the nonlinear medium.

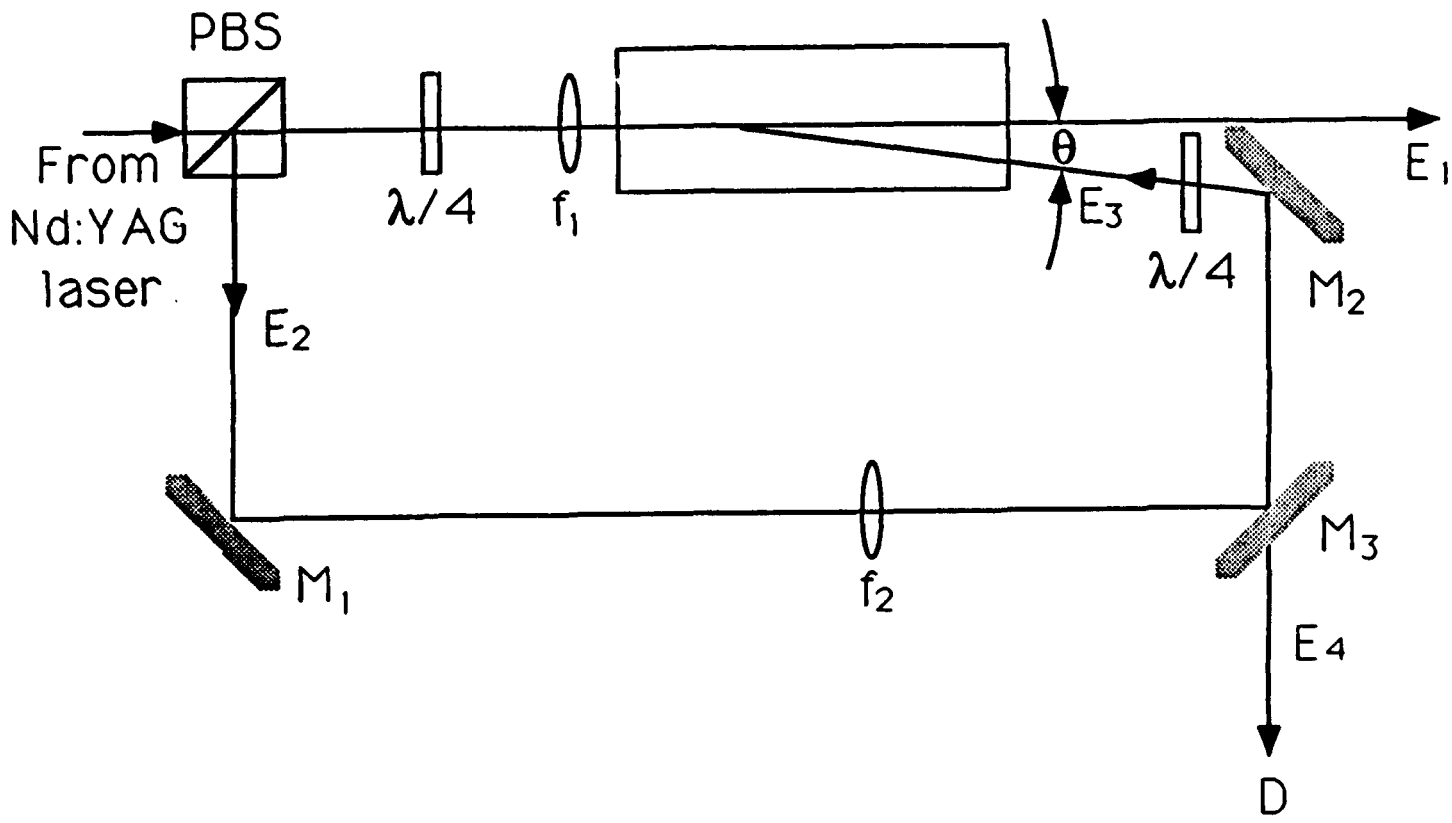
PBS
From
Nd:YAG
laser
λ/4
f1
θ
E1
E3
λ/4
M2
E2
M1
f2
M3
E4
D

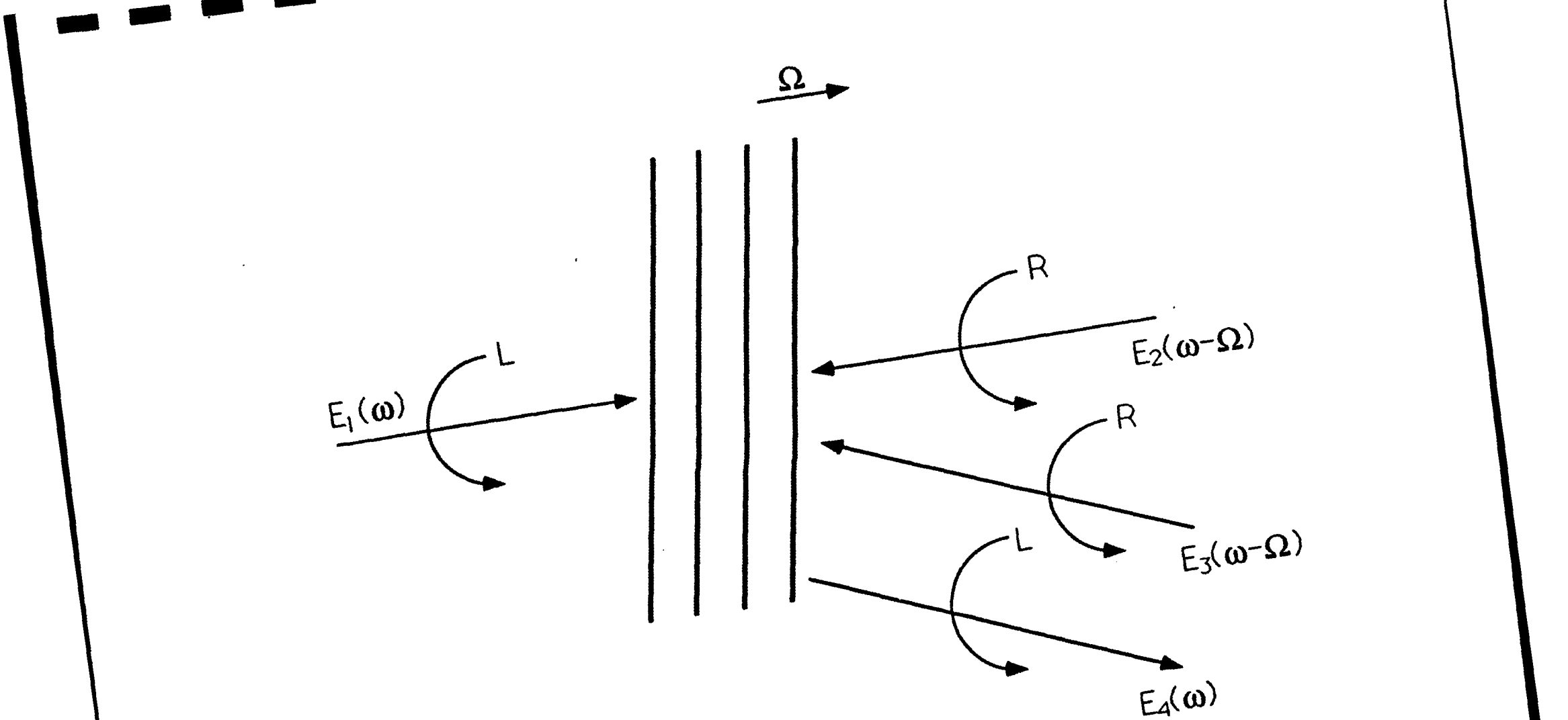
Ω
R
$E_2(\omega-\Omega)$
L
$E_1(\omega)$
R
$E_3(\omega-\Omega)$
L
$E_4(\omega)$

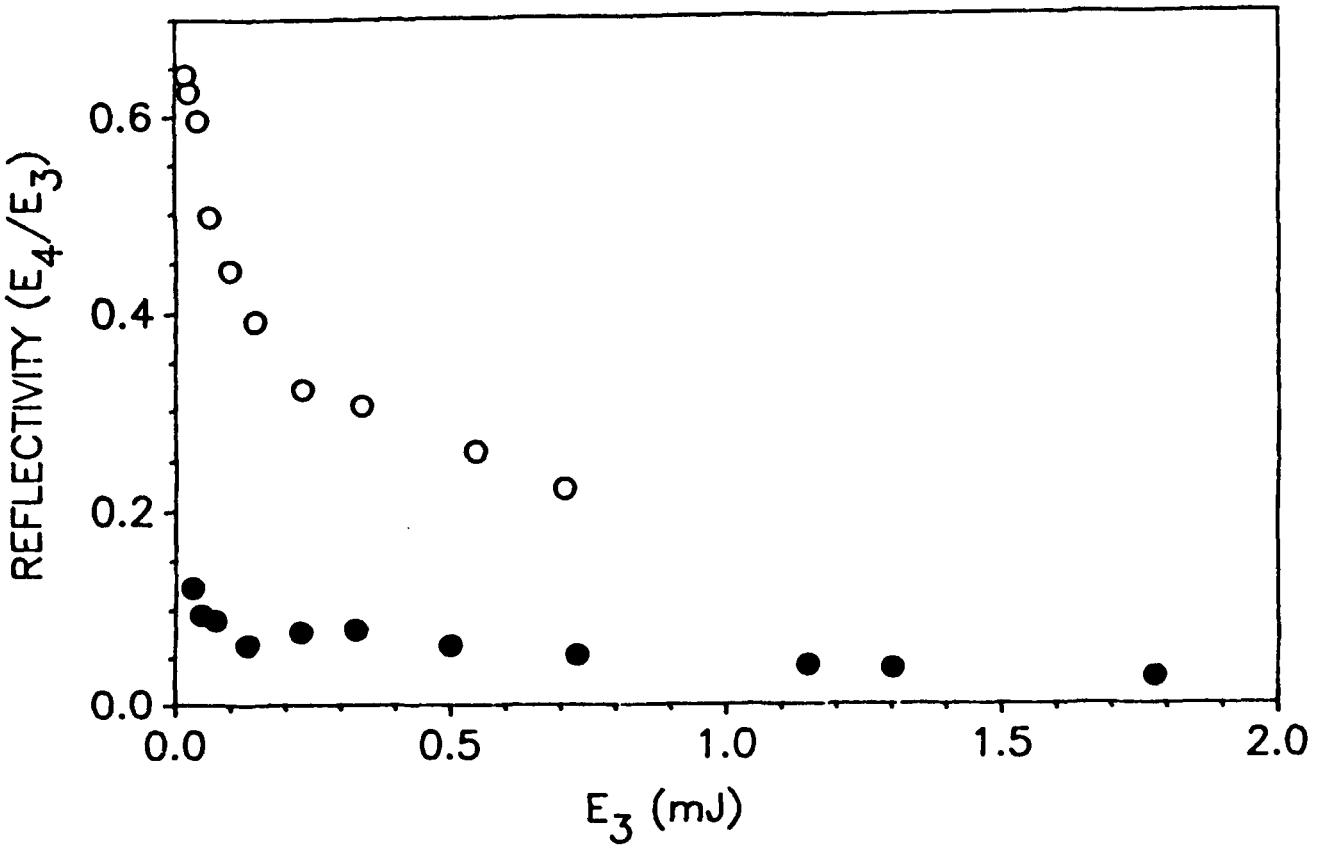

Fig. 3

Widely tunable, high power external cavity semiconductor lasers

Yuan Li, Cun-kai Wu, Morris B. Snipes, Jr. and John G. McInerney

Optoelectronic Device Physics Group, Center for High Technology Materials
University of New Mexico, Albuquerque, NM 87131-6081

ABSTRACT

While considerable attention has rightly been paid to the spatial coherence properties of high-power semiconductor lasers, very little work has been done to optimize their temporal coherence, as might be required by applications such as pulsed-Doppler laser radar, widespread optical clock distribution in dispersive channels, and spectroscopy.

Here we describe the operation of a wide stripe (100 μm) GRIN-SCH-SQW GaAs/AlGaAs device, which when first fabricated with a threshold current of ~400 mA. A high-reflectivity (R ~ 85 %) dielectric-metal coating wa deposited on one side and a two-layer anti-reflection coating (R < 1%) was deposited on the other (internal) facet. Various external cavities were constructed and their spectral properties examined. A simple mirror external cavity gave a maximum threshold reduction (to original threshold current) but the longitudinal mode spectrum was broad and unstable. By contrast, when a 1200 line/mm diffraction grating was coupled so that its rulings were parallel to the laser junction, the laser has a threshold of 550 mA and operated up to at least 2.5 I_{th} in a single,narrow (< 0.5 Å, instrument limited) longitudinal mode which was tunable from 7770 to 8080 Å by rotating the grating. Using this configuration the laser produced more than 500 mW in pulsed mode (0.8 μs, 10 kHz). The output wavelength was extremely stable with respect to variations in current and temperature.

1. INTRODUCTION

Narrow linewidth and wavelength tunability of semiconductor lasers with high output power are highly desirable in many applications[1] . Such devices are needed in areas of coherent optical fiber communications, free space communications, microwave energy transmissions and nonlinear optical frequency generations. We have developed a system which uses a pulsed semiconductor laser coupled to an external grating to produce 500 mW peak power of output power, with a linewidth of 0.5 Å or less, and a tuning range of about 300 Å.

Using an external cavity to achieve single longitudinal modes and narrow linewidth has been done previously by several groups [2-6]. One such group has reported a tuning range of 200 nm using a grating external cavity with a 10 mW single-mode output power[4]. However, to our knowledge only Mittelstein *et al.* have produced significant output power of 200 mW using an external cavity system[6].

Because semiconductor laser material have a wide and flat gain spectra, it is possible to achieve lasing over a wide tuning range. The grating functions as a wavelength filter so single longitudinal-mode operation of the semiconductor laser can be easily achieved with such configuration. The wavelength selectivity of the grating allows the lasing wavelength of the external cavity laser to be adjusted to a desired wavelength, even though this wavelength may locate a distance away from the gain peak for the active material. Wavelength tuning by mechanically rotating the grating is discontinuous because of the fixed longitudinal-mode frequency. Continuous frequency tuning within a longitudinal-mode spacing can be realized by varying the cavity length and consequence frequency shift of the longitudinal mode. Also, by using grating external cavity, the lasing wavelength can be stabilized against the change of injection current or device temperature.

One problem inherent in an external cavity system is that both the solitary laser and external cavity compete for dominance. To eliminate this problem, the semiconductor laser should have the internal facet antireflection (AR) coated, so that the external cavity has dominant influence on the lasing condition.

2. EXPERIMENT

The laser material used in our experiment was a graded-index separate-confinement heterostructure (GRIN-SCH) with a single quantum well, grown by metalorganic chemical vapor deposition (MOCVD) at CHTM, UNM. The laser structure is shown in Figure 1. In the lateral dimension the laser is purely gain guided. The finished laser diodes had a cavity length of 500 μm, and a stripe width of 100 μm. The threshold of the laser diode was about 400 mA when first fabricated. As mentioned previously, the front facet of the laser diode then was AR coated (< 1%) to increase the external cavity coupling efficiency. The rear facet was high-reflection (HR) coated to improve single-ended power output. In addition to producing high output power, such kind of wide stripe laser are advantageous due to their simple structure and easy to fabrication.

In our experimental arrangement, a blazed grating having 1200 lines/mm was used in the second diffraction order for optical feedback. The grating lines were aligned parallel to the epitaxial growth plane of the laser diode, hence the active layer waveguide acts as the entrance slit of a monochromator in coupling the feedback into the diode. It is noted that the external cavity is less effective when the grating lines are perpendicular to the growth plane in the case of wide stripe lasers, although it works well for narrow stripe lasers. The length of the external cavity is about 1 meter.

The experimental setup which was used for tunable external cavity laser is depicted in Figure 2. The laser diode was driven by a pulsed current source, with a pulse width of 1 μs and a repetition rate of 10 kHz. The optical spectra were measured using a Spex 1704 grating monochromator, with a resolution of 0.5 Å. Optical output power was monitored with a Photodyne 44 XLA power meter. To take power measurements with and without optical feedback, a beam splitter was used to extract a portion of the beam from the external cavity and the cavity was blocked to eliminate feedback.

A simple mirror external cavity gave a maximum threshold reduction (to original threshold current) but the longitudinal mode spectrum was broad and unstable. In Figure 3 we show typical laser diode spectra (a) without optical feed back , and (b) with feedback from a conventional mirror. By contrast, when a 1200 line/mm diffraction grating was coupled so that its rulings were parallel to the laser junction, the laser has a threshold of about 550 mA and operated up to at least 2.5 I_{th} in a single,narrow (< 0.5 Å, instrument limited) longitudinal mode. Figure 4 shows the optical spectra of the laser diode with feedback from a grating external cavity under the same operating condition as in Figure 3. This shows that grating coupling of the laser diode produces a narrowing of the spectra by 2 to 3 orders of magnitude.

Figure 5 shows the output power variation as the operating wavelength is changed by adjusting the tilt angle of the grating. The spectra width is less than 0.5 Å (the instrument resolution limit). The operating condition is same as before.

Figure 6 shows the stability of the grating external cavity laser. The driving current varied, but the operating wavelength is very stable and the spectra remains single longitudinal mode.

As the grating tilt angle is mechanically rotated, the operating wavelength of the laser can be tuned in a wide range. Figure 7 shows the tuning of the wavelength. The peak output power of the laser diode is about 550 mW. From Figure 7 we can see that the tuning range is above 300 Å, from 7770 to 8085 Å. At either end of the tuning curve, the feedback from the grating is insufficient to support lasing action.

In a seperate experiment, using the configuration shown in Figure 8, we use two grating external cavities simultaneously. When the two gratings are tilted in such a way that they correspond to two lasing wavelengths and these two wavelengths locate at opposite side of the peak of gain curve of the laser diode, it is possible to obtain a two-wavelength laser. Figure 9 shows the spectra of this two-grating external cavity laser. The separation between these two wavelengths can be adjusted by two gratings. Also, one of the two gratings in the experiment arrangement can be replaced by a mirror, which will give an improved power output. Such a device could be used in wavelength-division-multiplexing system and in optical frequency mixing experiments.

3. SUMMARY

To summarize, using a grating external cavity, a high power, narrow linewidth semiconductor laser has been realized. Specifically, our external grating cavity laser has: 1) less than a 0.5 Å linewidth single longitudinal mode, 2) greater than 300 Å wavelength tuning range at a wavelength ~ 800 Å, 3) more than 550 mW of optical power in pulsed mode, 4) excellent wavelength stability, and 5) the capability of two-wavelength operation.

4. ACKNOWLEDGEMENTS

We first wish to thank our colleagues at the CHTM Crystal Growth Facility for the growth of our laser material. We would also like to thank Dave Reicher and Bob McNeil of the CHTM Thinfilms Group for allowing us the use of their optical film deposition equipment and for providing invaluable optical coating experience.

5. REFERENCES

1. Kohroh Kobayashi and Ikuo Mito, "Single frequency and tunable laser diode," *J. Lightwave Technol.*, vol.6, no. 11, pp. 1623-1633, Nov. 1988.

2 R. Wyatt, and W.J. Devlin, "10 kHz linewidth 1.5 μm InGaAsP external cavity laser with 55 nm tuning range," *Electron. Lett.*, Vol. 19, pp. 110 - 112, Feb. 1983.

3. V.Yu. Bazhenov, A.P. Bogatov, P.G. Eliseev, O.G. Okhotnikov, G.T. Pak, M.P. Rakhvalsky, M.S. Soskin, V.B. Tararenko, K.A. Khairetdinov, " 35 mW CW single-frequency injection laser with an external dispersive cavity," *IEE Proceedings*, pp. 9-11, Vol. 132, Part J, No. 1, Feb. 1985.

4. A. Lidgard, T. Tanbun-Ek, R.A. Logan, H. Temkin, K.W. Wecht, N.A. Olsson, "External cavity InGaAs/InP graded index multiquantum well laser with 200 nm tuning range," *Appl. Phys. Lett.*, vol. 56(9), pp. 816-817, Feb. 1990.

5. M. Notomi, O. Mitomi, Y. Yoshikuni, F. Kano, Y. Tohmori, "Broad-band tunable two-section laser diode with external grating feedback," *Photon. Technol. Lett.*, vol. 2, pp. 85-87, 1990.

6. M. Mittelstein, D. Mehuys, A. Yariv, J.E. Ungar, and R. Sarfaty, "Broadband tunability of gain-flattened quantum well semiconductor lasers with external grating," *Appl. Phys. Lett.* 54, vol. 12, pp. 1092-1094, 1989.

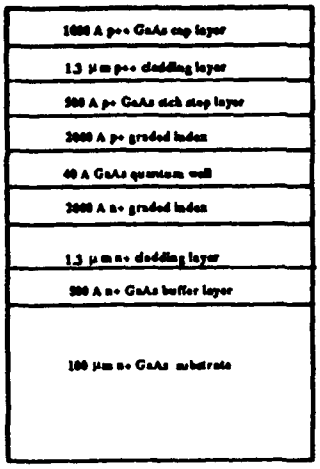

Fig.1 The structure of laser material used in the experiment.

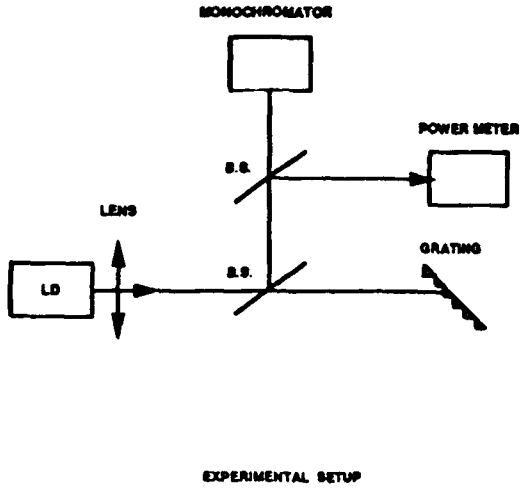

Fig.2 Experimental arrangement of grating external cavity laser diode.

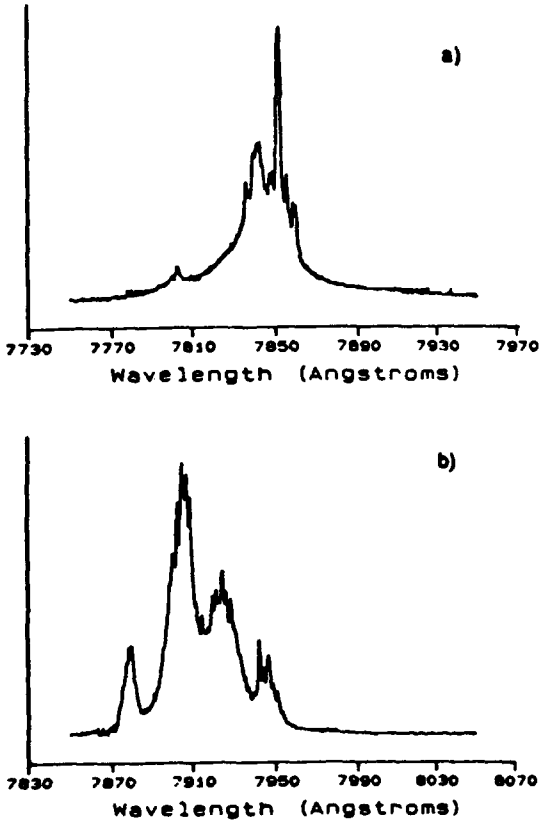

Fig.3 Spectra for laser diode a) free running, b) with from mirror external cavity.

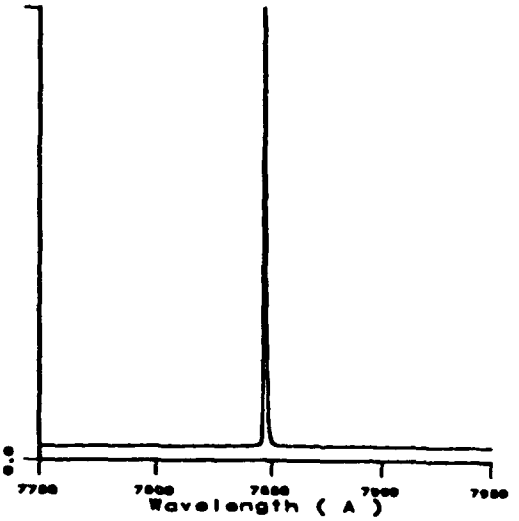

Fig.4 The spectrum output of the laser diode with feed back from grating external cavity.

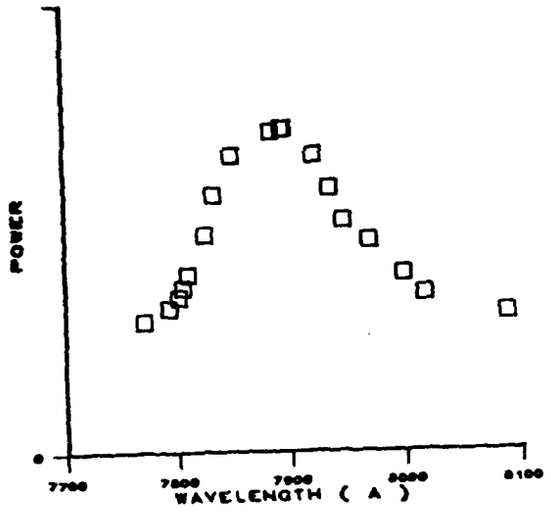

Fig.5 The output power variation as the operating wavelength is changed by adjusting the tilt angle of the grating.

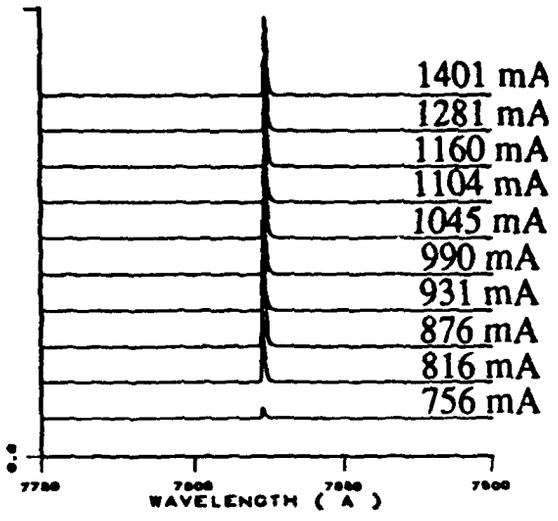

Fig.6 The wavelength stability of the grating external cavity laser diode under different injection current.

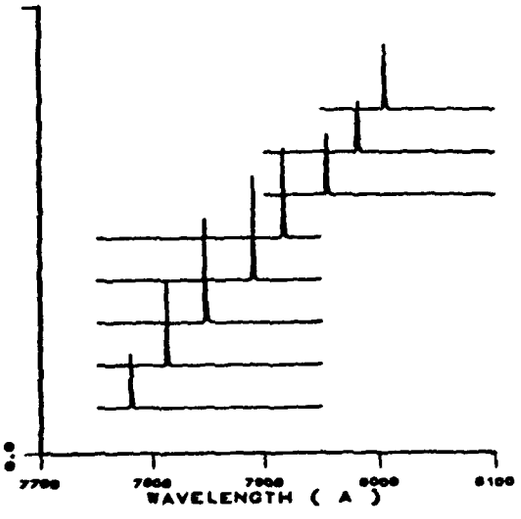

Fig.7 The tuning of the output wavelength by rotating the grating.

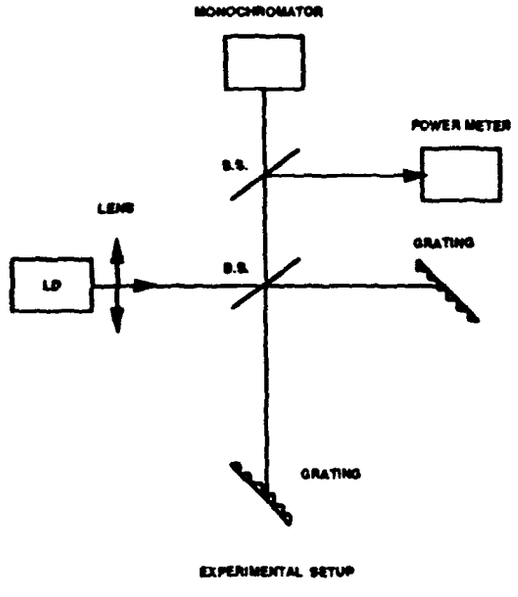

Fig.8 Experimental arrangement for two-wavelength laser operation.

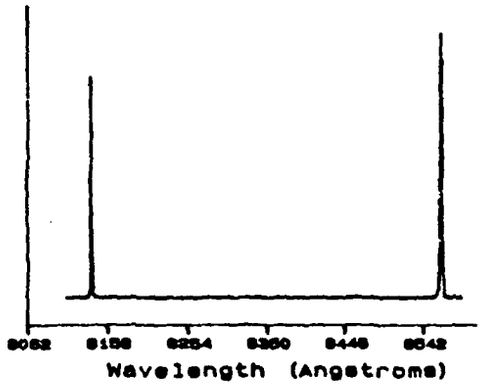

Fig.9 Spectra of two-wavelength operated laser diode.

Conclusions: In summary, a simple numerical technique is presented to calculate eigenenergies and eigenfunctions of QWs of arbitrary potential profile which also takes into account the nonparabolicity of bands. The validity of the technique is confirmed by calculating the eigenenergies of rectangular and graded wells. This approach can also be extended to calculate eigenenergies of multiple quantum wells and superlattices.

Acknowledgment: The author is grateful to H. F. Taylor for his support and encouragement. Thanks are also due to Dr. Hensley for helpful discussions.

D. P. DAVÉ

Department of Electrical Engineering
Texas A&M University
College Station, TX 77843, USA

11th July 1991

References

1 HIROSHIMA, T., and LANG, R.: 'Effect on conduction-band nonparabolicity on quantized energy level of a quantum well', *Appl. Phys. Lett.*, 1986, 49, pp. 456–457

2 ADACHI, A.: 'GaAs, AlAs, and $Al_xGa_{1-x}As$: Material properties for use in research and device applications', *J. Appl. Phys.*, 1987, 58, pp. R1–R29

3 HIROSHIMA, T., and NISHI, K.: 'Quantum confined Stark effect in graded-gap quantum wells', *J. Appl. Phys.*, 1987, 62, pp. 3360–3364

4 NAKAMURA, K., SHIMIZU, A., and HAYATA, K.: 'Finite element analysis of quantum wells of arbitrary semiconductors with arbitrary potential profile', *IEEE J. Quantum Electron.*, 1989, 25, pp. 889–894

STABLE-LOCKING BANDWIDTH IN SIDEMODE INJECTION LOCKED SEMICONDUCTOR LASERS

Indexing terms: Semiconductor lasers, Optoelectronics, Lasers and laser applications

An analytical expression for the possible sidemode locking bandwidth, consistent with the formula for peak-mode injection locking, is derived. Small-signal analysis is then applied to investigate the stable part of the locking range. The results demonstrate that sidemode injection locking offers relaxed operational requirements for frequency matching, with enhanced bandwidth, while retaining the traditional benefits of injection locking.

Introduction: An injection locking technique has been used to improve or to control static and dynamic lasing characteristics of semiconductor lasers for various applications, including long-distance high-speed digital fibre transmission and coherent communication systems. For example, singlemode operation under high-speed modulation has been achieved,[1] spectral linewidth[2] and frequency chirping[3] have been reduced, and mode partition noise has been suppressed,[4] thus enabling longer repeater spacings and faster data rates in coherent communication systems. However, a strong phase-amplitude coupling in semiconductor lasers[5] imposes stringent operational requirements for stable locking and limits the practical benefits of this technique. It is therefore important to examine whether these limitations can be reduced by choosing a target mode different from the free-running dominant mode.

Since the pioneering work of Goldberg *et al.*[6] who applied the sidemode (intermodal) injection locking to measure the semiconductor laser gain spectra, virtually no further research on this technique has been reported. We demonstrate that sidemode injection locking deserves more attention because it enhances the stable locking range.

Theory: The injection locking range for various target modes can be obtained from multimode rate equations describing temporal evolution of photon density for all modes and phase evolution of the injected mode. Consideration of multimode effects is especially important when the target mode is different from the free-running dominant mode. The rate equations for any mode m and for the target mode a are as follows:

$$\frac{dF_m}{dt} = (G_m - \gamma)F_m + 2f(F_aF_I)^{1/2}\cos\phi_L\delta_{ma} + \Gamma\beta_m R_{sp} \quad (1)$$

$$\frac{d\phi_a}{dt} = -\frac{\mu_a}{\mu_g}(\omega_a - \Omega_a) + \tfrac{1}{2}\alpha_a\Delta G_a - f(F_I/F_a)^{1/2}\sin\phi_L \quad (2)$$

with F_m, F_I the average photon densities of the mode m and the injected light, respectively, taken over the effective volume occupied by the transverse mode, G_m the temporal modal gain, γ the photon decay rate, f the intermodal spacing in the frequency domain, $\phi_L[=(\omega_a - \omega_I)t + \phi_a - \phi_I]$ the relative phase between the injected light with the phasor $\omega_I t + \phi_I$ and the target mode with the phasor $\omega_a t + \phi_a$, Γ the transverse-mode-dependent confinement factor, β_m the spontaneous emission coupling factor, R_{sp} the total spontaneous emission rate per unit volume, μ_a, μ_g the effective mode and the effective group index, respectively, ω_a, Ω_a the angular frequencies of the target mode and the cavity resonance, α_a the linewidth enhancement factor, and ΔG_a the carrier-induced gain change due to external light injection. Although the second term on the right hand side of eqn. 1 representing the external injection is similar to the one for peak-mode injection locking,[7] its magnitude for the sidemode case can be much larger due to the gain curve rolloff. The gain function is assumed to vary linearly with carrier concentration and parabolically with the wavelength difference between the gain peak and the mode under consideration.[8]

Eqns. 1 and 2 are complemented by the standard carrier-concentration rate equation.[8] For strongly index-guided semiconductor laser structures the active-region lateral dimensions are often small compared to the diffusion length, and hence we can neglect carrier diffusion effects.

Under steady-state conditions, eqns. 1 and 2 yield a detuning relation, which in turn gives the following expression for the possible locking range:

$$-\rho(1 + \alpha_a^2)^{1/2} \leq \omega_a - (\Omega_a + \Delta\Omega_a) \leq \rho \quad (3)$$

where $\rho = f(\mu_a/\mu_g)(F_I/F_a)^{1/2}$ and $\Delta\Omega_a = \frac{1}{2}(\alpha_a\mu_a/\mu_g)(\delta G_a - \Gamma\beta_a R_{sp}/F_a)$. Correspondingly, the possible locked phase ϕ_L is limited to $-\pi/2 \leq \phi_L \leq \pi/2 - \arctan\alpha_a$. The excess temporal gain δG_a, necessary for the injected mode to reach the nominal threshold level γ when the carrier density n is at its reference value $n_{ref} \simeq n_{th}$, requires more injected optical power in sidemode injection than in the gain-peak-mode case, thus leading to stronger damping. Larger values of F_I required for sidemode injection also result in larger ρ, enhancing the possible locking range.

Numerical simulation and discussion: The possible locking range for the sidemode injection, given by eqn. 3, differs from the conventional peak-mode-injection result[9] by an extra frequency offset term $\Delta\Omega_a$ due to an increased threshold gain deficit. Similarly to peak-mode injection,[9,10] only a part of the possible locking range is dynamically stable. A simple and meaningful analytical expression for stable locking bandwidth is not obtainable.

We therefore investigate the dynamical stability of injection-locked states by considering small fluctuations around the stationary solutions. After taking a Laplace transform of linearised rate equations containing only first-order fluctuation terms, we determine the stability of the solutions by examining the roots of the secular determinant.

A typical index-guided InGaAsP/InP laser emitting at $\sim 1{\cdot}54\,\mu m$ wavelength with a $240\,\mu m$ long Fabry-Pérot cavity is considered as an example. 11 longitudinal modes are included in the calculations. Longitudinal mode selection by external light injection is illustrated in Fig. 1, showing the relative injection level required to maintain a constant mode-

suppression ratio (MSR) of 20 at a fixed driving current of $1{\cdot}2I_{th}$, where I_{th} denotes the free-running laser threshold.

The spectral dependence of the phase interval and the corresponding frequency bandwidth for stable locking are illustrated in Figs. 2 and 3. The bias and MSR conditions are the same as in Fig. 1. The stable locked-phase interval is rather narrow except for weak relative injection into the 0 mode, where the boundary for stable locking extends down to $-\pi/2$ and the full locking range becomes dynamically stable.[10] For strong injection required to achieve higher MSR values (say, 60, not shown in the Figures), the stable-phase interval tends to expand gradually as the target mode moves away from the gain peak, while the corresponding range for 0-mode injection shrinks to less than $\pi/4$. The latter is consistent with experimental observations.[9,10] Owing to nonzero α_p, the zero phase is not located at the centre of the stable locked-phase interval, but it is always within the interval. As shown in Fig. 3, the frequency matching bandwidth for stable locking is increased significantly when the target mode moves away from the free-running dominant mode. This result implies that better locking and eased operational tolerances can be expected with sidemode injection locking technique.

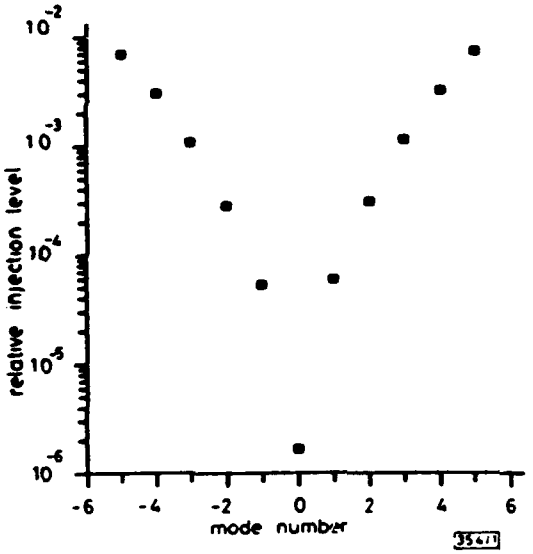

Fig. 1 *Relative injection levels required to achieve MSR of 20 at bias level of 20% above free-running threshold for various injected target modes*

Relative injection level is defined as ratio of injected photon density and resultant photon density in target mode at zero-phase injection Negative mode numbers correspond to longer-wavelength side of free-running spectrum

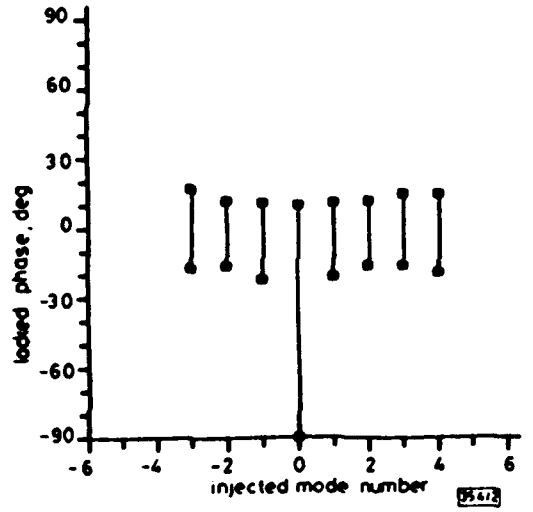

Fig. 2 *Stable locked-phase intervals at bias level of 20% above free-running threshold for various injected modes*

Optical injection level for each mode is such that zero-phase MSR of 20 is maintained

Conclusions: Sidemode injection locking of semiconductor lasers has been analysed using multimode rate equations. An analytical expression for the possible locking bandwidth has been obtained. Small-signal numerical study has revealed that sidemode injection offers enhanced stable-locking bandwidth, thus relaxing operational requirements for frequency matching. Equivalently, the modulation bandwidth can be increased by this technique, while retaining the traditional benefits of injection locking such as enhancing the field damping, narrowing the spectral linewidth, increasing modal stability, and reducing the dynamic frequency chirp during the direct modulation.

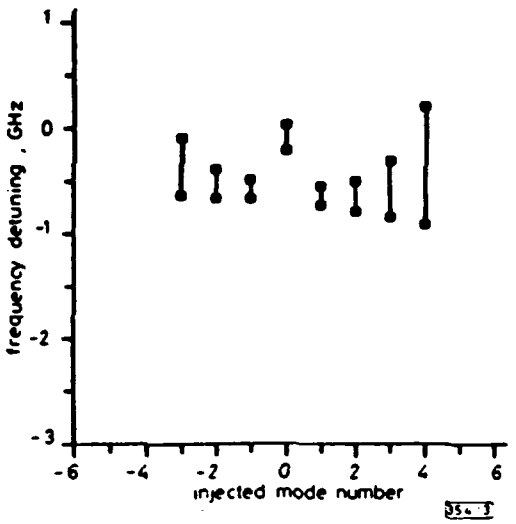

Fig. 3 *Stable frequency-detuning intervals for same optical injection conditions as in Fig. 2*

Note that frequency range for stable 0-mode locking is small despite wide range of permitted phases

Acknowledgments: This work was partially supported by the US Air Force Office for Scientific Research. A grant from Cray Research, Inc., which provided access to the National Center for Supercomputing Applications, is gratefully acknowledged.

J.-M. LUO

Physical Optics Corporation
20600 Gramercy Place
Suite 103
Torrance, California 90501, USA

M. OSIŃSKI

Center for High Technology Materials
University of New Mexico
Albuquerque, New Mexico 87131-6081, USA

22nd July 1991

References

1 TOBA, H., KOBAYASHI, Y., YANAGIMOTO, E., NAGAI, H., and NAKAHARA, M.: 'Injection-locking technique applied to a 170 km transmission experiment at 445·8 Mbit/s', *Electron. Lett.*, 1984, **20**, pp. 370–371

2 MOGENSEN, F., OLESEN, H., and JACOBSEN, G.: 'FM noise suppression and linewidth reduction in an injection-locked semiconductor laser', *Electron. Lett.*, 1985, **21**, pp. 696–697

3 LIN, C., ANDERSEN, J. E., and MENGEL, F.: 'Frequency chirp reduction in a 2·2 Gbit/s directly modulated InGaAsP semiconductor laser by CW injection', *Electron. Lett.*, 1984, **21**, pp. 80–81

4 IWASHITA, K., and NAKAGAWA, K.: 'Suppression of mode partition noise by laser diode light injection', *IEEE J. Quantum Electron.*, 1982, **QE-18**, pp. 1669–1674

5 OSIŃSKI, M., and BUUS, J.: 'Linewidth broadening factor in semiconductor lasers—an overview', *IEEE J. Quantum Electron.*, 1987, **23**, pp. 9–29

6 GOLDBERG, L., TAYLOR, H. F., and WELLER, J. F.: 'Intermodal injection locking and gain profile measurement of GaAlAs lasers', *IEEE J. Quantum Electron.*, 1984, **QE-20**, pp. 1226–1229

7 CARTLEDGE, J. C.: 'Theoretical performance of multigigabit-per-second lightwave systems using injection-locked semiconductor lasers', *J. Lightwave Technol.*, 1990, **8**, pp. 1017–1022

8 ADAMS, M. J., and OSTREICH, M.: 'Longitudinal mode competition in semiconductor lasers. Rate equations revisited', *IEE Proc. I*, 1982, 129, pp. 271–274
9 PETITBON, I., GALLION, P., DEBARGE, G., and CHABRAN, C.: 'Locking bandwidth and relaxation oscillations of an injection-locked semiconductor laser', *IEEE J. Quantum Electron.*, 1988, QE-24, pp. 148–154
10 MOGENSEN, F., OLESEN, H., and JACOBSEN, G.: 'Locking conditions and stability properties for a semiconductor laser with external light injection', *IEEE J. Quantum Electron.*, 1985, QE-21, pp. 784–793

PICOSECOND OPTICAL FIBRE SAMPLING OSCILLOSCOPE

Indexing terms: Optical fibres, Oscilloscopes, Optical measurement

An optical sampling oscilloscope, based simply on a dual wavelength, stroboscopic switching operation, in a nonlinear loop mirror has been used to directly measure, with picosecond resolution, the pulses generated from a gain switched semiconductor laser. The detected pulses were directly compared to those obtained with an electronically driven, optical sampling oscilloscope.

Introduction: Over the past few years, the nonlinear fibre loop mirror[1–3] has been successfully introduced as the switching element, both for soliton and nonsoliton pulses in various geometries.[4–9] Probably one of the most important applications of these devices is in dual wavelength operation,[10,11] and its relevance to ultrafast, all optical demultiplexing.[12] This is especially so because operation has recently been demonstrated using all semiconductor laser driving, in association with 'long' (~km) fibre loop lengths.[13]

The successful demonstration of dual wavelength operation of the nonlinear loop mirror device has given rise to the idea of an all optical, pulse sampling technique,[14] which is conceptually similar to the original, optical Kerr gate pulsewidth measurement method.[15]

The principle of operation[14] can be described by considering a simple nonlinear Sagnac loop mirror (see for example Fig. 1), constructed from a coupler which has a 3 dB splitting ratio at the signal wavelength and is unbalanced at the sampling wavelength. In the absence of the sampling pulses, the loop acts simply as a Sagnac interferometer for the weak signal pulses and the transmission through the device is zero. In the presence of the sampling pulses, because different intensities of the sampling signal propagate in the clockwise and anticlockwise directions, the signal develops a phase mismatch due to the crosscoupling term. If a long signal pulse is assumed, this phase difference only occurs for a time which is equal to the duration of the sampling pulse, i.e. where they temporally overlap, assuming no group velocity mismatch effects are present. Consequently, on traversing the loop, that part of the signal with the imposed phase difference will be switched out with a duration equal to the sampling pulse. If a fixed frequency difference is introduced between the signal and sampling pulses, then the sampling pulse will strobe through the signal, switching out and sampling at a rate determined by the frequency difference. A large area detector in association with high gain, low bandwidth amplifiers can be used to detect and display a sampled image of the signal, with a temporal resolution limited only by the duration of the sampling pulse and the walkoff due to dispersion where it is considered. However, it should be possible, either through the application of dispersion flattened fibre in the loop or appropriate fibre and wavelength selection, to minimise the dispersive effects.

Experiment: A schematic diagram of the experimental arrangement is shown in Fig. 1. The signal source was obtained initially from a GaInAsP ridge waveguide semiconductor laser, operating at 1·55 μm, gain switched at 100 MHz to produce 250 ps pulses, with an average power of 100 μW. No attempt was made to optimise the electronic drive characteristics to obtain shorter optical pulses or to minimise electrical ringing on the drive signals, to investigate the sensitivity of the measurement technique to the structured components so generated.

The probe (sampling) pulses were derived from a CW pumped, mode-locked Nd : YAG laser, operating at 1·32 μm, producing 80 ps pulses at a 100 MHZ repetition rate. A conventional optical fibre grating pair compressor was used to generate probe pulses of 6 ps duration, allowing a maximum peak power of 160 W in the nonlinear loop. Two frequency synthesisers, driven from a common oscillator were used to provide the modulation to the laser systems. This ensured highly stable fixed phase operation of the laser systems with a variable and selectable pulse repetition frequency difference Δf.

The signal and probe pulses were combined in a wavelength division multipler (WDM) and injected into the fibre loop mirror. This consisted of a 10 m length of dispersion shifted, nonpolarisation preserving, singlemode fibre spliced between two ports of a fibre coupler. The minimum dispersion of the fibre was at 1·45 μm, lying between the signal and probe pulse wavelengths, so reducing the group delay between the two pulses and minimising the pulse walkthrough which is a limitation to the temporal resolution of the technique. At 1·55 μm the coupler had a coupling ratio of $\alpha = 0.5$ and $\alpha = 0.08$ at 1·32 μm. The transmitted signals from the loop were incident on a large area (18 mm diameter) germanium detector and after amplification were displayed on a 20 MHz bandwidth storage oscilloscope.

Results and discussion: Fig. 2 shows a low temporal resolution measurement of a typical, gain-switched, semiconductor laser pulse train using the technique described above. The pulses appear 100 ms apart, consistent with the 10 Hz strobe frequency employed. With a greater temporal resolution, a representative sampled pulse profile is presented in Fig. 3a. This

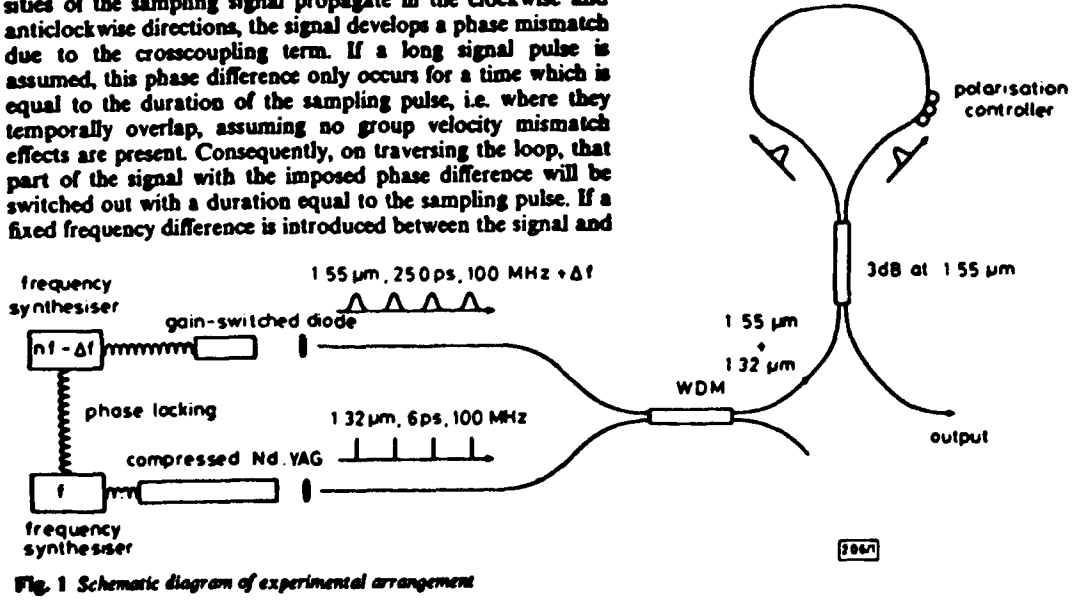

Fig. 1 *Schematic diagram of experimental arrangement*

Submitted to Jpn. J. Appl. Phys. (Lett.)

MULTIMODE SMALL-SIGNAL ANALYSIS OF SIDE-MODE INJECTION-LOCKED SEMICONDUCTOR LASERS

Jhy-Ming LUO* and Marek OSIŃSKI**

Center for High Technology Materials, University of New Mexico, Albuquerque, New Mexico 87131-6081, USA

---

* Present address: American Optical Corporation, Precision Product Division, 14 Mechanic Street, Southbridge, Massachusetts 01550, USA.

** Also with the Department of Electrical and Computer Engineering and the Department of Physics and Astronomy, University of New Mexico, Albuquerque, New Mexico 87131, USA.

Abstract

Temporal response of side-mode injection-locked semiconductor lasers is studied using a small signal analysis of multimode rate equations. The relaxation oscillation frequency and the decay rate are shown to be sensitive to the choice of the injection target mode. Modes with shorter wavelengths have higher relaxation frequencies due to their larger differential gain. Maximum enhancement of the relaxation frequency occurs within that group of target modes. The analysis, together with the previously predicted enhancement of stable locking range, suggests feasibility of applying the side-mode injection technique to increase the modulation bandwidth of semiconductor lasers and hence the transmission speed in optical communication systems, while preserving the usual benefits of injection locking.

KEYWORDS: Semiconductor lasers, injection locking, relaxation frequency, side-mode injection, optical communications

§1. Introduction

Since the first demonstration by Kobayashi and Kimura[1,2] in 1980, injection locking technique has been widely used either to improve static and dynamic performance of semiconductor lasers in general, such as single-mode operation under high-speed modulation[3], reduction of spectral linewidth[4] and frequency chirping[5,6], and suppression of mode partition noise[7], or for specific applications[8-10] as optical transmitter, repeaters, or local oscillators in long-distance high-speed fiber communications and in coherent transmission systems. This technique is expected to enhance the prospects for applications of semiconductor lasers in various fields. Unfortunately, due to a strong phase-amplitude coupling[11] in semiconductor lasers, a substantial part of the locking range is dynamically unstable[12,13]. The remaining stable locking range, shrinking with increasing strength of the phase-amplitude coupling, is sometimes so small that it becomes very difficult to achieve locking[12,13].

With very few exceptions[14-17], virtually all work on injection locking of semiconductor lasers, whether experimental or theoretical, focused on addressing the free-running dominant mode (gain-peak injection). Recently, we have shown[18] that choosing a side mode as injection target may result in an increased stable locking range and hence can be beneficial from the practical application point of view. In this letter, we show that side-mode injection locking has also some other attractive features. In particular, the relaxation oscillation frequency ν_r can be adjusted in a manner similar to detuning a distributed-feedback (DFB) laser from the gain-peak wavelength, since ν_r is related to the wavelength-dependent differential gain. The frequency response of a directly modulated diode laser usually peaks at ν_r and rolls off sharply above this value. Increasing ν_r therefore enhances the modulation frequency response, a result which is desirable for such applications as optical communications, fast switching and ultrashort pulse generation.

§2. Rate equation analysis

In order to investigate side-mode injection locking characteristics, we have developed a model based on multimode rate equations, including a phase equation for the injected mode. Consideration of multimode effects is especially important when the target mode is different from the free-running dominant mode. Assuming spatially uniform distributions of the carrier concentration and photon density inside the active region, the rate equations for any longitudinal mode "m" and for the target mode "a" are:

$$\frac{dF_m}{dt} = (G_m - \gamma)\, F_m + 2f\, (F_m F_I)^{1/2} \cos \phi_L\, \delta_{ma} + \Gamma \beta_m R_{sp} \quad , \tag{1}$$

$$\frac{d\phi_a}{dt} = -(\mu_e/\mu_g)\, (\omega_a - \Omega_a) + \tfrac{1}{2}\alpha_a \Delta G_a - f\, (F_I/F_a)^{1/2} \sin \phi_L \quad , \tag{2}$$

where F_m and F_I are the average photon densities of the mode "m" and of the injected light, respectively, both taken over the effective volume occupied by the transverse mode. G_m is the temporal modal gain of the mode "m", γ is the photon decay rate, f is the intermodal spacing in the frequency domain, ϕ_L [$= (\omega_a - \omega_I)t + \phi_a - \phi_I$] is the relative phase between the injected light with the phasor $\omega_I t + \phi_I$ and the target mode with the phasor $\omega_a t + \phi_a$, Γ is the transverse-mode-dependent confinement factor, β_m is the spontaneous emission coupling factor, R_{sp} is the total spontaneous emission rate per unit volume, μ_e and μ_g are the effective mode and the effective group index, respectively, ω_a and Ω_a are the angular frequencies of the target mode and the cavity resonance, α_a is the linewidth broadening factor for the mode "a", and ΔG_a is the carrier-induced gain change due to external light injection. With the second term on the right hand side of Eq. (1) representing the external light injection, Eq. (1) is identical in its form to any coherent model of peak-mode injection locking. However, the magnitude of that term can be much larger for side-mode injection, due to the gain-curve roll off. The gain

function is assumed to vary linearly with carrier concentration and parabolically with the wavelength difference between the gain peak and the mode under consideration[19]. The carrier-concentration dependence of the refractive index is included via the linewidth broadening factor. Nonlinear gain suppression effects, which may occur at high pumping currents or at high optical injection, are also taken into account by incorporating a photon-density-dependent term in the gain function.

For strongly index-guided semiconductor laser structures where the active-region lateral dimensions are often small compared to the diffusion length, carrier diffusion effects can be neglected. The rate equation for the carrier concentration n in the active region is

$$\frac{dn}{dt} = \frac{J}{d} - \frac{n}{\tau_e} - \sum_{m=\text{all}} \frac{G_m}{\Gamma} F_m \ , \tag{3}$$

where J is the rate of carrier injection per unit area, d is the active layer thickness, and τ_e is the carrier lifetime.

We investigate the stability of injection-locked states by considering small fluctuations around the stationary solutions and examining if these perturbations are dynamically stable. After taking a Laplace transform of linearized rate equations containing only first-order fluctuation terms, we find the roots h of the secular determinant and confine our attention to the roots situated in the left half of the complex h plane. The real part of h gives the decay constant Γ_r of the relaxation oscillation, with negative values indicating an oscillatory approach to equilibrium, while the imaginary part determines the relaxation oscillation frequency ν_r. .

We have applied this procedure to a general multimode case as well as to a simple single-mode approximation, assuming that single-mode operation has been reached by

virtue of a sufficiently strong external light injection.

An analytic solution for ν_r can be obtained in the single-mode case by assuming a zero locked phase. This assumption corresponds to the case of the most effective phase locking, with the highest achievable mode suppression ratio (MSR). When the injected mode is within a few longitudinal mode spacings away from the gain peak, the expression for the relaxation oscillation frequency ν_r can be simplified considerably by retaining the two dominant terms

$$\nu_r \simeq \frac{1}{2\pi}\left[\frac{F_a G_a G_{a,n}}{\Gamma} - \frac{f^2 F_I}{4F_a}\right]^{1/2}, \tag{4}$$

where $G_{a,n} \equiv dG_a/dn$ represents the differential temporal modal gain of the injected target mode. Similarly, the decay rate Γ_r can be expressed approximately as

$$\Gamma_r \simeq -\tfrac{1}{2} f\,(F_I/F_a)^{1/2}\ . \tag{5}$$

The first term in Eq. (4) is similar to that for a solitary laser[20], except that all quantities now refer to the injection-locked mode rather than the free-running mode. The second term, whose magnitude may become comparable to the first one when the target mode is sufficiently far away from the gain peak, represents the stabilizing effect of injected light which tends to reduce ν_r. It is clear that an increase in ν_r can be expected only when the injected power necessary to reach a required level of mode suppression is still sufficiently small to preserve the first term in Eq. (6) as dominant. This limits the available spectral range to a few longitudinal mode spacings away from the gain peak, where a relatively weak injection is sufficient to select the target mode. In the latter case a simple approximation represented by the first term in Eq. (6) should give a reasonably good estimate of ν_r.

Eq. (5) suggests that side-mode injection, which normally needs more injected power to achieve a specific MSR than peak-mode injection, may lead more easily to stable locking. This is consistent with our analysis of the stable locking range reported in Ref. 18.

§3. Numerical results and discussion

To illustrate results of stability analysis, we consider a typical index-guided InGaAsP laser emitting at 1.54 μm, with a 240 μm-long Fabry-Pérot cavity. 11 modes are included in the multimode calculations.

Longitudinal mode selection by external light injection is illustrated in Fig. 1, showing the relative injection level required to maintain a constant MSR of 20, which we regard as adequate for the single-mode approximation to hold. Negative mode numbers correspond to the long-wavelength side of the free-running spectrum. A constant driving current density of $1.2J_{th}$ is assumed, where J_{th} denotes the free-running laser threshold.

We have examined the wavelength dependence of the differential temporal modal gain dG/dn and obtained a ~25% variation at 5 mode spacings from the gain peak, with a linear increase from the long-wavelength side to the short-wavelength side. The first term in Eq. (4), illustrated by open diamonds in Fig. 2, is strongly dominated by this variation. As expected, when both terms in Eq. (4) are included (illustrated by open circles in Fig. 2), additional bending towards lower resonance frequencies occurs at both sides of the spectrum. Full multimode stability test results, indicated by solid circles in Fig. 2, confirm that detuning the lasing mode towards the short-wavelength side (increasing positive mode numbers) of the gain peak does increase the resonance frequency. As shown in Fig. 2, at $J = 1.2J_{th}$ the maximum enhancement of the relaxation oscillation frequency is seen to occur when light is injected into mode +3. As illustrated

in Fig. 3, further increase of ν_r is possible at higher driving currents, when longitudinal modes at even shorter wavelengths are targeted.

Our analysis shows that compared to full multimode stability test, single-mode rate equation analysis slightly underestimates the relaxation frequency but gives correctly its variation with wavelength, as long as the injected mode is within a few mode spacings from the free-running dominant mode and the injection is strong enough. Further increase of the injection level does not help in enhancing ν_r, even though it does improve the accuracy of the single-mode approximation.

Fig. 4 illustrates the decay rate of relaxation oscillations for various injected modes. Again, the results of full multimode analysis (full circles) are compared with a single-mode approximation (open circles) and a zero-locked-phase approximation of Eq. (5) (open triangles). Increased damping with increasing distance from the gain-peak mode is caused primarily by stronger injection required to maintain a fixed MSR.

§4. Conclusions

Side-mode injection locking of semiconductor lasers has been analyzed using multimode rate equations. Particular attention was paid to the behavior of the relaxation oscillation frequency and the decay rate. Feasibility of side-mode injection locking as a means of increasing the modulation frequency response of a semiconductor laser has been suggested. An additional benefit is that the optical injection enhances the field damping, thereby narrowing the spectral linewidth, increasing modal stability and reducing the dynamic frequency chirp during direct modulation. The results of our analysis are consistent with the enhancement of ν_r observed in DFB lasers detuned to the short-wavelength side of the material gain peak, and suggest a novel way to enhance the relaxation oscillation frequency of a semiconductor laser by side-mode injection locking.

Acknowledgment

Partial support of this work by the U.S. Air Force Office for Scientific Research and the U.S. Air Force Phillips Laboratory is gratefully acknowledged.

References

1) S. Kobayashi and T. Kimura: Electron. Lett. 16 (1980) 668.

2) S. Kobayashi and T. Kimura: IEEE J. Quantum Electron. QE-17 (1981) 681.

3) H. Toba, Y. Kobayashi, K. Yanagimoto, H. Nagai and M. Nakahara: Electron. Lett. 20 (1984) 370.

4) F. Mogensen, H. Olesen and G. Jacobsen: Electron. Lett. 21 (1985) 696.

5) C. Lin, J. K. Andersen and F. Mengel: Electron. Lett. 21 (1985) 80.

6) S. Piazzolla, P. Spano and M. Tamburrini: IEEE J. Quantum Electron. QE-22 (1986) 2219.

7) K. Iwashita and K. Nakagawa: IEEE J. Quantum Electron. QE-18 (1982) 1669.

8) Y. Yamamoto and T. Kimura: IEEE J. Quantum Electron. QE-17 (1981) 919.

9) S. Kobayashi and T. Kimura: IEEE J. Quantum Electron. QE-18 (1982) 1662.

10) N. A. Olsson, H. Temkin, R. A. Logan, L. F. Johnson, G. J. Dolan, J. P. van der Ziel and J. C. Campbell: J. Lightwave Techn. LT-3 (1985) 63.

11) M. Osiński and J. Buus: IEEE J. Quantum Electron. QE-23 (1987) 9.

12) F. Mogensen, H. Olesen and G. Jacobsen: IEEE J. Quantum Electron. QE-21 (1985) 784.

13) N. Schunk and K. Petermann: IEEE J. Quantum Electron. QE-22 (1986) 642.

14) L. Goldberg, H. F. Taylor and J. F. Weller: Electron Lett. 20 (1984) 809.

15) L. Goldberg, H. F. Taylor and J. F. Weller: IEEE J. Quantum Electron. QE-20 (1984) 1226.

16) L. Goldberg, A. M. Yurek, H. F. Taylor and J. F. Weller: Electron. Lett. 21 (1985) 814.

17) G. R. Hadley: IEEE J. Quantum Electron. QE-22 (1986) 419.

18) J.-M. Luo and M. Osiński: Electron Lett. 27 (1991) 1737.

19) M. J. Adams and M. Osiński: IEE Proc. Pt. I. (Solid State & Electron Dev.) 129 (1982) 271.

20) G. P. Agrawal and N. K. Dutta: *Long-Wavelength Semiconductor Lasers*, (Van Nostrand Reinhold, New York, 1986), Ch. 6, p. 246.

Figure Captions

Fig. 1. Relative injection levels required to achieve a mode suppression ratio (MSR) of 20 for injection locking of various longitudinal modes with pumping current density $J = 1.2J_{th}$. Negative mode numbers correspond to the longer-wavelength side of the free-running spectrum.

Fig. 2. Relaxation oscillation frequency ν_r calculated for various injected target modes with $J = 1.2J_{th}$ and MSR = 20. Solid circles - multimode stability test; open circles - single-mode approximation (Eq. 4); open diamonds - single-mode approximation with neglected injection term.

Fig. 3. Injection current dependence of relaxation oscillation frequency ν_r calculated for various injected target with MSR = 20 and $J = 1.2J_{th}$ (circles), $J = 1.3J_{th}$ (triangles), and $J = 1.4J_{th}$ (squares). Solid symbols - multimode stability test; open symbols - single-mode approximation (Eq. 4). Note that the maximum enhancement of ν_r shifts from mode +3 at $J = 1.2J_{th}$ to mode +4 at $J \geq 1.3J_{th}$.

Fig. 4. Decay rate of relaxation oscillations Γ_r calculated for various injected target modes with $J = 1.2J_{th}$ and MSR = 20. Solid circles - multimode stability test; open circles - single-mode approximation; open triangles - single-mode approximation with zero locked phase [Eq. (5)].

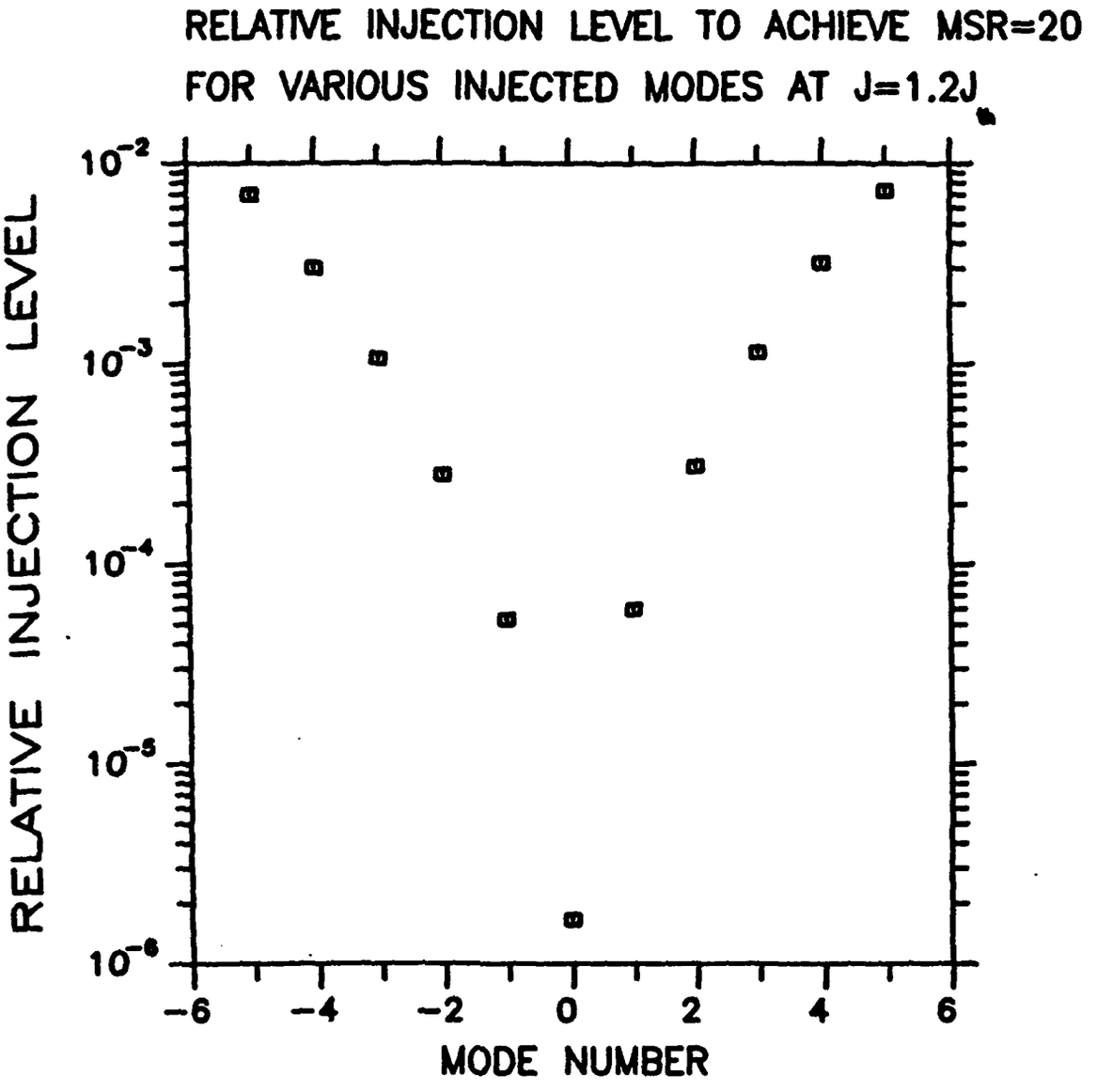
RELATIVE INJECTION LEVEL TO ACHIEVE MSR=20
FOR VARIOUS INJECTED MODES AT J=1.2J
RELATIVE INJECTION LEVEL
10^-2
10^-3
10^-4
10^-5
10^-6
-6
-4
-2
0
2
4
6
MODE NUMBER

Fig. 1

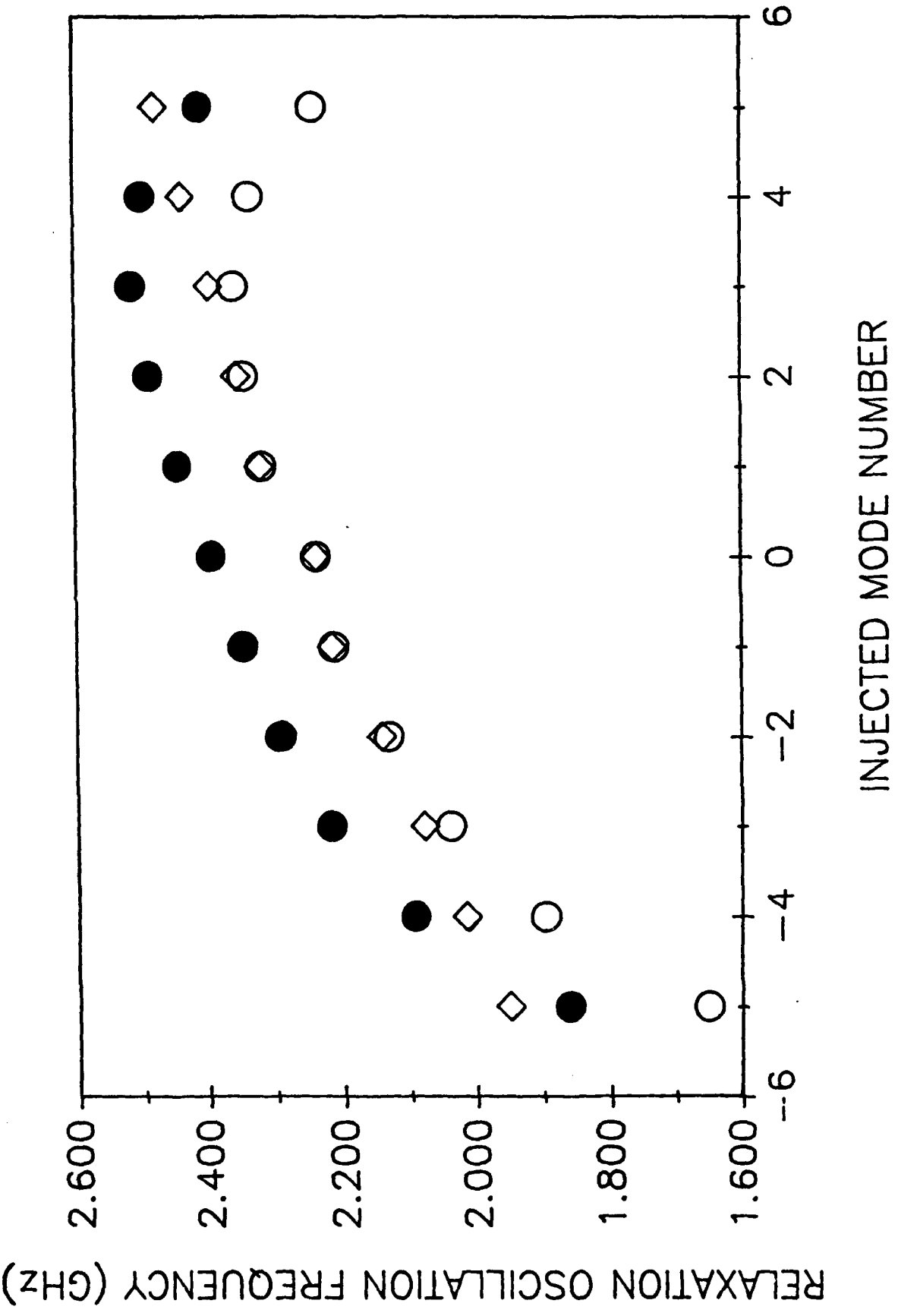
RELAXATION OSCILLATION FREQUENCY (GHz)
2.600
2.400
2.200
2.000
1.800
1.600
INJECTED MODE NUMBER
6
4
2
0
−2
−4
−6

Fig. 2

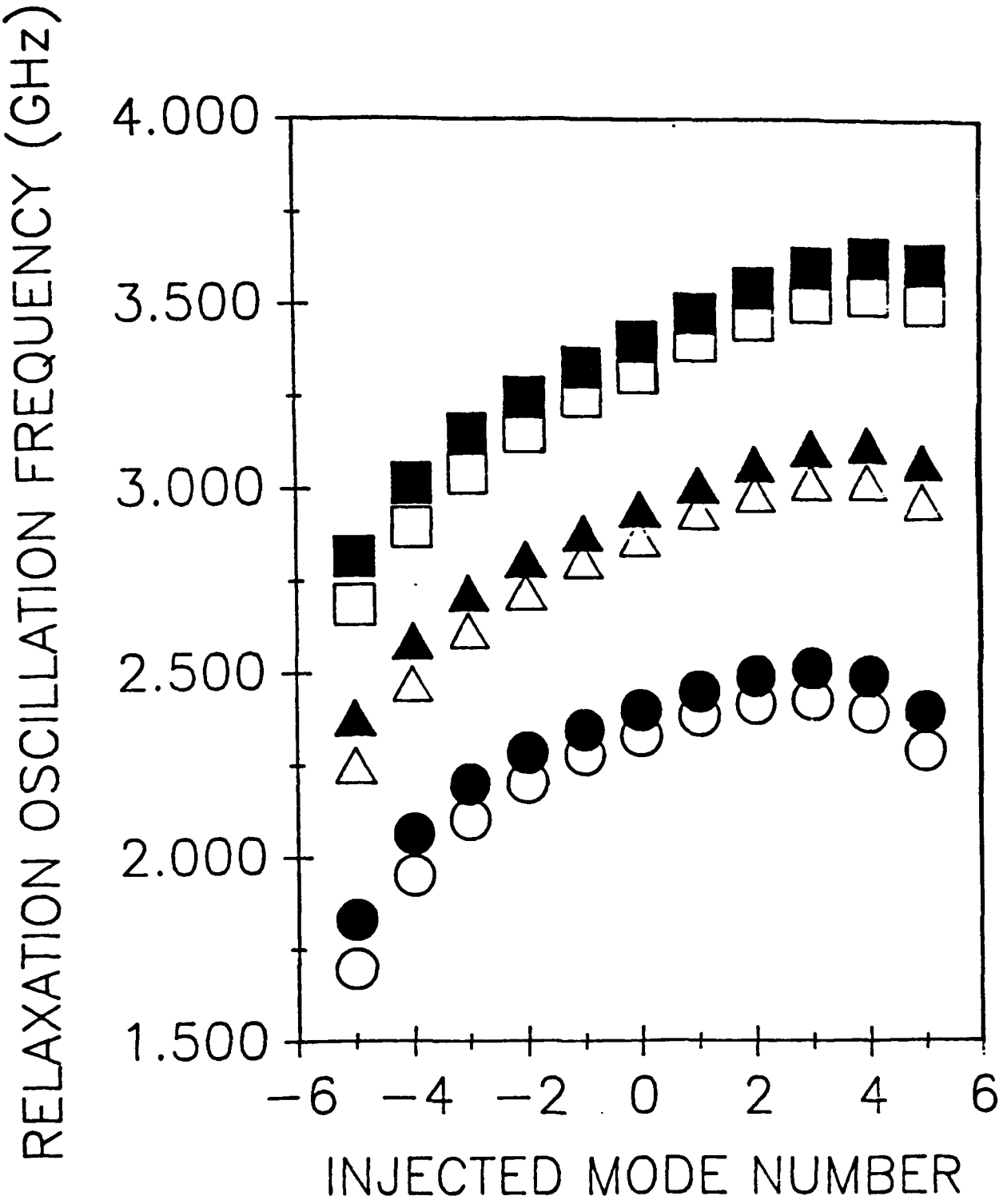
RELAXATION OSCILLATION FREQUENCY (GHz)
4.000
3.500
3.000
2.500
2.000
1.500
−6
−4
−2
0
2
4
6
INJECTED MODE NUMBER

Fig. 3

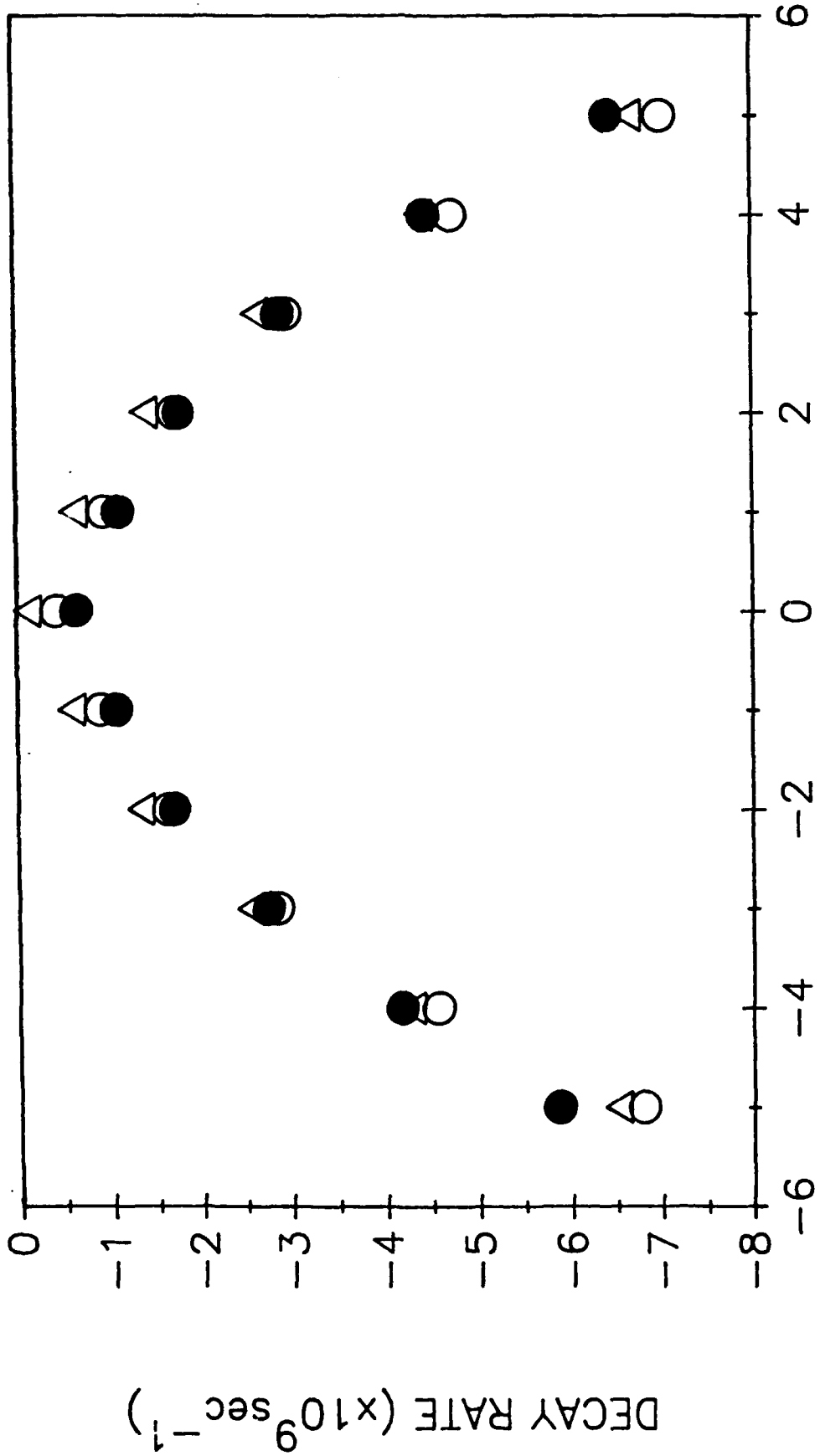
DECAY RATE (x10^{9}sec^{-1})
0
-1
-2
-3
-4
-5
-6
-7
-8
INJECTED MODE NUMBER
6
4
2
0
-2
-4
-6

Fig. 4

PROCEEDINGS REPRINT

SPIE–The International Society for Optical Engineering

Reprinted from

Laser Diode Technology and Applications III

23–25 January 1991
Los Angeles, California

Volume 1418

©1991 by the Society of Photo-Optical Instrumentation Engineers
Box 10, Bellingham, Washington 98227 USA. Telephone 206/676-3290.

NOVEL DISTRIBUTED-FEEDBACK STRUCTURE FOR SURFACE-EMITTING SEMICONDUCTOR LASERS

Mohammad Mahbobzadeh* and Marek Osiński**

Center for High Technology Materials, University of New Mexico, Albuquerque, New Mexico 87131-6081

ABSTRACT

A novel distributed feedback structure for wavelength-resonant surface-emitting semiconductor lasers is proposed and demonstrated. Compared to earlier resonant-periodic-gain devices, the total thickness of the new structure can be considerably smaller while retaining the characteristic features of the resonant-periodic-gain active medium. Room-temperature cw and pulsed operation of first distributed-feedback resonant-periodic-gain AlGaAs/GaAs/AlAs laser is reported.

1. INTRODUCTION

Surface-emitting semiconductor lasers are attracting considerable attention due to a wide range of their potential applications. There have been several approaches (vertical resonators, second-order grating coupling, and inclined mirrors) to achieve emission of the laser beam through the top surface. Among these, vertical-cavity surface-emitting lasers (VC-SELs)[1,2] offer distinct advantages of planar geometry, stable single-longitudinal-mode oscillation, and low-divergence circular output beam. Small-area low-threshold-current lasers can be used in optical computing and can be integrated with other optoelectronic devices to form part of monolithic optoelectronic integrated circuits and optical interconnects. Their low beam divergence simplifies the optics requirements and facilitates coupling into optical fibers. VC-SELs can also be easily arranged in one- or two-dimensional arrays to form high-power sources with possible applications in free-space optical communications and in solid-state laser pumping.

Conventional VC-SELs suffer from low external efficiencies and consequently low output powers. The primary reason for their poor performance lies in the competition between the desirable vertical emission and parasitic amplification of radiation emitted spontaneously in the directions parallel to the substrate plane. In order to suppress the amplified spontaneous emission (ASE) in the transverse directions and reduce the lasing threshold, a resonant-periodic-gain (RPG) structure has been proposed[3-6]. The RPG design takes advantage of the vertical geometry of VC-SELs by aligning quantum-well active regions, spaced at half the wavelength of a selected optical transition, with the maxima of the longitudinal mode pattern at the design wavelength. This enhances the gain along the vertical direction at the design wavelength and discriminates against the ASE parallel to the wafer surface. In addition, more efficient pumping is achieved and excitation of regions adjacent to the nulls of the standing wave is eliminated. In order to achieve low threshold, the RPG active region is normally sandwiched between two multilayer high reflectors (MHR), thus forming a distributed-Bragg-reflector (DBR) cavity with

---

* Also with the Department of Electrical and Computer Engineering, University of New Mexico.

** Also with the Department of Physics and Astronomy, University of New Mexico.

?194-0508-6/91/$4.00

relatively large total thickness.

In this paper, we present a new distributed-feedback (DFB) structure for RPG lasers which eliminates the need for end reflectors by interlacing the quarter-wave multilayer high reflectors with the gain medium. This reduces considerably the total thickness of the device, while retaining the characteristic features of the RPG active medium. We report on the first implementation of the new concept, using an optically pumped MO-CVD grown wafer. Both cw and pulsed operation is investigated. Preliminary results indicate that the new structure has indeed potential for very high output power.

2. CONCEPT OF DISTRIBUTED-FEEDBACK RESONANT-PERIODIC-GAIN MEDIUM

The length of DBR-type structures is inherently greater than that of otherwise equivalent DFB devices because the amplifying and feedback sections overlap in the latter structures. For VC-SELs, the device length is of primary concern, since apart from issues of technological complexity and cost it also affects the ability to pump the device uniformly. To reduce the DBR-RPG device length, we have proposed[7] that the RPG medium be converted into a DFB section by replacing the half-wave spacers with alternating quarter-wave layers which would provide reflectivity required for feedback. The resultant DFB-RPG structure is schematically illustrated in Figs. 1 and 2. A vertical resonator with highly reflective mirrors is created by a stack of alternating high- and low-refractive-index quarter-wave layers that form a DFB medium (layers C and D of Fig. 1, with refractive indices μ_C, μ_D). Within the DFB region, an RPG active medium is interspersed, represented in Fig. 1 by thick lines A. Each element of the RPG active medium can consist of a single quantum well or a group of coupled quantum wells positioned in such a way that they coincide with the antinodes of the standing wave at the designed wavelength of operation. This wavelength corresponds to a particular optical transition in the quantum well. The elements of the embedding DFB medium form spacers between active regions. One of the spacers, composed entirely of the high-index material B, serves as a phase shifter to satisfy the roundtrip phase matching condition.

In the following, we will describe particular design that was used to grow the first DFB-RPG AlGaAs/GaAs/AlAs wafer and report on initial results of cw and pulsed optical pumping of that prototype device.

3. PROTOTYPE DISTRIBUTED-FEEDBACK RESONANT-PERIODIC-GAIN LASER STRUCTURE

A prototype AlGaAs/GaAs/AlAs DFB-RPG VC-SEL sample was designed to operate at $n = 1$ subband transition in the quantum well. The active region consists of a stack of 10-nm thick GaAs single quantum wells separated by half-wave passive spacers. Except for a phase shifter in the central part of the structure, every spacer comprises two layers of AlAs (63.4-nm thick) and $Al_{0.15}Ga_{0.85}As$ (54.3 nm), each having an optical thickness of approximately a quarter of the design wavelength λ_r = 840.4 nm. The refractive indices for GaAs, $Al_{0.15}Ga_{0.85}As$, and AlAs were taken as 3.60, 3.50, and 3.00, respectively.[8] The lower and upper portions of the structure are separated by an $Al_{0.15}Ga_{0.85}As$ phase shifter with optical thickness of approximately $\lambda_r/2$. The whole structure contains 42.5 periods, of which 24 periods, counting from the center of the phase shifter, are at the bottom (*i.e.*, at the GaAs substrate side) and 18.5 periods are at the top. The output light is collected through the top surface. Since no quantum well is adjacent to the very first quarter-wave layer located at the top surface, the Al content in this layer is increased to 20% in order to avoid undesirable absorption of the pump light. The thickness of that layer is 59.9 nm, corresponding to the refractive index of 3.47.[8]

The total thickness of the structure described above, including the quantum-well layers, is approximately 5.42 μm. For the sake of comparison, a DBR-RPG laser with the same cumulative thickness of the active medium and the same reflectivities of multilayer reflectors would be almost two times thicker (10.55 μm) than the DFB-RPG structure.

Figs. 3(a) and 3(b) illustrate cavity reflectivity and gain spectra calculated for the DFB-RPG structure described above and for an equivalent RPG device with Bragg reflectors. The method of calculation follows a standard approach for periodic stratified media[9]. The transfer matrix for the structure is simplified by noting that products of identical unimodular matrices can be calculated analytically. Calculated reflectivities of the lower and upper reflectors are 99.76% and 99.56%, respectively. The most remarkable difference between the two structures is the absence of any side modes within the high-reflectivity band of the DFB-RPG laser. This is a direct consequence of shorter cavity length. Strong enhancement of gain at the resonance illustrates excellent wavelength selectivity of our structure.

In the process of designing the DFB-RPG structure, we used the reflectivity calculations to check for the wavelength of resonant mode. When the total optical thickness of a single period, consisting of a quantum well and an AlAs/$Al_{0.15}Ga_{0.85}As$ "half-wave" spacer, was chosen to be exactly equal to half of the design wavelength taken as 840.4 nm, the calculated resonant wavelength was longer (~848 nm) than the design wavelength. We attribute this shift of resonant wavelength to a phase-disturbing effect of quantum well layers. In order to correct for this shift, we have slightly reduced thicknesses of all spacer layers, thus bringing the resonance back to 840.4 nm.

4. EXPERIMENTAL RESULTS

The MOCVD-grown prototype structure described in previous section was optically pumped through the top mirror. The as-grown wafer was mounted in a holder, without any provision for heat-sinking. In order to enhance pumping efficiency, pumping wavelengths of 735-740 nm was selected. The corresponding photon energies of 1.68-1.69 eV are larger than the bandgap of $Al_{0.15}Ga_{0.85}As$ spacers (1.63 eV)[10] but smaller than the bandgap of the cap $Al_{0.2}Ga_{0.8}As$ layer (1.70 eV).[10] Hence, the pumping light was absorbed in $Al_{0.15}Ga_{0.85}As$ spacers, generating free carriers which subsequently could fall into quantum well GaAs active regions. This indirect pumping combined with absorption in quantum wells results in an improved pumping efficiency.

Since no heat sink was used, we anticipated that cw output power would be seriously limited by thermal effects. Therefore, with the aim of determining the potential of DFB-RPG lasers for high-power operation, we performed both pulsed and cw input/output measurements.

The experimental arrangement used for measurements of the pulsed input/output characteristics is shown schematically in Fig. 4. For pumping the DFB-RPG structure through the top surface, we used a dye laser (Quanta-Ray PDL-1, 230 μJ single-pulse energy), pumped by a Nd:YAG laser (Quanta-Ray DCR-2). The dye laser emitted 7 ns pulses at 10 Hz repetition rate, and was tuned to 735 nm wavelength. The pump beam power could be altered gradually by adjusting a variable neutral-density (ND) attenuator. A high-transmission, low-reflection (90/10) beam splitter BS allowed a direct measurement of the input power by reading the transmitted part of the pump power and multiplying it by a calibration factor that converted the transmitted power into the input power. A calibrated Gentec photodetector was used for this purpose. A calibrated dichroic beam splitter DBS was used to redirect the pump beam on its path towards the sample and to separate the reflected portion of the pump beam from the DFB-RPG output. Additional calibrated ND filter was inserted between the beam splitters BS and DBS to further attenuate the pump beam. A 10× microscope objective served a dual purpose of focusing the

pump beam and collimating the output. The DFB-RPG output power was measured using a Si photodetector calibrated to give the single-pulse output energy. Residual reflected pump beam was eliminated by an interference filter placed between the beam splitter DBS and the Si detector.

The experimental setup for cw measurements was essentially similar to that shown in Fig. 4. A dye laser (Coherent CR-599, 200 mW) operating at 740-nm wavelength, pumped by cw argon-ion laser (Spectra Physics Series 2000), was used as a pump source. The beam splitter BS was replaced by another beam splitter having low transmission (10%) and high reflection (90%), and no detector was placed behind BS. Calibrated power meters were employed to measure pumping and output power just prior to microscope objective and just after the interference filter, respectively. Spectral measurements were performed by coupling the DFB-RPG laser output into a high-resolution spectrometer by means of an optical fiber placed in a position of Si detector in Fig. 4. Appropriate interference filters were used between the beam splitter DBS and the fiber to select either pump signal or DFB-RPG output.

Fig. 5 shows a typical input/output characteristic for room-temperature cw pumping. The pump power values have been corrected for measured reflection from the surface (~32%) and calculated transmission (8%) through the DFB-RPG section. The lasing threshold for 10-μm spot size is ~60 mW, with top-surface output power efficiency of 9.3%, and differential quantum efficiency exceeding 80%. The maximum output of 6.7 mW is obviously limited by heating effects.

The output spectra centered at ~878 nm were rather broad (0.8 nm) with a complex structure indicating multiple transverse mode operation. Further work on improving the design with the goal of reducing the spectral width is in progress.

An input/output characteristic under pulsed pumping conditions is shown in Fig. 6. The output power of 8.5 W over 7 ns pulsewidth with power conversion efficiency of 10.5% is obtained. To our best knowledge, this is the highest peak power ever reported for VC-SEL devices. These data are preliminary and at this time a reliable estimate of maximum power density cannot be given. This is due to the fact that the beam was defocused slightly in order to maximize the output power and therefore the spot size is not exactly known. Further experiments are underway to determine the actual spot size. However, the several orders of magnitude difference between the pulsed and cw maximum output power density is a clear indication that easing the heating problems by employing efficient heat sinking should lead to significantly higher cw output power.

5. CONCLUSIONS

A novel DFB-RPG structure for vertical-cavity surface-emitting lasers has been proposed and demonstrated. Compared to recently developed DBR-RPG structures, a reduction in the total thickness of the device by almost a factor of two is achieved by eliminating the end reflectors and by interlacing the quarter-wave multilayer high reflectors with the RPG medium. The DFB-RPG devices offer the advantages of considerably simpler fabrication process, improved wavelength selectivity, and strong discrimination against excitation of secondary longitudinal modes. Preliminary data obtained on optically pumped bare wafer sample without any heat sink indicate that very high output power should be possible. 6.7 mW cw and 8.5 W pulsed output power was measured.

6. ACKNOWLEDGMENTS

This work was partially supported by the US Air Force Office of Scientific Research and Defense Advanced Research Projects Agency. The authors are grateful to Dr. C. F. Schaus for growing the prototype DFB-RPG sample, to Miss E. Gandjbakhch for assistance in performing optical pumping experiments, and to Drs. S. R. J. Brueck and A. Mukherjee for numerous helpful discussions.

7. REFERENCES

1. M. Osiński, "Vertical-Cavity Surface-Emitting Semiconductor Lasers: Present Status and Future Prospects", this volume.

2. M. Ogura, "Progress of Surface-Emitting Lasers in Japan", this volume.

3. R. Geels, R. H. Yan, J. W. Scott, S. W. Corzine, R. J. Simes, and L. A. Coldren, "Analysis and Design of a Novel Parallel-Driven MQW-DBR Surface-Emitting Diode Laser", Techn. Digest, CLEO '88 Conf. on Lasers and Electro-Optics, Anaheim, California, 25-29 April 1988, Paper WM1, pp. 206-207.

4. M. Y. A. Raja, S. R. J. Brueck, M. Osiński, C. F. Schaus, J. G. McInerney, T. M. Brennan, and B. E. Hammons, "Wavelength-Resonant Enhanced Gain/Absorption Structure for Opto-electronic Devices", in Post-Deadline Papers, XVI Int. Conf. on Quantum Electron. IQEC'88, Tokyo, Japan, 18-21 July 1988, Paper PD-23, pp. 52-53.

5. M. Y. A. Raja, S. R. J. Brueck, M. Osiński, C. F. Schaus, J. G. McInerney, T. M. Brennan, and B. E. Hammons, "Resonant Periodic Gain Surface-Emitting Semiconductor Lasers", *IEEE J. Quantum Electron.*, vol. 25, pp. 1500-1512, June 1989.

6. S. W. Corzine, R. S. Geels, J. W. Scott, R.-H. Yan, and L. A. Coldren, "Design of Fabry-Perot Surface-Emitting Lasers with a Periodic Gain Structure" *IEEE J. Quantum Electron.*, vol. 25, pp. 1513-1524, June 1989.

7. M. Mahbobzadeh and M. Osiński, "Novel Distributed-Feedback Resonant-Periodic-Gain Structure for Vertical-Cavity Surface-Emitting Semiconductor Lasers", *Electron. Lett.*, vol. 26, pp. 1716-1718, 27 Sept. 1990.

8. J.-P. Weber, "Propagation of Light in Periodic Structures: Application to Surface-Emitting Laser Diode", Ph.D. Dissertation, University of California at Berkeley, June 1990, Appendix A, pp. 227-246.

9. M. Born and E. Wolf, Principles of Optics, 6th Edition, Pergamon Press, Oxford 1980, Ch. 1.6, pp. 51-70.

10. C. Bosio, J. L. Staehli, M. Guzzi, G. Burri, and R. A. Logan, "Direct-energy-gap dependence on Al concentration in $Al_xGa_{1-x}As$", *Phys. Rev. B*, vol. 38, pp. 3263-3266, 15 Aug. 1988.

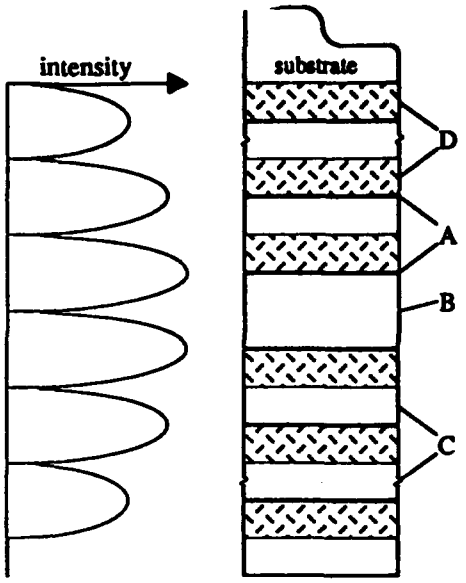

Fig. 1. A schematic illustration of the DFB-RPG structure and a corresponding intensity distribution of resonant mode. Thick lines (A) represent quantum-well active layers, unshaded region (B) - half-wave phase shifter, unshaded regions (C) - high-index quarter-wave spacers, shaded regions (D) - low-index quarter-wave spacers.

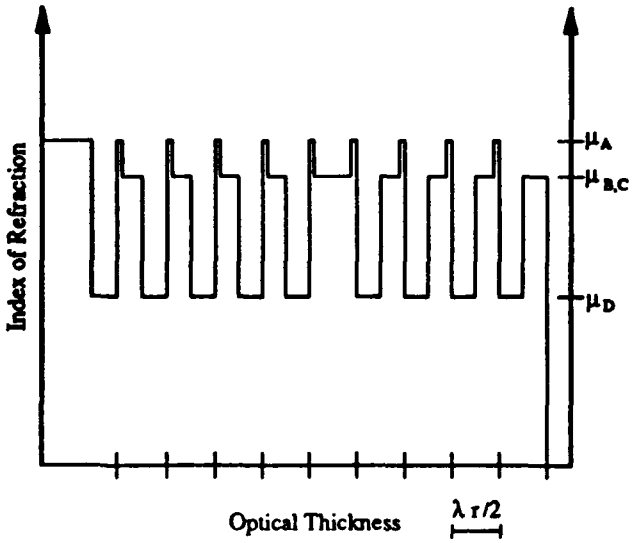

Fig. 2. Refractive index profile of the DFB-RPG structure with layer designation (A,B,C,D) the same as in Fig. 1. The number of periods is reduced to simplify graphical illustration.

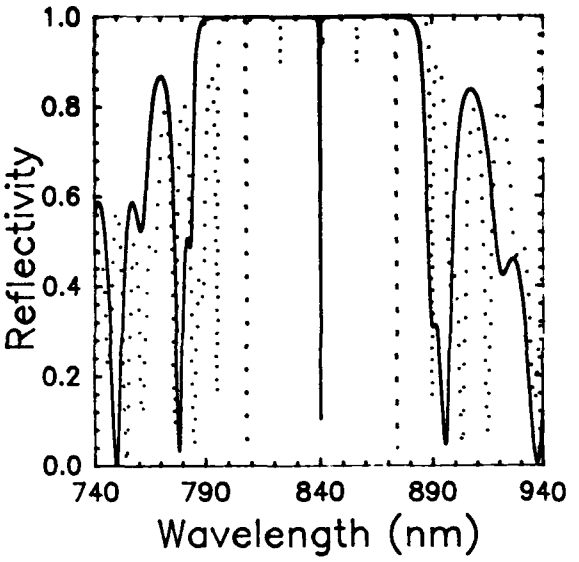

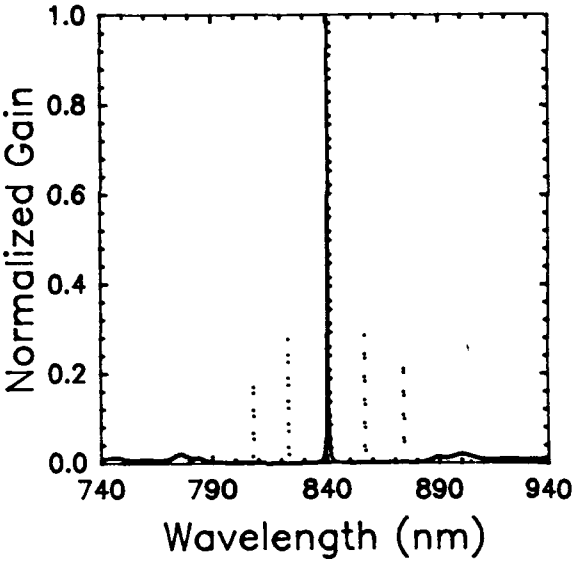

Fig. 3. Calculated reflectivity and gain spectra for a AlGaAs/GaAs/AlAs DFB-RPG VC-SEL (broken lines) and an equivalent DBR-RPG device with the same active medium thickness and MHR reflectivities (dotted lines).

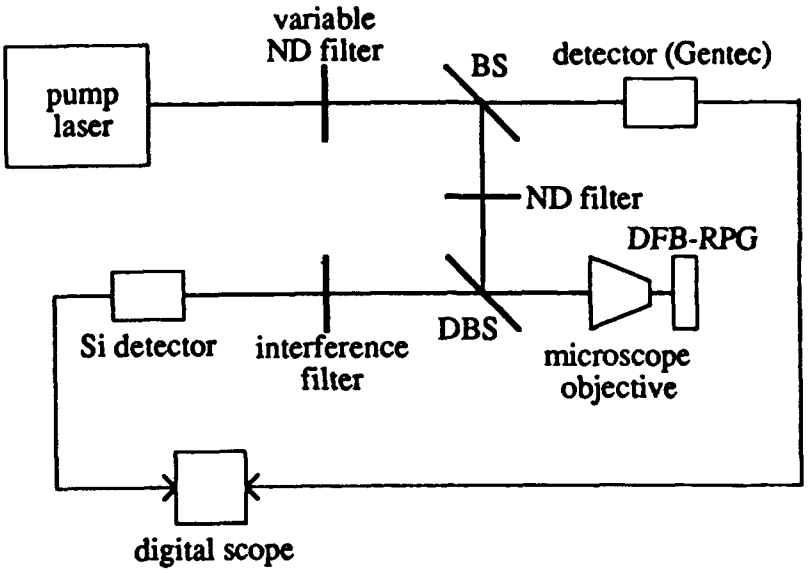

Fig. 4. Experimental setup for measurements of input/output characteristics of optically pumped VC-SELs.

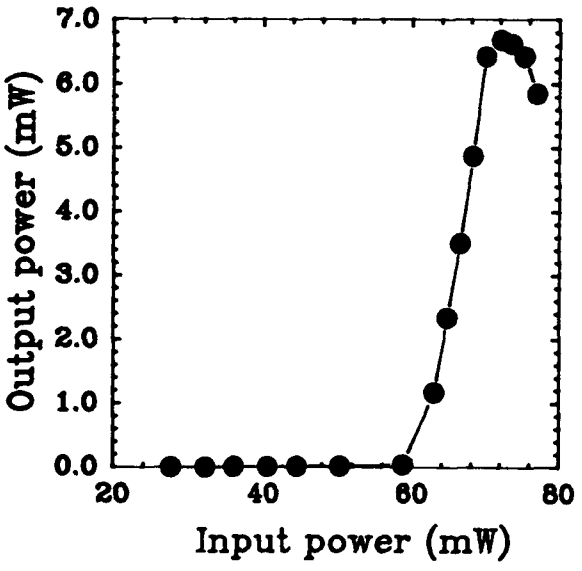

Fig. 5. Typical input/output characteristic for room-temperature cw pumping of DFB-RPG sample.

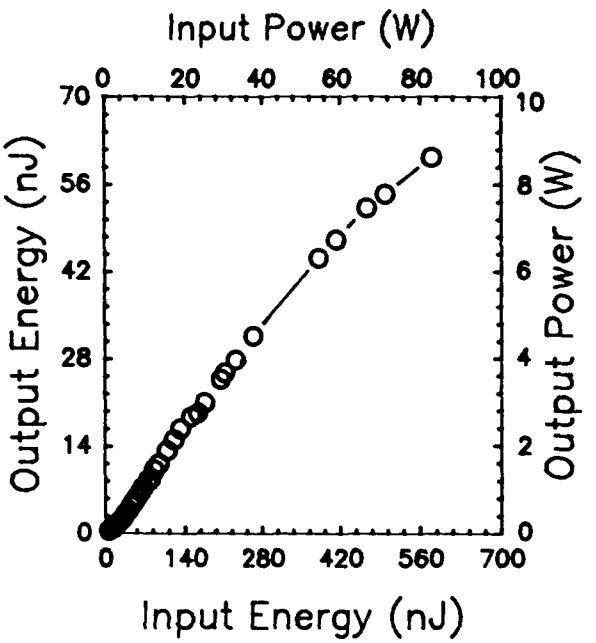

Fig. 6. Input/output characteristic for room-temperature pulsed operation of DFB-RPG laser.

ntegrated Optoelectronics for Communication & Processing, SPIE Symp. on Optical Fiber Materials & Devices, OE/Fibers '91, Boston, MA, Sept. 3-6, 1991, Paper 1582-15.

HIGH-POWER OPERATION OF DISTRIBUTED-FEEDBACK RESONANT-PERIODIC-GAIN SURFACE-EMITTING LASERS

Mohammad Mahbobzadeh*, Emmanuelle Gandjbakhch, and Marek Osiński*****

Center for High Technology Materials, University of New Mexico
Albuquerque, New Mexico 87131-6081

ABSTRACT

An experimental study of a prototype optically-pumped distributed-feedback resonant-periodic-gain vertical-cavity surface-emitting laser (DFB-RPG VCSEL) is reported. Both cw and pulsed conditions are investigated. The results obtained on bare wafer samples without any heat sink indicate that very high output power should be possible. Thermally limited cw output power of 6.7 mW cw was obtained with 10-μm diameter of the pumping beam. Under pulsed conditions, the output power of 8.5 W over 7 ns pulsewidth with power conversion efficiency of 10.5% was achieved. To our best knowledge, this is the highest peak power density ever reported for any semiconductor laser.

1. INTRODUCTION

Spectacular progress in vertical-cavity surface-emitting lasers (VCSELs) brought forth a variety of novel device structures. Most of these structures take advantage of the unique opportunities offered by the vertical-cavity configuration, in which the lasing modes propagate in the direction perpendicular to interfaces between layers of constituent semiconducting materials. This situation contrasts with that of conventional edge-emitting semiconductor lasers, where the lasing light propagates in the direction parallel to interfaces between the active region and the cladding layers. An excited lasing mode can be visualized as a standing electromagnetic wave. At any particular wavelength, only the regions in the vicinity of standing-wave maxima can provide gain required to sustain lasing oscillations, while pumping of regions near the nodes provides gain for competing longitudinal modes. If the resonator supports only one mode (for example, in single-mode distributed-feedback edge-emitting lasers), the carriers injected into the nodal regions can take part in stimulated recombination transitions only if they first diffuse towards the antinodes. The uniform pumping, typical for edge-emitting lasers, is therefore suffering from the lack of matching between the longitudinal distribution of injected carriers and the intensity distribution of optical field.

In this paper, we report on high-power operation of optically pumped distributed-feedback resonant-periodic-gain (DFB-RPG) lasers. Recently developed surface-emitting laser structures utilizing vertical-cavity configuration for improved pumping efficiency are discussed in Section 2. In Section 3, we briefly comment on early DFB VCSEL designs, to introduce the reader to DFB-RPG VCSELs in Section 4. In Section 5, we give a detailed account of our experiments on

* Also with the Department of Electrical and Computer Engineering and the Department of Physics and Astronomy, University of New Mexico.

** Present address: Optoelectronics Laboratory, Ecole Nationale Supérieure des Télécommunications, 46, rue Barrault, F-75634 Paris Cédex 13, France.

*** Also with the Department of Electrical and Computer Engineering and the Department of Physics and Astronomy, University of New Mexico.

Mahbobzadeh

cw and pulsed optical pumping of a prototype MOCVD-grown DFB-RPG sample. In particular, we have observed a record-high pulsed output power density.

2. WAVELENGTH-RESONANT VCSEL STRUCTURES

Conventional VCSELs with bulk (double-heterostructure, DH) active regions suffer from high threshold, low external efficiency, and low output power [Iga 1988]. The primary reason for their poor performance lies in the competition between the desirable vertical emission and parasitic amplification of radiation emitted spontaneously in the directions parallel or vicinal to the substrate plane.

It has been recognized that when a VCSEL optical cavity is carefully designed, such that a quantum-well active region would coincide with a standing-wave maximum at a designed wavelength of operation, more efficient pumping can be achieved compared to a medium with uniform gain [Geels 1988], [Raja 1988], [Brueck 1989]. The effect is obviously wavelength-sensitive, since at non-resonant wavelengths the gain drops down. Application of this concept to multiple active regions lead to introduction of distributed-Bragg-reflector resonant-periodic-gain (DBR-RPG) lasers [Raja 1989], [Corzine 1989a]. The multiple active regions in a DBR-RPG structure, illustrated schematically in Fig. 1, are separated by half-wave spacers and sandwiched between two multilayer high reflectors. The device features an enhanced gain along the resonator axis (by up to a factor of 2 compared to a uniformly pumped medium), improved wavelength selectivity, and reduced amplified spontaneous emission (ASE). Discrimination against ASE is caused mainly by anisotropy of the RPG medium. It can be expected that the increased number of active layers should result in boosting the optical output power. However, it is also more difficult to pump electrically VCSELs with multiple active regions, and optical pumping has been routinely used to excite DBR-RPG lasers [Gourley 1989], [Corzine 1989b], [McDaniel 1990]. Transverse-junction scheme is the most promising method for electrical pumping, but to date only limited success has been reported [Schaus 1991]. In addition to difficulties with electrical pumping, large total thickness of epitaxial material (typically 8-10 μm [Schaus 1989], [Mukherjee 1990]) renders the DBR-RPG structure ill suited for monolithic integration.

It is significantly easier to achieve electrical pumping in a DBR VCSEL with only a single active region satisfying the resonant gain condition, often referred to as a microlaser [Jewell 1989], [Jewell 1990]. The microlaser resonator, shown schematically in Fig. 2, preserves the characteristic features of the RPG medium. While the microlaser structure has been very effective in reducing the room-temperature cw threshold and is clearly dominating present designs of electrically-pumped VCSELs [Osinski 1991], its performance in terms of maximum output power has not at all been impressive. The highest reported room-temperature cw output power from GaAs/AlGaAs planar microlasers is 1.5 mW for 10-μm diameter devices with a four-quantum-well active region, and slightly over 3 mW for 30-μm diameter devices [Tell 1990]. The most recent results obtained for InGaAs/GaAs/AlGaAs microlasers with strained-quantum-well active regions, grown by phase-locked epitaxy, are 3 mW for 15-μm square devices, ~5.5 mW for 30-μm square, 9 mW for 45-μm square, and 10 mW for 85-μm square [Walker 1991].

3. DISTRIBUTED-FEEDBACK VCSEL STRUCTURE

DFB configuration has been realized in the past in the context of conventional VCSELs [Ogura 1984], [Ogura 1985], [Ogura 1987a], [Ogura 1987b]. The DFB structure, shown schematically in Fig. 3, consists of a stack of alternating quarter-wavelength layers of high-index low-bandgap material (for example, GaAs) constituting the active region, and of low-index high-bandgap material (AlGaAs), providing reflectivity in the DFB cavity. One half-wavelength layer

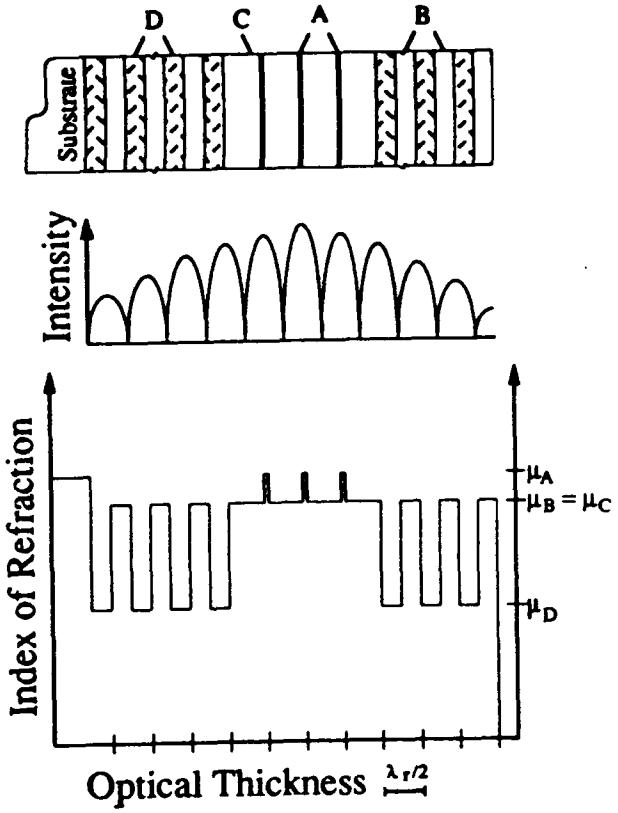

Fig. 1. Schematic illustration of layer structure, optical intensity distribution, and refractive index profile for a DBR-RPG laser. Thick lines (A) represents high-index quantum-well active layers, unshaded regions (B) - intermediate-index quarter-wave spacers, unshaded regions (C) - intermediate-index half-wave spacers, shaded regions (D) - low-index quarter-wave spacers.

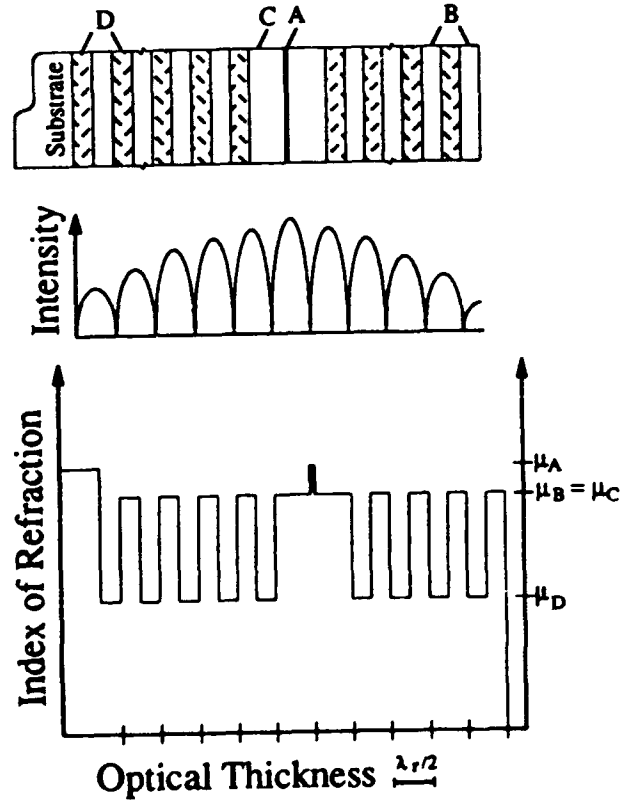

Fig. 2. Schematic illustration of layer structure, optical intensity distribution, and refractive index profile for a microlaser. Layer designation (A, B, C, D) is the same as in Fig. 1.

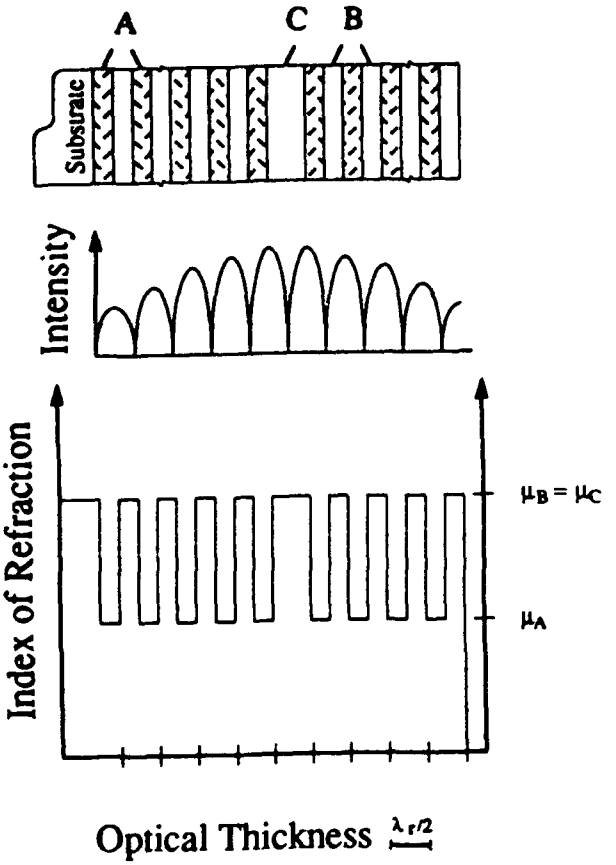

Fig. 3. Schematic illustration of layer structure, optical intensity distribution, and refractive index profile in a DFB VCSEL. Layer designation is the same as in Fig. 1.

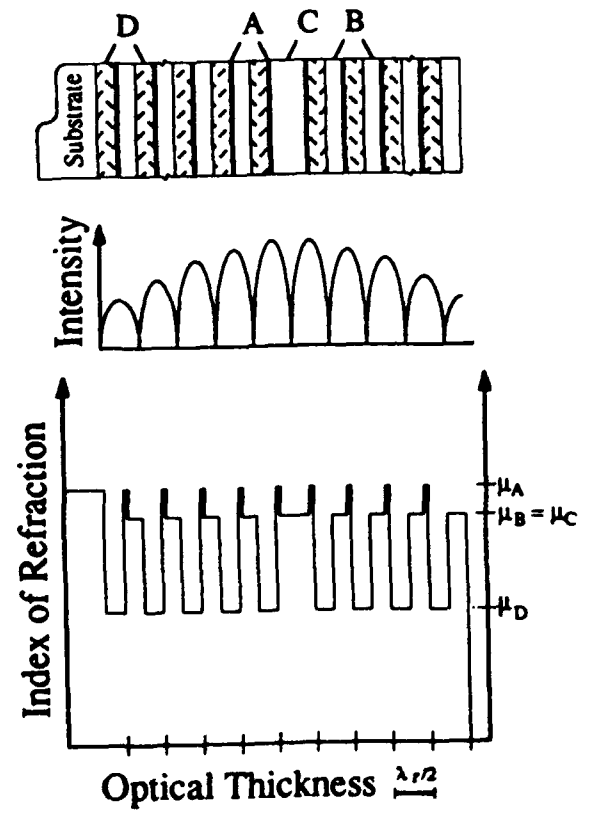

Fig. 4. Schematic illustration of layer structure, optical intensity distribution, and refractive index profile in a DFB-RPG laser. Layer designation is the same as in Fig. 1.

in the central part of the structure provides a phase-shift necessary to select a desired DFB mode.

A modified version of DFB VCSEL, utilizing a higher gain coefficient of quantum-well material, was proposed by Nomura *et al.* [Nomura 1987]. The high-index bulk quarter-wave layers have been replaced with multiple GaAs/AlGaAs quantum wells, with the Al composition in the barriers smaller than that in the low-index quarter-wave layers.

Lasing action in bulk and MQW DFB VCSELs was demonstrated both by optical pumping and by lateral current injection. However, since no attempt was made to arrange the quantum wells in register with the standing wave pattern inside the resonator, the performance of DFB VCSELs was at best similar to that of conventional DH VCSELs.

4. DISTRIBUTED-FEEDBACK RESONANT-PERIODIC-GAIN VCSEL STRUCTURE

The most recent advance in RPG laser structures is a distributed-feedback resonant-periodic-gain (DFB-RPG) VCSEL [Mahbobzadeh 1990], shown schematically in Fig. 4. By interlacing the RPG active medium with the quarter-wave multilayer high reflectors, the structure combines features of RPG, microlaser, and DFB designs. In particular, the effective cavity length is comparable to that of a microlaser. Consequently, the structure favors only one longitudinal mode within the entire gain spectrum.

The prototype MOCVD-grown DFB-RPG sample has been described in detail in [Mahbobzadeh 1991]. Here, we only give the most essential device parameters. The whole structure contains 42.5 half-wave periods, of which 24 periods, counting from the center of the phase shifter C, are at the bottom (*i.e.*, at the GaAs substrate side) and 18.5 periods are at the top. The layer thicknesses are, respectively, 63.4 nm for a low-index quarter-wave AlAs layer D, 54.3 nm for an intermediate index $Al_{0.15}Ga_{0.85}As$ layer B, and 10 nm for an active GaAs single-quantum well layer A. The total number of quantum wells is 42. The quarter-wave layer located at the top surface is made transparent to the pumping light (λ = 740 nm) by increasing the Al content to 20% (not shown in Fig. 4), with the thickness adjusted to 59.9 nm.

For RPG VCSELs, the total device thickness is of primary concern, since apart from issues of technological complexity and cost it also affects the ability to pump uniformly the active regions. As mentioned in Section 2, the total thickness of DBR-RPG structures is significantly larger than that of the microlaser. By replacing the DBR-RPG design with DFB-RPG, the total thickness of the device can be almost halved without compromising the characteristic features of the RPG active medium, to reach essentially the same thickness as the microlaser. Specifically, the total thickness of the prototype structure is 5.42 μm. An equivalent DBR-RPG device, having the same number of single quantum wells and the same reflectivities of top and bottom reflectors (99.56% and 99.7%) would be ~10.47-μm thick. Thus, compared to DBR-RPG structures, the DFB-RPG design offers the advantages of considerably simpler fabrication process, improved wavelength selectivity, and strong discrimination against excitation of satellite longitudinal modes.

5. OPTICAL PUMPING EXPERIMENTS

The prototype DFB-RPG sample was optically pumped both cw and pulsed through the top mirror. The pumping wavelength of 740 nm was selected in order to pump both $Al_{0.15}Ga_{0.85}As$ spacers and GaAs quantum-well active regions for a better pumping efficiency. In this way carriers generated within the $Al_{0.15}Ga_{0.85}As$ spacers can in turn fall into the quantum-well active regions. This results in a higher pump absorption and, consequently, a higher pumping ef-

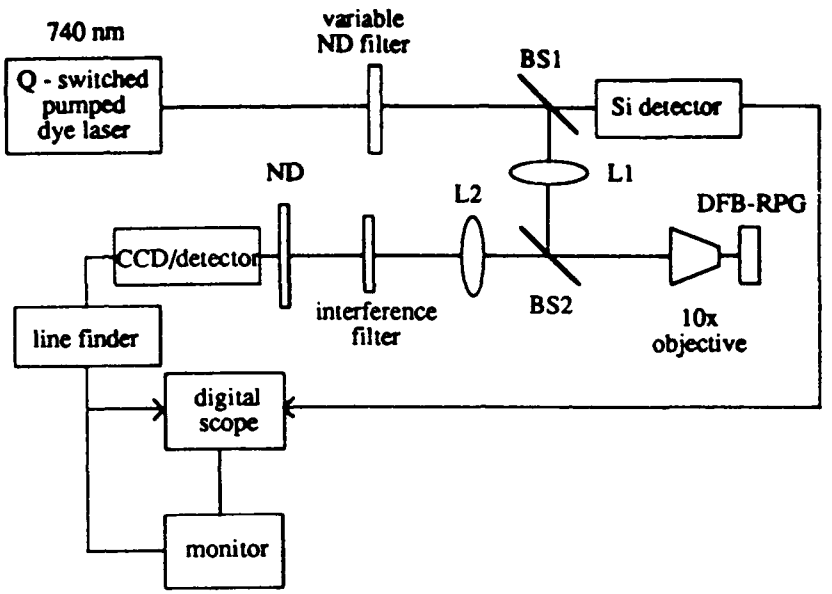

Fig. 5. Experimental setup for measurements of pulsed input/output characteristics of optically pumped VCSELs.

ficiency.

The experimental setup used for measurement of the pulsed input/output power is sketched in Fig. 5. A Q-switched pumped dye laser operating at 740 nm was used for pumping the DFB-RPG structure through the top mirror. Pulse duration was 7 ns and the repetition rate was 10 Hz. Power of the pump beam could be continuously varied by a circular variable attenuator. The beam splitter BS1 had high transmission and low reflection. This allowed a direct estimate of the input power by measuring the transmitted part of the pump power and multiplying it by a calibration factor that converted the transmitted power into the input power. A calibrated Gentec power meter was used for this purpose. The output power was measured using a Si detector calibrated to give the output energy. A calibrated dichroic beam splitter BS2 was used to pump the sample and at the same time to couple out the output beam. Additional calibrated ND filters, not shown in Fig. 5, were used next to the beam splitter BS2 to further attenuate the pump beam. The pump beam was focused using a 10× microscope objective. The microscope objective served for a dual purpose of focusing the pump beam and collimating the output. Appropriate interference filters were used to select pump or DFB-RPG output. The studied sample was simply placed in holder, without any provision for heat sinking.

A similar arrangement was used to perform the cw input/output measurements. A cw-dye laser operating at the 740-nm wavelength was used as a pump source. For the cw measurements, the beam splitter BS1 was replaced with another beam splitter having low transmission and high reflection. Rather than measuring the pump beam power after its passage through BS1, calibrated power meters were employed to measure the power of the input pump beam and the output just prior to microscope objective and just after the interference filter, respectively.

Fig. 6 shows a typical input/output characteristics for cw room-temperature pumping. The pump power has been corrected for measured surface-reflection (~30%) and calculated transmission (8%) through the substrate. Estimated threshold is ~60 mW with output power efficiency

of 10% (single ended), and differential quantum efficiency exceeding 80% per facet. The roll-off of the output power at high input powers is caused by heating effects. This is confirmed by the absence of any such roll-off for pulsed operation. Undoubtedly, thermal problems will be alleviated by placing the wafer on a heat sink.

The maximum measured peak pulsed output power reported in [Mahbobzadeh 1991] was 8.5 W. In order to determine the corresponding output power density, the following method of lasing spot-size measurement was adopted. The lens L2 (see Fig. 5) was used to image the sample into a CCD camera. The combination of the lens L2 and the objective is equivalent to a microscope. In order to calibrate the video and/or the scope against the translation of the sample, we used the lense L1 to expand the pump beam so that a larger area of the sample could be illuminated. By using a defect or dust spot, or another characteristic feature on the sample surface, we could perform the calibration. To this aim, the sample was translated in a transverse direction by a known distance as measured by a micrometer, while noting on the screen/scope the movement of the defect spot. Translation should only be done in transverse directions to ensure that the spot size does not change during the calibration phase. The lense L1 was then removed so that the camera was recording the actual size of the pumped spot. By having the calibration factor and noting the spot size as seen on the screen/scope, the spot size could be calculated.

Using the method described, we were able to determine the diameter of the lasing spot as ~16 μm. Fig. 7 shows the input/output characteristic for the pulsed conditions (7 ns pulsewidth, 10 Hz repetition rate). The efficiency of conversion of the estimated absorbed pump power into the lasing output emitted through the top surface was ~10%. Using the measured lasing spot size, the maximum peak output power of 8.5 W corresponds to ~4.5 MW/cm^2. To our knowledge, this is the highest power density ever reported for any semiconductor laser. It is approximately one order of magnitude higher than the maximum power density obtained from DBR-RPG lasers under similar pumping conditions [Wu 1991].

6. CONCLUSIONS

Distributed-feedback resonant-periodic-gain laser structure is very promising for high-power applications. While the total device thickness is comparable to that of a microlaser, a multiplicity of active layers in the DFB-RPG structure results in a record-high pulsed output power. Preliminary data obtained on optically pumped bare wafer DFB-RPG samples without any heat sinking illustrate a tremendous potential of these devices. Under cw conditions, thermally limited output power of 6.7 mW was obtained with 10-μm diameter of the pumping beam. The same device, when pumped by 7 ns pulses with 10 Hz repetition rate, produced as much as 8.5 W of the peak output power out of a 16-μm diameter lasing spot. The corresponding output power density was 4.5 MW/cm^2. To our best knowledge, this is the highest peak power density ever reported for semiconductor lasers.

7. ACKNOWLEDGMENTS

Support of the U.S. Air Force Office of Scientific Research, the Air Force Phillips Laboratory, and the Defense Advanced Research Projects Agency is gratefully acknowledged. The authors wish to express their gratitude to Dr. Christian Schaus for growing the prototype sample, to Drs. Anadi Mukherjee and Steven Brueck for valuable discussions and advice during the course of experiments, and to Mr. Andrew Frauenglass for his expert technical assistance.

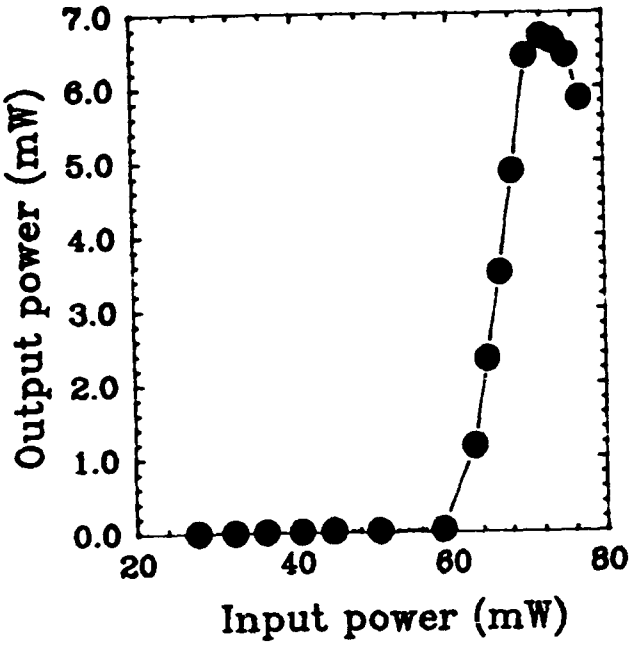

Fig. 6. Typical input/output characteristic for room-temperature cw pumping of the prototype DFB-RPG sample.

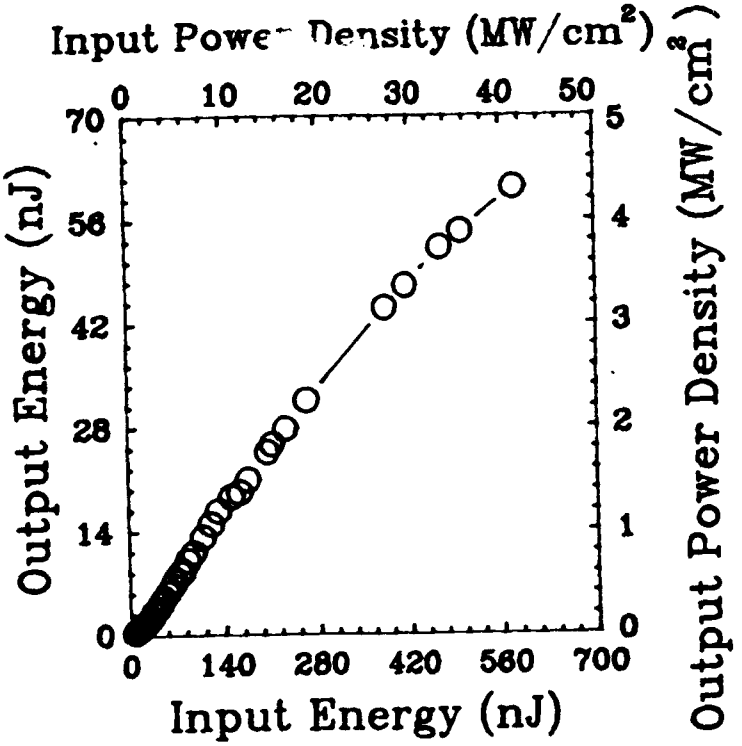

Fig. 7. Input/output energy and power-density characteristic of the prototype DFB-RPG laser pumped by 7 ns pulses at 10 Hz repetition rate.

8. REFERENCES

[Brueck 1989] S. R. J. Brueck, M. Y. A. Raja, M. Osiński, C. F. Schaus, M. Mahbobzadeh, J. G. McInerney, and K. J. Dahlhauser, "Optical Cavity Design for Wavelength-Resonant Surface-Emitting Semiconductor Lasers (Invited Paper)", *SPIE Proc. Vol. 1043 - Laser Diode Technology and Applications* (L. Figueroa, Ed.), SPIE Symp. on Lasers and Optics OE/LASE'89, Los Angeles, California, Jan. 18-20, 1989, pp. 111-122.

[Corzine 1989a] S. W. Corzine, R. S. Geels, R. H. Yan, J. W. Scott, L. A. Coldren, and P. L. Gourley, "Efficient, Narrow-Linewidth Distributed-Bragg-Reflector Surface-Emitting Laser with Periodic Gain", *IEEE Photon. Technol. Lett.*, vol. 1, pp. 52-54, March 1989.

[Corzine 1989b] S. W. Corzine, R. S. Geels, J. W. Scott, R.-H. Yan, and L. A. Coldren, "Design of Fabry-Perot Surface-Emitting Lasers with a Periodic Gain Structure", *IEEE J. Quantum Electron.*, vol. 25, pp. 1513-1524, June 1989.

[Geels 1988] R. S. Geels, R. H. Yan, J. W. Scott, S. W. Corzine, R. J. Simes, and L. A. Coldren, "Analysis and Design of a Novel Parallel-Driven MQW DBR Surface-Emitting Diode Laser", *CLEO '88 Conf. Lasers & Electro-Optics, Techn. Digest Series Vol. 7*, Anaheim, CA, April 25-29, 1988, Paper WM1, pp. 206-207.

[Gourley 1989] P. L. Gourley, T. M. Brennan, B. E. Hammons, S. W. Corzine, R. S. Geels, R. H. Yan, J. W. Scott, and L. A. Coldren, "High-Efficiency TEM_{00} Continuous-Wave (Al,Ga)As Epitaxial Surface-Emitting Lasers and Effect of Half-Wave Periodic Gain", *Appl. Phys. Lett.*, vol. 54, pp. 1209-1211, 27 March 1989.

[Iga 1988] K. Iga, F. Koyama, and S. Kinoshita, "Surface Emitting Semiconductor Lasers", *IEEE J. Quantum Electron.*, vol. 24, pp. 1845-1855, Sept. 1988, and the references quoted therein.

[Jewell 1989] J. L. Jewell, K. F. Huang, K. Tai, Y. H. Lee, R. J. Fischer, S. L. McCall, and A. Y. Cho, "Vertical Cavity Single Quantum Well Laser", *Appl. Phys. Lett.*, vol. 55, pp. 424-427, 31 July 1989.

[Jewell 1990] J. L. Jewell, Y. H. Lee, A. Scherer, S. L. McCall, N. A. Olsson, J. P. Harbison, and L. T. Florez, "Surface-Emitting Microlasers for Photonic Switching and Interchip Connections", *Opt. Eng.*, vol. 29, pp. 210-214, March 1990.

[Mahbobzadeh 1990] M. Mahbobzadeh and M. Osiński, "Novel Distributed-Feedback Resonant-Periodic-Gain Structure for Vertical-Cavity Surface-Emitting Semiconductor Lasers", *Electron. Lett.*, vol. 26, pp. 1716-1718, 27 Sept. 1990.

[Mahbobzadeh 1991] M. Mahbobzadeh and M. Osiński, "Novel Distributed-Feedback Structure for Surface-Emitting Semiconductor Lasers", SPIE Proc. Vol. 1418 - Laser Diode Technology and Applications III (D. Renner, Ed.), SPIE Symp. on High Power Lasers, OE/LASE'91, Los Angeles, California, January 20-25, 1991, pp. 25-31.

[McDaniel 1990] D. L. McDaniel, Jr., J. G. McInerney, M. Y. A. Raja, C. F. Schaus, and S. R. J. Brueck, "Vertical Cavity Surface-Emitting Semiconductor Laser with CW Injection Laser Pumping", *IEEE Photon. Technol. Lett.*, vol. 2, pp. 156-158, March 1990.

[Mukherjee 1990] A. Mukherjee, M. Mahbobzadeh, C. F. Schaus, and S. R. J. Brueck, "Ultrafast Operation of Optically Pumped Resonant-Periodic-Gain GaAs Surface Emitting Lasers", *IEEE Photon. Technol. Lett.*, vol. 2, pp. 857-859, Dec. 1990.

[Nomura 1986] Y. Nomura, K. Shinozaki, K. Asakawa, and M. Ishii, "GaAs/AlGaAs Distributed-Feedback Structure with Multiquantum Well for Surface-Emitting Laser", *J. Appl. Phys.*, vol. 60, pp. 874-877, 1 Aug. 1986.

[Ogura 1984] M. Ogura, T. Hata, and T. Yao, "Distributed Feed Back Surface Emitting Laser Diode with Multilayered Heterostructure", *Jpn. J. Appl. Phys. (Lett.)*, vol. 23, pp. L512-L514, July 1984.

[Ogura 1985] M. Ogura and T. Yao, "Surface Emitting Laser Diode with $Al_xGa_{1-x}As$/GaAs Multilayered Heterostructure", *J. Vac. Sci. Technol*, vol. B 3, pp. 784-787, March 1985.

[Ogura 1987a] M. Ogura and S. Mukai, "Distributed-Feedback, Surface-Emitting Laser Diode with Lateral Double Heterostructure", *Electron. Lett.*, vol. 23, pp. 758-760, 2 July 1987.

[Ogura 1987b] M. Ogura, W. Hsin, M.-C. Wu, S. Wang, J. R. Whinnery, S. C. Wang, and J. J. Yang, "Surface-Emitting Laser Diode with Vertical GaAs/GaAlAs Quarter-Wavelength Multilayers and Lateral Buried Heterostructure", *Appl. Phys. Lett.*, vol. 51, pp. 1655-1657, 23 Nov. 1987.

[Osiński 1991] M. Osiński, "Vertical-Cavity Surface-Emitting Semiconductor Lasers: Present Status and Future Prospects (Invited Paper)", SPIE Proc. Vol. 1418 - Laser Diode Technology and Applications III (D. Renner, Ed.), SPIE Symp. on High Power Lasers, OE/LASE'91, Los Angeles, California, January 20-25, 1991, pp. 2-24.

[Raja 1988] M. Y. A. Raja, S. R. J. Brueck, M. Osiński, C. F. Schaus, J. G. McInerney, T. M. Brennan, and B. E. Hammons, "Novel Wavelength-Resonant Optoelectronic Structure and Its Application to Surface-Emitting Semiconductor Lasers", *Electron. Lett.*, vol. 24, pp. 1140-1142, 1 Sept. 1988.

[Raja 1989] M. Y. A. Raja, S. R. J. Brueck, M. Osiński, C. F. Schaus, J. G. McInerney, T. M. Brennan, and B. E. Hammons, "Resonant Periodic Gain Surface-Emitting Semiconductor Lasers", *IEEE J. Quantum Electron.*, vol. 25, pp. 1500-1512, June 1989.

[Schaus 1989] C. F. Schaus, H. E. Schaus, S. Sun, M. Y. A. Raja, and S. R. J. Brueck, "MOCVD Growth of GaAs/AlGaAs Wavelength Resonant Periodic Gain Vertical Cavity Surface-Emitting Laser", *Electron. Lett.*, vol. 25, pp. 538-539, 13 April 1989.

[Schaus 1991] C. F. Schaus, A. J. Torres, J. Cheng, S. Sun, C. Hains, K. J. Malloy, H. E. Schaus, E. A. Armour, and K. Zheng, "Transverse Junction Vertical-Cavity Surface-Emitting Laser", *Appl. Phys. Lett.*, vol. 58, pp. 1736-1738, 22 April 1991.

[Tell 1990] B. Tell, Y. H. Lee, K. F. Brown-Goebeler, J. L. Jewell, R. E. Leibenguth, M. T. Asom, G. Livescu, L. Luther, and V. D. Mattera, "High-Power CW Vertical-Cavity Top Surface-Emitting GaAs Quantum Well Lasers", *Appl. Phys. Lett.*, vol. 57, pp. 1855-1857, 29 Oct. 1990.

[Walker 1991] J. D. Walker, D. M. Kuchta, and J. S. Smith, "Vertical-Cavity Surface-Emitting Laser Diodes Fabricated by Phase-Locked Epitaxy", *Appl. Phys. Lett.*, vol. 59, pp. 2079-2081, 21 Oct. 1991.

[Wu 1991] C. Wu and J. G. McInerney, "Power Scaling in High-Power Optically Pumped Vertical Cavity Surface-Emitting Semiconductor Lasers", *Techn. Digest, OSA '91 Annual Meeting, Techn. Digest Series Vol. 17*, San Jose, CA, Nov. 3-8, 1991, Paper MHH6, p. 38.

SPIE Proc. Vol. 1634 - Laser Diode Technology & Applications IV (D. Renner, Ed.), OE/LASE '92, Los Angeles, CA, Jan. 19-24, 1992, Paper 1634-49, in print.

DISTRIBUTED-FEEDBACK VERTICAL-CAVITY SURFACE-EMITTING LASER WITH RESONANT-PERIODIC-GAIN ACTIVE REGION

Mohammad Mahbobzadeh*, Emmanuelle Gandjbakhch, Eric A. Armour*, Kang Zheng, Shang-Zhu Sun, Christian F. Schaus***, and Marek Osiński****

Center for High Technology Materials, University of New Mexico
Albuquerque, New Mexico 87131-6081

ABSTRACT

Fabrication and lasing characteristics of prototype MOCVD-grown GaAs/AlGaAs/AlAs distributed-feedback resonant-periodic-gain surface-emitting lasers are reported. The new structure eliminates the need for end reflectors in earlier resonant-periodic-gain lasers, thereby reducing considerably the total thickness of the device. A new hybrid distributed-Bragg-reflector/distributed-feedback resonant-periodic-gain structure, compatible with the transverse-junction electrical pumping scheme, is also proposed.

1. INTRODUCTION

Surface-emitting semiconductor lasers are very attractive for applications in optical computing, coherent communications, high-power two-dimensional arrays and integrated optoelectronics. Early designs of VCSELs with bulk active regions suffered, however, from low external efficiency and consequently low output power [Iga 1988]. The primary reason for their poor performance was the competition between the desirable vertical emission and parasitic amplified spontaneous emission (ASE) in the transverse directions. In order to reduce the lasing threshold and suppress the ASE, two concepts of VCSELs with quantum-well (QW) active regions have been pursued in parallel: a distributed-Bragg-reflector resonant-periodic-gain (DBR-RPG) structure, with multiple active layers spaced at half the wavelength of a selected optical transition [Raja 1989], [Corzine 1989], [Schaus 1989a], and a microlaser structure [Jewell 1989], [Jewell 1990], with a single QW placed in a Bragg resonator. Both designs achieve gain enhancement in the vertical direction by aligning the active regions with the maxima of the longitudinal mode pattern at the emission wavelength. The most recent advance in RPG laser structures is a distributed-feedback resonant-periodic-gain (DFB-RPG) VCSEL [Mahbobzadeh 1990], where an RPG active region is intercalated with the multilayer high reflectors (MHRs). The new design eliminates the need for end reflectors in previous RPG structures and reduces the total thickness of the device, while retaining the characteristic features of RPG medium (gain enhancement in vertical direction, wavelength selectivity, ASE suppression, *etc.*).

In this paper, we describe fabrication of the first DFB-RPG laser structures grown by MOCVD and their performance under optical pumping conditions. Various versions of the RPG

* Also with the Department of Electrical and Computer Engineering, University of New Mexico.

** Present address: Optoelectronics Laboratory, Ecole Nationale Supérieure des Télécommunications, 46, rue Barrault, F-75634 Paris Cédex 13, France.

*** Present address: Eyeonics Corporation, 15895 SW 72nd Ave., Suite 200, Portland, Oregon 97224.

**** Also with the Department of Electrical and Computer Engineering and the Department of Physics and Astronomy, University of New Mexico.

structure design utilizing vertical-cavity configuration are discussed in Section 2. In Section 3, we describe the crystal growth and calibration process. Experimental results on quasi-cw and pulsed optical pumping of the prototype samples are given in Section 4.

2. CLASSIFICATION OF RPG VCSEL STRUCTURES

A characteristic feature of VCSELs that distinguishes them from edge-emitting semiconductor lasers is their small single-pass gain, reminiscent of gas lasers. As a direct consequence of small gain, in order to avoid prohibitively high lasing threshold it is necessary to place the active medium in a high-Q resonator. In today's state-of-the-art VCSELs, this is almost invariably achieved by providing a Bragg resonator consisting of a stack of high-reflectivity quarter-wave layers on either side of the active medium.

The vertical-stack geometry of VCSELs offers unique opportunities for designing novel devices with properties significantly different from those of conventional edge-emitting lasers. When a VCSEL optical cavity is carefully designed, such that a quantum-well active region would coincide with a standing-wave maximum at a designed wavelength of operation, more efficient pumping can be achieved compared to a medium with uniform gain [Geels 1988], [Raja 1988], [Brueck 1989]. The effect is wavelength-sensitive, and at non-resonant wavelengths the gain drops down to its bulk level. Application of this concept to multiple active regions lead to introduction of distributed-Bragg-reflector resonant-periodic-gain (DBR-RPG) lasers [Raja 1989], [Corzine 1989a], illustrated schematically in Fig. 1. The multiple active regions in a DBR-RPG structure are separated by half-wave spacers and sandwiched between two multilayer high reflectors. In devices designed for optical pumping, which is the standard excitation method in RPG VCSELs [Gourley 1989a], [Corzine 1989], [McDaniel 1990], the Bragg reflectors are transparent to a pumping wavelength while the spacers (regions B in Fig. 1) are absorbing. The output light is normally collected through the top reflector, although in devices with strained-quantum-well active regions [Gourley 1989b] the bottom reflector may be used to transmit light through the substrate. The device features an enhanced gain along the resonator axis (by up to a factor of 2 compared to a uniformly pumped medium), improved wavelength selectivity, and reduced amplified spontaneous emission (ASE). Discrimination against ASE is caused mainly by anisotropy of the RPG medium which counteracts the unfavorable aspect ratio for vertical emission in double-heterostructure lasers.

Optically pumped bare DBR-RPG wafers without any heat sink exhibited very good performance with up to 45% power conversion efficiency and over 20 mW of cw output power out of ~18-μm diameter near-field spot size [Schaus 1989b], [Schaus 1989c]. However, large total thickness of epitaxial material (typically 8-10 μm [Schaus 1989a], [Mukherjee 1990]) renders the DBR-RPG structure rather costly and ill-suited for monolithic integration.

A hybrid DBR/DFB structure, illustrated in Fig. 2, was introduced in [Schaus 1989a]. The active (DFB-RPG) section consisted of GaAs quantum wells intercalated with AlGaAs/AlAs multilayer reflectors and was surrounded on both ends by DBR reflectors. Again, the Bragg reflectors are transparent to pumping wavelength while the AlGaAs layers adjacent to quantum wells are absorbing. Due to practical difficulties in matching the resonant wavelength in the DFB region with that in the DBR reflectors, this device did not perform nearly as well (in fact, only pulsed operation was possible) as the DBR-RPG lasers.

The most recent advance in RPG laser structures is a distributed-feedback resonant-periodic-gain (DFB-RPG) VCSEL [Mahbobzadeh 1990] (Fig. 3), where DBR reflectors are entirely eliminated. In order to avoid unwanted absorption of pump radiation at the top quarter-wave layer, the composition of that layer (layer C in Fig. 3) is altered to slightly increase its bandgap compared to the remaining intermediate index layers (layers B in Fig. 3).

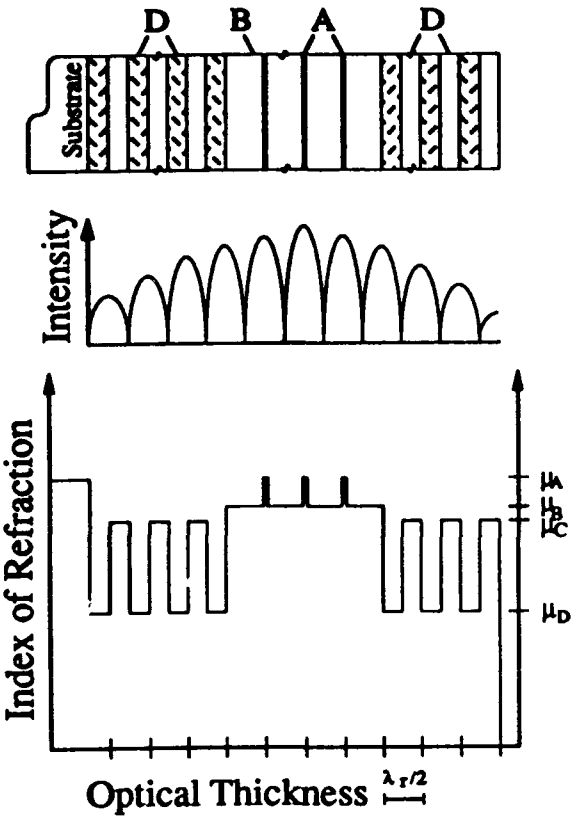

Fig. 1. Schematic illustration of a DBR-RPG structure, corresponding intensity distribution of resonant mode of wavelength λ_r, and refractive index profile. Thick lines (A) represent high-index quantum-well active layers, unshaded regions (B) - intermediate-index half-wave spacers absorbing at the pump wavelength, unshaded regions (C) - intermediate-index quarter-wave layers transparent at the pump wavelength, shaded regions (D) - low-index quarter-wave layers. For the sake of simplicity, the number of periods is reduced.

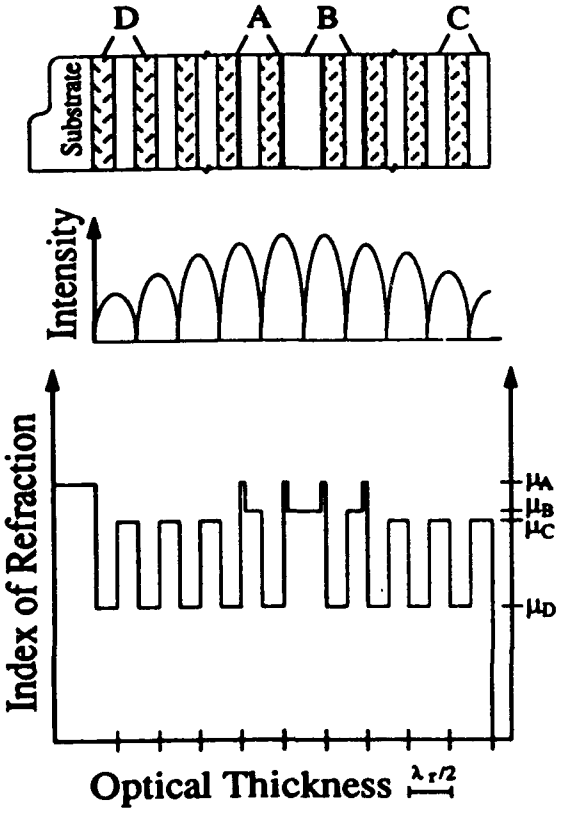

Fig. 2. Schematic illustration of layer configuration, optical intensity distribution, and refractive index profile in a hybrid DFB/DBR RPG VCSEL of [Schaus 1989a]. Layer designation is the same as in Fig. 1, except for the unshaded regions (B) which now represent an intermediate-index half-wave phase shifter and quarter wave layers, all absorbing at the pump wavelength.

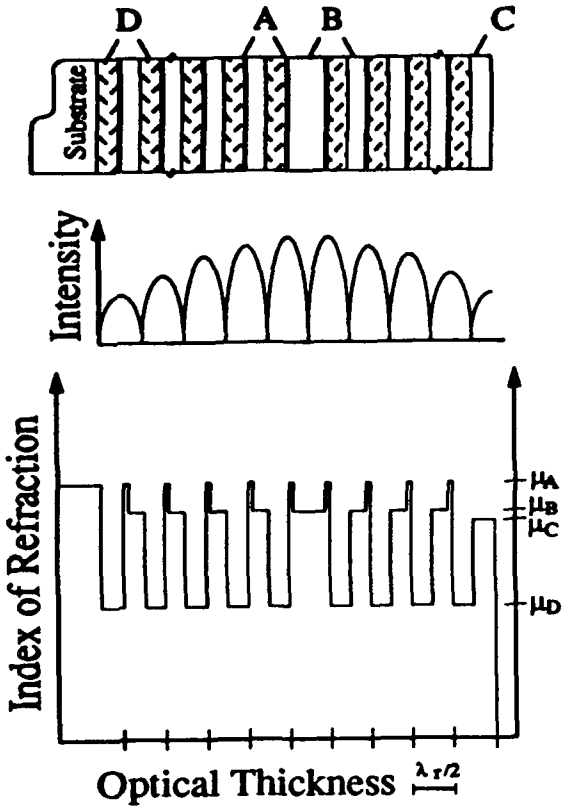

Fig. 3. Schematic illustration of layer configuration, optical intensity distribution, and refractive index profile in a DFB-RPG structure. Layer designation is the same as in Fig. 2.

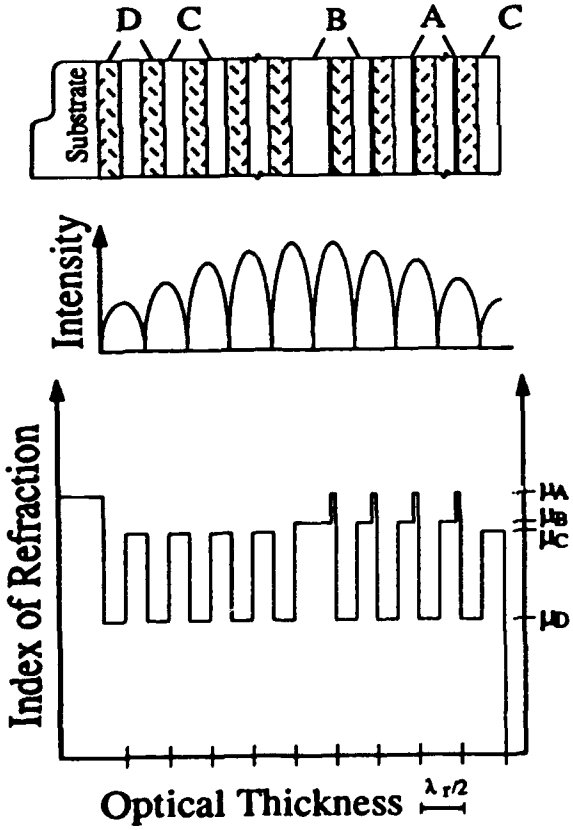

Fig. 4. Schematic illustration of layer configuration, optical intensity distribution, and refractive index profile in a hybrid DFB/DBR RPG VCSEL proposed in this paper. Layer designation is the same as in Fig. 2.

For RPG VCSELs, the total device thickness is of primary concern, since apart from issues of technological complexity and cost it also affects the ability to pump uniformly the active regions. By replacing the DBR-RPG design with DFB-RPG, the total thickness of the device can be almost halved without compromising the characteristic features of RPG active medium, to reach essentially the same thickness as the microlaser. Compared to DBR-RPG structures, the DFB-RPG design offers the advantages of considerably simpler fabrication process, improved wavelength selectivity, and strong discrimination against excitation of satellite longitudinal modes. It is, however, somewhat more demanding than the DBR-RPG structure when tolerances on layer thicknesses and compositions are considered. Since the DBR section in a DBR-RPG VCSEL is entirely passive, the tolerances in that section are not as stringent as in the active part of the device [Brueck 1989].

Another hybrid DFB/DBR design, presented for the first time in this paper, is shown in Fig. 4. We consider this structure as a prime candidate for electrically pumped RPG lasers. RPG VCSELs are notoriously difficult to pump electrically. The usual vertical current injection scheme, applied commonly in microlasers, is impractical in case of RPG lasers due to prohibitively high electrical resistance and lack of control over the uniformity of carrier injection over the entire thickness of the device. Transverse-junction scheme is the most promising method for electrical pumping, but to date only limited success has been reported [Schaus 1991]. Compared to the structures shown in Figs. 1-3, the DFB/DBR design of Fig. 4 has the advantage of an easy access to the active section (no need to bypass the top DBR reflector present in Figs. 1, 2) and a shorter depth of lateral contacts.

3. FABRICATION OF DFB-RPG VCSEL STRUCTURES BY MOCVD

Nominal compositions and layer thicknesses of DFB-RPG and DFB/DBR RPG VCSELs of Figs. 3 and 4 are shown schematically in Fig. 5. It should be emphasized that the structures illustrated in Fig. 5 only served as a guideline for fabricating the actual devices. In practice, a multiple-step calibration process is needed to satisfy the condition that the resonant wavelength should be close to the photoluminescence peak. The calibration procedure is described in a later part of this section.

During the design process, we used reflectivity calculations to ensure that the wavelength of resonant mode coincides with the optical transition wavelength corresponding to $n = 1$ subband transition in the quantum well [Mahbobzadeh 1991]. The design wavelength was taken as $\lambda_r = 840.4$ nm. The refractive indices for GaAs, $Al_{0.15}Ga_{0.85}As$, $Al_{0.25}Ga_{0.75}As$, and AlAs were taken as 3.60, 3.50, 3.45, and 3.00, respectively [Weber 1990]. It should be noted that the total optical thickness of a single period in the active (DFB) region, consisting of a quantum well and an AlAs/$Al_{0.15}Ga_{0.85}As$ "half-wave" spacer, is slightly smaller than the resonant wavelength.

The DFB-RPG structure consists of a stack of 10-nm thick GaAs single quantum wells sandwiched between AlAs and $Al_{0.15}Ga_{0.85}As$ layers, each slightly thinner than a quarter-wave. The whole structure, topped by a transparent $Al_{0.25}Ga_{0.75}As$ quarter-wave layer, contains 42.5 periods, of which 24 periods, counting from the center of the phase shifter, are at the GaAs substrate side, and 18.5 periods are at the top. The total number of quantum wells is 42. Calculated reflectivities of the lower and upper reflectors, separated by a half-wave $Al_{0.15}Ga_{0.85}As$ phase shifter, are 99.76% and 99.56%, respectively.

The top section of the DFB/DBR RPG structure is identical to that of the DFB-RPG device. The bottom Bragg reflector consists of a stack of alternating quarter-wave layers of AlAs and $Al_{0.25}Ga_{0.75}As$. The total number of periods is 45.5, of which 27 periods are below the center of the $Al_{0.15}Ga_{0.85}As$ phase shifter, and, as in the DFB-RPG laser, 18.5 periods are at the top. The total number of quantum wells is 18. Calculated reflectivity of the bottom reflec-

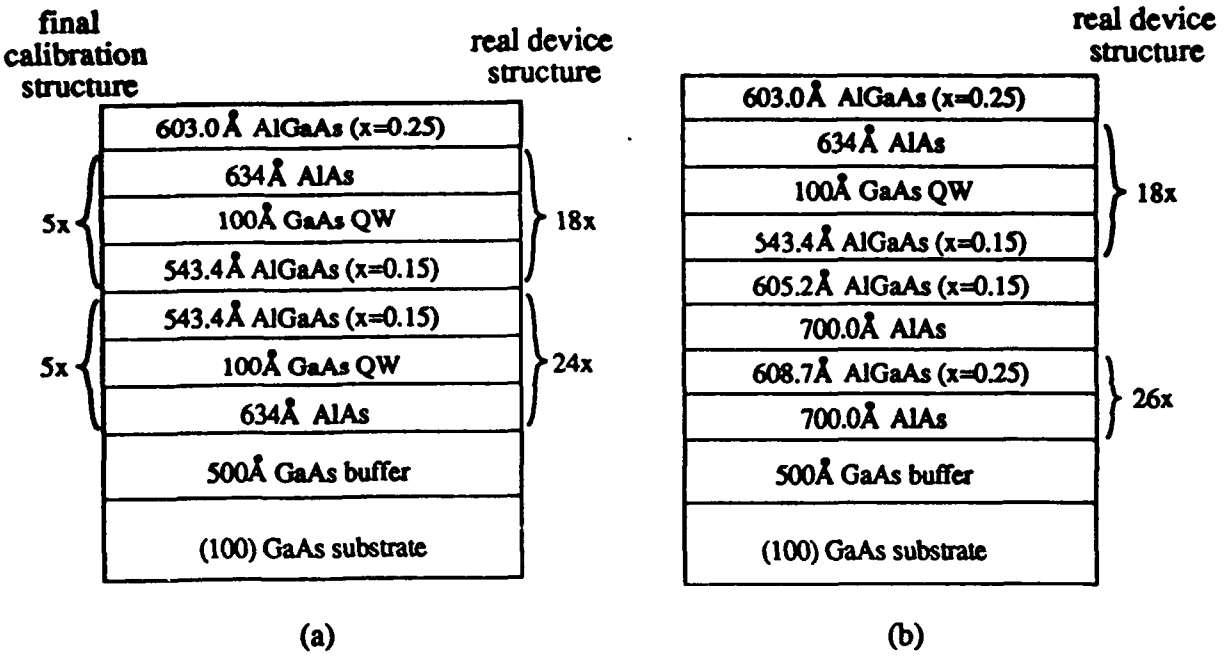

Fig. 5. Structure design of (a) DFB-RPG and (b) DFB/DBR RPG GaAs/$Al_xGa_{1-x}As$/AlAs VCSELs. The layer thicknesses are not drawn to scale.

tor, comprising 26.5 half-wave periods, is 99.80%.

Prototype DFB-RPG and DFB/DBR RPG structures were grown by MOCVD in a horizontal reactor at 100 torr and a growth temperature of 725 °C. The sources used were 100% arsine, trimethylgallium (TMGa) and trimethylaluminum (TMAl) which were maintained at a V/III ratio of 50. The growth rate was 500 Å/minute. The structures were undoped and produced in a single growth cycle.

In order to tune the resonant cavity and quantum-well emission wavelength to the design wavelength of λ_r = 840 nm, several calibration structures were needed before the growth of the final structures. First, a $3\lambda_r/2$ $Al_{0.25}Ga_{0.75}As$ layer, approximately 3652 Å thick, was grown on a GaAs buffer. Room-temperature photoluminescence (PL) was used to measure the layer alloy composition and infrared (IR) reflectometry was used to measure the reflectivity peak of the calibration layer. The reflectivity peak along with the associated alloy composition allows us to determine the exact layer thickness, giving us an accurate growth rate and TMAl incorporation constant. A more detailed description of the calibration procedure for VCSELs, including several examples of IR reflectometry spectra, is given in [Armour 1992]. When a satisfactory alloy composition and layer thickness for the calibration structure was obtained, a second calibration structure was grown which contained a $3\lambda_r/2$ AlAs layer (~4886 Å thick) on top of a $\lambda_r/4$ $Al_{0.25}Ga_{0.75}As$ layer (~628 Å thick). PL was used to verify the composition of the $Al_{0.25}Ga_{0.75}As$ layer, and IR reflectometry was used to measure the reflectance profile of the sample. The third and final calibration structure, shown in Fig. 5(a), resembled the actual DFB-RPG device but the number of periods above and below the center of the phase shifter was reduced to 5. PL was used to measure the quantum well emission and IR reflectometry was used to check the reflectance spectra. Using the TMAl incorporation coefficient obtained from the first $Al_{0.25}Ga_{0.75}As$ calibration structures, $Al_{0.15}Ga_{0.85}As$ layers could be grown without a separate calibration run by using a linear relationship between the Al content and the TMAl flow rates.

After the calibration runs, a DFB-RPG wafer (sample #610) was grown. The complete run sequence took ~4 hours, with 20 second growth interruptions between each layer. To accomplish this task, the MOCVD reactor is run via a dedicated DEC MicroVAX II computer which monitors and controls the reactor status every 10 ms. A second wafer (#613) was grown following the growth of a DFB/DBR RPG sample described below.

The growth of the DFB/DBR RPG structure was preceded by a single calibration run in which 5 periods of the DBR section and 5 periods of the DFB-RPG section were grown to verify the resonant wavelength. The structure was measured to resonate at 853 nm and thus the DFB/DBR RPG sample (wafer #612) was grown in the subsequent run.

TEM measurements were used to determine the actual layer thicknesses in the MOCVD-grown samples. Fig. 6 shows a TEM image of a piece of wafer #610. The measured thicknesses were: 549 Å for top $Al_{0.25}Ga_{0.75}As$ layer, 705 Å for AlAs layers, and 527 Å for $Al_{0.15}Ga_{0.85}As$ layers.

Fig. 6. TEM image of the prototype DFB-RPG VCSEL. The diameter of the exposed area is 6.4 μm. Quantum-well layers are not resolved. The top $Al_{0.25}Ga_{0.75}As$ layer is not visible because it was milled off in that portion of the sample.

4. OPTICAL PUMPING EXPERIMENTS

In quasi-cw experiments, the as-grown wafers were optically pumped using the 740 nm line of Ar-ion-pumped dye laser, with the pumping beam diameter of ~15 μm. As a precaution, in order to reduce the risk of sample overheating, a 10% duty-cycle chopper was used to modulate the pump beam at 1 kHz. The input power was measured with a calibrated NRC power meter. A high-sensitivity silicon detector was used to measure the output power.

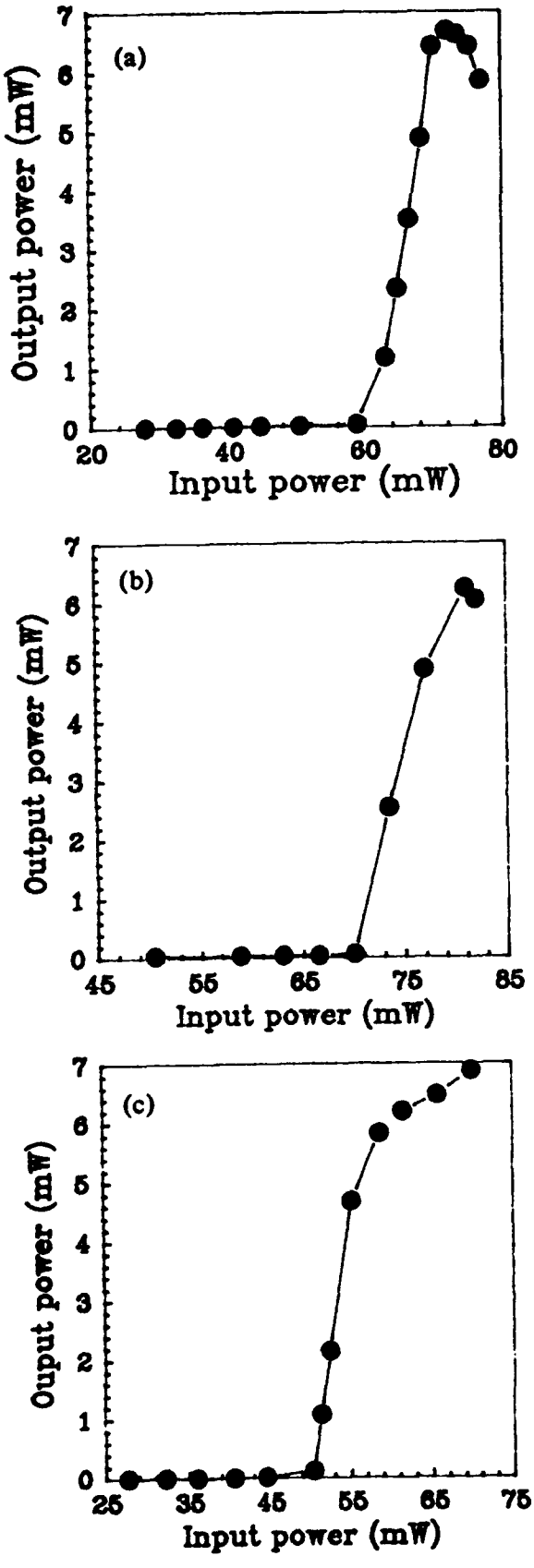

Fig. 7. Typical room-temperature input-output characteristics of (a) DFB-RPG sample #610, (b) DFB-RPG sample #613, and (c) DFB/DBR RPG sample #612 quasi-cw optically pumped without any heat sink. The input power refers to power absorbed within the DFB section of the device.

Fig. 7 shows typical quasi-cw characteristics of samples #610, 612, and 613. The average lasing threshold, obtained by pumping various spots on the same wafer, was 58 mW for wafer #610, 52 mW for wafer 612, and 74 mW for wafer 613. The increased threshold of wafer 613 was related to its poor surface morphology indicating an inferior crystalline quality.

Even though no heat sink was used, the maximum quasi-cw output power reached nearly 7 mW for any of the prototype wafers. This power level is considerably higher than that obtainable from single-quantum-well microlasers of the same active-region diameter, while it is comparable to that of DBR-RPG devices.

The cw output spectra of DFB-RPG device, centered at ~878 nm, were rather broad (0.8 nm) with a complex structure indicating multiple transverse mode operation. We note that the lasing wavelength is shifted towards the red, compared to the design wavelength of 840 nm. This is primarily caused by the disparity between the "ideal" specifications of Fig. 5 and the actually grown samples. As established by TEM measurements, the AlAs and $Al_{0.15}Ga_{0.85}As$ layer thicknesses in the prototype samples are greater than the original design parameters of Fig. 5. This shifts the resonant wavelength towards the red by ~27 nm, and even though it may no longer coincide with the gain peak, the resonant gain enhancement is sufficient to favor lasing at longer wavelengths. In addition, sample heating under the quasi-cw conditions also contributes to the red shift of the lasing wavelength.

In pulsed optical pumping experiments, we used a Q-switched Nd:YAG-laser-pumped dye laser that emitted 7 ns pulses at 735 nm, with 10 Hz repetition rate. The pumping beam power was measured using a calibrated Gentec detector.

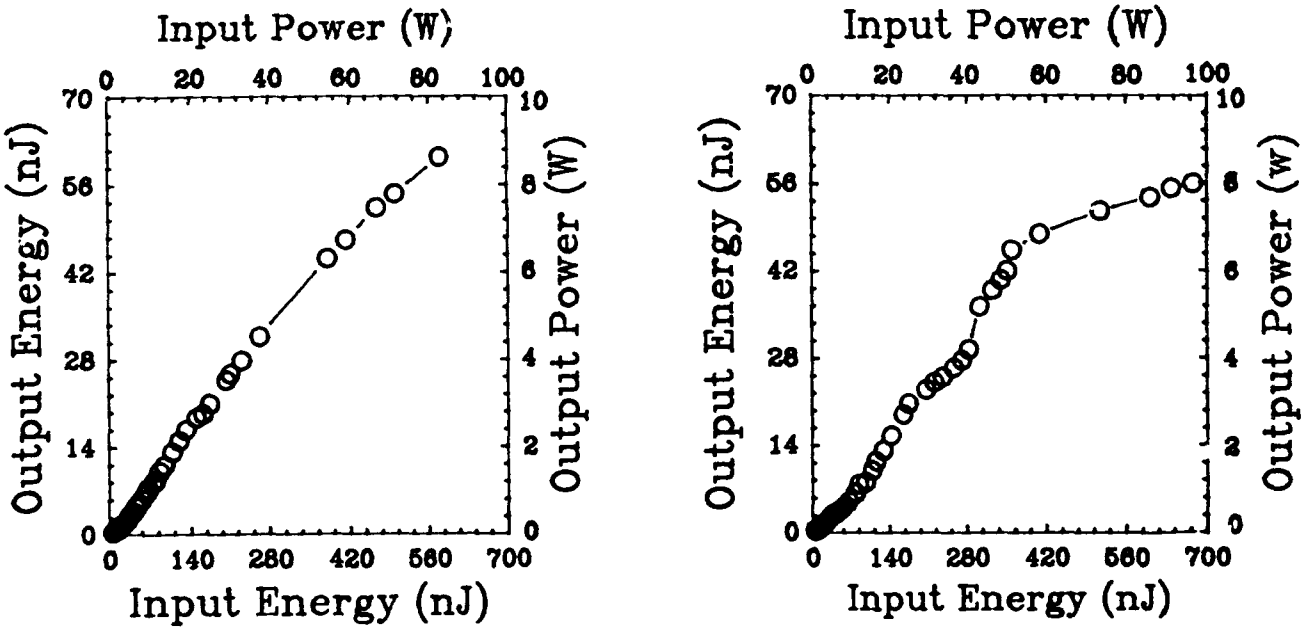

Fig. 8. Typical room-temperature input-output characteristics of the DFB-RPG sample #610, optically pumped with 7-ns pulses at 10 Hz repetition rate.

Fig. 8 shows examples of pulsed input-output characteristics measured for the DFB-RPG sample #610. The lasing threshold is about 30 nJ per pulse which corresponds to ~4 W peak

power. The peak output power reaches very high values, exceeding 8 W out of a 15-μm diameter lasing spot. This very large peak power illustrates the tremendous potential of RPG VCSELs as sources of very high-power well collimated laser light.

5. CONCLUSIONS

We have described fabrication process and lasing characteristics of prototype MOCVD-grown GaAs/AlGaAs/AlAs DFB-RPG VCSELs. The new structure eliminates the need for end reflectors in earlier resonant-periodic-gain lasers, thereby reducing considerably the total thickness of the device. A hybrid version of DFB-RPG device, with a passive Bragg reflector on the substrate side, is particularly attractive for electrical pumping.

6. ACKNOWLEDGMENTS

Support of the U.S. Air Force Office of Scientific Research, the Air Force Phillips Laboratory, and the Defense Advanced Research Projects Agency is gratefully acknowledged. The authors wish to express their gratitude to Drs. Anadi Mukherjee and Steven Brueck for valuable discussions and advice during the course of experiments, to Mr. Saket Chadda and Dr. Abhaya Datye for performing the TEM measurements, and to Mr. Andrew Frauenglass and Miss Xiaoxin D. Kuai for their technical assistance.

7. REFERENCES

[Armour 1992] E. A. Armour, S.-Z. Sun, D. P. Kopchik, K. Zheng, P. Zhou, J. Cheng, and C. F. Schaus, "Application of Metal-Organic Chemical Vapor Deposition to Vertical-Cavity Surface-Emitting Lasers", *SPIE Proc. Vol. 1634 - Laser Diode Technology and Applications IV* (D. Renner, Ed.), SPIE Laser & Sensor Engineering Symp., OE/LASE'92, Los Angeles, CA, Jan. 19-24, 1992, this volume.

[Brueck 1989] S. R. J. Brueck, M. Y. A. Raja, M. Osiński, C. F. Schaus, M. Mahbobzadeh, J. G. McInerney, and K. J. Dahlhauser, "Optical Cavity Design for Wavelength-Resonant Surface-Emitting Semiconductor Lasers (Invited Paper)", *SPIE Proc. Vol. 1043 - Laser Diode Technology and Applications* (L. Figueroa, Ed.), SPIE Symp. on Lasers & Optics, OE/LASE'89, Los Angeles, CA, Jan. 18-20, 1989, pp. 111-122.

[Corzine 1989] S. W. Corzine, R. S. Geels, J. W. Scott, R.-H. Yan, and L. A. Coldren, "Design of Fabry-Perot Surface-Emitting Lasers with a Periodic Gain Structure", *IEEE J. Quantum Electron.*, vol. 25, pp. 1513-1524, June 1989.

[Geels 1988] R. S. Geels, R. H. Yan, J. W. Scott, S. W. Corzine, R. J. Simes, and L. A. Coldren, "Analysis and Design of a Novel Parallel-Driven MQW-DBR Surface-Emitting Diode Laser", *CLEO '88 Conf. Lasers & Electro-Optics, Techn. Digest Series Vol. 7*, Anaheim, CA, April 25-29, 1988, Paper WM1, pp. 206-207.

[Gourley 1989a] P. L. Gourley, T. M. Brennan, B. E. Hammons, S. W. Corzine, R. S. Geels, R. H. Yan, J. W. Scott, and L. A. Coldren, "High-Efficiency TEM_{00} Continuous-Wave (Al,Ga)As Epitaxial Surface-Emitting Lasers and Effect of Half-Wave Periodic Gain", *Appl. Phys. Lett.*, vol. 54, pp. 1209-1211, 27 March 1989.

[Gourley 1989b] P. L. Gourley, S. K. Lyo, and L. R. Dawson, "High-Efficiency, Continuous-Wave, Epitaxial Surface-Emitting Laser with Pseudomorphic InGaAs Quantum Wells", *Appl. Phys. Lett.*, vol. 54, pp. 1397-1399, 10 April 1989.

[Iga 1988] K. Iga, F. Koyama, and S. Kinoshita, "Surface Emitting Semiconductor Lasers", *IEEE J. Quantum Electron.*, vol. 24, pp. 1845-1855, Sept. 1988, and the references quoted therein.

[Jewell 1989] J. L. Jewell, K. F. Huang, K. Tai, Y. H. Lee, R. J. Fischer, S. L. McCall, and A. Y. Cho, "Vertical Cavity Single Quantum Well Laser", *Appl. Phys. Lett.*, vol. 55, pp. 424-427, 31 July 1989.

[Jewell 1990] J. L. Jewell, Y. H. Lee, A. Scherer, S. L. McCall, N. A. Olsson, J. P. Harbison, and L. T. Florez, "Surface-Emitting Microlasers for Photonic Switching and Interchip Connections", *Opt. Eng.*, vol. 29, pp. 210-214, March 1990.

[Mahbobzadeh 1990] M. Mahbobzadeh and M. Osiński, "Novel Distributed-Feedback Resonant-Periodic-Gain Structure for Vertical-Cavity Surface-Emitting Semiconductor Lasers", *Electron. Lett.*, vol. 26, pp. 1716-1718, 27 Sept. 1990.

[Mahbobzadeh 1991] M. Mahbobzadeh and M. Osiński, "Novel Distributed-Feedback Structure for Surface-Emitting Semiconductor Lasers", *SPIE Proc. Vol. 1418 - Laser Diode Technology and Applications III* (D. Renner, Ed.), SPIE Symp. on High Power Lasers, OE/LASE'91, Los Angeles, CA, Jan. 20-25, 1991, pp. 25-31.

[McDaniel 1990] D. L. McDaniel, Jr., J. G. McInerney, M. Y. A. Raja, C. F. Schaus, and S. R. J. Brueck, "Vertical Cavity Surface-Emitting Semiconductor Laser with Injection Laser Pumping", *SPIE Proc. Vol. 1219 - Laser-Diode Technology and Applications II* (D. Botez and L. Figueroa, Eds.), OE/LASE'90, Los Angeles, CA, Jan. 16-19, 1990, pp. 284-291.

[Raja 1988] M. Y. A. Raja, S. R. J. Brueck, M. Osiński, C. F. Schaus, J. G. McInerney, T. M. Brennan, and B. E. Hammons, "Novel Wavelength-Resonant Optoelectronic Structure and Its Application to Surface-Emitting Semiconductor Lasers", *Electron. Lett.*, vol. 24, pp. 1140-1142, 1 Sept. 1988.

[Raja 1989] M. Y. A. Raja, S. R. J. Brueck, M. Osiński, C. F. Schaus, J. G. McInerney, T. M. Brennan, and B. E. Hammons, "Resonant Periodic Gain Surface-Emitting Semiconductor Lasers", *IEEE J. Quantum Electron.*, vol. 25, pp. 1500-1512, June 1989.

[Schaus 1989a] C. F. Schaus, H. E. Schaus, S. Sun, M. Y. A. Raja, and S. R. J. Brueck, "MOCVD Growth of GaAs/AlGaAs Wavelength Resonant Periodic Gain Vertical Cavity Surface-Emitting Laser", *Electron. Lett.*, vol. 25, pp. 538-539, 13 April 1989.

[Schaus 1989b] C. F. Schaus, M. Y. A. Raja, J. G. McInerney, H. E. Schaus, S. Sun, M. Mahbobzadeh, and S. R. J. Brueck, "High-Efficiency CW Operation of MOCVD-Grown GaAs/AlGaAs Vertical-Cavity Lasers with Resonant Periodic Gain ", *Electron. Lett.*, vol. 25, pp. 637-638, 11 May 1989.

[Schaus 1989c] H. E. Schaus, C. F. Schaus, S. Sun, M. Y. A. Raja, A. Jacome-Torres, and J. G. McInerney, "Growth of High-Efficiency Resonant Periodic Gain Vertical Cavity Surface-Emitting Lasers", *Gallium Arsenide and Related Compounds 1989, Proc. 16th Int. Symp. on Gallium Arsenide & Related Compounds*, Karuizawa, Japan, 1989, Inst. Phys. Conf. Ser. Number 106, pp. 749-754, Institute of Physics, Bristol 1990.

[Schaus 1991] C. F. Schaus, A. J. Torres, J. Cheng, S. Sun, C. Hains, K. J. Malloy, H. E. Schaus, E. A. Armour, and K. Zheng, "Transverse Junction Vertical-Cavity Surface-Emitting Laser", *Appl. Phys. Lett.*, vol. 58, pp. 1736-1738, 22 April 1991.

[Weber 1990] J.-P. Weber, "Propagation of Light in Periodic Structures: Application to Surface-Emitting Laser Diode", Ph.D. Dissertation, Univ. of California at Berkeley, June 1990, Appendix A, pp. 227-246.

Submission to CLEO '92

Classification: Applications of Nonlinear Optics and Laser Spectroscopy

(Nonlinear Dynamics in Devices: Solitons, Instabilities and Chaos)

NONLINEAR DYNAMICS OF DOUBLE EXTERNAL CAVITY SEMICONDUCTOR LASERS

John G. McInerney*, Jong-Dae Park[+] Dong-Sun Seo[#], Hua Li and Jun Ye

Optoelectronic Device Physics Group

Center for High Technology Materials

University of New Mexico

Albuquerque, NM 87131-6081

* Corresponding Author: Professor John G. McInerney. Tel. (505) 277-0768, Fax (505) 277-6433.

+ Present address: Department of Physics, Pai Chai University, Taejon, Korea.

Present address: Department of Electronic Engineering, Yon Sei University, Seoul, Korea.

ABSTRACT

Under certain well-defined conditions, semiconductor lasers subject to two independent sources of coherent feedback can exhibit self-pulsing instabilities, leading to chaos via period-doubling or quasiperiodicity. Experimental data and calculations are presented.

NONLINEAR DYNAMICS OF DOUBLE external cavity semiconductor lasers

John G. McInerney, Jong-Dae Park Dong-Sun Seo Hua Li and Jun Ye

Optoelectronic Device Physics Group
Center for High Technology Materials
University of New Mexico
Albuquerque, NM 87131-6081

SUMMARY

Semiconductor injection lasers are frequently operated in external cavities for spectral narrowing and mode stabilization, although the result can also be self-pulsations and chaos. External cavity lasers are also alignment-sensitive and are generally troublesome. Why then would anyone want to study double external cavity lasers?

Firstly, suppose one requires a single longitudinal and transverse mode with a narrow linewidth. Single-mirror external cavities can select a single longitudinal mode (cavity length L_{ext} < laser diode optical length L_d) or narrow the modal linewidth ($L_{ext} >> L_d$), but not both. Grating external cavities can select and narrow a single mode, but at a much lower level of feedback, severely restricting the available power ($\sim$1 mW). A combination of two external cavities [1] - one short plus one long, or two short cavities with a small length offset (a vernier combination) - can provide effective mode selection and linewidth narrowing even in medium-to-high power semiconductor lasers, while intracavity etalons or external high-finesse resonators are also effective in this regard [2]. However, in each case there are multiple sources of feedback which must be taken into account to determine the laser modes and dynamical properties.

Secondly, there are many situations in which conventional (single-mirror) external cavities are subjected to one or more sources of additional (often inadvertent) feedback - in OEICs, optical storage and inspection, fiber communication systems, for example - and again these must be included in systems design.

Finally, there are many fundamental issues to be examined - mode mixing, frustrated instabilities and the interplay between cooperative and competitive dynamics - which can be studied in a particularly convenient and flexible manner using double external cavities.

In this paper we describe experimental and theoretical studies of the static and dynamic properties of double external cavity semiconductor lasers. Our experiments have used GaAs/GaAlAs index-guided lasers (Hitachi HLP-1400) coupled to two long (10-60 cm) linear external cavities, without frequency-selective elements such as gratings or etalons. Our theory rests on rate equations for the carrier density, electric field amplitude and phase, including two coherent optical feedback terms. These are solved for the steady-state modes, then a linear stability analysis is performed to study the self-pulsations observed experimentally. Finally, the rate equations are integrated numerically with optional Langevin noise terms.

When the ratio of the cavity lengths is 2:1, the observed behavior is very similar to that of the single external cavity laser with off-axis tilt asymmetry [3,4], showing coherence collapse at low levels of feedback ($\sim 10^{-4}$ in intensity) and spectral mode splitting and slow self-pulsations due to mode mixing at high feedback ($\sim 10^{-1}$). These self-pulsations initiate period-doubling or quasiperiodic routes to chaos, and these effects are exacerbated by weak modulation close to the self-pulsing frequency. The existence of chaotic attractors has been confirmed by calculating correlation dimensions and bifurcation diagrams for the double external cavity laser.

References

[1] G. Wenke, R. Gross, P. Meissner and E. Patzak, *J. Lightwave Technol.* LT-5, 608 (1987).

[2] H. Li and H. R. Telle, *IEEE J. Quantum Electron.* 25, 257 (1989).

[3] J. D. Park, D. S. Seo and J. G. McInerney, *IEEE J. Quantum Electron.* 26, 1353 (1990).

[4] D. S. Seo, J. D. Park, J. G. McInerney and M. Osinski, *IEEE J. Quantum Electron.* 25, 2229 (1989).

A Simple High-Speed Si Schottky Photodiode

B. W. Mullins, S. F. Soares, K. A. McArdle, C. M. Wilson, and S. R. J. Brueck

Abstract—Design, fabrication, and UV-heterodyne characterization of Ni-Si-Ni metal-semiconductor-metal Schottky barrier photodetectors is reported. Planar detectors were fabricated, with a simple 3-level lithography process on bulk Si, in both simple-gap and interdigitated geometries with gap dimensions from 1 to 5 μm. Frequency response of these devices was characterized using a CW-laser heterodyne system at 334.5 nm. For a 4.5-μm interdigitated device, a 3-dB response of 16 GHz is measured, giving 22 GHz when deconvolved from the package/connector. A detailed theoretical model of the photodiode response incorporating effects of carrier transport and device geometry is in excellent agreement with the measurement. This model predicts an 86-GHz 3-dB response for the 1-μm gap geometry devices.

Introduction

THERE has been extensive research on high-speed low-noise photodetectors in the 0.8–1.5 μm wavelength range for use in optical communication systems. Four general device designs, p-i-n [1], [2], vertical Schottky barrier [3], planar Schottky barrier [4]–[7], and avalanche photodiode [8], have been developed. Device materials include Si [5], [9], InGaAs [8], and strained-layer superlattices [10]. In the near infrared region, very fast, highly responsive detectors have been fabricated. Frequency responses up to 67 GHz and quantum efficiencies of 80% have been reported for p-i-n devices [2]. The fastest Schottky-barrier devices reported have a 110-GHz frequency response [4].

In contrast, relatively little work has been reported on ultraviolet detectors. As ultrafast UV sources become available, there is increasing interest in high-speed detectors for monitoring photochemical and other high-speed phenomena.

The most salient materials characteristic at UV wavelengths that determines detector design is the very high absorption coefficient of $\sim 10^6$ cm^{-1} for almost all semiconductors. This dictates a design with very shallow junctions in traditional vertical geometries and favors the planar structure.

Manuscript received October 31, 1990; revised January 15, 1991. This work was supported in part by the Naval Research Laboratory.

B. W. Mullins was with the Center for High Technology Materials and the Department of Physics and Astronomy, University of New Mexico, Albuquerque, NM. He is now with Phillips Laboratory, Kirtland Air Force Base, Albuquerque, NM 87117.

S. F. Soares is with the Center for High Technology Materials and the Department of Electrical and Computer Engineering, University of New Mexico, Albuquerque, NM 87131.

K. A. McArdle and C. M. Wilson are with the Center for High Technology Materials and the Department of Physics and Astronomy, University of New Mexico, Albuquerque, NM 87131.

S. R. J. Brueck is with the Center for High Technology Materials, the Department of Physics and Astronomy, and the Department of Electrical and Computer Engineering, University of New Mexico, Albuquerque, NM 87131.

IEEE Log Number 9144500.

High-speed UV detectors have been reported using vertical Schottky barrier [11], planar interdigitated Schottky barrier [9], Si p-n junction, and vertical p-i-n with a thin p-layer [12], with only moderate success. A promising design used a planar interdigitated Schottky barrier with a low-frequency quantum efficiency of 12% at 337 nm and a frequency response of 5.3 GHz, measured at 800 nm [9]. No picosecond impulse, autocorrelation, or heterodyne response measurements at UV wavelengths have been reported.

We report on fabrication and UV-heterodyne characterization of high-speed planar Ni-Si-Ni Schottky barrier photodetectors. For a 4.5-μm gap geometry, a 16-GHz 3-dB heterodyne response limited by packaging effects, is measured at a wavelength of 334 nm. This is the highest reported speed for an Si-based detector. A photodiode transport model, including carrier drift, diffusion, and recombination, is in good agreement with the measured detector frequency response. This model gives a 24-GHz 3-dB point for the present detector exclusive of packaging limitations. For a 1-μm gap geometry, the model predicts an 86-GHz 3-dB response for these simple Si detectors.

The detector consists of a side-by-side pair of metal-semiconductor junctions comprising a metal-semiconductor-metal (MSM) diode. The exposed semiconductor, between the metal pads, is fully depleted with an appropriate applied bias. This depleted region is the photosensitive region of the diode, and high applied fields result in very fast, saturated drift velocities of the charge carriers. It is important to appreciate that both electron and hole velocities are equally important in this configuration. In this regime, Si offers performance comparable to GaAs and InP, in contrast to the situation in which only electron velocities and mobilities are important. The direct access to the depletion region by UV photons avoids the short absorption length problem inherent in other designs.

A common phenomenon, reported for all MSM devices, is a spurious gain mechanism leading to an anomalous effective quantum efficiency, >100%, at low frequencies [9], [13]. Tentative explanations have been put forth [14], but no definitive models have been presented. This phenomenon is also seen in the devices tested in this study. Our results indicate that this gain is most likely photoconductive resulting from junction leakage; a more detailed analysis will be published elsewhere.

Fabrication of Ni-Si-Ni MSM Schottky Barrier Photodiodes

MSM photodiodes were fabricated with Ni Schottky contacts on bulk Si ($n \sim 8 \times 10^{14}$ cm^{-3}). A planar, lateral geometry with both contacts on the top surface of the Si was

1041-1135/91/0400-0360$01.00 ©1991 IEEE

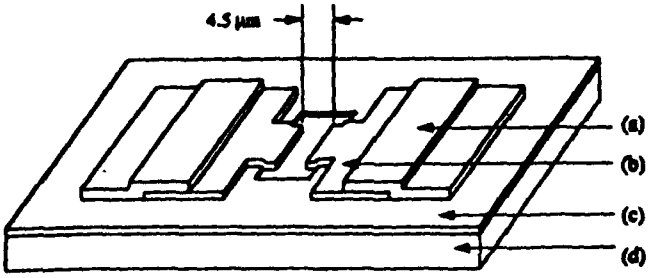

Fig. 1. MSM detector structure. Bonding pad: 75 × 75 μm^2. Window: 25 × 20 μm^2. (a) Cr/Au (200 nm). (b) Ni (30 nm). (c) SiO_2 (80 nm). (d) Si (bulk).

used; both simple-gap and interdigitated, or serpentine-gap, devices were fabricated with gap widths varying from 1 to 4.5 μm. A representative structure is shown in Fig. 1. The first layer is an 80-nm-thick SiO_2 film. Windows, ranging from 100 to 500 μm^2, expose the semiconductor surface where the Schottky contacts are formed. The oxide serves to isolate optically inactive metallization areas and reduce junction capacitance and dark current. The second layer is a 30-nm-thick Ni film with a series resistance of 50–60 Ω and a transmission of 17% at 334.5 nm. The Ni–Si contacts form the MSM photodiode. The photosensitive semiconductor region between the contacts varies in area from 15 to 90 μm^2 in the simple-gap geometry. The final layer is a 30/170 nm Cr/Au film to form the 75 × 75 μm^2 bonding pads.

Photodiodes were fabricated using conventional photolithography, including standard liftoff techniques for metal definition. Si wafers were cleaned and inserted into a preheated furnace (1100°C), with an O_2 flow of 4 l/min, for 25 min, to grow the 80-nm oxide. The windows in the oxide film were etched, and the metal films deposited in three photolithographic steps. Metal films were deposited in an electron-beam evaporator at a rate of 0.5 nm/s.

After fabrication, wafers were cleaved to separate dies incorporating detectors with variations in geometry and dimensions. An individual die was mounted at the edge of an Au-on-alumina microstrip high-speed package using heat-conductive epoxy. The package was mounted on an Au-coated Al block and an SMA connector (18-GHz bandwidth) was pressure fitted to the strip. Gold wires (25-μm diameter) were wire bonded between the photodiode, the package, and ground. Care was taken to ensure short bond wires so that packaging inductance did not affect the measurements. Dark currents, in this nonoptimized design, were <50 nA for a 25-μm-long device at a 10-V bias. For broad-band photodiode applications, the noise associated with this low dark current is negligible in comparison to RF-amplifier input noise.

Experimental Arrangement

A UV-heterodyne system was developed to characterize these detectors [15]. A single-mode Ar^+-ion laser, λ = 334.5 nm, and an intracavity doubled ($LiIO_3$), frequency stabilized dye laser provided the local oscillator and signal beams, respectively. Careful attention was placed on beam and polarization overlap. A typical local-oscillator intensity of 10^7 W/cm^2 (~2-μm FWHM) at the detector was necessary to reach shot-noise-limited detection. The gain of the RF-amplifiers and cabling from the SMA connector to the RF-spectrum analyzer was calibrated from 1 MHz to 18 GHz using a vector network analyzer. Absolute responsivity $R(\omega)$ was confirmed by comparison to the measured dc responsivity of a well-characterized low-frequency commercial detector.

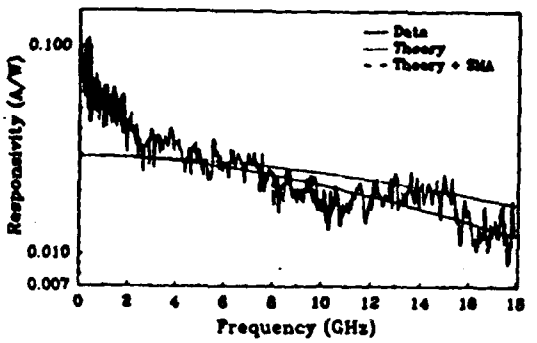

Fig. 2. Frequency response of a 4.5-μm gap interdigitated detector at 30 V bias.

Results

Measurements of $R(\omega)$ were made on several different detectors under a variety of conditions. The bulk of these measurements were used to validate an MSM detector response model that predicts high-speed detector performance as a function of bias and beam diameter and position on the detector, using Si carrier transport properties [15]. The model includes effects of carrier drift, diffusion, and recombination. A more detailed description will be published elsewhere. The model was compared to the measured frequency response for gap dimensions of 4.5, 3, and 1 μm with differing biases and beam positions.

$R(\omega)$ curves are shown for a 4.5-μm gap interdigitated detector at 30- and 10-V bias. (Figs. 2 and 3) Heterodyne signal levels were greater than 20 dB above the shot-noise floor across the entire frequency range; the ~ ±1 dB variations are due to package and electronics resonances as can be seen by noting the pattern similarity in the two figures. The 2-μm FWHM beam was centered in the detector gap, and $R(\omega)$ was measured out to 18 GHz. The 30-V data (Fig. 2) have been extended to show the low-frequency gain region, inherent in all MSM photodiodes. Two theoretical plots are shown. The upper curve in both graphs is the detector model which is in good agreement with the data out to about 14 GHz. At these frequencies, the bandwidth limitations of the SMA connector on the detector package become important. The SMA connector–detector package can be modeled as the product of a simple single pole, with a characteristic frequency of 18 GHz, due to the SMA connector, and the detector response. This leads to the lower modeling curve. An excellent fit is obtained out to the experimental frequency limit of 18 GHz, constrained by available amplifiers. The effect of the SMA connector can be seen on both the 30- and 10-V data. The variation in the frequency response for these two cases arises because of the (slight) change in carrier velocities at the two applied field strengths in this saturated regime. The only adjustable parameter is the overall quantum efficiency.

An extrapolation of the detector bandwidth can be made

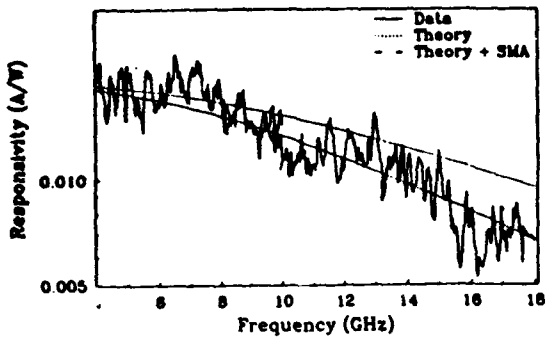

Fig. 3. Frequency response of a 4.5-μm gap interdigitated detector at 10 V bias.

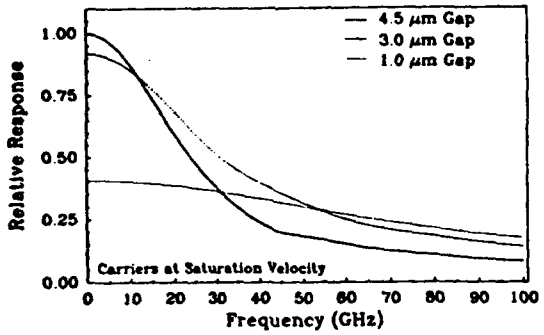

Fig. 4. Theoretical frequency response curves for varying gap dimensions. The calculation was carried out for a fixed 2-μm illumination spot and a fixed bias of 10^5 V/cm. The reduced responsivity for the smaller detectors is simply a geometrical effect due to the reduced overlap between the beam and the active detector area.

from the model, assuming an ideal RF package. At 30-V bias, the bandwidth of this 4.5-μm gap detector is 21.5 GHz. Increasing the bias will result in slightly higher carrier velocities and should give a 24-GHz bandwidth for a 4.5-μm gap Si-based detector. Scaling the response to smaller detector gap widths of 3 and 1 μm, the model predicts bandwidths of 34 and 86 GHz, respectively (cf. Fig. 4). The lower responsivity shown for the smaller detectors is simply a geometrical effect as the calculation is carried out for a fixed incident spot size. This high-speed response is comparable to the fastest reported GaAs detectors. The high-frequency ultraviolet responsivity of these detectors, 0.032 A/W (~12% quantum efficiency) with no antireflective coating, is very high for detectors with these large bandwidths. The quantum efficiency of the smaller gap detectors scales only with the gap dimension/spot size ratio. Thus, if the incident spot is smaller than the gap dimension, then the quantum efficiency remains nearly constant. Smaller detectors and tighter focusing will lead to a significantly improved quantum-efficiency bandwidth product.

Conclusion

A high-speed MSM photodiode, based on bulk Si and fabricated by a simple, inexpensive process, has been demonstrated. The bandwidths of these devices compare well to the fastest reported GaAs devices. A major advantage of this device for UV applications is the relative robustness of Si compared to GaAs when subjected to intense ultraviolet radiation. GaAs devices were also fabricated; however, they showed severe degradation, on a time scale of minutes, when subject to the intense local oscillator irradiation. This degradation was irreversible and severely limits the applicability of the unpassivated GaAs devices for ultraviolet applications. In contrast, the Ni-Si devices were extremely robust with no changes in speed or responsivity observed over time scales of several months—both for devices stored in laboratory ambient and devices subjected to many hours of high-intensity UV irradiation.

The simplicity, manufacturability, interconnection compatibility, and robustness of the planar-Si MSM photodiode make it a strong candidate for applications where the ultimate connection is to a silicon VLSI circuit. The high-speed high-responsivity detector presented here is an ideal candidate for many applications due to its materials compatibility with standard Si technology and the absence of complex and expensive epitaxial growths.

Acknowledgment

Helpful discussions with D. L. Spears and V. Diadiuk are gratefully acknowledged. C. F. Schaus provided extensive guidance in device design.

References

[1] W. Lenth, A. Chu, L. J. Mahoney, R. W. McClelland, R. W. Mountain, and D. J. Silversmith, "Planar GaAs p-i-n photodiode with picosecond time response," *Appl. Phys. Lett.*, vol. 46, pp. 191-193, 1985.

[2] R. S. Tucker, A. J. Taylor, C. A. Burrus, G. Eisenstein, and J. M. Wiesenfeld, "Coaxially mounted 67 GHz bandwidth InGaAs PIN photodiode," *Electron. Lett.*, vol. 22, pp. 917-918, 1986.

[3] S. Y. Wang and D. M. Bloom, "100-GHz bandwidth planar GaAs Schottky photodiode," *Electron. Lett.*, vol. 19, pp. 554-555, 1983.

[4] D. G. Parker, P. G. Say, A. M. Hansom, and W. Sibbett, "110 GHz high-efficiency photodiodes fabricated from indium tin oxide/GaAs," *Electron. Lett.*, vol. 23, pp. 527-528, 1987.

[5] T. Sugeta, T. Urisu, S. Sakata, and Y. Mizushima, "Metal-semiconductor-metal photodetector for high-speed optoelectronic circuits," *Japan. J. Appl. Phys.*, vol. 19, supp. 19-1, 1980.

[6] B. J. Van Zeghbroeck, C. Harder, J.-M. Halbout, H. Jakel, H. Meier, W. Patrick, P. Vettiger, and P. Wolf, "5.2 GHz monolithic GaAs optoelectronic receiver," in *Tech. Dig.*, IEEE IEDM, 1987, pp. 229-232.

[7] O. Wada, H. Hamaguchi, L. LaBella, and C. Y. Boisrobert, "Noise characteristics of GaAs metal-semiconductor-metal photodiodes," *Electron. Lett.*, vol. 24, p. 1574, 1988.

[8] J. C. Campbell, W. S. Holden, G. J. Qua, and A. G. Dentai, "Frequency response of InP/InGaAsP/InGaAs avalanche photodiodes with separate absorption, grading and multiplication regions," *IEEE J. Quantum Electron.*, vol. QE-21, pp. 1743-1746, 1985.

[9] R. J. Seymour and B. K. Garside, "Ultrafast silicon interdigital photodiodes for ultraviolet applications," *Can. J. Phys.*, vol. 63, pp. 707-711, 1985.

[10] G. E. Bulman, D. R. Myers, T. E. Zipperian, and L. R. Dawson, "Proton isolated $In_{0.2}Ga_{0.8}As/GaAs$ *strained-layer superlattice* avalanche photodiode," *Appl. Phys. Lett.*, vol. 48, pp. 1015-1017, 1986.

[11] H. Fabricius, T. Skettrup, and P. Bisgaard, "Ultraviolet detectors in thin sputtered ZnO films," *Appl. Opt.*, vol. 25, pp. 2764-2767, 1986.

[12] C.-Y. Wingo, C. Salupo, L. F. Szabo, G. P. Ceasar, and W. Javurek, "A new type of stable and sensitive UV detector fabricated with amorphous silicon-based alloys," presented at the MRS Spring Meet., 1988.

[13] D. K. Donald, S. Y. Wang, T. R. Ranganath, S. A. Newton, and W. R. Trutna, "Photocurrent amplification in Schottky photodiodes," *Appl. Phys. Lett.*, vol. 49, pp. 567-568, 1986.

[14] M. Ito and O. Wada, "Low dark current GaAs metal-semiconductor-metal (MSM) photodiodes using WSi_x contacts," *IEEE J. Quantum. Electron.*, vol. QE-22, pp. 1073-1077, 1986.

[15] B. W. Mullins, "Heterodyne characterization of high speed photomixers for the ultraviolet," Ph.D. dissertation, Dep. Phys., Univ. New Mexico, 1989 (unpublished).

Large second-order nonlinearity in poled fused silica

R. A. Myers, N. Mukherjee, and S. R. J. Brueck

Center for High Technology Materials, University of New Mexico, Albuquerque, New Mexico 87131

Received July 15, 1991

A large second-order nonlinearity [$\chi^{(2)} \sim 1$ pm/V $\sim 0.2\ \chi^{(2)}_{33}$ for $LiNbO_3$] is induced in the near-surface (~4 μm) region of commercial fused-silica optical flats by a temperature (250–325°C) and electric-field ($E \sim 5 \times 10^4$ V/cm) poling process. Once formed, the nonlinearity, which is roughly 10^2–10^4 times larger than that found in fiber second-harmonic experiments, is extremely stable at room temperature and laboratory ambient. The nonlinearity can be cycled by repeated depoling (temperature only) and repoling (temperature and electric field) processes without history effects. Possible mechanisms, including nonlinear moieties and electric-field-induced second-order nonlinearities, are discussed.

Fused silica is ubiquitous in modern technology. Its extremely low linear optical losses have enabled the growth of the fiber-optics industry. SiO_2 also plays a dominant role in microelectronics technology, in which the unique properties of the Si–SiO_2 interface are largely responsible for the behavior of metal–oxide semiconductor devices underlying advances in computer hardware.

Unlike its related quartz crystalline phase, fused silica is amorphous with a macroscopic inversion symmetry that forbids second-order nonlinear processes. Thus the discovery by Österberg and Margulis[1] of efficient second-harmonic generation (SHG) in a variety of Si–Ge glass fibers on training with optical fields has generated considerable interest in the physics and applications of this unexpected phenomenon. Stolen and Tom[2] proposed a mechanism based on electric-field-induced nonlinearities in which the field arises from a third-order optical rectification process. Bergot *et al.*[3] have observed an enhancement of the nonlinearity with the application of a transverse electric field. Recently Anderson *et al.*[4] proposed a photovoltaic effect based on interference between the fundamental and harmonic fields that phenomenologically accounts for the observed strength of this field.[5] This field interacts with the material third-order nonlinearity $\chi^{(3)}$ to provide an effective $\chi^{(2)} = \chi^{(3)}E_{dc}$. Similar field-induced nonlinearities have been observed in a variety of material systems, e.g., paraelectric lead–lanthanum zirconate–titanate.[6]

In this Letter we report what is to our knowledge the first observation of a permanent second-order nonlinearity in the near-surface region of bulk fused SiO_2 induced by a temperature/static electric-field poling process. The induced $\chi^{(2)}$'s achieved are 3 to 4 orders of magnitude larger than those found in the fiber experiments and approach that of traditional nonlinear-optical materials such as $LiNbO_3$.

The preparation process for generating the $\chi^{(2)}$ nonlinearity in a sample involves heating it to 250–325°C in a laboratory ambient while applying a dc bias of 3–5 kV across the nominally 1.6-mm-thick samples. After ~15 min of poling the heater is turned off and the sample is cooled to room temperature. Once cooled, the electric field is removed, and a stable $\chi^{(2)}$ nonlinearity is observed. For most experiments, electrodes (stainless steel and Si) were simply physically contacted to the sample. Samples have been maintained at room temperature without special precautions for several months without any noticeable degradation of the nonlinearity. Application of heat alone, above ~ 250°C, removes the nonlinearity. The necessary voltage did not scale with the sample thickness. Attempts to pole commerical fused-silica coverslips (180 μm thick) with a linearly scaled voltage were unsuccessful. However, large nonlinearities were observed when these same samples were placed atop a 1.6-mm-thick sample and the larger voltage was applied across both samples.

The SHG signal from these poled samples was obtained with 10-ns pulses at 1.06 μm from a 1-mm-diameter Q-switched Nd:YAG laser beam operating at 10 Hz at an intensity of 10 MW/cm². The SHG signals were recorded with a photomultiplier tube (maximum signal-to-noise ratio ~500:1).

The second-harmonic polarization induced normal to the surface along the poling field (the z direction) is given by

$$\mathcal{P}_z^{2\omega} = 2\epsilon_0[\chi^{(2)}_{31}(E_x^2 + E_y^2) + \chi^{(2)}_{33}E_z^2]. \quad (1)$$

If we measure the relative contributions of the vertical and the horizontal input polarizations to the SHG signal, the ratio of $\chi^{(2)}_{33}$ to $\chi^{(2)}_{31}$ is determined to be 7:1. A model of the angular dependence of the SHG power, including angular-dependent Fresnel reflectivity coefficients, shows that the signal should maximize at an incident angle of approximately 60°. Indeed a large harmonic signal was measured at a 60° angle of incidence as shown in Fig. 1. The ratio $\chi^{(2)}_{33}/\chi^{(2)}_{31}$ that best fits this angular SHG scan is ~2:1. This disagreement with the ratio obtained from the relative power measurements has not been resolved.

Scanning the laser spot transversely yields a smooth nonlinearity profile over the area covered by the 1-cm² electrode used for poling. No observable

0146-9592/91/221732-03$5.00/0 © 1991 Optical Society of America

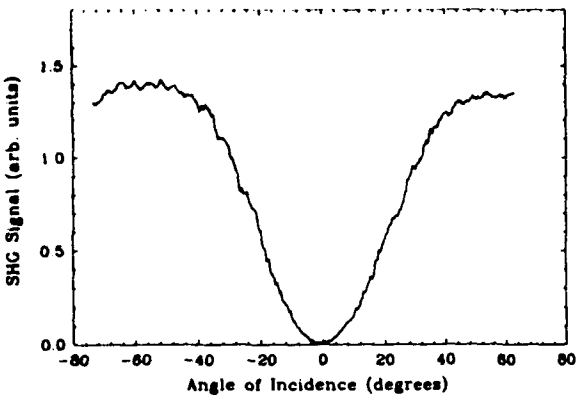

Fig. 1. SHG signal from a poled Optosil sample versus the angle of incidence for a TM-polarized fundamental beam at 1.06 μm.

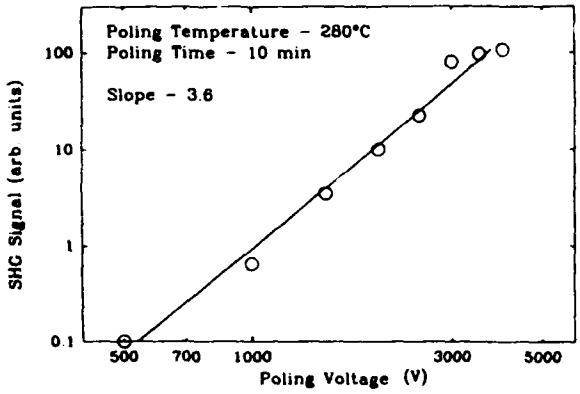

Fig. 2. SHG signal versus the poling voltage for a fixed temperature and poling time. The signal was obtained on a single sample with successive polings at higher poling voltages.

SHG signal was obtained for poling temperatures below 210°C. The SHG signal increased as a ~3.5 power law with the applied voltage as shown in Fig. 2. The nonlinearity could be recycled through a number of depoling (by application of heat alone) and repoling cycles (by application of heat and electric field) without degradation of the signal. Irradiation at a peak power level of 100 mW/cm^2 at 257 nm using a frequency-doubled Ar-ion laser for over an hour did not affect the nonlinearity. This is in contrast to the fiber results, where UV irradiation does erase the nonlinearity.[7]

No fringes were observed as the angle of incidence was varied at fundamental wavelengths of 1.06 μm, 740 nm, and 533 nm. This indicates that the nonlinear layer thickness is less than or comparable with the coherence length, which is 3 μm at 533 nm.[8] The absence of Maker fringes also indicates that the nonlinearity is generated only on one side of the sample. Interference fringes were observed from two adjacent samples, and, from the periodicity of those fringes, it was possible to determine that the nonlinearity was always on the side of the sample that had been positively biased during poling. The nonlinearity moved from one side to the other for repoling with reversed polarity.

The depth profile of the nonlinearity was determined by differential chemical etching using a 49% HF acid solution. Figure 3 shows the variation of the SHG as a function of the layer depth for samples poled for a duration of 15 min and for a duration of 2 h. Etch depths were determined by surface profilometer scans at each etch step. There was significant roughening of the sample surface by the etching. An index-matching fluid was used to ensure an optically smooth surface for comparability of the results. While the initial SHG signal measured using 1.06-μm pulses was approximately the same for both samples, the increase of the layer thickness on longer poling time is significant. For the nominal 15-min poling used in most of the experiments reported here, the characteristic length was ≤ 4 μm.

The $\chi^{(2)}$ coefficient was measured by comparing the SHG power generated in crystal quartz (1 mm thick) with that in $LiNbO_3$ (76 μm thick) reference samples at four different wavelengths. The maximum SHG signal, generated over a full coherence length, is given by $P^{2\omega} \propto 4|\mathcal{P}|^2 \cos^2 \theta L_c^2/\pi^2$, where L_c $(=\pi/\Delta k)$ is the coherence length for the SHG at the corresponding wavelength. For an exponentially decaying nonlinearity, as found for the poled fused-silica samples in the etching experiment, the SHG power is

$$P^{2\omega}(L) \propto |\mathcal{P}(0)|^2 \times \left[\frac{\exp(-2\alpha L) + 1 - 2\exp(-2\alpha L)\cos \Delta k L}{\Delta k^2 + \alpha^2}\right], \quad (2)$$

where α^{-1} is the characteristic length of the nonlinearity. In the limit of $L \to \infty$ the SHG power $P^{2\omega}$ becomes proportional to $P^{2\omega} \to |\mathcal{P}(0)|^2[1/(\Delta k^2 + \alpha^2)]$. Using the available indices of refraction,[6] we calculated the coherence lengths of quartz, $LiNbO_3$, and fused silica. From the observed etching rate we measured the inverse characteristic length α of 0.25 μm^{-1}. An average value of approximately 1×10^{-12} m/V for $\chi_{33}^{(2)}$, the largest $\chi^{(2)}$ coefficient of the poled fused silica, was obtained. The value of $\chi_{33}^{(2)}$ showed no dispersion over the three wavelengths used. The measured $\chi_{33}^{(2)}$ value of fused silica is almost 20% of the $\chi_{22}^{(2)}$ value of $LiNbO_3$.

We used several commercial grades of amorphous silica, including Optosil, Homosil, Infrasil, and

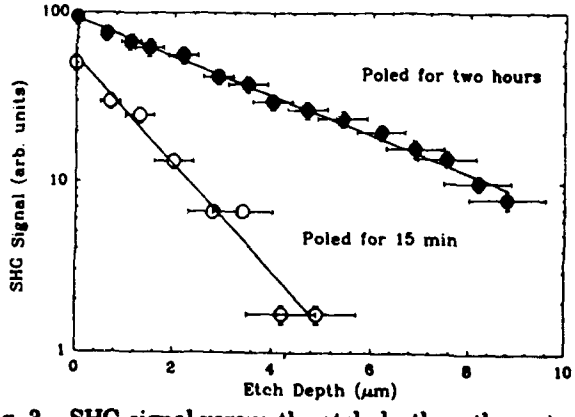

Fig. 3. SHG signal versus the etch depth as the material is successively etched away for two samples with identical poling voltages (5 kV) and temperatures (280°C) but different poling times.

Suprasil. The strength of the SHG signal was approximately the same for all samples (within a factor-of-2 variation) except for Suprasil, which showed a signal only ~10% as large. Suprasil, manufactured by a synthetic process, has a level of metal impurities only 10% that of the other grades.[9]

This large difference in SHG signals suggests that impurities play a role in the generation of the large observed nonlinearity. Typically the dominant metal impurity in Optosil and related materials is Al with a concentration of 20–50 parts in 10^6 (ppm).[9] Al is known to substitute for Si in as-grown fused-silica samples. Brower[10] has investigated the formation of paramagnetic impurity centers associated with these Al impurities including $AlO_{3/2}^-$ and $AlO_{3/2}^-$–Na^+ complexes formed under ionizing radiation. The temperature-induced destabilization of these complexes is similar to the observed dependence of the SHG signal on poling temperature. Indeed, almost all trapping centers observed in SiO_2 films have shown thermal discharge temperatures in the range of 100–400°C.[11]

If such localized moieties are indeed present and oriented, then the individual hyperpolarizability β can be estimated from the measured $\chi^{(2)}$. If an impurity density of 50 ppm is assumed, β is estimated to be 10^{-37} m^4/V, many orders of magnitude larger than that of urea or 2-methyl-4-nitroaniline.[12] This casts significant doubt on a localized impurity model for the nonlinearity.

Another possibility is a field-induced third-order process similar to that proposed for the fiber experiments. With the known fused-silica $\chi^{(3)} \sim 10^{-22}$ m^2/V^2,[13] the dc field required to generate the observed $\chi^{(2)}$ is $\sim 10^7$ V/cm. This large field might be generated in the fused silica by charge separation at high temperature followed by trapping as the temperature is lowered with the field applied. The major charge carriers in fused silica (9-eV band gap) in this temperature range are likely to be cations such as Na^+. Under the applied temperature and bias, these cations will drift to the cathode and leave a space-charge region with a fixed concentration of trapped negative charge similar to that in Schottky barriers. Under these conditions, the major part of the externally applied potential is dropped over a depletion region of only several micrometers, which enhances the field strength. Assuming an impurity density of 50 ppm (the nominal total impurity concentration) and a poling voltage of 5 kV, a space-charge width of 5–6 μm and a maximum field strength of 10^7 V/cm are estimated across the depletion region, comparable with those of experimental observations. Additionally, this mechanism is consistent with the experimental observation of a fixed-voltage requirement rather than a fixed-field requirement on thickness scaling. This model provides for regions of high field at each end of the sample. Experimentally the nonlinearity is only observed on the anode side. This may be due to inequivalent charge distributions, which lead to varying field strengths and effective lengths.

In conclusion, we have generated an extremely large second-order nonlinearity in the near-surface regions of bulk fused silica. The $\chi^{(2)}$ coefficient of 1×10^{-12} m/V is of the same order as that of crystal quartz and is 3 orders of magnitude larger than that reported for fibers. A possibility for the microscopic mechanism of this nonlinearity involves the creation and orientation of nonlinear complexes during the poling process. However, this model leads to questionably large values for the hyperpolarizability. Another possibility is the generation of a large dc field (10^7 V/cm) by charge separation and trapping, which induces the large $\chi^{(2)}$ by a field-induced third-order process. Because of the ready manufacturability of silica optical materials and their integration with semiconductor optoelectronics, this nonlinearity may have important applications in waveguide and other optoelectronic devices.

We thank A. Mukherjee, K. Malloy, A. Y. Wu, and K. Brower for helpful discussions. Partial support for this research was provided by the Air Force Office of Scientific Research.

R. A. Myers is also with the Department of Physics and Astronomy, University of New Mexico.

S. R. J. Brueck is also with the Departments of Physics and Astronomy and Electrical and Computer Engineering, University of New Mexico.

References

1. U. Österberg and W. Margulis, Opt. Lett. **11**, 516 (1986).
2. R. H. Stolen and H. W. K. Tom, Opt. Lett. **12**, 587 (1987).
3. M.-V. Bergot, M. C. Farries, L. Li, L. J. Poyntz-Wright, P. St. J. Russell, and A. Smithson, Opt. Lett. **13**, 592 (1988).
4. D. Z. Anderson, V. Mizrahi, and J. E. Sipe, Opt. Lett. **16**, 796 (1991).
5. A. Kamal, M. L. Stock, A. Szpak, C. H. Thomas, D. A. Weinberger, M. Frankel, J. Nees, K. Ozaki, and J. Valdmanis, in *Digest of Optical Society of America Annual Meeting* (Optical Society of America, Washington, D.C., 1990), paper PD25.
6. A. Mukherjee, S. R. J. Brueck, and A. Y. Wu, Opt. Commun. **76**, 220 (1990).
7. I. C. S. Carvalho, P. M. P. Gouves, W. Margulis, J. P. von der Weid, and B. Lesche, in *Digest of Conference on Lasers and Electro-Optics* (Optical Society of America, Washington, D.C., 1991), paper JTuA3.
8. I. H. Malitson, J. Opt. Soc. Am. **55**, 1205 (1965).
9. Heraeus Amersil Quartz Catalog, Heraeus Amersil Inc., 100 Heraeus Boulevard, Bedford, Calif. 30518.
10. K. L. Brower, Phys. Rev. B **20**, 1799 (1979).
11. D. J. DiMaria, in *The Physics of SiO_2 and Its Interfaces: Proceedings of the International Topical Conference*, S. T. Pantelides, ed. (Pergamon, New York, 1978), p. 160.
12. D. S. Chemla and J. Zyss, eds., *Nonlinear Optical Properties of Organic Molecules and Crystals* (Academic, New York, 1987).
13. M. D. Levenson, IEEE J. Quantum Electron. **QE-10**, 110 (1974).

Invited Paper

VERTICAL-CAVITY SURFACE-EMITTING SEMICONDUCTOR LASERS: PRESENT STATUS AND FUTURE PROSPECTS

Marek Osiński*

Center for High Technology Materials, University of New Mexico, Albuquerque, New Mexico 87131-6081

ABSTRACT

A dramatic progress in the development of high-quality vertical-cavity surface-emitting lasers (VC-SELs) has been achieved during the last couple of years, with very strong contributions made by U.S. researchers. In particular, new concepts of microlasers and resonant-periodic-gain devices have been proposed and implemented, and devices with strained-quantum-well active regions have been demonstrated. This paper reviews the present status and future prospects for (VC-SELs), with emphasis on recent developments in the U.S.

1. INTRODUCTION

Vertical-cavity surface-emitting lasers (VC-SELs) have a unique history of long and painstaking development by a single research group, in the atmosphere of prevailing skepticism reigning in the semiconductor laser community. For over a decade since their invention in 1977, development and studies of vertical-cavity surface-emitting lasers (VC-SELs) have been limited to a single group at Tokyo Institute of Technology, led by Kenichi Iga [Iga 1988]. The apparent lack of interest in VC-SELs amongst semiconductor laser researchers was caused by notoriously poor performance of those devices (high threshold currents, low efficiencies, no cw operation at room temperature). For example, as recently as in 1988 the pulsed room-temperature threshold current densities were ~30 times larger than the corresponding cw densities in edge emitting lasers [Sakaguchi 1988]. Until very recently, VC-SELs have not even been seriously considered for any applications. This situation has changed dramatically over the last couple of years, during which a startling progress in the development of high-quality VC-SELs has been achieved. In this paper, we will examine the present status and future prospects for VC-SELs, with emphasis on recent advances in the U.S. Parallel developments in Japan are described elsewhere in this volume [Ogura 1991].

An important driving force behind the recent surge of interest in VC-SELs is a wide range of potential applications for two-dimensional (2-D) laser arrays. While individual VC-SELs may represent an alternative to existing edge-emitting lasers, they offer unique novel opportunities when assembled into 2-D arrays. Compared to conventional arrays of grating surface emitters or deflected-beam diode lasers, VC-SEL arrays offer the advantages of high packing density, larger emitting areas and consequently higher output power, unconstrained arrangement of emitters, wafer-scale processing, inherent single-longitudinal-mode operation, and narrow nearly-circular output beams that facilitate coupling to optical fibers or redirection and detec-

* Also with the Department of Electrical and Computer Engineering and the Department of Physics and Astronomy, University of New Mexico.

0-8194-0508-6/91/$4.00

tion in open-space systems. Compatibility with vertical stacking architecture allows to integrate these arrays into more complex system. Moreover, large numbers of VC-SELs with each emitter having a different wavelength can be integrated monolithically [Chang-Hasnain 1990b], [Chang-Hasnain 1991]. These features render them ideal for many new applications, such as chip-to-chip communications, free-space optical communications, optical recording, medicine, *etc.* Especially attractive are applications requiring high degree of parallelism, such as optical interconnections, optical computing, image processing, and optical pattern recognition.

Replacement of electrical interconnections with optical devices has many potential advantages such as high interconnection densities, high transmission speed, low power requirements, low loss, low dispersion, low mutual interference, immunity to RFI, EMI, and EMP, and reduced impedance matching and groundplane requirements [Goodman 1984], [Feldman 1988]. Both free-space and guided-wave configurations can be used. The successful implementation of optical interconnections in real systems largely depends, however, on the development of suitable two-dimensional arrays of low cost, high speed, high packing density, reliable optical sources that would operate at low driving currents and would deliver sufficient output power.

2. CLASSIFICATION OF VC-SEL STRUCTURES

Dramatic progress in VC-SELs over the last two years brought forth a variety of novel device structures. Conventional VC-SELs had bulk, double-heterostructure active regions. A typical geometry of etched-well ring-contact cylindrical structure is shown in Fig. 1. Recent development efforts concentrated on reducing the lasing threshold and/or increasing the maximum output power. Significant new concept was replacement of the bulk active region with narrow (single- or multiple-quantum-well) layers in a carefully designed cavity such that the position of the active layer would coincide with an antinode of laser radiation at a designed wavelength of operation. VC-SELs with a single active region satisfying this resonant condition are often called microlasers [Jewell 1989b], [Jewell 1990a] (see Fig. 2). A simple extension of the microlaser concept leads to introduction of distributed-Bragg-reflector resonant-periodic-gain (DBR-RPG) lasers [Raja 1989], [Corzine 1989b] (Fig. 3), in which multiple active regions are separated by half-wave spacers. The most recent advance in RPG laser structures is a distributed-feedback resonant-periodic-gain (DFB-RPG) VC-SEL [Mahbobzadeh 1990] (Fig. 4), where an RPG active region is intercalated with the multilayer reflectors.

A characteristic feature of VC-SELs that distinguishes them from edge-emitting semiconductor lasers is their small single-pass gain, reminiscent of gas lasers. As a direct consequence of small gain, in order to avoid prohibitively high lasing threshold it is necessary to place the active medium in a high-Q resonator. In today's state-of-the-art VC-SELs, this is almost invariably achieved by providing a Bragg resonator consisting of a stack of high-reflectivity quarter-wave layers on either side of the active medium.

3. PROGRESS IN PERFORMANCE OF VC-SELS

3.1. Threshold

Due to extremely short length of the active medium, it is imperative to achieve very high (close to unity) reflectivities of the mirrors defining the Fabry-Pérot resonator. Several concepts were employed to reach that goal: quarter-wave dielectric multilayer reflectors [Zinkiewicz 1989], [Yoo 1990], quarter-wave semiconductor multilayer reflectors [Jewell 1989a], [Scherer 1989], metallic reflectors [Deppe 1989], [Yang 1990], [Schubert 1990], [Tu 1990] and hybrid mirrors, combining semiconductor and metallic reflectors [Schubert 1989], [Fisher 1990] or semiconductor and dielectric layers [Ho 1990a]. The high reflectivity semiconductor mirror

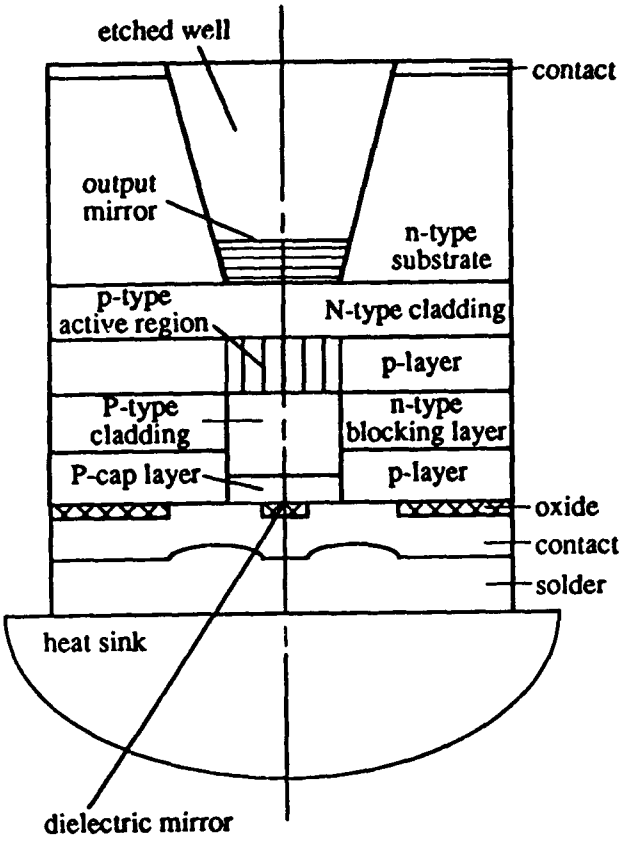

Fig. 1. Typical geometry of a conventional etched-well VC-SEL.

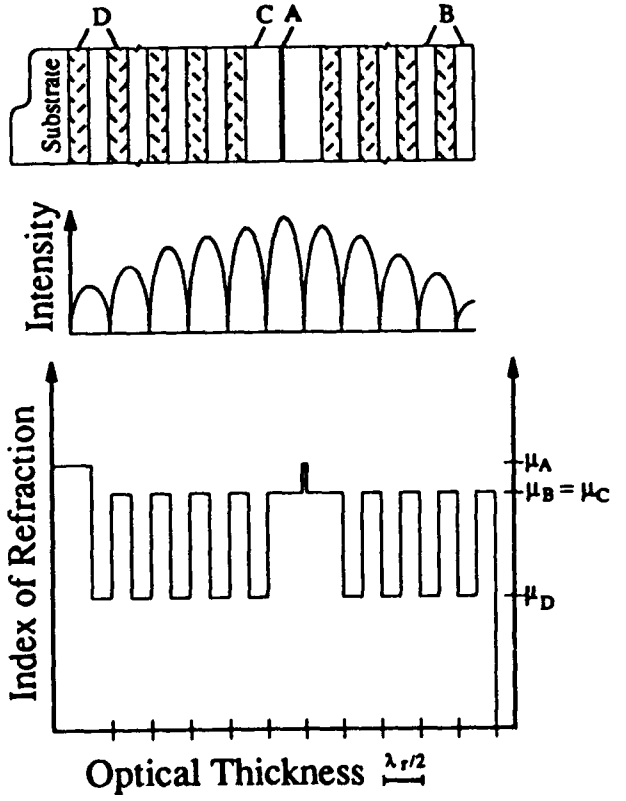

Fig. 2. Schematic illustration of layer structure, optical intensity distribution, and refractive index profile in a microlaser. Thick line (A) represents high-index quantum-well active layer, unshaded regions (B) - intermediate-index quarter-wave spacers, unshaded regions (C) - intermediate-index half-wave spacers, shaded regions (D) - low-index quarter-wave spacers.

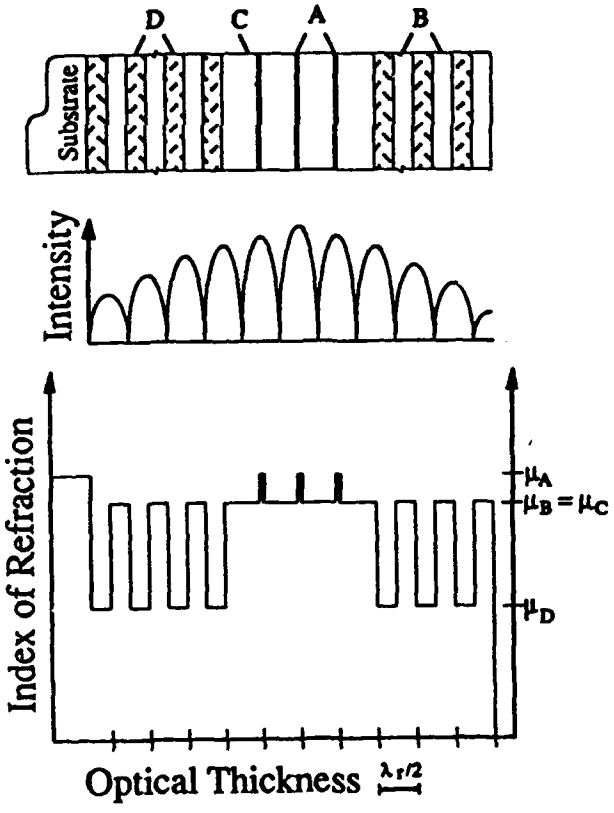

Fig. 3. Schematic illustration of layer structure, optical intensity distribution, and refractive index profile in a DBR-RPG laser. Layer designation is the same as in Fig. 2.

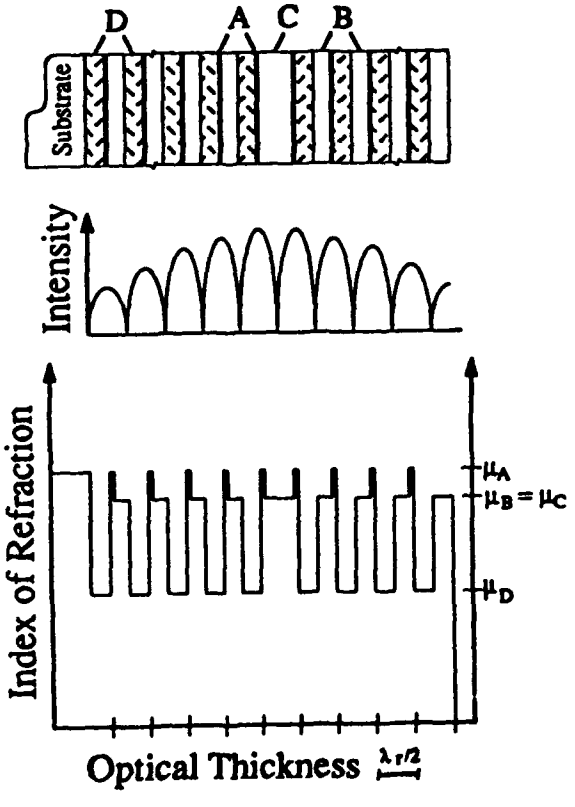

Fig. 4. Schematic illustration of layer structure, optical intensity distribution, and refractive index profile in a DFB-RPG laser. Layer designation is the same as in Fig. 2.

growth represents a significant technological challenge, since it requires a very good control of each layer thickness and composition. Calculations indicate that changing the thickness in one quarter-wave layer by only one unit cell (two monolayers) produces a shift of resonant wavelength up to 0.12 nm [Weber 1990]. In addition, rough interfaces reduce the reflectivity, introduce scattering and diffraction loss, and deform the wavefront of the lasing mode. Advanced crystal growth techniques, such as atomic layer epitaxy or phased-locked epitaxy [Walker 1990] may be utilized to provide ultimate perfection and uniformity of DBR layers with high reproducibility. Improved quality of interfaces can also be achieved by employing misoriented substrates [Wang 1990b].

Over the last two years, lasing threshold of VC-SELs for room-temperature operation has been reduced by orders of magnitude. The progress achieved in electrically pumped GaAs/AlGaAs devices is illustrated in Tables I and III for pulsed and cw operation, respectively.

So far, there have been relatively few reports of temperature dependence of lasing threshold. The characteristic temperature T_0 for pulsed threshold, given in Table II, is comparable to edge-emitting devices. However, as shown in Table IV, T_0 becomes significantly smaller for cw operation. Large difference between pulsed and cw values of T_0 indicates that strong temperature dependence of cw threshold in VC-SELs is primarily caused by thermal effects.

Optical pumping provides a convenient tool for studying VC-SEL structures. It can be used to evaluate potential performance of novel designs prior to achieving electrical pumping. It is worthwhile noting, however, that caution should be exercised when interpreting optical pumping data. With optical pumping, the active region is defined simply by the spot size of the pump beam, without any wafer processing. In electrically pumped structures, good confinement of carriers in columnar devices is accompanied by increased surface recombination at side walls, while planar structures suffer from current spreading. Hence, the threshold current density estimated from optical pumping data [Jewell 1989b] may lead to overoptimistic conclusions.

Another point of caution when interpreting the optical pumping results is a considerable uncertainty in evaluating the pump power actually absorbed in the active region. This somewhat corresponds to difficulties in establishing the pumping current in the active region in the presence of current spreading.

Tables V and VI contain data on room-temperature lasing threshold in optically pumped VC-SELs under pulsed and cw conditions, respectively.

3.2. Output power and efficiency

In evaluating progress in VC-SELs with respect to output characteristics, we have selected peak output power and overall power conversion efficiency as the main indicators. We have not included the slope efficiency η_d, since it can be made artificially high by reducing mirror reflectivities at the expense of increased threshold current. For example, η_d can be increased from ~15% to 54% by reducing the Ag mirror thickness from 400 Å to 300 Å [Tu 1990]. However, in the same instance, the pulsed threshold current density j_{th} in 20-μm diameter devices increases from 13 to 19 kA/cm^2 (I_{th} raising from 40 to 60 mA).

Tables VII and VIII contain data on output power and energy conversion efficiency for electrically-pumped VC-SELs operating under pulsed and cw conditions, respectively. Optical pumping results are summarized in Tables IX and X.

Table I. Room Temperature Pulsed Threshold

j_{th} [kA/cm^2]	I_{th} [mA]	V_{th} [V]	t_p [ns]	η_p [%]	Size [μm]	Structure	Reference
26	250		200	0.02	35 Ø	3 μm DH-DBR	[Zinkiewicz 1989]
25	20	1.3	100	1	10 Ø	0.6 μm DH-DBR, 400 Å Ag mirror	[Tu 1990]
18.4	1.3	15	50		3 Ø	unpassivated 3x8 nm MQW strained columnar μlaser	[Jewell 1989c]
16	115				30 Ø	0.7 μm DH-DBR 550 nm Ag mirror	[Deppe 1989]
15.3	12				10 Ø	0.5 μm DH-DBR	[Fischer 1990]
14.7	26				15 Ø	0.25 μm ion-implanted DH-DBR	[Tai 1989a]
14	16		200	2	12 Ø	20x15 nm GRINSCH-MQW-DBR	[Wang 1990a]
10.6	12	3.5	200	2	12 Ø	0.47 μm DH-DBR misoriented substrate	[Wang 1990b]
10.4	130		200	0.02	40 Ø	0.6 μm DH-DBR	[Botez 1989]
10.2	2	8	50		5 Ø	unpassivated 3x8 nm MQW strained columnar μlaser	[Jewell 1989c]
5.6	1.1		90		5 Ø	unpassivated 10nm SQW strained columnar μlaser	[Lee 1989]
3.2	3.2	4.2	100	2	10x10	3x8 nm MQW strained ion-implanted μlaser	[Lee 1990a]
2.3	45		90		50 Ø	unpassivated 10 nm SQW strained columnar μlaser	[Lee 1989]
1.9	7.5	10	300	0.3	20x20	3x8 nm MQW strained columnar μlaser	[Chang-Hasnain 1990a]
1.4	10.2		150	1	30 Ø	4x10 nm MQW proton-implanted μlaser	[Lee 1990b]
1.25	5	3.5	300	0.3	20x20	3x8 nm MQW proton-impanted strained μlaser	[Chang-Hasnain 1990a]
1.22	6		400	0.2	25 Ø	strained μlaser	[Yoo 1990b]
1.1	17	3	200	0.2	40x40	3x8 nm MQW proton-implanted strained μlaser	[Orenstein 1990]
0.74	3				20x20	strained columnar μlaser	[Clausen 1990]
0.6	26.5				75 Ø	8 nm SQW strained columnar μlaser	[Geels 1990a]

j_{th} - threshold current density
I_{th} - threshold current
V_{th} - threshold voltage
t_p - pulse length
η_p - duty cycle

Table II. Characteristic Temperature T_o for Pulsed Operations

T_o [K]	Range [°C]	Size [μm]	Structure	Reference
210	10-90	15 Ø	4x10 nm MQW GRINSCH proton-implanted μlaser	[Hasnain 1990]

T_o - characteristic temperature

Table III. Room Temperature CW Threshold

j_{th} [kA/cm^2]	I_{th}[mA]	V_{th} [V]	Size [μm]	Structure	Reference
130	2.3	27	1.5 Ø	unpassivated 3x8 nm MQW strained columnar μlaser	[Jewell 1990b]
31.8	1		2 Ø	passivated 3x8 nm MQW strained columnar μlaser	[Jewell 1990b]
22.6	40		15 Ø	0.5 μm DH-DBR	[Tai 1989b]
19.6	8		8 Ø	metallic mirror 0.6 μm DH-DBR	[Schubert 1990]
9.4	24	1.8	18 Ø	metallic mirror 0.6 μm DH-DBR	[Schubert 1990]
9.4	1.5		4x4	2 μm DH-DBR	[Hsin 1990]
6.6	2.5		7 Ø	3x8 nm MQW strained columnar μlaser	[Jewell 1990b]
6	1.5		5x5	10 nm SQW strained columnar μlaser	[Jewell 1990b]
4.1	0.8		5 Ø	passivated 3x8 nm MQW strained columnar μlaser	[Jewell 1990b]
3.6	3.6	3.7	10x10	3x8 nm MQW strained ion-implanted μlaser	[Lee 1990a]
2.8	2.2	7.5	10 Ø	4x10 nm MQW proton-implanted μlaser	[Lee 1990b]
1.4	0.7	4	7x7	8 nm SQW strained columnare μlaser	[Geels 1990b]
1.2	4.8		20x20	strained columnar μlaser	[Clausen 1990]
1.1	7.5	4	30 Ø	4x10 nm MQW proton-implanted μlaser	[Tell 1990]
0.8	1.1	4	12x12	8 nm SQW strained columnar μlaser	[Geels 1990a]

j_{th} - threshold current density
I_{th} - threshold current
V_{th} - threshold voltage

Table IV. Characteristic Temperature T_0 for CW Operation

T_0 [K]	Range [°C]	Size [μm]	Structure	Reference
115	15-50	15 Ø	0.5 μm DH-DBR	[Tai 1989b]
130	10-50	15 Ø	4x10 nm MQW GRINSCH proton-implanted μlaser	[Hasnain 1990]

T_0 - characteristic temperature

4. PERFORMANCE OF CONVENTIONAL VC-SELs

Conventional VC-SELs with thick active regions carry a potential for high-power operation, with the highest reported pulsed output power of 120 mW emitted by devices with diameter of 35 μm [Zinkiewicz 1989]. The cw output is however considerably lower, with thermally

limited light-output characteristics exhibiting a downward bend at output power levels near 1 mW for etched-well devices [Tai 1989b].

As recently as two years ago, the pulsed room-temperature threshold current densities of VC-SELs were ~30 times larger than the corresponding cw densities in edge emitting lasers [Sakaguchi 1988]. The threshold in conventional VC-SELs remains, however, very high (about 10 kA/cm^2 [Botez 1989], [Schubert 1990], compared to less than 1 kA/cm^2 in GaAs/AlGaAs edge emitters with similar bulk active regions), which indicates that thermal effects are still critical.

Conventional planar VC-SELs have been successfully integrated into closely packed phased-locked arrays [Deppe 1990], [van der Ziel 1990]. However, the familiar double-lobed far-field pattern that plagues the high-power edge-emitting phased arrays has been observed. Hence, one of the major attractions of VC-SELs which is its circular narrow output beam is lost when high-order 2-D supermodes are excited [Yoo 1990c]. It can be expected that achievement of stable single-lobe far-field in 2-D arrays will represent a formidable challenge.

Table V. Room-Temperature Pulsed Threshold - Optical Pumping

$\mathcal{P}_{th}$[kW/cm^2]	P_{th} [mW]	t_p [ns]	η_p [%]	Size [μm]	Structure	Reference
50900*	900*	0.01	0.08	1.5 Ø	1.6 μm DH-DBR	[Jewell 1989a]
1,600	1,250	12		10 Ø	150x10 nm MQW-DBR	[Gourley 1987]
820	410	0.01	0.08	8 Ø	20x8 nm strained MQW DBR	[Huang 1989]
30	24			10 Ø	20x60 nm DBR-RPG	[Corzine 1989b]
17.5	86	7	10^{-6}	25 Ø	20x10 nm hybrid DFB-DBR RPG	[Schaus 1989]

$\mathcal{P}_{th}$ - threshold irradiance (absorbed)
P_{th} - threshold pump power (absorbed)
t_p - pulse length
η_p - duty cycle
* - incident irradiance and power

Table VI. Room-Temperature CW Threshold - Optical Pumping

$\mathcal{P}_{th}$[kW/cm^2]	P_{th} [mW]	Size [μm]	Structure	Reference
0.7	1.5	20 Ø	8 nm SQW strained μlaser	[Jewell 1989b]

$\mathcal{P}_{th}$ - threshold irradiance (absorbed)
P_{th} - threshold pump power (absorbed)

Table VII. Room Temperature Pulsed Output Characteristics

p [kW/cm^2]	P_{max} [mW]	η [mW/mA, %]	t_p [ns]	η_p [%]	Size [μm]	Structure	Reference
0.28	0.4		500		12x12	8 nm SQW strained columnar μlaser	[Geels 1990a]
0.57	25				75 Ø	8 nm SQW strained columnar μlaser	[Geels 1990a]
0.75	3	0.16, 12			20x20	strained columnar μlaser	[Clausen 1990]
1.4	4.5	0.07, 5.0	100	1	20 Ø	0.6 μm DH-DBR, 3000 Å Ag mirror	[Tu 1990]
2.7	2.2	0.12, 9.4			9x9	strained columnar μlaser	[Clausen 1990]
2.7	3	0.07, 5.1	200	2	12 Ø	20x15 nm GRINSCH-MQW-DBR	[Wang 1990a]
2.8	45	0.07, 5.2	200	0.2	40x40	3x8 nm MQW proton-implanted strained μlaser	[Orenstein 1990]
5.3	6	0.12, 8.3	200	2	12 Ø	0.47 μm DH-DBR misoriented substrate	[Wang1990b]
12.5	120	0.11, 7.8	200	0.02	35 Ø	3 μm DH-DBR	[Zinkiewicz 1989]
14	11	0.14, 9.8	100	1	10 Ø	0.6 μm DH-DBR 400 Å AG mirror	[Tu 1990]
46.7	18				7 Ø	3x8 nm MQW strained columnar μlaser	[Jewell 1990b]

p - power density
P_{max} - maximum power
η - overall efficiency
t_p - pulse length
η_p - duty cycle

Table VIII. Room Temperature CW Output Characteristics

p [kW/cm^2]	P_{max} [mW]	η [mW/mA, %]	Size [μm]	Structure	Reference
0.31	0.55	0.10, 6.9	15 Ø	4x10 nm GRIN-SCH proton-implanted μlaser	[Hasnain 1990]
0.45	3.2	0.12, 8.3	30 Ø	4x10 nm GRIN-SCH proton-implanted μlaser	[Tell 1990]
0.68	1.2	0.02, 1.2	15 Ø	0.5 μm etched-well DH-DBR	[Tai 1989b]
0.70	0.7	0.06	10x10	3x8 nm MQW strained ion-impanted μlaser	[Lee 1990a]
0.76	0.6	0.11, 7.4	10 Ø	4x10 nm MQW proton-impanted μlaser	[Lee 1990b]
0.78	0.3	0.05, 3.9	7 Ø	3x8 nm MQW strained columnar μlaser	[Jewell 1990b]
1.91	1.5	0.21, 14.5	10 Ø	4x10 nm GRIN-SCH proton-implanted μlaser	[Tell 1990]

p - power density
P_{max} - maximum power
η - overall efficiency

Table IX. Room-Temperature Pulsed Ouput Characteristics - Optical Pumping

p [kW/cm^2]	P_{max} [mW]	η [%]	t_p [ns]	η_p [%]	Size [μm]	Structure	Reference
12.4	61	6.1	7	10^{-6}	25 Ø	20x10 nm hybrid DFB-DBR RPG	[Schaus 1989]

p - output power density
P_{max} - maximum power
η - overall efficiency
t_p - pulse length
η_p - duty cycle

Table X. Room-Temperature CW Output Characteristics - Optical Pumping

p [kW/cm^2]	P_{max} [mW]	η [%]	Size [μm]	Structure	Reference
56	40	36	10 Ø	60x10 nm DBR RPG	[Gourley 1989a]

p - output power density
P_{max} - maximum power
η - overall efficiency

5. PERFORMANCE OF MICROLASER VC-SELs

Strong interest in microlaser structures is to a large extent propelled by their relatively easy electrical pumping and capability of operating at low current levels. Originally, microlasers were fabricated in form of etched columns with side walls exposed to external environment. While this approach produces spectacular images [Lee 1989] and allows for a million of microlasers to be processed on a single wafer [Jewell 1990a], it is certainly not optimal from the point of view of reducing the threshold. In addition to very inefficient heat dissipation, surface recombination introduces a significant loss mechanism for structures of very small volume. In order to protect the etched columns from negative ambient influence, a buried-mesa geometry was proposed [Geels 1990a], in which the exposed surface is covered with polyimide (Fig. 5). Further improvement of device quality supplemented by a simplified fabrication process occurred with introduction of planar ion-implanted microlasers (Fig. 6) [Tai 1989a], [Tell 1990].

If the active region consists of a strained InGaAs/GaAs quantum well which radiates at a longer wavelength than GaAs, the output beam can be conveniently collected through a GaAs substrate without any necessity to etch a window. By the same token, reabsorption of laser emission in GaAs layers forming part of distributed Bragg reflectors can be greatly reduced.

Electrically pumped VC-SELs often suffer from increased threshold voltages caused by high series resistance of DBR reflectors, especially in the p-type doping case. Special precautions need to be taken to reduce excessive voltage drop at interfaces. An effective way to reduce height of barriers formed at abrupt interfaces is to utilize either short-period superlattices with gradually changing composition [Geels 1990a], [Tai 1990a] or "staircase" DBRs with additional intermediate bandgap layers [Tai 1990a]. The specific series resistance of conventional 10-period p-type GaAs/$Al_{0.7}Ga_{0.3}As$ DBRs (~7×10^{-3} Ωcm^2) can be reduced by as much as two orders of magnitude by introducing staircase DBRs (6.2×10^{-5} Ωcm^2) or superlattice DBRs (8.5×10^{-5} Ωcm^2) [Tai 1990a]. Even though peak reflectivity of staircase or superlattice DBRs is slightly re-

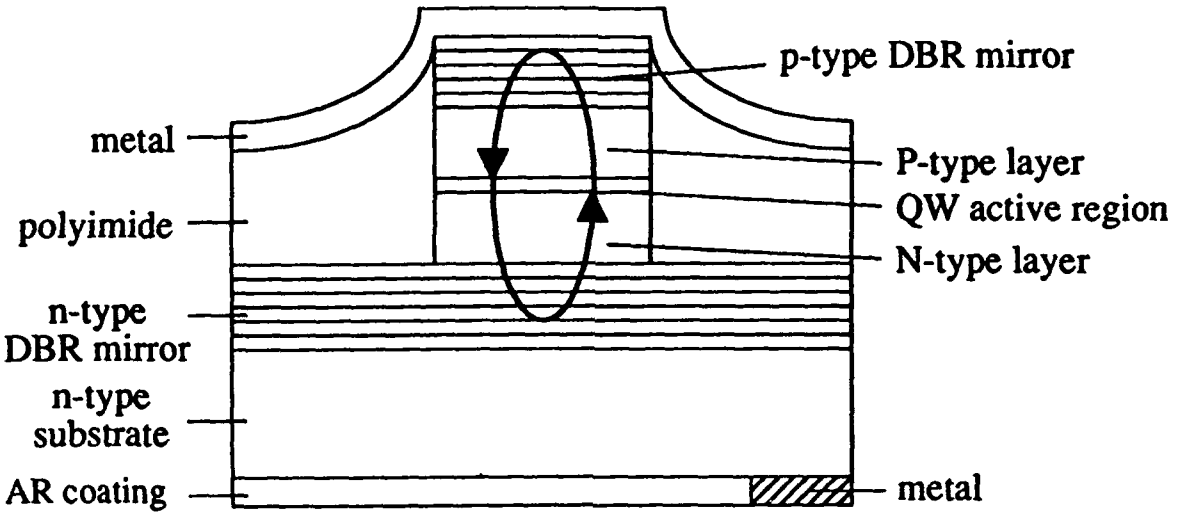

Fig. 5. Schematic illustration of a buried-mesa microlaser.

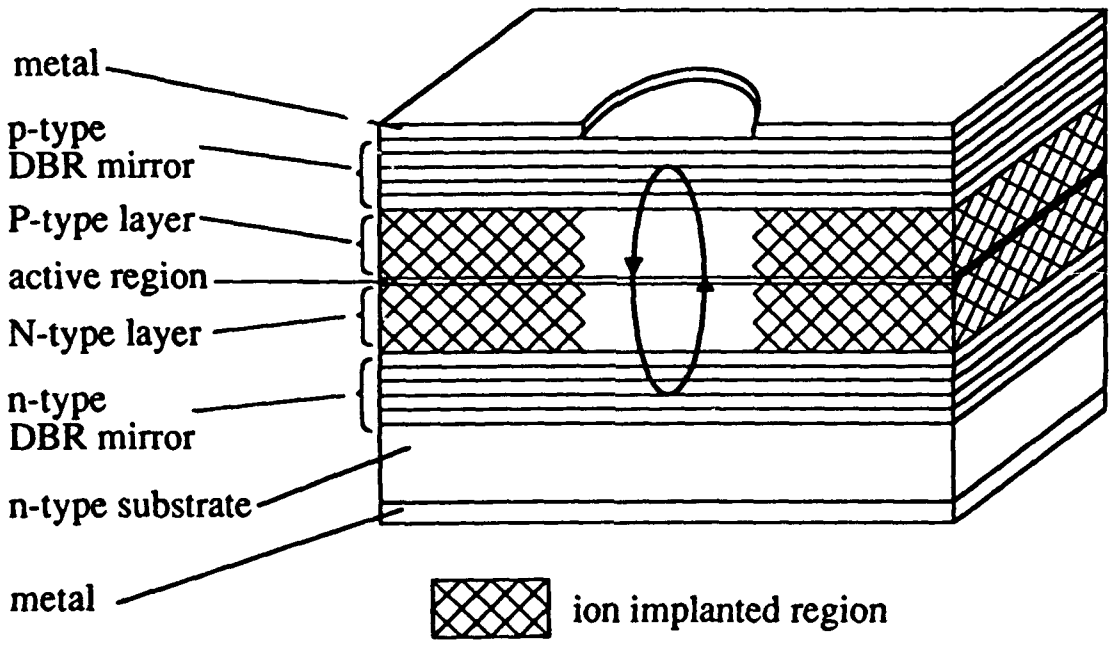

Fig. 6. Schematic illustration of a planar ion-implanted microlaser.

duced compared to quarter-wave DBRs, it is clear that even with one or two extra periods compensating for smaller reflectivity the series resistance will still remain very low. Staircase *p*-type DBRs have helped to reduce threshold voltages in gain-guided proton-implanted microlasers from 7-8 V to 3.7-4.2 V [Lee 1990c].

The highest reported cw output power from planar microlasers is 1.5 mW for 10-μm diameter GaAs/AlGaAs devices with four-quantum-well active region and over 3 mW for 30-μm diameter devices [Tell 1990]. It is important to note that although the emitting surface was increased ninefold, only twofold increase of the output power was achieved. This is a clear indication that the cw output was thermally limited and that the thermal problems deteriorate with increasing device diameter. The highest reported output power from columnar microlasers does not exceed 300 μW for a 7-μm diameter device with strained quantum well InGaAs/AlGaAs active region [Jewell 1990b].

Suitability of microlasers for fiber-optic applications has been demonstrated. Two-dimensional Gaussian-like transverse mode far field allow for much more efficient coupling into optical fibers than for conventional edge-emitting lasers. 50% butt coupling efficiency was measured for 8-μm core standard silica fibers with flat cleaved ends, and as much as 90% was achieved for fibers with etched lens-like ends [Tai 1990b]. This is the highest coupling efficiency ever reported for any diode laser. The best results obtained for edge-emitting lasers are in the range of 40-50% [Hillerich 1988]. Single-wavelength output with more than 50 dB side mode suppression ratio (again the highest ever reported), combined with 3-dB bandwidth exceeding 5 GHz [Hasnain 1990] clearly show that microlasers have reached the level of performance sufficient for first optical communication experiments to be attempted.

Coherent two-dimensional arrays of microlasers have been fabricated. Provided the size of individual emitters and their separation is sufficiently small, it is possible to maintain strong optical coupling between array elements. A phase-locked array comprised of 160 columnar microlasers of 1.3-μm diameter separated by less than 0.1 μm has been demonstrated [Yoo 1990a].

6. PERFORMANCE OF RPG VC-SELs

In parallel to microlasers, resonant-periodic-gain (RPG) structures have been pursued [Geels 1988], [Raja 1988a], [Raja 1988b], [Raja 1988c]. Both designs achieve gain enhancement in the vertical direction by aligning the active regions with the maxima of the longitudinal mode pattern at the designed wavelength, thus avoiding pumping the regions around the nulls of the standing wave. By the same token emission at non-resonant wavelengths is suppressed, and parasitic amplified spontaneous emission is reduced. Compared to microlasers, RPG structures carry a promise of generating higher output powers, by virtue of extended thickness of the active material. The alignment of peaks of an optical standing wave with quantum-well active layers leads to a significant reduction of the threshold current and additional enhancement of the maximum output power.

For VC-SELs, the total thickness of the device is of primary concern, since apart from issues of technological complexity and cost it also affects the ability to pump uniformly the device. First RPG structures were all of DBR type (see Fig. 3), with the total thickness significantly larger than the microlaser. Remarkable reduction of RPG laser thickness can be achieved by introducing, in analogy with edge-emitting lasers, a DFB-RPG structure [Mahbobzadeh 1990], shown in Fig. 4. The length of a DFB-type structure is inherently shorter than that of a DBR device with the same reflectivity of multilayer high reflector, because the amplifying and feedback sections overlap in the former structure whereas they are separated in the latter one. By replacing the DBR-RPG design with DFB-RPG, the total thickness of the device can be almost halved without compromising the characteristic features of RPG active medium. Compared

to present DBR-RPG structures, the DFB-RPG devices offer the advantages of considerably simpler fabrication process, improved wavelength selectivity, and strong discrimination against excitation of satellite longitudinal modes.

A slight modification of the structure shown in Fig. 4 results in a version of DFB-RPG VC-SEL that resembles a microlaser structure. Extending the length of the phase shifter to a full wave and placing an additional active layer in its center produces a microresonator sandwiched between two DFB sections, as indicated in Fig. 7. Compared to a usual microlaser structure, considerably higher output power can be obtained from the DFB-RPG laser, without any penalty whatsoever in the total device thickness. It should be noted, however, that the DFB-RPG structure of Fig. 4 is preferable to that of Fig. 7, since the latter contains one quantum well (symmetric quantum well in the center of the phase shifter) that is different from all the remaining ones.

So far, most experiments with RPG lasers involved optical pumping techniques. However, in order for these devices to reach their full application potential, it is necessary to develop an electrical pumping scheme. The substantial thickness of the RPG active region makes it very difficult to adopt the usual vertical pumping configuration without incurring a substantial penalty in threshold due to a non-uniform and inefficient carrier injection. On the other hand, transverse-junction pumping schemes do seem to represent a better approach in that long injection paths can be avoided and parasitic pumping of Bragg reflectors can be eliminated. In fact, the very first electrically pumped quasi-cw room-temperature operation of an RPG laser was recently achieved by using the transverse-junction approach [Schaus 1991].

While a strained-quantum-well active region is attractive for microlasers, incorporation of strained-layer materials in the RPG structures [Gourley 1989b] still represents a significant technological challenge. Due to multiplicity of active layers their cumulative thickness may easily exceed the critical thickness for dislocation-free accommodation of strain, leading to a metastable configuration.

7. THERMAL EFFECTS

Excessive heating of surface-emitting lasers represents a major impediment preventing further increase of their output power and development of densely-packed two-dimensional arrays. Thermal power densities generated inside the active region of VC-SELs are extremely high [Nakwaski 1991b]. This leads to a substantial increase of temperature and a corresponding increase in the threshold current density. The fact that the first room-temperature cw operation of VC-SELs was only reported two years ago [Ibaraki 1989], [Koyama 1989b] is mainly due to difficulties with overcoming the heating problems. The active-region temperature of the VC-SELs at threshold of cw operation has been estimated to be 25-30 °C higher than that of the substrate [Tai 1989b]. In contrast, the active-region heating near threshold in edge-emitting stripe lasers does not typically exceed 2-5 °C [Duda 1979], [Yano 1981], [Ito 1981], [Manning 1981]. Efficient heat dissipation, along with ultra-low threshold, is therefore critical for applications requiring massive integration. In addition, since the operating lifetime of the device decreases exponentially with temperature, it is essential to design lasers with consistently low self-heating.

Thermal problems will be even more pressing in arrays of VC-SELs, where long-range thermal cross-talk will have to be avoided. As the technology of surface-emitting lasers matures, optimization of their thermal properties will represent a major task to be solved in order to meet the requirements of massive integration necessary for optical processing applications.

In spite of their importance for individual device performance, large-scale integration ca-

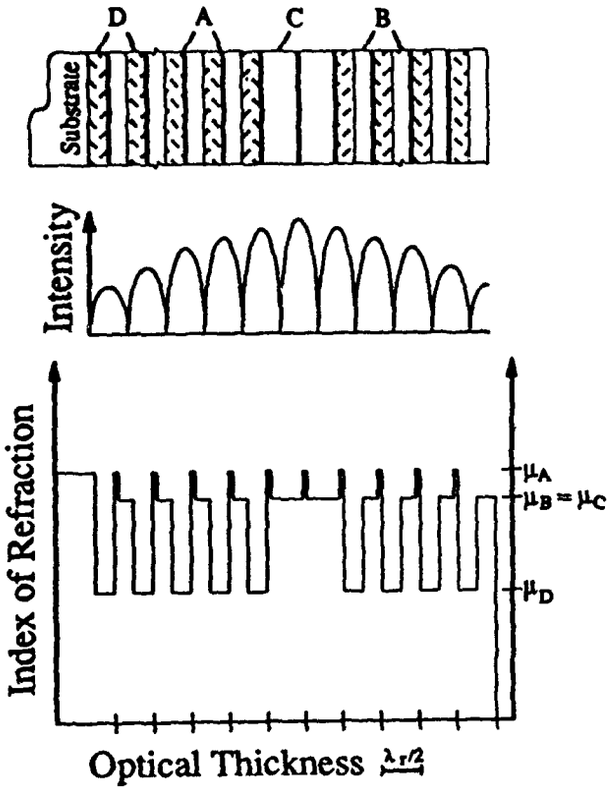

Fig. 7. Schematic illustration of layer structure, optical intensity distribution, and refractive index profile in a DFB-RPG analogue of microlaser. Layer designation is the same as in Fig. 2.

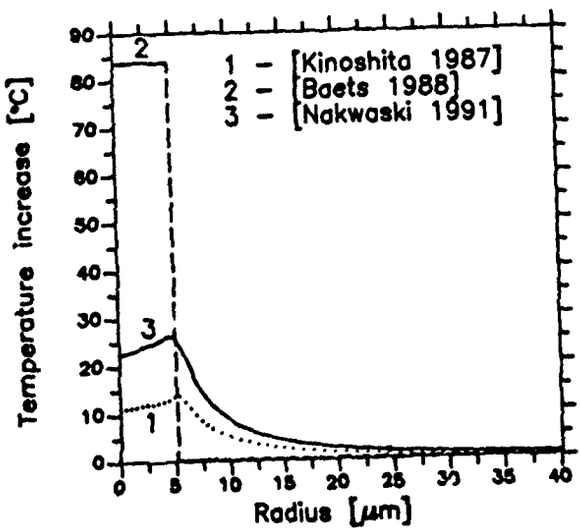

Fig. 8. Temperature profiles in an etched-well DH VC-SEL with 5-μm radius, calculated using various thermal models. The pumping current $I = 30$ mA $\simeq 2I_{th}$.

pabilities, and device reliability, thermal effects in VC-SELs received very little attention so far. The complexity of thermal problems in VC-SELs may be at least partially responsible for this. In contrast to edge-emitting diode lasers, where nonradiative recombination of charge carriers in the active region is a strongly dominant heat source, surface-emitting lasers have a much more complicated distribution of heat sources. In addition, analytical description of heat flux spreading in a cylindrically symmetric structure is more complicated than in a rectangular edge-emitting structure. Consequently, self-consistent solution of the thermal problem in a VC-SEL represents a difficult computational task.

Early attempts to address thermal problems in VC-SELs involved rather crude approximations. Kinoshita *et al.* [Kinoshita 1987] assumed a uniform heat source distribution in the active region and neglected the Joule heating, which in VC-SELs plays a much more important role than in edge emitters. Baets [Baets 1988] treated heat-spreading as one-dimensional, in addition to uniform distribution of heat sources. These deficiencies have been removed in a recent comprehensive treatment of thermal effects in etched-well vertical-cavity surface-emitting lasers, featuring realistic distribution of heat sources and two-dimensional analysis of both current and heat spreading [Nakwaski 1991b]. Fig. 8 illustrates inaccuracies in predicted temperature profiles that arise when unrealistic assumptions are made. Particularly inadequate is the one-dimensional treatment of [Baets 1988], strongly exaggerating thermal problems by neglecting the lateral heat spreading, which in structures of cylindrical symmetry is of critical importance. This results in errors as high as 220% in predicted temperature distribution in the active region [Nakwaski 1991a]. It is also shown in [Nakwaski 1991b] that by simple technological means it is possible to ease severity of heating effects.

Although in principle excessive heating should be avoided, it is worthwhile mentioning that thermal effects in VC-SELs are not always detrimental. In particular, increased temperature in the active region produces thermal waveguiding effect [Nakwaski 1991b] which may be responsible for reduced cw threshold currents in gain-guided proton-implanted microlasers [Lee 1990]. Pulsed thresholds over two times higher than in cw conditions were reported [Hasnain 1990].

Most VC-SEL structures exhibit increasing threshold current densities when device diameter is reduced below, say, 30 μm. Large diameter lasers experience smaller losses due to diffraction and diffusion, which results in lower thresholds. However, when the diameter is too large, the heating problems become more important, since the heat dissipation becomes essentially one-dimensional. There is, therefore, a trade-off between reducing losses and maintaining efficient heat sinking, which leads to optimal device size.

8. FUTURE PROSPECTS AND CONCLUSIONS

From an energy standpoint, replacing electrical interconnections with optical elements should in general reduce the total operating energy for communications over all but the shortest intrachip distances [Miller 1989]. Small arrays of VC-SELs should therefore be able to accomplish high-speed communication between electronic chips. Arrays of laser-based logic gates may be used for photonic switching in communication networks or for digital or neural computing. In all of these applications, it is essential to minimize the threshold current for lasing operation. To compete successfully against either electronic interconnections or optical modulators, the energy consumed by the laser per bit of transmitted information should compare favorably to energy requirements of the other sources. This translates to thresholds on the order of 100 μA [Jewell 1990a].

The lowest VC-SEL room-temperature cw threshold current reported to date is 0.7 mA for

a 7-μm square microlaser [Geels 1990b]. This compares very well with the lowest threshold in edge-emitting lasers (0.55 mA), achieved by optimizing a GRIN-SCH (graded-index separate confinement heterostructure) structure containing a single quantum well active region [Lau 1988]. Further progress should be possible, and the goal of 100 μA seems to be quite realistic. Improved passivation of sidewalls in columnar microlasers is expected to reduce threshold current in 1-μm diameter devices to less than 10 μA [Jewell 1990b].

The lowest cw threshold current density (800 A/cm^2) [Geels 1990a] reported for microcavity VC-SELs with strained quantum well active regions is still six times higher than the best result obtained in long-cavity edge-emitting structures (120 A/cm^2 [Chen 1990]). In addition, these low values of microlaser threshold current densities have been obtained solely for relatively broad-area emitters (~150 μm^2), while rapid increase of threshold was observed for small-area (<100 μm^2) devices. Further improvement in reducing the threshold current density will require very good quality of DBR mirrors with reflectivities exceeding 99% combined with suppressed nonradiative surface recombination in columnar microlasers or minimized current spreading in planar structures.

The microlaser structure, in which the active region coincides with an antinode of the lasing mode, has the advantage of very low threshold at the expense of small output power. On the other hand, resonant-periodic-gain (RPG) VC-SELs with multiple active regions offer impressively high output powers and high efficiencies. Consequently, the RPG devices represent a promising source for high-performance parallel networks with large numbers of processing elements, where the optical power requirements become more stringent. Another attractive area of applications for high-power VC-SELs is optical recording.

Possibility of photonic bandgaps in structures with three-dimensional periodicity [Yablonovitch 1987] represents a major attraction for VC-SELs since it implies effective inhibition of undesirable spontaneous emission. However, theoretical understanding of photonic bandgaps needs to be improved before such concept could be seriously entertained for semiconductor lasers. It has been recently shown [Leung 1990], [Zhang 1990], [Ho 1990b] that when the vector nature of the electromagnetic field is included in the analysis of fcc structures, the gaps obtained in scalar calculations disappear. At this point, it is not yet clear what conditions need to be satisfied in order to obtain the photonics bandgaps.

In summary, vertical-cavity surface-emitting semiconductor lasers are now at the stage of dynamic development. Their architecture is ideal for many novel applications. At a low-power end, such as interchip communication, microresonator VC-SELs with a single quantum well active region are the sources of choice. At a high-power end, corresponding for example to massively parallel interconnects or optical recording, highly-efficient resonant-periodic-gain structures with multiple active regions offer the best prospects. Among the most recent advancements, a novel DFB-RPG structure for vertical-cavity surface-emitting lasers seems particularly promising.

9. ACKNOWLEDGMENTS

The author wishes to thank his students and colleagues at the University of New Mexico, and particularly Mohammad Mahbobzadeh, Steven Kubica, and Drs. Christian Schaus, Włodzimierz Nakwaski, Julian Cheng, and Steven Brueck, for their fine collaboration and assistance during the course of research work on VC-SELs at UNM. Support of the U.S. Air Force Office of Scientific Research, the Phillips Laboratory, and the Defense Advanced Research Projects Agency is gratefully acknowledged.

10. REFERENCES

[Baets 1988] R. Baets, "Considerations on Geometry Design of Surface-Emitting Laser Diodes", *IEE Proc. Pt. J (Optoelectron.)*, vol. 135, pp. 233-241, June 1988.

[Botez 1989] D. Botez, L. M. Zinkiewicz, T. J. Roth, L. J. Mawst, and G. Peterson, "Low-Threshold-Current-Density Vertical-Cavity Surface-Emitting AlGaAs/GaAs Diode Lasers", *IEEE Photon. Technol. Lett.*, vol. 1, pp. 205-208, Aug. 1989.

[Chang-Hasnain 1990a] C. J. Chang-Hasnain, M. Orenstein, A. Von Lehmen, L. T. Florez, J. P. Harbison, and N. G. Stoffel, "Transverse Mode Characteristics of Vertical Cavity Surface-Emitting Lasers", *Appl. Phys. Lett.*, vol. 57, pp. 218-220, 16 July 1990.

[Chang-Hasnain 1990b] C. J. Chang-Hasnain, M. W. Maeda, N. G. Stoffel, J. P. Harbison, L. T. Florez, and J. Jewell, "Surface-Emitting Laser Arrays with Uniformly Separated Wavelengths", *Electron. Lett.*, vol. 26, pp. 940-942, 21 June 1990.

[Chang-Hasnain 1991] C. J. Chang-Hasnain, J. R. Wullert, J. P. Harbison, L. T. Florez, N. G. Stoffel, and M. W. Maeda, "Rastered, Uniformly Separated Wavelengths Emitted from a Two-Dimensional Vertical-Cavity Surface-Emitting Laser Array", *Appl. Phys. Lett.*, vol. 58, pp. 31-33, 7 Jan. 1991.

[Chen 1990] T. R. Chen, L. Eng, B. Zhao, Y. H. Zhuang, S. Sanders, H. Morkoç, and A. Yariv, "Submilliamp Threshold InGaAs-GaAs Strained Layer Quantum-Well Laser", *IEEE J. Quantum Electron.*, vol. 26, pp. 1183-1190 (1990).

[Clausen 1990] E. M. Clausen, Jr., A. Von Lehmen, C. Chang-Hasnain, J. P. Harbison, and L. T. Florez, "Greatly Improved Threshold Characteristics of Vertical-Cavity Surface-Emitting Lasers Fabricated by a Unique Etching Process", *Techn. Digest Postdeadline Papers, OSA 1990 Annual Meeting*, Boston, MA, Nov. 4-9, 1990, Paper PDP 21, pp. 52-54.

[Corzine 1989a] S. W. Corzine, R. S. Geels, R.-H. Yan, J. W. Scott, L. A. Coldren, and P. L. Gourley, "Efficient, Narrow-Linewidth Distributed-Bragg-Reflector Surface-Emitting Laser with Periodic Gain", *IEEE Photon. Techn. Lett.*, vol. 1, pp. 52-54, March 1989.

[Corzine 1989b] S. W. Corzine, R. S. Geels, J. W. Scott, R.-H. Yan, and L. A. Coldren, "Design of Fabry-Perot Surface-Emitting Lasers with a Periodic Gain Structure", *IEEE J. Quantum Electron.*, vol. 25, pp. 1513-1524, June 1989.

[Deppe 1989] D. G. Deppe, A. Y. Cho, K. F. Huang, R. J. Fischer, K. Tai, E. F. Schubert, and J. F. Chen, "AlGaAs-GaAs and AlGaAs-GaAs-InGaAs Vertical Cavity Surface Emitting Lasers with Ag Mirrors", *J. Appl. Phys.*, vol. 66, pp. 5629-5631, 1 Dec. 1989.

[Deppe 1990] D. G. Deppe, J. P. van der Ziel, N. Chand, G. J. Zydzik, and S. N. G. Chu, "Phase-Coupled Two-Dimensional $Al_xGa_{1-x}As$-GaAs Vertical-Cavity Surface-Emitting Laser Array", *Appl. Phys. Lett.*, vol. 56, pp. 2089-2091, 21 May 1990.

[Duda 1979] E. Duda, J.-C. Carballes, and J. Apruzzese, "Thermal Resistance and Temperature Distribution in Double-Heterostructure Lasers: Calculations and Experimental Results", *IEEE J. Quantum Electron.* vol. QE-15, pp. 812-817, Aug. 1979.

[Feldman 1988] M. R. Feldman, S. C. Esener, C. C. Guest, and S. H. Lee, "Comparison Between Optical and Electrical Interconnects Based on Power and Speed Considerations", *Appl. Opt.*, vol. 27, pp. 1742-1751, 1 May 1988.

[Fischer 1990] R. J. Fischer, K. Tai, M. Hong, J. M. Vanderberg, J. Y. Ying, J. P. Mannaerts, and A. Y. Cho, "Use of Hybrid Reflectors to Achieve Low Thresholds in All Molecular-Beam Epitaxy Grown Vertical Cavity Surface Emitting Laser Diodes", *J. Vac. Sci. Technol. B*, vol. 8, pp. 336-338, March 1990.

[Geels 1988] R. S. Geels, R. H. Yan, J. W. Scott, S. W. Corzine, R. J. Simes, and L. A. Coldren, "Analysis and Design of a Novel Parallel-Driven MQW-DBR Surface-Emitting Diode Laser", *CLEO '88 Conf. Lasers & Electro-Optics, Techn. Digest Series Vol. 7*, Anaheim, CA, April 25-29, 1988, Paper WM1, pp. 206-207.

[Geels 1990a] R. S. Geels and L. A. Coldren, "Low Threshold Planarized Vertical-Cavity Surface-Emitting Lasers", *IEEE Photon. Techn. Lett.*, vol. 2, pp. 234-236, April 1990.

[Geels 1990b] R. S. Geels and L. A. Coldren, "Submilliamp Threshold Vertical-Cavity Laser Diodes", *Appl. Phys. Lett.*, vol. 57, pp. 1605-1607, 15 Oct. 1990.

[Goodman 1984] J. W. Goodman, F. J. Leonberger, S.-Y. Kung, and R. A. Athale, "Optical Interconnections for VLSI Systems", *Proc. IEEE*, vol. 72, pp. 850-866, July 1984.

[Gourley 1987] P. L. Gourley and T. J. Drummond, "Visible, Room-Temperature, Surface-Emitting Laser Using an Epitaxial Fabry-Perot Resonator with AlGaAs/AlAs Quarter-Wave High Reflectors and AlGaAs/GaAs Multiple Quantum Wells", *Appl. Phys. Lett.*, vol. 50, pp. 1225-1227, 4 May 1987.

[Gourley 1989a] P. L. Gourley, T. M. Brennan, B. E. Hammons, S. W. Corzine, R. S. Geels, R. H. Yan, J. W. Scott, and L. A. Coldren, "High-Efficiency TEM_{00} Continuous-Wave (Al,Ga)As Epitaxial Surface-Emitting Lasers and Effect of Half-Wave Periodic Gain", *Appl. Phys. Lett.*, vol. 54, pp. 1209-1211, 27 March 1989.

[Gourley 1989b] P. L. Gourley, S. K. Lyo, and L. R. Dawson, "High-Efficiency, Continuous-Wave, Epitaxial Surface-Emitting Laser with Pseudomorphic InGaAs Quantum Wells", *Appl. Phys. Lett.*, vol. 54, pp. 1397-1399, 10 April 1989.

[Hasnain 1990] G. Hasnain, K. Tai, J. D. Wynn, Y. H. Wang, R. J. Fischer, B. E. Weir, and A. Y. Cho, "High Frequency Modulation and Efficient Fiber Coupling of Vertical Cavity Surface Emitting Lasers", *Post Deadline Papers, LEOS 1990 Annual Meeting*, Boston, MA, Nov. 4-9, 1990, Paper PD11, and *LEOS'90 Conf. Proc.*, pp. 662-663.

[Hillerich 1988] B. Hillerich, "Shape Analysis and Coupling Loss of Microlenses on Single-Mode Fiber Tips", *Appl. Opt.*, vol. 27, pp. 3102-3105, 1 Aug. 1988.

[Ho 1990a] S.-T. Ho, S. L. McCall, R. E. Slusher, L. N. Pfeiffer, K. W. West, A. F. J. Levi, G. E. Blonder, and J. L. Jewell, "High Index Contrast Mirrors for Optical Microcavities", *Appl. Phys. Lett.*, vol. 57, pp. 1387-1389, 1 Oct. 1990.

[Ho 1990b] K. M. Ho, C. T. Chan, and C. M. Soukoulis, "Existence of Photonic Gap in Periodic Dielectric Structures", *Phys. Rev. Lett.*, vol. 65, pp. 3152-3155, 17 Dec. 1990.

[Hsin 1990] W. Hsin, G. Du, J. K. Gamelin, K. J. Malloy, S. Wang, J. R. Whinnery, Y. J. Yang, T. G. Dziura, and S. C. Wang, "Low Threshold Distributed Bragg Reflector Surface Emitting Laser Diode with Semiconductor Air-Bridge-Supported Top Mirror", *Electron. Lett.*, vol. 26, pp. 307-308, 1 March 1990.

[Huang 1989] K. F. Huang, K. Tai, J. L. Jewell, R. J. Fischer, S. L. McCall, and A. Y. Cho, "Room-Temperature Pseudomorphic $In_xGa_{1-x}As/GaAs$ Quantum Well Surface-Emitting Lasers at 0.94-1.0 μm Wavelengths", *Appl. Phys. Lett.*, vol. 54, pp. 2192-2194, 29 May 1989.

[Ibaraki 1989] A. Ibaraki, K. Kawashima, K. Furusawa, T. Ishikawa, T. Yamaguchi, and T. Niina, "Buried Heterostructure GaAs/GaAlAs Distributed Bragg Reflector Surface Emitting Laser with Very Low Threshold (5.2 mA) under Room Temperature CW Conditions", *Jpn. J. Appl. Phys.*, vol. 28, pp. L667-L668, April 1989.

[Iga 1988] K. Iga, F. Koyama, and S. Kinoshita, "Surface Emitting Semiconductor Lasers", *IEEE J. Quantum Electron.*, vol. 24, pp. 1845-1855, Sept. 1988, and the references quoted therein.

[Ito 1981] M. Ito and T. Kimura, "Stationary and Transient Thermal Properties of Semiconductor Laser Diodes", *IEEE J. Quantum Electron.*, vol. QE-17, pp. 787-795, May 1981.

[Jewell 1989a] J. L. Jewell, S. L. McCall, Y. H. Lee, A. Scherer, A. C. Gossard, and J. H. English, "Lasing Characteristics of GaAs Microresonators", *Appl. Phys. Lett.*, vol. 54, pp. 1400-1402, 10 April 1989.

[Jewell 1989b] J. L. Jewell, K. F. Huang, K. Tai, Y. H. Lee, R. J. Fischer, S. L. McCall, and A. Y. Cho, "Vertical Cavity Single Quantum Well Laser", *Appl. Phys. Lett.*, vol. 55, pp. 424-427, 31 July 1989.

[Jewell 1989c] J. L. Jewell, A. Scherer, S. L. McCall, Y. H. Lee, S. Walker, J. P. Harbison, and L. T. Florez, "Low-Threshold Electrically Pumped Vertical-Cavity Surface-Emitting Microlasers", *Electron. Lett.*, vol. 25, pp. 1123-1124, 17 Aug. 1989.

[Jewell 1990a] J. L. Jewell, Y. H. Lee, A. Scherer, S. L. McCall, N. A. Olsson, J. P. Harbison, and L. T. Florez, "Surface-Emitting Microlasers for Photonic Switching and Interchip Connections", *Opt. Eng.*, vol. 29, pp. 210-214, March 1990.

[Jewell 1990b] J. L. Jewell, A. Scherer, Y. H. Lee, S. L. McCall, J. P. Harbison, L. T. Florez, R. S. Tucker, C. A. Burrus, C. J. Sandroff, and N. A. Olsson, "Vertical Cavity Surface Emitting Microlasers", , *LEOS'90 Conf. Proc., LEOS 1990 Annual Meeting*, Boston, MA, Nov. 4-9, 1990, Paper SDL1.2/MKK2, p. 378.

[Kinoshita 1987] S. Kinoshita, F. Koyama, and K. Iga, "Investigation of the CW Operation at Room Temperature for GaAlAs/GaAs Surface Emitting Laser", *Proc. Tech. Group Meet., IECE Japan*, paper OQE86-188, pp. 23-30, 16 March 1987.

[Koyama 1989b] F. Koyama, S. Kinoshita, and K. Iga, "Room-Temperature Continuous Wave Lasing Characteristics of a GaAs Vertical Cavity Surface-Emitting Laser", *Appl. Phys. Lett.*, vol. 55, pp. 221-222, 17 July 1989.

[Lau 1988] K. Y. Lau, P. L. Derry, and A. Yariv, "Ultimate Limit in Low Threshold Quantum Well GaAlAs Semiconductor Lasers", *Appl. Phys. Lett.*, vol. 52, pp. 88-90, 11 Jan. 1988.

[Lee 1989] Y. H. Lee, J. L. Jewell, A. Scherer, S. L. McCall, J. P. Harbison, and L. T. Florez, "Room-Temperature Continuous-Wave Vertical-Cavity Single-Quantum-Well Microlaser Diodes", *Electron. Lett.*, vol. 25, pp. 1377-1378, 28 Sept. 1989.

[Lee 1990a] Y. H. Lee, J. L. Jewell, B. Tell, K. F. Brown-Goebeler, A. Scherer, J. P. Harbison, and L. T. Florez, "Effects of Etch Depth and Ion Implantation on Surface-Emitting Microlasers", *Electron. Lett.*, vol. 26, pp. 225-227, 15 Feb. 1990.

[Lee 1990b] Y. H. Lee, B. Tell, K. Brown-Goebeler, J. L. Jewell, and J. V. Hove, "Top Surface-Emitting GaAs Four-Quantum-Well Lasers Emitting at 0.85 μm", *Electron. Lett.*, vol. 26, pp. 710-711, 24 May 1990.

[Lee 1990c] Y. H. Lee, B. Tell, K. Brown-Goebeler, J. L. Jewell, R. E. Leibenguth, M. T. Asom, G. Livescu, L. Luther, and V. D. Mattera, "High-Efficiency (1.2 mW/mA) Top-Surface-Emitting GaAs Quantum Well Lasers", *Electron. Lett.*, vol. 26, pp. 1308-1310, 2 Aug. 1990.

[Leung 1990] K. M. Leung and Y. F. Liu, "Full Vector Wave Calculation of Photonic Band Structures in Face-Centered-Cubic Dielectric Media", *Phys. Rev. Lett.*, vol. 65, pp. 2646-2649, 19 Nov. 1990.

[Mahbobzadeh 1990] M. Mahbobzadeh and M. Osiński, "Novel Distributed-Feedback Resonant-Periodic-Gain Structure for Vertical-Cavity Surface-Emitting Semiconductor Lasers", *Electron. Lett.*, vol. 26, pp. 1716-1718, 27 Sept. 1990.

[Manning 1981] J. S. Manning, "Thermal Impedance of Diode Lasers: Comparison of Experimental Methods and a Theoretical Model", *J. Appl. Phys.*, vol. 52, pp. 3179-3184, May 1981.

[Miller 1989] D. A. B. Miller, "Optics for Low-Energy Communication Inside Digital Processors: Quantum Detectors, Sources, and Modulators as Efficient Impedance Converters", *Opt. Lett.*, vol. 14, pp. 146-148, 15 Jan. 1989.

[Nakwaski 1991a] W. Nakwaski and M. Osiński, "Temperature Profiles in Etched-Well Surface-Emitting Semiconductor Lasers", *Jpn. J. Appl. Phys.*, vol. 30, 1 April 1991.

[Nakwaski 1991b] W. Nakwaski and M. Osiński, "Thermal Properties of Etched-Well Surface-Emitting Semiconductor Lasers", *IEEE J. Quantum Electron.*, vol. 27, June 1991.

[Ogura 1991] M. Ogura, "Progress of Surface-Emitting Lasers in Japan", this volume.

[Orenstein 1990] M. Orenstein, A. C. Von Lehmen, C. Chang-Hasnain, N. G. Stoffel, J. P. Harbison, L. T. Florez, E. Clausen, and J. E. Jewell, "Vertical-cavity surface-emitting InGaAs/GaAs lasers with planar lateral definition", *Appl. Phys. Lett.*, vol. 56, pp. 2384-2386, 11 June 1990.

[Raja 1988a] M. Y. A. Raja, S. R. J. Brueck, M. Osiński, C. F. Schaus, J. G. McInerney, T. M. Brennan, and B. E. Hammons, "Wavelength-Resonant Enhanced Gain/Absorption Structure for Optoelectronic Devices", *Post Deadline Papers, IQEC '88 XVI Int. Conf. Quantum Electron.*, Tokyo, Japan, July 18-21, 1988, Paper PD-23, pp. 52-53.

[Raja 1988b] M. Y. A. Raja, S. R. J. Brueck, M. Osiński, C. F. Schaus, J. G. McInerney, T. M. Brennan, and B. E. Hammons, "Novel Wavelength-Resonant Optoelectronic Structure and Its Application to Surface-Emitting Semiconductor Lasers", *Electron. Lett.*, vol. 24, pp. 1140-1142, 1 Sept. 1988.

[Raja 1988c] M. Y. A. Raja, S. R. J. Brueck, M. Osiński, C. F. Schaus, J. G. McInerney, T. M. Brennan, and B. E. Hammons, "Surface-Emitting Multiple Quantum Well GaAs/AlGaAs Laser with Wavelength-Resonant Periodic Gain Medium", *Appl. Phys. Lett.*, vol. 53, pp. 1678-1680, 31 Oct. 1988.

[Raja 1989] M. Y. A. Raja, S. R. J. Brueck, M. Osiński, C. F. Schaus, J. G. McInerney, T. M. Brennan, and B. E. Hammons, "Resonant Periodic Gain Surface-Emitting Semiconductor Lasers", *IEEE J. Quantum Electron.*, vol. 25, pp. 1500-1512, June 1989.

[Sakaguchi 1988] T. Sakaguchi, F. Koyama, and K. Iga, "Vertical Cavity Surface-Emitting Laser with an AlGaAs/AlAs Bragg Reflector", *Electron. Lett.*, vol. 24, pp. 928-929, 21 July 1988.

[Schaus 1989] C. F. Schaus, H. E. Schaus, S. Sun, M. Y. A. Raja, and S. R. J. Brueck, "MOCVD Growth of GaAs/AlGaAs Wavelength Resonant Periodic Gain Vertical Cavity Surface-Emitting Laser", *Electron. Lett.*, vol. 25, pp. 538-539, 13 April 1989.

[Schaus 1991] C. F. Schaus, A. Torres, J. Cheng, C. Hains, S. Sun, K. Zheng, and E. Armour, "Transverse-Injection Vertical-Cavity Surface-Emitting Lasers with Resonant Periodic Gain ", to be published in *Appl. Phys. Lett.*, vol. 58, 22 April 1991.

[Scherer 1989] A. Scherer, J. L. Jewell, Y. H. Lee, J. P. Harbison, and L. T. Florez, "Fabrication of Microlasers and Microresonator Optical Switches", *Appl. Phys. Lett.*, vol. 55, pp. 2724-2726, 25 Dec. 1989.

[Schubert 1990] E. F. Schubert, L. W. Tu, R. F. Kopf, G. J. Zydzik, and D. G. Deppe, "Low-Threshold Vertical Cavity Surface-Emitting Lasers with Metallic Reflectors", *Appl. Phys. Lett.*, vol. 57, pp. 117-119, 9 July 1990.

[Tai 1989a] K. Tai, R. J. Fischer, K. W. Wang, S. N. G. Chu, and A. Y. Cho, "Use of Implant Isolation for Fabrication of Vertical Cavity Surface-Emitting Laser Diodes", *Electron. Lett.*, vol. 25, pp. 1644-1645, 23 Nov. 1989.

[Tai 1989b] K. Tai, R. J. Fischer, C. W. Seabury, N. A. Olsson, T.-C. D. Huo, Y. Ota, and A. Y. Cho, "Room-Temperature Continuous-Wave Vertical-Cavity Surface-Emitting GaAs Injection Lasers", *Appl. Phys. Lett.*, vol. 55, pp. 2473-2475, 11 Dec. 1989.

[Tai 1990a] K. Tai, L. Yang, Y. H. Wang, J. D. Wynn, and A. Y. Cho, "Drastic Reduction of Series Resistance in Doped Semiconductor Distributed Bragg Reflectors for Surface-Emitting Lasers", *Appl. Phys. Lett.*, vol. 56, pp. 2496-2498, 18 June 1990.

[Tai 1990b] K. Tai, G. Hasnain, J. D. Wynn, R. J. Fischer, Y. H. Wang, B. Weir, J. Gamelin, and A. Y. Cho, "90% Coupling of Top Surface Emitting GaAs/AlGaAs Quantum Well Laser Output into 8 μm Diameter Core Silica Fibre", *Electron. Lett.*, vol. 26, pp. 1628-1629, 13 Sept. 1990.

[Tell 1990] B. Tell, Y. H. Lee, K. F. Brown-Goebeler, J. L. Jewell, R. E. Leibenguth, M. T. Asom, G. Livescu, L. Luther, and V. D. Mattera, "High-Power CW Vertical-Cavity Top Surface-Emitting GaAs Quantum Well Lasers", *Appl. Phys. Lett.*, vol. 57, pp. 1855-1857, 29 Oct. 1990.

[Tu 1990] L.-W. Tu, E. F. Schubert, R. F. Kopf, G. J. Zydzik, M. Hong, S. N. G. Chu, and J. P. Mannaerts, "Vertical-Cavity Surface-Emitting Lasers with Semitransparent Metallic Mirrors and High Quantum Efficiencies", *Appl. Phys. Lett.*, vol. 57, pp. 2045-2047, 12 Nov. 1990.

[van der Ziel 1990] J. P. van der Ziel, D. G. Deppe, N. Chand, G. J. Zydzik, and S. N. G. Chu, "Characteristics of Single- and Two-Dimensional Phase Coupled Arrays of Vertical Cavity Surface Emitting GaAs-AlGaAs Lasers", *IEEE J. Quantum Electron.*, vol. 26, pp. 1873-1882, Nov. 1990.

[Walker 1990] J. D. Walker, K. Malloy, S. Wang, and J. S. Smith, "Precision AlGaAs Bragg Reflectors Fabricated by Phase-Locked Epitaxy", *Appl. Phys. Lett.*, vol. 56, pp. 2493-2495, 18 June 1990.

[Wang 1990a] Y. H. Wang, K. Tai, J. D. Wynn, M. Hong, R. J. Fischer, J. P. Mannaerts, and A. Y. Cho, "GaAs/AlGaAs Multiple Quantum Well GRIN-SCH Vertical Cavity Surface Emitting Laser Diodes", *IEEE Photon. Techn. Lett.*, vol. 2, pp. 456-458, July 1990.

[Wang 1990b] Y. H. Wang, K. Tai, Y. F. Hsieh, S. N. G. Chu, J. D. Wynn, and A. Y. Cho, "Observation of Reduced Current Thresholds in GaAs/AlGaAs Vertical-Cavity Surface-Emitting Lasers Grown on 4° Off-Orientation (001) GaAs Substrates", *Appl. Phys. Lett.*, vol. 57, pp. 1613-1615, 15 Oct. 1990.

[Weber 1990] J.-P. Weber, K. Malloy, and S. Wang, "Effects of Layer Thickness Variations on Vertical-Cavity Surface-Emitting DBR Semiconductor Lasers", *IEEE Photon. Techn. Lett.*, vol. 2, pp. 162-164, March 1990.

[Yablonovitch 1987] E. Yablonovitch, "Inhibited Spontaneous Emission in Solid-State Physics and Electronics", *Phys. Rev. Lett.*, vol. 58, pp. 2059-2062, 5 18 May 1987.

[Yang 1990] L. Yang, M. C. Wu, K. Tai, T. Tanbun-Ek, and R. A. Logan, "InGaAsP(1.3 μm)/InP Vertical-Cavity Surface-Emitting Laser Grown by Metalorganic Vapor Phase Epitaxy", *Appl. Phys. Lett.*, vol. 56, pp. 889-891, 5 March 1990.

[Yano 1981] M. Yano, H. Imai, K. Hori, and M. Takusagawa, "High Temperature Characteristics of Stripe-Geometry InGaAsP/InP Double-Heterostructure Lasers", *IEEE J. Quantum Electron.*, vol. QE-17, pp. 619-626, May 1981.

[Yoo 1990a] H.-J. Yoo, A. Scherer, J. P. Harbison, L. T. Florez, E. G. Paek, B. P. Van der Gaag, J. R. Hayes, A. Von Lehmen, E. Kapon, and Y.-S. Kwon, "Fabrication of a Two-Dimensional Phased Array of Vertical-Cavity Surface-Emitting Lasers", *Appl. Phys. Lett.*, vol. 56, pp. 1198-1200, 26 March 1990.

[Yoo 1990b] H.-J. Yoo, J. R. Hayes, N. Andreadakis, E. G. Paek, G. K. Chang, J. P. Harbison, L. T. Florez, and Y.-S. Kwon, "Low Series Resistance Vertical-Cavity Front-Surface-Emitting Laser Diode", *Appl. Phys. Lett.*, vol. 56, pp. 1942-1944, 14 May 1990.

[Yoo 1990c] H.-J. Yoo, J. R. Hayes, E. G. Paek, A. Scherer, and Y.-S. Kwon, "Array Mode Analysis of Two-Dimensional Phased Array of Vertical Cavity Surface Emitting Lasers", *IEEE J. Quantum Electron.*, vol. 26, pp. 1039-1051, June 1990.

[Zhang 1990] Z. Zhang and S. Satpathy, "Electromagnetic Wave Propagation in Periodic Structures: Bloch Wave Solution of Maxwell's Equations", *Phys. Rev. Lett.*, vol. 65, pp. 2650-2653, 19 Nov. 1990.

[Zinkiewicz 1989] L. M. Zinkiewicz, T. J. Roth, L. J. Mawst, D. Tran, and D. Botez, "High-Power Vertical-Cavity Surface-Emitting AlGaAs/GaAs Diode Lasers", *Appl. Phys. Lett.*, vol. 54, pp. 1959-1961, 15 May 1989.

Marek Osiński

PROCEEDINGS

SPIE—The International Society for Optical Engineering

Laser Diode Technology and Applications III

Daniel Renner
Chair/Editor

23-25 January 1991
Los Angeles, California

Sponsored and Published by
SPIE—The International Society for Optical Engineering

Volume 1418

SPIE (Society of Photo-Optical Instrumentation Engineers) is a nonprofit society dedicated to the advancement of optical and optoelectronic applied science and technology.

Resonant periodic-gain surface-emitting semiconductor lasers and correlated emission in a ring cavity

M. Y. A. Raja* and S. R. J. Brueck†
Center for High Technology Materials, University of New Mexico, Albuquerque, New Mexico 87131

M. O. Scully and C. Lee
Center for Advanced Studies, Department of Physics and Astronomy, University of New Mexico, Albuquerque, New Mexico 87131
(Received 8 August 1990; revised manuscript received 19 June 1991)

A semiclassical theory of a resonant periodic-gain (half-wave spatially periodic-gain segments) laser in the context of a semiconductor medium is presented using an oversimplified picture. Terms arise in the polarization of this periodic-gain medium that lead to enhanced light-matter interaction, doubling the gain coefficient, and enhancing mode-pulling effects. Discussion of the physical processes is extended to include a comparison with the ring-cavity correlated-emission laser, which also utilizes a periodic-gain medium and exhibits a vanishing phase fluctuation between the degenerate counterpropagating modes. A simple physical picture of radiations from a half-wave-periodic, radiating dipole array illustrates the common mechanism and important relationship between these lasers.

PACS number(s): 42.50.−p, 42.60.Da, 42.55.Px, 42.60.By

I. INTRODUCTION

Recent reports of resonant periodic-gain (RPG) surface-emitting semiconductor lasers [1–4] have created a great deal of interest because of their potential application in optoelectronic integration [5], and two-dimensional arrays [6–8] for optical processing. These laser structures make use of half-wave-periodic, thin sections of gain medium (e.g., GaAs/$Al_{1-x}Ga_xAs$ quantum wells) similar to that proposed for a correlated emission in a ring cavity [9]. The concept of a correlated-emission laser (CEL) was first developed [10] some five years ago. In addition to its intrinsic interest to quantum optics, the CEL holds promise for applications in various areas of fundamental and applied physics, e.g., the laser gyroscope [11,12]. Several detailed investigations of various aspects of a CEL including linear [13–16] and nonlinear theories [17,18] have been reported. In these devices, two laser modes are coherently coupled either by preparing a three-level laser medium in a coherent superposition of upper states [10] or by using a spatially periodic gain medium in a ring cavity [9]. Figure 1(a) shows schematically a periodic gain medium CEL in a ring cavity. The periodic gain medium provides the correlation between the two degenerate counterpropagating waves in the ring cavity by constructive interference. When the light of a mode is partially reflected from a layer of the gain medium, constructive interference is achieved when the phase of counterpropagating mode matches that of the reflected wave. Much of this work, both theoretical [13–18] and experimental [19–24], has been directed towards three-level and two-photon systems [15].

In Fig. 1(b) the structure of a RPG surface-emitting laser with integrated epitaxial mirrors is shown [25–28] where only a few layers have been illustrated to simplify the picture. A standing-wave optical field is shown in registration with the quantum-well gain layers. This results

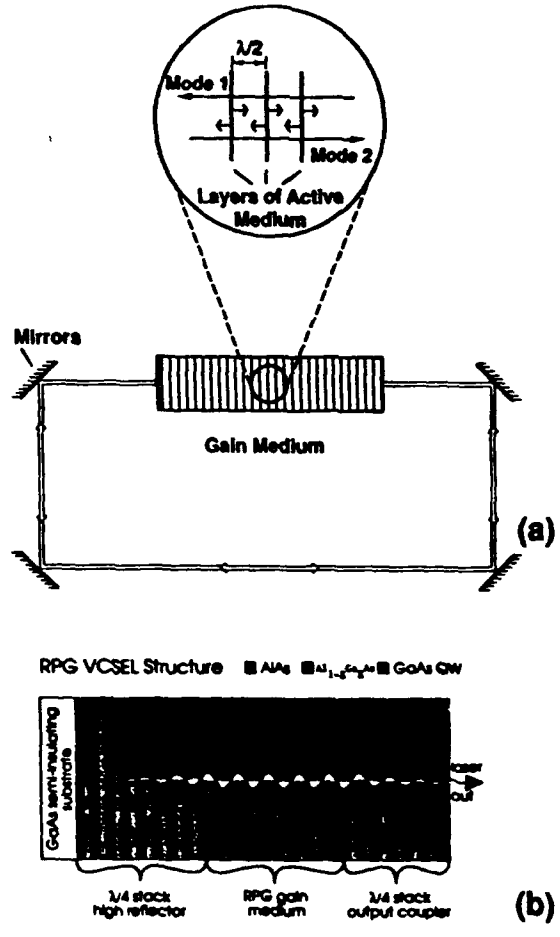

FIG. 1. Schematic representation of (a) a CEL in a ring cavity and (b) a RPG surface-emitting semiconductor laser. Both laser structures incorporate a λ/2 periodic-gain medium. For the CEL system this gain medium is placed in a ring cavity. For the RPG laser, high reflectors (λ/4 stacks of AlAs and $Al_{1-x}Ga_xAs$) are epitaxially grown along with the gain medium forming a high-Q Fabry-Pérot cavity.

 ©1991 The American Physical Society

in an enhanced light-matter interaction. These layers inherently operate in a single longitudinal mode because of the short cavity lengths and, hence, large free-spectral range compared to the gain bandwidth. Although a quantum theory of a CEL based on a spatially periodic gain medium in a ring cavity has been developed [29], the analysis was directed towards noise quenching and the enhanced light-matter interaction aspect (which is a key concept in RPG lasers) was not emphasized.

In this paper, we present an approximate semiclassical theory of RPG lasers (and compare with CEL), treating the valence and conduction bands of semiconductors as a homogeneously broadened two-level system [30] where the Fermi-Dirac distribution for the equilibrium carrier population is used instead of Maxwell-Boltzmann distribution. The RPG semiconductor medium is placed in a Fabry-Pérot cavity such that standing-wave optical-field interaction is enhanced by locating the thin sections of the gain medium (quantum wells) at the antinodes [1–4]. Enhancement in the gain coefficient and contributions to mode-pulling effects due to the RPG structure are evaluated. In RPG medium, amplified spontaneous emission in the directions transverse to the lasing axis is reduced because of the small overlap between optical field and gain sections [3]. It is straightforward to adapt the formalism for any two-level system, instead of two-band semiconductors which in reality are quite complex and require several approximations.

Relationships between a ring cavity CEL and a Fabry-Pérot cavity RPG surface-emitting laser are discussed. Although both lasers make use of spatially half-wave periodic-gain media, they differ in cavity feedback mechanism. In a CEL, the ring cavity does not influence the operating wavelength, rather counterpropagating running waves of the same frequency interact with periodic-gain medium and become correlated [29]. On the other hand, in RPG surface-emitting lasers [1–4], the Fabry-Pérot cavity mode strongly affects the operating frequency and influences [31] the interaction of the optical field with periodic-gain medium. A simple physical model, based on the radiation pattern of a periodic dipole array, demonstrates that, not surprisingly, common physical processes, e.g., quantum interference effects, govern the behavior of both CEL and RPG lasers.

The organization of this paper is as follows: In Sec. II we develop a semiclassical theory of RPG surface-emitting laser, where gain coefficient, mode pulling and pushing, and saturation terms are derived following the method of Ref. [32]. In Sec. III, the basic physical processes resulting from light-matter interactions in RPG surface-emitting lasers and CEL in a ring cavity are discussed. Common features and differences between RPG and CEL structure are identified. The relationships between these laser systems are further illuminated by considering the radiation pattern of a $\lambda/2$-spaced dipole array in Sec. IV. Finally, in Sec. V, concluding remarks summarize the present status of RPG lasers in the context of semiconductor-based CEL in a ring cavity.

II. SEMICLASSICAL THEORY OF RPG LASER

RPG surface-emitting semiconductor lasers were proposed [1] and demonstrated [1–4] recently. Progress has been rapid, and efficient cw operation under optical pumping has been achieved [26,27]. A schematic of the RPG structure is shown in Fig. 1(b); for details of various configurations Refs. [1–4, 25,26] should be consulted. In the following, an oversimplified semiclassical theory is developed using the density-matrix formalism.

The density-matrix formalism [32], developed originally for a two-level system, has been applied by several authors [30,33–37] to the analysis of the linear and nonlinear contributions to the optical gain in semiconductor lasers. The optical properties of a semiconductor are mainly determined by the conduction and the uppermost valence bands. In the case of quantum-well structures, the subband transitions with the $\Delta n = 0$ selection rule dominate. Physically, the dominant optical transitions are those which involve an electron-hole pair whose wave functions have maximum spatial overlap, i.e., an electron in the conduction subband and holes in the valence subbands having the same quantum numbers. This simplified picture suggests an analogy with a two-level atomic system. A theoretical derivation, as well as a geometrical picture of an equivalent electronic dipole moment in a direct band-gap bulk semiconductor, has been given [35]. The Bloch functions for electrons in the conduction band and holes in the valence bands were used for calculation of dipole matrix elements. At band edges, the periodic parts of the electron and hole Bloch functions have S-like and P-like symmetries, respectively, and light- and heavy-hole wave functions are orthogonal to each other. For quantum wells, the band gap increases and the electron-hole interaction is modified as a result of spatial localization. The dipole strength increases and the degeneracy between light- and heavy-hole subbands at $K = 0$ is lifted. For $GaAs/Al_{1-x}Ga_xAs$ quantum wells, the electron–heavy-hole band gap is smaller than that of the electron-light hole.

Here, density-matrix equations for a semiconductor, similar to those developed by Agrawal [30] and Kazarinov, Henry, and Logan [34], are used to determine the effects of the RPG spatial structure on the linear gain. The analysis begins with the relations between the medium polarization (driven by the electric fields) and the off-diagonal density-matrix elements and proceeds to calculate the polarization of the semiconductor medium inside a Fabry-Pérot cavity of total length L (along the z axis) following the procedure described in Ref. [32]. Then, the linear gain and frequency determining relations from the self-consistent laser theory are used to show the contribution of additional terms arising from the spatial periodicity of the medium.

As pointed out above, in the density-matrix approach for semiconductor lasers, the conduction-band state $|c\rangle$ and the corresponding valence-band state $|v\rangle$ participating in the band-to-band transitions are modeled as a "two-level system" analogous to that of Ref. [32]. The dipole moment between conduction and valence bands is denoted by d_{cv} and an explicit calculation is carried out following [35] except for the quantum confinement effects due to quantum wells. In a semiconductor medium, the carrier population follows Fermi-Dirac statistics (for both the electron and hole populations in their respective bands), as contrasted to the two-level atomic systems

obeying Maxwell-Boltzmann statistics. Coulomb-effects, carrier-carrier scattering, and phonon interaction all play an important role in establishing the Fermi-Dirac distribution on a subpicosecond time scale and medium behaves as a homogeneously broadened system [38].

The polarization $P(z,t)$ caused by the field $E(z,t)$ in a medium along the z axis can be obtained by taking the trace of the induced dipole moment d_{cv} with the density matrix and summing over all possible band-to-band transitions ω_t,

$$P(z,t)=\sum_{\omega_t}[d_{vc}\rho_{cv}(z,t)+d_{cv}\rho_{vc}(z,t)] \tag{1}$$

or

$$P(z,t)=\int d'D(\omega_t)[\rho_{cv}(z,t)+\rho_{vc}(z,t)]d\omega_t \tag{2}$$

where $d_{cv}=d_{vc}=d'$ is taken as real and $D(\omega_t)$ is the density of states per unit volume; ρ_{cv} and ρ_{vc} are the off-diagonal elements of the density matrix. The polarization in the medium in a Fabry-Pérot cavity can also be expanded in terms of complex amplitudes and the cavity eigenmodes [32],

$$P(z,t)=\sum_n \frac{P_n(t)}{2}\exp[-i(\nu_n t+\phi_n)]U_n(z)+\text{c.c.}\ , \tag{3}$$

where $P_n(t)$ is the complex amplitude, ν_n the frequency, ϕ_n the phase, and $U_n(z)$ the cavity mode profile for the nth-order mode of the empty resonator. The complex amplitude $P_n(t)$ is obtained from Eqs. (2) and (3) in the rotating-wave approximation [32,37],

$$P_n(t)=\frac{2}{\mathcal{L}}\exp[i(\nu_n t+\phi_n)] \times\int_0^L\left[\int D(\omega_t)d'\rho_{cv}(z,t)d\omega_t\right]U_n^*(z)dz\ , \tag{4}$$

where

$$\mathcal{L}\equiv\int_0^L|U_n(z)|^2dz$$

is a normalization factor.

To obtain $P_n(t)$, the off-diagonal element of the density matrix $\rho_{cv}(z,t)$ is evaluated by solving the formal density equations for a two-level or a two-band, i.e., for a semiconductor laser [30,33–37] under steady-state conditions. We take a special case of a semiconductor medium from which RPG structure can be fabricated relatively easily. The density-matrix equations for a semiconductor laser are used from Refs. [30,34], with a simplified notation for the components of $\rho(z,t)$,

$$\dot\rho_{cc}=-\gamma_c(\rho_{cc}-\bar\rho_{cc})-\frac{i}{\hbar}(V_{cv}\rho_{vc}-V_{vc}\rho_{cv})\ , \tag{5}$$

$$\dot\rho_{vv}=-\gamma_v(\rho_{vv}-\bar\rho_{vv})+\frac{i}{\hbar}(V_{cv}\rho_{vc}-V_{vc}\rho_{cv})\ , \tag{6}$$

$$\dot\rho_{cv}=-(\gamma+i\omega_t)\rho_{cv}+\frac{i}{\hbar}V_{cv}(\rho_{cc}-\rho_{vv})\ , \tag{7}$$

and

$$\dot\rho_{vc}=\dot\rho_{cv}^* \tag{8}$$

where the dot means the time derivative and where the light-matter interaction is contained in the term $V_{cv}=V_{vc}^*$, γ_c and γ_v are intraband energy relaxation rates for the conduction and valence band, respectively, and are connected to T_1 [32]. Here, γ is the polarization relaxation rate ($\gamma^{-1}=T_2$ where T_2 is the dipole dephasing time) and ω_t is the transition frequency. $\bar\rho_{cc}$ and $\bar\rho_{vv}$ are the occupation probabilities of electrons and holes in quasithermal equilibrium and are determined by quasi-Fermi levels of the conduction and valence bands, respectively. The quasi-Fermi levels result from the pump source, e.g., optical or electrical pumping. Spontaneous emission is not included in this simple model. The light-matter interaction term can be written explicitly as

$$V_{cv}=-\frac{d'}{2}\sum_n E_n(t)\exp[-i(\nu_n t+\phi_n)]U_n(z)+\text{c.c.}, \tag{9}$$

where the summation runs over all of the optical modes.

In order to calculate the first- and third-order terms of the induced polarization, Eqs. (5)–(8) are solved (see Appendix) using slowly varying amplitude approximation, leading to rate equation approximation. Contributions to the linear gain coefficient α, saturation parameter β, and frequency pulling and pushing terms are derived using the explicit expression for polarization in the self-consistency equations [32]. For a single longitudinal mode (RPG lasers inherently operate at a single longitudinal mode because of large mode spacing in the short cavity) including only up to third-order polarization terms, we find

$$\dot E=\frac{-\nu}{2Q}E+\alpha\left[1-\frac{\beta}{\alpha}E^2\right]E\ , \tag{10a}$$

$$\nu+\dot\phi=\Omega+\frac{\alpha(\omega_t-\nu)}{\gamma}\left[1-\frac{\beta}{\alpha}E^2\right], \tag{10b}$$

where Ω and Q denote the passive mode and "Q" of the resonator. Here,

$$\alpha=\alpha_0\left[1-\frac{\sin(k_nL_z)}{k_nL_z}\cos\left[2\varphi_n+(m-1)\frac{\pi k_n}{k_r}\right]\times\frac{\sin(m\pi k_n/k_r)}{m\sin(\pi k_n/k_r)}\right] \tag{11a}$$

and, where α_0 depends on quasi-Fermi levels $\bar\rho_{cc}$ and $\bar\rho_{vv}$ and polarization relaxation rate γ [see Appendix, Eq. (A17b)],

$$\beta=\frac{3}{8}\frac{d'^2\gamma}{\hbar^2}\left[\frac{\gamma_c+\gamma_v}{\gamma_c\gamma_v}\right]\frac{\alpha_0}{(\omega_t-\nu_n)^2+\gamma^2}\left[1-\frac{4}{3}\frac{\sin(k_nL_z)}{k_nL_z}\cos\left[2\varphi_n+(m-1)\frac{\pi k_n}{k_r}\right]\frac{\sin(m\pi k_n/k_r)}{m\sin(\pi k_n/k_r)}\right.$$
$$\left.+\frac{1}{3}\frac{\sin(2k_nL_z)}{2k_nL_z}\cos\left[4\varphi_n+2\pi(m-1)\frac{k_n}{k_r}\right]\frac{\sin(2m\pi k_n/k_r)}{m\sin(\pi k_n/k_r)}\right]. \tag{11b}$$

β, the saturation parameter, depends both on polarization relaxation γ and intraband relaxation rates γ_c and γ_v, and through α_0 it also depends on quasi-Fermi levels which take into account interband relaxations. Typically, large values of γ, 10^{13}/sec [34,36], allow the use of the rate-equation approximation. In the above expressions, $k_n = n\pi/L$ with n (integer) that the number of half wavelengths in the unpumped cavity mode and L the total cavity length, L_z ($\ll\lambda$) is the thickness of an individual quantum-well gain section, $k_r = 2\pi/\lambda_r$ where λ_r is the resonant wavelength set by the physical spacing of the quantum wells, m is the total number of quantum wells, and $\phi_n = k_n a_0$ where a_0 is the spacing of the first quantum well from the $z=0$ end of the resonator. Here, α_0 is the usual gain coefficient (scaled appropriately for the thin-gain sections) as given in the Appendix [cf. Eq. (A17b)]. These equations show a resonance behavior, the term $\{\sin(m\pi k_n/k_r)/[m\sin(\pi k_n/k_r)]\}$ is just $(-1)^{m+1}$ for $k_n = k_r$ and is of order $1/m$ for $k_n \neq k_r$, the width of the resonance scales inversely as the number of quantum wells. This behavior has been discussed previously for RPG lasers [3]. Additional insight can be gained into these equations by considering the resonance case $n=m$, $k_n = k_r$, and $\phi_n = \pi/2$. Under these conditions, $\cos[2\varphi_n + (m-1)\pi k_n/k_r] \rightarrow (-1)^m$ and Eqs. (11) simplify to

$$\alpha = \alpha_0 \left[1 + \frac{\sin(k_n L_z)}{k_n L_z} \right] \tag{12a}$$

and

$$\beta = \frac{3}{8}\frac{d'^2\gamma}{\hbar^2}\left[\frac{\gamma_c+\gamma_v}{\gamma_c\gamma_v}\right]\frac{\alpha_0}{(\omega_t-\nu)^2+\gamma^2} \times \left[1+\frac{4}{3}\frac{\sin(k_n L_z)}{k_n L_z}+\frac{1}{3}\frac{\sin(2k_n L_z)}{2k_n L_z}\right]. \tag{12b}$$

For $k_n L_z \ll 1$, which is the case for quantum-well structures, the gain is doubled on resonance and the saturation parameter is increased by a factor of $\frac{4}{3}$.

For an insight into the modal frequency behavior, we neglect $\dot{\phi}$, i.e., ignore dispersion effects [32,36], and write the equation

$$\nu \simeq \Omega + \frac{(\omega_t - \nu)}{\gamma}(\alpha - \beta E^2). \tag{13}$$

When the term βE^2 is small, we find that mode pulling is increased for RPG lasers (compared to the conventional uniform gain medium lasers) because of gain enhancement.

Equation (13) can be recast as

$$\nu = \frac{\Omega + S\omega_t}{1+S}, \tag{14}$$

where

$$S \equiv \frac{\alpha - \beta E^2}{\gamma}. \tag{15}$$

S is the stability factor. From Eq. (14) it is seen that the laser frequency ν is a weighted average of passive cavity mode frequency Ω and medium frequency ω_t with weighting factors unity and S, respectively. For $S \ll 1$ the laser frequency approaches Ω, and with $S \gg 1$ the operating frequency is "pulled" towards the medium frequency, especially in the case of a poor cavity Q, $\nu \approx \omega_t$.

In the steady-state case, Eq. (10a) gives

$$\alpha - \beta E^2 = \frac{\nu}{2Q}, \tag{16a}$$

which leads to a stability factor

$$S = \nu/2Q\gamma \tag{16b}$$

and

$$\nu = \frac{\gamma\Omega + (\nu/2Q)\omega_t}{\gamma + \nu/2Q} \tag{17}$$

which is the same as for the uniform gain medium lasers [32]. From this result, it is apparent that for low-Q cavities, i.e., $\nu/2Q \gg \gamma$, the operating frequency ν approaches ω_t, the medium frequency, and in case of high-Q cavities $\nu/2Q \ll \gamma$, the laser frequency ν approaches Ω, the cavity mode.

III. PHYSICAL PROCESSES IN RPG AND CEL LASERS

In this section, the fundamental processes resulting from enhanced light-matter interaction in RPG-based surface-emitting lasers [1–4,25–28] and a ring-cavity CEL [9,29] are discussed. The theory of correlated emission in the periodic-gain medium in a ring cavity was developed by Krause and Scully [29] using a fully quantum-mechanical treatment, where various coefficients for linear gain (α_{ij}) and nonlinear terms ($\beta_{ij;km}$) were derived. A complete quantum-mechanical formulation of the CEL problem was most appropriate to analyze the correlation of spontaneous emission which arises from the cross coupling of counterpropagating modes in the periodic-gain medium of a ring cavity. On the other hand, while considering a RPG medium in a Fabry-Pérot cavity, the electromagnetic fields can be described classically and a semiclassical laser theory described in Sec. II is sufficient to explain the results and predict the behavior.

Since both the ring-cavity CEL [9] and RPG surface-emitting [1–4] lasers (in a Fabry-Pérot resonator) utilize half-wave spatially periodic-gain medium, it is worthwhile to compare the fundamental principles involved in noise quenching via correlated spontaneous emission, and enhanced gain and saturation coefficients. The fundamental linewidth of laser radiation is due to spontaneous emission events in the lasing medium. In an atomic medium laser, this leads to the well-known Schawlow-Townes linewidth. In semiconductor devices, the strong coupling between the gain and the electronic contribution to the refractive index gives rise to substantial increases in this linewidth [39–41]. The linewidth in a RPG surface-emitting laser is as yet an open question. In the present discussion, we treat the problem as if it were a striated gain medium of independent oscillators and quote the results from the CEL calculations [29] for the diffusion coefficient of the relative phase angle $D(\theta)$

between the two degenerate counterpropagating modes in the ring cavity:

$$D(\theta)=(4\rho^2)^{-1}(\alpha_{11}+\alpha_{22}-2\alpha_{11}\cos\psi) -\tfrac{1}{8}(\beta_{11;11}+\beta_{22;22}+6\beta_{12;12}-8\beta_{11;22}\cos 2\psi)\ , \quad (18)$$

where α_{ij} and $\beta_{ij;km}$ are gain and saturation coefficients, ρ denotes the average number of photons in each mode, and $\psi=\theta+(\nu_1-\nu_2)t$ where the subscripts refer to the two counterpropagating modes in the ring cavity.

In order to achieve noise quenching between the two modes, the diffusion coefficient $D(\theta)$ should vanish. This can be achieved when all gain and saturation coefficients become equal, i.e., $\alpha_{11}=\alpha_{22}=\alpha_{12}\equiv\alpha$ and $\beta_{11;11}=\beta_{22;11}=\beta_{12;12}=\beta_{11;22}\equiv\beta$. Then the diffusion coefficient will vanish provided $\psi=0$ or nonlinear saturation effects lead to $D(\theta)=0$. The equality of various coefficients α_{ij} and $\beta_{ij;km}$ can be achieved by interference of two counterpropagating modes in a ring cavity at the thin sections of a periodic-gain medium.

To show the role of periodic-gain medium, we reproduce the expressions for α_{ij} and $\beta_{ij;km}$ from Ref. [29] in original notation:

$$\alpha_{ij}\equiv\alpha_0\int_{-l/2}^{l/2} n(z)u_i(z)u_j^*(z)dz \quad (19)$$

and

$$\beta_{ij;km}\equiv\beta_0\int_{-l/2}^{l/2} n(z)u_i(z)u_j(z)u_k^*(z)u_m^*(z)dz\ , \quad (20)$$

where $u_l(z)$ are normal mode functions and $n(z)$ is linear density of gain medium. For traveling waves in a ring cavity the normal mode functions can be expressed as

$$u_1(z)\approx\exp(ikz),\quad u_2(z)\approx\exp(-ikz)\ . \quad (21)$$

It is easy to show that with spatially periodic $n(z)$ with $z=j\pi/k$, i.e., $(j\lambda/2)$ periodicity with j an integer, the diffusion coefficient vanishes, whereas for a uniform gain medium with $n(z)=n_0$ (constant) it does not. It is important to note that the ring cavity does not influence the lasing frequency; rather the periodic-gain medium provides a constructive interference between the propagating modes.

On the other hand, in RPG surface-emitting lasers the Fabry-Pérot cavity plays an important role [31]. The Fabry-Pérot cavity formed by the integrated multilayer high reflectors around a 4–5-μm-thick RPG semiconductor provides a standing-wave optical field. The antinodes of the standing-wave optical field must be in registration with the thin sections of gain medium (i.e., quantum wells) for an optimal interaction between the light and active material. Also, the short cavity length and consequent large longitudinal mode spacing leads to single longitudinal mode operation of such microlasers. As seen from Eqs. (12a) and (12b) in Sec. II, additional terms arise in both the linear gain and nonlinear saturation coefficients as a result of the $\lambda/2$ periodic medium. The filling factor (L_z/λ_r) in Eq. (A17b) in the Appendix simply indicates that the gain is proportional to the cumulative thickness of the active medium. Compared to uniform gain medium of the same total length, RPG medium can provide twice the gain but it also saturates at lower intensities. It is interesting to note that the linear gain and saturation coefficients, i.e., Eqs. (12a) and (12b) can also be derived from Eqs. (19) and (20) simply using $u_j(z)$ as Fabry-Pérot mode functions for $i=j$, etc.

For the frequency behavior of RPG lasers, Eq. (13) of Sec. II predicts strong mode-pulling effects which should lead to a stable frequency operation. The nonlinear saturation term, however, counteracts at high intensities and reduces the stability factor given in Eq. (15). It is interesting to note that the steady-state modal frequency behavior of the RPG laser under saturation conditions approaches that of a uniform medium laser. However, under pulsed and modulated conditions, RPG would exhibit highly stable frequency operation.

IV. RADIATION PATTERN OF A PERIODIC DIPOLE ARRAY

Insight into the common physics underlying the behavior of both RPG and CEL lasers can be gained by considering the radiation patterns associated with a three-dimensional periodic radiating dipole array. Assume, as in Fig. 2, an array of dipole oscillators with equal dipole moments, $p=pe_3$, aligned in the z direction and located by the position vectors

$$\mathbf{r}=\sum_j m_j a_j e_j\ , \quad (22)$$

where the a_j are the unit-cell distances in the e_j direc-

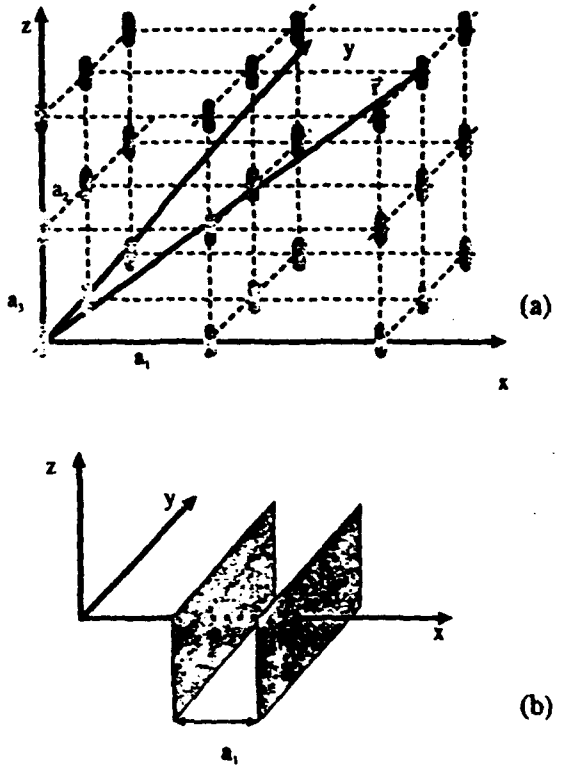

FIG. 2. A periodic dipole array. All of the dipoles are oriented in the z direction and spaced by a_1, a_2, and a_3 along the coordinate axes, respectively.

tions and m_j are integers. The radiated power from this array is simply given by [42]

$$S = S_0 (n_1 n_2 n_3)^2 \cos^2\theta \left[\prod_{j=1}^{3} \left| \frac{\sin(n_j \gamma_j/2)}{n_j \sin(\gamma_j/2)} \right|^2 \right], \quad (23)$$

where

$$\gamma_1 = k a_1 \sin(\theta)\cos(\varphi) + \beta_1 ,$$

$$\gamma_2 = k a_2 \sin(\theta)\sin(\varphi) + \beta_2 ,$$

$$\gamma_3 = k a_3 \cos(\theta) + \beta_3 ,$$

and $k = \omega/c$, n_j is the number of oscillators in the jth direction, β_j is the phase shift between adjacent oscillators in the jth direction, and $S_0 = (p/2\pi\epsilon_0)^2$ is the radiation intensity of a single oscillator. Note the similarity between the structure of this equation and the equation for the gain in the RPG structure derived earlier [cf. Eq. (11a)].

For stimulated emission, the phase relationships between these oscillators are simply set by the distances a_j and the propagation direction of the initial plane wave. For an incident wave propagating in the xy plane at an angle of ψ to the x axis and polarized in the z direction, the phase shifts are $\beta_1 = k a_1 \cos(\psi)$, $\beta_2 = k a_2 \sin(\psi)$, and $\beta_3 = 0$. Thus, in the equatorial xy plane the expression for the radiated power simplifies to

$$S = (n_1 n_2 n_3)^2 S_0 \frac{\sin^2(n_1\gamma_1/2)}{n_1^2 \sin^2(\gamma_1/2)} \frac{\sin^2(n_2\gamma_2/2)}{n_2^2 \sin^2(\gamma_2/2)} \quad (24)$$

with

$$\gamma_1 = k a_1 [\cos(\varphi) - \cos(\psi)]$$

and

$$\gamma_2 = k a_2 [\sin(\varphi) - \sin(\psi)] .$$

Figure 3 shows the angular distribution of the radiation from an ensemble of $32(x)\times 100(y)\times 100(z)$ oscillators with phases determined by an incident wave traveling along the x axis from the left ($\psi = 0$) with $a_2 = a_3 = 1/(40k)$; the values for $k a_1$ are shown. These angular distributions have been normalized by $[(n_1 n_2 n_3)^2 S_0]^{-1}$, i.e., the radiation in the forward direction as a result of the coherent addition of the fields from all the dipoles, is $(n_1 n_2 n_3)^2$ more intense than the radiation from a single dipole. The important point to note is that the radiation intensity in the backward direction is equal to that in the forward direction for a half-wave periodic structure (top). Deviations from this periodicity lead to a suppression of the backward radiation. Of course, the sensitivity of the backward radiation to the periodicity, or equivalently the wavelength, scales inversely as n_1. For increased n_2 the angular spread of the lobes is reduced, but the intensities in the forward and backward directions are unchanged. The radiation pattern in the equatorial plane is independent of n_3.

This backward radiation is a manifestation of the factor-of-2 enhancement of the gain in the RPG structure. The radiated fields add coherently to both forward and backward waves, i.e., they couple optimally to a standing-wave pattern, even in the absence of a Fabry-Pérot cavity. This also results in the elimination of spontaneous emission fluctuations in the phase between the two counterpropagating modes in a CCEL ring cavity. A photon spontaneously emitted into, say, the forward direction gives rise to amplified spontaneous emission and fluctuations in both the amplitude and phase of the radiation in the forward and backward propagating modes become correlated. On the $\lambda/2$ resonance, precisely the same fluctuation occurs for the counterpropagating

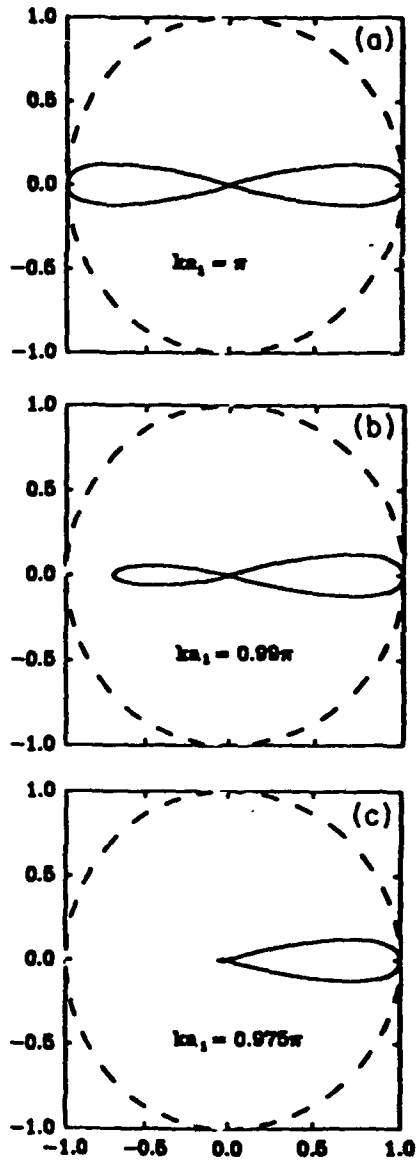

FIG. 3. Angular radiation pattern in the equitorial xy plane for a periodic array of $32(x)\times 100(y)\times 100(z)$ dipoles. The dipoles are closely spaced ($\lambda/40$) in the y and z directions. The spacing in the x direction is given in each segment. The relative phases have been adjusted to correspond to excitation by a plane wave incident from the x direction. Note that for a $\lambda/2$ spacing, (a) the radiation pattern is twofold symmetric with equal intensities in both the forward and backward directions. Away from the $\lambda/2$ condition, (b) and (c), the backward radiation decreases dramatically. This symmetry is responsible both for the suppression of noise fluctuations in a CEL and the gain enhancement in RPG lasers.

waves as a result of the bidirectional radiation (and gain) pattern. Off-resonance, and in particular for a homogeneous gain medium, this relationship is not preserved and the amplified spontaneous emission phase fluctuations for counterpropagating waves are uncorrelated.

V. CONCLUDING REMARKS

Before concluding, we summarize the present experimental status of RPG lasers and initial trial experiments using RPG medium in a ring cavity. Since the first demonstration of optically pumped RPG lasers [1–4], a great deal of progress has been made and cw operation of these laser structures has been achieved. Recently, high-efficiency (>45%), narrow-linewidth (~0.025 nm) cw lasing at room temperature has been demonstrated both in the GaAs/$Al_{1-x}Ga_xAs$- [26,27] and $In_{1-y}Ga_yAs/Al_{1-x}Ga_xAs$-based RPG structures. The $In_{1-y}Ga_yAs/Al_{1-x}Ga_xAs$ material system is very promising for the ring-cavity CEL, because the GaAs substrate is transparent at the lasing wavelengths. RPG structures with 20-period 8-nm-thick $In_{0.2}Ga_{0.8}As$ quantum wells and $Al_{0.2}Ga_{0.8}As$ half-wave spacers sandwiched between $Al_{0.25}Ga_{0.75}As$/AlAs integrated multilayer high-reflectors, all fabricated in a single metal-organic chemical-vapor deposition growth cycle, have delivered ~40-mW cw power at ~930–940 nm at room temperature. Single-ended power efficiencies >43% for optical pumping at 740 nm have been demonstrated. Based on these results, we have grown RPG structures with 40 and 60 periods of 8-nm-thick $In_{0.2}Ga_{0.8}As$ quantum wells and $Al_{0.2}Ga_{0.8}As$ half-wave spacers on GaAs substrates with both sides polished. Initial photoluminescence studies show intense radiation centered around ~930 nm with an anisotropic distribution in a narrow angle rather than a uniform photoluminescence (PL) from a Lambertian source. This directionality of amplified spontaneous emission is consistent with the calculations in Sec. IV. However, to use these $In_{1-y}Ga_yAs$ structures in CEL ring cavity, an antireflection coating (reflectivity ~0.1%) is required because of high Fresnel reflectivity of $Al_{1-x}Ga_xAs$ and GaAs surfaces (~30%) and it is very difficult to use these high-index materials ($n=3.40$–3.64) at very large Brewster's angles.

In conclusion, we have developed a semiclassical theory for resonant periodic gain lasers using the particular case of the surface-emitting semiconductor lasers. The theory based on a simple two-band model analogous to the two-level atomic system predicts the gain enhancement and frequency selectivity in the resonant periodic-gain laser. The common physics of the resonant periodic-gain medium and correlated emission ring cavity laser is also discussed.

ACKNOWLEDGMENTS

We would like to thank Dr. M. S. Zubairy of the Electronics Department, Quaid-i-Azam University, Islamabad, Pakistan, and Dr. C. F. Schaus and Dr. J. G. McInerney of the Center for High Technology Materials, University of New Mexico, for useful discussions. The CHTM portion of this work was partially supported by the U.S. Air Force Office of Scientific Research and the CAS portion by the Office of Naval Research.

APPENDIX

The solution of the density-matrix equations is carried out using a perturbative procedure [32], starting from a formal integration of Eq. (7) over the time interval from $-\infty$ to t (which includes all the contributions to the polarization up to the time t). The analytic evaluation is carried out in the rate equation approximation [32] which makes the assumptions that the population difference $(\rho_{cc}-\rho_{vv})$ and other quantities ϕ_n, d', and $E_n(t)$ do not vary appreciably in a time period γ^{-1} (dipole dephasing time T_2). For simplification, only a single-mode interaction is considered such that only the nth mode terms are used from Eq. (9) of Sec. II. The following expression is obtained for ρ_{cv}:

$$\rho_{cv}=\frac{-id'E_n(t)}{2\hbar}(\rho_{cc}-\rho_{vv}) \times\frac{\exp[-i(\nu_n t+\phi_n)]}{\gamma+i(\omega_t-\nu_n)}U_n(z)\,. \tag{A1}$$

Substitution of Eq. (A1) for ρ_{cv}, and using $\rho_{vc}=\rho_{cv}^*$ and $V_{cv}=V_{vc}^*$ in Eqs. (5) and (6) yields

$$\dot{\rho}_{cc}=-\gamma_c(\rho_{cc}-\bar{\rho}_{cc})-R(\rho_{cc}-\rho_{vv})\,, \tag{A2}$$

$$\dot{\rho}_{vv}=-\gamma_v(\rho_{vv}-\bar{\rho}_{vv})+R(\rho_{cc}-\rho_{vv}), \tag{A3}$$

where

$$R=\frac{d'^2}{2\hbar^2}E_n^2|U_n(z)|^2\frac{\gamma}{\gamma^2+(\omega_t-\nu_n)^2}\,. \tag{A4}$$

In a steady-state case the rate equations for carriers, i.e., ρ_{cc} and ρ_{vv} for electrons and holes, respectively, Eqs. (A2) and (A3) give

$$\rho_{cc}-\rho_{vv}=\frac{\bar{\rho}_{cc}-\bar{\rho}_{vv}}{1+R/R_s}\,, \tag{A5}$$

where

$$R_s=\gamma_c\gamma_v/(\gamma_c+\gamma_v)\,.$$

Substituting this in Eq. (A1) and then the resulting expression for ρ_{cv} into Eq. (4) leads to

$$P_n(t)=(-i/\mathcal{L}\hbar)\int_0^L\int\frac{D(\omega_t)d'^2E_n(t)}{\gamma+i(\omega_t-\nu_n)} \times\frac{(\bar{\rho}_{cc}-\bar{\rho}_{vv}}{1+R/R_s}d\omega_t|U_n(z)|^2dz\,. \tag{A6}$$

An exact evaluation of the integral over ω_t is difficult because R also involves terms containing $(\omega_t-\nu_n)$. However a simplification is possible from the consideration that only those transition frequencies are effective in the polarization which are nearly resonant with the optical mode ν_n in the cavity. This amounts to including a modified density of states in the interval $\Delta\omega$ of interest; so $D(\omega_t)\Delta\omega$ is replaced with $D(\omega)$ (number of states in the spectral interval $\Delta\omega$) resulting in

$$P_n(t)=-\frac{(\omega_l-\nu_n)+i\gamma}{(\omega_l-\nu_n)^2+\gamma^2}\frac{D(\omega)}{\mathcal{L}\hbar}\times\int_0^L d'^2E_n(t)\frac{\bar{\rho}_{cc}-\bar{\rho}_{vv}}{1+R/R_s}|U_n(z)|^2dz\ . \tag{A7}$$

This relation is the same as that found for gas lasers [32]. To evaluate the integral in (A7) the usual procedure is to expand $(1+R/R_s)^{-1}$ under the assumption that $E_n(t)$, the field amplitude, is small, and hence R is much smaller than the saturation parameter R_s. Therefore, we give here only up to third-order polarization terms explicitly,

$$P_n(t)=-\frac{1}{(\omega_l-\nu_n)-i\gamma}\frac{D(\omega)}{\mathcal{L}\hbar}\left[\int_0^L d'^2E_n(t)(\bar{\rho}_{cc}-\bar{\rho}_{vv})|U_n(z)|^2dz-\int_0^L d'^2E_n(t)\frac{(\bar{\rho}_{cc}-\bar{\rho}_{vv})R}{R_s}|U_n(z)|^2dz\right]+\cdots\ ,$$

where the ellipsis represents higher-order terms, or ignoring higher-order terms,

$$P_n(t)\approx-\frac{1}{(\omega_l-\nu_n)-i\gamma}\frac{D(\omega)}{\mathcal{L}\hbar}(I_1+I_2)\ . \tag{A8}$$

Consider the first integral I_1 in Eq. (A8). In the RPG medium, thin-gain sections (quantum wells) are spaced at half-wave intervals. The Fabry-Pérot cavity modes are represented by $U_n(z)=\sin k_n z$ where $k_n=n\pi/L$. Since only the quantum-well region provides the gain, i.e., $(\bar{\rho}_{cc}-\bar{\rho}_{vv})\neq 0$ only in these regions, the integral over the cavity length can be divided into n integrals each extending over the quantum-well thickness in each half-wave section with appropriate phase correlation between integrals. Thus,

$$I_1=d'^2E_n(t)\int_0^L\sin^2k_nz\left\{\sum_1^m\left[u_s\left[a_0+\frac{\pi(m-1)}{k_r}-\frac{L_z}{2}\right]-u_s\left[a_0+\frac{\pi(m-1)}{k_r}+\frac{L_z}{2}\right]\right]\right\}dz\ . \tag{A9}$$

Here u_s are unit step functions, $k_r=2\pi/\lambda_r$ where λ_r is the half-wave resonance set by the structure, a_0 is the distance from the edge of the cavity ($z=0$) to the center of the first quantum well, and m is the number of quantum wells of thickness L_z.

The transition dipole d' is approximately constant over the quantum-well dimension and has been pulled out of the integral. After some algebra, an analytic expression is derived for I_1, viz.,

$$I_1=d'^2E_n^2(t)(\bar{\rho}_{cc}-\bar{\rho}_{vv})\frac{mL_z}{2}\left[1-\frac{\sin k_nL_z}{k_nL_z}\cos\left[2\varphi_n+(m-1)\frac{\pi k_n}{k_r}\right]\frac{\sin(m\pi k_n/k_r)}{m\sin(\pi k_n/k_r)}\right]\ , \tag{A10}$$

where $\varphi_n=k_na_0$.

The second integral I_2 is similarly evaluated using the value of R from Eq. (A4),

$$I_2=\frac{md'^4E_n(t)}{2\hbar^2R_s}(\bar{\rho}_{cc}-\bar{\rho}_{vv})\frac{\gamma}{(\omega_l-\nu_n)^2+\gamma^2}\frac{3L_z}{8}\left[1-\frac{4}{3}\frac{\sin(k_nL_z)}{k_nL_z}\cos\left[2\varphi_n+(m-1)\frac{\pi k_n}{k_r}\right]\frac{\sin(m\pi k_n/k_r)}{m\sin(\pi k_n/k_r)}\right.$$
$$\left.+\frac{1}{3}\frac{\sin(2k_nL_z)}{2k_nL_z}\cos\left[4\varphi_n+2\pi(m-1)\frac{k_n}{k_r}\right]\frac{\sin(2m\pi k_n/k_r)}{m\sin(2\pi k_n/k_r)}\right]\ . \tag{A11}$$

Substituting Eqs. (A10) and (A11) for integral terms in Eq. (A8), the complex polarization $P_n(t)$ can be written up to third order as

$$P_n(t)=P_n^{(1)}(t)+P_n^{(3)}(t)\ , \tag{A12}$$

where the superscripts refer to the dependence of $E_n(t)$. Gain and lasing frequency are determined using the self-consistency equations from the semiclassical laser theory [32], namely,

$$\dot{E}_n+\frac{\nu}{2Q_n}E_n=\frac{-\nu}{2\epsilon_0}\mathrm{Im}[P_n(t)]\ , \tag{A13}$$

$$\nu_n+\dot{\phi}_n=\Omega_n-\frac{\nu}{2\epsilon_0E_n}\mathrm{Re}[P_n(t)]\ , \tag{A14}$$

where Q_n is the cavity Q and Ω_n is the nth mode of the cold cavity. Using the explicit expression for $P_n(t)$ in Eqs. (A13) and (A14) we find for the single-mode case,

$$\dot{E}=\frac{-\nu}{2Q}E+(\alpha-\beta E^2)E\ , \tag{A15}$$

$$\nu+\dot{\phi}=\Omega+\frac{\omega_l-\nu}{\gamma}(\alpha-\beta E^2)\ , \tag{A16}$$

where

$$\alpha=\alpha_0\left[1-\frac{\sin(k_n L_z)}{k_n L_z}\cos\left[2\varphi_n+(m-1)\frac{\pi k_n}{k_R}\right]\times\frac{\sin(m\pi k_n/k_r)}{m\sin(\pi k_n/k_r)}\right] \tag{A17a}$$

with

$$\alpha_0=\frac{\nu d'^2}{2\epsilon_0\hbar}\left[\frac{\gamma}{(\omega_t-\nu)^2+\gamma^2}\right]D(\omega)(\bar{\rho}_{cc}-\bar{\rho}_{vv})\left[\frac{L_z}{\lambda_r}\right] \tag{A17b}$$

and

$$\beta=\frac{3}{8}\left[\frac{d'^2\gamma}{2\hbar}\right]\left[\frac{\gamma_c+\gamma_v}{\gamma_c\gamma_v}\right]\frac{\alpha_0}{(\omega_t-\nu)^2+\gamma^2}\left[1-\frac{4}{3}\frac{\sin(k_n L_z)}{k_n L_z}\cos\left[2\varphi_n+(m-1)\frac{\pi k_n}{k_r}\right]\frac{\sin(m\pi k_n/k_r)}{m\sin(\pi k_n/k_r)}+\frac{1}{3}\frac{\sin(2k_n L_z)}{2k_n L_z}\cos\left[4\varphi_n+2(m-1)\frac{\pi k_n}{k_r}\right]\frac{\sin(2m\pi k_n/k_r)}{m\sin(2\pi k_n/k_r)}\right]. \tag{A17c}$$

*Present address: Department of Physics, University of North Carolina, Charlotte, NC 28262.

†Also with the Department of Electrical & Computer Engineering and the Department of Physics & Astronomy, University of New Mexico, Albuquerque, NM 87131.

[1] S. R. J. Brueck, C. F. Schaus, M. Osinki, J. G. McInerney, M. Y. A. Raja, T. M. Brennan, and B. E. Hammons, US Patent No. 4, 881, 236.

[2] M. Y. A. Raja, S. R. J. Brueck, M. Osinski, C. F. Schaus, J. G. McInerney, T. M. Brennan, and B. E. Hammons, Appl. Phys. Lett. 53, 1678 (1988).

[3] M. Y. A. Raja, S. R. J. Brueck, M. Osinski, C. F. Schaus, J. G. McInerney, T. M. Brennan, and B. E. Hammons, IEEE J. Quantum. Electron. QE-25, 1500 (1989).

[4] S. W. Corzine, R. S. Geels, J. W. Scott, L. A. Coldren, and P. L. Gourley, IEEE Photonics Technol. Lett. 1, 52 (1989), and references therein.

[5] H. Matsueda, J. Lightwave Technol. LT-5, 1382 (1987).

[6] S. Uchiyama and K. Iga, Electron. Lett. 21, 162 (1985).

[7] Z. L. Liau and J. N. Walpole, Appl. Phys. Lett. 50, 528 (1987).

[8] J. Nitta, Y. Koizumi and K. Iga, in *Conference on Lasers and Electroptics, San Francisco, 1986*, Technical Digest Series Vol. 8, "CLEO 1986" (Optical Society of America, Washington, DC, 1986), p. 382.

[9] M. O. Scully, Phys. Rev. A 35, 452 (1987).

[10] M. O. Scully, Phys. Rev. Lett. 55, 2802 (1985).

[11] M. O. SCully and J. Gea-Banacloche, Phys. Rev. A 34, 4043 (1986).

[12] W. W. Chow, J. Gea-Banacloche, L. M. Pedrotti, V. E. Sanders, W. Schleich, and M. O. Scully, Rev. Mod. Phys. 57, 61 (1985).

[13] M. O. Scully and M. S. Zubairy, Phys. Rev. A 35, 752 (1987).

[14] W. Schleich and M. O. Scully, Phys. Rev. A 37, 1261 (1988).

[15] M. O. Scully and M. S. Zubairy, Opt. Commun. 66, 303 (1988).

[16] M. O. Scully, K. Wodkiewicz, M. S. Zubairy, J. Bergou, Ning Lu, and J. Meyer ter Vehn, Phys. Rev. Lett. 60, 1832 (1988).

[17] J. A. Bergou, M. Orszag, and M. O. Scully, Phys. Rev. A 38, 754 (1988).

[18] K. Zaheer and M. S. Zubairy, Phys. Rev. A 38, 227 (1988).

[19] R. E. Slusher, L. W. Hollberg, B. Yurke, J. C. Mertz, and J. F. Valley, Phys. Rev. Lett. 55, 2409 (1985).

[20] R. M. Shelby, M. D. Levenson, S. H. Perlmutter, R. G. DeVoe, and D. F. Walls, Phys. Rev. Lett. 57, 691 (1986).

[21] L.-A. Wu, H. J. Kimble, J. L. Hall, and H. Wu, Phys. Rev. Lett. 57, 2520 (1986).

[22] B. L. Schumaker, S. H. Perlmutter, R. M. Shelby, and M. D. Levenson, Phys. Rev. Lett. 58, 357 (1987).

[23] M. Ohtsu and K.-Y. Liou, Appl. Phys. Lett. 52, 10 (1988).

[24] P. E. Toschek and J. L. Hall, in *Proceedings of the Fifth International Quantum Electron Conference, Baltimore, 1987*, IQEC Technical Digest Series Vol. 21 (Optical Society of America, Washington, D.C., 1987).

[25] C. F. Schaus, H. E. Schaus, S. Sun, M. Y. A. Raja, and S. R. J. Brueck, Electron. Lett. 25, 538 (1989).

[26] C. F. Schaus, M. Y. A. Raja, J. G. McInerney, H. E. Schaus, S. Sun, M. Mahbobzadeh, and D. R. J. Brueck, Electron. Lett. 25, 637 (1989).

[27] P. L. Gourley, T. M. Brennan, B. E. Hammons, S. W. Corzine, R. S. Geels, R. H. Yan, J. W. Scott, and L. A. Coldren, Appl. Phys. Lett. 54, 1209 (1989).

[28] P. L. Gourley, S. K. Lyo, and L. R. Dawson, Appl. Phys. Lett. 54, 1397 (1989).

[29] J. Krause and M. O. Scully, Phys. Rev. A 36, 1771 (1987).

[30] G. P. Agrawal, IEEE J. Quantum Electron. QE-23, 860 (1987).

[31] S. R. J. Brueck, M. Y. A. Raja, M. Osinski, C. F. Schaus, M. Mahbodzadeh, J. G. McInerney, and K. J. Dahlhauser, SPIE 1043, 111 (1989).

[32] See, for example, M. Sargent III, M. O. Scully, and W. E. Lamb, Jr., *Laser Physics* (Addison-Wesley, Reading, MA, 1974).

[33] M. Yamada and Y. Suematsu, IEEE J. Quantum Electron. QE-15, 743 (1979).

[34] R. F. Kazarinov, C. H. Henry, and R. A. Logan, J. Appl. Phys. 53, 4631 (1982).

[35] M. Asada and Y. Suematsu, IEEE J. Quantum Electron. QE-21, 434 (1985).

[36] W. W. Chow, G. C. Dente, and D. Depatie, IEEE J. Quantum Electron. QE-23, 1314 (1987).

[37] M. Sargent III, E Shou, and S. W. Koch, Phys. Rev. A 38, 4673 (1988).

[38] M. Sargent (private communication).

[39] A. Gamliel and N. George, J. Opt. Soc. Am. A 6, 1150 (1989).

[40] C. H. Henry, IEEE J. Quantum Electron. QE-18, 259 (1982).

[41] Y. Arakawa and A. Yariv, IEEE J. Quantum Electron. QE-22, 1887 (1986), and references therein.

[42] See, for example, J. A. Stratton, *Electromagnetic Theory* (McGraw-Hill, New York, 1941).

HIGH POWER, DIFFRACTION LIMITED,WIDE STRIPE INJECTION LASERS, USING AN EXTERNAL RESONATOR FOR TRANSVERSE MODE FILTERING

Morris B. Snipes, Jr., and John G. McInerney
Optoelectronic Device Physics Group, Center for High Technology Materials
University of New Mexico, Albuquerque, New Mexico 87131-6081

May 14, 1991

INTRODUCTION

During the last three decades tremendous progress has been made in the area of semiconductor injection laser research. Innovative laser structures, in particular the double-heterojunction, have made room temperature injection lasers a reality, and improvements in materials growth have given semiconductor lasers greater reliability, longevity and better performance than early devices. As the technology has grown, semiconductor lasers have been called upon to provide solutions to new and different engineering problems, and also to provide alternatives to other, more expensive and/or inefficient, technologies. One of the major engineering challenges has been to produce high power diode lasers, which operate in a single, diffraction-limited optical mode. A diffraction-limited beam can be focused to minimum spot size, and can easily be coupled to other optical components, with the most efficient optical power transfer. Efficient energy transfer is essential for waveguide to fiber coupling and long-distance propagation. Some of the applications for which high power laser diodes are needed are illumination, detonation, high speed optical printing, long-haul optical fiber communications, bio-medical lasers for use in surgery, and for pumping of solid state materials. Our research has focused on developing a new method of producing high power sources which require relatively easy processing, simple optical components, and produce diffraction limited output.

THEORY

The maximum optical power from a semiconductor laser is determined by the catastrophic facet damage threshold density. Since this limit is directly related to the emitting area, greater output power can be attained by increasing the lateral width of the pumped region. However, along with higher output power, the increased width promotes the propagation of higher order optical modes in the waveguide. Depending on the width of the laser stripe, and the level of pumping, it is possible to propagate several higher

order transverse modes concurrently. Higher order optical modes must be suppressed in order to achieve a diffraction-limited beam.

To avoid the creation and propagation of higher order modes, the phased array was developed. A laser array is formed by closely spacing individual emitters, all of which have common electrical contacts. Since the emitters are very closely spaced, their optical fields are coupled to one another. However, in general, adjacent emitters produce outputs which are 180 degrees out of phase with one another. Due to this out of phase condition, the far field pattern produced by laser arrays is typically double-lobed, and hence, not diffraction-limited.

Many schemes have been tried to force the fundamental mode operation of laser arrays, i.e. chirped arrays [1], Y-stripe arrays [2], and leaky mode arrays [3]. These have had only limited success over a narrow injection range. More recently, researchers have made use of external cavity schemes to control not only the undesirable double-lobed laser array far field, but also to suppress higher order modes in a simple wide stripe laser [4,5]. The experiment performed by Chang-Hasnain, et al. [4], used an anti-reflection (AR) coated laser array, coupled through a GRIN rod lens to a stripe mirror. The stripe mirror was used to couple one lobe of the far field back to the array cavity, and hence reinforce single mode operation. With their experimental setup they were able to attain a nearly diffraction-limited fundamental optical mode at upto twice the laser threshold current.

Our experiment employs a configuration similar to that used by Ruff, et al. [5], and is shown in Figure 1. This configuration allows a stable cavity to be formed in the transverse dimension, as shown in Figure 1a, and an unstable cavity in the lateral dimension, shown in 1b. To achieve the stable cavity, the beam is collimated in the transverse dimension by the first lens, it traverses the length of the cavity through the second (cylindrical) lens, is reflected by the external mirror, and returns via both of the lenses, to be coupled into the narrow optical waveguide of the laser diode's graded index region. The cylindrical lens has no effect on the beam in the transverse dimension. In the lateral dimension, the beam leaving the semiconductor gain medium is brought to a focus close to the second surface of the first lens because of the transverse collimation, and then diverges toward the second lens. The cylindrical lens causes the beam to converge onto the external mirror, where it is reflected back through the lens system. When the

lateral component of the beam arrives back at the facet of the laser diode it has been magnified, and a portion of the beam is spatially filtered by the optical waveguide formed by the laser diode. Since all of the waveguide modes form an orthogonal set, only outgoing and returning modes of the same order will interfere with one another. By adjusting the cavity such that the outgoing fundamental mode overlaps with the returning fundamental mode to a greater degree than higher order modes, the fundamental mode has less cavity loss, or larger modal gain, and as such will be the preferential lasing mode.

It has long been known that a good approximation of semiconductor lasing modes, in each transverse dimension, are simple Gaussian beams [6]. For our simple model, Gaussian beam optics were used to calculate the beam waist and the complex radius of curvature within the external cavity of the system [7]. Using this method we were able to calculate the outgoing and returning beam parameters at the facet of the laser, for a variety of separations between collimating lens and cylindrical lens, and between cylindrical lens and external mirror. Next analytic equations were developed to calculate the overlap of the outgoing and returning beams, and these beam parameters were used in these equations. A much more complete model has been developed by Dente [8], who included beam propagation within the gain medium.

EXPERIMENT

The laser structure used in our research was a GRaded INdex, Separate Confinement Heterostructure, with a Single Quantum Well (GRINSCH-SQW). A diagram of the laser material and band structure is shown in Figure 2. Using a simple processing sequence, requiring only a single mask, lasers having stripe widths of 50, 75, 100, and 150 μm were fabricated. The process makes use of a silicon nitride layer to define the pumped region. Processing of these lasers was begun by growing 1000 Å of Si_3N_4 onto the epitaxial layers, using standard LPCVD technique. Photo-resist was then spun onto the nitride, a soft bake was performed, and our mask was used to define the laser stripes. After photolithography, reactive ion etching (RIE) using CF_4 was employed to remove the nitride from the stripe region, and the photoresist was stripped. Next, a zinc diffusion was performed to create a p-side ohmic contact, and the wafer was metalized on the p-side, using 300 Å of titanium, 300 Å of platinum, and 300 Å of gold. The wafer was then thinned and polished to a thickness of approximately 100 μm. After lapping and polishing, 300 Å of

gold/germanium, 300 Å of nickel, and 3000 Å of gold was evaporated to form the n-side contact, and a rapid thermal anneal was performed to produce n-side ohmic contacts. Finally, the wafer was scribed and cleaved into bars, forming lasers having cavity lengths of 250, 375, 500 and 1000 μm, and each of the bars was scribed and cleaved into individual lasers. Initial testing of several of the unbonded lasers indicated threshold current densities near 300 A/cm^2, and differential quantum efficiencies approaching 80%. The completed lasers were mounted onto standard open heat sinks, p-side up; a mounted and wire bonded device is depicted in Figure 3.

One problem inherent to external cavity systems is that the laser diode cavity and the external cavity compete for dominance. It has been shown that the front facet reflectivity of the laser diode will determine the maximum drive current (and hence the maximum output power) for which the external cavity will select the dominant mode [9]. Experiments and calculations, have determined that, in order to maintain the fundamental mode at high injection levels (3-4 I_{th}), the front facet reflectivity should be less than 1%. Our preliminary experiments with uncoated lasers confirmed this, and demonstrated that the external cavity system would not remain single mode beyond more than a few percent above I_{th}. Above these current levels, the laser diode intrinsic facet reflectivity dominates, and the external cavity system reverted back to multimode behavior. To solve this problem, the front facet of the laser was anti-reflection (AR) coated. Very good AR coatings (<1%) were achieved, using a two layer V-coat design. A magnetron sputtering technique was used to sputter the two layers, consisting of Al_2O_3 and ZrO_2. Using the AR coated devices we were able to pump the system to greater than $3I_{th}$ before noticeable changes in the fundamental mode far-field profile appeared.

The setup used in the experiment is shown in Figure 4. It was designed so that the optical power, near-field and far-field could all be monitored at the same time. The laser was pumped using 1 μs current pulses, at a duty cycle of 1%. Optical power was measured with an integrating sphere and silicon photodetector combination. The output of the photodetector was channeled into a gated integrator/boxcar averager, so that the average output power versus current could be plotted. To measure the near-field profile of the system, a slit aperture was imaged onto a CCD camera, the slit was removed, and the beam at the image plane was stored onto a digital oscilloscope. From this near-field image, the effective aperture of the

system, d, was estimated, using the 1/e criterion to determine the cut-off [7]. This measurement is depicted in Figure 5. With this estimation, the diffraction limit for a lateral beam component can be approximated by $2\lambda R/d$, where R is the distance from the near-field plane to the plane of far-field best focus. With a second CCD camera, the far-field of the external cavity system, (i.e. the image best focus) was stored, and the calculated and measured far-fields were compared.

RESULTS:

Using our experimental setup, measurements at several current levels were taken, both with and without the cylindrical lens in the external cavity. Typical experimental far-field data for a 100 μm stripe with a 500 μm cavity length are shown in Figure 6a&b. For both Figures an arbitrary power scale is shown on the vertical axis. Figure 6a shows the diffraction-limited output profile at three different injection currents, using the cylindrical lens within the cavity. The horizontal scale has units of 0.25 mrad/div, showing that the majority of power lies within 0.5 mrad for all current levels. Using our estimate of the near-field aperture size, the diffraction limit was calculated to be 0.51 mrad. Figure 6b shows the far-field measured without the cylindrical lens in the cavity. Far-field measurements without the cylindrical lens showed very little change in profile at different injection levels, and hence only a single injection level is shown as representative. The horizontal axis of Fig. 6b is scaled at 1.25 mrad/div, so that the power is distributed over approximately 6.25 mrad, or more than 10 times the angular divergence of the external cavity without the cylindrical lens.

In Figure 7, a plot of the optical power versus current (PI) is shown for the system with the cylindrical lens, and reflects the total power of the system, i.e., the sum of both front mirror and back facet emitted powers. The power was measured without filtering outside of the main far-field lobe, and therefore contains power distributed over several milliradians. The usable power contained in the focused, diffraction limited spot was estimated to be approximately 85% of that shown in the curve, for current levels below 750 mA. Above this current level, the main lobe of the far-field did not increase further, and the increase in optical power shown in the PI curve was distributed into the side lobes. In addition, a comparison of total power from the solitary laser, measured before AR coating, and from the coupled system, indicate a large coupling loss occurred within the external cavity system, with and without

the cylindrical lens. We have concluded that the majority of this loss came about in coupling the transverse beam component back into the narrow aperture of the laser diode waveguide. It may be possible to alleviate this problem by increasing the active layer thickness and graded index region, or by using an asymmetric large optical cavity (ALOC) structure for the gain medium.

CONCLUSIONS AND DISCUSSION

It has been demonstrated that wide stripe injection lasers can be fabricated, anti-reflection coated, and coupled to an external cavity, to produce high power, diffraction limited, optical beams. The devices are easily fabricated, using a single mask process, and packaging/AR coating can easily be performed using well defined processes. A relatively simple stable/unstable external cavity configuration was employed to filter out the higher order transverse modes in the lateral dimension, to produce the diffraction limited output.

One shortcoming of our experimental technique is the somewhat arbitrary determination of the "near-field aperture" size to calculate the diffraction limit of the system. A more exact measurement of the diffraction limit can be made by assuming a particular phase front on the beam, and Fourier transforming the square root of the intensity profile, measured at the aperture, to the measurement plane. We will make use of this method in our next set of experiments.

A variety of ideas for future modifications and experiments have been explored. As was mentioned, we hope to attain better external cavity coupling using an ALOC. Preliminary results using an ALOC type waveguide structure, have shown better coupling efficiency than the simple GRIN-SCH waveguide. AR and high-reflection (HR) coatings have been a major area of work. We feel we can further improve the quality of the AR coatings, in order to drive the external cavity laser to higher diffraction-limited output power. Also, we can double the forward output power by HR coating the back facet of the device. One of the experiments which we intend to conduct is that of filtering the higher-order transverse modes using a grating for external feedback, and thus concurrently, select a single longitudinal mode. Using this system, we can conduct other, more important experiments, such as short pulse generation by mode locking and optical pumping of nonlinear materials for frequency doubling.

ACKNOWLEDGEMENTS

The authors would like to thank several

people who have greatly assisted in the preparation of this work. Greg Dente of the USAF, Phillips Laboratory (PILOT program) and Chuck Moeller, for their theoretical calculations and experimental design, Sean Kilcoyne and Alfonso Torres for helpful discussions of device fabrication techniques, Dave Reicher for use of his magnetron sputtering chamber and valuable coating experience, Ted Salvi for his consultation in the modeling of the external cavity, and finally Chris Schaus and Shang-Zhu Sun for growth of our laser material. We acknowledge financial support from the USAF Office of Scientific Research and the Phillips Laboratory (PILOT Branch).

REFERENCES:

[1] E. Kapon, C.P. Lindsey, J. Katz, S. Margalit, and A. Yariv, "Chirped arrays of diode lasers for supermode control," *Appl. Phys. Lett.*. vol. 45, p.200, August. 1984.

[2] D.F. Welch, W. Streifer, P.S. Cross, and D.R. Scifres,"Y-junction semiconductor arrays: part II-experiments," *IEEE J. Quantum Electron.*, vol. QE-23, pp. 752-756, June 1987.

[3] J.P. Hohimer, G.R. Hadley, D.C. Craft, T.H. Shiau, S. Sun, and C.F. Schaus, "Stable-mode operation of leaky-mode diode laser arrays at high pulsed and CW currents," *Appl.Phys. Lett.*,vol. 58, pp. 452-454, February 1991.

[4] C. Chang-Hasnain, D.F. Welch, D.R. Scifres, J.R. Whinnery, A. Dienes, and R. Burnham, "Diffraction-limited emission from a laser diode array in an apertured graded-index lens external cavity," *Appl.Phys. Lett.*,vol. 49, pp. 614-616, September 1986.

[5] J.A. Ruff, A.E. Siegman, and S.C. Wang, "Mode characteristics of broad area high power diode lasers in an external stable-unstable cavity," *Conference on Lasers and Electro-Optics, 1989 Technical Digest Series*, vol. 11 (Optical Society of America, Washington, D.C. 1989) p. 296.

[6] J.C. Dyment, "Hermite-gaussian mode patterns in GaAs junction lasers," *Appl. Phys. Lett.*. vol. 10, pp. 84-86, February 1967.

[7] A.E. Siegman, *Lasers*, University Science Books: Mill Valley, CA, pp. 663-697, 1986.

[8] Conversations with Greg Dente, Phillips Laboratory, Kirtland AFB, Albuquerque, NM, Spring 1991.

[9] W.F. Sharfin, A. Mooradian, C.M. Harding, and R.G. Waters, "Lateral-mode selectivity in external-cavity diode lasers with residual facet reflectivity," *IEEE J. Quantum Electron.*, vol. QE-26, pp. 1756-1763, October 1990.

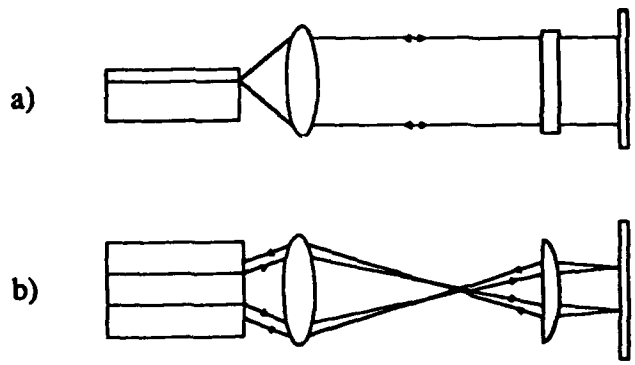

Figure 1 a) side view of laser and external cavity shows the stable cavity configuration, note that the cylindrical lens has no effect in this dimension, b) top view of the system shows the unstable cavity configuration, and demonstrates a cross-over and magnification of the beam

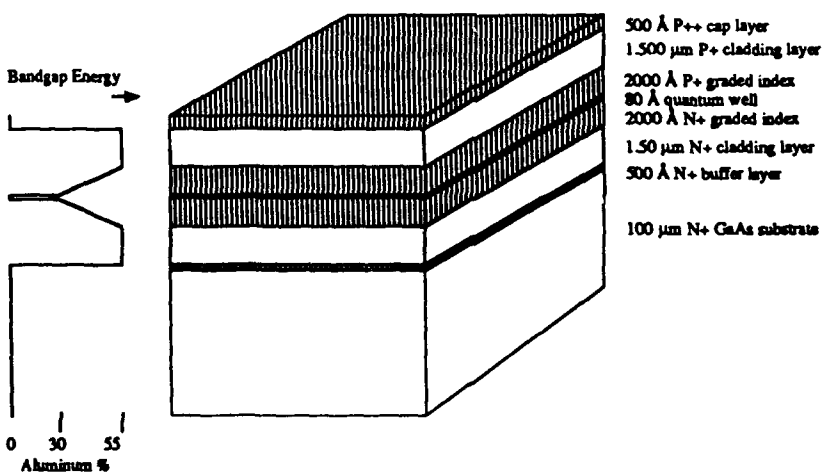

Figure 2 GRIN-SCH laser structure used for laser processing run SW1-125

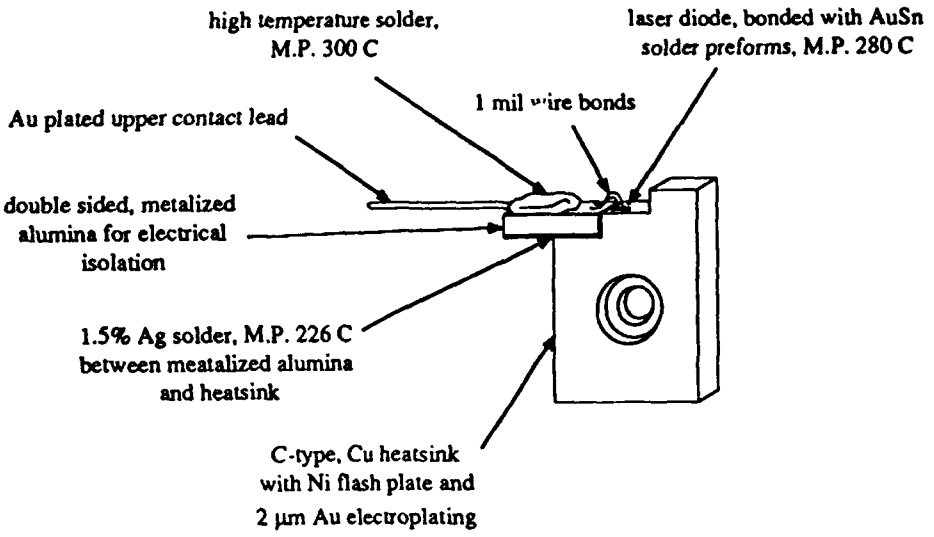

Figure 3 Standard package for high power lasers injected with 1usec pulse, at 1% duty cycle

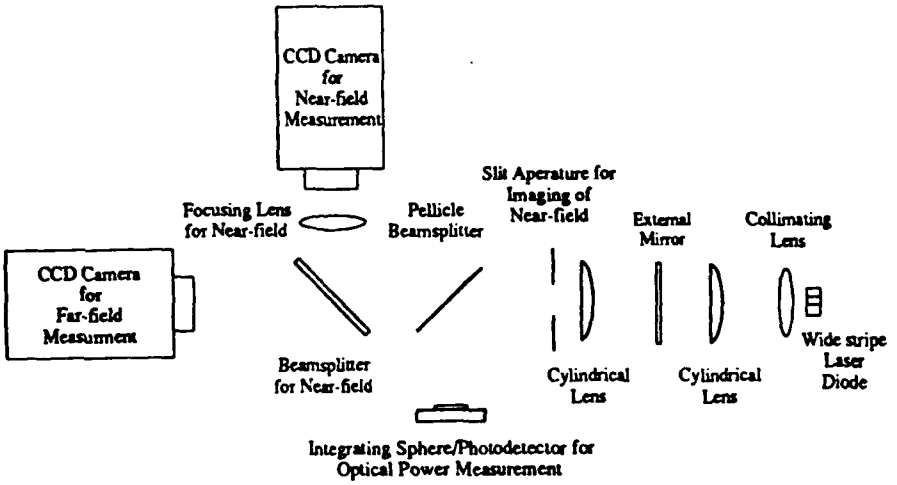

Figure 4 External cavity experimental setup, with diagnostics for measuring optical power, near-field, and far-field

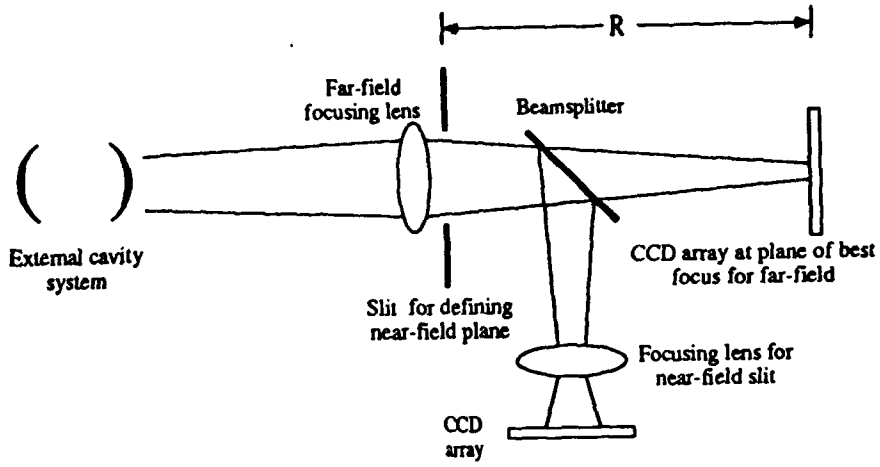

Figure 5 Simplified view of the measurement setup used in the calculation of the diffraction limit

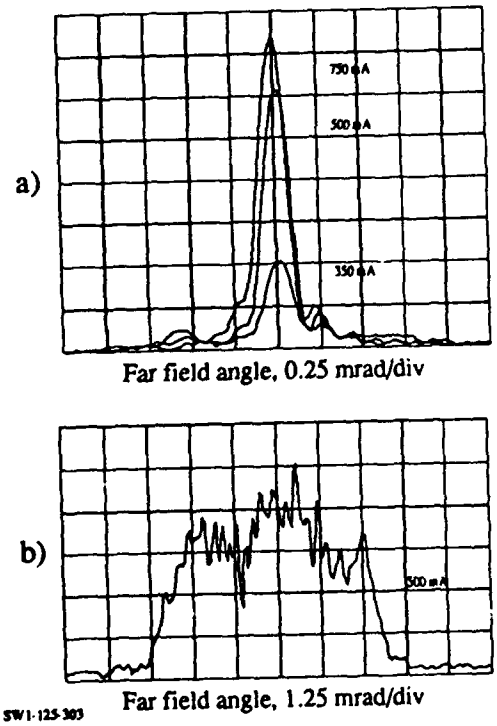

Figure 6 a) Far-field with cylindrical lens and mode filtering, b) far-field without cyl;indrical lens/without mode filtering

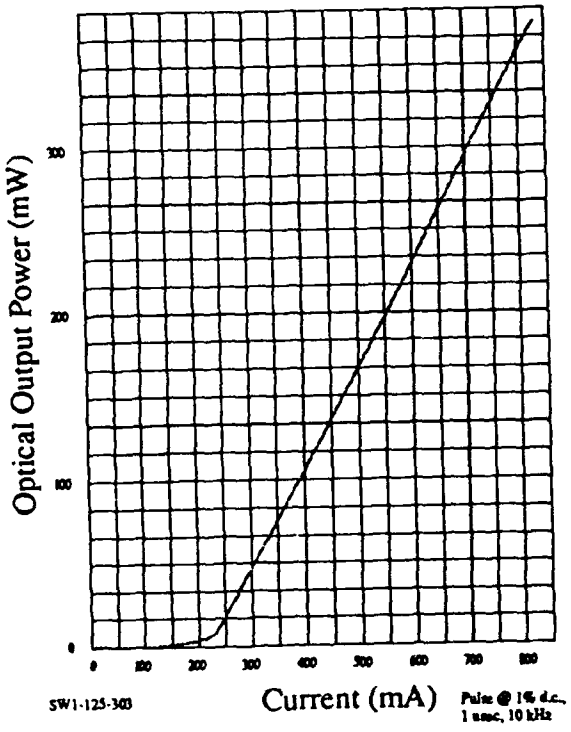

Figure 7 PI curve for device SW1-125-303, with external cavity mode filtering

Opt. Lett.

Phase-locking of Semiconductor Diode Lasers by Phase Conjugate Injection

Cunkai Wu, John G. McInerney, and Bruce W. Liby *

Optoelectronic Device Physics Group
Center for High Technology Materials
University of New Mexico
Albuquerque, NM 87131, USA

Phase-locking of two or three commercial diode lasers was achieved by uni- or bidirectional phase-conjugate injections. The phase-conjugate waves come from a double phase conjugate mirror. For the unidirectional injection locking the dependence of the locking bandwidth on the injection power was measured. Intermodal injection locking is demonstrated and the mode-coupling effect was included. For the bidirectional injection the quality of the phase-locking degrades as the injection power is increased. When it is increased to -30dB the phase-locking is unstable, it is larger than -30dB, the output spectra of the lasers are broadened.

If two or more lasers can be phase locked, they can be coherently combined into a single intense laser beam. This is useful for an array of semiconductor lasers. Nonlinear optical processes , for example, degenerate four-wave mixing, stimulated Brillouin scattering, provide a method by which phase conjugation backward wave of an incidence wave can be generated. If the

*Permanent address: NL Optics Ctr, USAF Phillips Lab, Kirtcano AFB, NM 87117-6008

Figure 1 shows the experimental configuration for the phase-locking of two or three semiconductor lasers. LD_1 is used as the master laser (ML), LD_2 and LD_3 are used as the slave lasers (SL). All of the lasers are Hitachi 1400 laser diodes, without antireflection coating. The operating wavelength is about 835 nm. The output of the laser diodes is an extraordinary polarization. They are incident upon opposite surfaces of a photorefractive crystal after passing through the telescopes. They provide the pumping beams, 1 and 2, of the DPCM. The angle between the beams 1 and 2 inside the crystal was approximately 173^0. The crystal is a single crystal of $BaTiO_3$ with dimensions of 7X6X5 mm^3 . The C-axis is of the crystal along the 7 mm side. Four-wave mixing in the crystal produces output beams 4 and 3, which are phase conjugates of the beams 1 and 2, respectively. The injection currents of the diode lasers of LD_1 and LD_2 are about 75 mA (about 1.4 I_{th}). The injection currents of both lasers are adjusted so that their longitudinal modes overlap. When I_1=73.5 mA and I_2=77.5 mA this case can be happened. In this case the powers of the pump beams of the DPCM are 1.8 mW and 1.6 mW, respectively. The pumping power density is about 150 mW/cm^2. The transmissivity of the DPCM is about 30%. The nonlinear coupling constant of the crystal γL=2.3. The output wavelengths of the lasers are measured by a grating monochromator. The temporal spectra are measured by two Fabry-Perot interferometers . Their free-spectral ranges are $2.5X10^3$ GHz and 1.6 GHz, respectively. The Farady's isolators provide a 40 dB isolation.

When the longitudinal modes of the two lasers overlap, their Fabry-Perot spectra coincide. The phase-locking between the master and slave lasers is signed by the interference fringes. The interference pattern is detected by a CCD camera and displayed on a video monitor. When the phase of the slave

laser is locked, the interference fringe appears, as shown in Fig.2 (a). If the phase conjugation beam 4 is blocked, the interference fringes disappear. Fig.2(b) shows intensity variation in interference fringes. The visibility obtained is V=0.95. Changing the current or/and temperature of the lasers we can tune the wavelength of the free-running lasers.

The phase locking of three laser diodes was carried out . Similar results were obtained.

Intermodal injection locking

For a weak injection power, in order to get good injection locking, the frequency of the free-running slave laser has to be tuned to within a relatively narrow bandwidth of the master laser frequency. Keeping the injection power a constant, adjusting the injection current and temperature of the master laser, as the frequency of the master laser is detuned from that of SL, the visibility of the fringe is reduce. But when the frquency of the ML is close to a nonlassing longitudinal mode (the longitudinal mode space is about 119 GHz) of the SL, the injection locking can be performed by using lower injection power. The SL constitutes a resonant amplifier for the light injected into a nonlassing mode. Because of the mode-coupling effect the injected SL mode power increases in proportion to the injection power, while the free-running SL mode power decreases due to the mode-coupling. The dependence of the locking bandwidth on the injection power was measured and shown in Fig.4. For weak injection the experimental data is in agreement with previous injection locking theory [5-7]. When the frequency of ML is close to nonlasing longitudinal mode of SL, the SL output power transfered completely to the injected mode. This is intermodal injection locking [8-10]. In this case the mode-coupling effect must be taken into account.

Under the usual plane-wave and slowly varying envelope approximation, the electric field inside the injected cavity can be expressed as

$$E_s(z,t) = \frac{1}{2} E_{so}(t) \exp j(\omega_s t - k_m z) + c.c. \quad (1)$$

where ω_s is the laser frequency and km the wave number of the mth mode, fixed by the cavity boundary conditions. The complex field of the injection laser is

$$E_i(z,t) = \frac{1}{2} E_{io}(t) \exp j(\omega_i t - k_i z) + c.c. \quad (2)$$

Including mode-coupling effects the coupled wave equation becomes

$$\frac{dE_{so}}{dt} = \{\frac{1}{2}(G - \frac{1}{\tau_p})(1+j\alpha) + \frac{C}{2Ln_g}\frac{E_{io}}{E_{so}} - j(\omega_s - \omega_i) + \xi |\frac{E_{io}}{E_{so}}|^2\} E_{so} \quad (3)$$

where G is the optical gain, τ_p is the photon lifetime, α is the ratio between the carrier-induced change in the refractive modal index n and the modal gain, n_g is the group index. ξ is the mode-coupling coefficient and can be represented as

$$\xi = \frac{1}{\Delta\Omega}(G - \frac{1}{\tau_p})[\Delta\Omega - (\omega_i - \omega_s)][\frac{C}{2Ln_g}\frac{1}{(\omega_i - \omega_s) - q\frac{C}{2Ln_g} + i\Gamma}] \quad (4)$$

where $\Delta\Omega$ is the bandwidth of the gain of the slave laser; Γ is the output linewidth of the master laser, and

$$q = \frac{\omega_i - \omega_s}{\frac{C}{2Ln_g}} \text{ integer}$$

Since $\omega_i - \omega_s$ is very close to $q\frac{C}{2Lng}$, the equetion (3) can be simplified to

$$\xi = -j\frac{1}{\Delta\Omega}(G - \frac{1}{\tau_p})[\Delta\Omega - (\omega_i - \omega_s)]\frac{C}{2Lng}\frac{1}{\Gamma} \quad (5)$$

Using $E_{so} = \sqrt{P_s}\exp(j\Phi_s)$ and converting eq.(3) into the rate equations for the total photon number P and the phase Φ of the laser field one obtains

$$\frac{dP_s}{dt} = [G - \frac{1}{\tau_p} + \frac{C}{2Ln_g}(\frac{P_i}{P_s})^{1/2}\cos\theta]P_s \quad (6)$$

$$\frac{d\Phi}{dt} = (G - \frac{1}{\tau_p})[\frac{\alpha}{2} - \frac{1}{\Gamma}\frac{C}{2Ln_g}(\frac{P_i}{P_s})(1 - \frac{\omega_i - \omega_s}{\Delta\Omega})] + \frac{C}{2Ln_g}(\frac{P_i}{P_s})^{1/2}\sin\theta - (\omega_s - \omega_i) \quad (7)$$

where P_i represents the number of injected photons in the cavity and $\theta = \Phi_i - \Phi_s$ is the difference between the phase of the optical field of the master laser and that of the injected slave field.

Stationary solutions

From eqs.(6) and (7) we can derive the steady-state solution of the system

$$\omega_i - \omega_s = \frac{C}{2Ln_g}(\frac{P_i}{P_s})^{1/2}(\alpha\cos\theta - \sin\theta - \frac{1}{\Gamma}\frac{P_i}{P_s}\cos\theta)$$
$$x[1 - \frac{2}{\Gamma}(1 - (\frac{C}{2Ln_g})^2(\frac{P_i}{P_s})^{3/2}\frac{1}{\Delta\Omega}\cos\theta]^{-1} \quad (8)$$

In general, $\frac{P_i}{P_s} < 1$, and $\frac{1}{\Gamma} << 1$, then then $\frac{1}{\Gamma}\frac{P_i}{P_s}\cos\theta$ term can be neglected. The solution (8) becomes

$$\omega_i - \omega_s = \frac{C}{2Ln_g}(\frac{P_i}{P_s})^{1/2}(\alpha\cos\theta - \sin\theta)[1 - \frac{2}{\Gamma}(\frac{C}{2Ln_g})^2(\frac{P_i}{P_s})^{2/3}\frac{1}{\Delta\Omega}\cos\theta]^{-1} \quad (9)$$

The second term in the denominator comes from the mode-coupling effect. Equetion (9) shows that when

$$\frac{2}{\Gamma}(\frac{C}{2Ln_g})^2(\frac{P_i}{P_s})^{3/2}\frac{1}{\Delta\Omega}\cos\theta = 1 \quad (10)$$

The locking bandwidth is largely enhanced by the mode-coupling effect. From eq.(10) we can obtain the required injection power for the maximum locking bandwidth

$$\frac{P_i}{P_s} = \left[\frac{1}{2}\frac{\Gamma\Delta\Omega}{\left(\frac{C}{2Ln_g}\right)^2}\frac{1}{\cos\theta}\right]^{2/3} \tag{11}$$

The Γ is determined by the linewidth of the laser and the accuracy of the detuning. The oscillating frequency of laser diodes changes with temperature. The temperature versus frequency shift characteristics are linear, and the slope is about - 30 GHz /^{0}C. We assume the accuracy of the detuning is about 200 MHz. We use the following set of parameters : $\Delta\Omega$ = 15 nm = 6.4 x 10^{12} Hz (at λ = 840 nm), Γ = 200 MHz, n_g = 4.3, L = 300 μm, α = 5. Substitution these data in eq.(11) yields

$$\frac{Pi}{Ps} = 0.13 \times (\cos\theta)^{-2/3} \tag{13}$$

When the mode-coupling effect is neglected, from the dependence of the locking bandwidth on the phase difference θ, we can get the maximum locking bandwidth at

$$\cos\theta_{max} = 0.98 \tag{14}$$

Substitution bmax in (13) yield

$$\left(\frac{P_i}{P_s}\right)_{max} = 1.3 \times 10^{-1} \tag{15}$$

The theoretical curve obtained from equation (9) is shown in Fig. 3. The theoretical curve [5] without the mode-coupling effect is also shown in the figure. Our theoretical curve is in agreement with the experimental results.

Bidirectional phase conjugation injection mutual phase-locking.

By removing the Faraday isolator from pumping beam 2, the phase-conjugate beam 3 can be injected into laser diode LD_1. This is the bidirectional mutual injection phase-locking configuration. For this scheme, the phase-locking

between the two diode lasers is stable only when the phase-conjugate injection level is less than - 40dB. When the injection level is increased to -30 dB, the frequencies of the lasers can not be adjusted to coincide, and the frequencies of the lasers are unstable. When the frequency difference between the two lasers is about 3 GHz, the relaxation oscillation can be easily excited. When the injection level is larger than -30 dB, the output spectra of the lasers are broadened and the case is driven into multimode operation, as shown in Fig.4. As increasing the injection power the two lasers free-running at a single longitudinal mode with different wavelengths will be pushed toward to multimode states, as shown in Fig.5.

In conclusion, it was experimentally demonstrated that the phase-locking of two and three commercial diode lasers without antireflection coating can be performed by phase-conjugate injection. The bidirectional injection locking is more unstable. For the intermodal injection locking the mode-coupling effect was included in the coupled wave equations. The theoretical results are in agreement in the experimental measurements.To get phase-locking of the diode lasers with difference of frequency of a few GHz, only needs the phase-conjugate injection power of a fraction of one microwatt. It means that nonlinear materials with fast respond time can be used in this technique, even they have low coupling efficiency. To extend to the phase-locking of more diode lasers is straightforward. This technique can also be applied for coherent processing of images transmitted through an optical fiber.

The authors would like to thank Dr. Hua Li, Yuan Li and Chi Yan for their help for experiment.

References

[1]. G.C.Dente, P.C.Durkin, K.A.Wilson, and C.E.Moeller, IEEE J.Quantum Electron., QE-24, 2441(1988).

[2]. J. Feinberg and G.D. Bacher, Appl. Phys. Lett., 48, 570(1986).

[3]. M. Cronin-Golomb, A.Yariv, and I Ury, Appl. Phys. Lett., 48, 1240(1986).

[4]. P.D.Hillman and M.Marciniak, J.Appl.Phys., 66, 5731(1989).

[5]. P.Gallion and G.Debarge, Electronics Lett., 21, 264(1985).

[6]. C.H.Henry, N.A.Olsson and N.K.Dutta, IEEE J Quantum Electron., 21, 1152(1985).

[7]. I.Petitbon, P.Gallion, G.Bebarge and C.Chabran, IEEE J. Quantum Electron., 24, 148(1988).

[8]. L.Goldberg, H.F.Taylor and J.F.Weller, Electronics Lett., 20, 809(1984).

[9]. L.Goldberg, H.F.Taylor and J.F.Weller, IEEE J.Quantum Electron., 20,1226(1984).

[10]. G.R.Harley, IEEE J.Quantum Electron., 22, 429(1986).

Figure captions

Figure 1. The experimental setup for the phase-locking of two and three semiconductor diode lasers.

Figure 2. The interference pattern between laser beams when the phases of the two diode lasers are locked (a), and (b) intensity variation in interference fringes, the visibility is 0.95.

Figure 3. Locking bandwidth vis injection rate (Pi/Ps). Solid line is the theoretical curve without mode-coupling [5], dashed line with mode-coupling, triangles experimental data.

Figure 4. Fabry-Perot interograms for high mutual phase-conjugate injection. (a)Without injection, and (b) with injection of 20 μW.

Figure 5. Bidirectional phase-conjugate mutual injection coupling between the two diode lasers. (a) free-running output wavelengths, (b) to (d) the phase-conjugate injection is increased from (b) to (d).

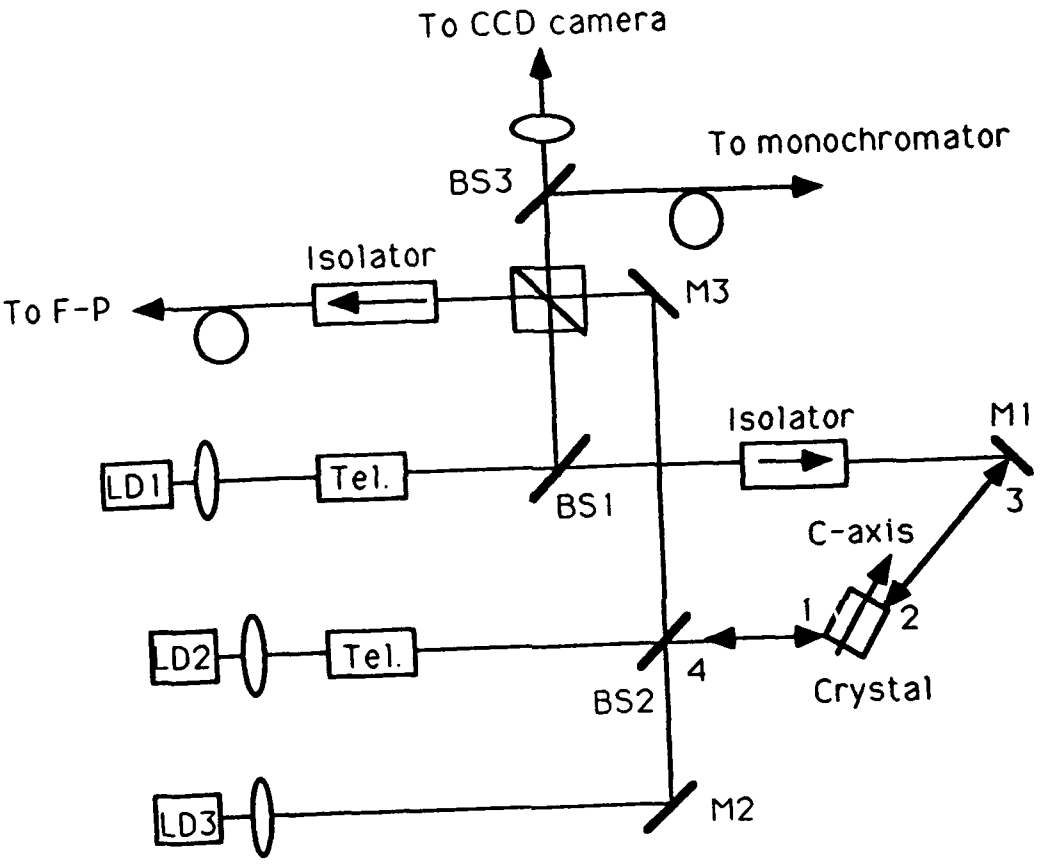
To CCD camera
To monochromator
BS3
Isolator
To F-P
M3
Isolator
M1
LD1
Tel.
BS1
3
C-axis
1
2
LD2
Tel.
4
BS2
Crystal
LD3
M2

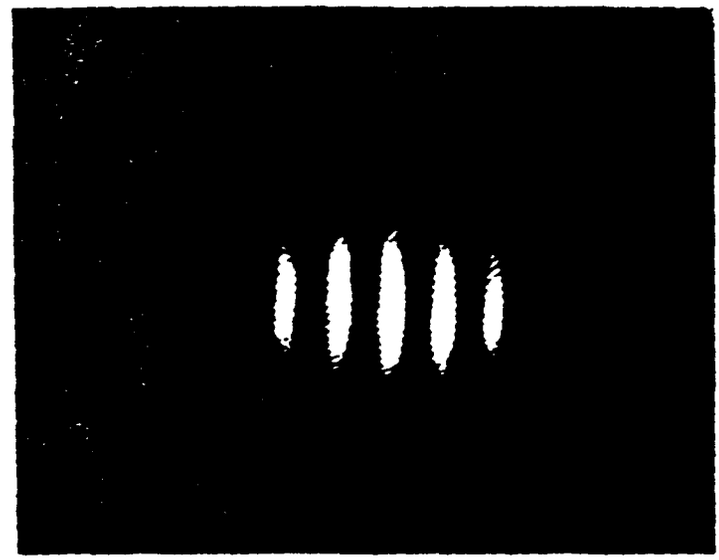

(a)

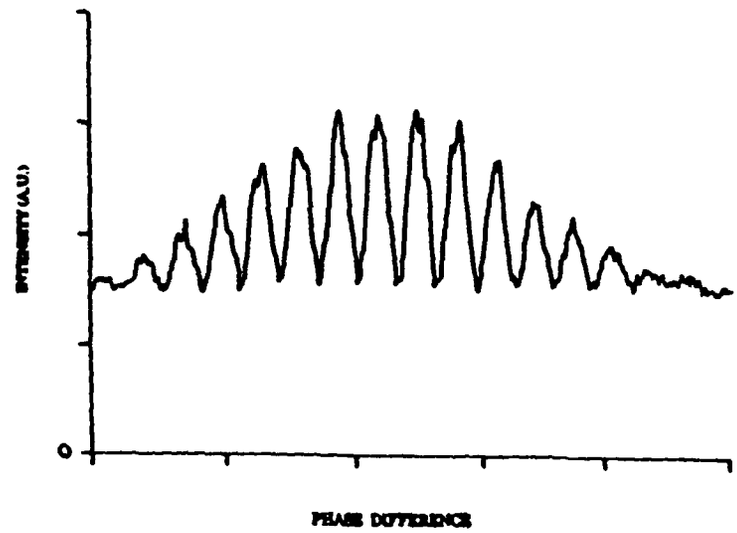

(b)

Fig. 2

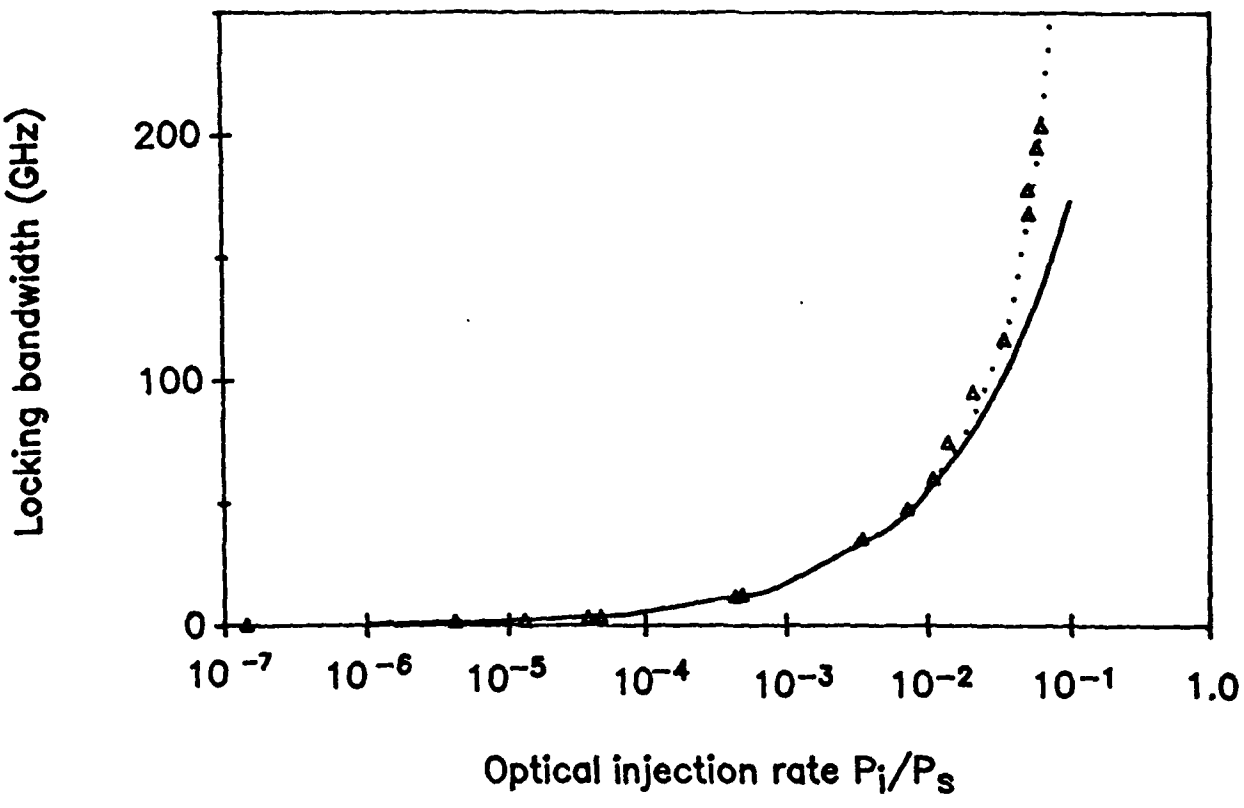
Locking bandwidth (GHz)
200
100
0
10 -7
10 -6
10 -5
10 -4
10 -3
10 -2
10 -1
1.0
Optical injection rate Pi/Ps

Fig. 3

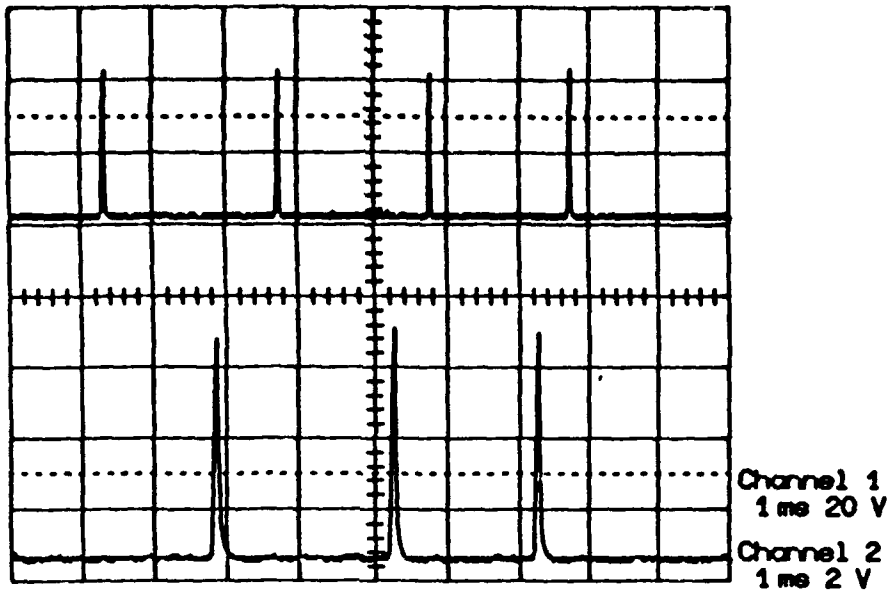
Channel 1
1 ms 20 V
Channel 2
1 ms 2 V

(a)

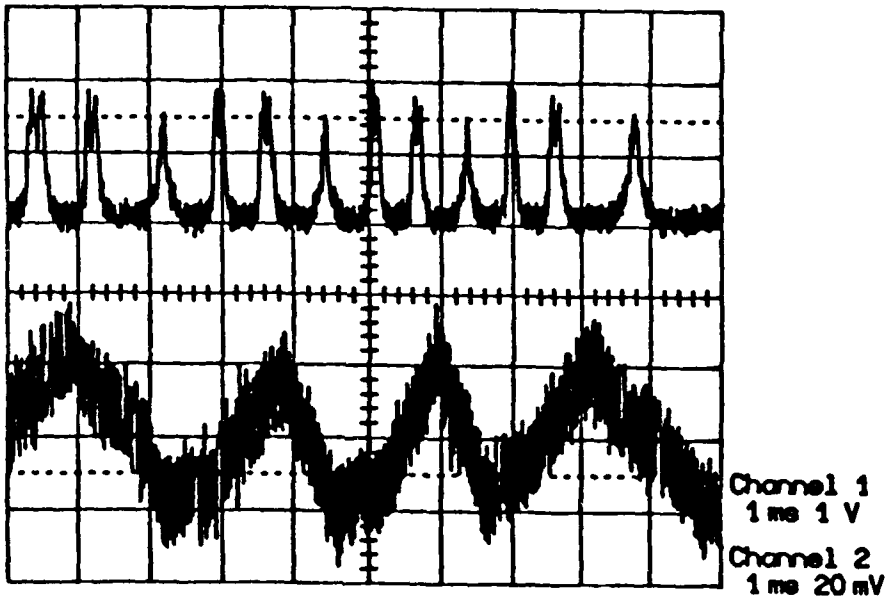
Channel 1
1 ms 1 V
Channel 2
1 ms 20 mV

(b)

Fig. 4

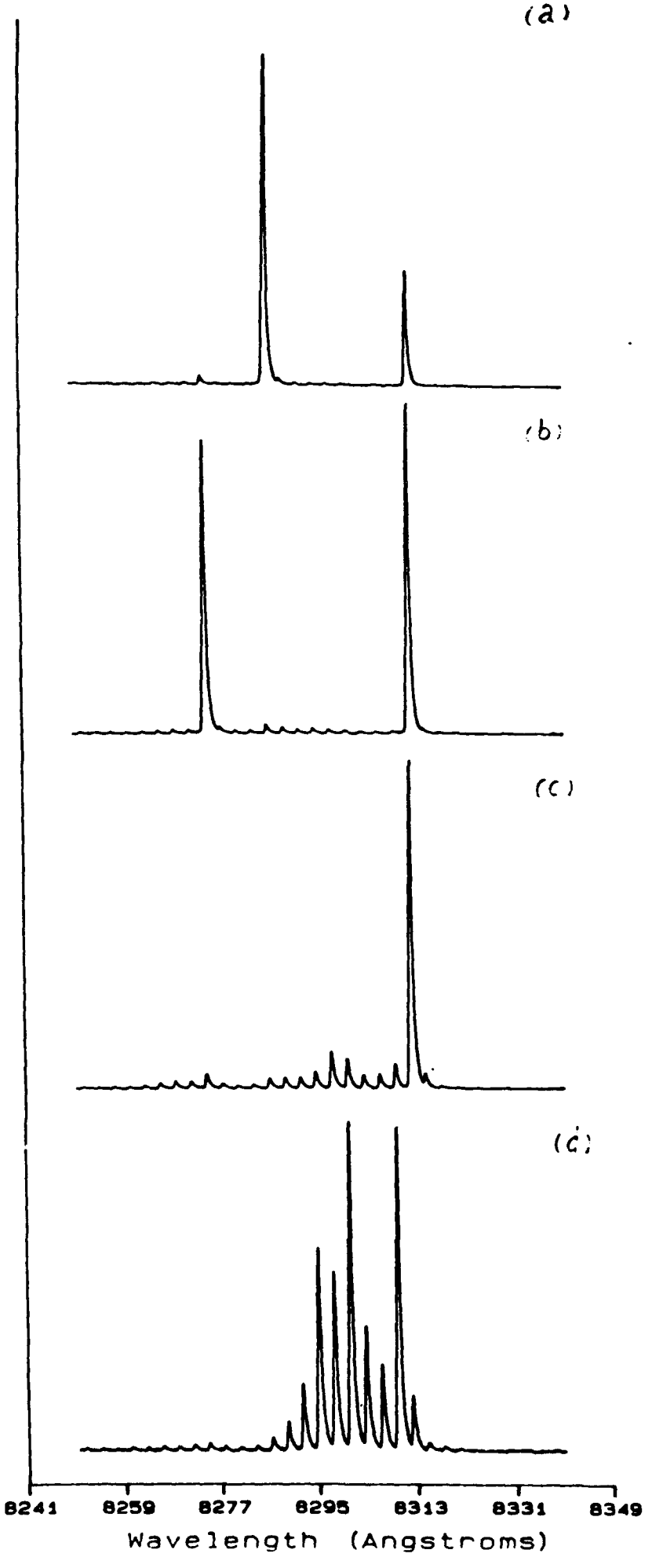
(a)
(b)
(c)
(d)
8241
8259
8277
8295
8313
8331
8349
Wavelength (Angstroms)

Fig 5

ISE '91

HIGH-POWER WIDELY TUNABLE LINE-NARROWED EXTERNAL CAVITY SEMICONDUCTOR LASERS

Cun-Kai Wu, Yuan Li, Morris B.Snipes,Jr,
and
John G. McInerney

Optoelectronic Device Physics Group, Center for High Technology Materials
University of New Mexico, Albuquerque, NM 87131-6081

INTRODUCTION

Narrow spectra and wavelength tunability of semiconductor lasers with high output powers are highly desirable. Such devices are needed in the areas of optical fiber telecommunications, free space communications, microwave energy transmission and nonlinear optical frequency generations. We have developed a system which uses a pulsed semiconductor laser coupled to an external grating to produce 500 mW peak of output power, with a linewidth of 0.05 nm or less, and a tuning range of 30 nm.

Using an external cavity to achieve these goals for low-power laser is not a novel idea [1-4]. A tuning range of 55 nm[2] has been reported with external grating cavities. However, none of the previous work has been concerned with producing high output power.

Because semiconductor laser materials have a wide gain spectra, it is possible to acheive lasing over a wide tuning range. However, wide range tuning can only be realized with a well defined lineshape, and also the wavelength should not drift with operating current or temperature variation. Both of these requirements can be achieved with an external cavity, using a grating for wavelength selection.

One problem inherent in an external cavity system, is that both the solitary laser and the external cavity compete for dominance. To eliminate this problem, the semiconductor laser should have the internal facet anti-reflection (AR) coated, so that the external cavity alone determines the lasing condition. An added benefit is that the operating wavelength will have little dependence on the temperature variations. In addition, if the length of

the external cavity is chosen to be much longer than that of the solitary laser, the wavelength separation of longitudinal modes is very small and the wavelength tuning becomes quasi-continuous.

EXPERIMENT

The semiconductor laser used in our experiment was fabricated at CHTM. The laser structure is a graded-index seperate-confinement heterostructure (GRIN-SCH) with a single quantum well, and is shown in Figure 1. In the lateral dimension the laser is purely gain guided. The device has a cavity length of 500 μm, and a stripe width of 150 μm. As mentioned previously, the front facet of the laser diode was AR coated (<1%) to increase the external cavity coupling efficiency. The rear facet was high-reflection (HR) coated (>75%) to improve single-ended power output. In addition to producing high output power, wide stripe lasers are advantageous due to their simple structure and ease of fabrication.

In our experimental arrangement, a blazed grating having 1200 lines/mm was used in the second diffraction order for optical feedback. The grating lines were aligned parallel to the epitaxial growth plane of the laser diode, hence the active layer acts as the entrance slit of a monochromator in coupling the feedback into the diode. It is noted that the external cavity is less effective when the grating lines are perpendicular to the growth plane in the case of wide-stripe lasers, although it works well for narrow-stripe lasers.

The experimental setup which was used is depicted in Figure 2. The laser was driven using a pulsed current source, with a pulse width of 1 microsecond and a repetition rate of 10 kHz. The optical spectra were measured using a Spex 1704 grating monochromator, with a resolution of less than 0.05 nm. Optical output power was monitered with a Photodyne 44 XLA power meter. To take power measurements with and without optical feedback, a beam splitter was used to extract a portion of the beam from the external cavity and the cavity was blocked to eleminate feedback. These results are shown in Figure 3. The output power versus wavelength curve, as shown in Figure 6, was measured at the grating.

In Figure 4 we show the laser diode spectra with and without optical feedback from an plane external mirror. The injection current is about twice threshold current. This demonstrates that even with external feedback from a mirror, the laser operates with a broad spectral envelope in multiple longitudinal modes. Figure 5 shows the optical spectra of the laser diode with feedback from a grating external cavity under the same operating condition as in

Figure 4. This clearly shows that grating coupling of the laser diode produces a narrowing of the spectra by 2 to 3 orders of magnitude.

Figure 6 shows the output power variation as the operating wavelength is changed by adjusting the tilt angle of the grating. The spectra width is less than 0.05 nm (the instrument resolution limit). The operating condition is same as before.

Figure 7 shows the stability of the laser with a grating external cavity. The driving current varied, but the operating wavelength is very stable and the spectra remains very narrow.

As the grating tilt angle is varied, the operating wavelength of the laser can be tuned continuously. Figure 8 shows the tuning of the wavelength. The result is abtained at same injection condition, i.e. about 2.0 times of threshold current. The peak output power of the laser at this condition is about 500 mW. From Figure 8 The tuning range is above 30 nm , from 777.0 nm to 808.5 nm . At either end of the tuning curve, the feedback from the grating is insufficient to support lasing action.

CONCLUSION

In conclusion, using a grating external cavity, a high power, narrow linewidth semiconductor laser has been realized. Specifically, the laser has:

1) very narrow linewidth;

2) wide wavelength tuning range;

3) high output power above 550 mW in pulsed mode;

4) excellent wavelength stability.

REFERENCES

1. Kohroh Kobayashi and Ikuo Mito, "Single frequency and tunable laser diodes," *J. Lightwave Technol.*, vol.6. no.11, pp. 1623-1633, November 1988.

2. R. Wyatt, and W. J. Devlin, "10 kHz linewidth 1.5 μm InGaAsP external cavity laser with 55 nm tuning range," *Electron. Lett.*, vol.19, pp. 110-112, February 1983.

3. V. Yu. Bazhenov, A. P. Bogatov, P. G. Eliseev, O. G. Okhotnikov, G. T. Pak, M. P. Rakhvalsky, M. S. Soskin,V.B.Tararenko, K. A. Khairetdinov, " 35 mW CW single - frequency injection laser with an external dispersive cavity," *IEE Proceedings*. pp. 9-11, Vol. 132, Pt.J. No.1. February, 1985

4. A. Lidgard, T. Tanbun-Ek, R. A.Logan, H. Temkin, K. W. Wecht, N.A.Olsson, "External-cavity InGaAs/InP graded index multiquantum well laser with 200 nm tuning range," *Appl.Phys.Lett.* 56(9), pp. 816-817, February 1990.

LASER STRUCTURE USED
FOR LASER PROCESSING RUNS MBS-562-1,2,3

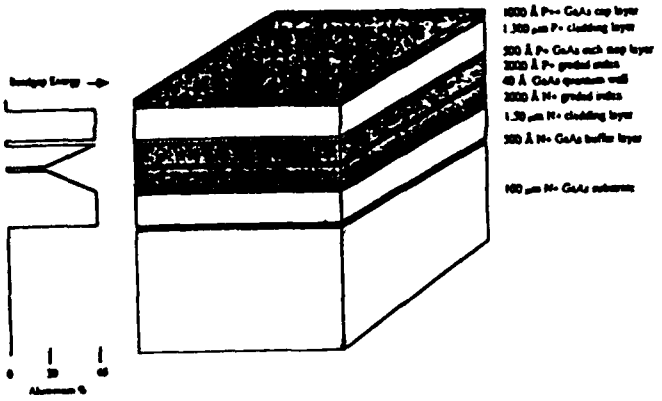

Figure 1 Semiconductor laser structure used in the experiment

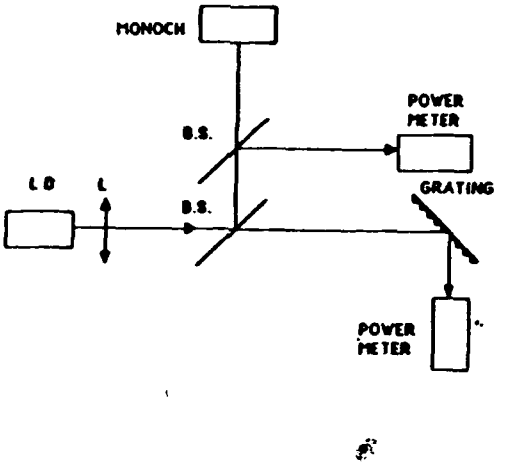

Figure 2 Experimental arrangement

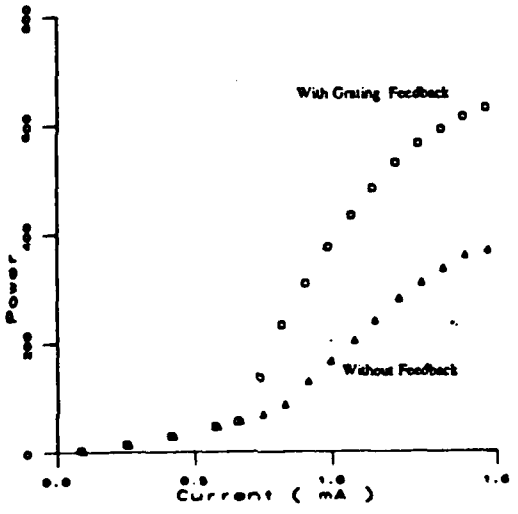

Figure 3 Power versus current for the laser diode with and without the external grating

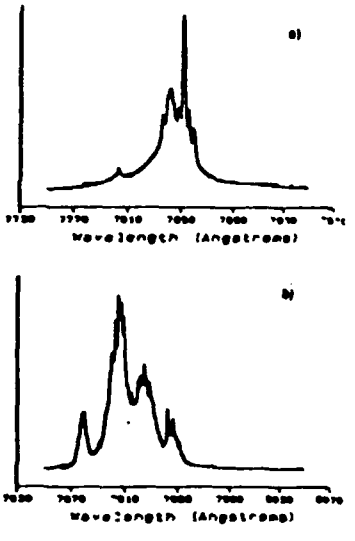

Figure 4 Spectra for laser diode a) without feedback from an external mirror, and b) with feedback from an external mirror

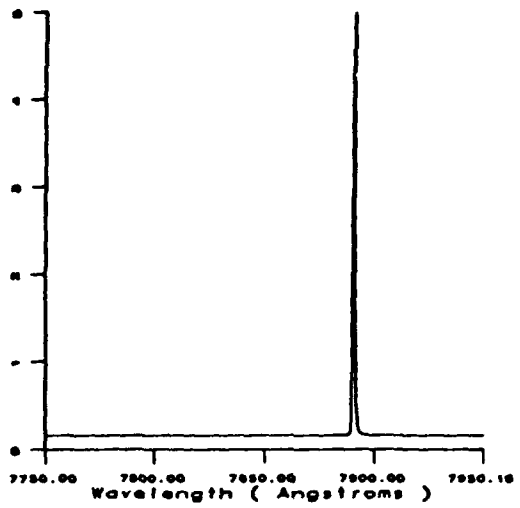

Fig.5 The spectrum output of the laser with the feedback from a grating external cavity.

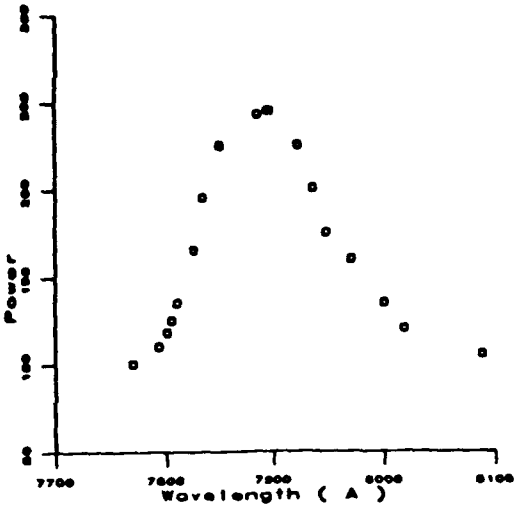

Fig.6 The output power variation as the operating wavelength is changed by adjusting the tilt angle of the grating. The spectrum width is less than 0.05 nm (the instrument resolution limit).

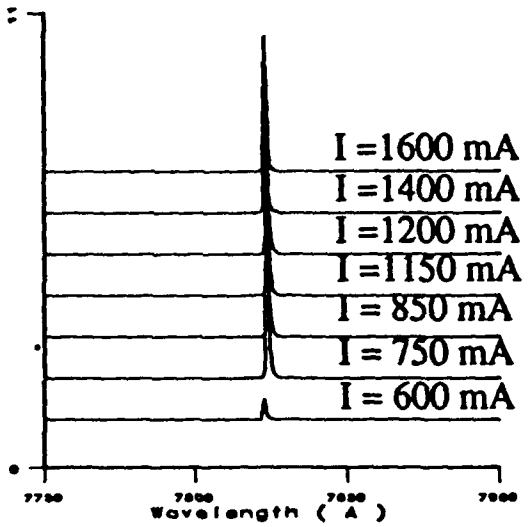

Fig.7 shows the wavelength stability of the laser with a grating external cavity under different injection current.

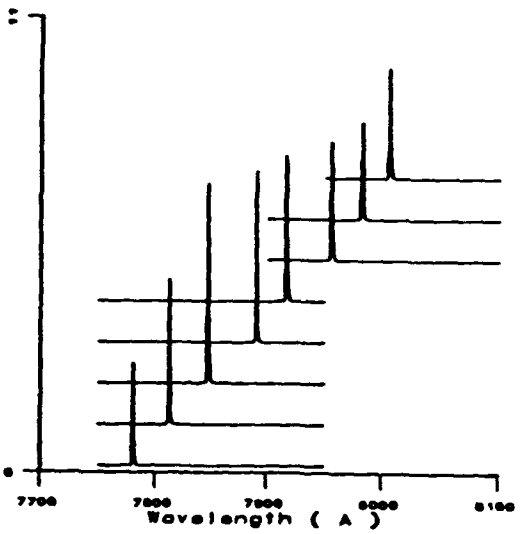

Fig.8 The tuning of the output wavelength by tilting the grating.

Submitted to PRL
Oct 91

Period-Doubling Route to Chaos in a Semiconductor Laser with Weak Optical Feedback

Jun Ye, Hua Li and John G. McInerney

Optoelectronic Device Physics Group
Center for High Technology Materials
University of New Mexico, Albuquerque, NM 87131

Abstract

We report the first experimental and theoretical observations of a period-doubling route to chaos in a semiconductor laser with optical feedback. Increasing the feedback produces a quasiperiodic route to chaos, manifested as a catastrophic increase in the laser linewidth. Under certain conditions, frequency locking occurs in preference to quasiperiodicity, and then period-doubling appears. Both phenomena are explained as interactions between the external cavity modes and the laser relaxation oscillations.

PACS Number: 42.50.Tj, 05.45.+b, 42.50.Kb., 42.55.Px

The dynamics of semiconductor lasers subject to coherent optical feedback have been studied for several years [1,2]. At high levels of feedback (~10% in intensity) and below the isolated laser threshold, the laser dynamics are dominated by the external resonator, and a distinct set of instabilities is observed: external cavity mode interactions [3] and low-frequency self-pulsations [4], subharmonic bifurcations [5] and an intermittent route to a linewidth-broadened chaotic state [6]. At lower levels of feedback (< 0.1% in intensity) and well above the isolated laser threshold, increasing the feedback level initially produces linewidth narrowing, then undamping of the relaxation oscillation, followed by excitation of external

cavity modes and finally a catastrophic increase in the laser linewidth, a phenomenon which has been called "coherence collapse" [1,2].

In this letter we report experimental and theoretical evidence that the coherence collapsed state is actually a chaotic one, usually obtained via a quasiperiodic route [7], but also via a period-doubling route under certain conditions. Moreover, we explain the physical basis for coherence collapse as the interaction between the external cavity modes (separated by frequency ν_{ext}) and the relaxation oscillation (ν_R) in the laser.

Our experiments have used GaAs/AlGaAs laser diodes (Hitachi HLP-1400) operating at ~830 nm with a single longitudinal mode when isolated, although multimode operation is common under external optical feedback. An external cavity was formed by one laser facet and a high-reflectivity plane mirror, the fraction of light coupled back being varied using a half-wave plate placed between a pair of linear polarizers. The laser was forced to oscillate in a single diode mode (containing many external cavity modes) by an intracavity solid etalon of thickness 100 μm, finesse 30 and free spectral range ~1000 GHz. The ratio f_{ext} of the output intensity coupled back into the lasing mode was obtained by measuring the external cavity transmission changes and observing the value of f_{ext} at very weak feedback (normally $<10^{-6}$) by noting the maximum feedback-induced shift in the optical frequency [8]

$$(\nu-\nu_0)|_{max} = p(f_{ext})^{1/2}(1+\alpha^2)^{1/2} \qquad (1)$$

where p is a constant determined by the laser resonator parameters and α is the linewidth enhancement factor. Optical spectra were measured using three scanning Fabry-Perot interferometers with free spectral ranges of 2150, 16.1 and 0.750 GHz, and finesses of 300,100 and 300, respectively. The laser intensity noise spectra were measured using a fast *pin*-photodiode coupled to a microwave spectrum analyzer.

Initially the laser was biased in the range $1.5\text{-}1.7I_{th}$, the external cavity length was chosen such that the relaxation oscillation frequency was an integer multiple of the external cavity mode spacing, and the external feedback ratio was increased gradually. Figure 1 shows intensity noise spectra near the relaxation oscillation resonance for increasing f_{ext} with $\nu_R = 6\nu_{ext}$: the free-running laser (with $f_{ext} = 0$) has damped relaxation oscillation which becomes undamped with increasing feedback. Strong features spaced by ν_{ext} also emerge, indicating the presence of multiple external cavity modes. With further increase of f_{ext}, a series of period-doubling bifurcations occurs marked by the appearance of peaks separated by $\nu_{ext}/2$ and $\nu_{ext}/4$. This process is confirmed by the observation of optical spectra. The power spectrum in the low frequency domain is simultaneously observed to insure that frequency locking ($\nu_R = n\nu_{ext}$, n an integer) is maintained. Eventually the discrete noise peaks diminish while the noise floor rises, leading to a nearly white intensity noise spectrum, and a broadened optical spectrum characteristic of coherence collapse.

In the more general case when ν_R is not an integer multiple of ν_{ext}, the relaxation oscillation again becomes undamped and external cavity modes are excited, followed by interaction between them and culminating once again in a coherence-collapsed state. This scenario occurs far more frequently than the period-doubling route to chaos, which requires careful monitoring of the optical spectra and control of the laser current, temperature and external cavity length to maintain the relationship $\nu_R \approx n\nu_{ext}$. However, in either case the mechanism responsible for the chaotic coherence-collapsed state is the nonlinear interaction between the relaxation oscillation and external cavity modes.

Theoretically, the system is described by rate equations for the carrier population N(t) and complex optical electric field E(t), the latter equation being decomposed into separate equations

for the intensity I(t) and phase $\phi(t)$ in the active region of the laser, with a delayed nonlinear feedback term [8,9,10]. The general form of these equations is

$$dX(t)/dt = g(X(t)) + (f_{ext})^{1/2}h(X(t), X(t-\tau)) + F(t) \qquad (2)$$

with the vector

$$X(t) = (I(t), \phi(t), N(t))$$

where g describes the isolated laser and $(f_{ext})^{1/2}h$ is the nonlinear feedback term with delay time τ and strength $(f_{ext})^{1/2}$. F is a Langevin force term describing white noise driving. Because the phase diffusion process causes difficulties in constructing trajectories in the $\{I,\phi,N\}$ phase space, we further transform the phase $\phi(t)$ into the instantaneous deviation of the optical frequency from its steady state value

$$\omega(t) = \lim_{\delta t \to 0} \{[\phi(t)-\phi(t-\delta t)]/\delta t\} \qquad (3)$$

to construct trajectories in the phase space $\{I,\omega,N\}$. We then integrate the delay-differential rate equations (2) numerically.

Initially, the effects of noise are not included in our calculations (Figures 2-4). Figure 2 gives calculated time series and power spectra for the intensity I(t), and Poincaré maps in the plane of constant N(t). The time series show that the faster relaxation oscillation is initially modulated by ν_{ext}, then $\nu_{ext}/2$, $\nu_{ext}/4$ and ultimately an irregular signature. The power spectra agree well with the experimental data presented in Figure 1. The bandwidth of the spectra is limited by the linewidth of the cold laser resonator which is about 20 GHz here. The frequency spacing of external cavity modes in the power spectra is smaller than $2L_{ext}/c$ (L_{ext} is the external cavity length), due to mode pulling effects. Figure 3 shows a calculated bifurcation plot for the frequency-locked condition, showing a clear period-doubling sequence. Taking the

peak values of the time series of I(t) gives the envelope of the external cavity modulation signature, and taking the local maxima of this envelope gives the bifurcation points for a given f_{ext}.

To confirm the chaotic nature of the irregular state, we calculated the correlation dimension D_2 [11] for each of the data sets in Figure 2. The resulting data (Figure 4) converged to a fractal dimension of 2.1-2.7, indicating a chaotic attractor. We have also calculated D_2 values for the system with white driving noise and no feedback; these values converged to 3 (with a small computational error) as expected for a purely stochastic process. The calculated D_2 for the coherence-collapsed state never reached 3 even with large feedback ratios and with large spontaneous emission noise included. We note in passing that the uncertainties in the calculated D_2 values are due to nonuniform attractor densities caused by the stiffness of this system which has time constants ranging from ~10 picoseconds to microseconds. The very large data sets required for accurate determination of the correlation dimension D_2 precludes experimental measurements using currently available equipment.

We have also studied the effects of adding realistic levels of white noise [12], indicating that noise causes no significant modifications of the essential features of the period-doubling or quasiperiodic routes to chaos, although it does obscure the details and make the correlation dimension more difficult to determine.

In conclusion, we have presented the first experimental and theoretical demonstration of a period-doubling route to chaos in a coherence-collapsed semiconductor laser. This route occurs in preference to the more usual quasiperiodic route when frequency locking conditions are maintained. In either case, the coherence-collapsed semiconductor laser is shown to be chaotic,

and the behavior is due to nonlinear interaction between the external cavity modes and the relaxation oscillation undamped by the optical feedback.

The authors are grateful to N. B. Abraham and A. M. Albano at Bryn Mawr College for helpful discussions, and to the USAF Phillips Laboratory for Cray-2 access. This work was supported by AFOSR, RADC and NSF.

REFERENCES:

[1] D. Lenstra, B. H. Verbeek and A. J. Den Boef,
IEEE J. Quantum Electron., QE-21, 674 (1985)

[2] G. C. Dente, P. S. Durkin, K. A. Wilson and C. E. Moeller,
IEEE J. Quantum Electron., QE-24, 2441 (1988)

[3] D. S. Seo, J. D. Park, John G. McInerney and M. Osinski,
IEEE J. Quantum Electron., 25, 2229 (1989)

[4] J.D. Park, D.S. Seo and J.G. McInerney,
IEEE J. Quantum Electron., 26, 1353 (1990)

[5] T. Mukai and K. Otsuka, Phys. Rev. Lett., 55, 1711 (1985)

[6] J. Sacher, W. Elsaesser and E.O. Goebel, Phys. Rev. Lett., 63, 2224 (1989)

[7] J. Mørk, J. Mark and B. Tromborg, Phys. Rev. Lett., 65, 1999 (1990)

[8] G.P. Agrawal and N.K. Dutta,
"Long-Wavelength Semiconductor Lasers",
Van Nostrand Reinhold Inc., 1986, Page 272

[9] R. Lang, and K. Kobayaski, IEEE J. Quantum Electron., QE-16, 347 (1980)

[10] G.P. Agrawal, IEEE J. Quantum Electron., 26, 1901 (1990)

[11] P. Grassberger and I. Procaccia, Phys. Rev. Lett., **50**, 346 (1983)

[12] R.F. Fox, I.R. Gatland, R. Roy and G. Vemuri, Phys. Rev. A., **38**, 5938 (1988)

FIG.1 Measured power spectra of the intensity with increasing feedback level f_{ext}, when the frequency locking condition is satisfied (A to F). The injection current I/I_{th} = 1.60, the external cavity length L_{ext} = 18 cm, the external cavity mode spacing ν_{ext}=0.7 GHz and the relaxation oscillation frequency ν_R=4.2 GHz.

FIG.2 Calculated intensity time series (1st column), power spectra (2nd column) and Poincaré maps (3rd column) for the period-doubling route to chaos as $(f_{ext})^{1/2}$ increases (A to F).

FIG.3 Calculated bifurcation picture for the period-doubling route to chaos as $(f_{ext})^{1/2}$ increases. The system parameters at the points marked A to E are the same as those in the graphs similarly designated in FIG.2.

FIG.4 Calculated correlation dimension D_2 at the points previously marked A to F during the period-doubling route to chaos.

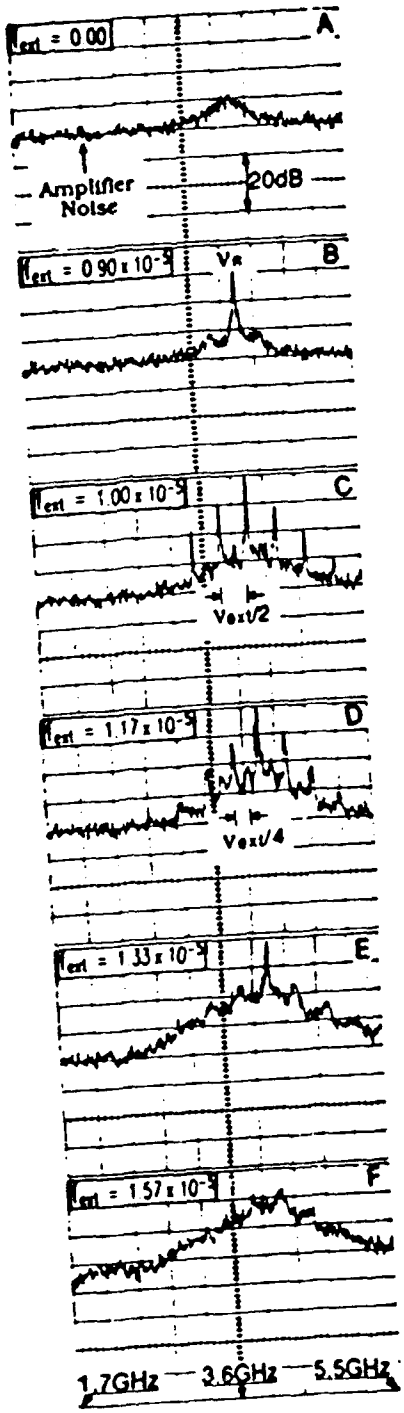

FIG. 1

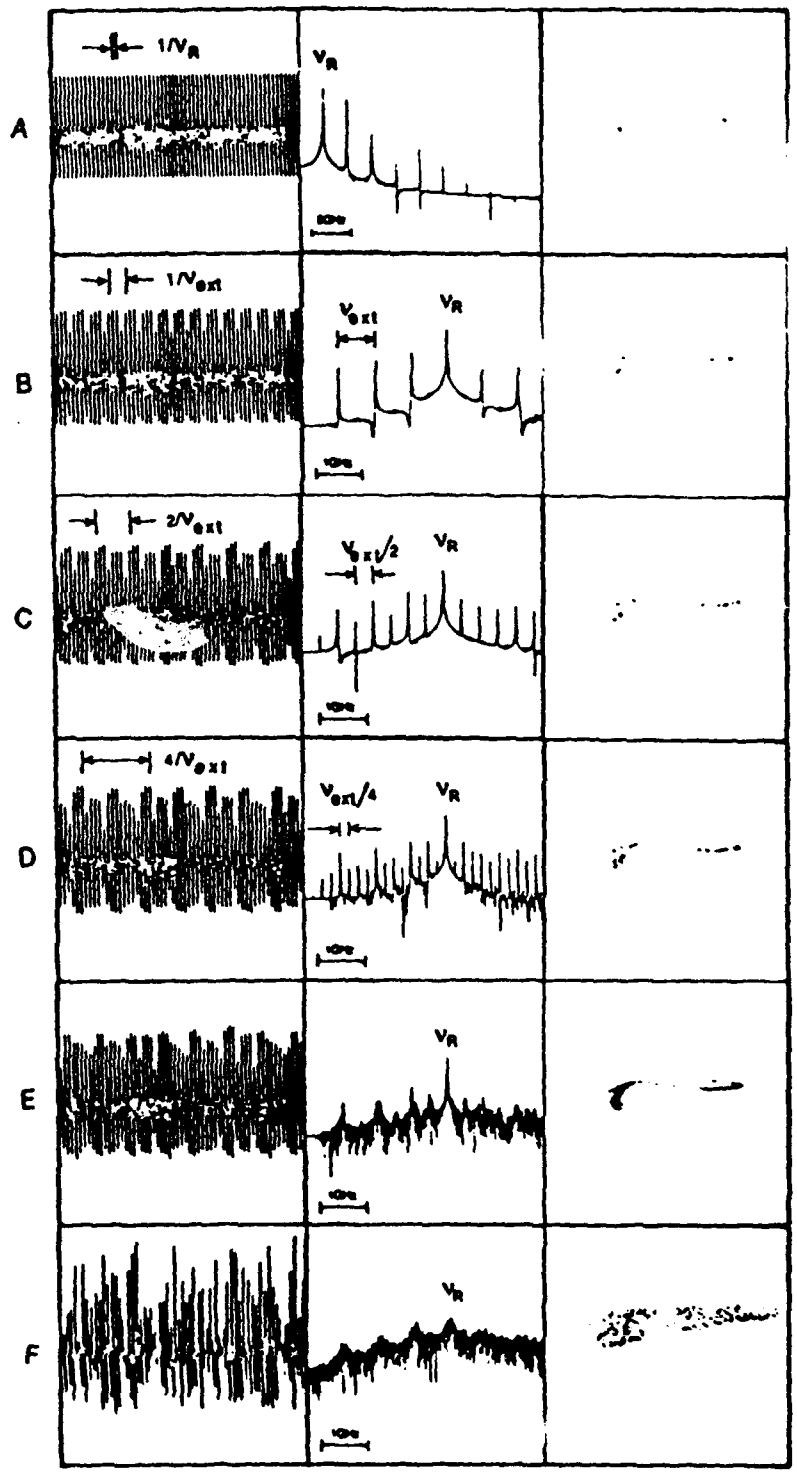
A
B
C
D
E
F
1/VR
VR
1/Vext
Vext
VR
2/Vext
Vext/2
VR
4/Vext
Vext/4
VR
VR
VR
100ms

Fig. 2

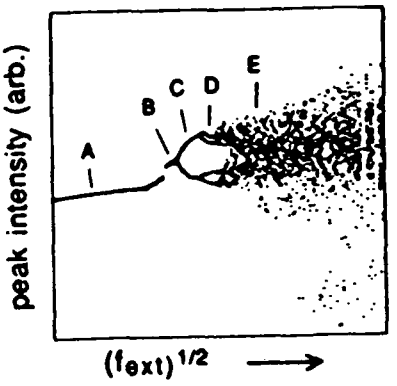

Fig 3

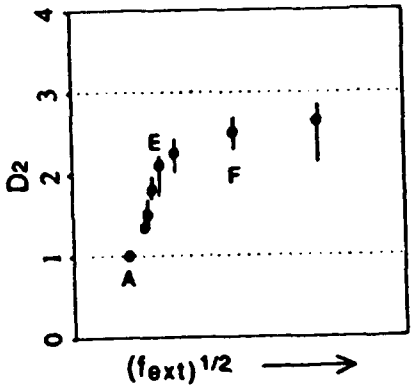

Fig. 4

Dynamic Analysis of Coherence Collapse in the External Cavity Semiconductor Laser

Jun Ye, Hua Li, and John G. McInerney

Optoelectronic Device Physics Group

Center for High Technology Materials

University of New Mexico, Albuquerque, NM 87131

ABSTRACT

We describe theoretical and experimental investigations of a particular interesting and important dynamical phenomenon: coherence collapse of a semiconductor laser with external optical feedback. In experiments, we observed that, as the feedback level increased, the laser linewidth increased tremendously, while the external cavity modes and relaxation oscillation resonances were greatly enchanced. We devised a novel method by which the feedback level can be measured using a frequency discriminator. In our computer simulations, we solved the time-dependent coupled rate equations for the intensity, the optical phase and the carrier number. The time evolution of the field intensity and the intensity spectrum were obtained to show resonant enhancement of the laser modes by the external feedback. The return map and the correlation dimension (D2) were calculated to describe the characteristics of the deterministic chaos in more detail.

I. INTRODUCTION

The dynamics of a semiconductor laser (SCL) can be influenced very strongly by external optical feedback. The dynamical complexity of the external cavity semiconductor laser has been observed experimentally for a long time [1-3]. One well-known but poorly-understood phenomenon is studied here - coherence collapse, in which the linewidth of the SCL is broadened from a few MHz to several tens of GHz by increasing optical feedback[4]. A crucial question is whether this process is deterministic chaos or a stochastic instability. Based on the definition of the deterministic chaos, some of the required properties are[5]: (1) the behavior in time of any variable of the

system is aperiodic; (2) the power spectrum of some variable has some broadband parts; (3) the dimension of a chaotic system must be greater than or equal to two, and the correlation dimension is usually a fractal number; (4) a return map shows an infinite number of points. Therefore by investigating these properties, we can begin to understand the nature of the process.

II. EXPERIMENTS

The experimental arrangement used is shown in FIG.1. An external resonator is formed with one uncoated facet of a GaAs/AlGaAs CSP laser diode, a microscope objective, two polarized beam splitters, a half-wave plate and a plane mirror (R>98.5%). Rotating the $\lambda/2$ plate can continuously change the feedback level. The slope of the resonance curve of the etalon plate is used here as a frequency-discrimination curve to measure the very weak feedback level since the external feedback can cause the lasing frequency of the laser diode to shift according to the equation

$$\omega-\Omega=-K(1+\alpha^2)^{1/2}\sin(\omega\tau+\arctan(\alpha)). \quad (1)$$

Here $(\omega-\Omega)$ represents the frequency shift induced by the feedback and τ is the optical round trip time in the external cavity. α is the linewidth enhancement factor. K is related to the feedback level f_{ext} by

$$K=\frac{1-R_m}{\tau_1}\left(\frac{f_{ext}}{R_m}\right)^{1/2}. \quad (2)$$

The change of the ratio of the intensities I_2/I_1 (refer to FIG. 1) is used to determine the relative feedback level change. A 30-picosecond photo diode is coupled to a microwave spectrum analyzer to measure the intensity spectrum, while a set of three Fabrry-Perot scanning etalons is used to obtain the optical field spectrum. The three F-P etalons have free spectral ranges of 3000GHz, 16.5GHz, and 750MHz with finesses of 300, 100, and 300 respectively. The combination of these three F-P cavities enables us to observe a very large part of the optical spectrum. In this experiment, F-P (1) is to ensure single mode oscillation of the laser diode. F-P (2) is suitable for observing coherence collapse and F-P (3) can be used to find the laser line-width.

III. EXPERIMENTAL RESULTS

FIG. 2 and FIG. 3 show our experimental results. FIG.2 shows the frequency discrimination curve as well as the optical output from the same etalon plate when the external mirror was oscillating and the feedback level was very low. This feedback level was measured from FIG. 2. Then we

increased the feedback intensity and measured the relative feedback level change. FIG. 3 shows the optical spectrum for several different feedback levels. As f_{ext} increases, the relaxation oscillations are enhanced, and both the main lasing mode and the relaxation peaks are modified by the resonantly enhanced external cavity modes. The single lasing mode operation collapses and the laser line-width increases by several orders of magnitude.

IV. THEORETICAL MODELING

The conventional rate equations for SCL need to be modified if the intraband relaxation of charge carriers and polarization within the conduction and valence bands is taken into account [6][7]. The optical gain g per unit length becomes

$$g=g_l/(1+m)^{1/2} \qquad (3)$$

where $m=p/p_s$, p is the intracavity mode intensity and the saturation intensity p_s is related to the intraband relaxation times. g_l is assumed to vary linearly with the change of the carrier population. The nonlinearity is introduced into the modified gain as spectral hole burning. The modified rate equations for a single mode laser have the following form

$$\frac{dp}{dt} = (G_l/(1+m)^{1/2} - \gamma)\, p + R_{sp} \qquad (4)$$

$$\frac{d\phi}{dt} = \frac{\alpha}{2}(G_l-\gamma) - \frac{\beta}{2}\frac{G_l p}{1+(1+m)^{1/2}} \qquad (5)$$

$$\frac{dN}{dt} = J/q - \gamma_e N - G_l p/(1+m)^{1/2} \qquad (6)$$

where

$$G_l = \Gamma v_g g_l = G_N (N-N_0) \qquad (7)$$

$$\gamma = \Gamma v_g g_{th} = G_N (N_{th}-N_0). \qquad (8)$$

The parameter γ represents the cavity loss rate, and the carrier life time is given by $\tau_c=1/\gamma_e$. The parameter β controls the nonlinear phase change and for a F-P laser $\beta=0$. Γ is the electromagnetic mode confinement factor. If external optical feedback is applied, then the rate equations will have some extra terms

$$\frac{dp}{dt} = (G_l/(1+m)^{1/2} - \gamma)\, p + R_{sp} + 2K \cdot [p(t)\ p(t-\tau)]^{1/2} \cos[\phi(t)-\phi(t-\tau)+\omega\tau] \qquad (9)$$

$$\frac{d\phi}{dt} = \frac{\alpha}{2}(G_l-\gamma) - (w-\Omega) - K\left[\frac{p(t-\tau)}{p(t)}\right]^{1/2} \cdot \sin[\phi(t)-\phi(t-\tau)+\omega\tau] \qquad (10)$$

$$\frac{dN}{dt} = J/q - \gamma_e N - G_l p/(1+m)^{1/2} \qquad (11)$$

where the parameter K is given in (2) and τ is the external cavity round trip time. These equations can be numerically solved in the time domain

and the solutions will give the time evolutions of the variables. It is very easy to observe the intensity p(t) experimentally, so its behavior is most conveniently used to describe and analyze the detailed dynamics of the system. First the phase space trajectory (as a return map) and the power spectrum of the intensity are calculated. Then the method of Grassgerger and Procaccia[8][9]to calculate the dimension (D2) is applied. Calculations have been performed for:

(1) a dc-biased semiconductor laser (SCL) without feedback, with realistic spontaneous emission noise included;

(2) a SCL with external feedback, but with the spontaneous emission noise artificially excluded;

(3) a SCL with external feedback, with realistic spontaneous emission noise included.

V. THEORETICAL RESULTS

The calculated results are shown in FIG. 4. Comparing the calculations for these three situations shows the following conclusions.

(1) The noise-driven isolated semiconductor laser has a noise-blurred point in the return map. The SCL is lasing in a stable state and fluctuating around that state under the influence of the spontaneous emission noise. The flat spectrum shows white noise. The dimension (D2) is zero in the relatively large reconstructed phase space, indicating globally stable behavior in the steady state solution. D2 is divergent as the embedding dimension n tends to infinity, showing purely stochastic behavior in the small phase space.

(2) The noise-free external cavity laser system shows an aperiodic behavior in time, with considerable resonant enhancement at the external cavity modes and at relaxation oscillation resonances. The fractal D2 value has a slightly wavy form as the observation range r is changed, showing the complexity of the system. D2 converges at a fractal value between 2 and 3, which is characteristic of deterministic chaos.

(3) The behavior shown in (2) is changed by the inclusion of noise. The trajectory in phase space (a return map) is again blurred by the noise. The resonantly enhanced external cavity modes and relaxation oscillations are still very clear in the time evolution and intensity spectrum. The convergent range of r for D2 is much shorter than that without noise. Although the deterministic chaos still has a clear signature, it is strongly perturbed by a noise-driven stochastic process. One must be very careful in examining the dynamics of the external cavity laser with spontaneous emission noise.

VI. CONCLUSIONS

We have demonstrated both experimentally and theoretically that external optical feedback can greatly increase the instability of SCL by resonantly enhancing the relaxation oscillations and the external cavity modes. The theoretical calculations show that deterministic chaos is present in the process of coherence collapse, but this process is affected by the presence of spontaneous emission noise. The experiments are continuing in order to provide more comparisons between experiment and theory in the future.

REFERENCES

[1] J. Mørk, J. Mark, and B. Tromborg, Phys. Rev. Lett. **65**,1999 (1990)

[2] Y. Cho and T. Umeda, Opt. Commun. **59**, 131 (1986)

[3] G.C. Dente, P.S.Durkin, K.A.Wilson, C.E. Moeller, IEEE J. Quantum Electron. **24**, 2441 (1988)

[4] D. Lenstra, B. H. Verbeek, and A. J. Den Boef, IEEE J. Quantum Electron. **21**, 674 (1985)

[5] J.R. Tredicce and N. B. Abraham, **"Lasers and Quantum Optics"**, Proceedings of the International School on Lasers and Quantum Optics Editors: L.M.Narducci, E.J. Quel, and J.R.Tredicce, World Scientific1988

[6] G.P. Agrawal, IEEE J. Quantum Electron. **26**, 1901 (1990)

[7] G.P. Agrawal, J. Appl. Phys. **63**, 1232 (1988)

[8] P. Grassberger and I. Procaccia, Phys. Rev. Lett. **50**, 346 (1983)

[9] N. B. Abraham, A. M. Albano, A. Passamante, and P.E.Rapp, Editors, **"Measures of Complexity and Chaos"**, Plenum Press, 1989

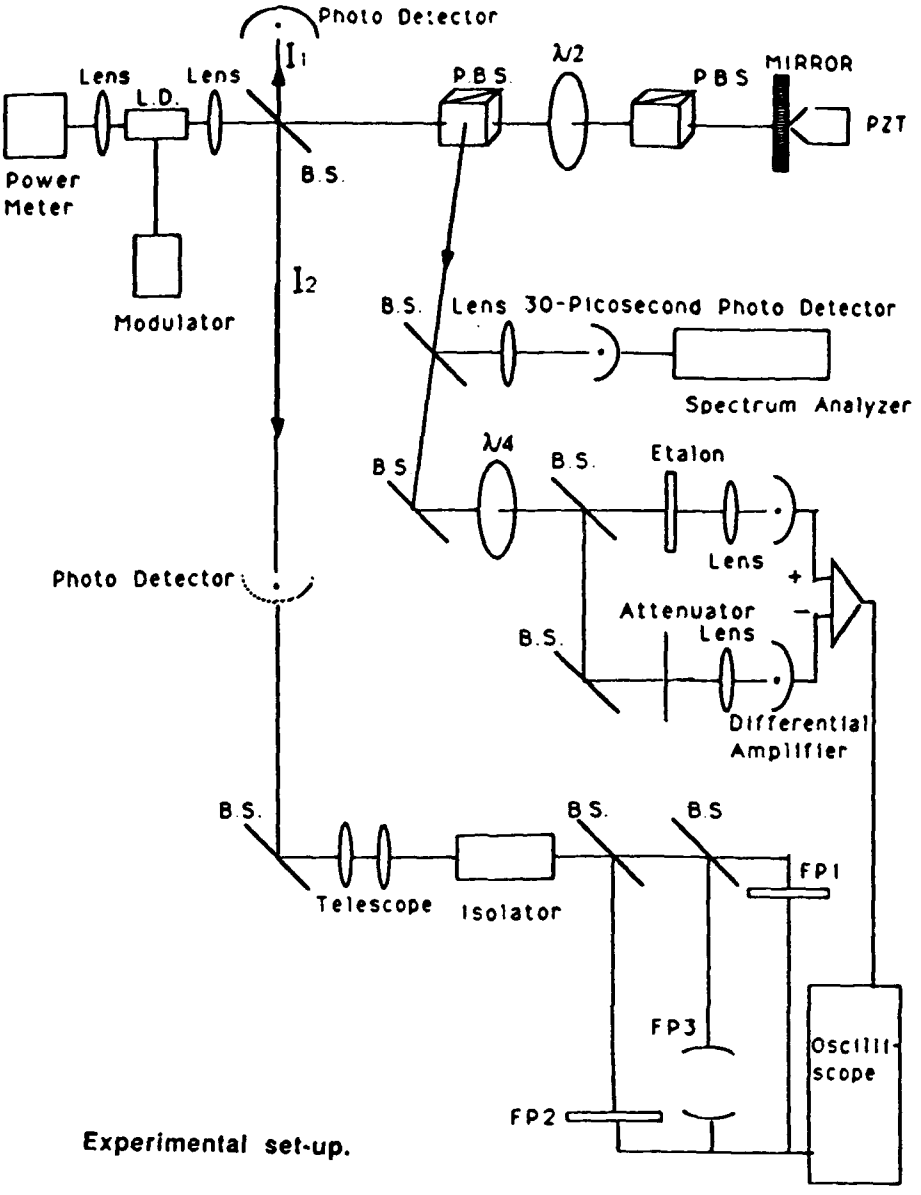

FIG.1. Experimental set-up.

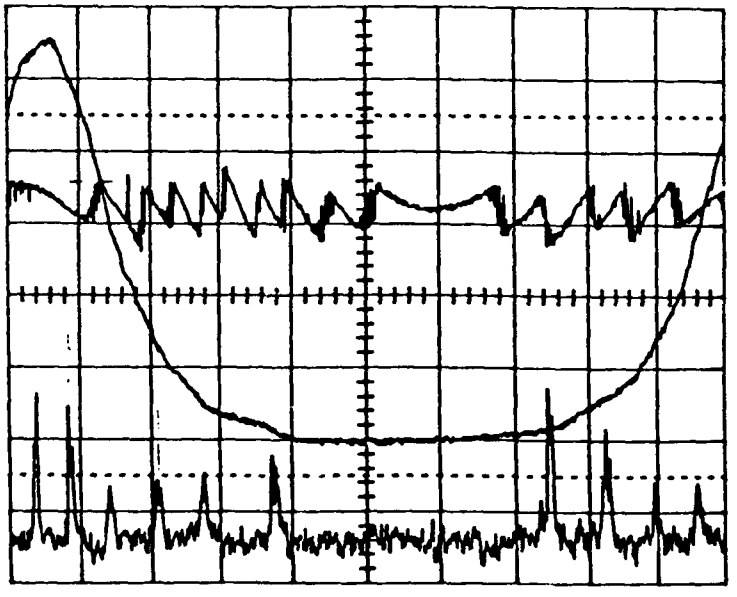

FIG.2. The measurement of the weak feedback level by modulating the external mirror. Injection current $J=1.17J_{th}$. The external feedback level f_{ext} is $1.3*10^{-6}$.

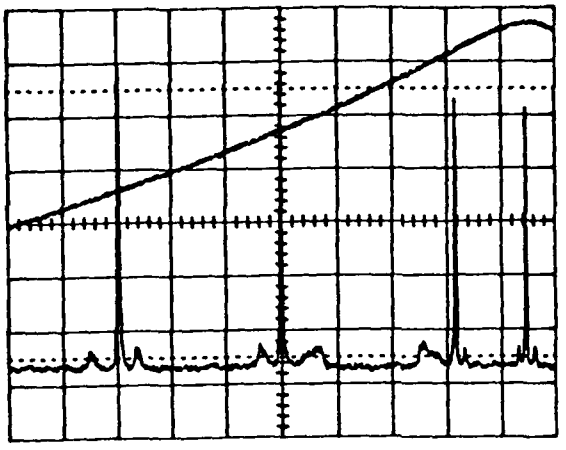

$J = 1.17\ J_{th},\ f_{ext} = 1.30 * 10^{-6}$

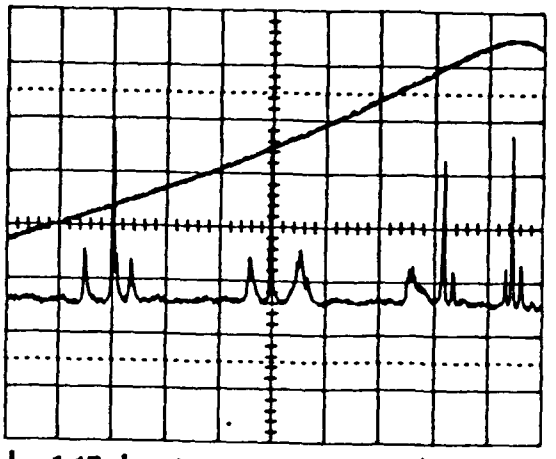

$J = 1.17\ J_{th},\ f_{ext} = 1.77 * 10^{-6}$

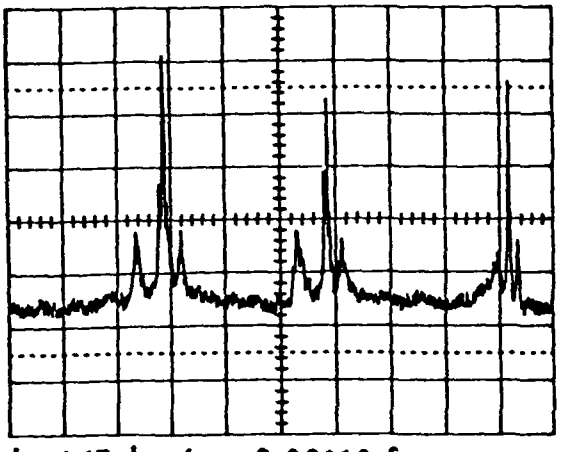

$J = 1.17\ J_{th},\ f_{ext} = 2.82 * 10^{-6}$

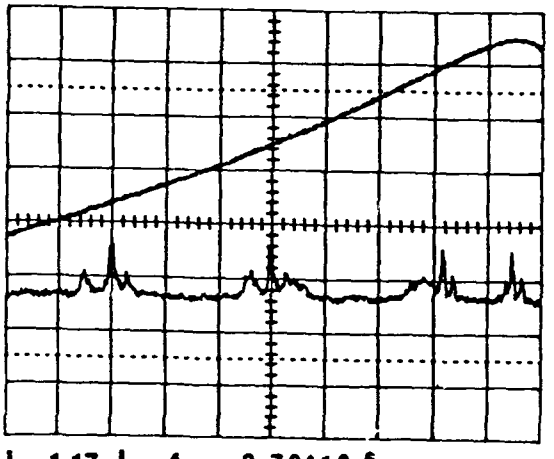

$J = 1.17\ J_{th},\ f_{ext} = 3.70 * 10^{-6}$

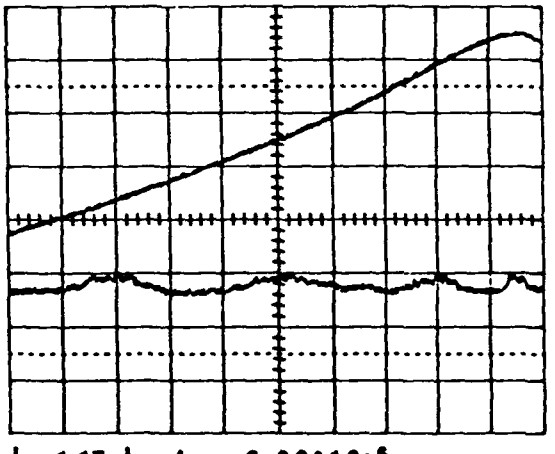

$J = 1.17\ J_{th},\ f_{ext} = 6.66 * 10^{-6}$

FIG.3. The observed optical spectrum from F-P (2) which has the free spectrum range 16.5 GHz and finesse 100. It is shown here that the single mode oscillation gradually turns to coherence collapse with the feedback level increased.

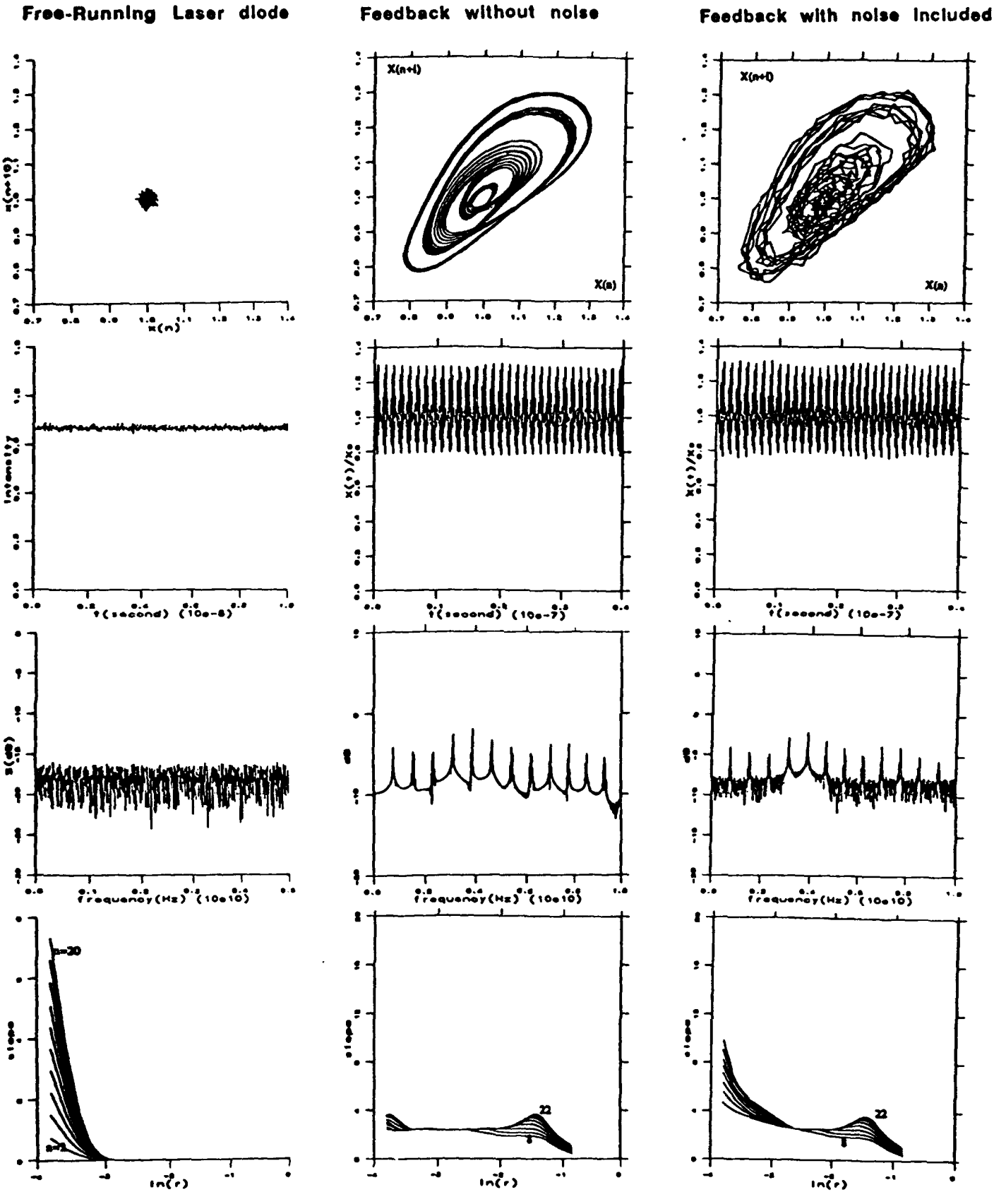

FIG. 4. Comparison of data sets for the three cases: (1) free-running laser diode; (2) external optical feedback without spontaneous emission noise; (3) external feedback with spontaneous emission noise included. Row 1: phase portraits (return maps); row 2: time evolutions of field intensity; row 3: intensity spectrum; row 4: slopes of the log-log plots of the correlation integral vs log(r) for embedding dimensions 8 to 22 (lower to upper).

Grating coupling to surface plasma waves. I. First-order coupling

Saleem H. Zaidi

Center for High Technology Materials, University of New Mexico, Albuquerque, New Mexico 87131

M. Yousaf*

Department of Physics, University of New Mexico, Albuquerque, New Mexico 87131

S. R. J. Brueck

Center for High Technology Materials, University of New Mexico, Albuquerque, New Mexico 87131

Received May 17, 1990; accepted October 18, 1990

A systematic experimental and theoretical study of first-order grating coupling to surface plasma waves existing at an air–Ag interface is presented. The experiment extends beyond previous work to grating depths comparable with the grating period. The grating profiles range from sinusoidal to rectangular. For TM-polarized incident radiation this grating depth range includes the entire spectrum of surface-plasma-wave-radiation coupling—from underdamped, to nearly 100% coupling, to overdamped and the disappearance of the resonance from the zero-order reflectance measurements. Strong polarization and absorption effects are observed for the deepest gratings. A simple theoretical model, based on the Rayleigh hypothesis and retaining only resonant diffraction terms without a small-signal approximation being made, provides good agreement with the experimental results.

INTRODUCTION

The study of the interaction of light with periodic structures (gratings) on metals has a long and distinguished history. In 1902 Wood[1] first noted the anomalous behavior (christened Wood's anomalies) displayed by diffraction gratings of large and rapid changes in diffraction intensities for small angular and spectral variations. Rayleigh[2,3] presented in 1907 the first theoretical explanation of these anomalies in suggesting that such behavior was due to the cutoff or the appearance of a new spectral order. In 1941 Fano first distinguished between two types of Wood anomalies: (1) an edge anomaly, with a sharp behavior related to the passing off of a diffraction order (i.e., a diffraction order passing over the horizon, 90° to the surface normal) and (2) a resonance anomaly due to excitation of a bound or surface wave at the metal–dielectric interface.[4]

Surface plasma waves (SPW's) are TM modes of the electromagnetic field bound to the interface between a metal and a dielectric. The condition for existence of the SPW mode is $\epsilon_m' < -\epsilon_d$, where ϵ_m' is the real part of the metal dielectric constant and ϵ_d is the dielectric constant of the dielectric. Related modes, first investigated by Sommerfeld,[5] exist when one of the media is highly lossy. The SPW phase velocity is less than the light velocity in the dielectric, and phase matching between an incident, freely propagating wave and the SPW is accomplished either by a prism[6] or by grating coupling techniques.

The SPW dispersion relation for a planar metal–air interface is simply given by[7]

$$k_{SPW} = k_0[\epsilon_m/(\epsilon_m + 1)]^{1/2}, \quad (1)$$

where $k_0 = 2\pi/\lambda$ is the free-space optical wave vector. The phase-matching condition for excitation of SPW's is satisfied whenever $k_0 \sin\theta$, the component of k_0 along the metal–air interface, satisfies the condition

$$k_0 \sin\theta = \pm k_{SPW}' + n2\pi/d, \quad (2)$$

where d is the grating period, θ is the angle of incidence, $n = \pm 1, \pm 2, \ldots$ is the coupling order, and k_{SPW}' is the real part of the SPW wave vector. In Eq. (2) the choice of a negative sign preceding k_{SPW}' corresponds to a SPW moving in the direction opposite the incident wave. This expression assumes that the grating wave vector is in the plane of incidence; i.e., the grating lines are perpendicular to the incident wave vector.

The SPW dispersion relationship is plotted in Fig. 1 for a lossless, free-electron metal ($\epsilon_m = 1 - \omega_p^2/\omega^2$), where the axes are normalized to the plasma frequency ω_p and the corresponding optical wave vector ($k_p = \omega_p/c$). Also shown as two vertical dashed lines, corresponding to the $n = \pm 1$ orders in Eq. (2), are the wave vectors of a surface grating. Finally, the wave vectors accessible in the $n = 0$ and $n = \pm 1$ orders by variations in the angle of incidence are shown as horizontal lines. This figure was drawn for a grating period smaller than the optical wavelength ($\lambda/d > 1$); note that there is only one point that satisfies Eq. (2), for $n = -1$, and at this incident angle there is no allowed diffraction order.

In 1967 Teng and Stern first detected SPW's optically by bombarding 1200-line/mm (833-nm-period) gratings with 10-keV electrons and observing the emitted optical radiation.[8] They observed that the line shape of the

0740-3224/91/040770-10$05.00 © 1991 Optical Society of America

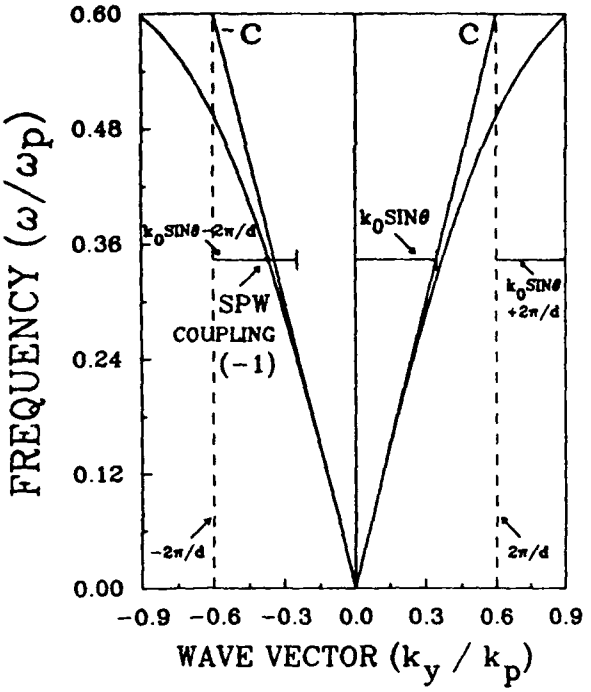

Fig. 1. Dispersion relation of SPW's for a lossless, free-electron metal ($\epsilon = 1 - \omega_p^2/\omega^2$). The axes are normalized to ω_p and $k_p = \omega_p/c$. The grating wave vectors corresponding to $n = \pm 1$ order of a grating of period d are shown as vertical dashed lines. The range of wave vectors accessible by variations in the input angle from normal to grazing incidence for $n = 0$ and $n = \pm 1$ is shown as horizontal lines. Note that for this choice of parameters ($\lambda/d < 1$) there is only one SPW coupling resonance, and at this resonance angle there is no propagating diffraction order.

emitted radiation was influenced by the surface condition of the metal but was independent of the energy of the bombarding electrons. Cowan and Arakawa carried out a detailed study of the SPW dispersion curves for dielectric-metal layers on concave diffraction gratings and also developed a quantum-mechanical formalism to describe their results.[9] Hutley and co-workers published in 1973 a detailed experimental study of the anomalies of sinusoidal profile gratings as a function of grating depth[10-12] and characterized the SPW line shapes for grating depths h ranging up to 60 nm for 500-nm-period gratings ($h/d \leq 0.12$). The integral formalism developed by Petit and others[13] was used to describe these results with good agreement. Pockrand and Raether, in an extensive series of publications,[14-18] characterized the SPW coupling as a function of grating period, depth, and profile. The gratings studied were sufficiently deep for better than 98% coupling into the SPW mode to be realized. A perturbation analysis, developed by Kroger and Kretschmann,[19] was used in modeling these results with good agreement, although clearly the perturbation approach must break down as the coupling efficiency approaches 100%. A complete theoretical treatment of grating coupling to SPW's was provided by Mills and co-workers.[20,21] Their approach uses an integral formulation of the boundary-value problem at the grating interface and an extinction theorem mechanism following from Green's theorem that was first applied by Toigo et al.[22] The latter study does not give simple analytic results but relies on extensive computational and numerical evaluation. Glass et al.[23] and Weber[24] simplified this treatment by developing a renormalized mode-coupling theory that retained the resonant terms and treated all other terms within perturbation theory. Yamashita and Tsuji[25] independently developed a differential formulation that treats the resonantly generated fields on a par with the incident fields and allows for saturation and decreases in coupling with increasing grating depths. They employed a power-series expansion in k_0h and restricted their study to small grating amplitudes; simple analytic expressions were obtained for the coupling strength as a function of h.

In this paper a comprehensive experimental and theoretical study of first-order grating coupling to SPW's for a wide range of grating parameters is presented. The experimental results establish, for the first time to our knowledge, a relationship between grating depth and grating period for SPW coupling and extend to grating depths that no longer support SPW's but rather show polarization and absorption effects. The theoretical approach is an extension of the Rayleigh hypothesis including only resonant terms in the Rayleigh expansion (cf. Refs. 23–25). This results in considerable simplification; reasonable agreement between theory and experiment is found out to depth/period ratios of ~0.5. Gupta et al.[26] used a similar approach to describe grating coupling to long-range SPW modes on thin, symmetrically bounded, metal films.

GRATING FABRICATION

Gratings were fabricated holographically in positive photoresist layers spun onto Si substrates with the use of the 488-nm line from a single-mode Ar-ion laser. The details of the grating fabrication were presented elsewhere.[27] The grating profiles were approximately sinusoidal for shallow depths, evolving toward rectangular profiles as the depth was increased (cf. Fig. 4 below). After development these gratings were coated with ~100-nm-thick electron-beam evaporated Ag films. Films were deposited at room temperature and at background pressures of low 10^{-6} Torr.

OPTICAL ARRANGEMENT

All of the measurements reported here are of the angular dependence of the zero-order reflectance for a fixed-frequency TM-polarized He–Ne laser beam at 633 nm. The samples were mounted as one surface in a 90° corner reflector attached to a computer-controlled rotation stage. This arrangement ensured that the reflected beam was always returned in the same direction and eliminated the necessity of a second rotation stage for the detector. The incident laser beam was focused with a long-focal-length (0.5-m) lens to a spot of ~2 mm. This provided an angular limitation of 0.05°, much smaller than the observed reflectance variations. Care was taken with the alignment to ensure that the axis of the rotation stage was in the plane of the grating so that the laser spot sampled the same area of the grating throughout a scan. Grating depths were measured in cross section with a scanning electron microscope (SEM). This introduces some errors, estimated at ±5 nm, owing to uncertainties in the SEM calibration and variations in the grating depth for the different areas sampled in the optical and SEM measurements.

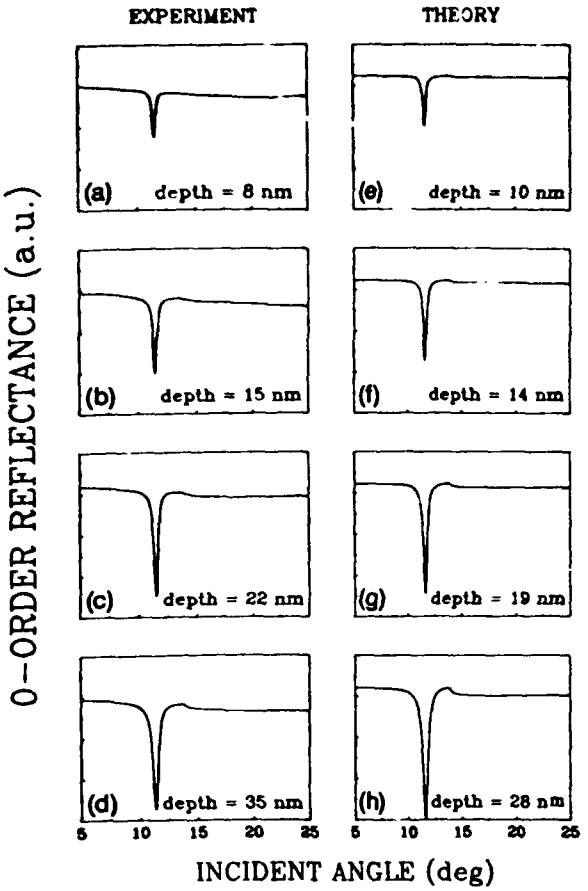

Fig. 2. Zero-order reflectance at 633 nm for 510-nm-period gratings with varying grating depths. The left side [(a)–(d)] presents experimental results; the right side [(e)–(h)] presents theoretical modeling. See the text for details.

EXPERIMENTAL RESULTS

Zero-order reflectance measurements for a series of 510-nm gratings with increasing depth are shown on the left-hand side of Fig. 2. The theoretical modeling shown on the right-hand side will be discussed below. The major features to be noted in these measurements include the following:

(1) The excitation of SPW's at $\theta \sim 11.6°$ corresponding to the sharp dip in the reflectivity (note that there is no diffracted order at this angle, so that this decrease corresponds directly to energy coupled into the SPW mode),

(2) The rapid increase in coupling efficiency with increasing grating depth to a maximum observed coupling of 94% at a grating depth of 35 nm,

(3) The horizon for the $n = -1$ diffracted order at $\theta \sim 13.8°$ (this is apparent as the cusp in the reflectivity as energy is transferred from the specularly reflected beam to the diffracted beam).

Similar results for deeper gratings are presented on the left-hand side of Fig. 3. Note the larger angular scale in this figure. Specific features to be noted include the following:

(1) The relatively gradual decrease in the coupling efficiency of SPW's,

(2) The clear broadening of the SPW resonance with increasing depth,

(3) The shift in the SPW resonance to smaller angles with increasing depth,

(4) The residual SPW coupling even at large grating depth/grating period ratios,

(5) The increasing coupling to the $n = -1$ diffraction order. (The sharp spike at $-38°$ corresponds to the collection of the $n = -1$ diffraction order in the optical system and is not part of the zero-order reflectance. It does provide a useful monitor of the energy in the diffracted order.)

SEM images of the gratings used for the measurements of Fig. 3, taken in cross section, are shown in Fig. 4. Note that the grating shapes are sinusoidal at low depths but gradually show increasing harmonic components and trend toward rectangular profiles for the deepest gratings investigated. This profile modification results from the grating fabrication technique.[27]

Similar experiments were performed for gratings with periods of 392 and 440 nm, in an investigation of the dependence of the coupling efficiency on grating depth and grating period. All the experiments were carried out at a wavelength of 633 nm, in avoidance of variations in the metal optical properties. Qualitatively similar behavior was observed, with comparable coupling efficiencies occurring at shallower grating depths for finer gratings. Experimentally determined coupling efficiencies, resonance angles, and resonance linewidths for all three sets

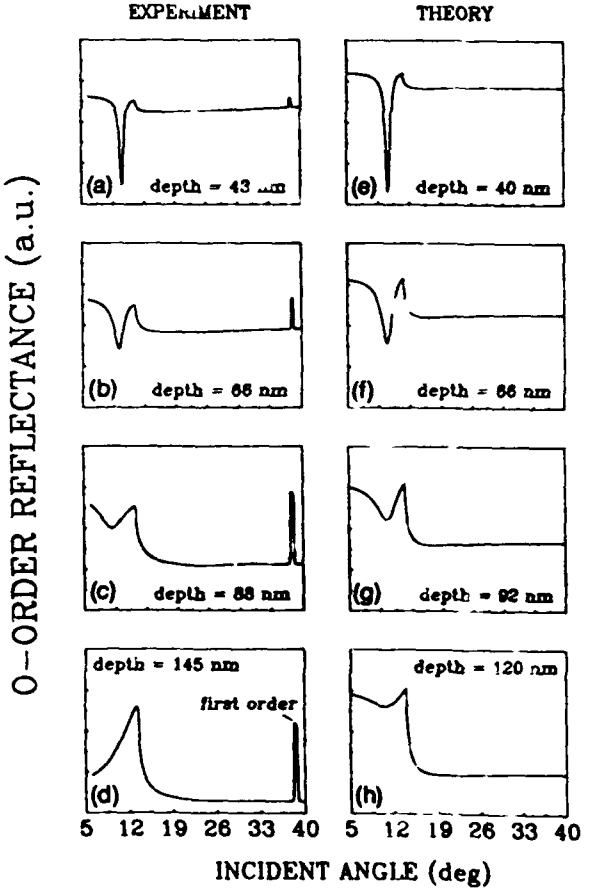

Fig. 3. Continuation of Fig. 2 for deeper gratings. Note the expanded angular scale. Again, the left side [(a)–(d)] presents experimental results; the right side [(e)–(h)], theoretical modeling. The sharp spikes on the experimental data at $-38°$ correspond to the $n = -1$ diffraction order entering the collection optics and are not a part of the zero-order reflectivity.

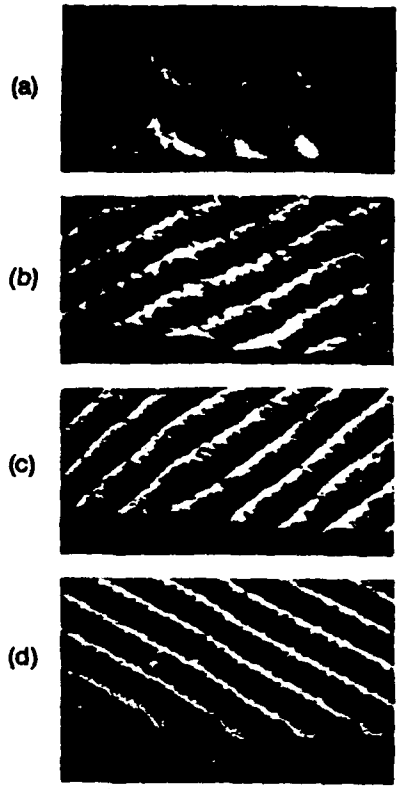

Fig. 4. Cross-section SEM pictures of the gratings used for the experiments. The measured depths are (a) 43 nm, (b) 57 nm, (c) 88 nm, and (d) 145 nm.

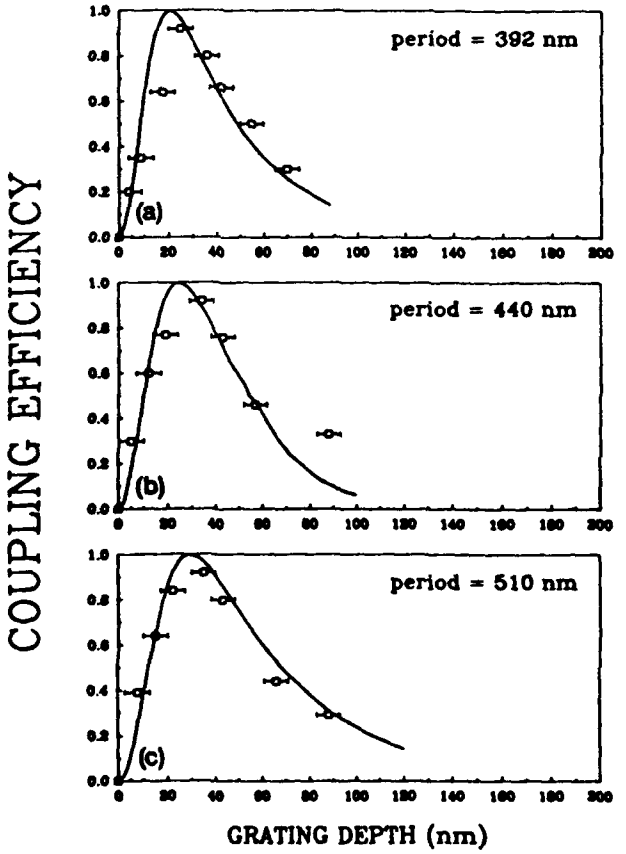

Fig. 5. Coupling efficiency into the SPW mode for gratings with periods of (a) 392 nm, (b) 440 nm, and (c) 510 nm and varying depths. The solid curves are the result of theoretical modeling; see the text for details.

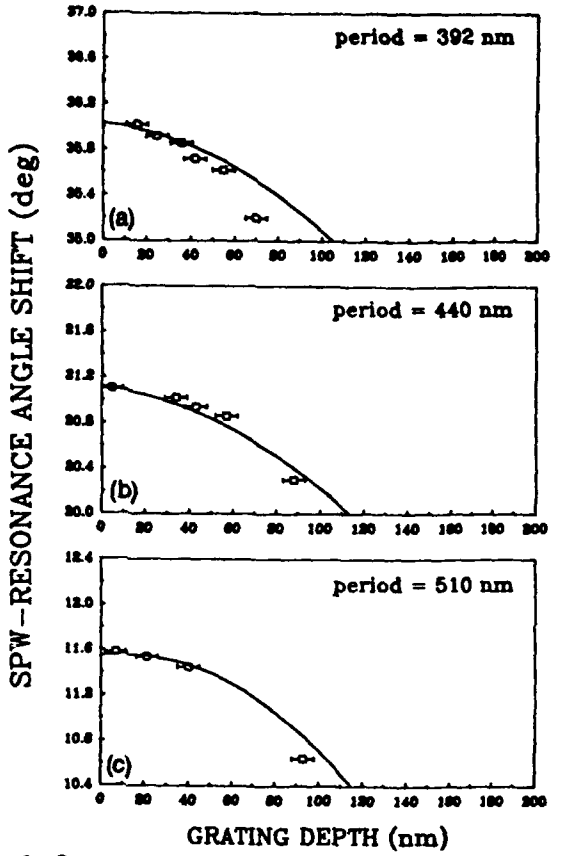

Fig. 6. Same as Fig. 5, except here for SPW resonance angle.

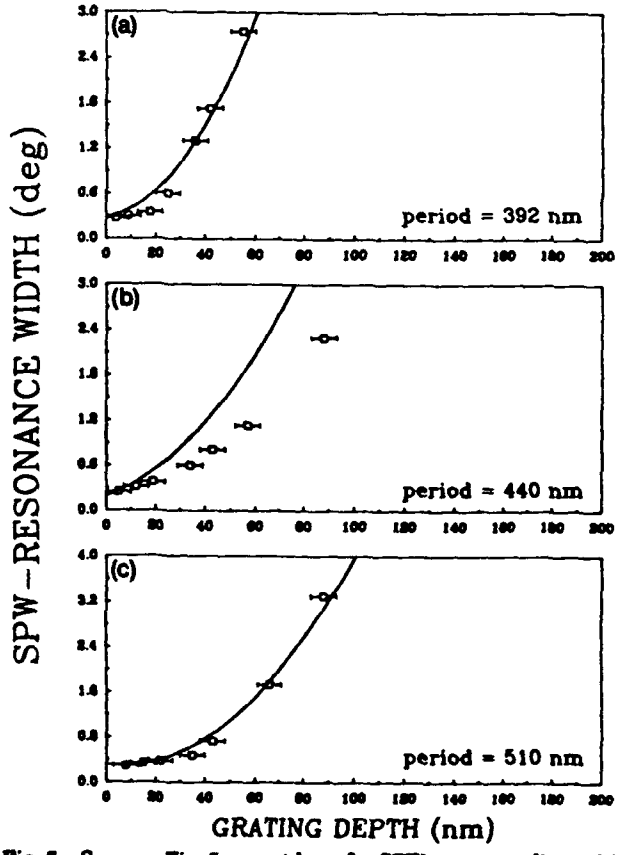

Fig. 7. Same as Fig. 5, except here for SPW resonance linewidth (FWHM).

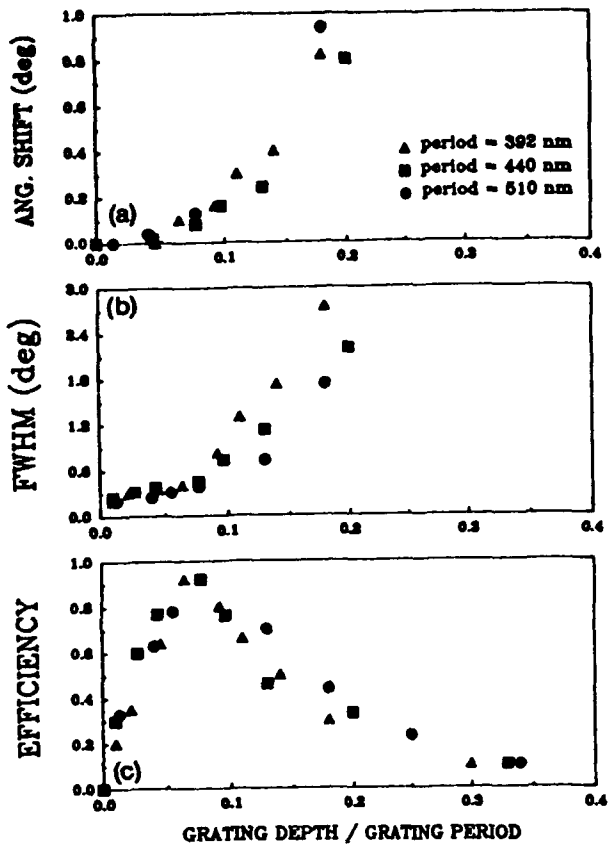

Fig. 8. Data of Figs. 5–7 for the SPW resonance angle, the resonance linewidth, and the coupling efficiency replotted against the dimensionless parameter h/d. Note that this parameter is approximately invariant for these three grating periods.

of gratings are presented in Figs. 5, 6, and 7, respectively. The solid curves are theoretical and will be discussed below. With increasing grating depth each of the data sets displays an initial rapid increase in coupling efficiency, peaking at over 90%, and a slower decrease in efficiency; an approximately quadratic decrease in the resonant coupling angle; and an approximately quadratic increase in the resonance width.

These results are summarized in Fig. 8, which shows all three sets of data plotted against the dimensionless parameter h/d, i.e., grating depth/grating period. Within experimental uncertainties these results appear to follow a common behavior. Some of the variability may well arise from differing grating profiles, especially for the deeper gratings.

Further increases in grating depth, accompanied by a change in profile to rectangular, lead to an elimination of SPW effects. For approximately square gratings strong polarization effects demonstrate the possibility of the fabrication of reflective polarizers for visible radiation. This is shown in Fig. 9, where reflectance scans for the three grating periods are given for depths of 200 nm (392-nm period), 170 nm (440-nm period), and 190 nm (510-nm period), which resulted in maximum polarization effects. Note that for TM polarization, almost 100% of the incident energy (~96% for the 510-nm-period grating) is coupled into the first-order diffraction peak for angles beyond the horizon for this order. In contrast, only approximately 20% of the energy polarized in the TE direction is coupled out of the zero-order reflected beam. Careful variations of grating depth and profile must be investigated for optimization of the polarization of the reflected beam. Such polarization behavior for square gratings was predicted[28,29] and demonstrated in the infrared[30]; to our knowledge, though, this is the first observation of these effects in the visible spectral region. SEM pictures of the gratings are shown in Fig. 10.

Further increases in grating depth result in rectangular profiles with decreasing line/space ratios. Angular reflectance scans for deep rectangular gratings are shown in Fig. 11 [(a) 320-nm depth, 392-nm period; (b) 330-nm depth, 440-nm period; (c) 300-nm depth, 510-nm period]. There is a broad absorption of TM-polarized radiation, while a large diffraction efficiency, increasing with increasing periods, is observed for TE polarization. Figure 12 shows SEM pictures of these gratings.

THEORY

During the past thirty years many grating theories based on the vector character of the electromagnetic field have been developed. An excellent summary can be found in Refs. 6, 13, and 20. Integral methods, developed by Petit and others, evaluate the field at any point in terms of an integral over the grating surface Λ (cf. Fig. 13). A variation of these integral techniques based on a Green's-function formalism specifically directed to the evaluation of the SPW dispersion relation on a periodic surface was extensively developed by Mills and co-workers[20,21] and Otagawa.[31] In addition, a differential formalism, developed by Nevierre *et al.*,[32] was applied to SPW's on a periodic surface by Numata.[33] All these approaches are fully rigorous, bold for arbitrary profiles, and require exten-

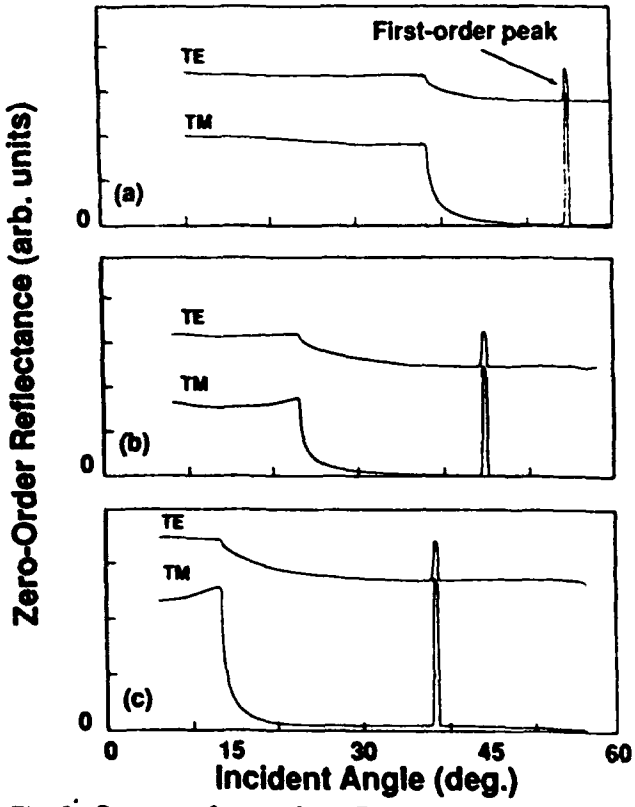

Fig. 9. Sequence of zero-order reflectance scans for approximately square gratings ($h/d \sim 0.5$) showing strong polarizing effects: (a) h = 200 nm, d = 392 nm; (b) h = 170 nm, d = 440 nm; and (c) h = 190 nm, d = 510 nm.

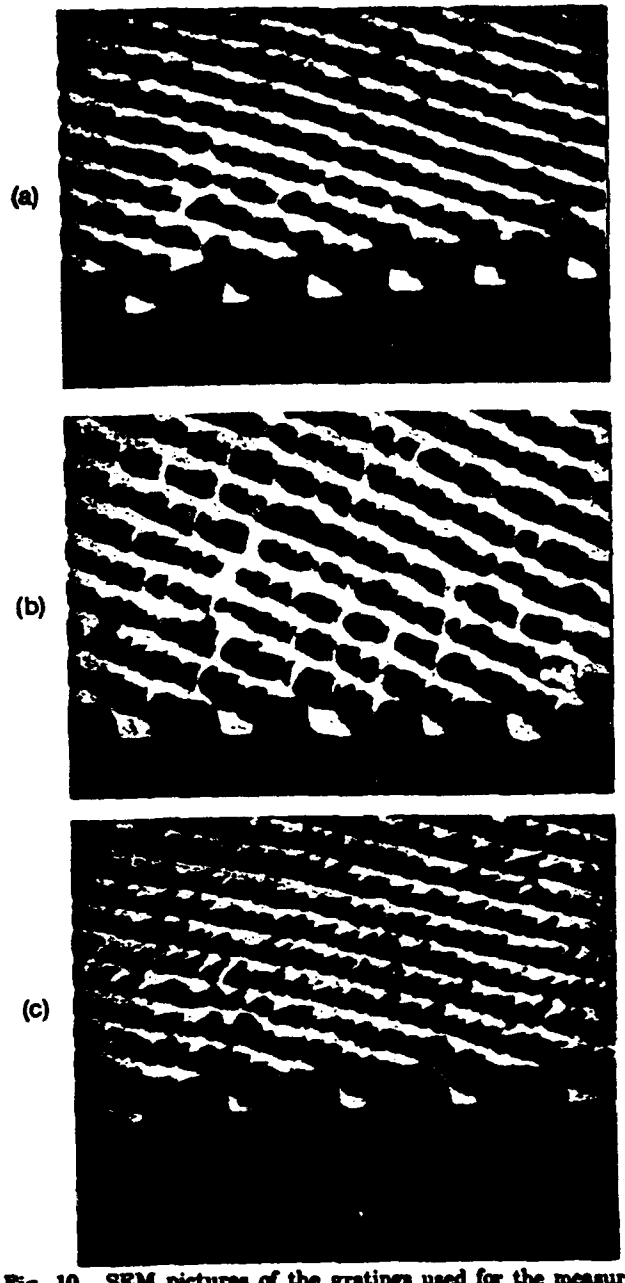

Fig. 10. SEM pictures of the gratings used for the measurements of Fig. 9.

sive computation, typically involving matrices of order 40 or higher.

A number of differential analyses, usually based on a perturbation expansion in k_0h, where h is the grating depth, and relying on a Rayleigh or plane-wave approach have also been presented.[18,34,35] In these treatments the scattered field amplitudes are also treated as small quantities, of the order of k_0h times the incident and reflected/transmitted field amplitudes. These models have the virtue of relatively simple analytic results and ready physical interpretation. These perturbational approaches clearly break down as the coupling efficiencies into SPW modes and diffraction orders approach unity, since they do not self-consistently describe the necessary decrease in the zero-order reflected and transmitted beams. Yamashita and Tsuji[25] treated the coupling problem within the Rayleigh hypothesis without making the small-signal approximation for the resonant scattered fields; however, their treatment retained the expansion in k_0h, which limits its applicability to larger grating amplitudes. Nevertheless, their model provided an elegant analytic result that included the quadratic [$\propto(k_0h)^2$] increase in the SPW intensity with grating depth for shallow gratings, the saturation of the SPW intensity at a coupling efficiency near 100%, and a gradual decrease of the coupling [$\propto(k_0h)^{-2}$] for deeper gratings as the energy is coupled back into the radiating fields, in qualitative agreement with the experimental results presented above. Weber[24] presented a related analysis, based on the extinction theorem, that retains the nonresonant terms in a perturbation-theory expansion in k_0h while also keeping the resonant terms.

These models begin with a time-harmonic, plane-wave expansion of the electromagnetic field in the regions outside the grating kerf ($z < 0$ and $z > h$, Fig. 13); the magnetic fields of the TM-polarized fields are given by

$$\mathbf{B}^r = B^r\mathbf{e}_x = \{\exp[i(k_y y + k_z z)] + \sum B^r_n \exp[i(k_n y - \alpha_n z)]\}\mathbf{e}_x, \quad z < 0 \quad (3a)$$

and

$$\mathbf{B}^m = B^m\mathbf{e}_x = \sum B^m_n \exp[i(k_n y + \beta_n z)]\mathbf{e}_x, \quad z > h, \quad (3b)$$

where $k_y = k_0 \sin\theta$, $k_z = k_0 \cos\theta$, $k_n = k_y + ng$, $n = 0, \pm1, \pm2, \ldots$, $g = 2\pi/d$ is the grating wave vector with d the grating period, $\alpha_n = i(k_n^2 - k_0^2)^{1/2}$, $\beta_n =$

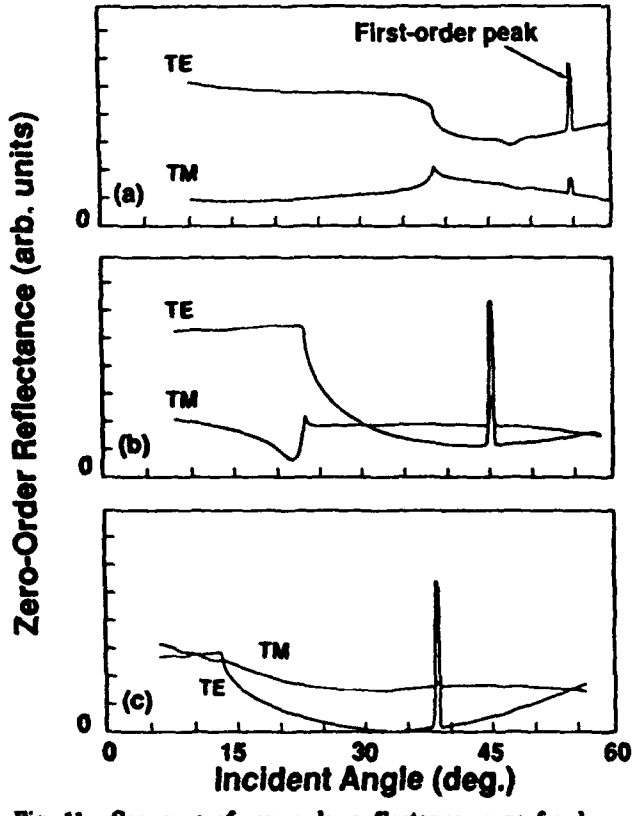

Fig. 11. Sequence of zero-order reflectance scans for deeper rectangular gratings ($h/d \sim 1$) showing strong absorption effects: (a) h = 320 nm, d = 392 nm; (b) h = 330 nm, d = 440 nm; and (c) h = 300 nm, d = 510 nm.

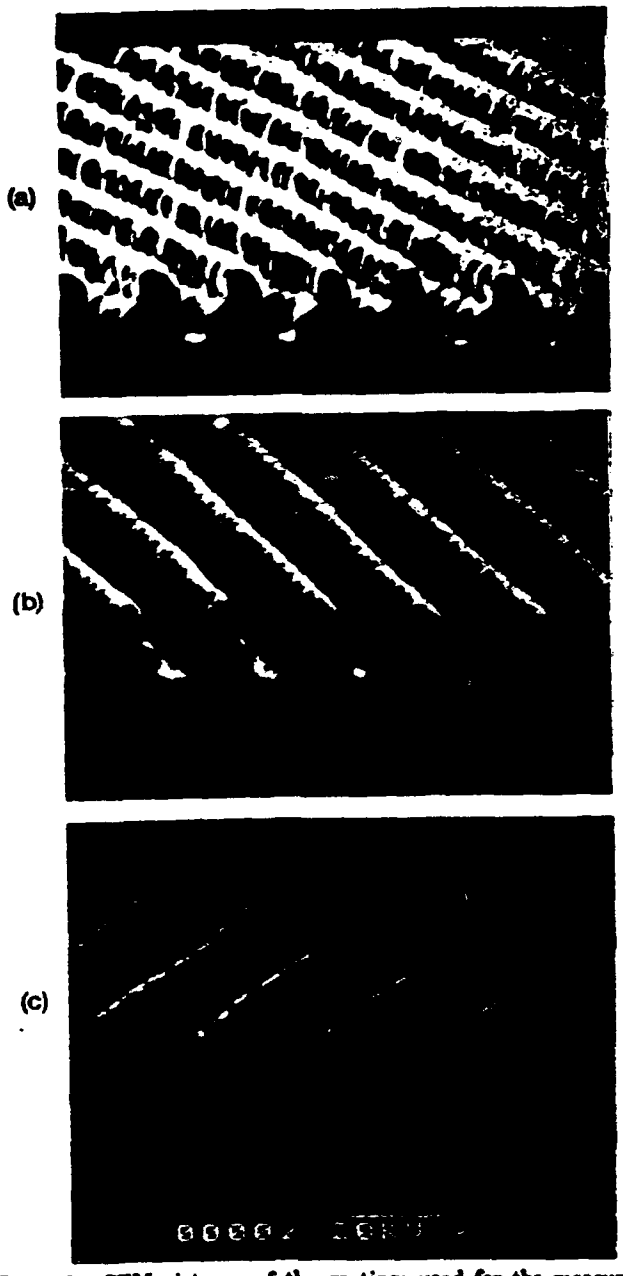

Fig. 12. SEM pictures of the gratings used for the measurements of Fig. 11.

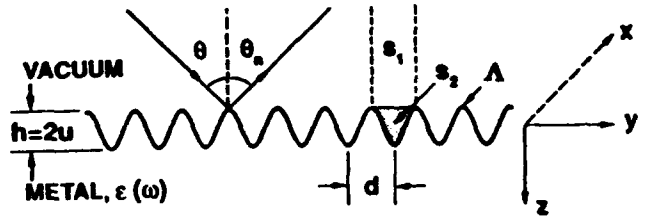

Fig. 13. Geometry used in the analysis.

$\iota(k_n^2 - \epsilon_m k_0^2)^{1/2}$, and ϵ_m is the metal dielectric constant. Within the grating kerf ($0 < z < h$), the validity of this expansion is not well established. Rayleigh made the assumption, known as the Rayleigh hypothesis, that for sufficiently shallow gratings this expansion is valid everywhere. This hypothesis was investigated by Van den Berg and Fokkema[36] and shown to be analytically correct; Petit and Cadilhac[36] showed that for TE polarization the Rayleigh expansion is convergent for $h/d < 0.14$, and pointed out that reliable results could be obtained even for h/d values as great as twice this limit. A detailed analysis of the applicability of the Rayleigh hypothesis to real materials was recently presented.[37] Glass *et al.*[38] pointed out that the extinction theorem formalism leads to the identical dispersion relation.

The approach used here in the comparison with experiment is to apply the Rayleigh hypothesis for TM-polarized input radiation. For the gratings used in these experiments, h/d extends to 0.8, although detailed comparisons are attempted only to ~0.3. The calculation does not make a small-signal approximation for either the grating depth or the diffracted field amplitudes. The plane-wave expansion [Eqs. (3)] is truncated by the retention of resonant terms, e.g., $n = 0$ and $n = -1$. In addition, the next terms, $n = -2$ and $n = +1$ are retained in the numerical evaluations and are determined to be small relative to the resonant terms. Energy conservation, i.e., a constant total of the energies in the diffracted beams and absorbed in the metal, is used as a further check on the calculation.

Thus Eq. (3) is assumed to hold up to the grating surface defined by

$$f(y) = u \sin(gy), \tag{4}$$

where $u = h/2$ is the grating amplitude. Using the generating function for Bessel functions, we can write

$$\exp[i\gamma f(y)] = \exp[i\gamma u \sin(gy)] = \sum \exp(ipgy) J_p(\gamma u). \tag{5}$$

The boundary conditions satisfied by these fields are

$$\{B^v(y, z) = B^m(y, z)\}|_{z=f(y)} \tag{6}$$

and

$$\left\{\frac{\partial B^v(y, z)}{\partial n} = \frac{1}{\epsilon_m}\frac{\partial B^m(y, z)}{\partial n}\right\}\Bigg|_{z=f(y)}, \tag{7}$$

where

$$\frac{\partial}{\partial n} = \left[1 + \left(\frac{\partial f}{\partial y}\right)^2\right]^{-1/2}\left(\frac{\partial}{\partial z} - \frac{\partial f}{\partial y}\frac{\partial}{\partial y}\right).$$

Applying these boundary conditions leads to an infinite set of coupled linear equations:

$$J_p(k_z u) + \sum B^v_n(-1)^{p-n} J_{p-n}(\alpha_n u) - \sum B^m_n J_{p-n}(\beta_n u) = 0 \tag{8}$$

and

$$\left(k_z - \frac{pgk_y}{k_z}\right)J_p(k_z u) - \sum\left[\alpha_n - \frac{(p-n)gk_n}{\alpha_n}\right]B^v_n(-1)^{p-n}J_{p-n} \times (\alpha_n u) - \frac{1}{\epsilon_m}\sum\left[\beta_n - \frac{(p-n)gk_n}{\beta_n}\right]B^m_n J_{p-n}(\beta_n u) = 0, \tag{9}$$

where p and n are integers extending from $-\infty$ to $+\infty$.

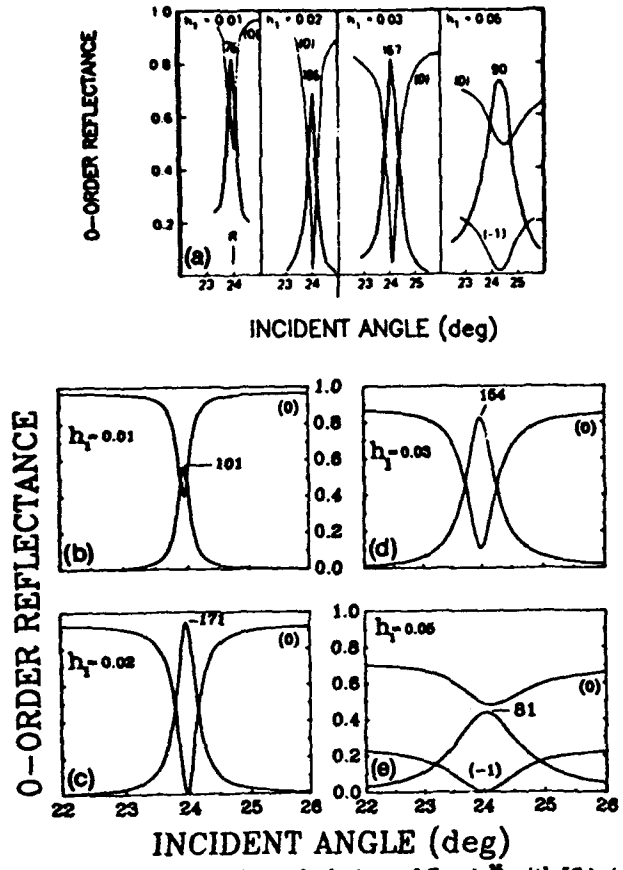

Fig. 14. Comparison of (a) calculations of Garcia[35] with [(b)–(e)] present calculations for 800-nm-period Au gratings at 633 nm ($h_1 = h/2d$).

Note that no small-signal approximation was made in the derivation of these equations. These equations are now truncated by the retention of only the fields for $n = 0$ and $n = -1$, the reflected/transmitted and resonant diffracted terms, which are expected to be large based on phase-matching arguments [cf. Eq. (2) and Fig. 1]. In addition, the fields for $n = +1$ and $n = -2$ were retained as a check on the convergence. The relative field intensities for these two orders for a 510-nm-period grating at a depth of 22 nm were 0.017 and 0.0018, respectively, lending support to this truncation procedure. This leads to solving an 8×8 matrix inversion for the field intensities.

Using the Green's-function approach developed by Toigo *et al.*,[23] Garcia evaluated the SPW fields and line shape for sinusoidal gratings.[35] The results, obtained by the inclusion of 60 terms in the numerical analysis, are shown in Fig. 14(a) for parameters appropriate to an 800-nm-period Au grating of various depths $h_1 = h/2d$. For this grating period and wavelength (633 nm), $\lambda/d < 1$, and there are two possible propagating diffraction orders. The resonance shown in Fig. 14 corresponds to the $n = +1$ SPW coupling; there is also a propagating $n = -1$ diffraction order throughout this angular range. The numbers labeling the SPW curves in the figure represent the relative intensity of the mode. The results from the present treatment for the same parameters are shown in Figs. 14(b)–14(d). Note the overall similarity of the calculated intensities and line shapes. Interestingly, the largest discrepancy is for the shallowest grating, $h_1 = 0.01$, where the present calculation yields a SPW intensity that is 24% larger than the more rigorous calculation of Garcia.[35] For deeper gratings the agreement is generally within 10%. A similar result was found by Weber[24] in his development of a coupled-mode analysis. This comparison indicates that despite the relative simplicity of the formulation the present model provides substantial insight into SPW coupling.

COMPARISON OF THEORY AND EXPERIMENT

The initial step in a comparison of this model with the experimental results is the establishment of the deposition-dependent dielectric properties of the Ag films. Various values of the Ag dielectric constant at a 633-nm wavelength have been reported, viz., $(-16.4, 0.54)$,[39] $(-17.9, 0.49)$,[40] and $(-18.9, 2.35)$.[41] As is reflected in this wide dispersion of reported values, the dielectric properties of thin films are dependent on deposition- and substrate-dependent columnar structure, granularity, subideal density, and incorporated impurities. Given this uncertainty, the approach adopted here is to adjust the dielectric properties to obtain a best fit to the experimental result for a single grating [510-nm period, 22-nm depth; Fig. 2(c)], which gives a value of $(-13.65, 0.82)$; this value was used for all the comparisons between theory and experiment. The fit for this grating is shown in Fig. 15; excellent agreement is obtained for a calculated depth of 19 nm. In subsequent measurements, which will be reported in detail elsewhere, the dielectric properties of Ag films deposited on Si substrates under identical conditions were determined independently by ellipsometric techniques to be $(-12.9, 0.76)$, within 7% of the values obtained here. The grating fabrication and the film deposition involved in the present study were carried out over a period of several months, and deposition conditions and the resulting film properties invariably drift over this time period; no adjustment was made in the dielectric values used in the comparison between theory and experiment.

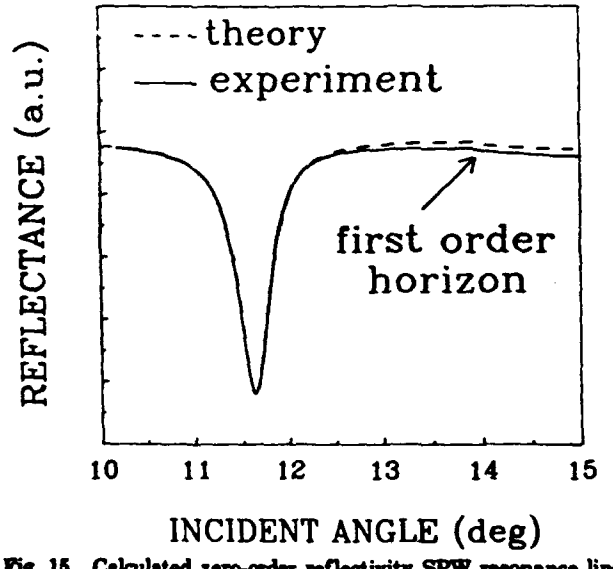

Fig. 15. Calculated zero-order reflectivity SPW resonance line shapes for $\epsilon = (-13.65, 0.82)$ at grating depth $h = 19$ nm. The experimental result ($h = 22$ nm) is shown as the solid curve.

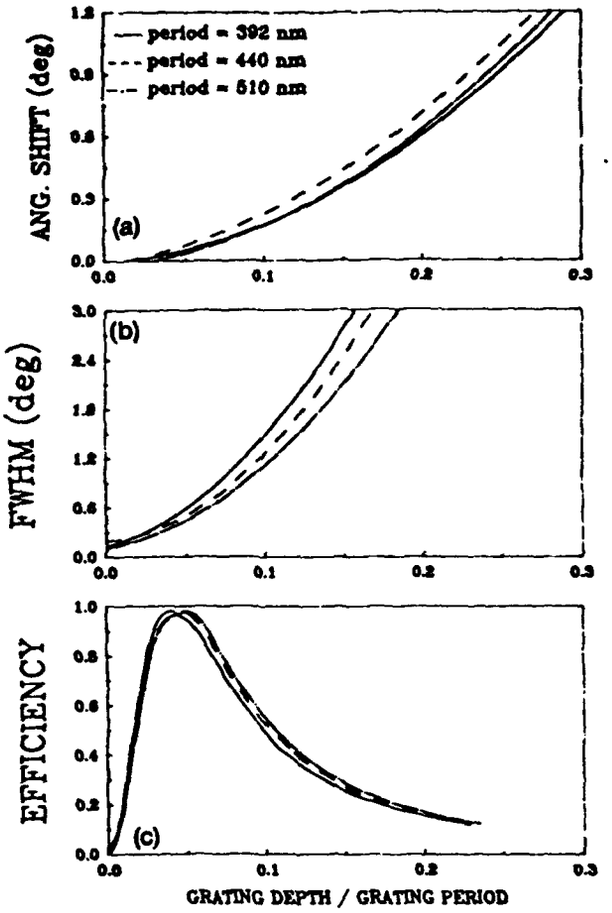

Fig. 16. Calculated SPW resonance parameters plotted against the dimensionless parameter h/d.

Comparisons with the experimental results are shown on the right-hand sides of Figs. 2 and 3. In each case the grating depth for the calculation is adjusted to give coupling efficiencies that match the experimental results. There is overall excellent agreement. For the deepest grating shown experimentally, $h = 145$ nm, there is a substantial difference with the model that is probably associated with the significant deviation from a simple sinusoidal profile at this depth (cf. Fig. 4). Figures 5–7 present the model results along with the experimental data for the coupling efficiency, the resonance angle, and the resonance linewidth for all three grating periods investigated. There is an excellent qualitative match between theory and experiment. The most significant deviation, that for the linewidth of the 440-nm-period gratings, is most probably due to a variation in the film dielectric properties for this set of gratings. The coupling efficiencies first increase rapidly as the grating depth is increased, saturate near 100% coupling, and then decrease as the resonance becomes overcoupled owing to radiative damping back into the zero-order radiation fields. This coupling change is accompanied by approximately quadratic changes in the resonance angle and linewidth with increasing grating depth. Remarkably similar qualitative behavior was predicted by Weber and Mills[21] in their numerical analysis of grating coupling for 800-nm-period Ag sawtooth gratings. They evaluated the third-order coupling at $\lambda = 480$ nm and found a maximum coupling strength for grating depths of 40–60 nm.

The model results are summarized in Fig. 16, which shows the calculated resonance angle, resonance linewidth, and coupling strength plotted against the dimensionless parameter h/d for the three grating periods investigated. For evaluation of the coupling efficiency this parameter is reasonably invariant; there are more significant deviations in the evaluation of the resonance line-shape parameters.

Overall, this simple model provides a good picture of the experimentally observed resonance variations. Disagreements between theory and experiment increase for deeper gratings and larger periods. A significant phenomenon not included in the theoretical model is the deviation from sinusoidal grating profiles, which increases as the grating depth is increased and also is more significant for larger grating periods. The films also exhibit significant surface roughness (see Fig. 4), which has not been included in the model and may influence the observed line shapes.

Calculated zero-order, TM-polarization reflectivity curves for deeper gratings, up to $h/d \sim 1$, are shown in Fig. 17. Again, there is good qualitative agreement with the large coupling into the diffraction order for deep gratings ($h/d \sim 0.5$), although detailed comparisons are not possible because of the strong deviation from a simple sinusoidal profile of the experimental gratings. The model does not show the absorption of TM-polarized radiation seen experimentally. A detailed comparison with experiment requires deep sinusoidal gratings, which are inherently difficult to fabricate because of the strong nonlinearities of existing photoresists.[37] More nearly sinusoidal gratings can be fabricated on a transparent substrate; research continues in the pursuit of a better experimental test of the model for deep gratings. The theoretical model loses much of its simplicity for rectangular gratings, where many Fourier components of the grating profile are comparable in intensity.

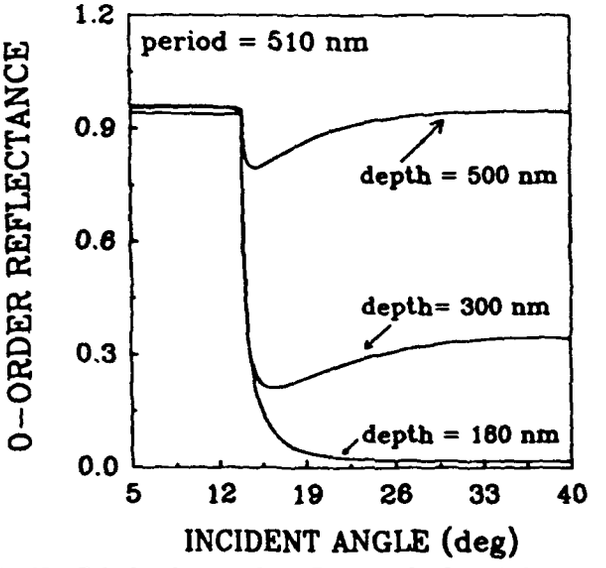

Fig. 17. Calculated zero-order reflectivity for deep ($h/d \sim 1$) sinusoidal gratings in TM polarization ($d = 510$ nm).

SUMMARY

A systematic experimental and theoretical study of first-order grating coupling to SPW's existing at an air–Ag interface was reported. The experiment extends the range of investigated grating depths to $h/d \sim 1$. For TM-polarized incident radiation this includes the entire range of SPW-radiation coupling—from underdamped, to nearly 100% coupling, to overdamped and the ultimate disappearance of the SPW resonance from the observed zero-order reflectance. Strong polarization and absorption effects are observed for the deepest gratings. A simple theoretical model, based on the Rayleigh hypothesis and retaining only resonant diffraction terms without making a small-signal approximation, provides good agreement with the experimental results.

Several extensions of this work are immediately apparent. For larger grating periods there are more diffraction orders and SPW coupling resonances. Interesting coupling effects occur when two of these resonances occur at approximately the same angle. These effects have been investigated experimentally and theoretically and will be reported in a subsequent publication. In addition, the SPW resonance can be used to characterize metal optical constants under a variety of deposition conditions. A study is under way that compares this technique with more conventional techniques such as ellipsometry.

ACKNOWLEDGMENT

This research was partially supported by the U.S. Air Force Office of Scientific Research.

S. R. J. Brueck is also with the Departments of Electrical Engineering and Physics, University of New Mexico, Albuquerque, New Mexico 87131.

*Present address, Electronics Division, PINSTECH, P. O. Box Nilore, Islamabad, Pakistan.

REFERENCES

1. R. W. Wood, Philos. Mag. 4, 396 (1902).
2. Lord Rayleigh, Philos. Mag. 14, 60 (1907).
3. Lord Rayleigh, Proc. R. Soc. London Ser. A 79, 399 (1907).
4. U. Fano, J. Opt. Soc. Am. 31, 213 (1941).
5. A. Sommerfeld, Ann. Phys. (Leipzig) 28, 665 (1909).
6. A. D. Boardman, ed., *Electromagnetic Surface Modes* (Wiley, New York, 1982).
7. E. A. Stern, as quoted in R. A. Ferrel, Phys. Rev. 111, 1214 (1958).
8. Y. Y. Teng and E. A. Stern, Phys. Rev. Lett. 19, 511 (1967).
9. J. J. Cowan and E. T. Arakawa, Z. Phys. 235, 97 (1970).
10. M. C. Hutley, Opt. Acta 20, 607 (1973).
11. M. C. Hutley and V. M. Bird, Opt. Acta 20, 771 (1973).
12. M. C. Hutley and D. Maystre, Opt. Commun. 19, 431 (1976).
13. R. Petit, ed., *Electromagnetic Theory of Gratings* (Springer-Verlag, Berlin, 1980).
14. I. Pockrand, Phys. Lett. A 49, 259 (1974).
15. I. Pockrand and H. Raether, Opt. Commun. 18, 395 (1976).
16. I. Pockrand, J. Phys. D 9, 2423 (1976).
17. I. Pockrand and H. Raether, Appl. Opt. 16, 1784 (1977).
18. H. Raether, Opt. Commun. 42, 217 (1982).
19. E. Kroger and E. Kretschmann, Phys. Status Solidi B 76, 515 (1976).
20. V. M. Agranovich and D. L. Mills, eds., *Surface Polaritons* (North-Holland, Amsterdam, 1982).
21. M. Weber and D. L. Mills, Phys. Rev. B 27, 2698 (1983).
22. F. Toigo, A. Marvin, V. Celli, and N. R. Hill, Phys. Rev. B 15, 5618 (1977).
23. N. E. Glass, M. Weber, and D. L. Mills, Phys. Rev. B 29, 6548 (1984).
24. M. G. Weber, Phys. Rev. B 33, 909 (1986).
25. M. Yamashita and M. Tsuji, J. Phys. Soc. Jpn. 52, 2462 (1983).
26. S. D. Gupta, G. V. Varada, and G. S. Agarwal, Phys. Rev. B 36, 6331 (1987).
27. S. H. Zaidi and S. R. J. Brueck, Appl. Opt. 27, 2999 (1988).
28. J. L. Roumiguieres, D. Maystre, and R. Petit, J. Opt. Soc. Am. 67, 557 (1977).
29. J. L. Roumiguieres, Opt. Commun. 19, 76 (1976).
30. K. Knop, Opt. Commun. 26, 28 (1978).
31. K. Utagawa, J. Opt. Soc. Am. 69, 333 (1979).
32. M. Naviere, P. Vincent, R. Petit, and M. Cadilhac, Opt. Commun. 9, 48 (1973).
33. H. Numata, J. Phys. Soc. Jpn. 51, 2575 (1982).
34. S. S. Jha, J. R. Kirtley, and J. C. Tsang, Phys. Rev. B 22, 3973 (1980).
35. P. M. Van den Berg and J. T. Fokkema, J. Opt. Soc. Am. 69, 27 (1979).
36. R. Petit and M. Cadilhac, C. R. Acad. Sci. 262, 468 (1966).
37. T. C. Paulick, Phys. Rev. B 42, 2801 (1990).
38. N. Garcia, Opt. Commun. 45, 307 (1983).
39. G. P. Motulevich, *Optical Properties of Metals* (Consultants Bureau, New York, 1973).
40. P. B. Johnson and R. W. Christy, Phys. Rev. B 6, 4370 (1972).
41. R. Weast and D. Lide, eds., *Handbook of Physics and Chemistry*, 70th ed. (CRC, Boca Raton, Fla., 1989).

Grating coupling to surface plasma waves. II. Interactions between first- and second-order coupling

Saleem H. Zaidi, M. Yousaf,* and S. R. J. Brueck

Center for High Technology Materials, University of New Mexico, Albuquerque, New Mexico 87131

Received May 17, 1990; accepted November 26, 1990; manuscript in hand January 25, 1991

For grating periods larger than the excitation wavelength, multiple-grating orders couple incident optical radiation to the surface plasma waves (SPW's) characteristic of the metal–air interface. For a grating period that is an integral multiple of the wave vector of these surface modes, two resonances become degenerate in coupling angle. There are also permitted diffraction orders at this coupling angle. The vicinity of this multiple-mode coupling resonance, where several free-space electromagnetic modes, as well as two surface modes, are coupled by different orders of a grating, is known as a minigap region. Not surprisingly, the response surface displays complex dependences on frequency, angle, and grating profile. A detailed experimental and theoretical study is presented of the optical response at 633 nm in the $(+1, -2)$ minigap region for Ag films deposited on photolithographically defined 870-nm-period gratings. Measurements of both the 0-order reflectance and the −1-order diffraction are presented for a wide progression of grating depths. The SPW resonances depend on the grating depth, and this variation is used to tune through the minigap region for a fixed wavelength and period. Similar measurements are presented for a single grating as a function of wavelength through the minigap region. In both measurements the 0-order response shows only a single broad minimum as the resonances approach degeneracy, while the −1-order diffraction shows clearly defined momentum gaps. A simple theoretical model based on the Rayleigh hypothesis is presented that gives a good qualitative picture of the response. The response surfaces are sensitive to the grating profile, and detailed modeling requires inclusion of higher-order grating components.

1. INTRODUCTION

Optical interactions with metallic gratings have long fascinated scientists. Wood's initial observations of grating anomalies[1] were classified by Fano[2] into (1) diffraction anomalies associated with the redistribution of energy among diffraction orders when one order passes over the horizon (i.e., the propagation direction reaches an angle of 90° to the grating normal) and (2) resonance anomalies associated with the propagation of guided waves along the grating interface. A large body of experimental and theoretical research relating to optical interactions with periodic surfaces has been accumulated.[3,4] This paper is concerned with resonance anomalies and is focused on the propagation of guided waves, known as surface plasma waves (SPW's), on bare metallic surfaces.

For grating periods less than the excitation wavelength, only first-order coupling to SPW's is permitted and has been described in detail elsewhere.[5] For grating periods larger than the incident wavelength it is possible to couple to SPW's in higher orders and to observe electromagnetic interactions between these couplings. These interactions are the major focus of this paper. The first experimental evidence of these interactions between different coupling orders was provided by Stewart and Gallaway,[6] who observed that in some cases Wood's anomalies did not become coincident but repelled each other as the optical wavelength was varied to bring the resonances closer together. Ritchie *et al.*[7] also observed gaps in the dispersion relation of the SPW's and attributed them to higher-order interactions between SPW's. Hutley[8] and Hutley and Bird[9] carried out a detailed experimental study of the anomalies of sinusoidal diffraction gratings in the visible spectrum. The anomalies were characterized in a Littrow configuration as a function of groove depth, period, and wavelength, and in some cases a reluctance of anomalies to merge was observed. Kroo *et al.*[10] observed similar gaps in the dispersion relation of SPW's in metal–oxide–metal structures and attributed them to the crossing of $(+1, -1)$ coupling to SPW's. Chen *et al.*[11] experimentally investigated grating coupling to SPW's in the minigap regions, i.e., degenerate coupling to SPW's in two different grating orders, such as $(+1, -2)$ or $(+2, -2)$, and measured energy gaps for various minigap regions. Weber and Mills[12] and Tran *et al.*[13] showed theoretically that interactions of elastically scattered SPW's result in complex response surfaces in the vicinity of the minigaps and that a direct interpretation in terms of a modal dispersion relation is difficult at best. Detailed modeling and careful evaluation of couplings in both amplitude and phase are necessary for a full appreciation of the experimental results. Heitman *et al.*[14] showed from experimental studies on metal–oxide–metal structures that the existence of energy or momentum gaps was dependent on the mode of excitation and the experimental observable; i.e., using fast electron excitation and light emitted from metal–oxide–metal structures, they observed energy and momentum gaps, but only energy gaps were observed from optical excitation (similar to Chen's results). They also pointed out that the anomalies strongly depend on grating period, depth, and profile as well as on the excitation mechanism and the method of detection.

0740-3224/91/061348-12$05.00 © 1991 Optical Society of America

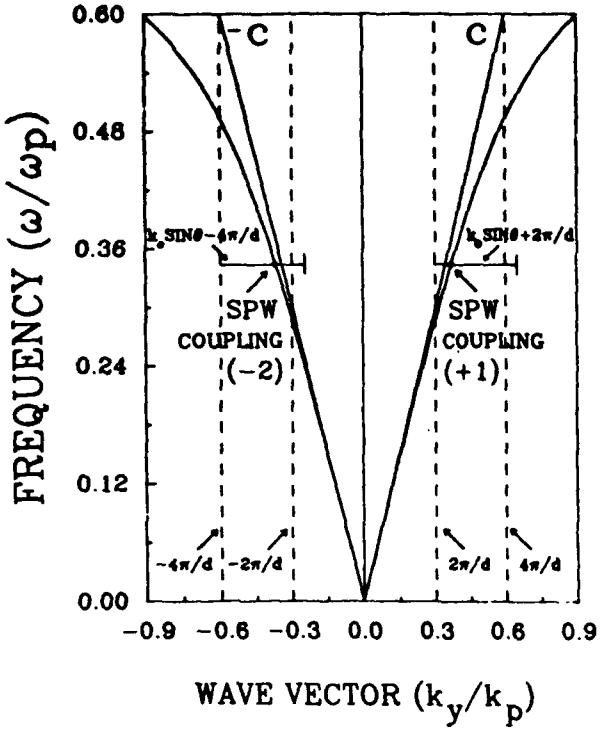

Fig. 1. Dispersion relation of SPW's for a lossless, free-electron metal ($\epsilon = 1 - \omega_p^2/\omega^2$). The axes are normalized to ω_p and $k_p = \omega_p/c$. The grating vectors corresponding to the $n = \pm 1$ and $n = \pm 2$ orders of a grating of period d are shown as vertical dashed lines. The range of wave vectors accessible by varying the input angle from normal to grazing incidence for $n = +1$ and $n = -2$ is shown as horizontal lines. Note that for this choice of parameters ($\lambda/d = 0.73$), there are two SPW resonances and that the -1 diffraction order propagates throughout the angular range.

When higher-order couplings to SPW's are studied, the permitted diffraction orders are strongly coupled to the SPW's; therefore the incident beam, all propagating diffracted beams, and the SPW's must be taken into account for a complete understanding of these complex interactions. The effect of SPW resonance on diffraction orders has been studied by many authors.[16-17] However, all those studies dealt with single SPW resonance; the effects of multiple couplings have not been investigated experimentally. Here, a systematic theoretical and experimental investigation of SPW interference in the $(+1, -2)$ minigap region is presented. Both the 0-order reflectance and the -1-order diffraction (the only permitted diffraction order in the angular region of SPW coupling) were measured at 633 nm as a function of the incident angle for various grating depths and profiles at a fixed grating period of 870 nm. The angular shifts in the SPW resonance angles as a result of the increasing grating depths were used to tune through the coupling degeneracy. By adding intensities in the 0-order reflectance and the -1-order diffraction to find the total reflected energy, we observed momentum gaps. Also, for a single-grating profile similar measurements were repeated as a function of wavelength. Consistent with the experimental results discussed above, momentum gaps were not found in the 0-order reflectance; however, well-defined momentum gaps were observed in the -1 diffraction order.

Finally, a simplified theoretical formalism, developed for the analysis of first-order coupling,[8] is extended. This analysis, based on a simple truncation of the plane-wave expansion of the scattered fields within the Rayleigh hypothesis, provided remarkably good agreement with the first-order coupling results. Not surprisingly, while the major features of the experiment are reproduced, the agreement is less satisfactory for this more demanding case.

The dispersion relation for SPW's at a metal–air interface is given by[18]

$$k_{SPW} = k_0[\epsilon/(1 + \epsilon)]^{1/2}, \quad (1)$$

where k_0 is the free-space propagation vector and ϵ is the metal dielectric constant. The excitation of SPW's takes place whenever the wave vector of the incident light parallel to the metal–air grating interface satisfies the condition

$$k_0 \sin\theta + 2\pi n/d = \pm k_{SPW}, \quad (2)$$

where θ is the incident angle, d is the grating period, and $n = 0, \pm 1, \pm 2, \ldots$ represents the coupling order. For a lossless free-electron metal ($\epsilon = 1 - \omega_p^2/\omega^2$), the dispersion relation [Eq. (1)] is plotted in Fig. 1, where $k_p = \omega_p/c$. The vertical dashed lines represent the various grating orders, and the horizontal lines indicate the accessible wave vectors ($2\pi n/d$ to $k_0 + 2\pi n/d$) in the $+1$ and -2 orders. Note that coupling to SPW's can be achieved for both of these orders for the choice of ω and d corresponding to the present experiment. Coupling in the $+1$ (-2) orders results in the propagation of SPW's in the forward (backward) [i.e., same (opposite)] direction as the y component of the incident wave vector. The -1 diffraction order is permitted throughout the angular range of the two SPW couplings, and its properties are strongly influenced by the SPW resonances. Also note that degeneracy in the coupling angle θ corresponds to the coupling of the oppositely directed SPW's by an integral multiple of the grating wave vector (3 in this case). In a fashion familiar from many examples of mode coupling, this degeneracy results in the interactions between the SPW modes that give rise to the minigap effects.

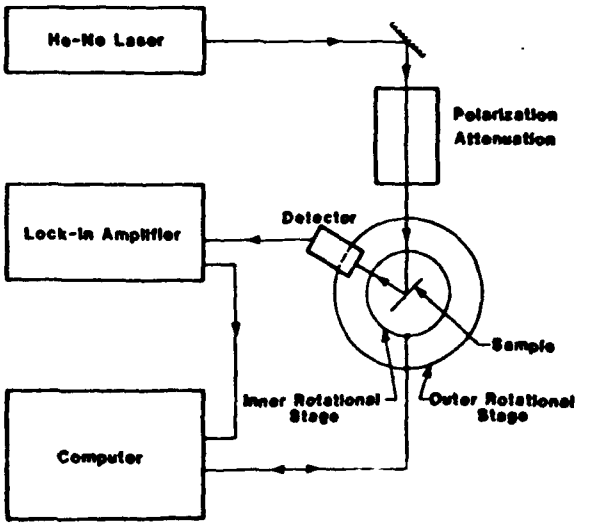

Fig. 2. Experimental arrangement for reflection and diffraction-order measurements.

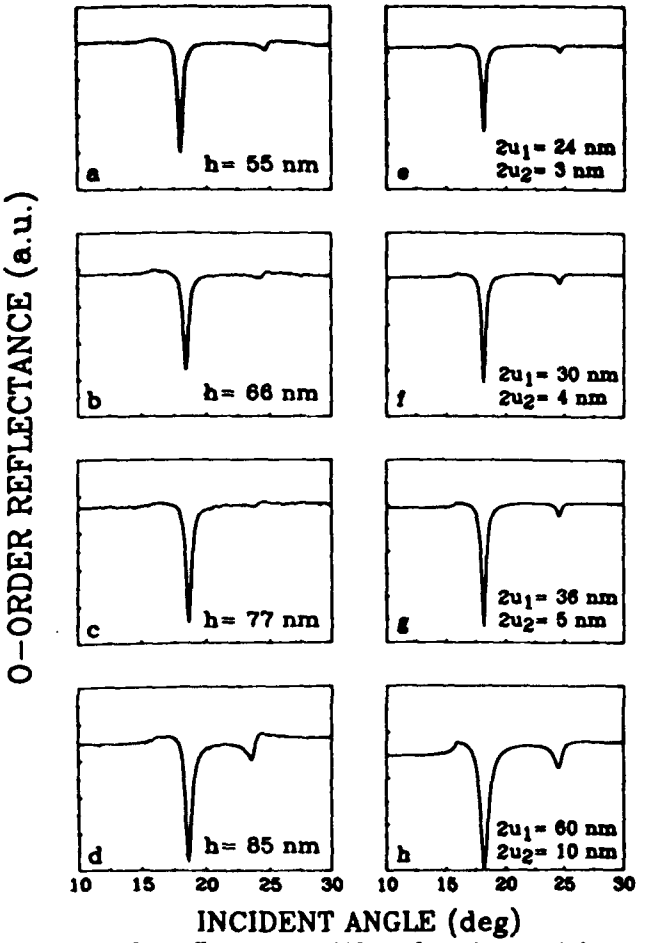

Fig. 3. 0-order reflectances at 633 nm for 870-nm-period gratings with varying grating depths h. The left-hand column presents experimental results; the right-hand column presents theoretical modeling. See the text for details.

2. EXPERIMENT

Gratings were fabricated holographically in positive photoresist on Si substrates with a single-frequency Ar-ion laser source at 488 nm.[19] Grating depths were varied by adjustment of the exposure time. This results in variations in both the depth and the grating profile, which varies from approximately sinusoidal at small depths to rectangular at the deepest gratings investigated. These photoresist gratings were coated with ~100-nm-thick Ag films with the use of an electron-beam evaporator system at room temperature and at a background vacuum of low-10^{-6} Torr.

The optical measurements were scans of reflectance (diffraction) versus incident angle in the experimental setup shown in Fig. 2. In this arrangement two concentric rotation stages are used, with the sample mounted on the inner stage and the detector mounted on the outer stage. The data acquisition step involved a personal computer interfaced with a stepper motor controller, which, in turn, controlled the two rotation stages. Most measurements were made at the He–Ne laser wavelength. For the variable-wavelength measurements a cw-dye-laser source was used. Grating depths were measured in cross section with a scanning electron microscope (SEM). This introduces errors, estimated at ±5 nm, owing to uncertainties in the SEM calibration and to variations in grating depths for the different areas sampled in the optical and SEM measurements.

3. 0-ORDER REFLECTANCE MEASUREMENTS

Figures 3a–3d show the 0-order reflectance scans as the grating depth is increased. The plots in Figs. 3e–3h are obtained from the modeling and will be discussed in Section 8. The following important features should be noted:

(1) The excitation of SPW's in the first ($n = +1$) and second ($n = -2$) orders at ~18° and 24.7°, respectively,

(2) The horizon for the associated diffraction orders at 15.8° and 27.1°, respectively,

(3) The increase in the first-order coupling efficiency as the grating depth is increased,

(4) The relative weakness of the second-order coupling,

(5) The decrease in the angular separation of the two coupling resonances as the grating depth is increased.

Also note that the angular shifts in the second-order resonance are almost twice those in the first order.

For deeper gratings the corresponding measurements are shown in Figs. 4a–4d; as before, Figs. 4e–4h are obtained from theory. Note the following features:

(1) The increase in the −2-order coupling strength,

(2) The merging of the first- and second-order couplings, resulting in a saddle-point line shape,

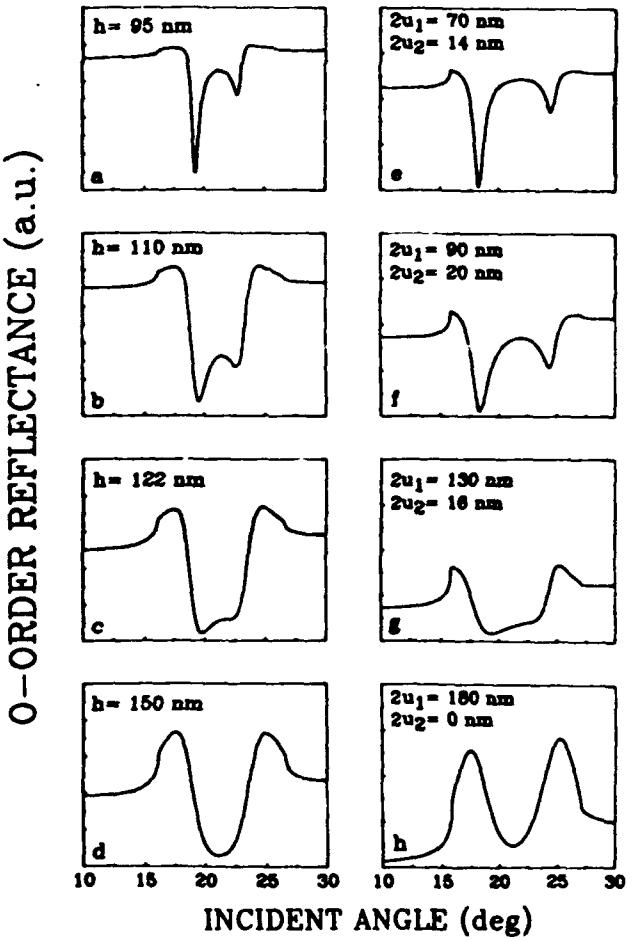

Fig. 4. Same as Fig. 3 but for deeper gratings.

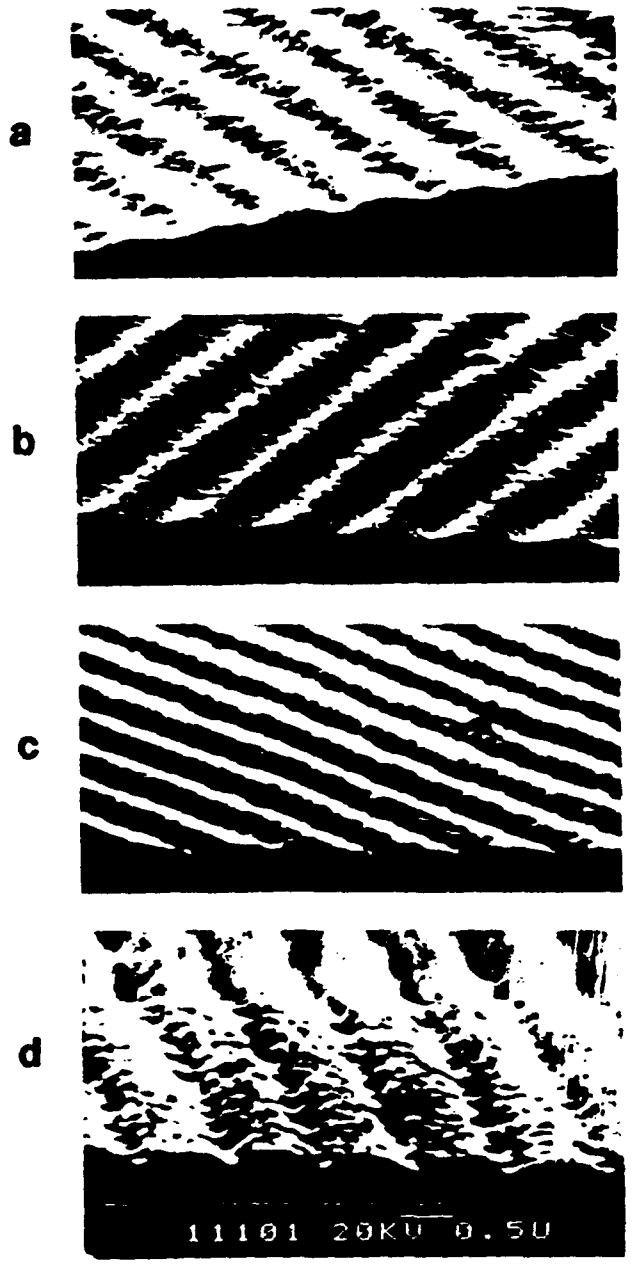

Fig. 5. Cross-section SEM photographs of the gratings used for the experiments. The measured depths are (a) 95 nm, (b) 110 nm, (c) 122 nm, and (d) 150 nm.

(3) The emergence of a broad minimum (Fig. 4d), where first- and second-order couplings can no longer be distinguished.

This is similar to the behavior observed[11] and calculated[12] for similar fixed-frequency reflectivity scans in the vicinity of a minigap. As a result of the saddle-point response surface, only a single, broad resonance is observed when θ is varied for fixed ω, while two distinct resonances and an energy gap are found when ω is varied for fixed θ.

In Fig. 5 SEM profiles of the gratings used to obtain Figs. 4a–4d are shown. Increasing grating depth also results in increasing deviation from sinusoidal profiles as a result of the grating fabrication technique.[10] For still deeper gratings the corresponding measurements are shown in Fig. 6, where the vertical scale is unchanged from that of Figs. 3 and 4. For these approximately rectangular grating structures (cf. Fig. 7), there is an overall decrease in the 0-order reflectance, an absence of clear SPW coupling resonances, and line shapes that do not lend themselves to simple interpretation.

4. −1-DIFFRACTION-ORDER MEASUREMENTS

For this grating period and measurement wavelength the −1 diffraction order is a propagating mode throughout the entire incident angle range including that of the SPW resonances. Coupling to this propagating order provides additional information on the SPW resonance characteristics. In fact, the first observations of Wood's anomalies were related to diffraction orders rather than to 0-order reflectance. Measurements of the energy coupled into the SPW mode must take into account both the reflectance and the energy coupled into the diffraction order. Diffraction-order scans corresponding to the 0-order scans of Figs. 3a–3d are shown in Figs. 8a–8d; as above, the plots in Figs. 8e–8h are obtained from theory. The vertical scale on these measurements is the same as that for the 0 order, so the diffracted energy in the −1 order is significant when compared with the reflectivity. The following features should be noted:

(1) The line shapes are derivativelike as the incident angle is varied through the SPW resonances,

(2) The coupling strengths are equal, in contrast with the much weaker −2-order coupling observed in the reflectivity (cf. Figs. 3a–3d),

(3) Neither the maxima nor the minima in the diffraction-order intensities correspond to the 0-order minima,

(4) There is an enhancement of the diffraction-order intensity in the region between the SPW interactions,

(5) As the grating depths increase, the angular separation between the SPW resonances as measured between

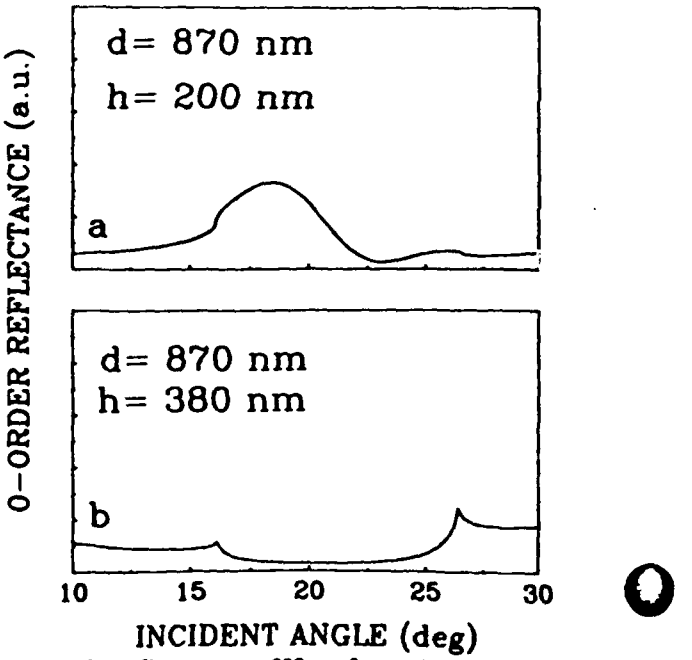

Fig. 6. 0-order reflectances at 633 nm for gratings with (a) residual SPW effects and (b) absorptive behavior.

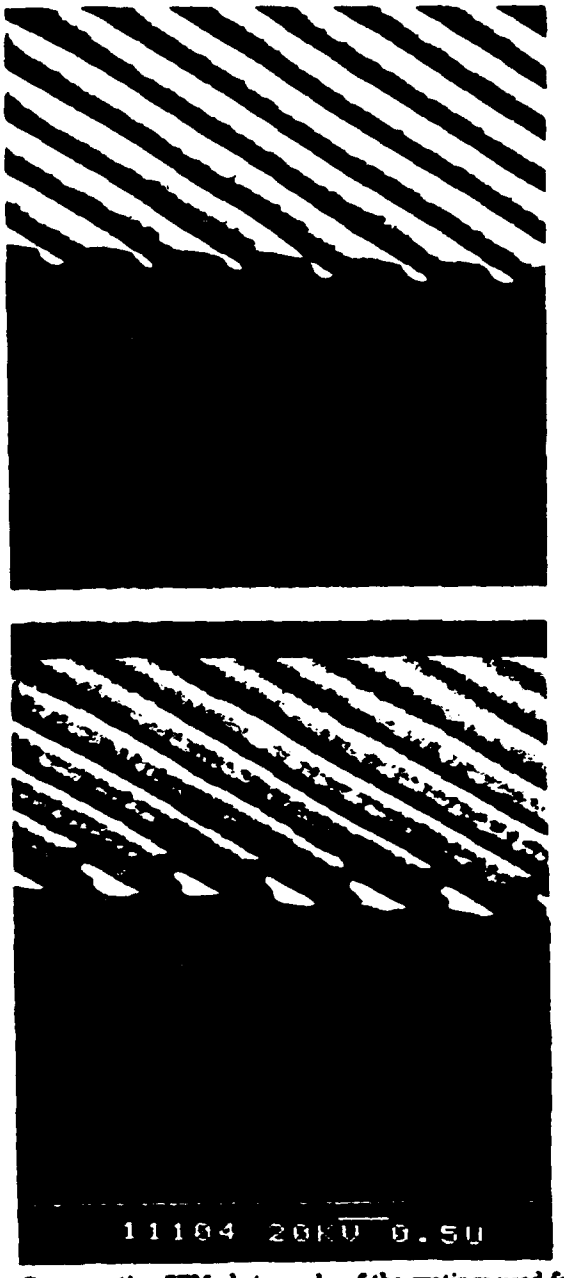

Fig. 7. Cross-section SEM photographs of the gratings used for the measurements in Fig. 6.

either the minima or the maxima of the line shapes first decreases (Figs. 8a–8c) and then increases (Fig. 8d).

For deeper gratings, corresponding to the 0-order scans of Figs. 4a–4d, the diffraction-order scans are shown in Figs. 9a–9d, where, as above, Figs. 9e–9h are the result of theoretical modeling that will be discussed in Section 8. The following features can be noted from these measurements:

(1) There is an increase in the angular separation of the two minima with increasing grating depth, in contrast with the behavior in the 0-order measurements, where the minima move toward each other and merge,

(2) There is a decrease in the angular separation of the two maxima (Figs. 9a–9c) and an emergence of a single maximum (Fig. 9d),

(3) The enhancement in the −1 diffraction order is such that the minimum in the 0 order (Fig. 4d) corresponds to the maximum in the −1 diffraction order (Fig. 9d).

A comparison of the 0-order (Figs. 4a–4d) and −1-diffraction-order (Figs. 9a–9d) measurements shows that much of the incident energy is re-emitted into the diffraction order. This enhancement in the diffraction-order intensity is mediated by SPW interactions.

Finally, the diffraction-order measurements are shown for gratings with residual SPW coupling effects (Fig. 10a) and without SPW effects (Fig. 10b), corresponding to the 0-order scans of Fig. 6. For the shallower grating, there is a decrease in intensity, and two broad minima, at 18.2° and 24°, are observed, with the minimum at 18° corresponding to the maximum in the 0 order (Fig. 6a) and the minimum at 24° corresponding to neither the minimum nor the maximum in the 0 order (Fig. 10a). For the deepest grating measured, there are no residual SPW effects but rather a substantial decrease in the diffraction-order intensity for all angles.

5. ENERGY-SUM MEASUREMENTS

For these measurements, only the 0 and −1 orders are propagating within the angular range of SPW interactions. Thus we can evaluate the total energy coupled to

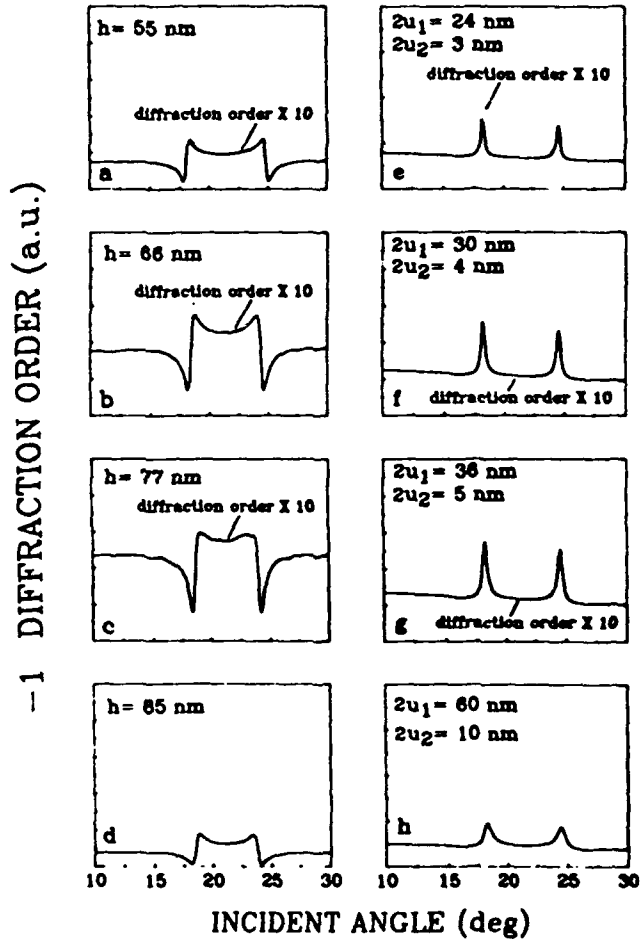

Fig. 8. −1-diffraction-order scans for the gratings used in Fig. 3. The left-hand column presents experimental results; the right-hand column presents theoretical modeling. See the text for details.

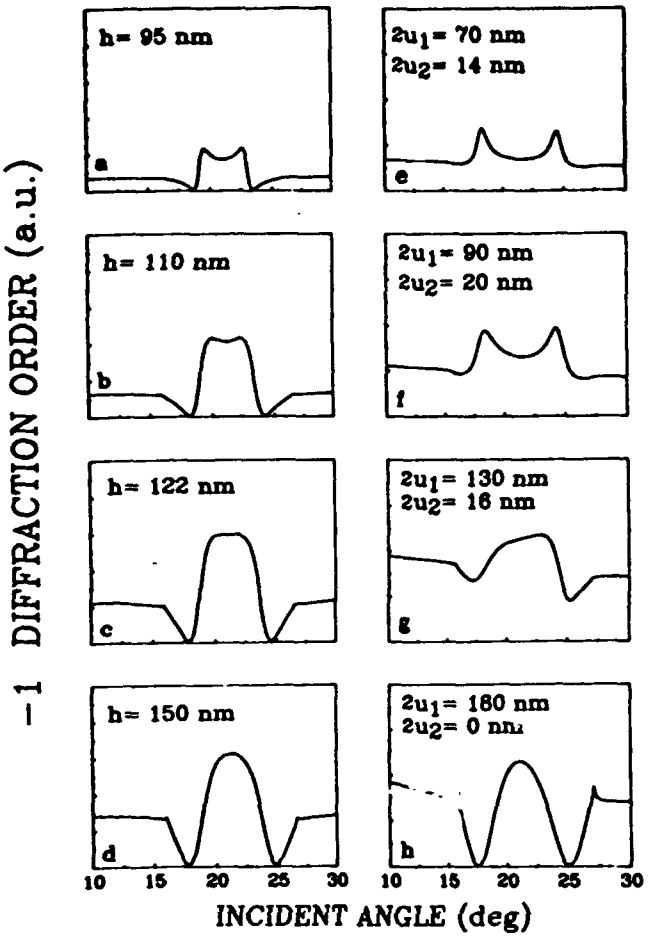

Fig. 9. −1-diffraction-order scans for the gratings in Fig. 4. The left-hand column presents experimental results; the right-hand column presents theoretical modeling. See the text for details.

SPW's by adding the energies in these orders. Figures 11a–11d show these energy sums for the measurements of Fig. 3 (0 order) and Fig. 8 (−1 diffraction order). The measurements for the deeper gratings (Figs. 4 and 9) are given in Figs. 11e–11h. Note that

(1) The coupling efficiencies are reduced in comparison with the 0 order, since some of the incident energy is also coupled into the diffraction order,

(2) The coupling of energy to SPW's in the −2 order is manifested by the resonance line shape, in comparison with the less-well-defined line shape of Figs. 3a–3d,

(3) There is a gradual increase in coupling efficiency and a broadening of the first-order resonance line shape followed by a decreasing efficiency at still deeper gratings,

(4) There is a decreasing angular separation (Figs. 11a–11f) followed by an increasing separation for deeper gratings.

Both the −1-order measurements and the energy-sum measurements show a well-defined momentum gap; i.e., they show two resonances as a function of θ at fixed ω that first approach each other and then diverge as the grating depth is increased.

The experiments exhibited strong dependence on the details of the grating profiles. For some cases, with approximately sinusoidal profiles, saddle-point line shapes were not observed in the 0-order reflectances. Also, the diffraction-order line shapes were similar to the 0-order line shapes at SPW resonance angles. Not unexpectedly, the higher-order Fourier components of the grating pro-

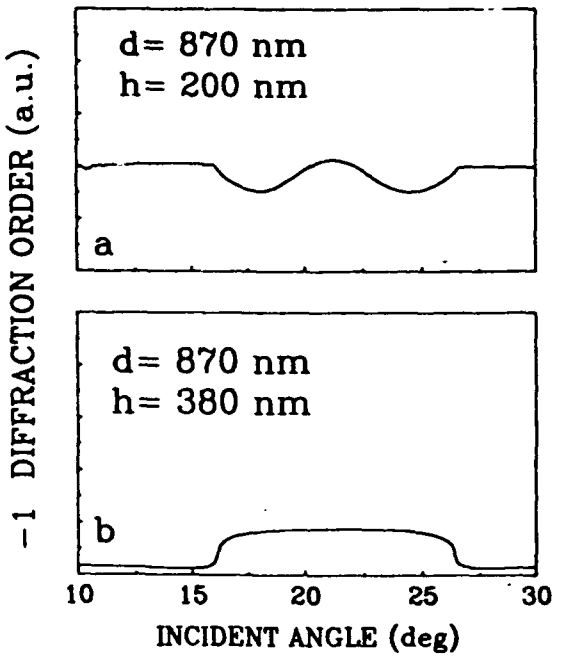

Fig. 10. −1-diffraction-order scans for the gratings used in Fig. 6.

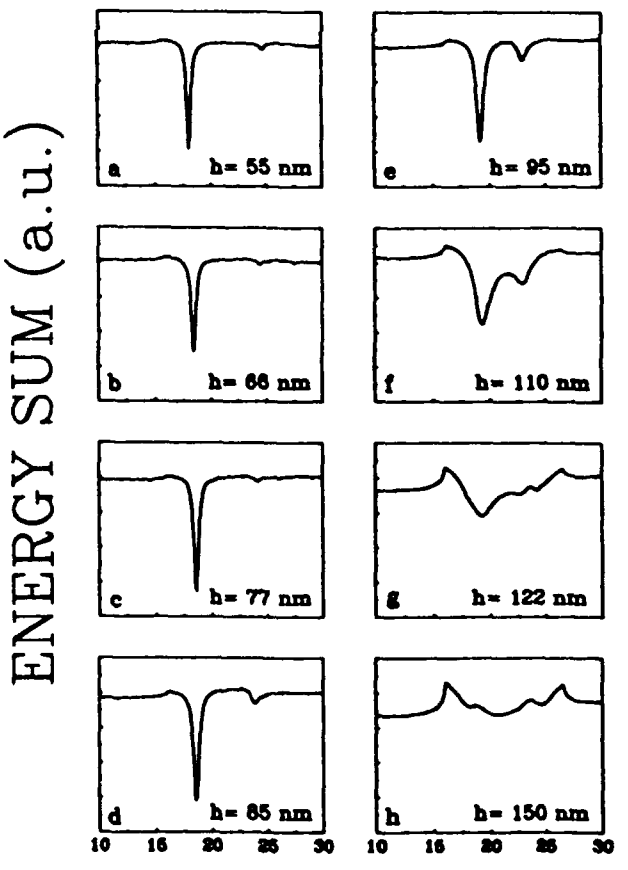

Fig. 11. Energy-sum (0-order reflectance plus −1-diffraction-order) scans for the gratings used in Figs. 3, 4, 8, and 9.

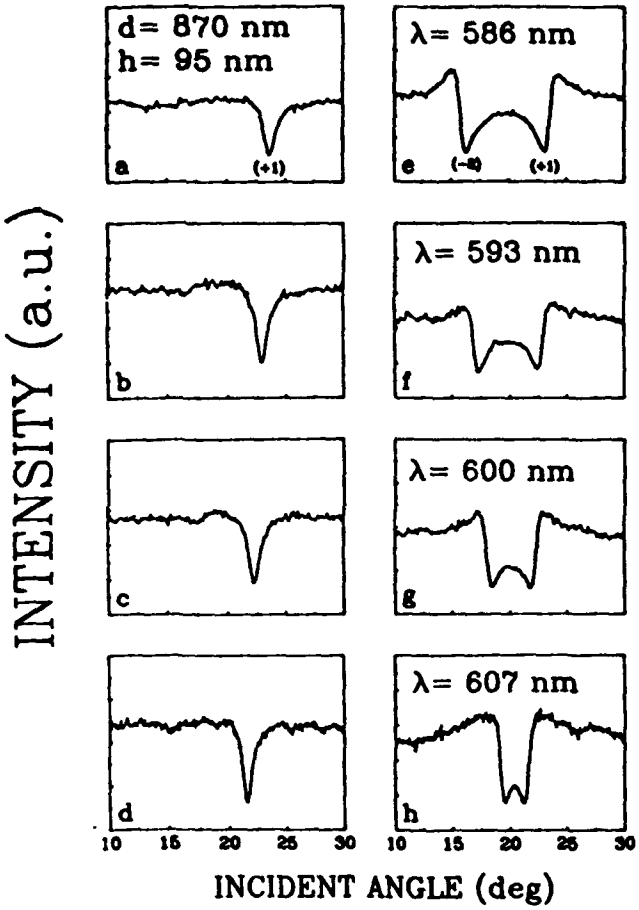

Fig. 12. 0-order reflectance and −1-diffraction-order scans for the 95-nm-deep gratings (Figs. 4a, 9a, and 11e) as the wavelength is increased from 586 to 607 nm. The left-hand column presents the 0-order measurements; the right-hand column presents the −1-diffraction-order measurements.

files substantially affect the first- and second-order coupling strengths and line shapes.

6. VARIABLE-WAVELENGTH MEASUREMENTS

For the 95-nm-deep grating (Figs. 4a, 9a, and 11e), a series of 0-order reflectance and −1-diffraction-order measurements was carried out as a function of wavelength. The output from a dye laser was tuned through the 580–633-nm range, sufficient to probe the (+1, −2) minigap region.

Figure 12 shows the 0-order reflectance (Figs. 12a–12d) and −1-diffraction-order (Figs. 12e–12h) scans as wavelength is increased from 586 to 607 nm; the vertical scale for the diffraction-order measurements is ten times more sensitive than the corresponding scale for the 0-order measurements. Note the following essential features:

(1) The angular separation decreases between the $n = +1$ and $n = -2$ couplings, with the angular shifts in the second order being almost twice those in the first order,

(2) A well-defined resonance is absent in the 0-order scans corresponding to the $n = -2$ coupling, and the broad SPW resonance corresponding to the $n = +1$ coupling moves toward smaller angular values (Figs. 12a–12d),

(3) The intensity in the −1 diffraction order is gradually reduced in the angular region between the two couplings,

(4) As in the previous measurements, the −1-diffraction-order measurements show comparable, mirror-image couplings for the two SPW resonances, while the −2-order coupling is barely observable in the 0-order reflection.

A further increase in wavelength brings the two couplings still closer, and some interference effects are observed as shown in Fig. 13. The major features are the following:

(1) The monotonic shift to smaller angular values in the 0-order reflectance scans corresponding to the $n = +1$ coupling as the wavelength is changed (Figs. 13a–13d),

(2) The appearance of a sharp feature at 23.8° in the −1-diffraction-order measurements (Figs. 13e–13f), which corresponds approximately to the horizon for the appearance of the −2 diffraction order,

(3) The appearance of a slight discontinuity in the −1-diffraction-order line shape (Fig. 13g),

(4) The decrease in the angular separation between the two couplings (Figs. 13e–13g),

(5) The sharp increase in the diffraction-order intensity as the two couplings cross each other.

In Fig. 14 these measurements are extended to still longer wavelengths, beyond the (+1, −2) minigap region. The major features include

(1) The appearance of $n = -2$ coupling in the 0-order scans (Figs. 14a–14d),

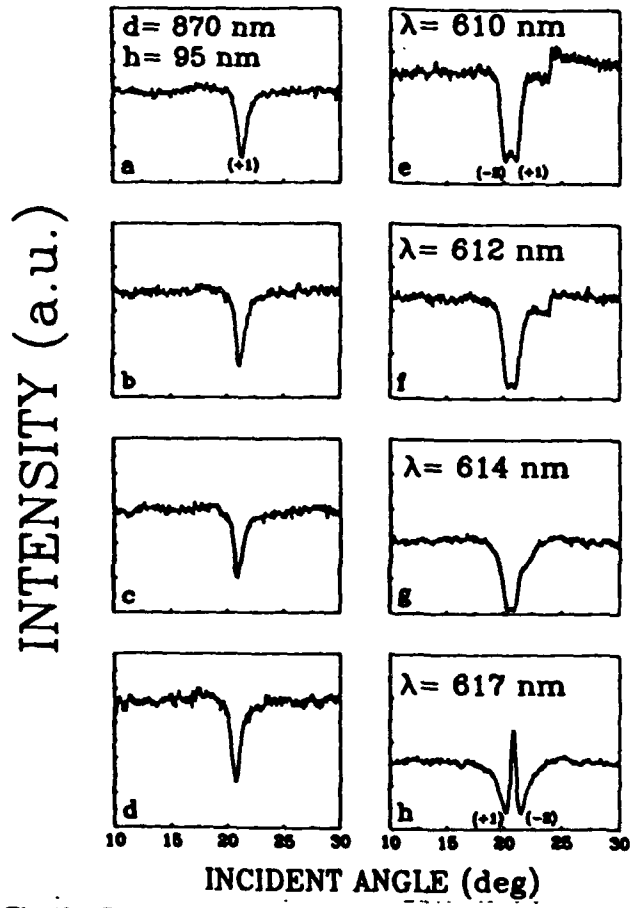

Fig. 13. Same as Fig. 12 but for an increase in wavelength from 610 to 617 nm.

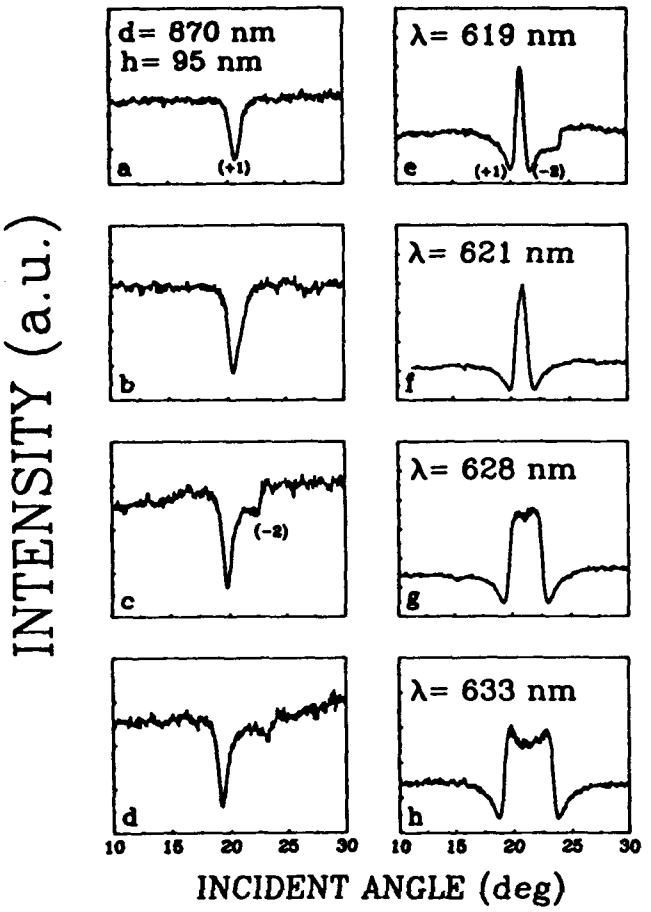

Fig. 14. Same as Fig. 12 but for an increase in wavelength from 619 to 633 nm.

(2) The appearance of a sharp feature at 24.2° (Fig. 14e) corresponding to similar features in Figs. 13e–13f,

(3) The increase in angular separation between the $n = +1$ and $n = -2$ couplings,

(4) The increase in −1-diffraction-order intensity in the region between SPW couplings,

(5) The reversal of the resonance line shapes in the diffraction-order measurements, evident from a comparison of Figs. 12e–12g and 14e–14g.

Thus, as couplings to SPW's in the first and second orders become degenerate, interference effects result in an enhancement in the diffraction-order intensity over a narrow angular range. When the modes cross each other, the resonances observed in 0 order show a single minimum and do not exhibit a momentum gap (Fig. 15a), while a clearly defined forbidden momentum gap is observed for the −1-diffraction-order scans (Fig. 15b). The magnitude of this gap is ~0.3° and is in good qualitative agreement with the momentum gaps observed by Heitman *et al.*[14]

7. THEORY

A variety of mathematical formalisms have been applied to describe optical interactions with periodic surfaces. Integral methods were first proposed by Petit and Cadilhac,[20] Wirgin,[21] and Uretski.[22] A number of integral formulations have been investigated, including a Green's-function formalism based on an extinction theorem mechanism developed by Glass *et al.*,[23] Laks *et al.*,[24] and Utagawa.[25] In addition, differential formalisms developed by Nevière *et al.*[26] and Numata[27] have also been used to study SPW dispersion relations. All these methods are rigorous, hold for arbitrary grating profiles, and require extensive computation.

Simpler, approximate formulations have been introduced starting from the Rayleigh hypothesis[5,28] and from the extinction theorem formalism.[29] These were demonstrated to offer a good approximation of the exact calculation[29] and to first-order coupling experiments.[5] While these formulations are lacking in ultimate rigor and accuracy, they offer a good intuitive physical picture of the interaction with a minimum of computational difficulty. Here, the extension of this simple formulation for the minigap region is briefly described. More details are presented in Appendix A.

For TM-polarized light incident on a sinusoidal surface with an excursion of $2u$, a straightforward but involved algebraic procedure results in the coupled linear differential equations

$$J_p(k_z u) + \sum_n B_n^{\prime}(-1)^{p-n} J_{p-n}(\alpha_n u) - \sum_n B_n^{\prime\prime} J_{p-n}(\beta_n u) = 0, \tag{3}$$

$$\left(K_z - pg\frac{k_0}{k_z}\right) J_p(k_z u) - \sum_n \left[\alpha_n - (p-n)g\frac{k_n}{\alpha_n}\right] B_n^{\prime}(-1)^{p-n} J_{p-n}(\alpha_n u) - \frac{1}{\epsilon}\sum_n \left[\beta_n - (p-n)g\frac{k_n}{\beta_n}\right] B_n^{\prime\prime} J_{p-n}(\beta_n u) = 0, \tag{4}$$

where all variables are defined in Appendix A.

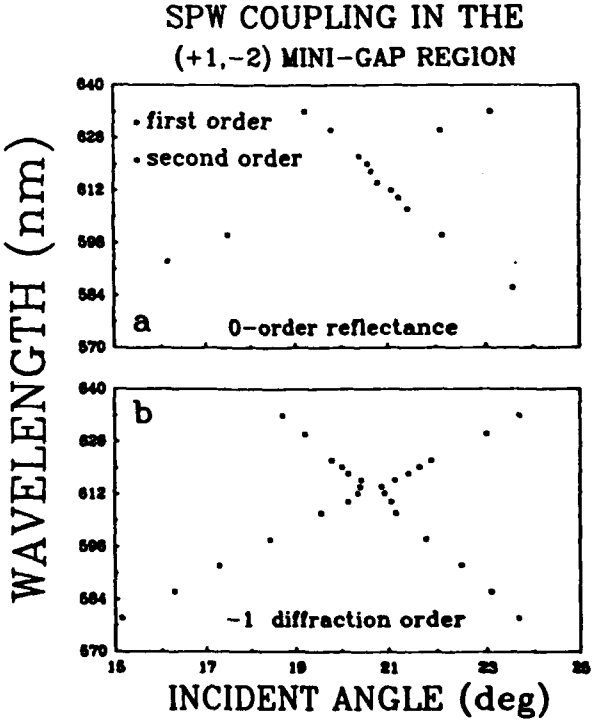

Fig. 15. Plot of the resonance behavior observed in Figs. 12–14. The 0-order reflectivity (a) shows a single dominant resonance becoming a single broad minimum in the minigap region. In contrast, the −1-diffraction-order scans (b) show a well-defined momentum gap corresponding to the (+1, −2) minigap region.

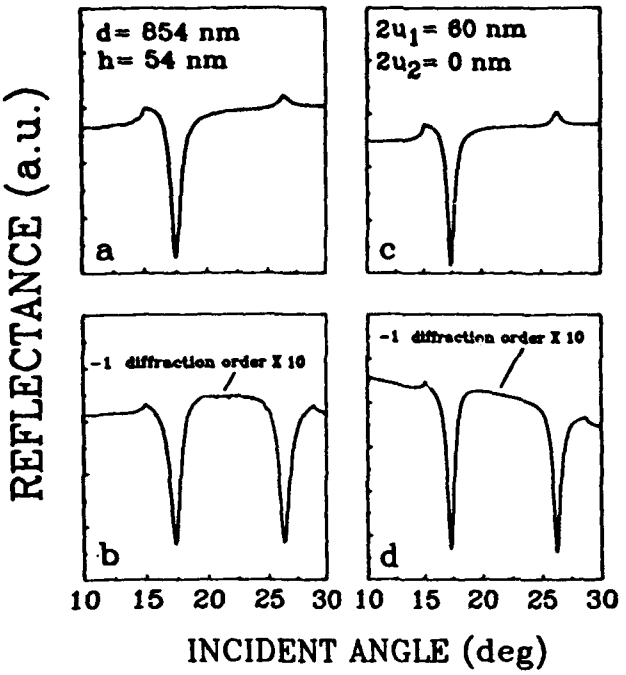

Fig. 16. Comparison between theory and experiment for a grating with a nearly sinusoidal profile. The left-hand column presents experimental results; the right-hand column presents theoretical modeling.

In the derivation of Eqs. (3) and (4) no small-signal approximation is made for either the grating depth or the diffraction-order amplitudes. From the dispersion-relation curve in Fig. 1, for the present case the only resonant terms in the above expansions [Eqs. (3) and (4)] are $n = +1$ and $n = -2$. The $n = -1$ term is the permitted diffraction order and is strongly influenced by SPW interactions. The infinite series was truncated at $n = 0, -1, 1, -2$, which resulted in an 8×8 matrix and considerable simplification. Previous analyses included many more terms and provided significantly greater accuracy. Since the experimental profiles were not precisely sinusoidal, additional Fourier components were included in the grating profile. It was shown by Van den Berg and Fokkema[20] that the Rayleigh hypothesis would still be valid if a profile could be described by a finite Fourier series. The mathematical analysis, however, becomes progressively more complex as the number of higher-order Fourier components is increased. For the present purpose the surface profile is redefined to include only one additional Fourier component:

$$z = u_1 \sin(gy) + u_2 \sin(2gy). \tag{5}$$

In general, u_2 is much smaller than u_1. For this profile we obtain

$$J_p(k_z u_1) J_0(k_z u_2) + \sum_n (-1)^{p-n} J_{p-n}(\alpha_n u_1) J_0(\alpha_n u_2) B_n^s - \sum_n B_n^m J_{p-n}(\beta_n u_1) J_0(\beta_n u_2) + \sum_{s=1}^{\infty} \left[A(p,s) + \sum_n B(p,n,s) + \sum_n C(p,n,s) \right] = 0 \tag{6}$$

and

$$D(p) + \sum_n E(p,n) - \frac{1}{\epsilon} \sum_n F(p,n) + \sum_{s=1}^{\infty} \left[G(p,s) + \sum_n I(p,n,s) - \frac{1}{\epsilon} \sum_n L(p,n,s) \right] = 0, \tag{7}$$

where A, B, C, D, E, F, G, I, and L are defined in Appendix A.

Equations (6) and (7) reduce to Eqs. (3) and (4) for $u_2 = 0$. The terms in these equations are of the general form $J_s J_{s'}$; in the numerical calculations terms are retained up to $s + s' = 3$; i.e., J_0J_0, J_0J_1, J_0J_2, J_0J_3, J_1J_1, and J_1J_2.

8. COMPARISON BETWEEN THEORY AND EXPERIMENT

In a previous analysis of first-order coupling to SPW's it was shown that the best fit to the experimental results was obtained for a Ag-film dielectric constant of $(-13.65, 0.82)$ (Ref. 5); this value was used without further adjustment. In Fig. 16 experimental and theoretical reflectance scans versus angle are shown for an 854-nm-period grating with a nearly sinusoidal profile. The theoretical calculations were carried out with the use of Eqs. (6) and (7). Note that the calculated +1-order coupling resonance line shape in the −1-diffraction-order scan (Fig. 16b) is similar to the 0-order line shape (Fig. 16a) and that the two resonances are comparable, although only a small enhancement rather than a coupling dip at the −2-order resonance is observed in the 0-order scan. The theoretical line shapes (Figs. 16c and 16d) closely follow the experimental line shapes, although the observed resonance widths are slightly larger than those predicted.

For grating profiles deviating from a sinusoidal shape, u_1 and u_2 were adjusted to produce line shapes closest to those experimentally observed. In Fig. 17 the experimen-

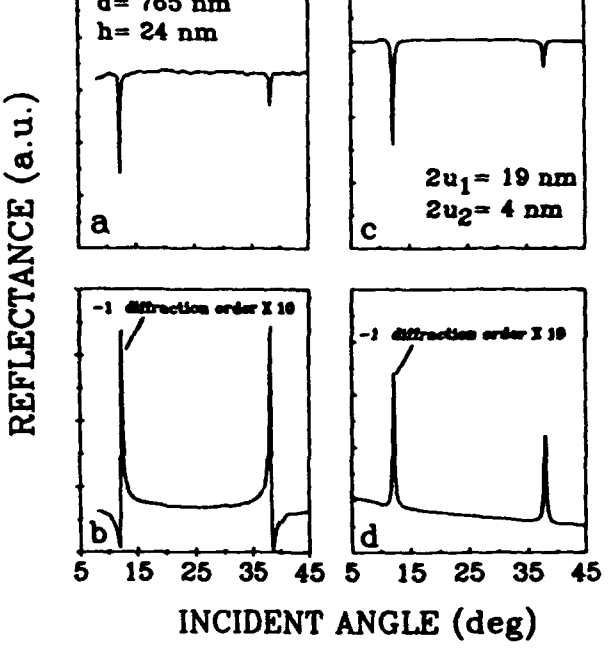

Fig. 17. Comparison between theory and experiment for a profile showing a slight deviation from a sinusoidal shape. The left-hand column presents experimental results; the right-hand column presents theoretical modeling.

tal and calculated plots for a grating with a 765-nm period are shown. This grating deviated from a sinusoidal profile and showed appreciable coupling in the second order (Fig. 17a). In the −1 diffraction order sharp spikes in intensity at SPW resonance minima are observed (Fig. 17b). The calculated 0-order plot (Fig. 17c) is similar to the experimental plot (Fig. 17a). The calculated −1-diffraction-order plot (Fig. 17d), although showing intensity spikes at both SPW resonances, fails to display the experimentally observed dispersionlike minima, shows unequal intensities at the SPW resonances, and does not replicate the observed diffraction efficiency enhancement in the region between the SPW resonances.

Thus this simple model includes many of the major features observed, but for a complete description higher Fourier coefficients must be included, as we can see in comparing the experimental and theoretical plots in Figs. 3a–3d and 3e–3h above. Note the following features:

(1) The resonance line shapes in the second order are different (Figs. 3a–3c and 3e–3g),
(2) The observed grating depths are much larger than those predicted (Figs. 3a–3c and 3e–3g),
(3) The calculated angular shifts are much smaller than those observed.

The large difference in grating depths and the second-order line shapes is due to the omission of higher Fourier coefficients in the grating profile that result in cancellation effects in second-order coupling. Specifically, the model at present does not include a third-order coefficient. Yet, as we discussed above, it is just this Fourier component of the grating that resonantly couples the counterpropagating SPW modes. For deeper gratings the comparison between observed (Figs. 4a–4d) and predicted (Figs. 4e–4h) reflectance scans show the following features:

(1) There is an evolution to a broad minimum (Figs. 4e–4h),
(2) The calculated and observed depths are similar (Figs. 4a–4c and 4e–4g),
(3) The calculated angular shifts are smaller than those observed,
(4) The calculated energy coupled to the diffraction order is much higher than that observed.

Note that the calculated plot in Fig. 4h is for a sinusoidal profile, while the actual profile shows considerable deviation from a sinusoidal shape (Fig. 5d). These comparisons emphasize the importance of knowledge of the exact profile for calculation of its reflectance behavior.

The comparison of calculated (Figs. 8a–8d) and observed (Figs. 8e–8h) diffraction-order line shapes shows the following features:

(1) There is a lack of energy enhancement in the region between intensity spikes (Figs. 8e–8h),
(2) The calculated spikes in intensity are slightly asymmetric (Figs. 8e–8g),
(3) The calculated energy in the diffraction order is higher than that observed.

For deeper gratings a similar comparison of observed (Figs. 9a–9d) and calculated (Figs. 9e–9h) diffraction-order line shapes shows the following features:

(1) An energy enhancement for the calculated line shapes in the region between SPW resonances (Figs. 9e–9h),
(2) The appearance of shallow minima (Figs. 9e–9h),
(3) The appearance of an asymmetric line shape in Fig. 9g,
(4) The sharp decrease in signal from −10° to 15° in Fig. 9h.

Thus the comparison of theory and experimental results indicates that, although the theory manages to show major features of our data, many finer details are not observed. A more detailed theoretical investigation, including both higher Fourier coefficients and a more rigorous formalism, is necessary to provide a detailed fit between theory and experiment.

9. SUMMARY

A systematic experimental study of interactions between SPW couplings in the (+1, −2) minigap regions is reported. The experiment covers the entire range of SPW interactions, ranging from weak-coupling to stronger-coupling effects and to deeper profiles showing absorption rather than SPW effects. The simple theoretical model, although missing many of the finer details, shows the major features of our experimental data. One can develop a better model by including several Fourier coefficients in the grating profile.

Several extensions of this work are immediately apparent. For larger grating periods there are more diffraction orders, and it would be interesting to see how energy is distributed in these orders at SPW resonance angles. Also, the appearance of momentum gaps in the 0 order depends on the strength of interactions.

As we noted above, there has been much discussion of the physical significance of momentum and energy gaps in the minigap regions. As this study, as well as others,[10,11,14] demonstrated, the response surface is quite complex in the vicinity of a minigap, and a complete analysis of the experimental situation is necessary. Most theoretical treatments of SPW effects on gratings can be cast as a linear algebraic problem of the general form $\mathbf{ME} = \mathbf{S}$, where the vector $\mathbf{E}$ represents the response fields, $\mathbf{M}$ is the medium response matrix, and $\mathbf{S}$ is the source of excitation vector. Formally, this is solved as $\mathbf{E} = \mathbf{M}^{-1}\mathbf{S}$, where each term in the inverse matrix is proportional to $(\det \mathbf{M})^{-1}$. In many situations knowledge of this determinant, and hence of the dispersion relation, is sufficient for an understanding of the main features of the response. For example, for the case of a single SPW resonance, the experimental dispersion relation obtained from the resonance angles and the linewidths of the 0-order coupling dips are in reasonable agreement with that calculated from the determinant of M; higher-order terms can be added to evaluate the effect of deeper gratings.[6] In the minigap region this procedure clearly is not appropriate; for example, neither of the extrema observed in the first-order coupling coincides with the 0-order coupling resonance angles. In this situation it is not possible simply to extract a dispersion relation from the experimentally observed line shapes. A full treatment of the system response is necessary for interpretation of the measurements in terms of modes and dispersion relations.

APPENDIX A

For a TM-polarized plane wave incident on a sinusoidal interface we can define a (magnetic) B field below and above the grating by using the Rayleigh hypothesis:

$$B^v(y,z) = \exp[i(k_y y + k_z z)] + \sum_n B_n^v \exp[i(K_n y - \alpha_n z)], \quad z < 0,$$

$$B^m(y,z) = \sum_n B_n^m \exp[i(K_n y + \beta_n z)], \quad z > 0,$$

where $k_y = k_0 \sin\theta$, $k_z = k_0 \cos\theta$, $k_0 = \omega/c$, $k_n = k_y + ng$ ($n = 0, \pm 1, \pm 2$), $g = 2\pi/d$ (d is the grating period), and

$$\alpha_n = i(k_n^2 - k_0^2)^{1/2}, \qquad \beta_n = i(k_n^2 - \epsilon k_0^2)^{1/2}.$$

For a sinusoidal surface the profile is given by

$$f(y) = u \sin(gy),$$

so that, by applying the generating function for Bessel functions, we obtain

$$\exp[i\gamma f(y)] = \exp[i\gamma u \sin(gy)] = \sum_{p=-\infty}^{\infty} \exp(ipgy) J_p(\gamma u).$$

By applying the boundary conditions

$$B^v(y,z) = B^m(y,z)|_{z=f(y)},$$

$$\frac{\partial}{\partial n} B^v(y,z) = \frac{1}{\epsilon} \frac{\partial}{\partial n} B^m(y,z)|_{z=f(y)},$$

where $\partial/\partial n$ is the normal derivative to the surface and is defined by

$$\frac{\partial}{\partial n} = \left\{1 + \left[\frac{\partial f(y)}{\partial y}\right]^2\right\}^{-1/2} \left[\frac{\partial}{\partial z} - \frac{\partial f(y)}{\partial y} \frac{\partial}{\partial y}\right],$$

we arrive at Eqs. (3) and (4) above. For a more complex sinusoidal surface the profile is given by

$$f(y) = u_1 \sin(gy) + u_2 \sin(2gy),$$

and we obtain

$$\exp[i\gamma f(y)] = \sum_{p,q} \exp[i(p + 2q)gy] J_p(\gamma u_1) J_q(\gamma u_2).$$

Again, applying the boundary conditions leads to Eqs. (6) and (7) above, where the constants are given by

$$A(p,s) = [J_{p-2s}(k_z u_1) + (-1)^s J_{p+2s}(k_z u_1)] J_s(k_z u_2),$$

$$B(p,n,s) = (-1)^{p-n} B_n^v [J_{p-n-2s}(\alpha_n u_1) + (-1)^s J_{p-n+2s}(\alpha_n u_1)] J_s(\alpha_n u_2),$$

$$C(p,n,s) = B_n^m [J_{p-n-2s}(\beta_n u_1) + (-1)^s J_{p-n+2s}(\beta_n u_1)] J_s(\beta_n u_2),$$

$$D(p) = [K_z - pg(k_y/k_z)] J_p(k_z u_1) J_0(k_z u_2) - gk_y u_2 \times [J_{p-2}(k_z u_1) + J_{p+2}(k_z u_1)] J_0(k_z u_2),$$

$$E(p,n) = -(-1)^{p-n} B_n^v [\alpha_n - (p - n)g(k_n/\alpha_n)] \times J_{p-n}(\alpha_n u_1) J_0(\alpha_n u_2) - gk_n u_2 B_n^v \times [J_{p-n-2}(\alpha_n u_1) + J_{p-n+2}(\alpha_n u_1)] J_0(\alpha_n u_2),$$

$$F(p,n) = B_n^m [\beta_n - (p - n)g(k_n/\beta_n)] \times J_{p-n}(\beta_n u_1) J_0(\beta_n u_2) - gk_n u_2 B_n^m \times [J_{p-n-2}(\beta_n u_1) + J_{p-n+2}(\beta_n u_1)] J_0(\beta_n u_2),$$

$$G(p,s) = [k_z - (p - 2s)g(k_y/k_z)] J_{p-2s}(k_z u_1) J_s(k_z u_2) + (-1)^s [k_z - (p + 2s)g(k_y/k_z)] J_{p+2s}(k_z u_1) \times J_s(k_z u_2) - gk_y u_2 [J_{p-2s-2}(k_z u_1) + (-1)^s J_{p+2s-2}(k_z u_1)] J_s(k_z u_2) - gk_y u_2 \times [J_{p-2s+2}(k_z u_1) + (-1)^s J_{p+2s+2}(k_z u_1)] J_s(k_z u_2),$$

$$I(p,n,s) = -(-1)^{p-n} B_n^v [\alpha_n - (p - n - 2s)g(k_n/\alpha_n)] \times J_{p-n-2s}(\alpha_n u_1) J_s(\alpha_n u_2) + (-1)^s B_n^v \times [\alpha_n - (p - n + 2s)g(k_n/\alpha_n)] \times J_{p-n+2s}(\alpha_n u_1) J_s(\alpha_n u_2) - gk_n u_2 B_n^v \times [J_{p-n-2s-2}(\alpha_n u_1) + (-1)^s J_{p-n+2s-2}(\alpha_n u_1)] \times J_s(\alpha_n u_2) - gk_n u_2 B_n^v [J_{p-n-2s+2}(\alpha_n u_1) + (+1)^s J_{p-n+2s+2}(\alpha_n u_1)] J_s(\alpha_n u_2),$$

$$L(p,n,s) = B_n^m [\beta_n - (p - n - 2s)g(k_n/\beta_n)] \times J_{p-n-2s}(\beta_n u_1) J_s(\beta_n u_2) + (-1)^s B_n^m \times [\beta_n - (p - n + 2s)g(k_n/\beta_n)] \times J_{p-n+2s}(\beta_n u_1) J_s(\beta_n u_2) - gk_n u_2 B_n^m \times [J_{p-n-2s-2}(\beta_n u_1) + (-1)^s J_{p-n+2s-2}(\beta_n u_1)] \times J_s(\beta_n u_2) - gk_n u_2 B_n^m [J_{p-n-2s+2}(\beta_n u_1) + (-1)^s J_{p-n+2s+2}(\beta_n u_1)] J_s(\beta_n u_2).$$

ACKNOWLEDGMENTS

This work was partially supported by the U.S. Air Force Office of Scientific Research. We appreciate the assistance of Anadi Mukherjee and An-Shiang Chu in the tunable laser measurements.

M. Yousaf is also with the Department of Physics and Astronomy, University of New Mexico, Albuquerque, New Mexico 87131. S. R. J. Brueck is also with the Department of Electrical and Computer Engineering and the Department of Physics and Astronomy, University of New Mexico, Albuquerque, New Mexico 87131.

*Present address, Electronics Division, PINSTECH, P.O. Box Nilore, Islamabad, Pakistan.

REFERENCES

1. R. M. Wood, Phys. Rev. 48, 928 (1935).
2. U. Fano, J. Opt. Soc. Am. 31, 213 (1941).
3. R. Petit, ed., *Electromagnetic Theory of Gratings* (Springer-Verlag, Berlin, 1980).
4. V. M. Agranovich and D. L. Mills, eds., *Surface Polaritons* (North-Holland, Amsterdam, 1982).
5. S. H. Zaidi, M. Yousaf, and S. R. J. Brueck, J. Opt. Soc. Am. B 8, 770 (1991).
6. J. E. Stewart and W. S. Gallaway, Appl. Opt. 1, 421 (1962).
7. R. H. Ritchie, E. T. Arakawa, J. J. Cowan, and R. N. Hamm, Phys. Rev. Lett. 21, 1530 (1968).
8. M. C. Hutley, Opt. Acta 20, 607 (1973).
9. M. C. Hutley and V. M. Bird, Opt. Acta 20, 771 (1973).
10. N. Kroo, Z. S. Szentirmay, and J. Felszerfalvi, Phys. Lett. A 86, 445 (1981).
11. Y. J. Chen, E. S. Koteles, R. J. Seymour, G. J. Sonek, and J. M. Ballantyne, Solid State Commun. 46, 95 (1983).
12. M. G. Weber and D. L. Mills, Phys. Rev. B 34, 2893 (1986).

13. P. Tran, V. Celli, and A. A. Maradudin, Opt. Lett. **13**, 530 (1988).
14. D. Heitman, N. Kroo, C. Schulz, and Zs. Szentirmay, Phys. Rev. B **35**, 2660 (1987).
15. D. Heitman, Opt. Commun. **20**, 292 (1977).
16. W. Rothballer, Opt. Commun. **20**, 429 (1977).
17. E. H. Rosengart and I. Pockrand, Opt. Lett. **1**, 194 (1977).
18. E. A. Stern, as quoted in R. A. Ferrel, Phys. Rev. **111**, 1214 (1958).
19. S. H. Zaidi and S. R. J. Brueck, Appl. Opt. **27**, 2999 (1988).
20. R. Petit and M. Cadilhac, C. R. Acad. Sci. **259**, 2077 (1964).
21. A. Wirgin, Rev. Opt. **9**, 449 (1964).
22. J. L. Uretski, Ann. Phys. **33**, 400 (1965).
23. N. E. Glass, M. Weber, and D. L. Mills, Phys. Rev. B **29**, 6548 (1984).
24. B. Laks, D. L. Mills, and A. A. Maradudin, Phys. Rev. B **23**, 4965 (1981).
25. K. Utagawa, J. Opt. Soc. Am. **69**, 333 (1979).
26. M. Nevière, P. Vincent, and R. Petit, Nouv. Rev. Opt. **5**, 6577 (1974).
27. H. Numata, J. Phys. Soc. Jpn. **51**, 2575 (1982).
28. M. Yamashita and M. Tsuji, J. Phys. Soc. Jpn. **52**, 2462 (1983).
29. M. G. Weber, Phys. Rev. B **33**, 909 (1986).
30. P. M. Van den Berg and J. J. Fokkema, J. Opt. Soc. Am. **69**, 27 (1979).

CHARACTERIZATION OF THIN Al FILMS USING GRATING COUPLING TO SURFACE PLASMA WAVES

Saleem H. Zaidi, D. W. Reicher, B. Draper[1], J. R. McNeil,[2] and S. R. J. Brueck[3]

Center for High Technology Materials, University of New Mexico

Albuquerque, NM 87131

ABSTRACT

A detailed characterization of the optical, microstructural and electrical properties of thin (5-50 nm) Al films grown by thermal evaporation, magnetron sputtering, and ion-assisted sputtering (IAS), is reported. Dielectric-function measurements were carried out by using grating coupling to surface plasma waves (SPW) and, for comparison, ellipsometric measurements were also performed . Scanning electron microscope (SEM) studies of film microstructure as well as dc electrical resistivity measurements were carried out and correlated with the optical data. Using the Bruggeman effective media approximation, good agreement was obtained for thicker films (30-50 nm), but for not for thinner films (< 30 nm) . SEM and resistivity measurements suggest that conditions of film growth influence the behavior of individual grains, resulting in increased electron reflectance at the grain boundaries with increasing energy delivered to the substrate during deposition. This resulted in lower electrical resistivities for evaporated films than for IAS films. Finally, the influence of 5-20 Å Al_2O_3 on thick Al films was investigated, both SPW and resistivity measurements suggest that the oxide film was not confined to film surface, but had penetrated inside the film leading to much higher electrical resistivities than would be otherwise expected.

To be published in Jour. of Appl. Phys. Nov 91

1. INTRODUCTION

Optical characterization of metal films is important for process control in the semiconductor industry. The standard ellipsometric and reflectometric techniques [1-4] possess the requisite sensitivity but require complex instrumentation and computations, in addition, a very careful and model dependent interpretation of the data is necessary for determining the optical parameters. A waveguide approach, using prism coupling to either dielectric waveguide modes [5] or to a surface-plasma-wave confined to a metal-dielectric interface [6-8] has also been used. The optical excitation of surface plasma waves (SPWs) has been carried out in both Kretschmann-Raether geometry [9] or in Otto geometry [10]. In the Kretschmann-Raether geometry, SPW excitation occurs by tunneling thru a thin metal film, which places severe constraints on the film thickness and dielectric constants, limiting its effectiveness mostly to Ag and Au films, and, of course, on the transparent substrate material which is typically a glass prism. In the Otto geometry the prism is placed in close proximity of the top surface of the film. The tunnel barrier between the metal film and the prism has to be very thin (< 500 nm) requiring significant pressure between the prism and the substrate. Both of these techniques are sensitive to film properties, and the theoretical formalism is provided by Fresnel theory.

Grating-coupling based characterization, in contrast, is free of all the above mentioned constraints. The theoretical formalism to describe the coupling process is, however, complex and requires detailed computational algorithms[11-12]. Recently, we have presented a detailed analysis of grating coupling to SPWs for a wide range of grating depths and profiles [13-14]. The theoretical analysis, based on the Rayleigh expansion, was very simple and provided good agreement with the experimental data. Here, we apply this analysis to measurement of metal film optical properties. Al films because of their importance in integrated circuit technology were used. These films were deposited by three different deposition techniques; thermal evaporation, magnetron sputtering, and ion-assisted magnetron sputtering. In addition, ellipsometric, resistivity, and SEM measurements were also carried out on these films to compare with the SPW data. In all cases, excellent agreement with SPW measurements was obtained.

2. EXPERIMENTAL ARRANGEMENT

An Al target was used which was 99.99 % pure. Room temperature depositions were carried out in a 45-cm diameter, cryogenically pumped bell jar vacuum system [15]. For thermal evaporation, a tungsten boat was used. Sputtered films were deposited at 0.5 mTorr Ar pressure using a planar magnetron source. For ion-assisted deposition, a beam of argon ions from a Kaufman ion source was directed at the substrate surface during magnetron sputtering. The beam voltage was maintained at 440 eV, and ion flux at the film surface was approximately 25 $\mu Amp/cm^2$. In all cases, depositions were carried out at a rate ~ 2 Å/s, starting vacuum was in the low 10^{-7} Torr range, and the film thickness was determined by a crystal monitor. The ellipsometric measurements were performed on films deposited on Si-wafers. For SPW measurements, the films were deposited on holographically defined submicrometer gratings on Si [16]. The zero order reflectance (λ=633 nm) from the coated gratings was monitored as a function of incident angle, the excitation of surface plasma waves is manifested by resonance like dip in the reflectance curve, and is described in detail elsewhere [13-14].

3. ELLIPSOMETRIC MEASUREMENTS

Ellipsometry involves measurement of the effect of reflection on the state of polarization of the reflected light [1]. The state of polarization is characterized by the phase and the amplitude relationships between the two orthogonal polarizations of the electric field vector of the polarized field. The electric field orientation of one, designated as TM, is in the plane of incidence, and of the other, designated as TE, is normal to the plane of incidence. In general, reflection causes a change in the relative phases of the TM and TE waves, and a change in the ratio of their amplitudes. The angle Δ is defined as the change in phase, and the angle Ψ as the arctangent of the factor by which the amplitude ratio changes. The angles Δ and Ψ are measured by the ellipsometer. There are a wide variety of commercial software packages which calculate the film dielectric constants and thickness, given Δ, Ψ, the light wavelength, and the substrate index. From our measurements, the dielectric constants were alculated by using a computational package developed by Urban [17]. Fig. 1 shows the measured variation of Ψ

and Δ as a function of film thickness, the values at zero thickness correspond to those of Si. The qualitative behavior of Ψ is the same for the films deposited by all three techniques. The behavior of Δ, however, is similar for sputtered and ion-assisted sputtered (IAS) films, but for evaporated films it remains approximately constant. Using these Δ and Ψ values, the dielectric constants of Table I were calculated. The real part of the dielectric constant shows much larger changes than the imaginary part. Also, the real and imaginary dielectric constants for evaporated and sputtered films were larger than for IAS films.

4. SPW MEASUREMENTS

In Figs. 2 and 3, we show a sequence of 0-order reflectance scans of sputtered Al films as thickness is increased approximately from 5 to 50 nm on Si grating (d=477 *nm*, depth=16 *nm*). The dotted curves present the results of the best fit to experimental lineshape, and will be discussed below. The main features of Fig. 2 , where the film thickness varies from about 5 to 20 nm can be characterized as follows:

1. the appearance of a broad SPW resonance at film thickness of 11 *nm* with intensity minimum at $\theta = 18.08^{o}$ and a cusp at $\theta = 18.9^{o}$ due to the emergence of the -1-diffraction order (i.e., for angles greater than 18.9^{o} there is an allowed -1-diffraction order that can take energy from the reflected beam, for angles less than 18.9^{o} this order is evanescent);
2. the decrease in SPW resonance width from about 1.5^{o} (Fig. 2b) to $.9^{o}$ (Fig. 2 d);
3. the increase in coupling efficiency from 0.1 (Fig. 2b) to 0.3 (Fig. 2d) and;
4. the slight shift in resonance angles (angles at which intensity minima occur) to larger angular values, i.e., a decrease in angular separation between SPW resonance angle and the cusp angle (the cusp angle remains constant determined by only by grating periodicity and the laser wavelength).

The behavior of the SPW resonance for thicker films (24-50 nm) is shown in Figure 3, and can be briefly summarized as follows:

1. the continuing decrease in SPW resonance width from 0.86^{o} (Fig. 3a) to 0.57^{o} (Fig. 3d);
2. the saturation of coupling efficiency at 0.52 (Figs. 3 c&d) from 0.34 (Fig. 3a) and;
3. the continuing small shifts in resonance angles to larger angular values.

In Fig. 4, we have plotted coupling efficiency, resonance width, and the resonance angle shifts as a function of film thickness for films deposited using all three deposition techniques. The salient features of these measurements are :

1. the coupling efficiencies reach ~ 52 % for both evaporated and sputtered films for film thickness in the range 30-40 nm, while for the IAS films, the corresponding efficiency was ~ 41 % for film thickness of above 50 nm ;
2. the resonance widths for the evaporated and sputtered films are almost identical, while those for IAS films were approximately 15 % larger and;
3. the absolute shifts in the resonance angles (i.e., the angular difference between SPW resonance and the cusp angle) decreased from 0.78^{o} to 0.74^{o} for evaporated films, and from 0.82^{o} to $.76^{o}$ for sputtered films, while for IAS films weak dependence with film thickness was observed.

In general, the evaporated and sputtered films were observed to have similar characteristics, while the IAS films showed significantly different patterns. In contrast with the ellipsometric measurements where there were two observable quantities, the SPW measurements provide three observed quantities, the resonance width, resonance angle, and the coupling efficiency. In addition the variations in optical properties for the different films are more evident in these measurements than they were in the ellipsometric measurements

5. THEORETICAL MODELING

The grating coupling to SPWs has been treated by a large number of authors [11-13]. Most of these theoretical formalisms are very complex, and require extensive computational efforts. Here, we have used an elegant and simple analysis for SPWs at a single grating interface with any arbitrary profile developed by Toigo et al. [18]. We have extended this analysis to two interfaces to model optically thin films.The theoretical analysis is based on the Rayleigh hypothesis and is briefly reviewed here.

For TM-polarized light incident at a grating surface at an angle θ, we can write the magnetic field in the three regions (vacuum, metal film, and Si-substrate) as follows:

$$B_{vac}(y,z) = \exp(i(k_y y + k_z z)) + \sum_n R_n \exp(i(k_n y - \alpha_n z)); \quad 1.$$

$$B_{met}(y,z) = \sum_n [A_n \exp(i(k_n y + \beta_n z)) + B_n \exp(i(k_n y - \beta_n z))]; \quad 2.$$

$$B_{sub}(y,z) = \sum_n C_n \exp(i(k_n y + \gamma_n z)); \quad 3.$$

where

$$k_y = k\sin\theta, \qquad k_z = k\cos\theta, \qquad k = \omega / c;$$

$$k_n = k_y + ng, \qquad n = 0, \pm 1, \pm 2, \ldots, \qquad g = 2\pi / d;$$

$$\alpha_n^2 = k^2 - k_n^2, \qquad \beta_n^2 = \varepsilon_{met} k^2 - k_n^2, \qquad \gamma_n^2 = \varepsilon_{sub} k^2 - k_n^2. \quad 4.$$

and ε_{met} , ε_{sub} are metal and substrate (Si) dielectric constants, and d is the grating period. For a grating profile defined by f(y), a straightforward application of electromagnetic boundary conditions leads to the following set of coupled linear differential equations (as explained in the appendix):

$$\sum_n [-R_n X_{m-n}(-\alpha_n u) + A_n X_{m-n}(\beta_n u) + B_n X_{m-n}(-\beta_n u)] = X_m(k_z u); \quad 5.$$

$$\sum_n [A_n X_{m-n}(\beta_n u) \exp(\iota \beta_n t) + B_n X_{m-n}(-\beta_n u) \exp(-\iota \beta_n t) - C_n X_{m-n}(\gamma_n u)] = 0; \quad 6.$$

$$\sum_n [R_n \left(\frac{(\omega/c)^2 - k_m k_n}{\alpha_n}\right) X_{m-n}(-\alpha_n u) + A_n \left(\frac{\varepsilon_{met}(\omega/c)^2 - k_m k_n}{\varepsilon_{met}\beta_n}\right) X_{m-n}(\beta_n u)$$
$$+ B_n \left(\frac{\varepsilon_{met}(\omega/c)^2 - k_m k_n}{\varepsilon_{met}\beta_n}\right) X_{m-n}(-\beta_n u)] = \left(\frac{(\omega/c)^2 - k_m k_y}{k_z}\right) X_m(k_z u); \quad 7.$$

$$\sum_n [A_n \left(\frac{\varepsilon_{met}(\omega/c)^2 - k_m k_n}{\varepsilon_{met}\beta_n}\right) X_{m-n}(\beta_n u) \exp(\iota \beta_n t) + B_n \left(\frac{\varepsilon_{met}(\omega/c)^2 - k_m k_n}{\varepsilon_{met}\beta_n}\right) X_{m-n}(-\beta_n u) \exp(-\iota \beta_n t)$$
$$- C_{m-n} \left(\frac{\varepsilon_{sub}(\omega/c)^2 - k_m k_n}{\varepsilon_{sub}\gamma_n}\right) X_{m-n}(\gamma_n u)] = 0; \quad 8.$$

where $X_p(\rho)$ is the Fourier transform of the grating profile defined by

$$X_p(\rho) = \frac{1}{d}\int_{-d/2}^{d/2} \exp(-\iota\, pgy)\exp(\iota\, \rho\, f(y))\, dy. \qquad 9.$$

Here p (=m-n) is an integer and ρ is given by $\alpha_n u$, $\beta_n u$, or $\gamma_n u$. In Eqs. 5-8 both n and m go from $-\infty$ to $+\infty$. Computationally, however, the series is truncated at values for which inclusion of next higher order term does not result in any change of the previously calculated value. The Fourier transform integral can be evaluated for any given grating profile. In particular, for sinusoidal profiles eq. 9 gives the familiar Bessel function expansion, and has been investigated in detail elsewhere [13]. Convergence for this particular profile is obtained for n,m = 2. For other nonanalytical profiles, i.e., square or rectangular, the Rayleigh assumption is usually not valid, however, it was pointed out by Hill et al. [19] that fc .hallow gratings (u/d ~ .07), this method can still be applied with reliable results. In our numerical calculations, we have tested for consistent results for n,m as large as 10 leading to an 84 x 84 matrix inversion. For numerical calculations, the grating profile used for evaluating the integral Eq. 9 is shown in Fig. 5 (see appendix for more details). The actual SEM profile of Si grating (depth =16 nm) used in the experiments is shown in Fig. 8c. The real and imaginary parts of the dielectric constant of Al were allowed to vary independently to obtain the best fit to the experimentally observed resonance lineshapes. The shift in the resonance angle was strongly dependent on the real part of the dielectric constant, the width of the resonance was a function of both the real and imaginary parts of the dielectric constant. Also a 5% variation in either the film thickness or the grating depth did not result in a shift of the resonance angle.

6. COMPARISON OF ELLIPSOMETRIC AND SPW DATA

In Table 1, we have compared the dielectric constants calculated by the two different techniques. For film thickness below 10 nm, the metal films did not show the characteristic SPW lineshape, therefore it was not possible to calculate the corresponding dielectric constants. The comparison of the data shows that, in general, the values calculated from the two methods were within 6% of each other, although for some cases, especially for ~

10-nm thick films, the difference was much larger. For both cases, the variation of the dielectric constants were similar. The values calculated by SPW method were in general larger than the ellipsometric values for thinner (< 30 nm) and smaller for thicker films. The SPW results were in good agreement with the literature [20-21]. The lineshape of the SPW resonance is influenced by grating profile, by the substrate on which grating is defined as well as by the presence of very thin Al_2O_3 films on Al films, effects of all of these variations are evaluated in the following sections.

6a. INFLUENCE OF GRATING PROFILES

In our work, the depth of the grating was chosen to keep the coupling strength well within the Rayleigh criterion (h/d ~ .07). In Fig. 6, we have calculated SPW lineshapes for three different profiles assuming same period (d=477 nm), depth (h=16 nm), and dielectric constant (ε=-46,16), the difference in profile changes coupling efficiencies, but there are no significant changes in the resonance angles and widths. In addition to the grating profile, the substrate in which the grating is fabricated also plays an important part. In Fig. 7, we have shown experimental and calculated SPW lineshapes for 50-nm thick Al films deposited on Si (h=16nm), SiO_2 (h=17 nm), and photoresist (h=36 nm) gratings. The profiles of these gratings are shown in Fig. 8. The dielectric constants of the films on SiO_2 and photoresist are characterized by (-40.1,14,6) and (-32.2, 12.8) . It is seen that dielectric constant of the film deposited on photoresist is significantly different from the values in Table I. This suggests that the photoresist surface being significantly rougher than either SiO_2 or Si results in the growth of poor quality films.

6b. INFLUENCE OF OXIDE LAYERS

When a freshly deposited Al-film is exposed to the atmosphere at room temperature, a transparent, amorphous oxide layer immediately forms on the metal surface. Hass reported that the oxide within a few hours grows to a thickness of approximately 15-20 Å , but further growth occurs slowly reaching a maximum of 45 Å after one month [22]. In order to investigate the influence of Al oxide film on the SPW resonance lineshape of Al

films, we deposited very thin (5-20 Å) films of Al_2O_3 on an approximately 40-nm thick Al film. In Fig. 9, we have shown the results of 5 and 20 Å oxide on the SPW lineshape. The solid line represents bare Al film (thickness = 40 nm, Fig. 3c). 5 Å oxide film significantly alters the SPW resonance characteristics increasing the resonance width by 17%, resonance angle by 6%, and decreasing coupling efficiency by 11%. The corresponding numbers for 20 Å film were 31%, 25%, and 21%. Assuming the dielectric constants of bulk Al [21] in literature (-46.36, 16.69), our calculations showed that the resonance angle was .6° in comparison with the corresponding values of .74° and .76° for evaporated and sputtered films (thickness = 50 nm). Assuming an oxide layer of 20 Å (n = 1.66) on bare Al substrate, our calculations showed that the resonance angle increased by .16°, which is in good agreement with our data. However, deposition of 5-20 Å Al_2O_3 resulted in increases in resonance angles which were almost twice .32°. Therefore, it appears that the oxide film is not limited to the surface, but also penetrates in the Al film and changes its composite dielectric constant. This is reflected in the much higher resistivity of oxide coated films as will be shown later.

7. SEM MEASUREMENTS

Grain boundaries, voids, and other inhomogeneities significantly affect the optical properties of thin films [23-24]. This is reflected in the large differences of the dielectric constants of the films (Table 1). In Fig. 10, we have shown a series of scanning electron micrographs (SEMs) of the Al films as a function of thickness. The increase in grain sizes is consistent with similar behavior for metal films, such as silver [25]. The grain sizes and boundaries for evaporated films (Fig. 10a) are significantly larger than the films deposited by sputtering and ion-assisted sputtering (Figs. 10b & 10c). For evaporated films, the film discontinuities decrease rapidly with thickness, and also the film surface appears very smooth. The behavior of both sputtered and IAS films is different; the grain size increase with film thickness is slow, and the film surface appears rough and discontinuous. These results indicate that the process of film growth by evaporation and sputtering is fundamentally different. In evaporated films, the grain boundaries are interconnected, the individual grains are not spherically symmetric, and the structure as a whole appears continuous. With sputtered and IAS films, however, the grain boundaries are not interconnected, the individual grains are approximately spherical, and the structure as a whole appears

discontinuous. The dielectric response (Table 1) of these films provides us with a simple means of calculating the density of the films [3]. Using the Bruggeman effective medium approximation [26], it is possible to define an effective dielectric constant, ε, for the film in terms of the bulk dielectric constant (ε_{met} = -46.36, 16.69) and the volume fraction of voids in the film,

$$\varepsilon = \frac{(2X-1) + \varepsilon_{met}(2-X) + \sqrt{[(2X-1) + \varepsilon_{met}(2-X)]^2 + 8\varepsilon_{met}(1+X)^2}}{4(1+X)}, \qquad 10.$$

where X is the ratio of void volume fraction to the metal volume fraction. Using this equation, and given the measured dielectric constants in table 1, we calculated the void fractions of 0.01, 0.06, and 0.17 for evaporated, sputtered, and IAS films. For thinner films (< 20 nm) corresponding measured dielectric constants (Table 1) were not in good agreement with calculated values from Eq. 10 for any value of X. A comparison of the structures of sputtered and IAS films (Figs. 10b & 10c) shows that the film morphology is very similar for both films, and therefore the large void fraction difference as predicted by Eq. 10 is misleading. This, coupled with increasing disagreement for thinner films, suggests that the Bruggeman effective media approximation is not appropriate to describe the composite metal structure. As will be seen in the next section, the structural changes at the grain boundaries play a major role in determining the dielectric properties.

8. RESISTIVITY MEASUREMENTS

Resistance measurements provide information about the internal structure of the metal films [24]. Using standard four-point probe technique [27], the resistivity of all films for which optical measurements had been performed was determined. In Fig. 11, the resistivity is plotted as a function of film thickness. The solid and dotted lines are the result of theoretical modeling and will be discussed below. From the data, the following salient features are apparent:

1. for evaporated films, the resistivity ratios, i.e., film resistivity/bulk resistivity, where ρ_b = 2.73 $\mu\,\Omega$-cm [28] varied from 11.24 to 1.18 for film thickness increasing from approximately 7 to 100 nm;

2. for sputtered films, the resistivity ratios varied from 36 to 2.65 as film thickness increased from 5 to 50 mm, and;

3. for IAS films, the resistivity ratios varied from 13 to 3.96 as film thickness increased from 6 to 100 nm.

The resistivity of vacuum deposited thin metal films depends on the thickness, grain size, and the impurities present in the film. Various theories have been developed to account for the thickness variation of the resistivity [29-34]. In the Fuchs-Sondheimer (F-S) theory [29], assuming free electron model the increase in the resistivity of the film with decreasing film thickness is modeled by assuming that the electron scattering at the film surfaces modifies the electron distribution resulting in an expression for the thickness dependence of the resistivity. This theory, however, shows small thickness dependent contribution for films thicker than the mean free path of the electrons. For films much thinner than the electron mean free path, Lovel and Appleyard (L-A) also developed an expression for resistivity dependence of thickness [30]. We have not been able to fit our data with either of these theories. In F-S theory, the high resistivity ratios obtained experimentally force the calculations to pick abnormally high mean free paths reducing the applicability of the theory to either very low temperatures, or to very thick films at room temperatures. The L-A theory is not suitable for the range of film thicknesses in our experiment. We therefore used a very simple empirical expression due to Planck [35] to fit our resistivity data for the films. According to this expression, the film resistivity as a function of thickness is simply given by

$$\rho_t = \rho_b \left(1 + \frac{A}{t}\right), \qquad 11.$$

where ρ_t is the thickness dependent resistivity, ρ_b is the bulk resistivity, and t is the film thickness. The constant A was later specified to be $4\, l_e / \pi$, where l_e is the electron mean free path, by simply averaging over the reduction of electron mean free path for film thickness less than the electron mean free path [36]. For films thicker than the mean free path, a smaller value of $A \sim 3\, l_e / 8$ is appropriate since some of the electrons are not stopped by the film surfaces [31]. In Fig. 11a., we have plotted Eq.11 with $A = 4\, l_e / \pi$ for mean free paths of 14 nm (dotted line), as calculated from basic principles [37, 28] and 30 nm (solid line) as given by Mayadas, et al.

[33]. With l_e = 14 nm, the fit is better for thicker films (40-60 nm), while for thinner films, the fit is better at l_e = 30 nm. The same calculation, however, does not predict the higher resistivities found for sputtered and IAS films (Table 1). Therefore, in addition to thickness dependence, there is also structure (grain size, boundaries, defects, etc.) dependence of resistivity. According to Mathiessen's rule [36], the total resistivity of the metal film can then be expressed as the sum $\rho = \rho_t + \rho_g$ where ρ_g is the resistivity due to the scattering of electron by lattice defects, grain size, and impurities, and ρ_t is given by Eq. 11. For films deposited by different techniques ρ_t shows approximately similar behavior. The grain-dependent resistivity, ρ_g, varies according to the growth conditions of the film. Mayadas and Shatzkes developed a model to predict qualitatively the effects of grain boundary scattering [33]. Their calculations showed that the measured resistivities increase significantly due to the scattering from the grain boundaries. In this model, the grain boundaries are represented as partially reflecting surfaces normal to the plane of the film, separated by an average distance D. The ratio between the grain and the bulk resistivity is given by

$$\frac{\rho_g}{\rho_b} = 1 - \frac{3\alpha}{2} + 3\alpha^2 - 3\alpha^3 \ln(1+\alpha^{-1}), \qquad 12.$$

where α is defined by $\left(\frac{l_e}{D}\frac{R}{1-R}\right)$ with R being the electron reflection coefficient at the reflecting planes (corresponding to grain boundaries). From the SEM analysis, it is evident that the distance D, which has also been identified as grain size, is similar for both sputtered and IAS films. Therefore, the increased contribution to resistivity appears to come from increased reflectance at the grain boundaries. In Figures 11b & 11c, we have plotted the sum $\rho = \rho_t + \rho_g$ for R = .05 and .65. It is seen that a reasonably good agreement is obtained with 30 nm mean free path. The large value of R for IAS films suggests that the ion bombardment during sputtering results in significant changes in the shape of the Fermi surface, and the potential barrier at the grain boundaries. Similar behavior has been observed for Ag films by Parmigiani, et al. [7]. Finally, in Fig. 12, we have plotted the measured resistivities as a function of SPW resonance angle and width. The experimental data of Fig. 12a represents five films of approximately 40-nm thickness deposited by thermal evaporation, magnetron sputtering, Ion-assisted sputtering, and sputtered films with 5 and 20 Å Al_2O_3 films. The solid line presents a first order

polynomial fit thru the data points. The increase in resonance angle corresponds to a similar increase in film resistivity providing an excellent non-invasive monitor for film characterization. Similar behavior is also observed by plotting the SPW resonance width versus film resistivity as thickness is increased from 10-60 nm for thermally evaporated films(Fig. 12b). This shows that the wider the resonance, the larger is the film resistivity. Both of these parameters (Res. angle and width) are related to the film dielectric constants, which are related to the resistivity. For metals with imaginary part of the dielectric constant much smaller than the real part (Au, Ag, etc.) simple analytical relationships exist between resonance parameters and the dielectric constants. In case of Al, however, it is not possible to determine a simple analytical relationship. Our calculations and the experimental data (Figs. 12a & 12b), however, suggest a linear response of resistivity with increase in resonance angle and width.

9. CONCLUSIONS

A detailed investigation of the optical, structural, and electrical properties of Al films in the 5-60 nm thickness range has been carried out. The measurement of metal film optical properties using grating excitation of SPWs is shown to provide simple, readily interpretable results. The influence of different substrates and profiles has been investigated. A comparison of the film structure of evaporated, sputtered, and IAS films by SEM analysis, and optical measurements suggests that a description of effective medium dielectric constant in terms of the presence of voids is inappropriate. A comparison of the electrical resistivities shows that the scattering from the grain boundaries substantially increases the resistivities of the films grown by ion-bombardment . It has been shown by Zieman et al. [38] that for the films grown under ion-bombardment, two distinct regimes exist: one regime where resistivity increases and grain size decreases with increasing energy delivered to the substrate during deposition process, and the second regime, which occurs at higher deposition rates where the reverse behavior is observed. The experimental data presented here show that these films correspond to the the first regime where energy delivered to the substrate increases from evaporated to IAS films along with an increase in resistivity, although our SEM measurements did no show a significant change in the grain sizes of IAS films. It is suggested that the increased resistivity of the sputtered and IAS films is due to an increase in grain boundary reflectance.

APPENDIX

The boundary conditions at the two interfaces, metal-air and metal-substrate, are given by

$$B_{vac} - B_{met} = 0, \tag{1.}$$

$$B_{met} - B_{sub} = 0, \tag{2.}$$

$$\left(\frac{\partial}{\partial n} - \frac{1}{\varepsilon_{met}}\frac{\partial}{\partial n}\right)(B_{vac} - B_{met}) = 0, \tag{3.}$$

$$\left(\frac{\partial}{\partial n} - \frac{1}{\varepsilon_{sub}}\frac{\partial}{\partial n}\right)(B_{met} - B_{sub}) = 0, \tag{4.}$$

where

$$\frac{\partial}{\partial n} = \sqrt{1+\left(\frac{\partial f(y)}{\partial n}\right)^2}\left(\frac{\partial}{\partial z} - \frac{\partial f(y)}{\partial y}\frac{\partial}{\partial y}\right). \tag{5.}$$

On applying these boundary conditions at $z = -t+uf(y)$ and $z = uf(y)$, where u is the grating amplitude and f(y) defines the grating profile, and taking the Fourier transform of the resulting set of equations, one arrives at the set of equations (5-8) given in the text. The Fourier transform integral (Eq. 9) for the grating profile (Fig. 5) can be solved analytically by assuming that in the region $\pm b_1 d/2$ to $\pm b_2 d/2$, the grating profile can be described by the straight line equation $y=mx+c$, with $m = \frac{\pm 4u/d}{b_1 - b_2}$, and $c = \frac{b_1+b_2}{b_1-b_2}$, where b_1 and b_2 were determined from SEM measurements (Fig. 7c) to .606 and .367 respectively. The integral in Eq. 9 can therefore be evaluated for p=0 as

$$X_0(\rho) = \exp(-\rho)(1-b_1) + \exp(\rho)\, b_2 + \frac{r_1 \exp(\rho r_2)}{2\rho}\left(\exp(-2\rho r_3) - \exp(-2\rho r_4)\right), \tag{6.}$$

and for $p \neq 0$,

$$X_p(\rho) = \frac{\iota \exp(-\rho)}{2\pi p}\left(\exp(\iota \pi p b_1) - \exp(-\iota p\pi b_1)\right) + \frac{\iota \exp(\rho)}{2\pi p}\left(\exp(-\iota p\pi b_2) - \exp(\iota p\pi b_2)\right)$$

$$+ \frac{\exp(\rho r_2)}{\left(\frac{4\rho}{r_1} - \iota 2\pi p\right)}\left(\exp[-(\frac{2\rho}{r_1} - \iota \pi p)b_2] - \exp[-(\frac{2\rho}{r_1} - \iota \pi p)b_1]\right)$$

$$+ \frac{\exp(\rho r_2)}{\left(\frac{4\rho}{r_1} + \iota 2\pi p\right)}\left(\exp[-(\frac{2\rho}{r_1} + \iota \pi p)b_2] - \exp[-(\frac{2\rho}{r_1} + \iota \pi p)b_1]\right). \quad 7.$$

with $r_1 = \frac{b_1 - b_2}{r_2}$, $r_2 = \frac{b_1 + b_2}{r_1}$, $r_3 = \frac{b_2}{r_1}$, $r_4 = \frac{b_1}{r_1}$, and ρ is defined in the text. For a square profile, Eqs.. 6 and 7 assume much simpler forms.

$$X_0(\rho) = \cosh(\rho), \quad 8.$$

and

$$X_p(\rho) = \frac{2\iota}{\pi p}\sinh(\rho)\sin(\frac{\pi p}{2}). \quad 9.$$

ACKNOWLEDGEMENTS

This work was supported by SEMATECH / SRC. We would also like to acknowledge the assistance of Alfonso Torres, Chris Krannenberg, Scott Wilson, Susan Hietala, M. Yousaf, and Mike Lang during the course of this work.

1. B. Draper is with the Sandia National Laboratories, Albuquerque, New Mexico.

2. J. R. McNeil is with the Department of Electrical Engineering, University of New Mexico.

3. S. R. J. Brueck is with the Departments of Electrical Engineering and Physics, University of New Mexico.

REFERENCES

Archer, J. O. S. A. 52, 970 (1962).

Aspness and A. A. Studna, Phys. Rev. B 27, 985 (1983).

Aspness, Thin Solid Films 89, 249 (1982).

Johnson and R. W. Christy, Phys. Rev. B 6, 4370 (1973).

King and S. P Talim, Optica Acta 28, 407 (1981).

Zhizhin, , M. A. Moskalova, E. V. Shomina, and V. A. Yakovlev, 1980a, Fiz Met i Met 50, N3.

Parmigiani, E. Kay, T. C. Huang, J. Perrin, M. Jurich, and J. D. Swalen, Phys. Rev. B 33, 879 (1986).

Fuzi, G. W. Bradberry, and J. R. Sambles, Jour. Mod. Opt. 36, 1405 (1989).

Kretschmann and M. Raether, Z. Naturf (a) 24, 2135 (1968).

Otto, Z. Phys. 261, 398 (1968).

Electromagnetic Surface Modes, Edited by A. D. Boardman, Wiley (1982).

Surface Polaritons, Edited by V. M. Agranovich and D. L.Mills, North-Holland (1982).

Saleem H. Zaidi, M. Yousaf, and S. R. J. Brueck, J. O. S. A. B 8, 770 (1991).

Saleem H. Zaidi, M. Yousaf, and S. R. J. Brueck. J. O. S. A. B 8, 1348 (1991).

Mcnally, J. R. McNeil, J. M. Bennett, and H.H.Hurt Appl.Opt. 25, 3631 (1986).

Saleem H. Zaidi and S. R. J. Brueck, Appl. Opt. 27, 2999 (1988).

Urban III, Applied Surf. Sci. 33/34, 934 (1988).

Toigo, A. Marvin, V. Celli, and N.R. Hill, Phys. Rev. B 15, 5618 (1977).

Hill and V. Celli, Phys. Rev. B 17, 2478 (1978).

Schulz, J. O. S. A. 44, 357 (1954).

Optical Properties of Metals, G.P. Motulevich, Consultants Bureau (1973).

Hass G., Z. Anorg. Chem. 254, 96 (1947).

Optical Properties of Thin Solid Films, O. S. Heavens, Dover Publications Inc. (1955).

Vacuum Deposition of Thin Films, L. Holland, Wiley (1969).

Sennet and G. D. Scott, J. O. S. A. 40, 203 (1950).

G. Bruggeman, Ann. Phys. (Leipzig) 24, 636 (1935).

Smits, Bell Sys. Tech. Journal, 711 (1958).

Handbook of Physics and Chemistry, edited by Weast, CRC Press (1989-90).

Sondheimer, Advan. Phys. 1, 1 (1952).

S. Appleyard and A. C. B. Lovell, Proc. Roy. Soc. A 158, 718 (1937).

Chopra and L. C. Bobb, Acta Metallurgica 12, 807 (1964).

Mayadas, Jour. Appl. Phys. 39, 4241 (1968).

Mayadas and M. Shatzkes, Phys. Rev. B 1, 1382 (1970).

Mayadas, M. Shatzkes, and J. F. Janak, Appl. Phys. Lett. 14, 345 (1969).

Wilkinson, Jour. Appl. Phys. 22, 419 (1951).

Weale, Proc. Roy. Soc. Lon. A 62, 135 (1949).

Solid State Physics, N. W. Ashcroft, Holt, Rinehart and Winston (1976).

Zieman and E. Kay, J. Vac. Sci. Tech. A 1, 512 (1983).

TABLE 1 Dielectric constants and dc resistivities of Al as a function of film thickness for evaporated, sputtered, and IAS films.

ABLE I. OPTICAL PARAMETERS AND dc RESISTIVITIES S A FUNCTION OF FILM THICKNESS

Film hickness (nm)	Ellip. Measurements (ε_r, ε_i)	SPW Measurements (ε_r, ε_i)	Resistivity (10-6 Ω-cm)
<u>. Evaporated Films</u>			
7.5	(-33.1, 15.3)	----------	30.7
10.	(-28.8, 17.9)	(-36, 20)	18.
18.	(-42.1, 16.1)	(-42.6, 14.9)	7.9
29.	(-44.8, 16.3)	(-40.1, 14.2)	5.6
40.	(-45.1, 16.5)	(-40. 14.8)	4.2
52.	(-44.3, 16.6)	(-41.4,15)	4.1
<u>2. Sputtered Films</u>			
5.2	(-13.7, 13.4)	----------	98.8
11.	(-29.2, 15.2)	(-33., 22.)	18.8
15.	(-36.4, 15.4)	(-39.5, 16.5)	15.3
20.	(-34.8, 14.)	(-36.5, 14.)	16.1
30.	(-40.6, 14.2)	(-37.7,14.8)	8.9
40.	(-41.1, 15.4)	(-40.1,14.6)	7.5
50.	(-40.8, 15.)	(-40.3,14.7)	7.2
<u>3. IAS Films</u>			
6.1	(-27.7, 17.4)	----------	36.5
13.5	(-28.2, 15.7)	(-32.2, 15.8)	30.4
21.	(-30.2, 11.8)	(-33., 13.8)	21.4
31.	(-28.3, 12.2)	(-30., 13.5)	20.7
42.	(-33.3, 12.8)	(-33,13)	14.6
55.	(-29.2,11.4)	(34.1, 12.8)	17.4
73.	(-32.8,12.7)	(-31.3, 12.5)	9.6

FIGURE CAPTIONS

Fig. 1. Experimental variation of ellipsometric parameters Δ and Ψ with film thickness for Al films deposited by three different techniques.

Fig. 2 Variation of SPW lineshape for Al film thickness from 5 to 20 nm.

Fig. 3 Variation of SPW lineshape for Al film thickness from 24 to 50 nm.

Fig. 4 Experimental variation of SPW parameters, coup. eff., res. width, and res. angle shift, with film thickness for films deposited by three different techniques.

Fig. 5 Profile of the Si grating used for numerical calculations.

Fig. 6 Variation of the SPW lineshape for sinusoidal, square, and Fig. 5. grating profiles

Fig. 7 Variation of SPW lineshape for sputtered Al film (thickness = 50 nm) deposited on three different substrates.

Fig. 8 SEM profiles of three gratings (Si, Photoresist, and SiO_2) used for SPW characterization.

Fig. 9 Influence of thin oxide films on SPW lineshape of approximately 40 nm sputtered Al films.

Fig. 10 SEM measurements of Al films deposited by three techniques, a. thermal evaporation, b. magnetic sputtering, and c. ion-assisted magnetic sputterig.

Fig. 11 Variation of Al film resistivity with thickness and grain boundary reflection for films deposited by three different techniques assuming two different values of electron mean free path.

Fig. 12 Variation of Al film resistivity with SPW resonance angle for constant film thickness (a), and (b) resistivity variation with SPW resonance width for film thickness from 10 to 60 nm.

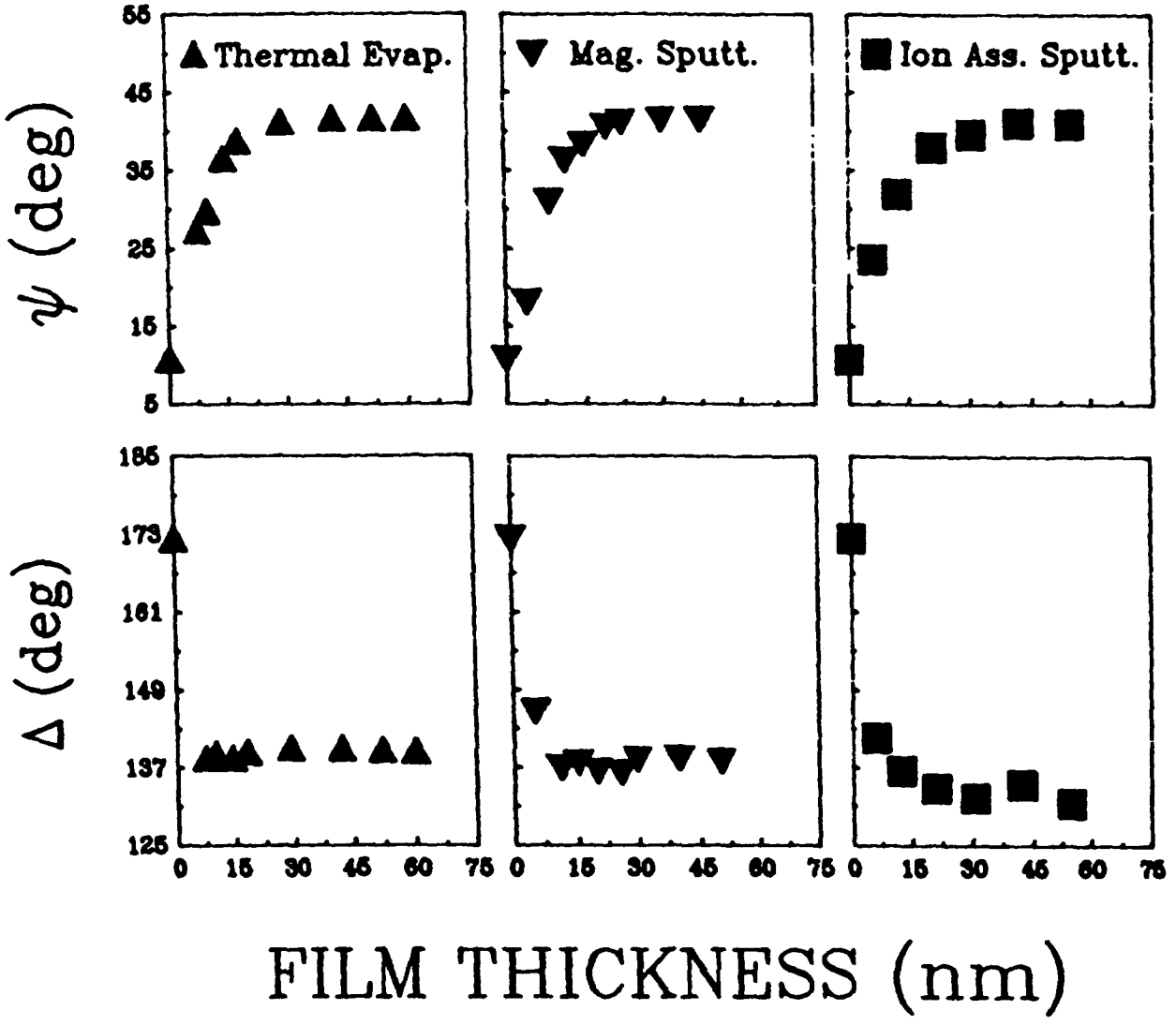
Thermal Evap.
Mag. Sputt.
Ion Ass. Sputt.
ψ (deg)
Δ (deg)
55
45
35
25
15
5
185
173
161
149
137
125
0
15
30
45
60
75
FILM THICKNESS (nm)

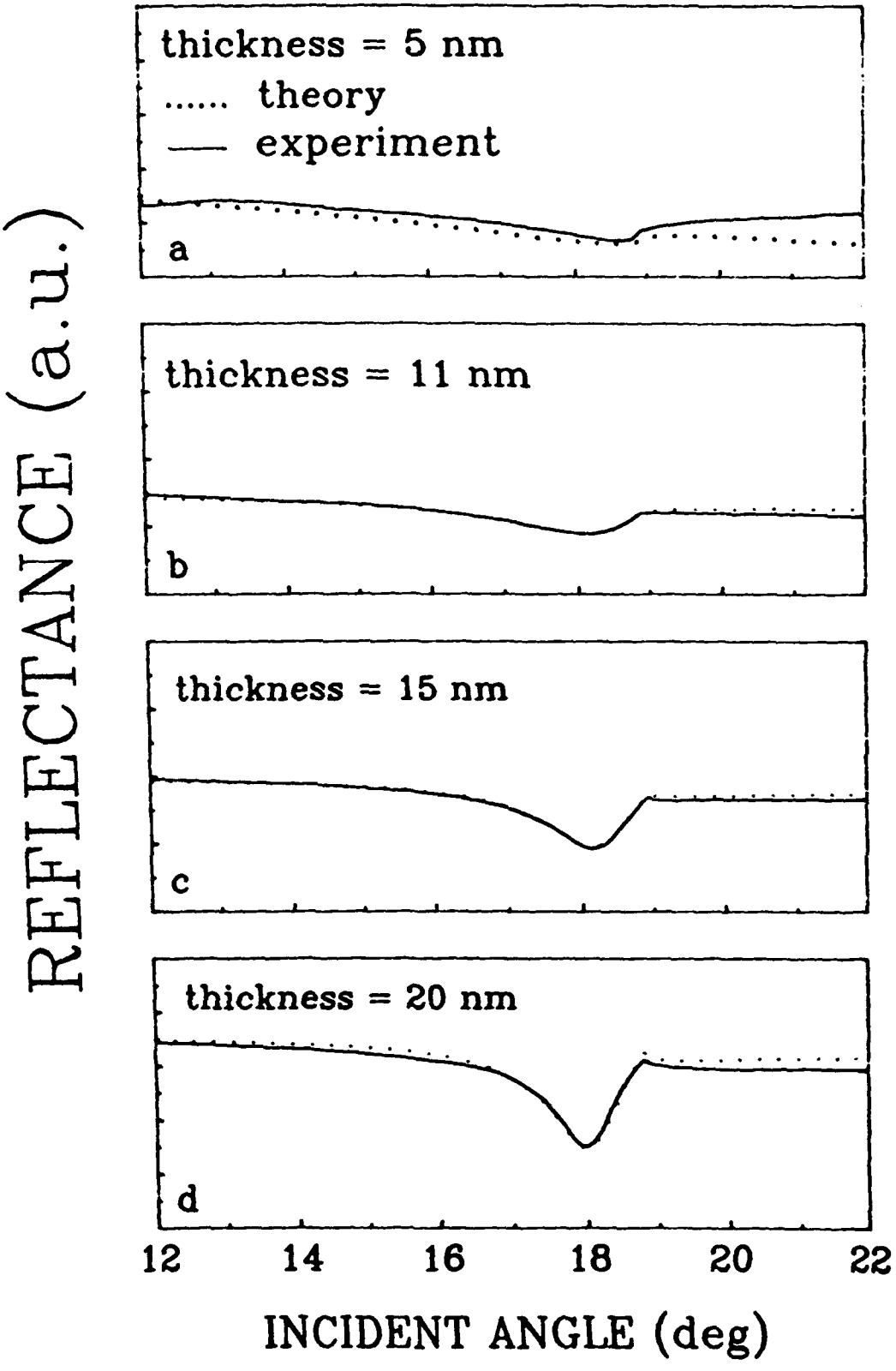
thickness = 5 nm
..... theory
—— experiment
a
thickness = 11 nm
b
thickness = 15 nm
c
thickness = 20 nm
d
REFLECTANCE (a.u.)
12
14
16
18
20
22
INCIDENT ANGLE (deg)

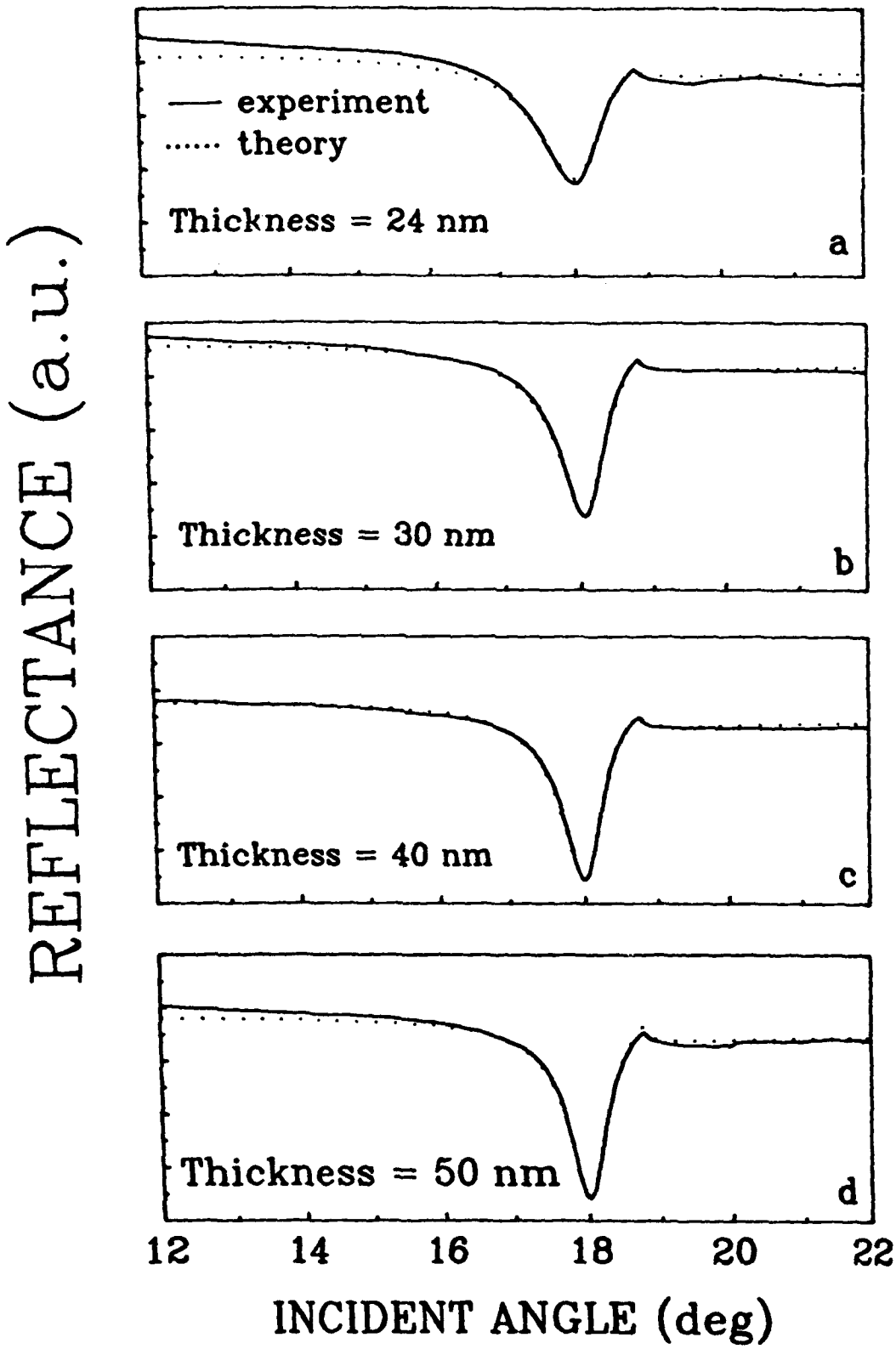
REFLECTANCE (a.u.)
experiment
theory
Thickness = 24 nm
a
Thickness = 30 nm
b
Thickness = 40 nm
c
Thickness = 50 nm
d
12
14
16
18
20
22
INCIDENT ANGLE (deg)

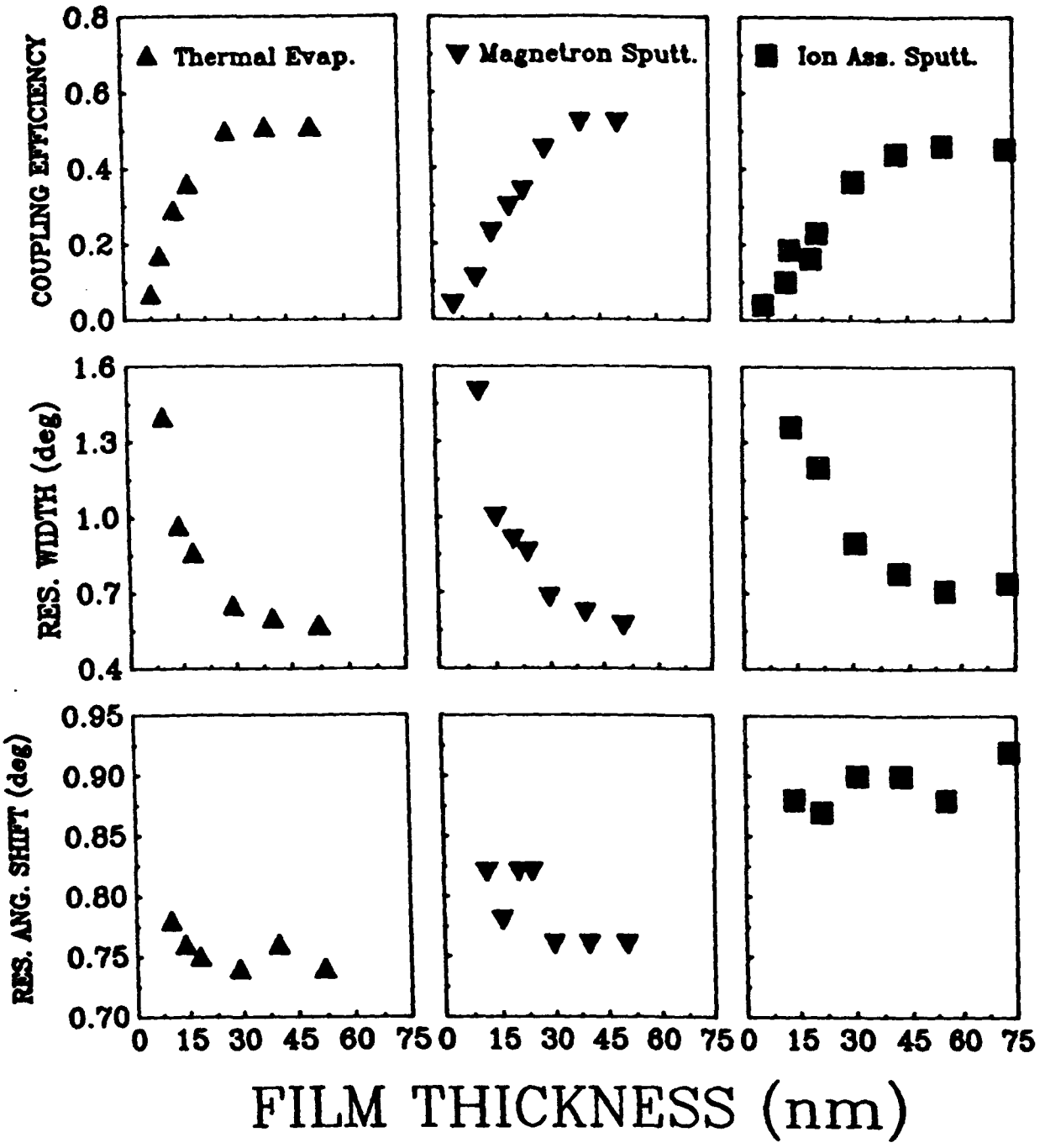
Thermal Evap.
Magnetron Sputt.
Ion Ass. Sputt.
COUPLING EFFICIENCY
0.8
0.6
0.4
0.2
0.0
RES. WIDTH (deg)
1.6
1.3
1.0
0.7
0.4
RES. ANG. SHIFT (deg)
0.95
0.90
0.85
0.80
0.75
0.70
0 15 30 45 60 75
0 15 30 45 60 75
0 15 30 45 60 75
FILM THICKNESS (nm)

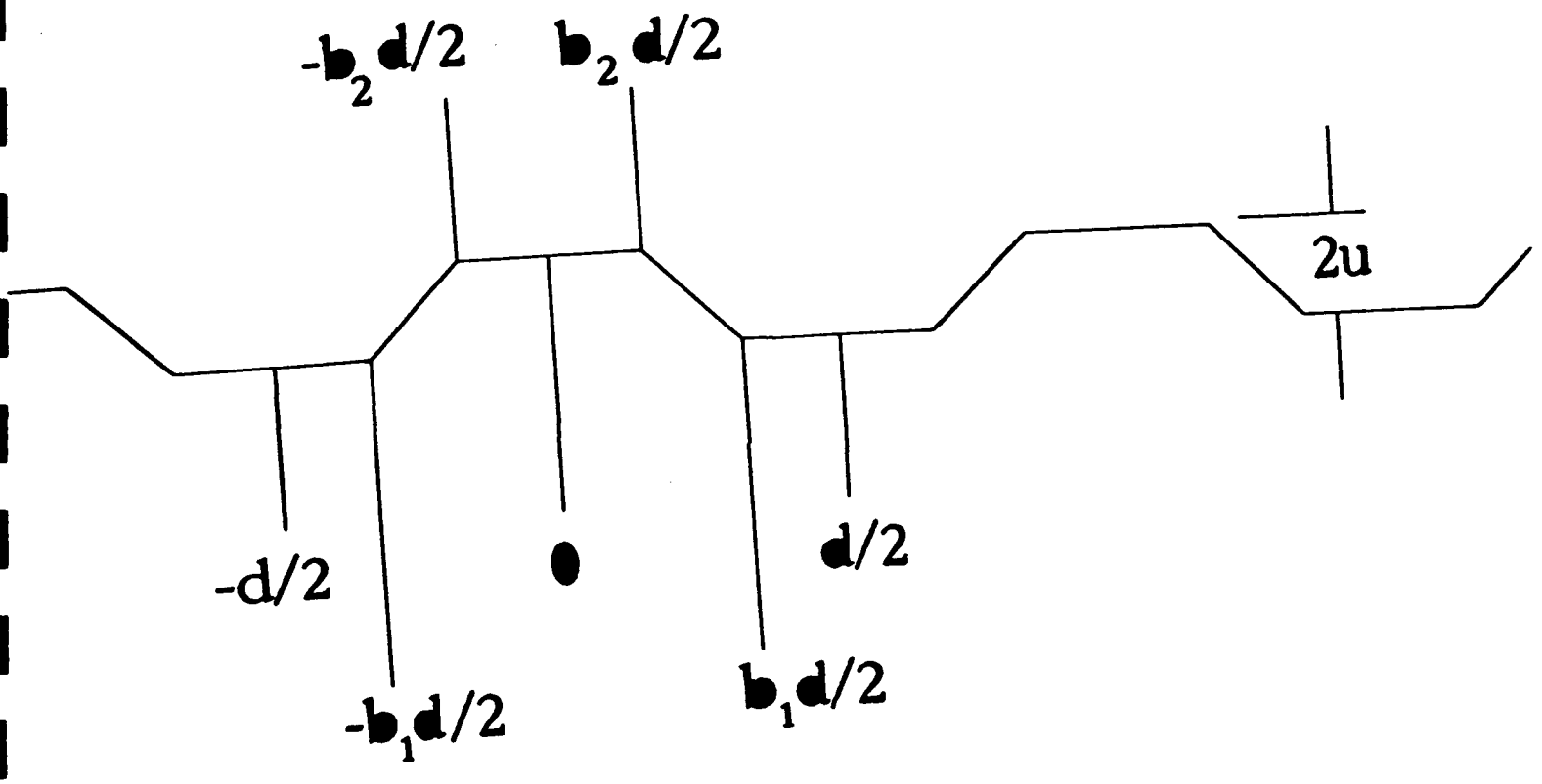
$-b_2 d/2$
$b_2 d/2$
2u
$-d/2$
0
$d/2$
$-b_1 d/2$
$b_1 d/2$

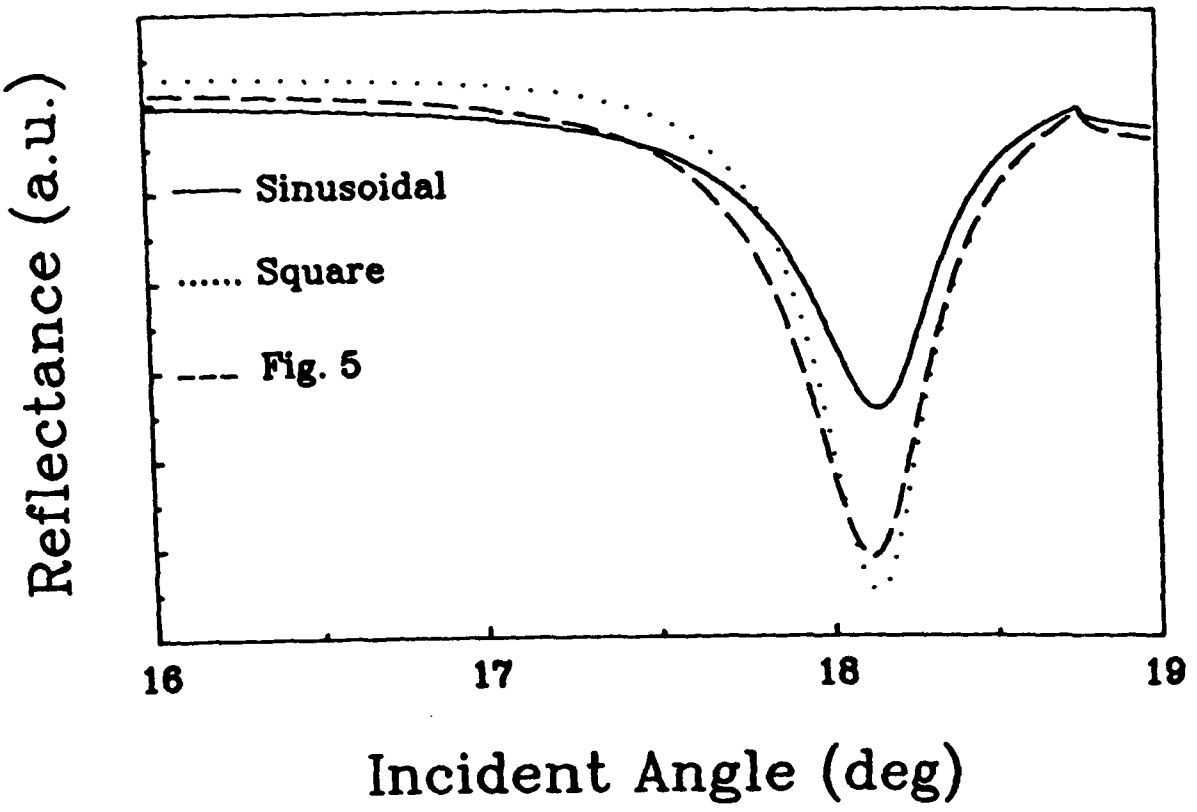
Reflectance (a.u.)
Sinusoidal
Square
Fig. 5
16
17
18
19
Incident Angle (deg)

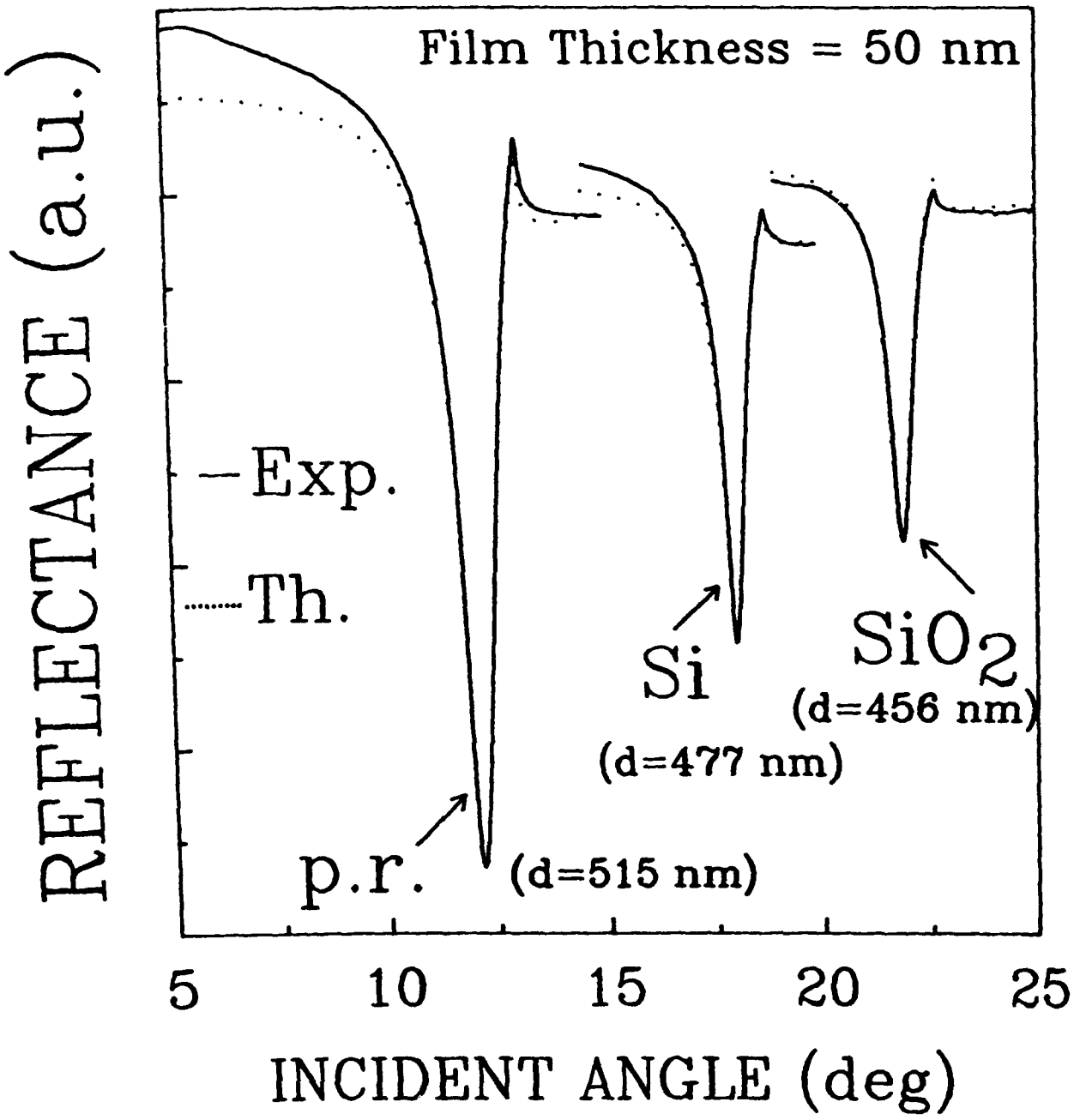
Film Thickness = 50 nm
REFLECTANCE (a.u.)
Exp.
Th.
p.r.
(d=515 nm)
Si
(d=477 nm)
SiO2
(d=456 nm)
5
10
15
20
25
INCIDENT ANGLE (deg)

SEM Profiles of gratings used for SPW characterization

Photoresist

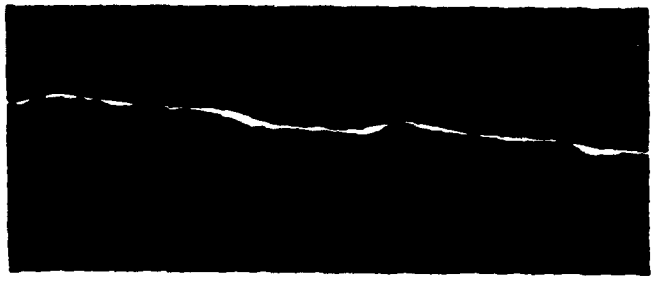

Si

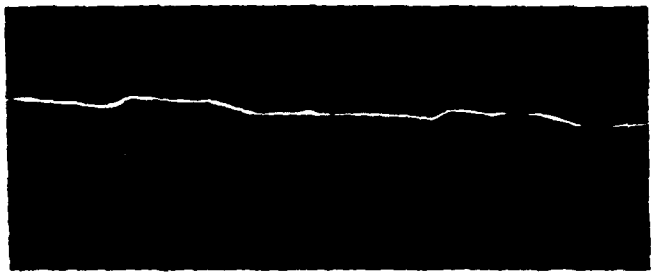

SiO_2

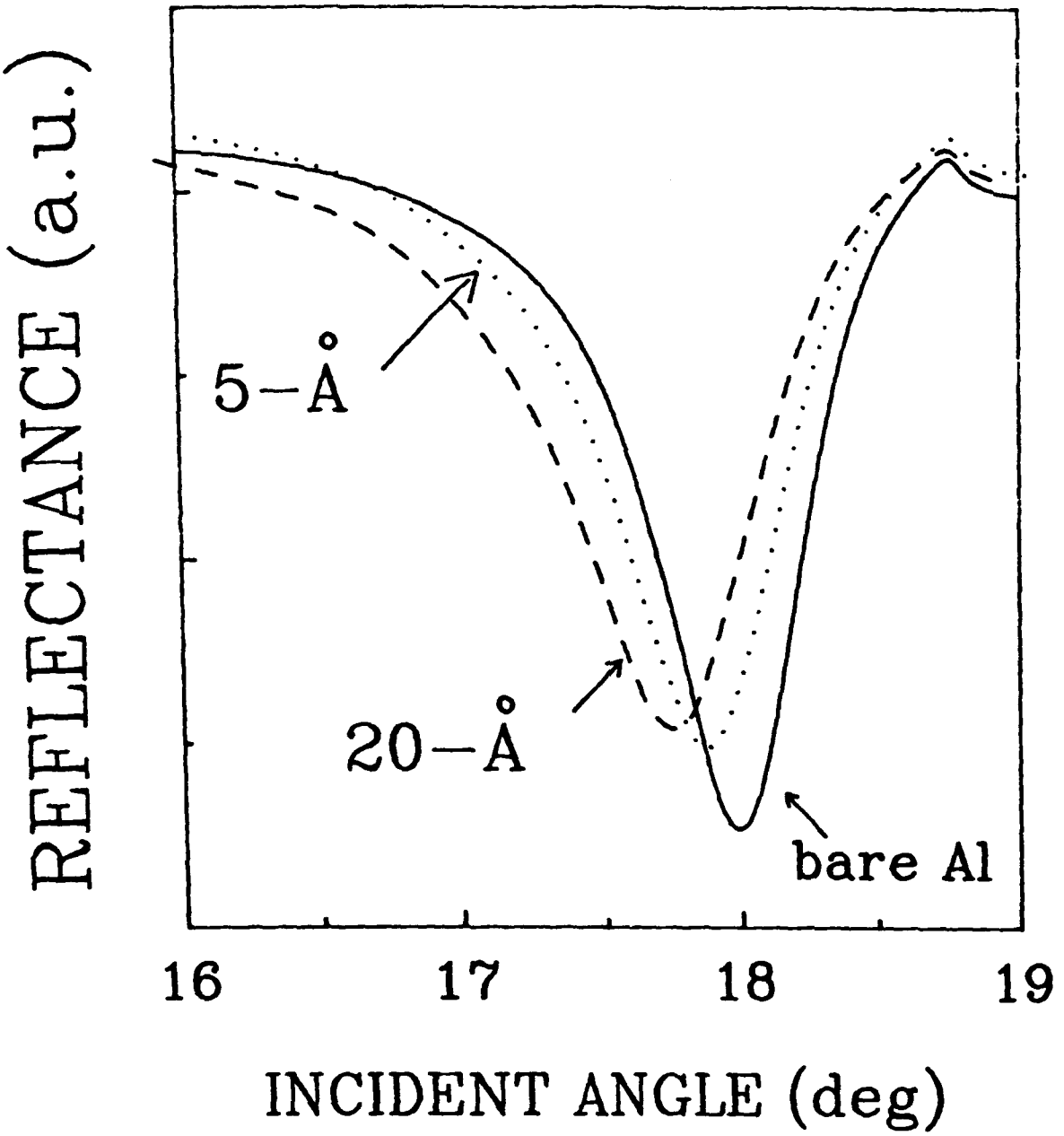
REFLECTANCE (a.u.)
5-Å
20-Å
bare Al
16
17
18
19
INCIDENT ANGLE (deg)

Evap. Films

Thickness:

7nm

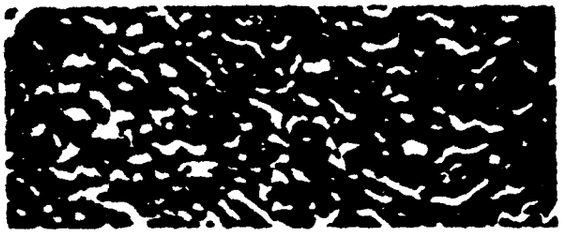

14nm

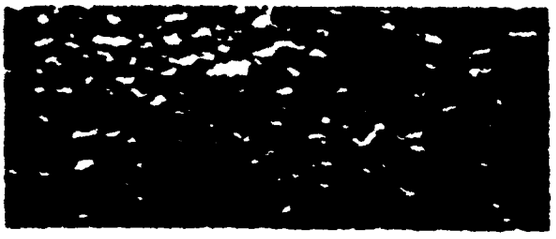

29nm

42nm

60nm

Sputt. Films

Thickness:

5nm

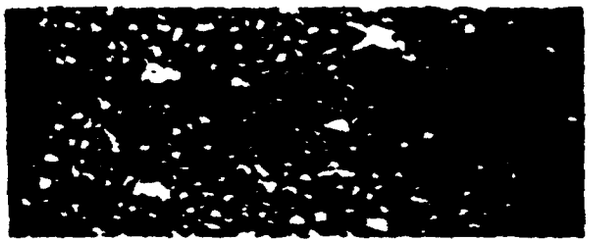

11nm

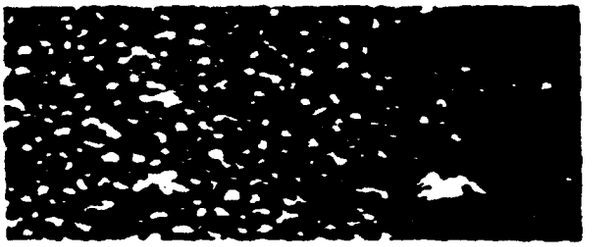

20nm

30nm

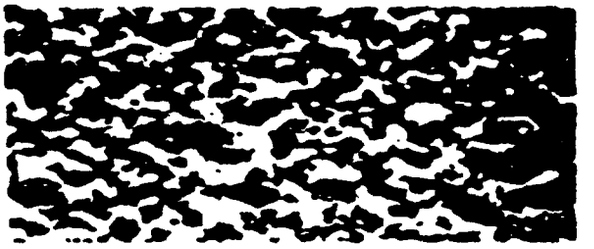

50nm

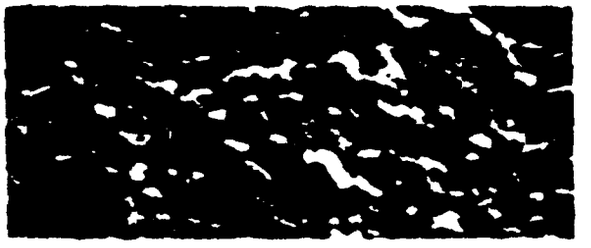

IAS Films

Thickness:

6nm

12nm

21nm

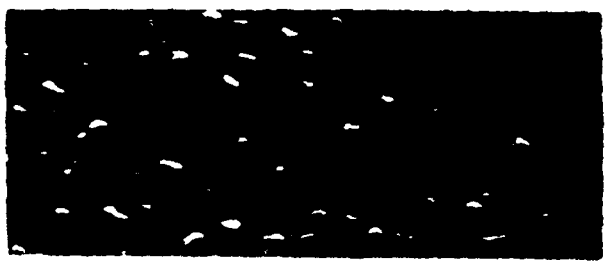

31nm

55nm

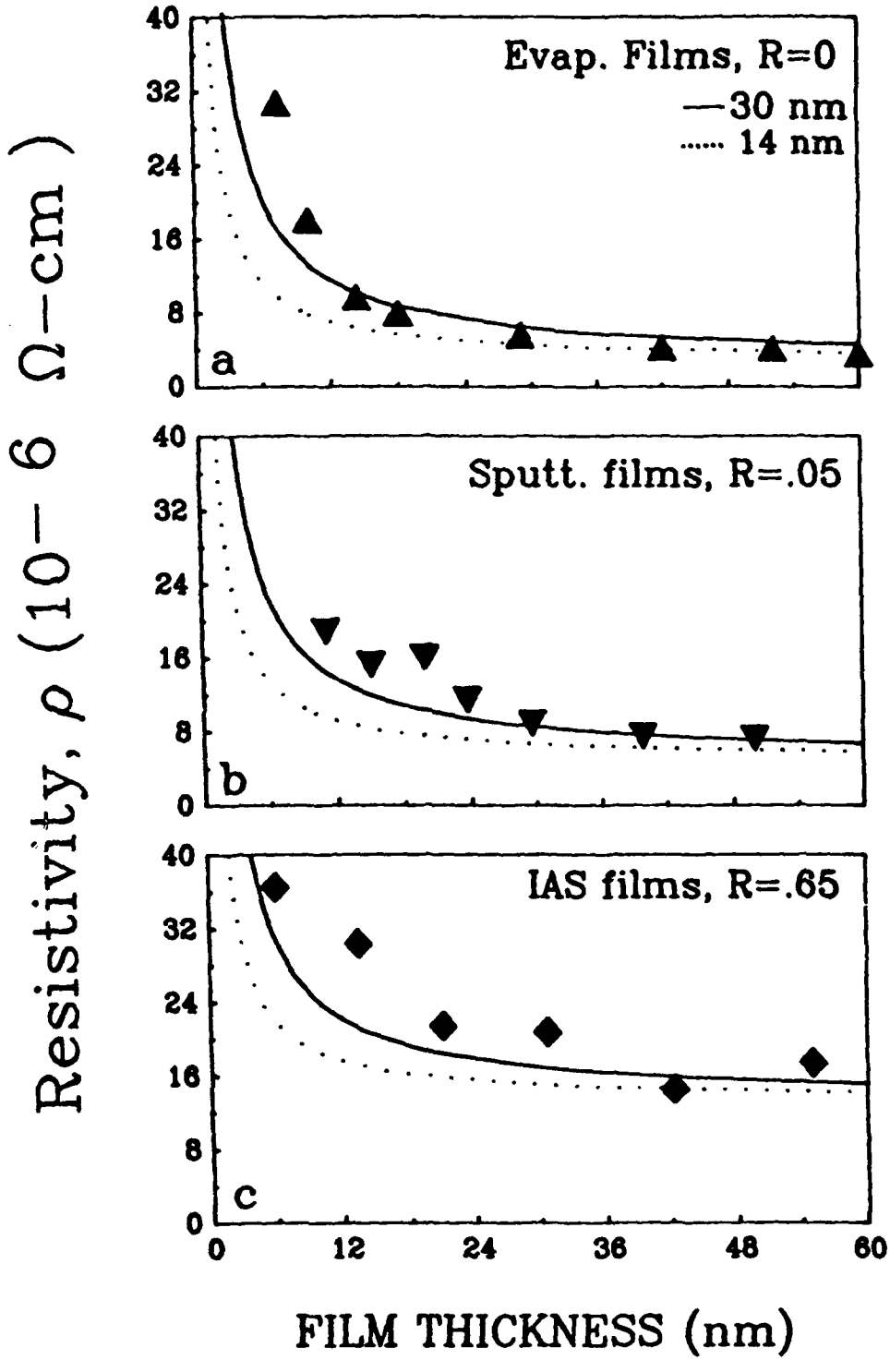
Evap. Films, R=0
—30 nm
····· 14 nm
a
Sputt. films, R=.05
b
IAS films, R=.65
c
40
32
24
16
8
0
0
12
24
36
48
60
Resistivity, ρ (10− 6 Ω−cm)
FILM THICKNESS (nm)

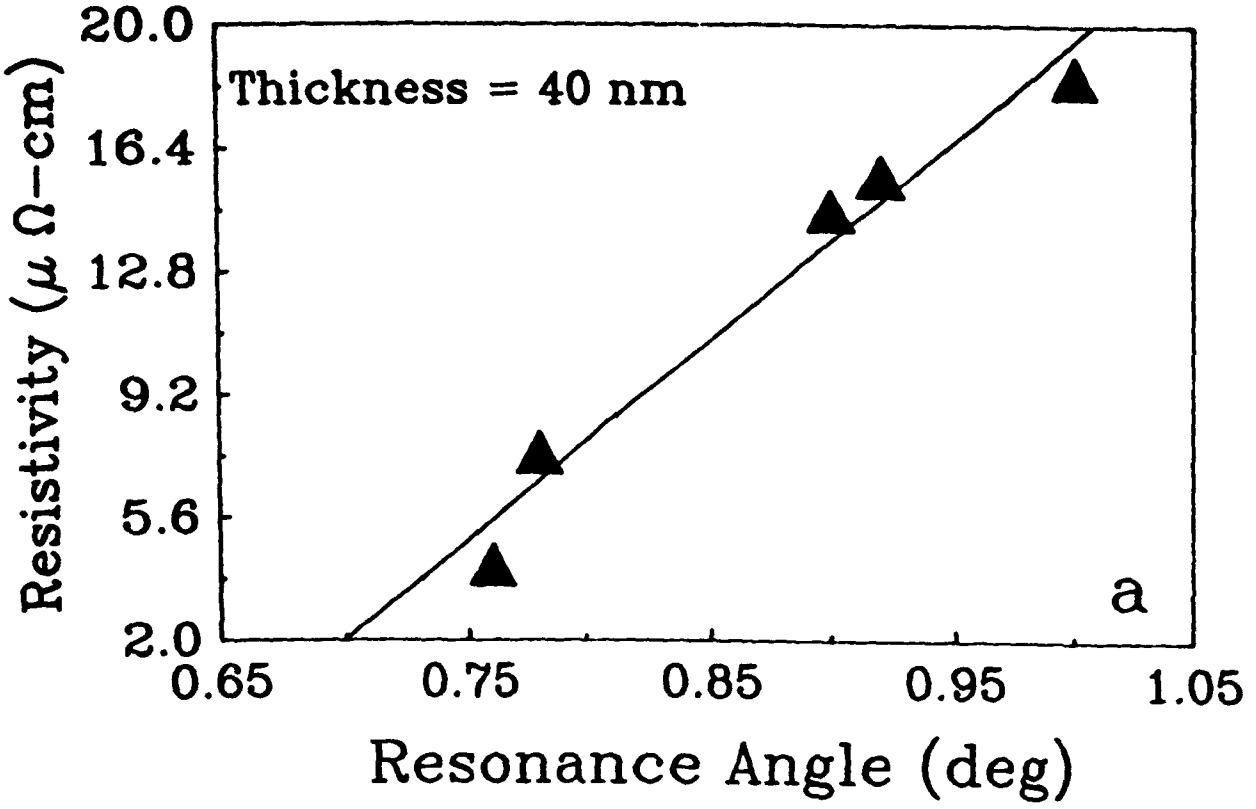
Thickness = 40 nm
Resistivity (μ Ω−cm)
20.0
16.4
12.8
9.2
5.6
2.0
0.65
0.75
0.85
0.95
1.05
Resonance Angle (deg)
a

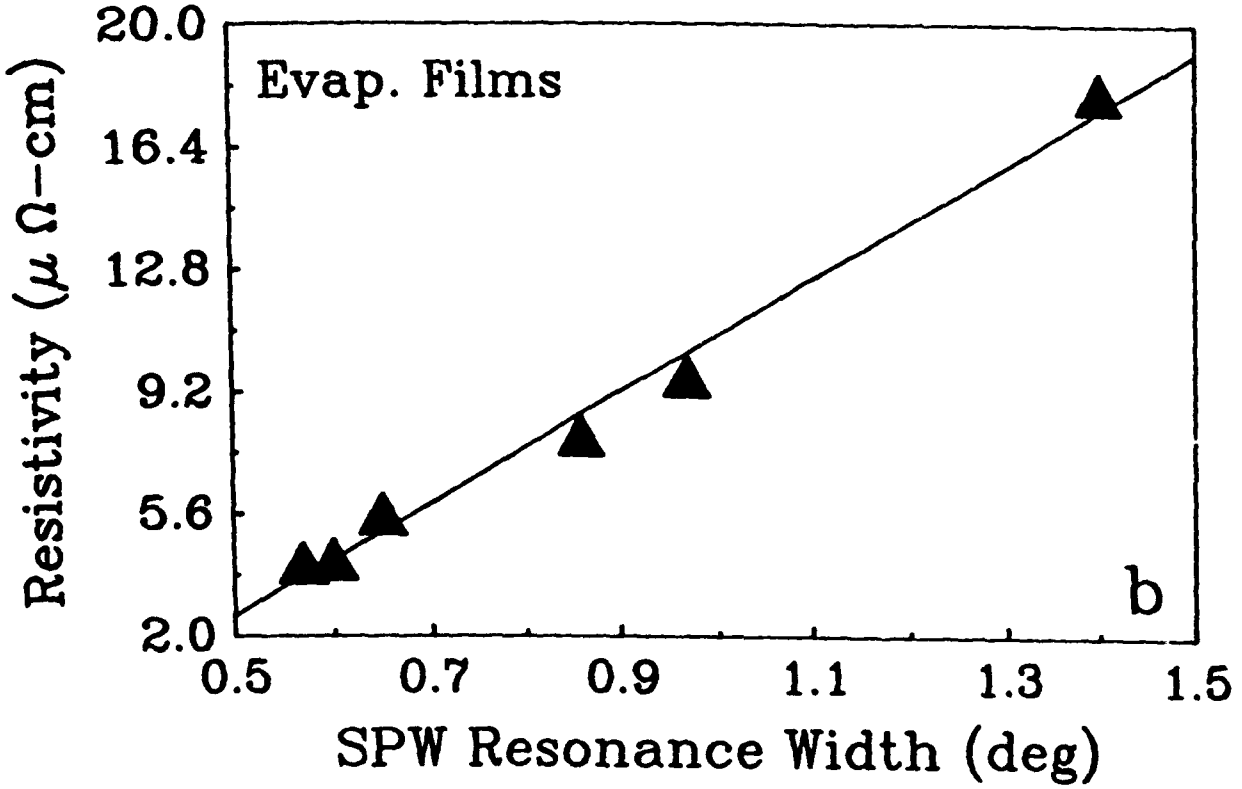
Evap. Films
Resistivity (μ Ω−cm)
20.0
16.4
12.8
9.2
5.6
2.0
0.5
0.7
0.9
1.1
1.3
1.5
SPW Resonance Width (deg)
b

Low Series Resistance High-Efficiency GaAs/AlGaAs Vertical-Cavity Surface-Emitting Lasers with Continuously Graded Mirrors Grown By MOCVD

P. Zhou, Julian Cheng, C. F. Schaus, S. Z. Sun, K. Zheng, E. Armour, C. Hains, Wei Hsin, D. R. Myers, and G. A. Vawter

Abstract—**GaAs/AlGaAs vertical-cavity top-surface-emitting lasers with a continuously graded mirror composition have been grown by MOCVD, and planar devices with proton-implant current confinement have been characterized. Continuous grading of the heterointerfaces in the Bragg reflectors eliminated the energy-band discontinuities, thus improving carrier transport and resulting in a substantial reduction in the series resistance and threshold voltage of the laser diodes. These VCSEL's have excellent room-temperature CW electrical characteristics, including some of the lowest series resistance, highest power efficiency, and lowest operating voltages ever reported.**

VERTICAL-CAVITY surface-emitting lasers (VCSEL's) are well suited for use in parallel, two-dimensional, optical switching [1], [2] and computing [2] architectures because of their surface-normal format, high power [3], low beam divergence [4], and good modal properties [5]. The room-temperature CW operation of top-surface-emitting VCSEL's with high output power has been demonstrated [3], although the series resistance and threshold voltage of these diodes remain high. A high series resistance increases the operating voltage and electrical power dissipation, which may limit the output optical power, the temperature range for CW operation, and the overall power efficiency. The last, representing the efficiency of converting electrical power into optical power, is particularly important in the design of high-density parallel arrays, in which high power dissipation exacerbates thermal management problems and limits the packing density of the array. The large series resistance arises from a combination of contact resistance, spreading resistance, and the impedance to carrier transport arising from the energy barriers at the heterointerfaces of the distributed Bragg reflectors (DBR mirrors). These factors also contribute to increased operating voltages. Contact resistance has been reduced by increasing the contact area and confining the current via proton implantation [3], or by the FSELD process [6] in which the current is injected laterally from large-area contacts. To reduce the series resistance arising from the energy-band discontinuities at the heterointerfaces, various grading techniques have been proposed for molecular-beam epitaxy (MBE), including the interposition of a supperlattice [7] or a piecewise-linear gradient with one or more $Al_xGa_{1-x}As$ layers of intermediate Al composition [7], [3] at each interface. These efforts have significantly reduced the series resistance from the range of kiloohms to several hundred ohms, but these values remain too high to achieve good electrical-to-optical power conversion efficiency. It is also highly desirable to reduce the operating voltages of the VCSEL to below 2.5 V to render them compatible with 5-V silicon driver integrated circuits. The superlattice grading of the heterointerface by MBE is particularly difficult to implement [7].

On the other hand, the continuous grading of an arbitrary composition profile can be readily achieved by metalorganic vapor-phase epitaxy (MOVPE or MOCVD). In this letter, we report the properties of high-quality VCSEL's with continuously graded DBR heterointerfaces grown by low-pressure MOCVD. Room-temperature CW operation of these VCSEL's was achieved, demonstrating high output power (2 mW), narrow spectral width (0.4 Å), low threshold current (2 mA) and voltage (2.5 V), high differential quantum efficiency (up to 80%), low series resistance (22 Ω), and high power efficiency (4.5%). We believe that the electrical characteristics are comparable to the best values reported to date [3], [10], [11].

The VCSEL epilayer structure (Fig. 1) consists of an undoped active region bounded by the p-doped and n-doped DBR mirror stacks, all of which were grown on a buffered (100) n-GaAs substrate. The upper p-doped DBR mirror contains 24 pairs of quarter-wave $Al_xGa_{1-x}As$ and AlAs layers. The Al content of the $Al_xGa_{1-x}As$ is 15%, except at the heterointerfaces, where it is linearly graded from 15 to 100% over a distance of 120 Å. The lower n-doped DBR mirror contains 43.5 pairs of quarter-wave $Al_xGa_{1-x}As$ and AlAs layers with similarly graded Al composition as in the p-mirror. The active layer contains a symmetrical, graded-index, separate-confinement heterostructure (GRINSCH) with four 80-Å quantum wells separated by 20-Å spacers. The

Manuscript received April 12, 1991; revised May 1, 1991. This work was supported in part by the Air Force Office of Scientific Research, the National Science Foundation, and the Defense Advanced Research Projects Agency.

P. Zhou, J. Cheng, C. F. Schaus, S. Z. Sun, K. Zheng, E. Armour, C. Hains, and W. Hsin are with the University of New Mexico, Center for High Technology Materials, Albuquerque, NM 87131.

D. R. Myers and G. A. Vawter are with the Sandia National Laboratories, Albuquerque, NM 87175.

IEEE Log Number 9101310.

1041-1135/91/0700-0591$01.00 ©1991 IEEE

total thickness of the GRINSCH-MQW structure corresponds to a single wavelength of the cavity mode, which is designed to lase at 846 nm. Room-temperature pulsed operation of VCSEL's with a GRINSCH active layer at room temperature has been reported previously [8].

The MOCVD growth was carried out at 725°C and 100 torr in a conventional horizontal reactor. The reactor details and general approach to the growth of VCSEL's have been given elsewhere [9]. Sources were trimethylgallium (TMGa), trimethylaluminum (TMAl), and 100% arsine in a hydrogen flow of 10 L/min. The growth rate and V/III ratio were 50 nm/min and 50, respectively. Linear grading was accomplished by simultaneous ramping of TMGa and TMAl flows in 0.1-s increments. Diethyltellerium (DETe 74 ppm in H_2) and carbon tetrachloride (CCl_4 400 ppm in H_2) were used for nominal doping levels of 3×10^{18} cm^{-3} in the mirror layers. The 60-Å GaAs p-contact layer was doped using diethylzinc (DeZn) to a level of 1×10^{20} cm^{-3}. A combination of photoluminescence and reflectance spectroscopy were used to calibrate the layer thicknesses.

The VCSEL device structure is a planar, top-surface-emitting, large-contact-area design similar to that described in [3]. Current confinement is achieved by the implantation of 310-keV protons at a dosage of $3 \times 10^{14}/cm^2$ around a masked active area whose diameter ranges from 5 to 40 μm. A post-implant anneal at 430°C for 30 s was carried out. Large-area Ti-Pt-Au p-contacts and Au-Ge-Ni-Au n-contacts were used.

Fig. 2 shows the room-temperature CW electrical (current–voltage) and optical (light–current) characteristics of representative VCSEL's with active area diameters of 8, 11, 20, and 35 μm. Their lasing thresholds occur at 2.2 mA (3.4 V), 2.7 mA (3.2 V), 6.0 mA (3.0 V), and 9.6 mA (2.1 V), corresponding to threshold current densities of 4.4, 2.8, 1.9, and 1.2 kA/cm^2. The series resistances are 75, 50, 30, and 22 Ω, (measured at a current of 20 mA) respectively, which are at least a factor of 3 lower than the values for comparably sized devices reported in [3]. Peak output optical power ranges from 0.5 mW for the 8-μm devices to 2.0 mW for the 35-μm devices, which are not solder bonded or optimally heat sunk. The differential quantum efficiency ranges from 50% for the 35-μm devices to 80% for the 8-μm devices. The lower efficiency of the larger size devices are largely due to a lower rate of stimulated emission resulting from the larger spatial intensity variations in a multimode optical field, which does not effectively utilize the more-or-less uniform carrier (gain) distribution in the active region.

The lower operating voltages and the very low series resistances of the VCSEL's indicate that the electrical characteristics have been substantially improved by the grading, and that thermal dissipation has been significantly reduced. However, the optical output is not yet optimal, due in large part to the misalignment of the cavity mode with the gain peak, and in part to the very large number of quarter-wave pairs in the DBR mirrors and to inadequate heat sinking. The thickness uniformity of wafers grown by MOCVD across a 2-in-diameter wafer is about 1–2%, which results in a ±15-nm variation in the position of the Fabry–Perot mode. No effort was

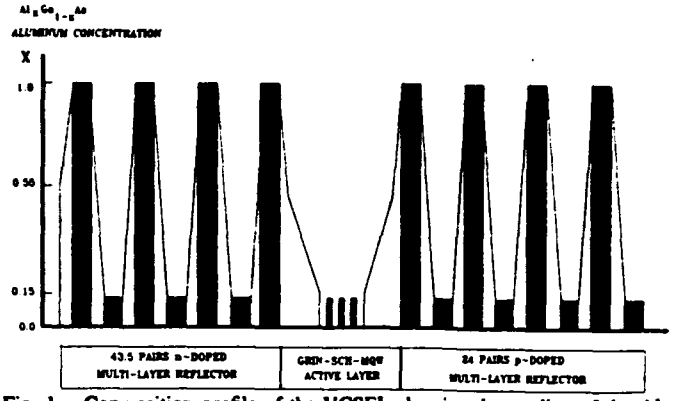

Fig. 1. Composition profile of the VCSEL showing the grading of the Al composition in the p-doped and n-doped DBR mirror layers, and in the GRINSCH active layer, which contains four GaAs quantum wells.

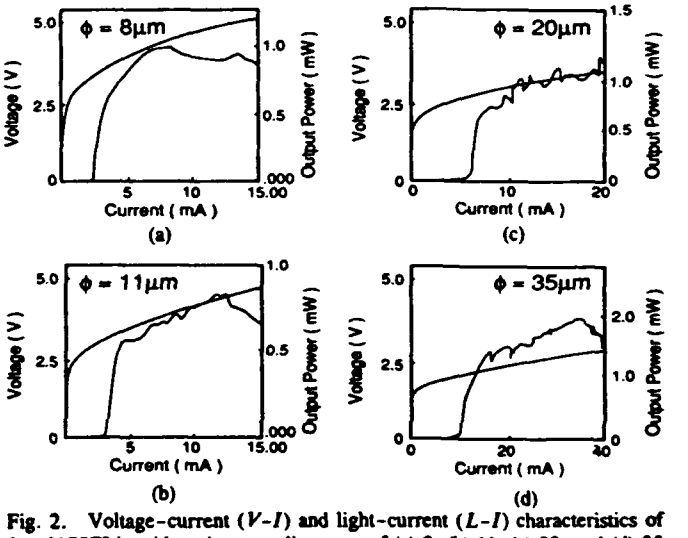

Fig. 2. Voltage–current (V–I) and light–current (L–I) characteristics of four VCSEL's with active area diameters of (a) 8, (b) 11, (c) 20, and (d) 35 μm.

made to select the portion of the wafer in which the mode position is best aligned to the gain peak. With improved alignment and better thermal management, higher optical power and thus improved power efficiencies (in excess of 10%) should be possible. Despite the nonoptimal optical alignment, the demonstration of a power efficiency of 4.5% (which is the highest value reported, to our knowledge) is indicative of the excellent electrical characteristics that have been achieved. Nearly all the VCSEL's showed good lasing characteristics, and the device parameters have good local uniformity. However, due to processing inhomogeneities, significant systematic variations in the device parameters occur across some parts of the wafer. To obtain a meaningful comparison of devices of different sizes, the average values of the threshold current density, series resistance, and threshold voltage for VCSEL's from the same part of a wafer, whose active areas range from 8 to 35 μm, are shown in Fig. 3. The data show the monotonic decrease of all three characteristics with increasing device diameter. The average threshold of 0.88 kA/cm^2 for the 35-μm devices is comparable to the best results for similar device structures [3]. The lowest threshold current density of 780 A/cm^2 was achieved by a 40-μm-diameter device. Lasing was observed up to a temperature of 82°C, with an output power of 0.2 mW.

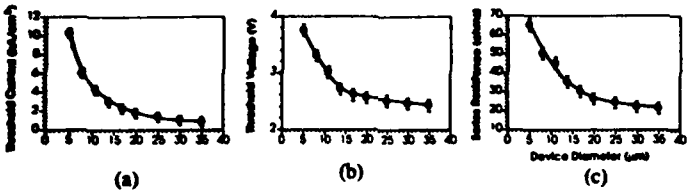

(a) (b) (c)

Fig. 3. Variations of the (a) threshold current density, (b) diode series resistance, and (c) threshold voltage of the VCSEL's as a function of active area diameter.

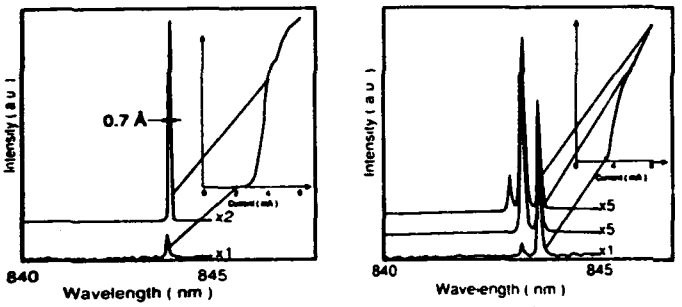

(a) (b)

Fig. 4. Pulsed light–current characteristics and the spectral properties of the light output at several values of drive current for a VCSEL whose active area diameter is (a) 11 μm and (b) 14 μm.

The series resistances and threshold voltages are, to our knowledge, the lowest values ever reported for vertically-injected, top-surface-emitting VCSEL's and can be directly attributed to the continuous grading of the heterointerfaces. Slightly higher resistances (than the 24 Ω for our 20-μm-diameter devices) were reported for bottom-surface-emitting VCSEL's (40 Ω for 20-μm squares [10]) and VCSEL arrays (28 Ω for 20-μm squares, pulsed [11]), in which a continuous top electrode was used to reduce the contribution from the spreading resistance. However, the threshold voltages (4–5 V [10], [11]), differential quantum efficiency (8% [11]) and the overall power efficiency (0.8% [10]) of these devices are not comparable to the values reported in this work (2.6 V, 60%, and 3%, respectively).

Fig. 4 shows the spectra for VCSEL's with active area diameters of 11 and 14 μm at different drive current levels. Also shown are their pulsed light–current characteristics (0.1% duty cycle) at room temperature. Well above threshold, the spectrum of the smaller device shows a single peak with a full width at half maximum (FWHM) of 0.7 Å. The best devices show an FWHM of less than 0.4 Å, which is resolution limited. Even below threshold, the spectrum is relatively narrow, which is indicative of the very high Q of the resonant cavity. For the larger device, the spectrum shows a dominant peak at threshold, although a vestige of a second mode is already apparent. As the drive current increases, a discontinuity in slope of the L–I characteristics can be observed, concomitant with the growth of a second dominant peak in the spectrum (shifted toward higher energies). This corresponds to the appearance of a higher order optical mode. At still higher drive currents, a third and even higher energy mode appears.

In conclusion, we have presented the room-temperature CW electrooptical characteristics of planar proton-implanted VCSEL's with continuously graded DBR heterointerfaces grown by MOCVD. These results represent the best VCSEL characteristics that have been reported for MOCVD-grown materials, with excellent threshold current density, differential quantum efficiency, and spectral characteristics. With respect to series resistance, operating voltages, and overall power efficiency, these results represent, to our knowledge, the best data reported for a top-surface-emitting VCSEL, and compare very favorably with bottom-surface-emitting VCSEL's. This can be attributed to the effectiveness of MOCVD in grading the heterointerfaces and thus minimizes the series resistance contribution from the energy-band discontinuities. Further improvement in optical output power and higher power efficiencies can be achieved by optimization of the DBR mirror characteristics, improved heat sinking, and optimized processing conditions.

Acknowledgment

The authors would like to acknowledge the assistance of Dr. B. Tell of AT&T Bell Laboratories and helpful discussions with Dr. G. R. Olbright and Dr. R. P. Bryan of Sandia National Laboratories.

References

[1] G. R. Olbright, R. P. Bryan, K. Lear, T. M. Brennan, G. Poirier, Y. H. Lee, and J. L. Jewell, "Cascadable laser logic devices: Discrete integration of phototransistors with surface-emitting laser diodes," *Electron. Lett.*, vol. 27, no. 3, p. 216, 1991.

[2] J. Cheng, G. R. Olbright, and R. P. Bryan, "Binary arithmetic using optical symbolic substitution and cascadable surface-emitting laser logic devices," in *Tech. Dig. Optical Comput.*, vol. 6, 1991, p. 10; also to be published in *Appl. Opt.*, July 1991.

[3] B. Tell, Y. H. Lee, K. F. Brown-Goebeler, J. L. Jewell, R. E. Leibenguth, M. T. Asom, G. Livescu, L. Luther, and V. D. Mattera, "High-power CW vertical-cavity top surface-emitting GaAs quantum well lasers," *Appl. Phys. Lett.*, vol. 57, p. 1855, 1990.

[4] K. Tai, G. Hasnain, J. D. Wynn, R. J. Fischer, Y. H. Wang, B. Weir, J. Gamelin, and A. Y. Cho, "90% coupling of top surface emitting GaAs/AlGaAs quantum well laser output into 8 μm diameter core silica fibre," *Electron. Lett.*, vol. 26, no. 19, p. 1628, 1990.

[5] C. J. Chang-Hasnain, M. Orenstein, A. von Lehmen, L. T. Florez, J. P. Harbison, and N. G. Stoffel, "Transverse mode characteristics of vertical-cavity surface-emitting lasers," *Appl. Phys. Lett.*, vol. 57, p. 218, 1990.

[6] H.-J. Yoo, J. R. Hayes, N. Andreadakis, E. G. Paek, G. K. Chang, J. P. Harbison, L. T. Florez, and Y.-S. Kwon, "Low series resistance vertical-cavity front-surface-emitting laser diode," *Appl. Phys. Lett.*, vol. 56, no. 20, p. 1942, 1990.

[7] K. Tai, L. Yang, Y. H. Wang, J. D. Wynn, and A. Y. Cho, "Drastic reduction of series resistance in doped semiconductor distributed Bragg reflectors for surface-emitting lasers," *Appl. Phys. Lett.*, vol. 56, p. 2496, 1990.

[8] Y. H. Wang, K. Tai, J. D. Wynn, M. Hong, R. J. Fischer, J. P. Mannaerts, and A. Y. Cho, "GaAs/AlGaAs multiple quantum well GRIN-SCH vertical cavity surface emitting laser diodes," *IEEE Photon. Technol. Lett.*, vol. 2, no. 7, p. 456, 1990.

[9] H. E. Schaus, C. F. Schaus, S. Sun, M. Y. A. Raja, A. Jacome-Torres, and J. G. McInerney, in *Inst. Phys. Conf. Ser. no. 106, Gallium Arsenide and Related Compounds*, 1989, p. 749.

[10] C. J. Chang-Hasnain, C. E. Zah, G. Hasnain, J. P. Harbison, L. T. Florez, N. G. Stoffel, and T. P. Lee, "Effect of operating electric power on the dynamic behavior of quantum well vertical-cavity surface-emitting lasers," *Appl. Phys. Lett.*, vol. 58, p. 1247, 1991.

[11] M. Orenstein, A. C. Von Lehmen, C. Chang-Hasnain, N. G. Stoffel, J. P. Harbison, and L. T. Florez, "Matrix-addressable vertical-cavity surface-emitting laser array," *Electron. Lett.*, vol. 27, p. 438, 1991.

Cascadable, Latching Photonic Switch with High Optical Gain by the Monolithic Integration of a Vertical-Cavity Surface-Emitting Laser and a pn-pn Photothyristor

Ping Zhou, Julian Cheng, C. F. Schaus, S. Z. Sun, C. Hains, K. Zheng, E. Armour, W. Hsin, D. R. Myers, and G. A. Vawter

Abstract—**We report the first demonstration of a cascadable photonic switch based on the monolithic integration of a multiquantum-well vertical-cavity surface-emitting laser (VCSEL) and a latching pn-pn photothyristor grown by LP-MOCVD. The VCSEL and pn-pn photothyristor structures can be independently optimized for optical switching, logic and memory functions. Optical switching with high gain (30 000), high contrast (30 dB), low switching power (11 nW), and latching memory have been demonstrated.**

VERTICAL-CAVITY surface-emitting lasers (VCSEL's) are well-suited for use in parallel, two-dimensional, optical switching and computing [1], [2] architectures because of their surface-normal format, parallel optical access, high output power, low beam divergence, and good modal properties. Optical switches based on the integration of heterojunction phototransistors (HPT's) or photothyristors (pn-pn devices) with a VCSEL provide optical gain, switching, control, and logic without an electronic intermediary. By varying the degree of positive optical or electrical feedback between the VCSEL and HPT, these structures can function alternatively as an optical amplifier, an optical switch, or a bistable logic or memory device.

Surface-normal optical switches based on the monolithic integration of a HPT with an LED, [3]–[5] or an edge-emitting AlGaAs/GaAs laser [6] have been extensively studied. The former, sometimes called the VSTEP (vertical-to-surface transmission electrophotonic switch) [5], has been integrated into large (32 × 32), monolithic, optically addressable arrays [7]. However, LED-based switches are power-inefficient devices with low optical gain and serious optical crosstalk problems, while edge-emitting laser-based photothyristors are incompatible with two-dimensional array architectures. The advent of VCSEL's presents a solution to these problems and opens new vistas for compact two-dimensional laser-based switching arrays, provided that their thermal dissipation can be made tractable. Recent improvements in VCSEL characteristics, including lower series resistance, threshold voltage, current density, and higher quantum and power efficiencies [8], have significantly enhanced the propects for VCSEL-based switching arrays.

Boolean optical logic functions [1] and binary arithmetic operations [2] have been demonstrated by the use of optical switches and logic gates based on GaAlAs/GaAs VCSEL's and HPT's. These thresholding VCSEL/HPT optical switches have high optical gain (20) and contrast (32 dB), but do not exhibit bistable or latching characteristics in the absence of positive optical feedback, which requires that the HPT and VCSEL be vertically aligned. VCSEL-based optical switches have also been demonstrated by the monolithic integration of an InGaAs VCSEL with a GaAlAs/GaAs HPT [9] or an embedded pn-pn structure [10]. In these designs, a strained InGaAs quantum-well active layer facilitates through-substrate optical transmission without vias. However, cascading is not possible in the former [9] since the GaAs HPT is transparent to the InGaAs VCSEL emission, and although latching has been observed, the mechanism is not understood. The latter [10] attempts to circumvent this problem by embedding a pn-pn structure within the VCSEL cavity, using the same InGaAs quantum-well layers for both light emission and absorption. Here, latching operation is likely to be a result of positive electrical feedback. But since the same InGaAs quantum wells serve as the active layer of the laser as well as the absorber of the HPT, the detector responsivity is reduced, while poor spectral overlap between the source and detector on different devices makes precise wavelength control imperative for cascaded operation.

In this letter we demonstrate a new monolithic switch design that circumvents many of these problems by integrating a GaAs VCSEL with a self-contained GaAs photothyristor. Here, a stand-alone pn-pn structure (a VSTEP) provides

Manuscript received June 28, 1991; revised August 27, 1991. University of New Mexico work was supported by the Air Force Office of Scientific Research under Contract AFOSR-91-0345 DEF and by DARPA; Sandia National Laboratory work was supported by the Department of Energy under Contract DEAC04DP00789.

P. Zhou, J. Cheng, C. F. Schaus, S. Z. Sun, C. Hains, K. Zheng, E. Armour, and W. Hsin are with the Center for High Technology Materials, University of New Mexico, Albuquerque, NM 87131.

D. R. Meyers and G. A. Vawter are with Sandia National Laboratories, Albuquerque, NM 87185.

IEEE Log Number 9103693.

1041-1135/91$01.00 ©1991 IEEE

its own positive feedback and latching characteristics, while the VCSEL serves as an active load. This eliminates the reliance on the VCSEL for positive optical feedback, which is impractical since optical logic functions often require multiple inputs that are spatially separated, while there is only a single VCSEL output. It also permits the independent optimization of the photothyristor and VCSEL parameters without compromising them for compatibility. Cascadability is also preserved by the use of a GaAs active layer. We describe below the design, fabrication, and operating characteristics of the first monolithic, cascadable, latchable, VCSEL-based optical switch, with very high optical gain (30 000) and contrast (30 dB), and low switching power (11 nW).

The operating principles of a latching pn-pn/VCSEL optical switch can be understood from the electrical characteristics of a two-terminal photothyristor in series with a VCSEL. The principles of a pn-pn thyristor are explained by the conventional two-transistor model with positive electrical feedback [11]. In the case of a photothyristor, which is comprised of a photosensitive npn-HPT and a single-heterostructure LED, radiative recombination in the latter can also provide positive optical feedback. The combination of optical and electrical feedback produces the familiar bistable electrical characteristic, with a negative differential resistance region separating the conductive (ON) and resistive (OFF) states. While their relative contributions have not been determined, experimental evidence has shown that switching did not occur in the absence of efficient electroluminescence from the LED. Optical switching is implemented by noting that the voltage V_s, at which switching occurs from the OFF-state to the ON-state, is reduced by the input optical power, i.e., by the optically injected virtual base current, which plays the role of the gate current in a silicon-controlled rectifier (SCR). By biasing the pn-pn structure at a voltage below V_s in the dark, thus keeping it in the OFF-state, and applying an optical pulse to reduce V_s below the bias voltage, switching to the ON-state can be optically effected. In principle, the optical switching energy is somewhat arbitrary since it depends on the desired reduction of V_s. In practice, this must be tempered by considerations of the desired input optical signal dynamic range. The switched photothyristor current in the conducting state powers the VCSEL above threshold. The latter stays on (without optical bias) as long the bias voltage exceeds that required to bias the VCSEL above lasing threshold.

The device structure (Fig. 1), which consists of a photothyristor vertically integrated with a VCSEL, is grown by low-pressure metalorganic vapor phase epitaxy (LP-MOCVD). The VCSEL active layer contains four 8 nm thick GaAs quantum wells separated by 2 nm thick $Al_{0.15}Ga_{0.85}As$ spacers layers, embedded between two multilayer distributed Bragg reflector (DBR) stacks containing 43.5 and 24 pairs of quarterwave AlAs and $Al_{0.15}Ga_{0.85}As$ layers, respectively. The heterointerfaces in the DBR mirrors are continuously graded to improve the electrical characteristics of the VCSEL [8]. The photothyristor structure is epitaxially regrown on the VCSEL by MOCVD, although the entire structure can be grown in a single step. The pn-pn epilayers contain a 100 nm undoped AlAs stop-etch layer, a 1.5 μm undoped GaAs isolation layer, a 1 μm n^+-GaAs contact layer ($5 \times 10^{18}/cm^3$ Te), a 25 nm $Al_x \times Ga_{1-x}As$ layer (graded from $x = 0$ to $x = 0.3$), a 300 nm n-$Al_{0.3}Ga_{0.7}As$ emitter layer ($5 \times 10^{17}/cm^3$ Te), a 25 nm $Al_xGa_{1-x}As$ layer (graded from $x = 0.3$ to $x = 0$), a 100 nm p^+-GaAs base layer ($5 \times 10^{18}/cm^3$ C), a 300 nm n-GaAs collector layer ($1 \times 10^{17}/cm^3$ Te), a 600 nm n^+-GaAs subcollector layer ($1 \times 10^{18}/cm^3$ Te), a 500 nm $Al_{0.3}Ga_{0.7}As$ cladding layer ($5 \times 10^{18}/cm^3$ C), and a 100 nm p^+-GaAs contact layer ($1 \times 10^{19}/cm^3$ C). The reverse-biased n^+-i-p^+ junction formed by the thick i-GaAs isolation layer between the pn-pn and VCSEL structures isolates the two devices electrically.

The pn-pn and VCSEL device structures are horizontally integrated with a metallic interconnection between the n-contact of the photothyristor and the p-contact of the VCSEL. The device fabrication starts with two chemical mesa-etches ($1\ NH_4OH : 1\ H_2O_2 : 40\ H_2O$) that define the photothyristor (150×100 μm) and n-contact areas, respectively. An 18 μm diameter active area is next photolithographically defined and is isolated by proton-implantation [8]. The p-contact (Ti/Pt/Au) and n-contacts (Au-Ge/Ni/Au) are patterned photolithographically. Finally, the devices are isolated with a mesa etch that cuts through the active layer of the VCSEL.

Fig. 2(a) shows the room-temperature, CW, current-voltage-light characteristics of the integrated switch and the light-current characteristic of the VCSEL. The optical input from a 830 nm laser source is coupled to the pnpn device via a multimode optical fiber. The *I-V* data show the desired negative differential resistance characteristic, with bistable branches above 2.6 V. The lasing threshold is 2.8 mA and the output power (0.35 mW) is limited by self-heating due to a high-series resistance resulting from processing problems. The magnified low-current bistable region is shown in Fig. 2(b), which illustrates the reduction of V_s by input light. The voltage barrier between the ON and OFF states can be eliminated by an input power of less than 30 nW.

Fig. 3(a) shows the scanned dc optical transfer characteristic of the device under a 4.2 V bias, which shows the abrupt onset of switching at an input power level of 15 nW, and a switched VCSEL output power of 0.35 mW, which represents an optical gain of 23 000. The switched output achieves a peak power level of 1.3 mW, which is reduced to 0.35 mW by excessive self-heating as the input power continues its upward scan. The power remains latched at the 0.35 mW level when the input power is scanned downward past the switching threshold towards zero, provided that the device is biased above the threshold voltage for lasing. The optical contrast, defined as the ratio of the switched output power level to the spontaneous emission level below threshold, is about 30 dB. Fig. 3(b) shows the time-domain response of the switch to a transient dc optical signal, which again illustrates latching of the switched optical output without any input optical bias. The inset shows its time response to a single 15 μs optical pulse, which shows that the switched VCSEL output remains turned on until the electrical bias is removed. The switching speed (about 5 μs) is currently limited by the large area of the photothyristor. These switches are cascadable since the emission of the GaAs VCSEL (847

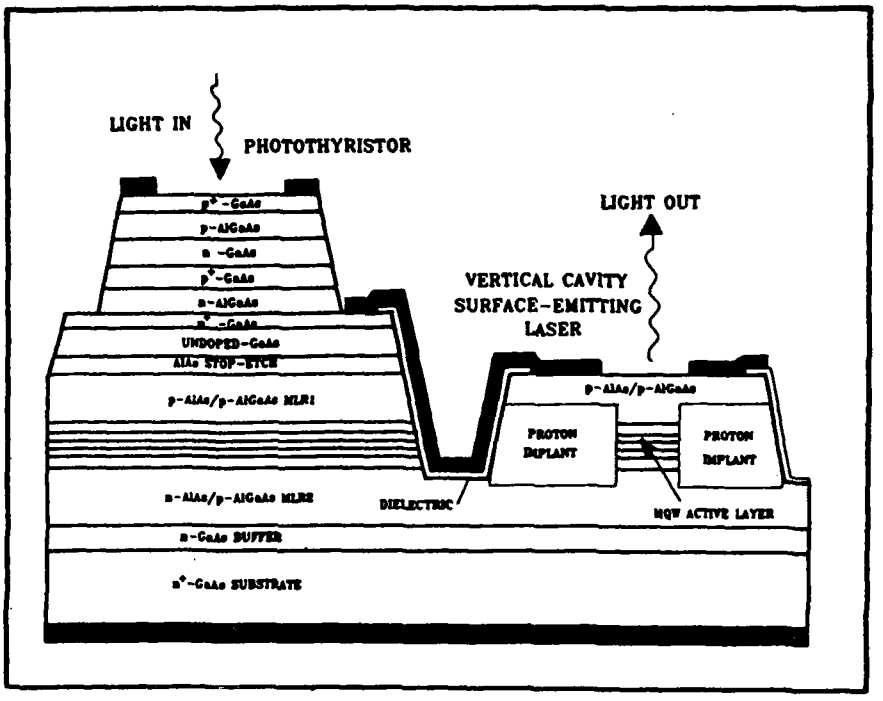

Fig. 1. Epilayer structure for a monolithic integrated VCSEL/photothyristor latching optical switch, with a pn-pn structure regrown on a VCSEL structure by LP-MOCVD.

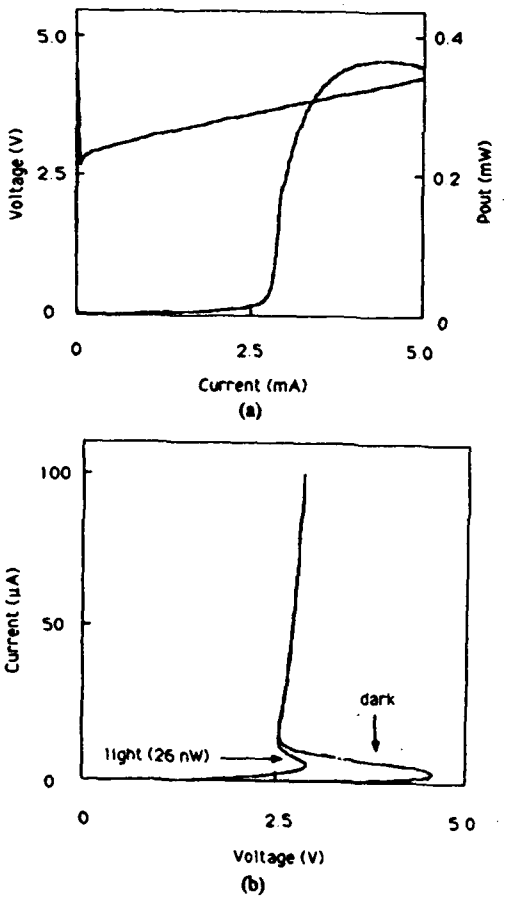

Fig. 2. (a) Light-current characteristic of the VCSEL and current-voltage characteristic of an integrated VCSEL/photothyristor switch. (b)Magnification of (a) at low current levels showing the reduction of switching voltage with illumination.

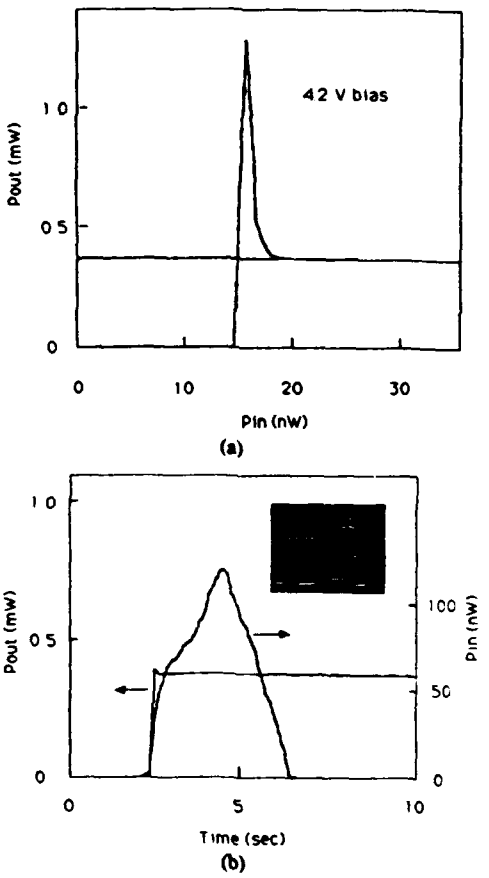

Fig. 3. (a) The scanned dc optical transfer characteristic and (b) the temporal response of the switch to a transient dc signal and to a 15 μs input optical pulse (inset) showing optical threshold switching and latching behavior.

nm) is readily absorbed by the GaAs collector-base layers of the HPT. We have confirmed this by achieving latchable switching using a GaAs VCSEL source over a wide range of input optical power up to a milliwatt.

The switching energy is a function of the desired level of reduction in V_s, which therefore decreases with increasing V_s. This is shown in Fig. 4, which plots the switching power and output power as a function of bias voltage. A threshold can be seen at 3.7 V, which is the bias voltage at which the switched photothyristor current becomes sufficient to drive the VCSEL well above threshold. Above 3.7 V, the output laser power increases with bias voltage (current) while the switching power is reduced since less optical power is needed to effect a smaller reduction in V_s. Thus, a switching threshold as low as 11 nW, corresponding to an optical gain of 30 000, has been achieved.

In summary, we have demonstrated the operation of a monolithic latching optical switch based on the integration of a photothyristor with a VCSEL. Latching optical switching characteristics have been demonstrated, along with high optical gain (30 000) and high optical contrast (30 dB). The integrated pn-pn/VCSEL switch represents not only a volatile optical memory, but can also be used to implement a new class of optical logic gates with latching logical outputs.

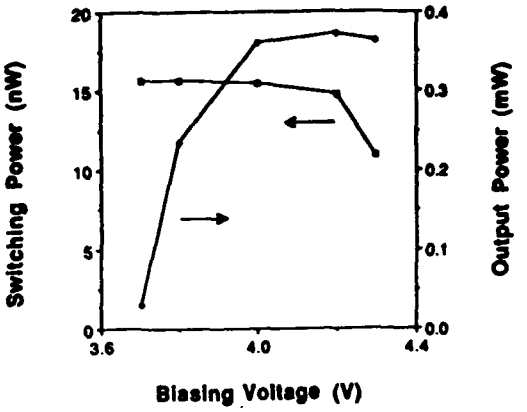

Fig. 4. Input switching power and switched output power of the integrated optical switch as a function of bias voltage.

ACKNOWLEDGMENT

We acknowledge the technical assistance of Dr. C.-K. Wu and A. Torres.

REFERENCES

[1] R. P. Bryan, G. R. Olbright, and J. Cheng, "Cascadable surface-emitting laser logic: Demonstration of Boolean logic," *Electron. Lett.*, vol. 27, no. 11, pp. 893-894, May 23, 1991.

[2] J. Cheng, G. R. Olbright, and R. P. Bryan, "Binary arithmetic using optical symbolic substitution and cascadable surface-emitting laser logic devices," in *Proc. OSA Top. Meet. Opt. Computing*, vol. 6, Mar. 1991, pp. 10-13.

[3] A. Sasaki, K. Matsuda, Y. Kimura, and S. Fujita, "High-current InGaAsP-InP phototransistors and some monolithic optical devices," *IEEE Trans. Electron Devices*, vol. ED-29, pp. 1382-1388, Sept. 1982.

[4] J. C. Campbell, A. G. Dentai, C. A. Burrus, Jr., and J. F. Ferguson, "InP/InGaAs heterojunction phototransistors," *IEEE J. Quantum Electron.*, vol. QE-17, pp. 264-269, Feb. 1981.

[5] I. Ogura, Y. Tashiro, S. Kawai, K. Yamada, M. Sugimoto, K. Kubota, and K. Kasahara, "Reconfigurable optical interconnection using a two-dimensional vertical to surface transmission electrophotonic device array," *Appl. Phys. Lett.*, vol. 57, pp. 540-542, 1990.

[6] C. F. Schaus, J. R. Shealy, F. E. Najjar, and L. F. Eastman, "Integrated laser/phototransistor optoelectronic switching device by organometallic vapor phase epitaxy," *Electron. Lett.*, vol. 22, pp. 454-456, 1986.

[7] K. Matsuda, K. Takimoto, D.-H. Lee, and J. Shibata, "Integration of 1024 InGaAsP/InP optoelectronic bistable switches," *IEEE Trans. Electron Devices*, vol. 37, pp. 1630-1634, 1990.

[8] P. Zhou, J. Cheng, C. F. Schaus, S. Z. Sun, K. Cheng, E. Armour, W. Hsin, D. R. Myers, and G. A. Vawter, "Low series resistance high efficiency vertical-cavity surface-emitting lasers with continuously graded mirrors grown by MOCVD," *IEEE Photon. Technol. Lett.*, vol. 3, pp. 591-593, July 1991.

[9] W. K. Chan, J. P. Harbison, A. C. von Lehmen, L. T. Florez, C. K. Nguyen, and S. A. Schwarz, "Optically controlled surface-emitting lasers," *Appl. Phys. Lett.*, vol. 58, pp. 2342-2344, May 1991.

[10] T. Numai, M. Sugimoto, I. Ogura, H. Kosaka, and K. Kasahara, "Surface-emitting laser operation in vertical-to-surface transmission electrophotonic devices with a vertical cavity," *Appl. Phys. Lett.*, vol. 58, pp. 1250-1252, 1991.

[11] S. M. Sze, *Physics of Semiconductor Devices*. New York: Wiley, 1981, p. 200.

APPENDIX B: PRESENTATIONS

An inclusive presentation list from the initiation of this grant (2/1/89) is included. Presentations originating within this incremental reporting period are highlighted in bold, and abstracts are included where available.

E. A. Armour, S. Z. Sun, K. Zheng, D. P. Kopchik and C. F. Schaus, "MOCVD Regrowth of AlGaAs on AlGaAs," post-deadline paper presented at Advanced Processing and Characterization Technologies (APCT'91), Clearwater Beach, FL, (1991).

L.J. Baca, J.G. McInerney, and D.E. Mathews, "Design of a Broadband High-Frequency Antenna on Gallium Arsenide Using the Effective Index Method," Electron. Lett., Vol. 26, pp. 1083-1085, July 1990.

L. Baca, J.G. McInerney and D.E. Mathews, *Integrable Broadband Atennas on GaAs*, Proc. ISE'89, Albuquerque, NM, May 1989.

S.R.J. Brueck, M.Y.A. Raja, M. Osinski, C.F. Schaus, M. Mahbobzadeh, J.G. McInerney, and K.J. Dahlhauser, *Optical Cavity Design for Wavelength-Resonant Surface-Emitting Semiconductor Lasers*, SPIE Proc. 1043, 175, 1989.

R.P. Bryan, G.R. Olbright, and J. Cheng, "AND, OR, and XOR Digital Optical Logic: Binary Addition Using Optical Symbolic Substitution," 1991 Conference on Lasers and Electrooptics; May 1991, Paper CMB1.

E.A. Callan and J. G. McInerney, "Sensitive Doppler Velocimetry and Anemometry Using Semiconductor Lasers," submitted to CLEO '92.

C.-P. Cherng, J.G. McInerney, and M. Osinski, "Stable Single-Lobed Emission from a Semiconductor Laser Array by Spatial Filtering in an External Cavity," CLEO '90 Conference on Lasers and Electrooptics, Anaheim, CA, May 21-25, 1990, Technical Digest Series 1990 Vol. 7, OSA 1990, Paper CThII3, pp. 388-390

C-P. Cherng, T. C. Salvi, M. Osinski, and J. G. McInerney, "Lateral Wavefront Measurements of High-Power Semiconductor Lasers Using a Three-Mirror Cyclic Interferometer," SPIE Proceedings, Vol. 1319, 15th Congress of the International Commission for Optics, Optics in Complex Systems (F. Lanzl, H.-J. Preuss, G. Weigelt, Eds.) Garmisch-Partenkirchen, Germany, August 5-10, 1990, pp. 40-41

C.-P. Cherng and M. Osinski, "Observation of Low-Order Lateral Modes in Broad-Area Diode Lasers," Technical Digest, OSA 1990 Annual Meeting, Boston, MA, November 4-9, 1990, Technical Digest Series 1990, Vol. 15, Paper MK9, pp. 15-16

C.-P. Cherng and M. Osinski, "Improved Coupled-Mode Analysis of Diffraction-Coupled Diode Laser Arrays," IEEE LEOS 1990 Annual Meeting, Boston, MA, Nov. 4-9, 1990, Paper SDL3.6, LEOS '90 Conference Digest, p. 21, and LEOS '90 Conference Proceedings, pp. 426-427

C.P. Cherng, M. Osinski and J.G. McInerney, *Diffraction-limited, Single-lobed Emission from Carrier-guided Diode Laser Array in an External Cavity with Spatial Filter*, Published in Proc. IEEE-LEOS Ann. Meet. (LEOS'89, Orlando, FL, Oct. 1989), paper OE4.2., pp. 78-79.

C.P. Cherng, T.C. Salvi, M. Osinski and J.G. McInerney, *Phase Front Reconstruction of Diode Laser Arrays Using a Ring Interferometer*, Published in Proc. 1989 Ann. Meet. Opt. Soc. of Am. (OSA'89, Orlando, FL), paper MAA2, p. 50.

K-H. Chung, J.G. McInerney and M. Osinksi, *Spectral Properties of Short External Cavity Semiconductor Lasers*, Proc. Int. Conf. on Lasers and Electro-Optics (CLEO '89), OSA, Washington, DC, April 1989, Paper ThK27.

V.L. Farley-Leadbetter, J.G. McInerney, S. Mancha, G.C. Dente and D. Gallant, *Stability Properties of Semiconductor Lasers under Current Modulation*, Proc. ISE'89, Albuquerque, NM, May 1989.

V.L. Farley-Leadbetter, J.G. McInerney, S. Mancha, G.C. Dente and D. Gallant, *Nonlinear Dynamics of Semiconductor Injection Lasers Under Large-signal Modulation*, Published in Proc. 1989 Ann. Meet. OSA (OSA'89, Orlando, FL Oct. 1989), paper WL48.

J.A. Hutchinson, D.P. Caffey, C.F. Schaus, and C.W. Trussel, "Diode Pumped Eyesafe Erbium Glass Laser," Conference on Lasers and Electro-Optics Post Deadline Papers, CLEO'90, paper CPDP19-1, May, 1990

D.S. Lee and K. Malloy, "Reduced Absorption in Semiconductor Quantum Wells through Coherently-derived Quantum Interference," submitted to OSA 92.

H. Li, J. Ye, and J.G. McInerney, "Chaos in Semiconductor Lasers," submitted to NDOS '92.

H. Li, Y. Ye, A. Bahm, and J.G. McInerney, "Influence of Noise on Deterministic Chaos in a Coherence-collapsed Semiconductor Laser," OPCON, San Jose, CA, Nov. 1991.

Y. Li, T.C. Salvi and J.G. McInerney, *Lateral Mode Bistability Due to Nonlinear Guiding in Active Semiconductor Waveguides*, Published in Proc. IEEE-LEOS 1989 Ann. Meet. (LEOS'89, Orlando, FL, Oct. 1989), paper OE13.6.

J.-M. Luo and M. Osinski, "Multimode Stability Analysis of Side-Mode Injection-Locked Semiconductor Lasers," Optics '89 OSA Annual Meeting, Orlando, Florida, October 15-20, 1989, Technical Digest Series Vol. 18, Optical Society of America 1989, Paper TuP5, p. 87.

J.-M. Luo and M. Osinski, "Simulation of Field-Noise Spectra in Injection-Locked Semiconductor Lasers," QELS'91 Conference on Quantum Electronics Laser Science, Baltimore, Maryland, May 12-17, 1991, 1991 Technical Digest Series Vol. 11, Optical Society of America 1991, Paper QWD29, pp. 150-151.

J.-M. Luo and M. Osinski, "Simulation of Frequency Noise Spectra in Injection Locked Semiconductor Lasers," IQEC'90 XVII International Quantum Electronics Conference, Anaheim, California, May 21-25, 1990, Technical Digest Series 1990 Vol. 8, Optical Society of America 1990, Paper QThI25, pp. 248-249.

J.-M. Luo and M. Osinski, "Enhanced Stable-Locking Range in Side-Mode Injection Locked Semiconductor Lasers," Technical Digest, OSA 1990 Annual Meeting, Boston, Massachusetts, November 4-9, 1990, Technical Digest Series 1990 Vol. 15, Paper TuA3, p. 61.

M. Mahbobzadeh, E. Gandjbakhch, E. A. Armour, K. Zheng, S.-Z. Sun, C. F. Schaus, and M. Osinski, "Distributed-Feedback GaAs/AlGaAs/AlAs Vertical-Cavity Surface-Emitting Laser with Resonant-Periodic-Gain Active Region," Technical Digest, 3rd Annual Symposium on Ceramics and Advanced Materials, Albuquerque, New Mexico, October 24-25, 1991, pp. 17-18.

M. Mahbobzadeh and M. Osinski, "High-Power-Density Pulsed Operation of Distributed-Feedback Vertical-Cavity Surface-Emitting Laser with Resonant-Periodic-Gain Active Region," accepted for QELS '92 Conference on Quantum Electronics and Laser Science, Anaheim, California, May 10-15, 1992.

M. Mahbobzadeh, M.Y.A. Raja, J.G. McInerney, C.F. Schaus and S.R.J. Brueck, *Mode Stability of Resonant Periodic Gain Surface-emitting Semiconductor Lasers*, Proc. SPIE, Vol. 1219, pp. 264-276, Jan. 1990.

M. Mahbobzadeh and M. Osinski, "Novel Distributed-Feedback Surface-Emitting Laser Design," Technical Digest, OSA 1990 Annual Meeting, Boston, Massachusetts, November 4-9, 1990, Technical Digest Series 1990 Vol. 15, Paper FJ3, p. 240; and LEOS '90 Conference Proceedings, IEEE LEOS 1990 Annual Meeting, Paper OE13.3/FJ3, pp. 366-367.

M. Mahbobzadeh, A.S. Chu, A. Mukherjee, C.F. Schaus, and S.R.J. Brueck, "Generation and Characterization of Picosecond Optical Pulses From resonant Periodic Gain GaAs Surface Emitting Lasers," IEEE Lasers and Electro-Optics Society Annual Meeting, paper SDL1.4/MKK4, Boston, MA, Nov. 4-8, 1990

D.L. McDaniel Jr. and J.G. McInerney, "Absorptive Optical Bistability and Switching in MQW Etalons with Optical Half-Wave Periodicity," submitted to CLEO '92.

D.L. McDaniel Jr. and J.G. McInerney, "Optical Bistability in a MQW Etalon with Optical Half-Wave Periodicity," Proc. OSA Annual Meeting, Boston, MA, Nov. 1990.

D.L. McDaniel Jr., L. LI, and J.G. McInerney, "Diode Laser Pumped Vertical-Cavity Surface-Emitting Semiconductor Lasers for Free-Space Commu cation," Proc. OSA Annual Meeting, Boston, MA, Nov. 1990.

D.L. McDaniel, Jr., M.Y.A. Raja, D.S. Seo, J.G. McInerney, S.R.J. Brueck and C.F. Schaus, *External Cavity Operation of Resonant Periodic Gain Semiconductor Lasers*, Proc. ISE'89, Albuquerque, NM, May 1989.

D.L. McDaniel, Jr., J.G. McInerney, M.Y.A. Raja, C.F. Schaus and S.R.J. Brueck, *Diode Laser Array Pumping of Vertical-cavity Surface-emitting Lasers*, Presented at LEOS'89 (postdeadline paper), Oct. 1989.

J.G. McInerney, *Dynamical Properties of Semiconductor Injection Lasers*, Proc. 12 IEEE Conf. on Ideas in Science and Electronics (ISE '89), Albuquerque, NM, May 1989.

J.G. McInerney, *Vertical-cavity Surface-emitting Semiconductor Lasers*, Proc. XX Winter Colloquium on Quantum Optics, Snowbird, Utah, Jan. 1990 (Invited Paper).

J.G. McInerney, V.L. Farley-Leadbetter, J.D. Park and D.S. Seo, *Nonlinear Dynamics of Modulated Semiconductor Lasers*, Published in Proc. Int. Conf. on Laser Science (Laser'89, New Orleans, LA, Jan. 1990) (Invited Paper).

M. Mojahedie and M. Osinski, "Determination of Operator Ordering in Effective-Mass Hamiltonian from Optical Transition Energies in GaAs/AlGaAa Superlattices and Quantum Wells," submitted to Qels '92.

M. Mojahedie and M. Osinski, "Operator Ordering in Effective-Mass Hamiltonian for Semiconductor Superlattices and Quantum Wells," Technical Digest, 3rd Annual Symposium on Ceramics and Advanced Materials, Albuquerque, New Mexico, October 24-25, 1991, pp. 18-19.

M. Mojahedie and M. Osinski, "Effects of Operator Ordering in Effective-Mass Hamiltonian on Transition Energies in Semiconductor Quantum Wells," Technical Digest, OSA 1991 Annual Meeting, San Jose, California, November 3-8, 1991, Technical Digest Series Vol. 17, Optical Society of America 1991, Paper WH4, p. 113.

A. Mukherjee, "Photorefractive Effects in Thin Film PLZT," *CLEO '90*, Paper #047, Anaheim, CA, May 5 1990.

A. Mukherjee, *Pulsed Laser Processing of High Temperature Superconducting Thin Films*, International SAMPE Electronic Materials and Processes Conference, Albuquerque, NM, 1990.

A. Mukherjee, *Photorefractive Effects in PLZT Thin Films*, CLEO '90, Paper #047, Anaheim, CA, May 25, 1990.

A. Mukherjee, S.R.J. Brueck, A.Y. Wu, *Electrooptics of Thin Film PLZT*, Presented at CLEO Baltimore, MD, 24-28 April, 1989.

M. Osinski, "Heavy-Hole Effective Mass in InP - A Critical Examination," Conference Proceedings, Second International Conference on Indium Phosphide and Related Materials, Denver, Colorado, April 23-25, 1990, Paper P37, pp. 330-333.

M. Osinski and C.-P. Cherng, "Broad-Area Mode-Coupling Model for Carrier-Guided Diode Laser Arrays," Technical Digest, 3rd Annual Symposium on Ceramics and *Advanced Materials, Albuquerque, New Mexico*, October 24-25, 1991, p. 18.

M. Osinski and C.-P. Cherng, "Thermal Focusing Effects in Gain-Guided Diode Laser Arrays," Technical Digest, OSA 1991 Annual Meeting, San Jose, California, November 3-8, 1991, Technical Digest Series Vol. 17, Optical Society of America 1991, Paper WS4, p. 132.

M. Osinski and C.-P. Cherng, "Broad-Area Mode Coupling in Gain-Guided Diode Laser Arrays," LEOS '91 Conference Digest, IEEE LEOS 1991 Annual Meeting, San Jose, California, November 4-7, 1991, Paper SDL 1.6, p. 13.

M. Osinski and C.-P. Cherng, "Array Mode Evolution in Gain-Guided Diode Laser Arrays," submitted to CLEO '92 Conference on Lasers and Electro-Optics, Anaheim, CA, May 10-15, 1992.

J.D. Park, D.S. Seo and J.G. McInerney, *Quasi-subharmonic Bifurcation Routes to Chaos in an External-cavity Semiconductor Laser*, Proc. Sixth National Conference on Quantum Optics CQO6, Rochester, NY, June 1989.

J.D. Park, D.S. Seo and J.G. McInerney, *Self-pulsations and Chaos in Asymmetric External-cavity Semiconductor Lasers*, Published in Proc. 1989 Ann. Meet. OSA (OSA'89, Orlando, FL, Oct. 1989), paper FL3.

J. D. Park, D. S. Seo, J. G. McInerney, and M. Osinski, "Nonlinear dynamics of semiconductor lasers: low frequency self-pulsations due to asymmetric optical feedback", QELS'89 Conference on Quantum Electronics and Laser Science, Baltimore, Maryland, April 24-28, 1989, Technical Digest Series Vol. 12, Paper TuJJ4, pp. 74-75, Optical Society of America 1989.

M.Y.A. Raja, A. Mukherjee, M. Mahbobzadeh, C.F. Schaus, and S.R.J. Brueck, *Dynamics of Resonant Periodic Gain GaAs/AlGaAs Surface Emitting Lasers under Picosecond Optical Excitation*, LEOS'89, Orlando, FL, October 1989.

M.Y.A. Raja, S.R.J. Brueck, M. Osinski, C.F. Schaus, J. McInerney, T.M. Brennan, and B.E. Hammons, *Surface-Emmitting Semiconductor Lasers: Comparisons of Resonant Periodic Gain and Conventional Structures*, Proc. Int. Conf. on Lasers and Electro-Optics (CLEO '89), Opt. Soc. of America, Washington, DC, April 1989), Paper FC4, pp. 382-383.

M.Y.A. Raja, J.G. McInerney, C.F. Schaus, S.R.J. Brueck, H.E. Schaus and S. Sun, *Transverse Mode Structure of Optically Pumped Resonant Periodic Gain Semiconductor Lasers*, Published in Proc. IEEE-LEOS 1989 Ann. Meet. (LEOS'89, Orlando, FL, Oct. 1989), paper OE11.4.

T.C. Salvi, M.B. Snipes, Jr., and J.G. McInerney, *Nonlineaer Waveguiding and Self-focusing in Wide Stripe Semiconductor Lasers*, Proc. ISE'89, Albuquerque, NM, May 1989.

C.F. Schaus, S-Z. Sun, H.E. Schaus, M.Y.A. Raja, S.R.J. Brueck, J.G. McInerney, and M. Mahbobzadeh, *Growth of CW Vertical-Cavity Surface Emitting GaAs/GaAlAs Lasers with Resonant Periodic Gain*, Proc. CLEO '89, postdeadline paper.

H. E. Schaus, C. F. Schaus, S. Z. Sun, M. Y. A. Raja, A. Jacome-Torres, J. G. McInerney, "Growth of High-Efficiency Resonant Periodic Gain Vertical Cavity Surface-Emitting Lasers," 16th Int. Symp. GaAs Related Compounds, Inst. Phys. Conf. Ser. p. 749 (1990).

H.E. Schaus, C.F. Schaus, S. Sun, M.Y.A. Raja, A. Jacome-Torres and J.G. McInerney, *Growth of High-Efficiency Resonant-Periodic-Gain Vertical Cavity Surface-Emitting Lasers*, Proc. 16th Int. Symp. on GaAs Related Compounds (Inst. of Phys. Conf. Ser. 1990) Jan. 1990.

D-S. Seo, J-D. Park, and J.G. McInerney, *Modal Properties of Semiconductor Lasers with Asymmetric Optical Feedback*, Proc. Int. conf. on Quantum Electron. and Laser Sci. (QELS '89), (Opt. Soc. of America, Washington, DC, April 1989), paper TuJJ3, pp.72-75.

D-S. Seo, J-D. Park, and J.G. McInerney, *Self-pulsation in Asymmetric External Cavity Semiconductor Lasers Due to Multiple Feedback Effects*, Proc. Int. Conf. on Quantum Electron. and Laser Sci. (WELS '89), OSA, Washington DC, April 1989)Paper TuJJ4.

D.S. Seo, J.D. Park and J.G. McInerney, *Spectral and Intensity Noise Characteristics of Double External Cavity Semiconductor Lasers*, Published in Proc. 1989 Ann. Meet. Opt. Soc. of Am. (OSA'89, Orlando, FL, Oct. 1989), paper WL26.

T.H. Shiau, S.Sun, C.F. Schaus, K. Zheng, and G.R. Hadley, "Strained Quantum Well Leaky-Mode Diode Laser Arrays," IEEE Lasers and Electro-Optics Society 1990 Annual Meeting, paper SDL3.2, Boston, MA, Nov. 4-8, 1990.

M.B. Snipes, Jr., T.C. Salvi, J.G. McInerney and C.F. Schaus, *High Power, Wide Stripe Semiconductor Injection Lasers*, Proc. ISE'89, Albuquerque, NM, May 1989.

S.T. Srinivasan, C.F. Schaus, E. A. Armour, J.G. McInerney, and S. Hersee, "High Power Single-Laterral-Mode Unstable Resonator Wide-Stripe Semiconductor Lasers," submitted to CLEO '92.

S.T. Srinivasan, C.F. Schaus, S.Z. Sun, E. Armour, A.H. Paxton, D.J. Gallant, and C.E. Moeller, "Semiconductor Laser with Unstable Resonator Consiting of Negative Cylindrical Lenses," presented at SPIE/OE Lase 92,Los Angeles, CA, Jan. 19-25.

W. E. Thompson, C.-P. Cherng, and M. Osinski, "Array-Mode Selection in Nonabsorbing-Mirror Diode Laser Arrays," Technical Digest, OSA 1991 Annual Meeting, San Jose, California, November 3-8, 1991, Technical Digest Series Vol. 17, Optical Society of America 1991, Paper WS5, p. 132.

W.E. Thompson and M. Osinski, "Longitudinal Behavior in Semiconductor Laser Diodes," Technical Digest, OSA 1990 Annual Meeting, Boston, MA, November 4-9, 1990, Technical Digest Series 1990, Vol. 15, Paper MK11, p. 16

J. Ye, H. Li, and J.G. McInerney, "Period-Doubling Route to Chaos in a Coherence-Collapsed Semiconductor Laser," submitted to CLEO '92.

P. Zhou, J. Cheng, C.F. Schaus, S.Z. Sun, D. Kopchik, C. Hains, W. Hsin, C.H. Chen, D..R.. Myers, and G.A. Vawter, "Low Series Resistance Continuously-Graded-Mirror GRIN-SCH-MQW Vertical-Cavity Surface-Emitting Lasers Grown by MOCVD," Device Research Conference, 1991.

L.C. Zou, K.J. Malloy, and A.Y. Wu, "Surface Normal Second Harmonic Generation in PLZT and GaAs Thin-Film Waveguides," Third Annual Symposium on Ceramics and Advanced Materials, Albuquerque, NM, Oct. 24-25, 1991.

Submitted to CLEO 21 November 1990 to be considered for category 10. Optical Switching, Logic, and Storage Systems

AND, OR and XOR Digital Optical Logic: Binary Addition Using Optical Symbolic Substitution

R. P. Bryan and G. R. Olbright
Sandia National Laboratories[†], *Albuquerque, New Mexico 87185*
Voice: (505) 844-8548, FAX: (505) 844-3211

Julian Cheng
University of New Mexico[††], *Center for High Technology Materials, Albuquerque, NM 87131*

ABSTRACT

Cascadable optical logic (AND, OR and XOR) based on heterojunction phototransistors and vertical-cavity surface-emitting lasers is demonstrated. We also discuss a scheme for implementing binary arithmetic using optical symbolic substitution and these logic elements.

AND, OR and XOR Digital Optical Logic: Binary Addition Using Optical Symbolic Substitution

R. P. Bryan and G. R. Olbright
Sandia National Laboratories[†], *Albuquerque, New Mexico 87185*
Voice: (505) 844-8548, FAX: (505) 844-3211

Julian Cheng
University of New Mexico[††], *Center for High Technology Materials, Albuquerque, NM 87131*

Summary

We describe cascadable optical logic gates (AND, OR and XOR) based on heterojunction phototransistors (HPT) and vertical-cavity surface-emitting laser (VCSEL) structures.[1] Here, a single device provides electronic amplification, optical gain and switching, and we eliminate the need for an additional external optical source or an optical bias beam. We describe optical logic functions such as inversion, AND, NAND, OR, NOR, and exclusive OR (XOR), etc., using simple combinations of phototransistors and lasers, and provide a specific example of binary arithmetic based on optical symbolic substitution. In Fig. 1 we show the optical circuit configuration for AND-, OR-, and XOR-gate operation. The phototransistors are optically switched from a high-bias voltage, low collector current OFF-state to a low-bias voltage, high conductance ON-state which then drives the VCSEL above threshold. If multiple optical inputs (each of sufficient intensity to switch on the VCSEL), are incident on the HPT, then an optical OR gate is obtained (see Fig. 2a). To operate as an AND-gate, the intensity of each optical input to the HPT must be such that they can collectively, but not individually, produce enough current gain to switch on the VCSEL (see Fig. 2b). By configuring two HPTs and two VCSELs as shown in Fig. 1b, we have demonstrated XOR (see Fig. 2c). For the case of XOR operation, when light is present at both or neither HPTs, the potential between them is at ground and no current flows through the VCSELs and the output is the 0-state. However, if only one HPT is illuminated, then current flows through a VCSEL and the output is the 1-state

Boolean logic recognizes a combination of input bits and outputs one bit. Symbolic substitution,[2] recognizes not only a combination of bits but also their relative spatial configuration. We illustrate this with the example of a two-dimensional binary half-adder, using a two-dimensional array of phototransistor/VCSEL surface-normal logic gates. Binary addition involves the SUM and CARRY operations, which can be simulated using the AND- and XOR-gates, respectively. The states 0 and 1 are symbolically represented by a VCSEL in the ON-state or OFF-state. For binary addition, inputs

consist of two N-bit words (two linear arrays) arranged as parallel rows of optical bits. The addition algorithm requires both pattern shifts and transformations that simulate the SUM (XOR) and CARRY (AND) operations. Each bit in the sum of A + B is replaced by the corresponding left and right-shifted CARRY and SUM bits (VCSEL outputs), thus replacing the original rows of A and B with new, spatially-shifted symbols representing rows of CARRY and SUM bits. These are fed into the next logic array to undergo N-successive symbolic substitution cycles until there are no 1-bits remaining. The complete arithmetic operation can also be done more simply cycling the output through the logic array N times, using the optical scheme shown in Fig. 3. This requires that the logic array be reset after each of N passes through the half-adder, while preserving the previously generated optical outputs as the inputs for the next pass.

† SNL research is supported by DOE contract No. DE-AC04-76DP00789.

†† UNM research is supported in part by AFOSR and DARPA.

1. Sandia Patent no. SD-4896, S-71, 738 pending, January (1990).

2. A. Huang, in Tech. Digest, IEEE Tenth Int'l. Optical Computing Conf., (1983), pp.13-17.

Figure Captions

Figure 1. Digital optical circuit configurations for a) AND and OR, and b) XOR.

Figure 2. Digital optical logic operations a) OR, b) AND, and c) XOR.

Figure 3. Optical circuit for a multi-pass binary half-adder, which includes a logic array (S1) and a memory array (S2). Also shown are the rules for addition using symbolic substitution and a 4-bit binary addition.

a)

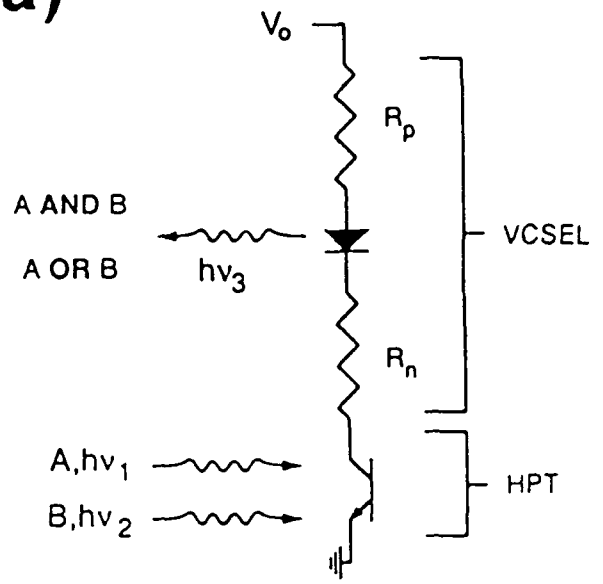
V_o
R_p
A AND B
A OR B
$h\nu_3$
VCSEL
R_n
A,$h\nu_1$
B,$h\nu_2$
HPT

b)

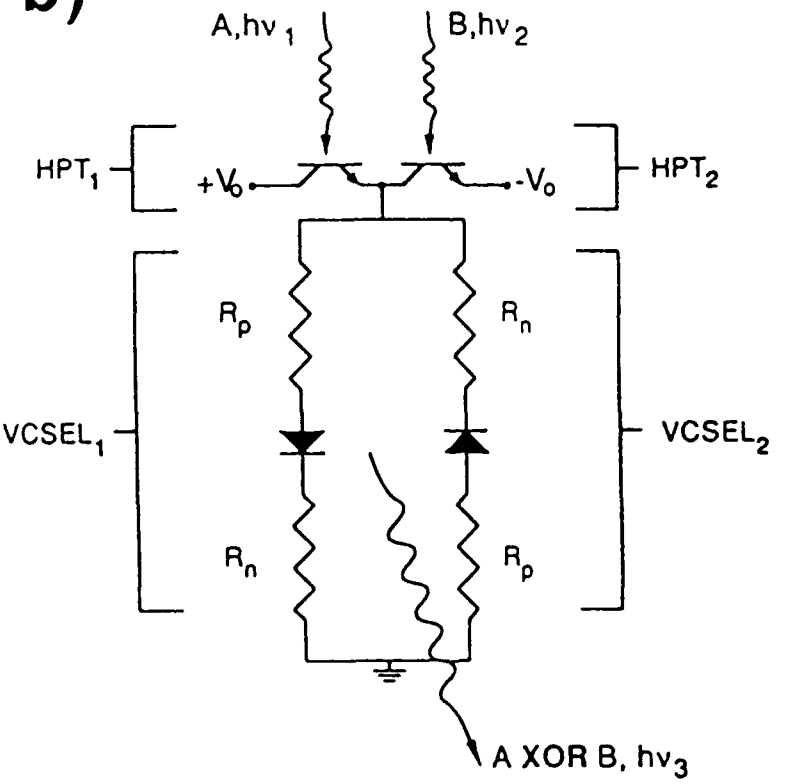
A,$h\nu_1$
B,$h\nu_2$
HPT_1
$+V_o$
$-V_o$
HPT_2
R_p
R_n
$VCSEL_1$
$VCSEL_2$
R_n
R_p
A XOR B, $h\nu_3$

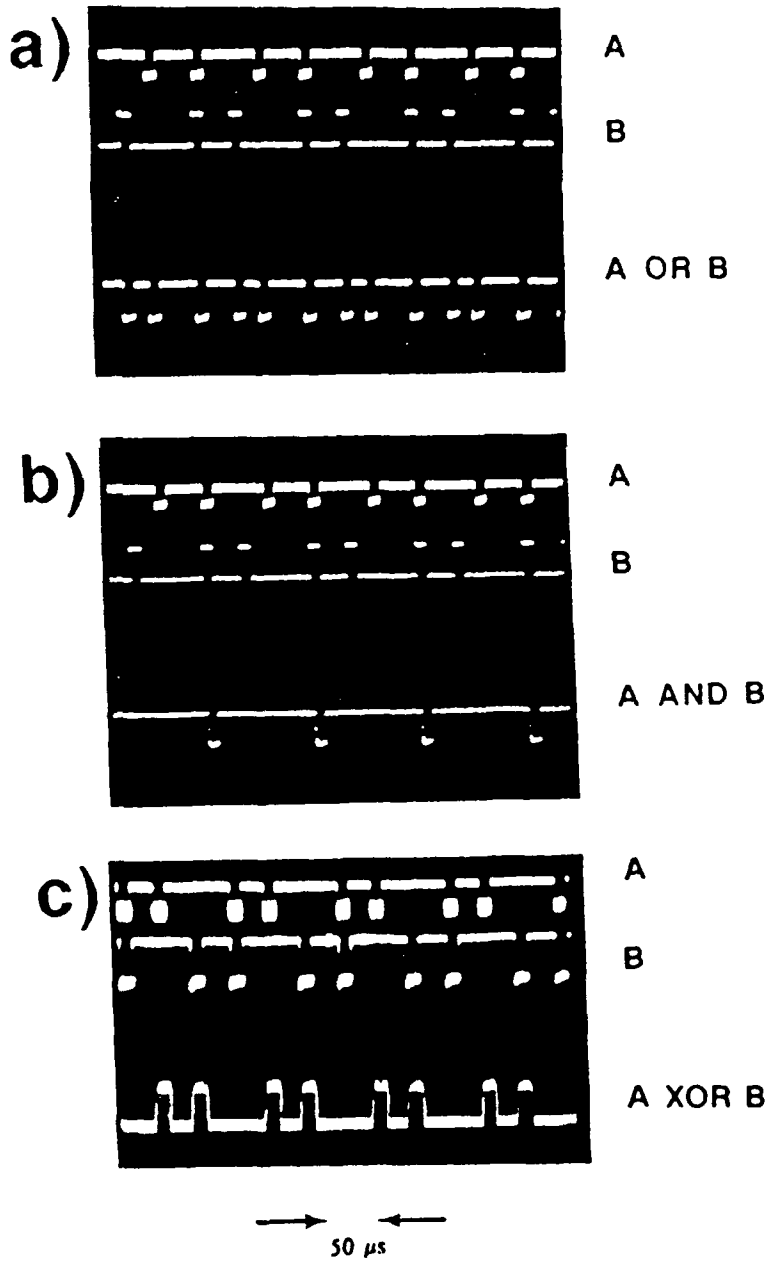
a)
A
B
A OR B
b)
A
B
A AND B
c)
A
B
A XOR B
50 μs

Submission to CLEO '92

Classification: Semiconductor Lasers (Semiconductor laser applications)

SENSITIVE DOPPLER VELOCIMETRY AND ANEMOMETRY USING SEMICONDUCTOR LASERS

Elizabeth A. Callan and John G. McInerney*

Optoelectronic Device Physics Group

Center for High Technology Materials

University of New Mexico

Albuquerque, NM 87131-6081

ABSTRACT

Velocities of diffusely reflecting objects have been measured in the range 0.5-20 m s^{-1} using compact, self-referencing and sensitive (-60 dB) systems based on laser diodes. Airflow velocities have also been determined.

* Corresponding Author: Professor John G. McInerney. Tel. (505) 277-0768, Fax (505) 277-6433.

SENSITIVE DOPPLER VELOCIMETRY AND ANEMOMETRY USING SEMICONDUCTOR LASERS

Elizabeth A. Callan and John G. McInerney

Optoelectronic Device Physics Group
Center for High Technology Materials
University of New Mexico
Albuquerque, NM 87131-6081

SUMMARY

The extreme sensitivity of laser diodes to minute amounts of optical feedback has long been considered a nuisance, but this same attribute, if properly controlled, makes laser diodes ideal for remote sensing. Here we describe the construction and evaluation of compact and sensitive diode-laser-based velocimeter/anemometer systems which are self-referencing (*i.e.* need no phase or frequency adjustment) and which require only simple optical alignment, in contrast to the more usual interferometric laser sensors. In each case, a low-power ($\sim$1 mW) laser beam was collimated and directed onto a moving and diffusely reflecting target (white bond paper), from which the Doppler-shifted optical backscatter was coupled back into the lasing mode, causing an easily detected intensity modulation at the Doppler frequency shift.

Two data extraction schemes have been examined. In the first, a beam-splitter was placed in the collimated beam to direct a portion of the returning backscatter into a photodiode, and the Doppler backscatter modulation appeared on the intensity noise spectrum; this signal was amplified and detected using a microwave spectrum analyzer. In a second experiment, the junction voltage was amplified and input to the microwave spectrum analyzer. In each case, compact frequency mixer/counter electronics could replace the spectrum analyzer in practical applications.

Having determined the laser-lens coupling factor by measuring the threshold reduction in a separate strongly coupled external cavity, we measured the total coupled backscatter into the lasing mode to be approximately -60 dB for a signal-to-noise ratio of 10 dB or better. The SNR varied considerably with measured velocity (*i.e.* with Doppler frequency) due to the amplifier response and modulation response of the laser diode. The velocimeter was linear to within 2% in the range from 0.5 to 20 m s^{-1}, the lower limit being due to the amplifier low-frequency roll-off and the upper limit was restricted by packaging limitations on the laser diodes.

Applications of the semiconductor laser Doppler velocimeter include anti-collision sensing, anemometry, wind shear detection, guiding robots or docking vehicles. To evaluate the system as a simple anemometer, we replaced the moving paper target with a tube attached to a vacuum hose, then illuminated the resulting airflow with the laser diode. While clean laboratory air produced very little backscatter and consequently unreliable Doppler signals, addition of small amounts of scattering particulates into the airstream produced excellent results.

In summary, we have demonstrated compact, self-referencing and sensitive velocimeter/anemometer using Doppler-shifted optical backscatter to modulate the intensity or junction voltage in a diode laser. Measurements of velocities in the range 0.5-20 m s^{-1} with SNR greater than 10 dB required only -60 dB of backscatter. The system has many possible applications, including measurement of air flow velocities.

For Office Use

category #

For Office Use

paper #

CLEO® '92

CONTRIBUTED PAPER CATEGORIZATION FORM
(Attach to Original)

Paper Title Sensitive Doppler velocimetry

Corresponding Author J. McInerney

Address CHTM, Univ of NM, Albuquerque NM 87131

Phone (505) 277-0768

Fax (505) 277-6433

Mode of Presentation

The program committee will schedule both oral and poster sessions. For poster sessions each author is provided a 4-foot-high x 8-foot-wide bulletin board on which to display a summary of the paper. Authors remain in the vicinity of the bulletin board for the duration of the session to answer the questions of attendees. The abstract and summary of both oral and poster papers are published in the same fashion, both in the advance program and in the digest.

Check one

☐ To be scheduled for poster presentation only.

☐ To be scheduled for oral presentation only.

☒ To be scheduled for poster presentation only if oral presentation is not possible or desirable.

☐ To be scheduled for oral presentation only if poster presentation is not possible or desirable.

☐ To be scheduled only for demonstration presentation.

THE FINAL DECISION WILL BE MADE BY THE PROGRAM COMMITTEE. IN CASES WHEN NO PREFERENCE IS STATED, SCHEDULING WILL BE AT THE OPTION OF THE PROGRAM COMMITTEE.

☐ **To be scheduled only for the CLEO® '92 Conference.**

CLEO® '92 TOPICS TO BE CONSIDERED

☐ **1. Gas and Free-Electron Lasers**

Gas laser technology and engineering • Gas laser science, including kinetics, spectroscopy, chemistry, materials, pulse power, and novel applications • VUV and XUV gas laser sources • Free-electron lasers

☐ **2. Solid-State and Liquid Lasers**

Advances in solid-state laser media • Advances in liquid lasers including dye lasers • Novel pump sources including high-power laser diodes • Novel resonator geometries, fiber lasers • Modeling of solid-state and liquid lasers/resonators

☒ **3. Semiconductor Lasers**

High-power semiconductor lasers and arrays • Short and long wavelength lasers • Coherent diode arrays • Surface-emitting lasers • Semiconductor laser applications • Narrow linewidth and tunable lasers • Quantum-well, wire, and dot structures • Superlattice devices, novel materials, and processes

☐ **4. Applications of Nonlinear Optics and Laser Spectroscopy**

Nonlinear-optical probing of surfaces • Cooperative phenomena and up-conversion lasers • Nonlinear dynamics in devices, solitons, instabilities, and chaos • Nonlinear optics in fibers • Frequency conversion and optical parametric oscillators • Nonlinear spectroscopy for material and device studies • Multiwave mixing processes

☐ **5. Phase Conjugation and Photorefractive Devices**

Mechanisms and applications of phase conjugation • Phase conjugation by SRS and SBS • Phase-conjugate lasers • Photorefractive materials and mechanisms • Photorefractive devices and applications

☐ **6. Optical Materials and Fabrication**

Crystal growth • Microfabrication techniques • Quantum well, line, and dot fabrication techniques • Microprogrammable materials • Materials with enhanced nonlinear optical response • Materials for high-power and nonlinear propagation

☐ **7. Lasers for Fusion and Strong-Field Physics**

Laser fusion technology • Laser plasma interactions • Picosecond and femtosecond lasers for strong-field physics • Applications of laser-produced plasmas • Laser-driven accelerators

☐ **8. Ultrafast Optics and Electronics**

Generation of ultrashort pulses • Measurement of ultrafast optical and electronic properties of materials and devices • Ultrahigh-speed optoelectronic devices and switching techniques

☐ **9. Atmospheric, Space, and Ocean Optics**

Lidar and laser radar systems • Ranging, tracking, and navigation • Free-space optical communications • Media effects on optical propagation and system performance • Optical remote sensing • Atmospheric, space, and underwater optical systems • Optical devices for use in atmospheric, space, and ocean systems

☐ **10. Optical Switching, Logic, and Storage Systems**

Optical storage components and systems • Optical switching and logic devices • Optical computing and neural networks • Integrated optics • Quantum well and superlattice devices • Bistability and bistable devices • Optical signal processing

☐ **11. Electro-Optical Device and Infrared Sensor Technologies**

Electro-optical devices and instruments for metrology • Beam conditioning, isolation, modulation, switching, sensing, and pulse power applications • Electro-optical displays • Passive and active infrared sensors • Focal plane arrays and imaging systems • Innovative detector technology

☐ **12. Diagnostic, Analytical, and Industrial Applications**

Flow, combustion, and plasma diagnostics • Chemical analysis • Sensors and detectors • Visualization and imaging • Process monitoring • Robotic sensing and control • Materials processing and surface treatment

☐ **13. Medical and Biological Applications**

Laser angioplasty • Lasers in ophthalmology • Laser surgery • Laser photodynamic therapy • Fiber optic delivery systems for surgery, diagnostics, and photodynamic therapy • Laser design and engineering for the medical environment • Laser photobiology • Optoelectronic medical sensors and devices

☐ **14. Lasers in Electronic and Optical Device Processing**

Laser modification of materials, including etching, deposition, doping and mixing • Laser ablation and recrystallization of solids • Laser-induced chemistry • Projection printing and lithography by lasers • Lasers in process diagnostics and materials characterization

☐ **15. Lightwave Communications**

Fiber optics • Sources, detectors, optical amplifiers, and integrated components • Transmitters, receivers, and performance considerations • System applications

OPTICAL SOCIETY OF AMERICA
COPYRIGHT AGREEMENT

Technical Digest: **Conference on Lasers and Electro-Optics (1992)**

Title of Article: "Sensitive Doppler velocimetry . . ."

Author(s): E. A. Callen and J. G. McInerney

The undersigned hereby assigns to the Optical Society of America (the "Society") copyright ownership in the above-titled work to be effective as of the date published, this assignment to be effective as of the date published and to the extent transferable under applicable national law. If each author's signature does not appear below, then the signing author(s) represent that they sign this agreement as authorized agent(s) for and on the behalf of all the authors. The Society shall have the right to register copyright to the above-titled book in its name as claimant. Also, the Society shall have the right to grant reprint permission to third parties and to negotiate and receive reasonable royalties in such instances.

Authors (or their employers, in the case of works made for hire) reserve all other rights to the above book including: (a) The right to use the work in future works of their own; (b) All proprietary rights other than copyright; (c) The right of the employer to make copies of the work. If prepared under U.S. Government contract, the government shall have the rights under copyright to the extent required by the contract.

[signature]	
Signature	Signature
J. McINERNEY	
Print name	Print name
ASSOC. PROF. NOV 21, 1991	
Title Date	Title Date

Each author who is not a U.S. Government employee should sign above, if reasonably practicable; and each author's employer should sign if the work was prepared within the scope of the author's employment.

If all authors were U.S. Government employees at the time this article was prepared, and such article was prepared as part of official duties, then one author should sign below to certify that this is true and that the article is therefore not subject to U.S. copyright protection.

Signature Print name Title and Date

PLEASE COMPLETE AND RETURN THIS FORM TO:
CLEO® '92
Optical Society of America
Meetings Department
2010 Massachusetts Avenue, NW
Washington, DC 20036

Submitted to OSA 92

Reduced absorption in semiconductor quantum wells through coherently-derived quantum interference.

Reduced Absorption Mechanisms in Semiconductor Quantum Well. DONG S. LEE, KEVIN J. MALLOY, CHTM University of New Mexico.- - - Ultra high refractive indices without absorption[1] and reduced absorption[2] have been predicted and observed for atomic systems. We apply these considerations to semiconductor structures with complicated energy bands and strong phonon interactions. Bulk semiconductors offer limited flexibility, while quantum well structures offer the ability to tailor the dielectric response through control of the conduction subband states and the separation between heavy and light hole states. To observe high indices without absorption, Raman pumping from the ground conduction state should result in a coherent state at the bottom of heavy hole and light hole bands. The high index then exists between the first excited conduction subband and the range of separation between the holes. Since this scheme gives a large refractive index change, we can observe results by photo- or electro-reflectance. However, interactions between subbands and the strong phonon scattering may inhibit the coherent state. To observe reduced absorption without changes of refractive index, two conduction subbands should be coupled by a CO_2 laser. Reduced absorption should be observable from the bottom of hole state to the range between the two dressed states of the conduction subbands. This approach is simpler than coherent pumping, and modulated transmission offers the best chance for observation.

1. M. Scully, Phy. Rev. Lett. **67**, 1855(1991)
2. S. E. Harris et al., Phys. Rev. Lett. **67**, 3062(1991)

NDOS '92

CHAOS IN SEMICONDUCTOR LASERS

Hua Li, Jun Ye and John G. McInerney*

Center for High Technology Materials

The University of New Mexico

Albuquerque, NM 87131-6081, USA

*Corresponding author: Tel. (505) 277-0768

Fax. (505) 277-6433

Bitnet "MCINERNY@UNMB"

Abstract

We report investigations of the onset of chaos in a semiconductor laser with weak external optical reflection, and in an AR-coated semiconductor laser in an external cavity.

CHAOS IN SEMICONDUCTOR LASERS

Hua Li , Jun Ye and John G. McInerney
Center for High Technology Materials
The University of New Mexico
Albuquerque, NM 87131, USA
Tel. (505) 277-0768

Semiconductor lasers are typical class-B lasers in which the decay rates obey $\gamma_p, \gamma \ll \gamma_\parallel$, where γ_p, γ and $\gamma_\parallel$ are the decay rates of the photons, population inversion and polarization, respectively. Therefore an isolated semiconductor laser is well described by rate equations with only two independent variables (photon number and carrier population) so that chaos is not observed. Here we show two different geometries to make chaos feasible in a semiconductor laser system. The results clearly demanstrate the origin of instability in the semiconductor laser: the interaction in the nonlinear laser medium between undamped relaxation oscillation (which expresses the energy exchange between carrier population and photons) and some external modulation (which may include optical feedback).

In the first experiments we used a commercial CSP semiconductor laser (Hitachi HLP1400) with an external reflector which provides weak optical feedback (<0.1% in power) to the laser. This optical feedback modulates the carrier population N and the optical field (both intensity I and phase Φ) in the laser resonator and also causes coupling between them. Using this geometry a rich variety of dynamic behavior has been observed /1,2/, but the physical basis for the instability was hitherto unclear. We show here the measured intensity noise spectrum by changing system parameters, mainly by changing feedback levels (Figs.1 and 2). For increasing feedback level the relaxation oscillation is undamped at first, then the external cavity modes are excited. Fig. 1 shows that chaos can be reached through a pure period-doubling route if the relaxation oscillation frequency ν_R remains an integer multiple of the external cavity mode spacing ν_{ext}, i.e. $\nu_R=n\nu_{ext}$ (n: integer). The fundamental period corresponds to the roundtrip time of photons in the external cavity ($T=1/\nu_{ext}$). Fig.2 shows the quasiperiodic route to chaos observed when $\nu_R \neq n\nu_{ext}$. The latter situation is found more frequently in the experiment. The optical spectra are also monitored during the measurements, clearly showing symmetry breaking in the system.

Although the pure period-doubling route to chaos happens only in a narrow range of system parameters, initial period-doubling is found in quasiperiodic behavior (Fig.2), indicating that period-doubling is a fundamental process in the system. For most system parameters we see a mixture of period-doubling and quasiperiodicity, culminating in chaos.

The above experiment has been modeled theoretically /3/ using a rate equation approximation including coupling between the intensity and phase, weak feedback and gain saturation effects. The rate equations are integrated numerically to obtain the time series of the three variables $N(t), I(t), \Phi(t)$ which are further utilized to calculate the autocorrelation function, correlation dimension and other fundamental dynamical properties. Period-doubling and quasiperiodic routes to chaos are obtained in the theoretical analysis, in good agreement with the experimental measurements /4/.

The phenomena described above are easy to understand in the general context of nonlinear oscillators: the interaction of two or more modulations applied to a nonlinear oscillator can cause chaotic behavior. If the two modulation frequencies have a rational ratio, frequency locking may result and period-doubling will occur when the system symmetry is broken. Otherwise the two incommensurate modulation frequencies will beat together, and for increasing modulation depth more new frequencies corresponding to combinations of the existing frequencies will appear because of nonlinearity of the oscillator. Both processes cause chaos in the oscillator. In our laser system only one external modulation is added due to the external cavity modes, but the intrinsic relaxation oscillations are also undamped by the optical

feedback, so in effect two oscillations are applied to the laser system, and interaction between them causes the chaos.

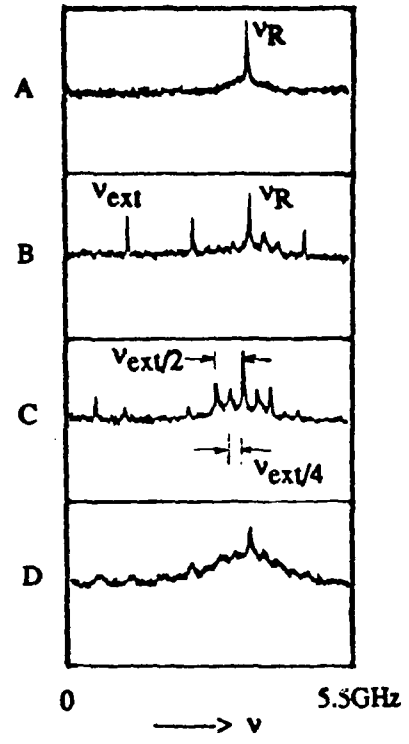

Fig.1 Measured intensity power spectra for the laser diode with an external reflector. $L_{ext} \equiv 9$cm, pump current $I/I_{th} \equiv 1.38$. Feedback level was increased from A to D.

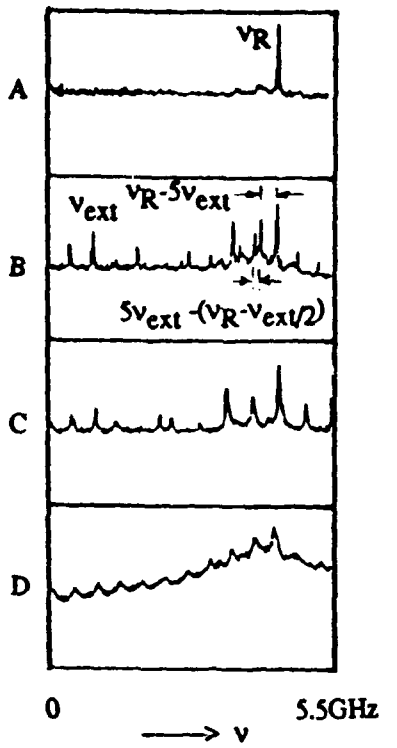

Fig.2 Measured intensity power spectra for the laser diode with an external reflector. $L_{ext} \equiv 15.5$cm, pump current $I/I_{th} \equiv 1.59$. Feedback level was increased from A to D.

Armed with this understanding, we set up another experiment to investigate the dynamic behavior of an anti-reflection (AR) coated semiconductor laser in an external cavity with a grating reflector. The residual reflectivity of the AR-coating on the internal facet was less than 0.1%. A solid etalon with FSR ≡ 100 GHz and finess ≡ 30 was inserted in the cavity to create strong dispersion and hence longitudinal mode selection. The external cavity mode spacing was chosen as ≡ 520MHz so that the envelope of the etalon resonance curve could include several cavity modes, therefore multi-mode behavior was possible. At first the cavity detuning was chosen so that the cavity resonance was at the center of the etalon resonance curve. In this case a single external cavity mode was obtained (Fig.3A) and maximum output power observed. As the external cavity was detuned from the center of the etalon resonance, a sharp peak at several tens of MHz appeared (marked in Fig.3 as ν_R) which was accompanied by a low frequency component (marked as ν_1 in Fig.3) and its harmonics. With different cavity detuning the value of ν_R was almost constant but ν_1 changed, so that different ratios of ν_R to ν_1 were obtained. The corresponding intensity spectra showed quasiperiodicity (Fig.3D) or period-doubling (Fig.3C). The corresponding optical spectra showed multi-mode behavior and different ansymmetries. Chaotic behavior appeared upon further cavity detuning(Fig.3E).

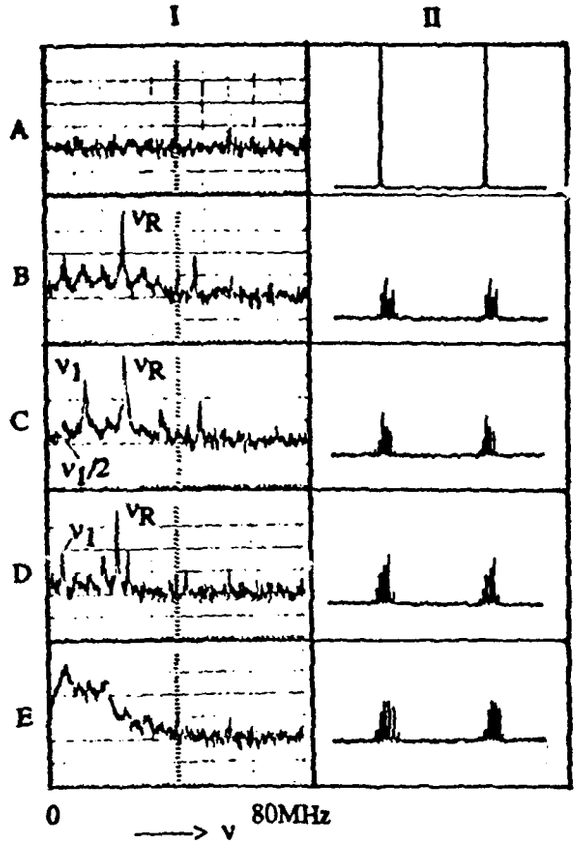

Fig.3 Measured intensity power spectra (I) and optical spectra (II) for an AR-coated laser diode in an external cavity. $L_{ext} \cong 26$cm, pump current $I/I_{th} = 1.07$. External cavity length is detuned from A to D by an amount $< \lambda/2$. Optical spectra were measured by using a plane-plane scanning F-P interferometer with FSR=11GHz and finesse>100.

In the experiments ν_R could be changed most effectively by adjusting the pump current, while ν_1 could be varied mainly by setting the cavity detuning. This suggests that ν_R was the relaxation oscillation frequency of the external cavity laser, and ν_1 was the beat frequency between different cavity modes; these modes had unequal mode spacings because they were located at different parts on the etalon dispersion curve. Further experimental measurements are continuing.

Both experiments agree in associated indicating strongly that the origin of instabilities in a semiconductor laser system is the interaction between undamped intrinsic relaxation oscillation and same external modulation.

References:

/1/ G. C. Dente, P. S. Durkin, K. A. Wilson and C. E. Moeller, IEEE J. Quantum Electron., QE-24, 2441(1988).
/2/ J. Mork, J. Mark and B. Tromborg, Phys. Rev. Lett., 65, 1999(1990).
/3/ Jun Ye, Hua Li and John G. McInerney, Submitted to Phys. Rev. Lett..
/4/ Hua Li, Jun Ye and John G. McInerney, unpublished.

OPCON SANJOSE 11/91

Influence of noise on deterministic chaos in a coherence-collapsed smiconductor laser

Hua Li

Jun Ye

Alan Bahm*

John G. McInerney

Optoelectronic Physics Group

Center for High Technology Materials

University of New Mexico

Albuquerque, NM 87131

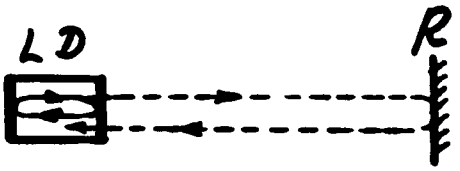

GaAs/AlGaAs
Hitachi HLP1400
single mode above I_{th}.

$$f_{ext} = \frac{P_{feedback}}{P_{in\ LD}}$$

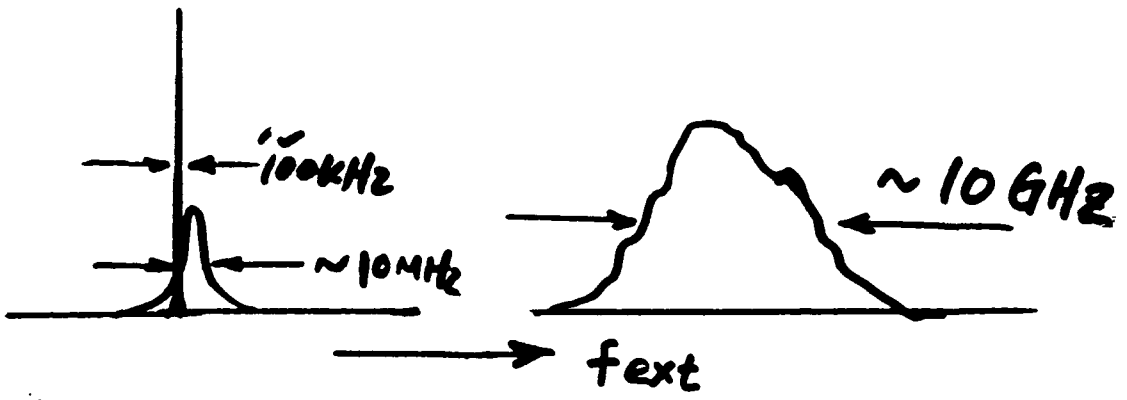

A. Linewidth narrowing

B. coherence collapsed State

Questions.

1. what happens between A → B ?
2. what is the coherence collapsed state ?
3. noise influence on 1. 2. ?

experimental study

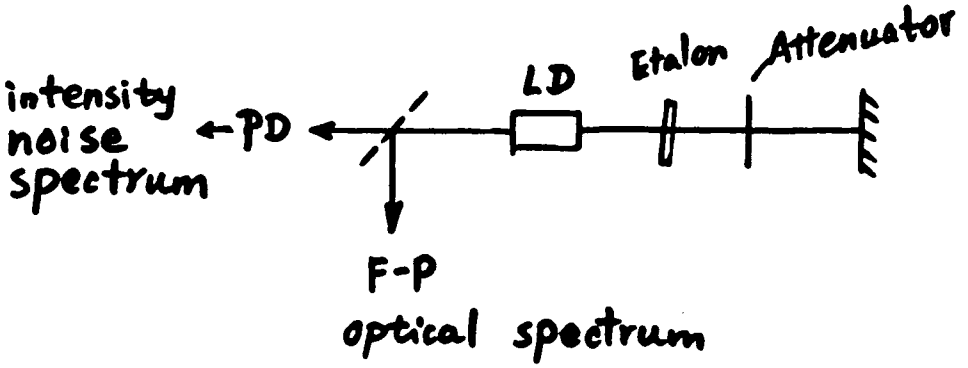

THEORETICAL STUDY

$$\frac{dX(t)}{dt} = \underbrace{f(X(t))}_{①} + \underbrace{k \cdot g(X(t), X(t-\tau))}_{②} + \underbrace{F(t)}_{③}$$

① isolated lasing process /1,2/

② delayed nonlinear feedback /1,3/

t: delay time;

k: feedback strength

$\propto (f_{ext})^{1/2}$

③ Langevin force, noise driving /4,5/

$$X(t) = \begin{pmatrix} I(t) \\ \Phi(t) \\ N(t) \end{pmatrix} \longrightarrow X(t) = \begin{pmatrix} I(t) \\ \Omega(t) \\ N(t) \end{pmatrix}$$

$$\Omega(t) = \omega(t) - \omega_s = \lim_{\Delta t \to 0} \frac{\Phi(t) - \Phi(t-\Delta t)}{\Delta t}$$

Refenrences:

/1/G.P.Agrawal and N.K.Dutta, "Long-Wavelength semiconductor Lasers", Van Nostrand Reinhold Inc., 1986

/2/G.P.Agrawal, IEEE J.Quantum Electron., **26**, 1901(1990)

/3/B.Dorrizi and B.Grammaticos, Phys. Rev. A, **35**, 328(1987)

/4/M.Lax, Reviews of Modern Physics, **38**, 541(1966)

/5/R.F.Fox, I.R.Gatland,R.Roy and G.Vemuri, Phys. Rev. A.,**38**, 5938(1988)

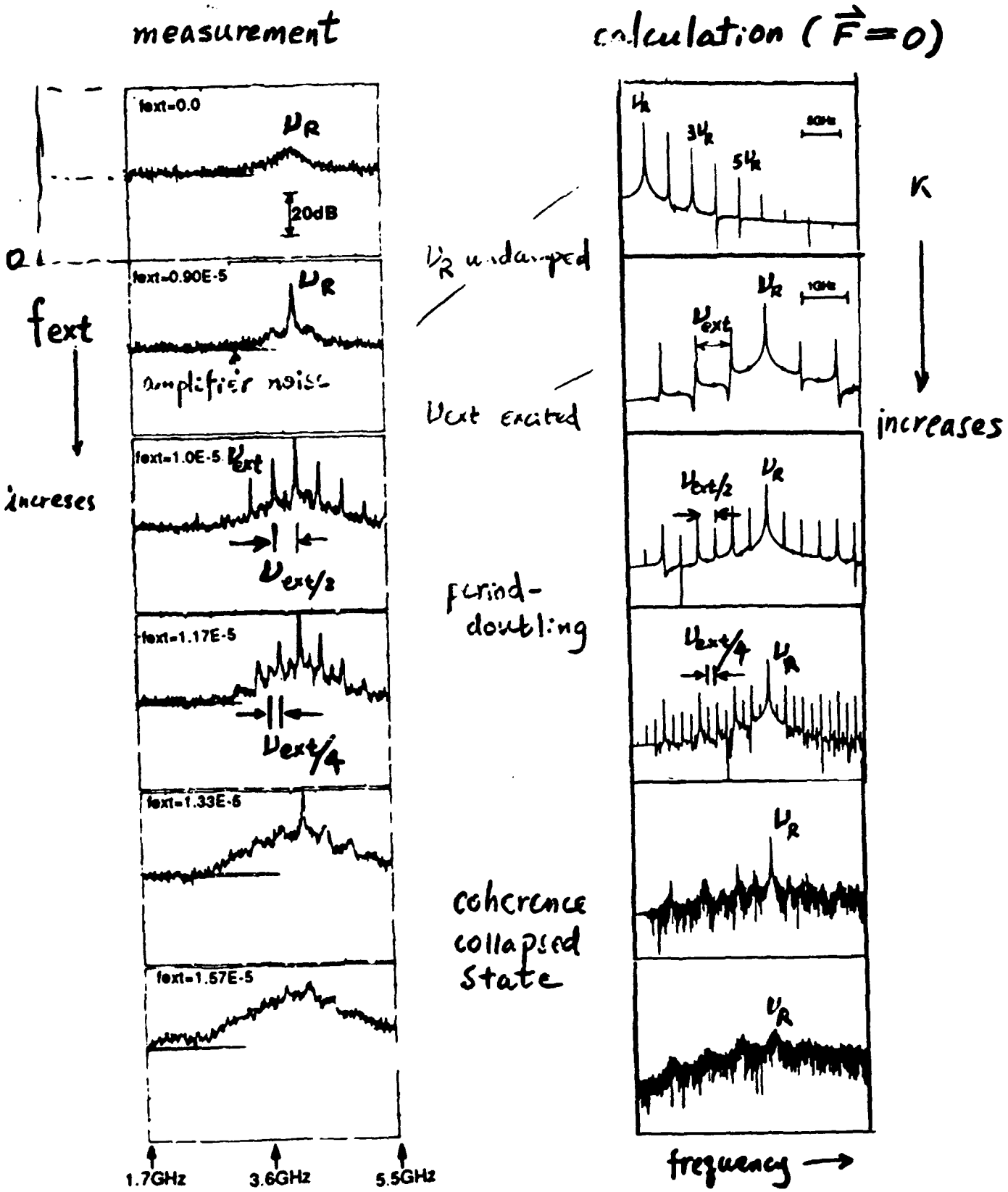
measurement
calculation ($\vec{F}=0$)
fext=0.0
ν_R
20dB
fext=0.90E-5
ν_R
amplifier noise
fext=1.0E-5
ν_{ext}
$\nu_{ext/2}$
fext=1.17E-5
$\nu_{ext/4}$
fext=1.33E-6
fext=1.57E-5
1.7GHz
3.6GHz
5.5GHz
fext
increases
ν_R undamped
ν_{ext} excited
period-doubling
coherence collapsed state
ν_R
$3\nu_R$
$5\nu_R$
50Hz
ν_{ext}
10Hz
$\nu_{ext/2}$
$\nu_{ext/4}$
K
increases
frequency →

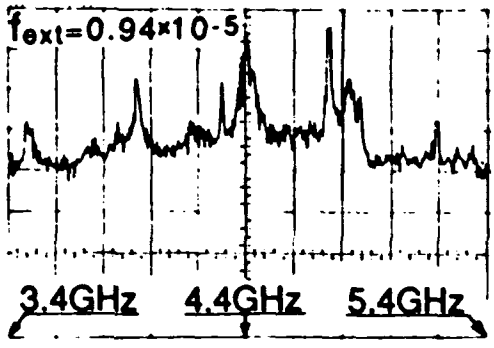

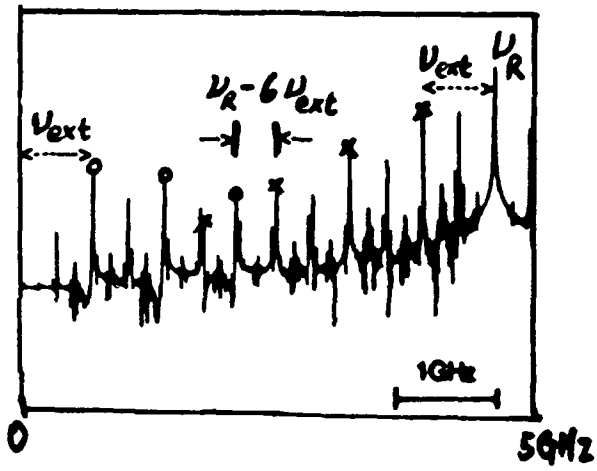

$\nu_R \neq n \cdot \nu_{ext}$ Quasiperiodic route
→ coherence collapse

$\nu_R = n \cdot \nu_{ext}$ period-doubling route
→ coherence collapse

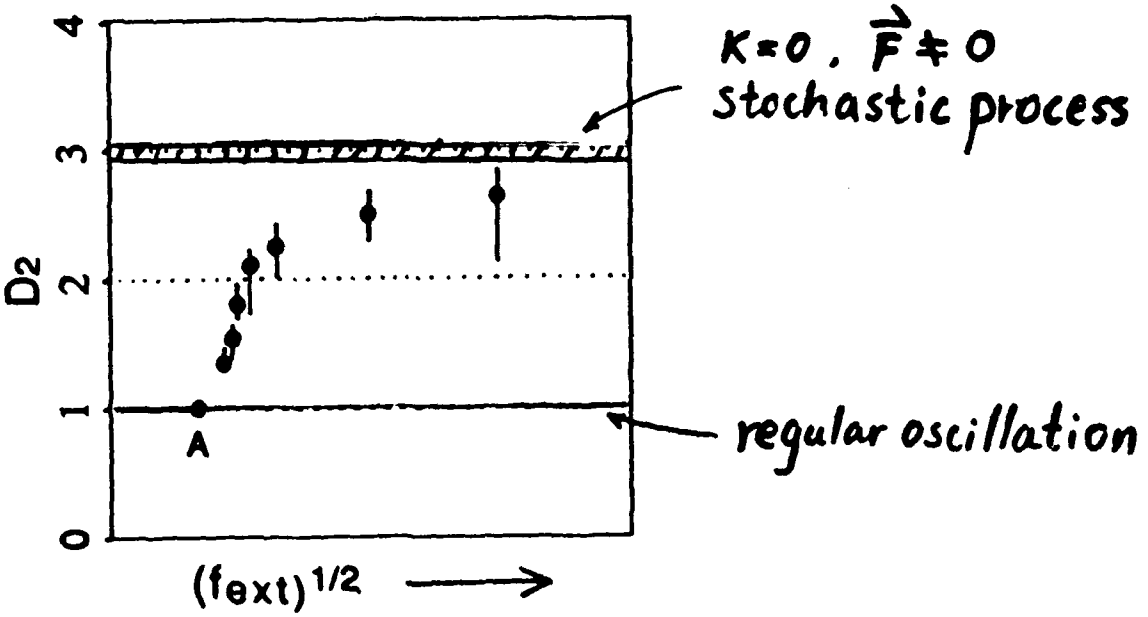
K=0, $\vec{F} \neq 0$
stochastic process
regular oscillation
D2
0
1
2
3
4
A
(fext)1/2

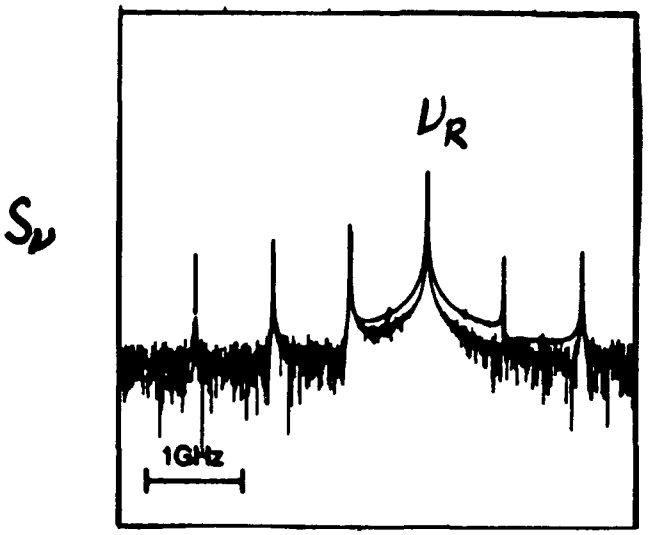
S_ν
ν_R
1GHz

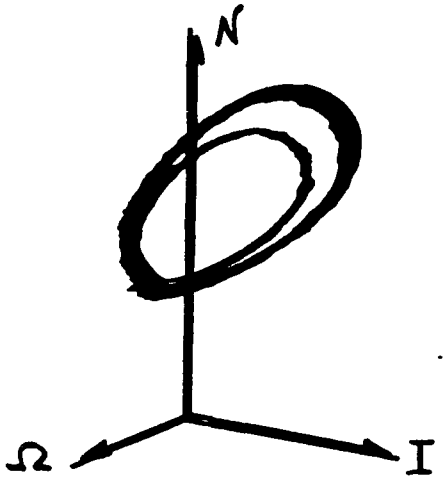
N
Ω
I

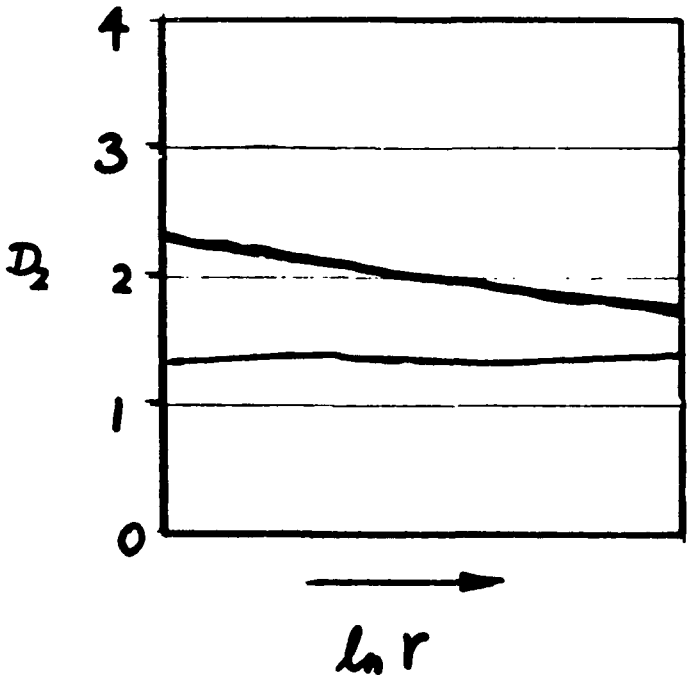
4
3
D_2
2
1
0
ln r

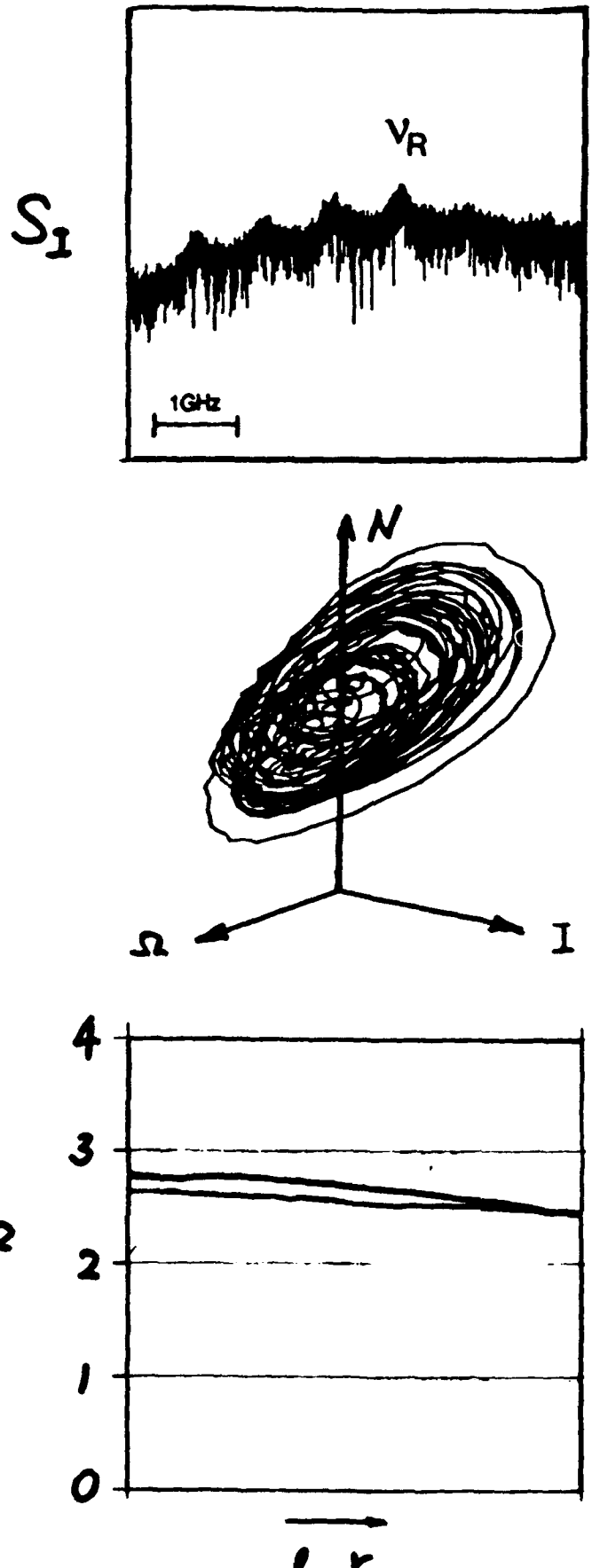
S_I
ν_R
1GHz
N
Ω
I
D_2
4
3
2
1
0
ln r

CONCLUSION

1. a semiconductor laser with weak optical feedback for increasing feedback level undergoes:

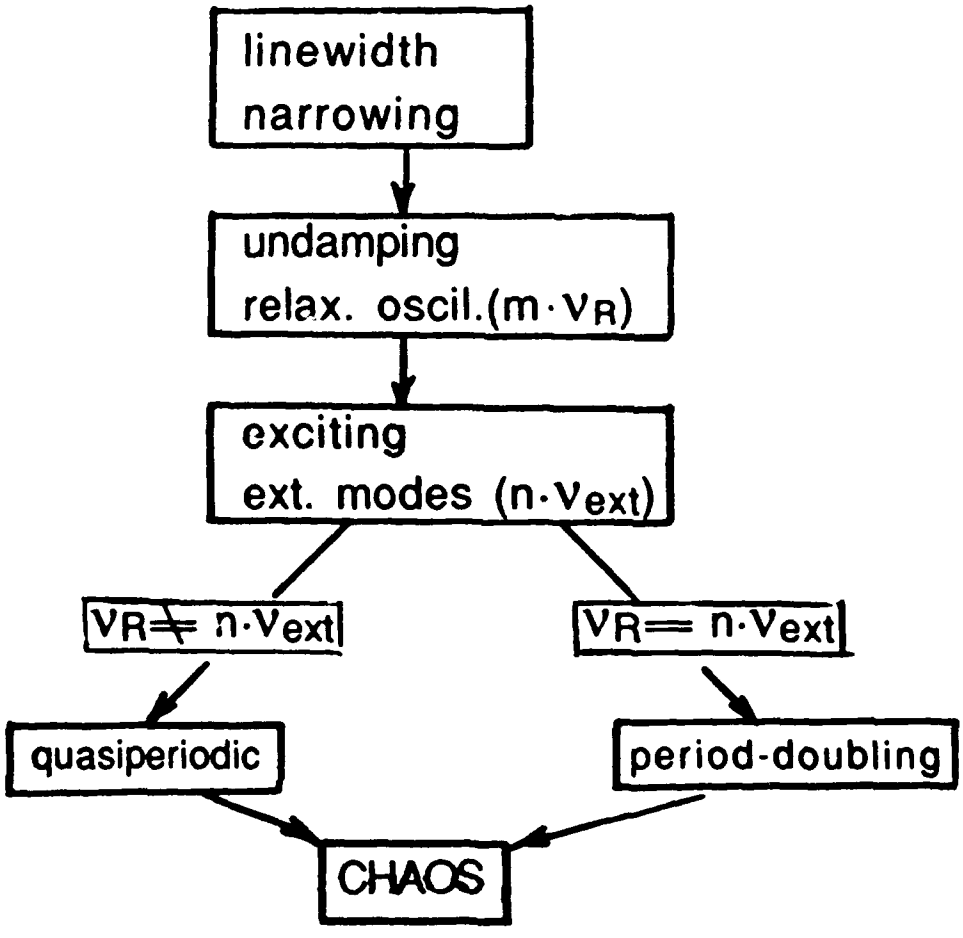

2. White noise with a realistic level does not have strong influence to the dynamics but obscure the details and make the correlation dimension more difficult to determine.

quency modulation (FM) are essential in semiconductor laser based angular modulated coherent optical fiber communication systems. Two-electrode DFB lasers (2E-DFB) show great potentials for all the requirements mentioned above. We report in this paper a study of the FM responses of two-electrode DFB lasers vs the condition that one section (front) is biased to obtain lasing action whereas the other (back) section is moderately biased and modulated.[1]

The 2E-DFB laser is based on an etched mesa buried heterostructure (EMBH) laser with current blocking regions of semi-insulating InP material grown by hydride vapor phase epitaxy.[2] These lasers have both facets cleaved and have about equal length in each section (≈254 μm).

We have studied the FM responses at several I_b such that $I_b \leq I_{b,th}$ and I_f = 100 mA. Two main features are noteworthy. First, the FM sensitivities from 300 kHz up to a few hundred megahertz are uniform. Second, the bandlimited FM sensitivities resemble the responses of an electrical low pass filter. The 3-dB FM bandwidth evolves from 360 MHz at I_b = 10 mA to 900 MHz at I_b = 30 mA, right below $I_{b,th}$. Also the sensitivity reduces from 2 GHz/mA at I_b = 10 mA to 440 MHz/mA at I_b = 30 mA. Thus, both the FM sensitivity and the bandwidth can be altered by varying I_b to satisfy system needs. The general FM response shows drastically different behavior when I_b exceeds $I_{b,th}$. At I_b = 35 mA, when the back section is barely lasing, the FM sensitivity shows a pronounced resonance peak at ≈500 MHz. As I_b is increased further, the relaxation oscillation frequency increases beyond our measurement limit of 3 GHz. Finally, at I_b = 80 mA, the FM response resembles that of a regular DFB laser and exhibits the typical sensitivity dip and a phase reversal around 1 MHz.

1. C. Y. Kuo and N. K. Dutta, "Characteristics of Two-Electrode DFB Lasers," Electron. Lett. 24, 947 (1988).
2. Y. Twu, C. Y. Kuo, J. D. Wynn, R. F. Karlicek, Jr., W. V. Werner, R. L. Brown, and N. K. Dutta, "Two-Electrode DFB Lasers for Optical FSK Heterodyne Systems," unpublished.

11:15 AM
TUP3 Multigigahertz bandwidth FM response of two-electrode DFB lasers

A. E. WILLNER, M. KUZNETSOV, I. P. KAMINOW, U. KOREN, T. L. KOCH, C. A. BURRUS, G. RAYBON, AT&T Bell Laboratories, Crawford Hill Laboratory, Box 400, Holmdel, NJ 07733.

We report the experimental and theoretical characterization of the FM response of a two-section DFB laser emitting at 1.3 μm. Such tunable lasers have emerged as important components for various FDM and FSK optical communication systems. Experimentally determined FM responses for similar structures have been reported previously only for modulation frequencies below ~1 GHz. We extend these measurements of two-section DFB lasers into the multigigahertz frequency range. The FM response magnitude is large and flat for frequencies from 10 kHz up to several hundred megahertz. This is followed by a dip in the response at ~1 GHz and a relaxation resonance peak at a few gigahertz. However, this dip does not limit the speed of the device, as is evident from the flat AM response of this laser at 1 GHz. In proper bias conditions, an FM response magnitude >1 GHz/mA and a 3-dB FM bandwidth of ~5 GHz is demonstrated, including the shallow dip and increased response of the resonance; we believe this to be the widest FM bandwidth reported to date for such lasers. As the bias is increased in the modulated section, the resonance peak becomes damped and moves out to higher frequencies. Both the characteristic response dip found at ~1 GHz and the resonance at a few gigahertz depend strongly on the bias conditions. The laser can be biased in a regime where there is either a red or blue frequency shift with static current tuning. In comparison with the static red-shifted FM response, the blue-shifted response has a more severe dip at ~1 GHz and a strongly damped resonance. Consequently, a blue-shift-bias produces a much lower 3-dB bandwidth than a red-shift bias. The observed behavior is well represented by theoretical curves derived from a small-signal analysis of the coupled rate equations. This model characterizes the laser behavior by only a few parameters; namely, the relaxation frequency, the photon and carrier lifetimes, a damping factor, and the asymmetry between the two sections.

We thus successfully demonstrate and characterize the multigigahertz FM response for two-electrode DFB lasers.

11:30 AM
TUP4 Single-mode semiconductor lasers with optical feedback: a theoretical approach

M. MILANI, U. Milan, Physics Dept., Milan 20133, Italy; F. BRIVIO, G. CHIARETTI, ITALTEL SIT, 20019 Castelletto di Settimo Milanese, Italy.

Different classes of behavior appear in semiconductor laser dynamics depending on the feedback ratio for fixed geometry of the feedback generating system. Feedback is usually reported to give rise to a decrease of the threshold current I_{th} and an increase of the differential quantum efficiency η_D; sometimes it is reported that η_D remains constant. In some experiments it is possible to see that η_D decreases. The response of the system to optical feedback is investigated by means of a microscopic model introduced to describe laser diode dynamics, and their changes, for example, in the presence of a small current modulating signal. As a first approximation the role of the phase of the electromagnetic field is neglected. A unifying way to describe the three different behaviors can be obtained by taking into account the dependence of interband carrier lifetime t_S on optical feedback (i.e., the changes in the photon number inside the optical cavity driven by optical feedback):

$$t_S = [\gamma_s(1 + An_{ph})]^{-1};$$
$$\gamma_s^{-1} = t_S(I = I_{th}).$$

A steady state analysis gives information on I_{th}, η_D, and the characteristic curve: the three classes of behavior are ruled by the sign of a function F linking cavity losses K, feedback ratio f, and coupling B between the actual electromagnetic field and the active cavity:

$$F = K[B(1 - f) - f].$$

11:45 AM
TUP5 Multimode stability analysis of side-mode injection-locked semiconductor lasers

JHY-MING LUO, U. New Mexico, Center for High Technology Materials, Albuquerque, NM 87131; MAREK OSINSKI, U. Tokyo, Research Center for Advanced Science & Technology, 4-6-1 Komaba, Meguro-ku, Tokyo 153, Japan.

Semiconductor lasers with their relatively low-Q Fabry-Perot cavities typically have multimode spectra and poor frequency stability. Injection locking has proved useful in achieving single-mode operation under high-speed modulation and enabling pure amplitude or phase modulation. Compared with a conventional setup, where light is injected into the free-running dominant mode, side-mode injection locking permits us to extend the available range of device parameters such as lasing frequency, linewidth, or modulation bandwith. Also, spectral variation of laser characteristics, e.g., gain or linewidth enhancement factor, can be determined by scanning the injected longitudinal modes of the slave. In our analysis, we use multimode rate equations including a phase equation for the injected mode. The dynamic stability is investigated by considering small fluctuations around the stationary solutions. The results are then compared with a simple single-mode approximation. As an example, a typical index guided 1.54-μm InGaAsP laser is considered. A full multimode stability test confirms the single-mode result that detuning the lasing mode toward the short-wavelength side of the gain peak increases the resonance frequency ν_r. At a pumping level 20% above the free-running threshold, the maximum enhancement of ν_r occurs three mode spacings away from the central mode. An additional benefit is that optical injection enhances the field damping, thereby narrowing the spectral linewidth, increasing modal stability, and reducing the dynamic frequency chirp. We conclude that the side-mode injection locking may be useful for such uses as optical communication, fast switching, and ultrashort pulse generation.

1989

ANNUAL MEETING
OPTICAL SOCIETY OF AMERICA
TECHNICAL DIGEST

Summaries of papers
presented at the Annual Meeting of the Optical Society of America

15–20 October 1989
Orlando, Florida

Conference Edition

Optical Society of America
1816 Jefferson Place, NW
Washington, DC 20036
(202) 223-8130

inversionless amplification can occur with any nonvanishing number of atoms in the upper level. This latter configuration is, therefore, more interesting for inversionless amplification.

1. O. Kocharovskaya and P. Mandel, Phys. Rev. A 42, 523 (1990).

QWD28 Phase-driven dynamics of a multimode semiconductor laser

C. Etrich, Paul Mandel, N. B. Abraham,* and H. Zeghlache†
Optique Nonlinéaire Théorique, Université Libre de Bruxelles, Campus Plaine C.P. 231, B-1050 Bruxelles, Belgium

We derive the following set of equations to describe a two-mode semiconductor laser:

$$\partial_\tau E_1 = -E_1 + (1 - i\alpha)A(E_1F + E_2G^*),$$
$$\partial_\tau E_2 = -(\chi - i\delta)E_2 + (1 - i\alpha)A(E_2F + E_1G),$$
$$\partial_\tau F = \gamma - \gamma(1 + |E_1|^2 + |E_2|^2)F - \gamma(E_1E_2^*G + E_1^*E_2G^*),$$
$$\partial_\tau G = -\gamma(1 + |E_1|^2 + |E_2|^2)G - \gamma E_1^*E_2F, \quad (1)$$

where $\chi = \chi_1/\chi_2$ is the ratio of the decay rates of the electric fields E_1 and E_2; it is fixed to be larger than unity. γ is proportional to the decay rate of the population inversion., A is the pump, α is the linewidth enhancement factor, and $\tau = \chi_1 t$ is the scaled time. E_1 and E_2 are complex, so the phase dynamics are fully included in Eqs. (1). The variables F and G are related to the population inversion. The steady-state solutions of Eqs. (1) are the trivial solution

$$E_1 = E_2 = 0, \quad G = 0, \quad F = 1 \quad (2)$$

and the two single-mode solutions

$$E_1 = \sqrt{A - 1}\exp(-i\Omega_1\tau), \; E_2 = 0, \; G = 0, \; F = 1/A, \quad \Omega_1 = \alpha, \quad (3)$$

$$E_2 = \sqrt{A/\chi - 1}\exp(-i\Omega_2\tau), \; E_1 = 0, \; G = 0, \quad F = \chi/A, \quad \Omega_2 = \alpha\chi - \delta, \quad (4)$$

which exist for $A > 1$ and $A > \chi$, respectively. There are also two-mode solutions with both electric fields different from zero and oscillating with different frequencies. The steady-state solutions are steady in the sense that the corresponding intensities are constant. If we neglect the phase interaction in Eqs. (1), i.e., cancel G, Eqs. (3) and (4) remain solutions and no two-mode solutions can be found. In this case a linear stability analysis around the single-mode solutions shows that Eqs. (3) are always stable and Eqs. (4) are always unstable. No instabilities occur on either branch. On the contrary, when we deal with the full Eqs. (1), the generic situation is that Eqs. (3) become unstable by a Hopf bifurcation (A_1) and restabilize for a sufficiently high pump. Because this restabilization occurs at a relatively high value of A, this point is not considered here. On the branch of solutions of Eqs. (4), up to three Hopf bifurcation points (A_2, A_3, and A_4) may be found. The mode of Eqs. (4) can be stable between A_2 and A_3 and eventually stabilizes for sufficiently high pump at A_4.

Figure 1 gives a typical example of the relative position of the Hopf bifurcation points A_i in the parameter plane (χ, δ). The boundaries where A_1 is equal to either A_2 or A_3 are shown, as well as the lines of degeneracy where two of the A_i on the branch of solutions of Eqs. (4) coincide. The topology of the boundaries in this parameter plane changes neither with γ nor with α where $4 \le \alpha \le 5$. Two-mode solutions emerge from the Hopf bifurcations A_i. Figure 2 shows an example for $A_1 < A_2$ with a stable branch of two-mode solutions connecting A_1 and A_2. The branch of two-mode solutions emerging from A_3 connects to A_4, which is very large in this case. There is an interval of instability on this branch that is marked by a pair of Hopf bifurcations (A_5, A_6). The restabilization at A_6 occurs for relatively high pump. A_5 and A_6 are connected by a stable branch of quasi-periodic solutions that are governed by one additional frequency, the frequency appearing at one of the Hopf bifurcations.

*Department of Physics, Bryn Mawr College, Bryn Mawr, Pennsylvania 19010.
†Laboratoire de Spectroscopie Hertzienne, USTL 1, 59655 Villeneuve d'Ascq, France.

QWD29 Simulation of field-noise spectra in injection-locked semiconductor lasers

Jhy-Ming Luo and Marek Osiński
Physical Optics Corporation, 20600 Gramercy Place, Torrance, California 90501

There has been growing interest recently in application of injection-locking techniques to semiconductor lasers. A primary motivation for these studies is the prospect of applying injection-locked lasers to coherent optical communication systems. The performance of such systems is greatly influenced by the noise characteristics of the light source. Recently, we reported[1] on numerical investigations of diode-laser frequency-noise spectra under external signal injection. In particular, we examined side-mode injection locking, in which the target mode differs from the free-running dominant mode, and we showed that it is possible to achieve considerable reduction in frequency noise in the low-frequency regime. Here we describe the first multimode numerical studies of field-noise spectra in injection-locked semiconductor lasers. Field-noise spectra are important because they carry direct information about linewidth and line shape.

In the simulations, we consider InGaAsP/InP index-guided master and slave lasers emitting at ~ 1.54 μm, with the respective linewidth enhancement factors of 4 and 5.5. The master oscillator wavelength is adjusted to match various modes of the slave laser. First, stationary solutions of the multimode rate equations without any noise terms are found for both the master and slave oscillators. These solutions are then used as initial conditions in simulations of temporal evolution with Langevin noise terms included. The temporal behavior of the master laser is found first to provide an injected signal with a noise component. Two longitudinal modes are included, with the side-mode intensity 20 dB lower than that of the peak mode. Hence, in addition to the spontaneous-emission noise and electron-population fluctuations, the injected signal also contains partition noise. The multimode stochastic rate equations with external injection terms[2] are then solved for the slave laser, with 11 modes included in the calculations. This allows us to investigate side-mode injection locking and the competition between the target mode and the dominant free-running mode. The field-noise spectra are obtained from the time-dependent solution by a fast Fourier transform algorithm.

We start by performing a small-signal analysis without the noise terms, which indicates that the stable locking bandwidth can be increased significantly by injection into a side mode. As shown in Fig. 1, the stable locking range is predicted to increase with the detuning from the gain peak. This implies that better locking and eased operational tolerances can be expected with side-mode injection. This prediction is confirmed by numerical simulation of noise spectra with different target modes. Although the noise spectra for the peak-mode injection indicate poor locking of the free-running dominant mode (Fig. 2), the field-noise spectrum of the slave laser is almost a replica of the master oscillator when mode +3 (short-wavelength side of the gain spectrum) is chosen (Fig. 3). Contrary to noiseless small-signal calculations, however, the locking quality degrades when higher detuning is attempted, which demonstrates the importance of noise effects.

In summary, the first multimode numerical simulations of field-noise spectra in injection-locked diode lasers are reported. Small-signal predictions of improved locking are verified, and an optimal target mode is identified. We demonstrate that by proper choice of the injected mode, it is possible to achieve nearly perfect locking. The results are consistent with our earlier calculations of frequency-noise spectra. To our best knowledge, these are the first calculations of field-noise spectra for injection-locked semiconductor lasers.

1. J.-M. Luo and M. Osiński, in *Technical Digest, International Quantum Electronics Conference* (Optical Society of America, Washington, D.C., 1990), paper QThI25.
2. N. Schunk and K. Petermann, IEEE J. Quantum Electron. QE-22, 642 (1986).

QWD30 Orthogonal-field noise coupling in the half-waveplate/polarizer attenuator

Brian H. Kolner
Hewlett-Packard Laboratories, P.O. Box 10350, Building 26M16, Palo Alto, California 94303-0867

The conventional optical attenuator for linearly polarized light is constructed with a half-wave retardation plate and a polarizer and works by rotating incident linearly polarized light so that the power transmitted by the polarizer has a $\cos^2 2\theta$ dependence, where θ is the angle between the optic axis of the waveplate and the incident electric field vector. If the incident light is not completely linearly polarized, but has a small orthogonal component, then as the waveplate is rotated to reduce the net power, the unwanted orthogonal field component is increased as measured past the polarizer. Hence, the net power does not go to zero.

Now, consider the nature of the transmitted power when amplitude fluctuations on the two orthogonal components are included. When $\theta = 0$, the noise results entirely from the main polarization field, and when $\theta = 45°$, the noise results only from the weaker orthogonal field. In many cases, lasers are constructed with intracavity loss elements that are polarization dependent, so the laser tends to operate in a single polarization. However, light emerging from the cavity in the unwanted polarization will be much closer to threshold (above or below) and will have a larger relative noise component.[1] Hence, as the attenuator reduces the optical power and the contribution of the quieter polarization field, the contribution of the noisier unwanted field is enhanced. We thus have the interesting situa-

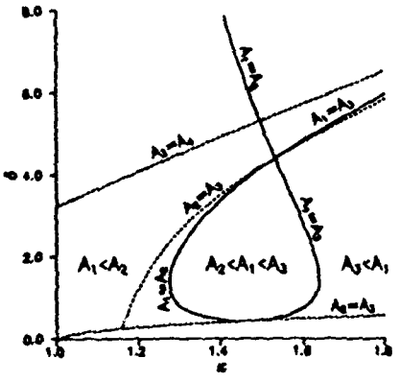

QWD28 Fig. 1. Boundaries where A_1 is equal to either A_2 or A_3 (solid lines) and loci of degeneracy where two of the A_i on the branch of solutions of Eqs. (4) coincide (dashed lines) for $\lambda = 0.15$ and $\alpha = 4$.

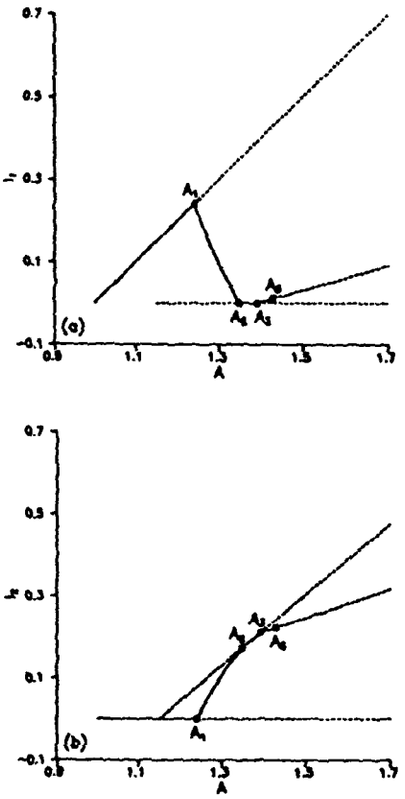

QWD28 Fig. 2. Bifurcation diagram showing the intensities I_1 and I_2 of the single-mode and two-mode solutions versus the pump A for $\chi = 1.15$, $\delta = 0.8$, $g = 0.15$, and $\alpha = 4$. A branch of stable quasiperiodic solutions emerges from A_5.

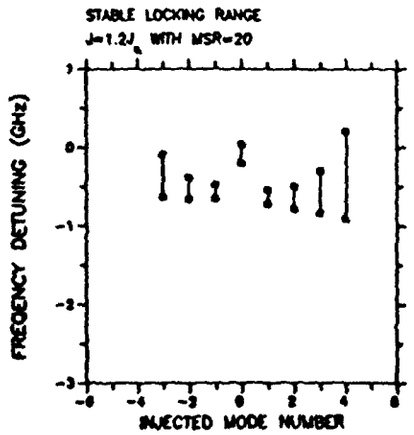

QWD29 Fig. 1. Stable locking range for various injected modes at the bias level of 20% above the free-running threshold, calculated by small-signal analysis. The optical injection level for each mode is such that a zero-phase mode-suppression ratio of 20 is maintained.

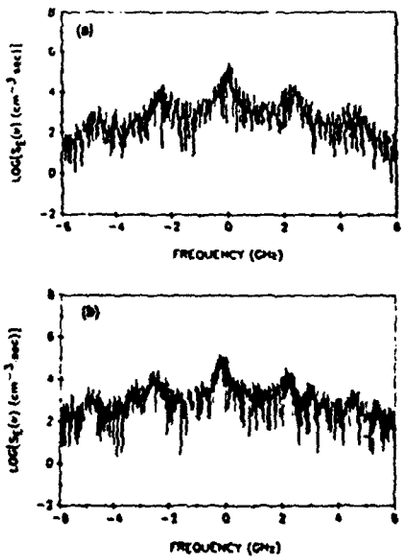

QWD29 Fig. 2. Field-noise spectra of slave laser (a) under free-running conditions and (b) under the peak-mode injection with relative injection levels to achieve a mode-suppression ratio of 20. The slave laser is biased at $1.2I_{th}$, and the master is biased at $1.5\ I_{th}$.

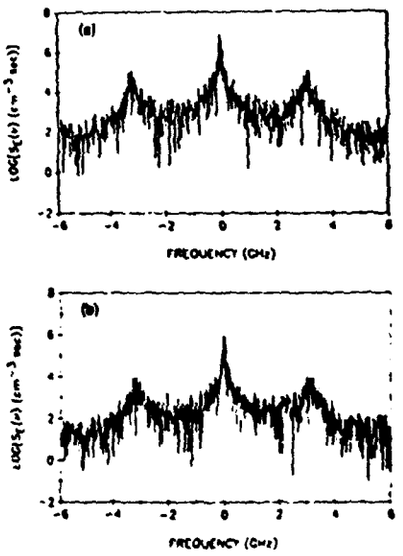

QWD29 Fig. 3. Field noise spectra of (a) the master laser biased at $1.5\ I_{th}$ and (b) the slave laser biased at $1.2\ I_{th}$, injected into mode 3. The injection level is such that a mode-suppression ratio of 20 is achieved between the target mode and the free-running gain-peak mode.

Poster Wednesday

Marek Osiński

Conference on Quantum Electronics Laser Science

1991 Technical Digest Series Volume 11

Conference Edition

Summaries of papers presented at the
Conference on Quantum Electronics
Laser Science
May 12–17, 1991
Baltimore, Maryland

Sponsored by:
American Physical Society
IEEE/Lasers and Electro-Optics Society
Optical Society of America
in cooperation with
Quantum Electronics Division of the European Physical Society
Japanese Quantum Electronics Joint Group

Optical Society of America
2010 Massachusetts Ave., NW
Washington, DC 20036

Articles in this publication may be cited in other publications. In order to facilitate access to the original publication source, the following form for the citation is suggested:

Name of Author(s), Title of Paper, in Quantum Electronics Laser Science, 1991 Technical Digest Series (Optical Society of America, Washington, D.C. 1991), pp. xx-xx.

ISBN Number

Conference Edition	1-55752-190-5 (softcover)
Postconference Edition	1-55752-191-3 (hardcover)
1991 Technical Digest Series	1-55752-192-1 (hardcover)

Library of Congress Catalog Card Number

Conference Edition	90-63173
Postconference Edition	90-63172

IEEE Catalog number: 91CH2946-2

Copyright © 1991, Optical Society of America

Individual readers of this digest and libraries acting for them are permitted to make fair use of the material in it, such as to copy an article for use in teaching or research, without payment of fee, provided that such copies are not sold. Copying for sale is subject to payment of copying fees. The code 1-55752-192-1/91/$2.00 gives the per-article copying fee for each copy of the article made beyond the free copying permitted under Sections 107 and 108 of the U.S. Copyright Law. The fee should be paid through the Copyright Clearance Center, Inc., 21 Congress Street, Salem, MA 01970. Permission is granted to quote excerpts from articles in this digest in scientific works with the customary acknowledgment of the source, including the author's name and the name of the digest, page, year, and name of the Society. Reproduction of figures and tables is likewise permitted in other articles and books provided that the same information is printed with them, permission of one of the original authors is obtained, and notification is given to the Optical Society of America. Republication or systematic or multiple reproduction of any material in this digest is permitted only under license from the Optical Society of America; in addition, the Optical Society may require that permission also be obtained from one of the authors. Address inquiries and notices to the Director of Publications, Optical Society of America, 2010 Massachusetts Avenue, NW, Washington, DC 20036. In the case of articles whose authors are employees of the United States Government or its contractors or grantees, the Optical Society of America recognizes the right of the United States Government to retain a nonexclusive, royalty-free license to use the author's copyrighted article for United States Government purposes.

Printed in the U.S.A.

Comparison of the power generated by various heat sources, obtained by integrating local yields over the respective layers, reveals the most important heat sources in the device. In contrast to edge-emitting lasers, the active-region heating dominates only at relatively small values of pumping current. At large current levels, Joule heating in the *P*-AlGaAs layer becomes the single most important heat source. The aggregate effect of Joule heating in all layers is the dominant heat source over the entire current range considered ($2I_{th}$ - $4I_{th}$).

We have also investigated the effect of changing various structural parameters on thermal behavior of etched-well VCSELs. It will be shown that excessive heating can be reduced substantially by simple technological improvements in the device design.

MICROSTRUCTURE OF $InAs_xSb_{1-x}$ INFRARED DEVICES

S. Chadda, A. K. Datye, Department of Chemical Engineering, University of New Mexico, Albuquerque, NM 87131 and L. R. Dawson, Sandia National Laboratories, Albuquerque, NM 87185.*

III-V alloy devices are being considered for applications as infrared detectors, by several research groups due to processing advantages over II-VI alloy devices. $InAs_{0.4}Sb_{0.6}$ has the lowest band gap at 77 K among all III-V compounds, which corresponds to a cut off wavelength of 9 μm. The use of strained layer superlattices (SLS) was first proposed by Osboum[1] for lowering the band gap and achieving absorption at wavelengths greater than 12 μm at 77 K. Devices were grown by Molecular Beam Epitaxy (MBE) and consisted of a p-n junction embedded in a $InAs_xSb_{1-x}$/InSb SLS with layers of equal thickness. The active device SLS was grown on a composition graded strain relief buffer on (100) face of InSb substrates. The samples were sliced, thinned, polished, dimpled and ion milled for making cross-section Transmission Electron Microscope (TEM) samples. This paper will discuss various types dislocations nucleating due to misfit strain in this system. Further it will correlate the growth conditions with dislocation density, type of dislocations, and electrical properties of the device.

[1]G. C. Osboum, J. Vac. Sci. Technol. B (1984) 2 (2), 176.

DISTRIBUTED-FEEDBACK GaAs/AlGaAs/AlAs VERTICAL-CAVITY SURFACE-EMITTING LASER WITH RESONANT-PERIODIC-GAIN ACTIVE REGION

Mohammad Mahbobzadeh, Emmanuelle Gandjbakhch, Eric A. Armour, Kang Zheng, Shang-Zhu Sun, Christian F. Schaus, and Marek Osinski, Center for High Technology Materials, University of New Mexico, Albuquerque, New Mexico 87131-6081.*

Dramatic progress in vertical-cavity surface-emitting lasers (VCSELs) achieved over the last two years brought forth a variety of novel device structures. Significant new concept, resulting in gain enhancement along the vertical direction, was the replacement of a bulk active region with thin (single- or multiple-quantum-well) layers in a carefully designed Bragg resonator such that the active layer would coincide with an antinode of laser radiation. VCSELs with a single active region satisfying this resonant condition are often called microlasers. A generalization of the microlaser concept, consisting in extending its active region to multiple layers separated by half-wave spacers, results in distributed-Bragg reflector resonant-periodic-gain (DBR-RPG) lasers. The most recent advance in RPG laser structures is a distributed-feedback resonant-periodic-gain (DFBRPG) VCSEL, where an RPG active region is intercalated with the multilayer high reflectors (MHRs). The new design eliminates the need for end reflectors in DBR-RPG structures and reduces the total thickness of the device, while retaining all characteristic features of RPG medium.

Our first DFB-RPG VCSEL laser has been fabricated by MOCVD in a single growth cycle. The structure, designed for operation at n = 1 subband transition, consists of a stack of 10-nm thick GaAs single quantum wells separated by halfwave AlAs/$Al_{0.15}Ga_{0.85}As$ spacers. The total device thickness of the DFB-RPG is ~5.5 μm. For the sake of comparison, a DBR-RPG laser with the same cumulative active medium thickness and MHR reflectivities would be almost two times thicker (~10.5 μm). A direct consequence of shorter cavity length is increased longitudinal mode spacing. Compared to an equivalent DBR-RPG device, a remarkable difference between the two structures is the absence of any side modes within the entire high-reflectivity band of the DFB-RPG laser.

The as-grown wafers were optically excited using the 740 nm line of Ar-ion-pumped dye laser, with the pumping beam diameter of 10 μm. Even though no heat sink was used, the cw output power of 7 mW is considerably higher than that obtainable from single-quantum-well microlasers, while it is comparable to that of DBR-RPG devices.

BROAD-AREA MODE-COUPLING MODEL FOR CARRIER-GUIDED DIODE LASER ARRAYS

Marek Osiński and Chung-Pin Cherng, Center for High Technology Materials, University of New Mexico, Albuquerque, New Mexico 87131-6081.*

The objective of this paper is to demonstrate suitability of a broad-area mode-coupling approach to describe modal properties of carrier-guided semiconductor laser arrays. The supermode theory often adopted to explain modal behavior of phased array lasers is suitable only for index-guided arrays, since it requires a basis of individual waveguide modes. For carrier-guided arrays, with no built-in lateral variation of refractive index, such approach fails to predict correctly the number of system modes and their relative gains. It is more appropriate to treat the carrier-guided array as a perturbed broad-area laser, since the number of lateral modes is not limited in this case by the number of array elements. Recently, a simple model of carrier-guided arrays was proposed, based on the standard perturbation theory. It assumes an infinite loss outside the active region and ignores differences between modal gains of all the unperturbed (broad area) modes, claiming that these simplifications would not affect the results significantly. In this paper, we show that either of these assumptions has important consequences on the calculated modal gains for the array modes.

Rather than using the perturbation theory, we follow the coupled mode formulation, but with a basis of broad-area modes instead of individual waveguide modes. An active broad-area waveguide is considered, with the gain-index coupling as well as spatially averaged temperature effects included. The perturbation due to array structure is assumed in form a raised sinusoidal modulation of permittivity, with gain maxima at stripe centers. A smooth half-period cosine profile of temperature is also included in the perturbation.

As an example, we consider a 10-stripe GaAs/AlGaAs carrier-guided array similar to commercially available devices (SDL-2410C, 6-μm stripes on 10-μm centers, multiple-quantum-well active region). A comparison of the present theory with earlier simplified perturbation analysis corresponding to a limit of very high loss and constant reveals that the previous treatment is unreliable in predicting the modal gains of high-order array modes (mode number larger than the number of emitters). It should be emphasized that these high-order modes usually dominate in carrier-guided arrays, hence precise knowledge of their modal gains is very important in considerations of mode ordering and mode suppression schemes.

Our results reveal that earlier agreement between the simplified model and experimental observations was fortuitous. On the other hand, broad-area coupled-mode theory can contribute to improved understanding of array laser behavior and constitutes an important design and interpretation tool.

OPERATOR ORDERING IN EFFECTIVE-MASS HAMILTONIAN FOR SEMICONDUCTOR SUPERLATTICES AND QUANTUM WELLS

Mohammad Moiahedie and Marek Osiński, Center for High Technology Materials, University of New Mexico, Albuquerque, New Mexico 87131-6081.*

In recent years, effective-mass theory has been used extensively as a computational tool for determining electronic states and other properties of abrupt heterostructures, superlattices, and quantum wells. It has been recognized that application of the effective mass theory to abrupt interfaces between different materials suffers from ambiguity in kinetic energy operator ordering, caused by non-vanishing commutator of the momentum operator and the position-dependent effective mass $m(z)$. This leads to non-uniqueness of Hamiltonian, which in its general form can be written as

Meeting Program

Third Annual Symposium on Ceramics and Advanced Materials

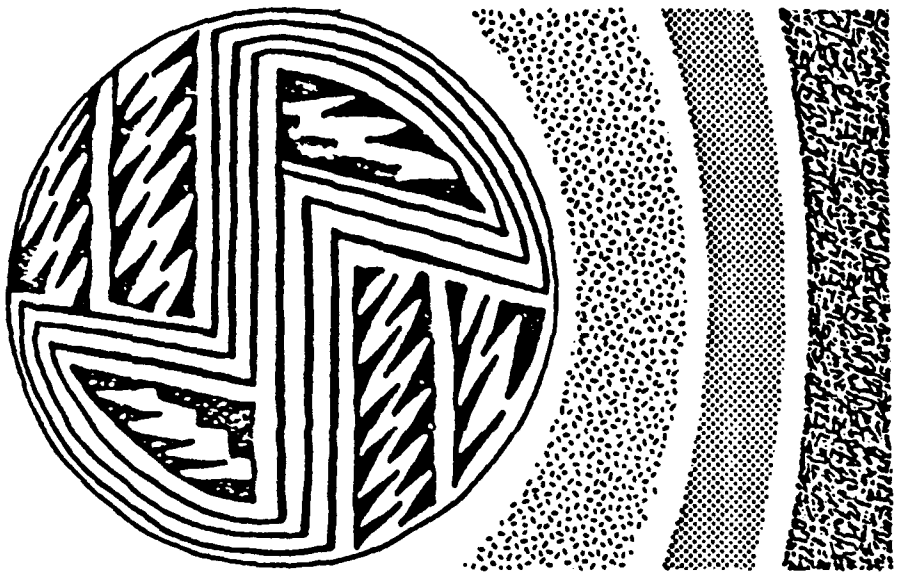

Hyatt Regency Hotel
Albuquerque, NM
October 24-25, 1991

Sponsored by:

The New Mexico Sections of the
American Ceramic Society and
the Materials Research Society

Accepted for QELS'92 Conf. Quantum Electron. & Laser Science, Anaheim, CA, May 10-15, 1992

HIGH-POWER-DENSITY PULSED OPERATION OF DISTRIBUTED-FEEDBACK VERTICAL-CAVITY SURFACE-EMITTING LASER WITH RESONANT-PERIODIC-GAIN ACTIVE REGION

by

MOHAMMAD MAHBOBZADEH and MAREK OSIŃSKI

Center for High Technology Materials, University of New Mexico, Albuquerque, New Mexico 87131-6081

Corresponding author: Professor Marek Osiński,
Center for High Technology Materials,
University of New Mexico,
Albuquerque, New Mexico 87131-6081.
Tel. (505) 277-6031
Fax (505) 277-6433

Abstract

Distributed-feedback resonant-periodic-gain surface-emitting lasers are pumped optically. The output power of 8.5 W over 7 ns pulsewidth with power conversion efficiency of 10.5% is achieved. This corresponds to a record peak-power density of 4.5 MW/cm^2.

HIGH-POWER-DENSITY PULSED OPERATION OF DISTRIBUTED-FEEDBACK VERTICAL-CAVITY SURFACE-EMITTING LASER WITH RESONANT-PERIODIC-GAIN ACTIVE REGION

by

MOHAMMAD MAHBOBZADEH and MAREK OSIŃSKI

Center for High Technology Materials, University of New Mexico,

Albuquerque, New Mexico 87131-6081

Corresponding author: Professor Marek Osiński,

Center for High Technology Materials,

University of New Mexico,

Albuquerque, New Mexico 87131-6081.

Tel. (505) 277-6031

Fax (505) 277-6433

Vertical-cavity surface-emitting semiconductor lasers (VCSELs) are very attractive for applications in optical computing, image processing, free-space communications, and high-power two-dimensional arrays. Conventional VCSELs with bulk active regions suffer, however, from low external efficiency and consequently low output power. The primary reason for their poor performance is the competition between the desirable vertical emission and parasitic amplified spontaneous emission (ASE) in the transverse directions. In order to reduce the lasing threshold and suppress the ASE, two concepts of VCSELs with quantum-well (QW) active regions have been pursued in parallel: a resonant-periodic-gain (RPG) structure, with multiple active layers spaced at half the wave-

length of a selected optical transition[1-2], and a microresonator structure[3], with a single QW placed in a Bragg resonator. Both designs achieve gain enhancement in the vertical direction by aligning the active regions with the maxima of the longitudinal mode pattern at the emission wavelength. Recently, a new distributed-feedback (DFB) structure for RPG VC-SELs has been proposed[4]. In that design, illustrated in Fig. 1, the QW active regions are interspersed within a stack of quarter-wave layers that form multilayer high reflectors (MHRs). The new design eliminates the need for end reflectors in the previous RPG structures and reduces the total thickness of the device, while retaining the characteristic features of RPG medium (gain enhancement in vertical direction, wavelength selectivity, ASE suppression, *etc.*).

Our DFB-RPG VCSEL GaAs/AlGaAs/AlAs laser was fabricated by MO-CVD. The device consists of a stack of 10-nm thick GaAs single quantum wells separated by half-wave AlAs/$Al_{0.15}Ga_{0.85}As$ spacers. The whole structure contains 42.5 periods, of which 24 are at the GaAs substrate side and 18.5 at the top. Calculated reflectivities of the lower and upper reflectors, separated by a half-wave $Al_{0.15}Ga_{0.85}As$ phase shifter, are 99.76% and 99.56%, respectively. The output light is collected through the top reflector.

The total thickness of the structure described above is ~5.5 μm. For the sake of comparison, a distributed Bragg reflector (DBR) RPG laser with the same cumulative active medium thickness and MHR reflectivities would be almost two times thicker (~10.5 μm).

The as-grown wafers were optically pumped through the top mirror. Under cw conditions, thermally limited output power of 6.7 mW was obtained with 10-μm diameter of the pumping beam. A Q-switched pumped dye laser operating at 740 nm was used for high-power pulsed pumping. Fig. 2 shows the input/output characteristic for pulsed conditions (7 ns pulse duration, 10 Hz repetition rate). The efficiency of conversion of

the estimated absorbed pump power into the lasing output emitted through the top surface was ~10%. Using a measured lasing spot size of ~16 μm, the maximum peak output power of 8.5 W corresponds to ~4.5 MW/cm^2. It is approximately one order of magnitude higher than the maximum power density obtained from DBR-RPG lasers under similar pumping conditions[5].

In conclusion, DFB-RPG laser structure is very promising for high-power applications. While the total device thickness is comparable to that of a microlaser, a multiplicity of active layers results in a record-high pulsed output power. Preliminary data obtained on optically pumped bare wafer DFB-RPG samples without any heat sinking illustrate the tremendous potential of these devices. To our best knowledge, the peak power density of 4.5 MW/cm^2 is the highest ever reported for any semiconductor laser.

References

1. M. Y. A. Raja, S. R. J. Brueck, M. Osinski, C. F. Schaus, J. G. McInerney, T. M. Brennan, and B. E. Hammons, IEEE J. Quantum Electron. 25, 1500 (1989).
2. S. W. Corzine, R. S. Geels, J. W. Scott, R. H. Yan, and L. A. Coldren, IEEE J. Quantum Electron. 25, 1513 (1989).
3. J. L. Jewell, Y. H. Lee, A. Scherer, S. L. McCall, N. A. Olsson, J. P. Harbison, and L. T. Florez, Opt. Eng. 29, 210 (1990).
4. M. Mahbobzadeh and M. Osiński, Electron. Lett. 26, 1716 (1990).
5. C. Wu and J. G. McInerney, *Techn. Digest, OSA '91 Annual Meeting*, San Jose, CA, Nov. 3-8, 1991, Paper MHH6, p. 38.

Figure Captions

Fig. 1. Schematic illustration of the DFB-RPG layer structure, corresponding intensity distribution of resonant mode, and refractive index profile. Thick lines (A) represent high-index quantum-well active layers, unshaded regions (B) - intermediate-index quarter-wave spacers, unshaded region C - half-wave phase shifter, shaded regions (D) - low-index quarter-wave spacers. λ_r - resonant wavelength.

Fig. 2. Input/output energy and power-density characteristic of the DFB-RPG laser pumped by 7 ns pulses at 10 Hz repetition rate.

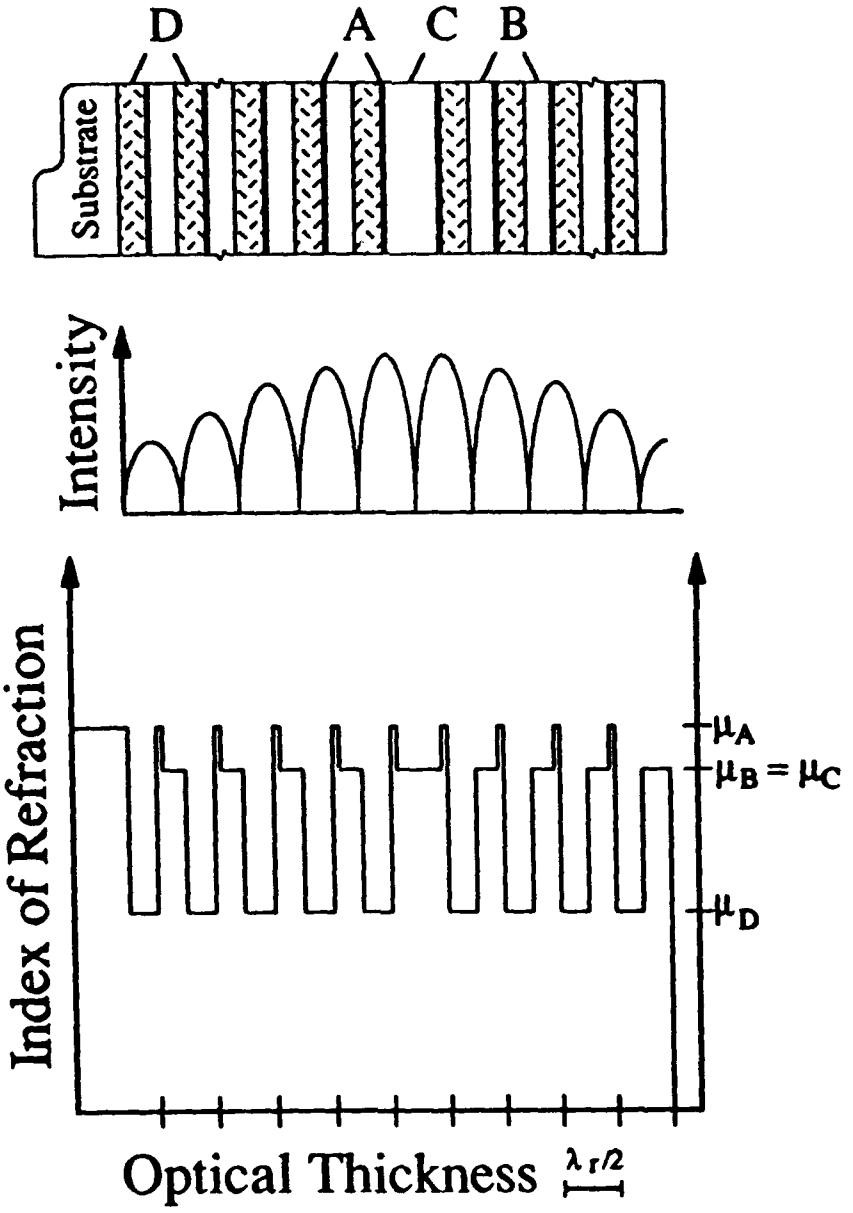
D
A
C
B
Substrate
Intensity
Index of Refraction
μ_A
$\mu_B = \mu_C$
μ_D
Optical Thickness
$\lambda_r/2$

Figure 1

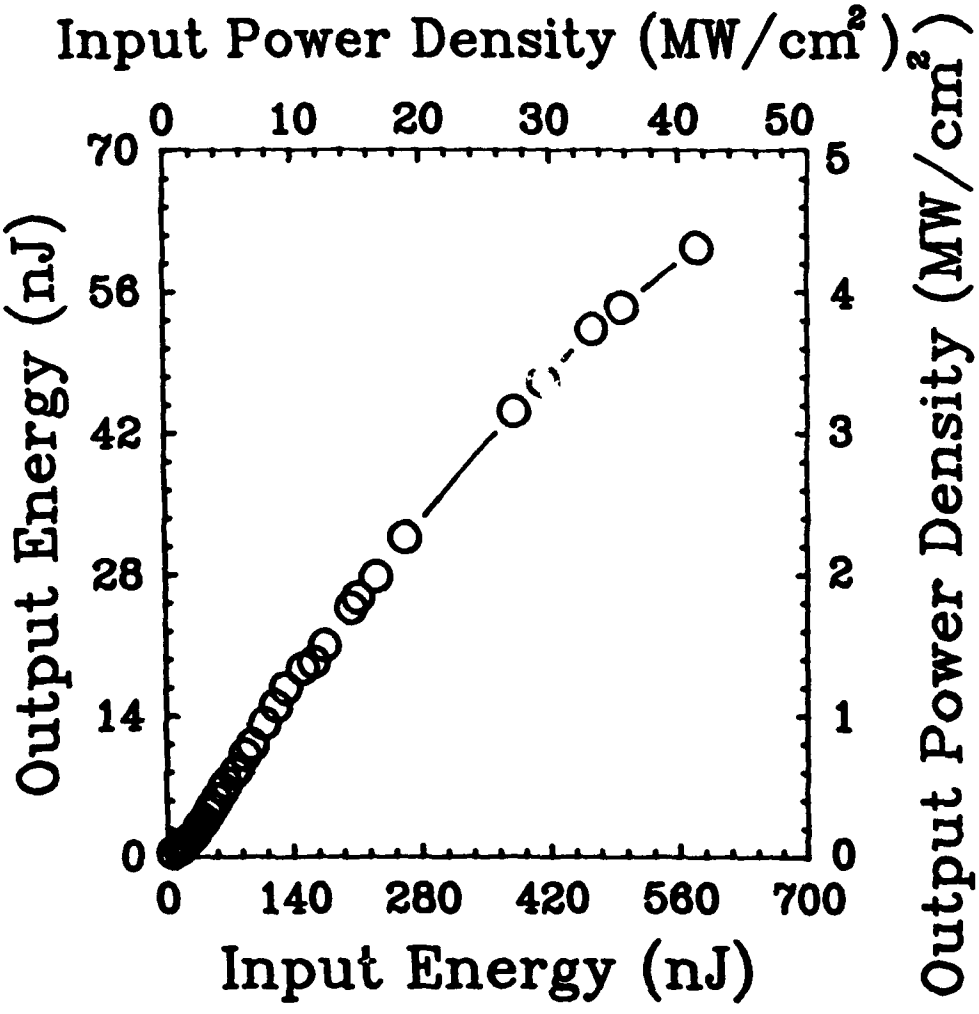
Input Power Density (MW/cm²)
0
10
20
30
40
50
70
56
42
28
14
0
Output Energy (nJ)
5
4
3
2
1
0
Output Power Density (MW/cm²)
0
140
280
420
560
700
Input Energy (nJ)

Figure 2

Submission to CLEO '92 Symposium on Optical Switching, Logic and Storage

Absorptive optical bistability and switching in MQW etalons with optical half-wave periodicity

Donald L. McDaniel Jr. and John G. McInerney*

Optoelectronic Device Physics Group

Center for High Technology Materials

University of New Mexico

Albuquerque, NM 87131-6081.

* Corresponding author. Tel. (505) 277-0768, -3317; Fax (505) 277-6433

ABSTRACT

Low-threshold bistable optical elements and saturably absorbing switches are possible using excitonic absorption in multiple quantum wells spaced by one-half the optical wavelength. For GaAs/AlGaAs etalons with twenty 10-nm quantum wells, thresholds may be as low as 18 W cm^{-2}.

Absorptive optical bistability and switching in MQW etalons with optical half-wave periodicity

Donald L. McDaniel Jr. and John G. McInerney

Optoelectronic Device Physics Group

Center for High Technology Materials

University of New Mexico

Albuquerque, NM 87131-6081.

SUMMARY

Optical bistability (OB) in passive nonlinear etalons such as those containing multiple quantum wells (MQW) of GaAs/AlGaAs is a promising alternative to other bistable optical switching mechanisms such as those which occur in semiconductor lasers and laser amplifiers [1]. Although OB in passive nonlinear etalons is somewhat slower, it is much more easily extendable to one- and two-dimensional arrays of switches. To realize this advantage, it is necessary to minimize the switching thresholds and optical absorption (and hence the power dissipation) in the MQW etalon. Following an approach which has already proven successful in reducing thresholds and increasing power efficiencies of vertical-cavity surface-emitting semiconductor lasers (VCSELs) [2], here we consider a resonant periodic absorption (RPA) device, consisting of an etalon enclosing several absorbing layers - ideally single quantum wells or closely-spaced groups of quantum wells - spaced one-half wavelength apart and positioned so that they align optimally with the antinodes of the standing wave optical field in the etalon.

We have analyzed the GaAs/GaAlAs RPA structure numerically using a wave propagation model in a thin-film matrix formalism [3]. The spacers are assumed to have constant indices, the unsaturated QW absorption α_0 follows the semi-empirical description of Chemla *et al.* [4], and the excitonic features saturate according to the simple rule $\alpha(I) = \alpha_0/(1 + I/I_{sat})$. In contrast to the situation where optically-pumped lasing occurs, here the spacers are non-absorbing and the input optical beam(s) for holding and switching are tuned close to the heavy-hole excitonic absorption peak in the quantum wells. As in the VCSEL, significant excitation of the quantum wells occurs primarily along the cavity axis and at the design wavelength, reducing the switching threshold. Figure 1 shows calculated optical input-output characteristics for a GaAs/GaAlAs RPA bistable switch with twenty absorbing layers (single 10-nm quantum wells) and different end reflectivities.

Comparison between resonant and non-resonant MQW absorbing switches shows that switching thresholds may be reduced by up to a factor of three when optical half-wave periodicity is introduced. This reduction, together with the low background absorption of the RPA structure, should enable efficient arrays of bistable optical switches to be constructed.

We acknowledge financial assistance from the US Air Force Rome Laboratory, Hanscom AFB and from the Air Force Office of Scientific Research.

REFERENCES

1 J. G. McInerney, *Proc. SPIE* **836**, 244 (1987), and references therein.

2 C. F. Schaus, M. Y. A. Raja, J. G. McInerney, H. E. Schaus, S. Sun, M. Mahbobzadeh and S. R. J. Brueck, *Electron. Lett.* **25**, 637 (1989).

3 M. Y. A. Raja, S. R. J. Brueck, M. Osinski, C. F. Schaus, J. G. McInerney, T. M. Brennan and B. E. Hammons, *IEEE J. Quantum Electron.* **25**, 1500 (1989).

4 D. S. Chemla, D. A. B. Miller, P. W. Smith, A. C. Gossard and W. Wiegmann, *IEEE J. Quantum Electron.* **QE-20**, 265 (1984).

Submitted to QELS'92

DETERMINATION OF OPERATOR ORDERING IN EFFECTIVE-MASS HAMILTONIAN FROM OPTICAL TRANSITION ENERGIES IN GaAs/AlGaAs SUPERLATTICES AND QUANTUM WELLS

by

MOHAMMAD MOJAHEDIE and MAREK OSIŃSKI

Center for High Technology Materials, University of New Mexico, Albuquerque, New Mexico 87131-6081

Corresponding author: Professor Marek Osiński,
Center for High Technology Materials,
University of New Mexico,
Albuquerque, New Mexico 87131-6081.
Tel. (505) 277-6031
Fax (505) 277-6433

Abstract

The magnitude of the subband-edge shift between the extreme cases of effective-mass operator ordering is shown to depend substantially on superlattice/quantum well parameters. Comparison with experimental data leads to a Hamiltonian consistent with earlier microscopic calculations.

DETERMINATION OF OPERATOR ORDERING IN EFFECTIVE-MASS HAMILTONIAN FROM OPTICAL TRANSITION ENERGIES IN GaAs/AlGaAs SUPERLATTICES AND QUANTUM WELLS

by

MOHAMMAD MOJAHEDIE and MAREK OSIŃSKI

Center for High Technology Materials, University of New Mexico,
Albuquerque, New Mexico 87131-6081

Corresponding author: Professor Marek Osiński,
Center for High Technology Materials,
University of New Mexico,
Albuquerque, New Mexico 87131-6081.
Tel. (505) 277-6031
Fax (505) 277-6433

In recent years, effective-mass theory has been used extensively as a computational tool for determining electronic states and other properties of abrupt heterostructures, superlattices, and quantum wells. It has been recognized[1-3] that application of the effective mass theory to abrupt interfaces between different materials suffers from ambiguity in kinetic energy operator ordering, caused by non-vanishing commutator of the momentum operator and the position-dependent effective mass $m(z)$. This leads to non-uniqueness of Hamiltonian, which in its general form can be written as[4]

$$H = -\tfrac{1}{2}\hbar^2 [m(z)]^{\alpha} \nabla [m(z)]^{\beta} \nabla [m(z)]^{\alpha} + V(z),$$

with $2\alpha + \beta = -1$. Corresponding with this one-parameter family of operators, the matching conditions for the envelope wave function $\psi(z)$ and its derivative $\psi'(z)$ are also parametrized, with continuity of $[m(z)]^{\alpha}\psi(z)$ and $[m(z)]^{\beta}\, d\{[m(z)]^{\alpha}\psi(z)\}/dz$ at the interfaces[2].

The values of α and β can in principle be determined by comparison with microscopic theory[2,3] or experiment[5]. Yet, while theoretical considerations indicate that only $\beta = -1$ ($\alpha = 0$) is consistent with microscopic treatment[2,3], Fu and Chao reported[5] that experimentally observable interband transition energies are not sensitive to the choice of β. In this paper, we resolve this apparent controversy by demonstrating that, contrary to Fu and Chao's assertion, the interband transition energies do vary substantially with β. Comparison with available data confirms that the choice of $\beta = -1$ provides the best fit with experiment.

Specifically, we have analyzed $GaAs/Al_xGa_{1-x}As$ superlattice and quantum well systems using the transfer matrix technique[5]. The results show that an increase in subband-edge energy within the conduction band is approximately linear with β ($-1 < \beta < 0$). We have also investigated the effects of superlattice parameters, such as subband index, thicknesses of both constituent materials, and barrier height (composition) on the shifts of subband-edge energy, between the two extreme cases of $\beta = -1$ and $\beta = 0$. As shown in Fig. 1, calculated energy levels are more sensitive to the choice of β for higher subbands. Even for the lowest-order subband, the effect gets substantially stronger with decreasing well thickness (Fig. 2). Increasing the barrier height or thickness will also result in a larger shift of the lowest-subband-edge energies (*e.g.*, 33.5 meV for $x = 0.4$ barrier vs. 15 meV for $x = 0.25$ in Fig. 3), thus in general the effect is stronger in

quantum wells than in superlattices.

Having determined that the choice of β can manifest itself in substantial shifts of transition energies, we have attempted to fit various experimental data available in the literature. In all cases we arrived at the same conclusion, namely that $\beta = -1$ fits experiments better than any other value of β within the range $-1 < \beta \leq 0$. Therefore, we conclude that the correct choice for the kinetic energy operator, consistent both with experimental data and the microscopic theory, is $\beta = -1$.

References

1. R. A. Morrow, Phys. Rev. B 35, 8074 (1987).

2. G. T. Einevoll, P. C. Hemmer, and J. Thomsen, Phys. Rev. B 42, 3485 (1990).

3. G. T. Einevoll, Phys. Rev. B 42, 3497 (1990).

4. R. A. Morrow and K. R. Brownstein, Phys. Rev. B 30, 678 (1984).

5. Y. Fu and K. A. Chao, Phys. Rev. B 40, 8349 (1989).

Figure Captions

Fig. 1. β-dependence of the subband structure in a $GaAs/Al_{0.25}Ga_{0.75}As$ superlattice with the well width d_1 = 150 Å and the barrier thickness d_2 = 25 Å, calculated for three lowest subbands.

Fig. 2. β-dependence of the lowest-subband structure in $GaAs/Al_{0.25}Ga_{0.75}As$ superlattices with d_2 = 25 Å, and d_1 = 150 Å (solid lines) or d_1 = 25 Å (broken lines).

Fig. 3. β-dependence of the lowest-subband structure in $GaAs/Al_xGa_{1-x}As$ superlattices with d_1 = 30 Å, d_2 = 25 Å, and x = 0.25 (solid lines) or x = 0.4 (broken lines).

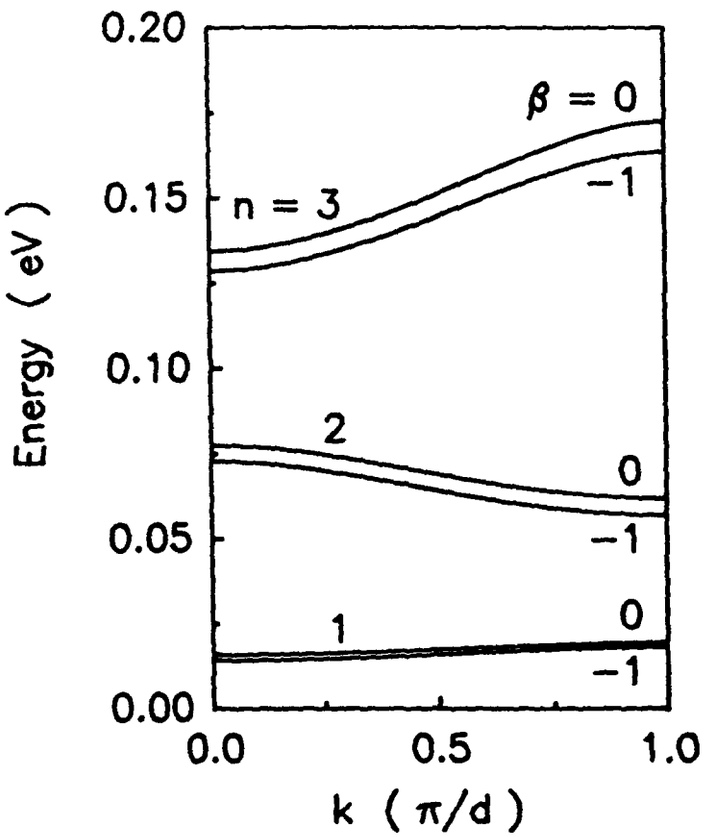

Figure 1

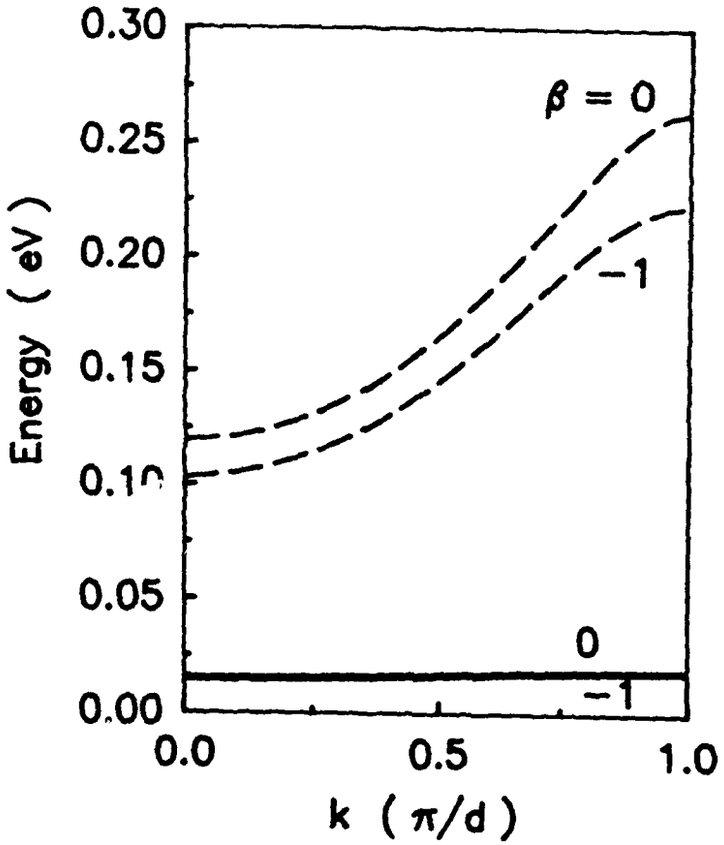

Figure 2

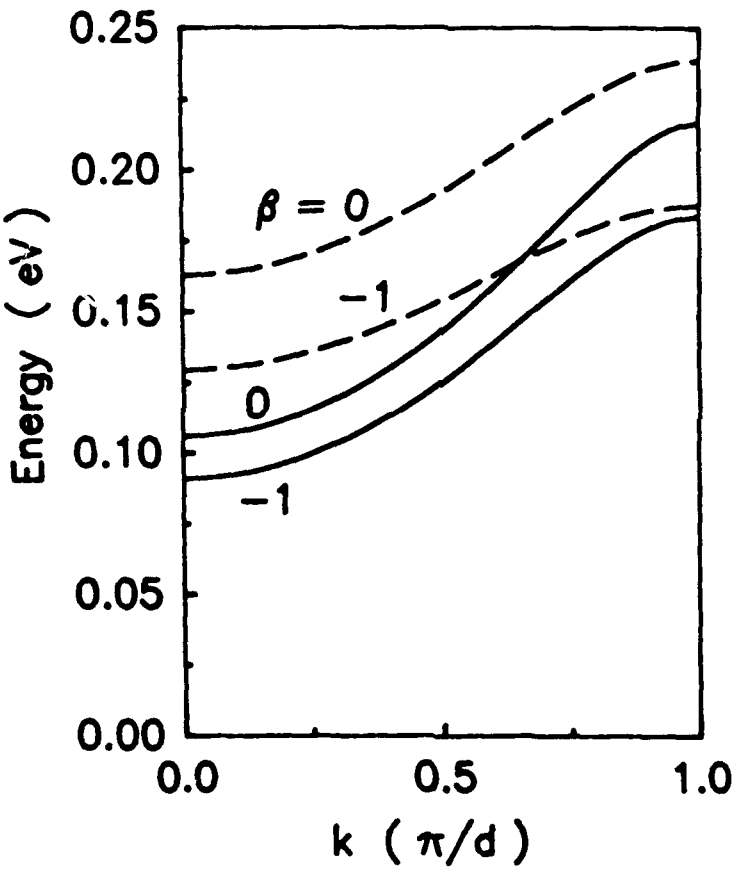

Figure 3

The as-grown wafers were optically excited using the 740 nm line of Ar-ion-pumped dye laser, with the pumping beam diameter of 10 μm. Even though no heat sink was used, the cw output power of 7 mW is considerably higher than that obtainable from single-quantum-well microlasers, while it is comparable to that of DBR-RPG devices.

BROAD-AREA MODE-COUPLING MODEL FOR CARRIER-GUIDED DIODE LASER ARRAYS

Marek Osinski and Chung-Pin Cherng, Center for High Technology Materials, University of New Mexico, Albuquerque, New Mexico 87131-6081.*

The objective of this paper is to demonstrate suitability of a broad-area mode-coupling approach to describe modal properties of carrier-guided semiconductor laser arrays. The supermode theory often adopted to explain modal behavior of phased array lasers is suitable only for index-guided arrays, since it requires a basis of individual waveguide modes. For carrier-guided arrays, with no built-in lateral variation of refractive index, such approach fails to predict correctly the number of system modes and their relative gains. It is more appropriate to treat the carrier-guided array as a perturbed broad-area laser, since the number of lateral modes is not limited in this case by the number of array elements. Recently, a simple model of carrier-guided arrays was proposed, based on the standard perturbation theory. It assumes an infinite loss outside the active region and ignores differences between modal gains of all the unperturbed (broad area) modes, claiming that these simplifications would not affect the results significantly. In this paper, we show that either of these assumptions has important consequences on the calculated modal gains for the array modes.

Rather than using the perturbation theory, we follow the coupled mode formulation, but with a basis of broad-area modes instead of individual waveguide modes. An active broad-area waveguide is considered, with the gain-index coupling as well as spatially averaged temperature effects included. The perturbation due to array structure is assumed in form a raised sinusoidal modulation of permittivity, with gain maxima at stripe centers. A smooth half-period cosine profile of temperature is also included in the perturbation.

As an example, we consider a 10-stripe GaAs/AlGaAs carrier-guided array similar to commercially available devices (SDL-2410C, 6-μm stripes on 10-μm centers, multiple-quantum-well active region). A comparison of the present theory with earlier simplified perturbation analysis corresponding to a limit of very high loss and constant reveals that the previous treatment is unreliable in predicting the modal gains of high-order array modes (mode number larger than the number of emitters). It should be emphasized that these high-order modes usually dominate in carrier-guided arrays, hence precise knowledge of their modal gains is very important in considerations of mode ordering and mode suppression schemes.

Our results reveal that earlier agreement between the simplified model and experimental observations was fortuitous. On the other hand, broad-area coupled-mode theory can contribute to improved understanding of array laser behavior and constitutes an important design and interpretation tool.

OPERATOR ORDERING IN EFFECTIVE-MASS HAMILTONIAN FOR SEMICONDUCTOR SUPERLATTICES AND QUANTUM WELLS

Mohammad Moiahedi and Marek Osinski, Center for High Technology Materials, University of New Mexico, Albuquerque, New Mexico 87131-6081.*

In recent years, effective-mass theory has been used extensively as a computational tool for determining electronic states and other properties of abrupt heterostructures, superlattices, and quantum wells. It has been recognized that application of the effective mass theory to abrupt interfaces between different materials suffers from ambiguity in kinetic energy operator ordering, caused by non-vanishing commutator of the momentum operator and the position-dependent effective mass $m(z)$. This leads to non-uniqueness of Hamiltonian, which in its general form can be written as

$$H = -\frac{1}{2}\hbar^2 [m(z)]^{\alpha}\nabla[m(z)]^{\beta}\nabla[m(z)]^{\alpha} + V(z),$$

with $2\alpha + \beta = -1$. Corresponding with this one-parameter family of operators, the matching conditions for the envelope wave function $\psi(z)$ and its derivative $\psi'(z)$ are also parametized, with continuity of $[m(z)]^{\alpha}\psi(z)$ and $[m(z)]^{\beta}d([m(z)]^{\alpha}\psi(z)]/dz$ at the interfaces.

The values of α and β can in principle be determined by comparison with microscopic theory or experiment. Yet, while theoretical considerations indicate that only $\beta = -1$ ($\alpha = 0$) is consistent with microscopic treatment, there have been reports that experimentally observable interband transition energies are not sensitive to the choice of β. In this paper, we resolve this apparent controversy by demonstrating that, contrary to earlier claims, the interband transition energies do vary substantially with β. Comparison with available data confirms that the choice of $\beta = -1$ provides the best fit with experiment.

Specifically, we have analyzed GaAs/$Al_xGa_{1-x}As$ superlattice and quantum well systems using the transfer matrix technique. The results show that within the conduction band a subband-edge energy shifts approximately linearly with β ($-1 \leq \beta \leq 0$). We have also investigated the effects of superlattice parameters, such as subband index, thicknesses of both constituent materials, and barrier height (composition) on the shifts of subband-edge energy, between the two extreme cases of $\beta = -1$ and $\beta = 0$. Calculated energy levels are more sensitive to the choice of β for higher subbands and for decreasing well thickness. Increasing the barrier height or thickness also results in larger shift of subband-edge energies.

SURFACE NORMAL SECOND HARMONIC GENERATION IN PLZT AND GaAs THIN-FILM WAVEGUIDES

L C. Zou, K. J. Malloy and A. Y. Wu, Center for High Technology Materials (CHTM), EECE Building, The University of New Mexico, Albuquerque, New Mexico 87131-6081.

We compare SHG in PLZT and GaAs thin-film waveguides. PLZT should offer higher conversion efficiencies and interaction with other optoelectronic devices. However, the difficulties presented by the polycrystalline structure of PLZT films need be examined for PLZT based devices.

Our waveguide structure requires the interaction of two counterpropagating laser beams to emit the second harmonic from the surface. The single crystal $LiNbO_3$- and GaAs-based structures have been studied previously. It is possible to deposit PLZT thin films with c axis (001) normal to the surface and with the a (and b) axes of the polycrystallites randomly oriented in the plane. Assuming such a microstructural model, our calculations show the second order nonlinear polarization for emission from the surface is present only when one of the incident laser beams is TE and the other is TM. $P^{2\omega}$, the source of the nonlinear output is independent of the orientation of the grains in the waveguide plane,

$$P^{2\omega} = d_{15}E_1^{\omega}E_2^{\omega}Y.$$

This result implies that, except for scattering losses at grain boundaries, a polycrystalline PLZT waveguide will have identical properties to a single crystal structure.

We report on these considerations for PLZT and compare them with our experimental results on single crystal GaAs-based structures. The technological advantages of GaAs and the difficulties encountered with PLZT will be discussed.

MICROSTRUCTURE AND ELECTRICAL PROPERTIES OF R.F. SPUTTERED BARIUM TITANATE FILM ON SILICON

Bi-Shiou Chiou and Jenq-I Jiang Institute of Electronics, National Chiao Tung University, Hsinchu, Taiwan.*

Meeting Program

Third Annual Symposium on Ceramics and Advanced Materials

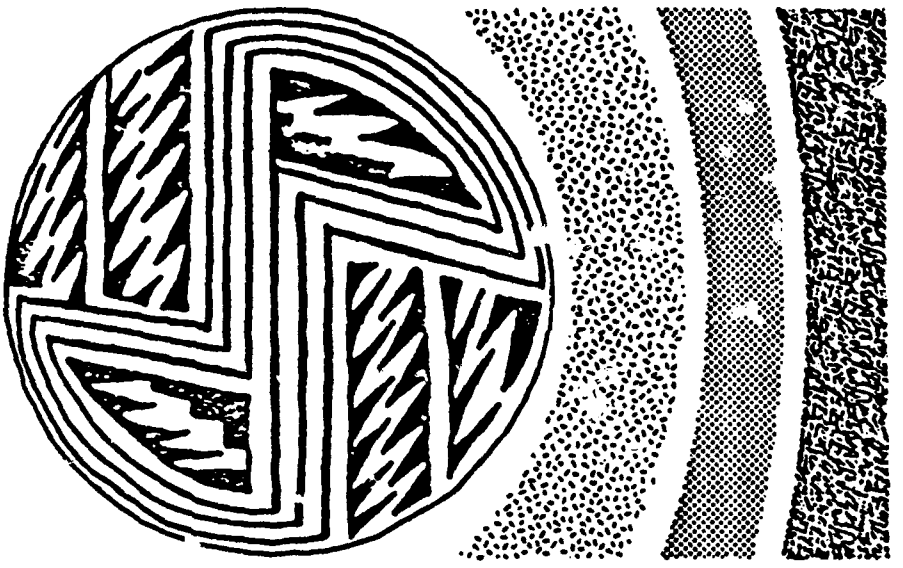

Hyatt Regency Hotel
Albuquerque, NM
October 24-25, 1991

Sponsored by:

The New Mexico Sections of the
American Ceramic Society and
the Materials Research Society

WH 8:30am MORNING
Fairmont Regency 1

Optical Materials
Alastair M. Glass, *AT&T Bell Laboratories, Presider*

8:30am

WH1 Stimulated emission and lasing studies of wide gap II–VI compounds using optical excitation

X. H. Yang, J. Hays, W. Shan, and J. J. Song
Oklahoma State University, Department of Physics, Stillwater, Oklahoma 74078

Stimulated emission and lasing effects of bulk ZnSe samples, grown by physical vapor-phase transport technique and MBE epilayers on GaAs substrates were investigated (using a 10-ns pulsed laser) in the frequency as well as in the time domain. For lasing studies, a laser cavity was formed by cleaving the sample's two parallel facets with the cavity lengths of a few hundred microns. The cleaved edges were not subjected to reflective coatings. The lasing threshold densities were found to be surprisingly low; ~7 kW/cm^2 for a sample with a cavity length of 300 μm. The longitudinal modes of the lasers were clearly resolved. Stimulated emission at both 10 and 300 K was observed. The stimulated emission was evidenced by the spectral narrowing of the emission peak, the highly superlinear dependence of the output signal on the pumping power density, and the narrowing of the temporal profile under high excitation. The gain values were measured by the variable excitation length method. The effect of the pumping photon energy on the stimulated emission at room temperature was investigated.

A comparison between the bulk and MBE samples is made and the physical mechanism involved is discussed.

8:45am

WH2 Noise performance of photorefractive crystal holograms

Q. Wang Song, Partha P. Banerjee, and Jaw-Jei Liu
Syracuse University, Department of Electrical Engineering, Syracuse, New York 13244

We analyze the temporal and spatial nature of the diffracted light from a photorefractive volume hologram under the influence of electronic noise in the material. Because of this noise, the holographic grating within the crystal is not strictly periodic; in other words, it has random fluctuations in both amplitude and period. Gaussian beam illumination at the nominal Bragg angle is assumed. The reason for this choice is that we can now evaluate not only the temporal statistics in the diffracted light, but also its spatial randomness. This quantitative evaluation achieved through defining a system transfer function that relates the output diffracted light to the input in the spatial frequency domain. For light nominally incident at the Bragg angle, this transfer function may be derived by Fourier transforming the paraxial wave equation in the presence of interaction terms. Estimation of spatial randomness is not possible to calculate assuming plane wave illumination since one cannot monitor transverse fluctuations along its wavefront. By using first-order approximation, the temporal and spatial noise ratios are obtained. Their dependence on reading time, reading beam intensity, grating spacing, and temperature are predicted.

9:00am

WH3 Self-trapped exciton enhanced photostructural transformation in AsSe fiber glass

A. W. Schmid, M. Kim, K. Cerqua, and W. D. LaCourse
University of Rochester, Laser Energetics Laboratory, 250 E. River Road, Rochester, New York 14623

Arsenic chalcogenide glasses for IR fiber and data storage uses exhibit photoinduced structural transformations when irradiated by below-band-gap light. We demonstrate that these transformations are enhanced by irradiating at a self-trapped exciton (STE) resonance wavelength. Rayleigh and Raman signals show that STE decay leads to instabilities among metastable structural states in bulk glass. With time constants of the order of seconds, these instabilities may switch abruptly into states of increased order. By varying the relative concentration in these binary compounds, we control the availability of the initial STE forming state. These measurements provide evidence that photoinduced structural transformations in arsenic selenides occur at 1–5 W/cm^2 irradiation levels.

9:15am

WH4 Effects of operator ordering in effective-mass Hamiltonian on transition energies in semiconductor quantum wells

Mohammad Mojahedie and Marek Osinski
University of New Mexico, Center for High Technology Materials, Albuquerque, New Mexico 87131-6081

It has been recognized that use of the effective mass theory for abrupt interfaces between different materials suffers from ambiguity in kinetic-energy operator ordering, caused by nonvanishing commutator of the momentum operator and the position-dependent effective mass. This leads to nonuniqueness of the Hamiltonian, which in its general form can be written as a one-parameter family of operators.[1] The matching conditions for the envelope wave function and its derivative at the interfaces are also parametrized.[1] Recently, Fu and Chao reported[2] that experimentally observable interband transition energies are not sensitive to the effective-mass operator ordering. In this paper, we demonstrate that optical transition energies do vary substantially with ordering. Specifically, we have analyzed GaAs/AlGaAs quantum wells using the transfer matrix technique.[2] We have investigated the effects of quantum well parameters, such as subband index, thicknesses of both constituent materials, and barrier height (composition) on the shifts of subband-edge energy, between the two extreme cases of operator ordering. Calculated energy levels are more sensitive to ordering for higher subbands and for decreasing well thickness. Increasing the barrier height or thickness in coupled quantum wells will also result in a larger shift of subband-edge energies. Comparison with available data allows us to choose the ordering that provides the best fit to experiment.

References

1. G. T. Einevoll, P. C. Hemmer, and J. Thomsen, Phys. Rev. B 42, 3485 (1990).
2. Y. Fu and K. A. Chao, Phys. Rev. B 40, 8439 (1989).

9:30am

WH5 Nonlinear optical characteristics of two-wave mixing in InP:Fe photorefractive crystals

Yang Zhao, Qingfeng Tang, and Zhaolin Li
Wayne State University, Department of Electrical & Computer Engineering, Detroit, Michigan 48202

InP:Fe photorefractive crystals are attractive materials for optical information processing due to their fast response time and relatively high nonlinearity. In this work, we investigate two-wave mixing in these crystals as a function of light intensity, beam intensity ratio, and external electric field intensity. The crystal used in our experiments was 2.2 × 2.5 × 3 mm with incident direction <110> normal to the 2.5 × 3-mm face. The laser wavelength is 1.06 μm. In addition to the energy transfer between the beams, we observed the beam path deflection effect in the crystal in our experiments. The amount of the path deflection depends on the input intensity levels. A change in the angle between the interaction beams by 2.4° was observed without external electric field on the crystal. In addition, we observed the energy transfer from the pump to signal with pump-to-signal intensity ratios >>1.

We also found that the nonlinear effects of the crystal depends on the exposure time of the crystal to the laser and illumination light.

9:45am

WH6 Beam diameter threshold for photoinduced polarization conversion in $LiNbO_3$:Fe

D. W. Wilson, E. N. Glytsis, N. F. Hartman, and T. K. Gaylord
Georgia Institute of Technology, School of Electrical Engineering and Microelectronics Research Center, Atlanta, Georgia 30332

Photoinduced polarization conversion is a form of optical damage in $LiNbO_3$ waveguide devices.[1] In an attempt to better understand this phenomenon, we have studied the effect in bulk $LiNbO_3$:Fe. In this work, we have observed nearly complete ordinary-to-extraordinary polarization conversion in $LiNbO_3$:Fe for input ordinary beam diameters greater than ~200 μm and no polarization conversion for beam diameters less

1991 Optical Society of America Annual Meeting

Summaries of papers presented at the Annual Meeting of the Optical Society of America

November 3–8, 1991
San Jose, California

1991 Technical Digest Series
Volume 17

CONFERENCE EDITION

Optical Society of America
2010 Massachusetts Avenue, NW
Washington, DC 20036

Articles in this publication may be cited in other publications. In order to facilitate access to the original publication source, the following form for the citation is suggested:

> Name of Author(s), "Title of Paper," in OSA Annual Meeting Technical Digest, 1991 (Optical Society of America, Washington, D.C., 1991), Vol. 17, pp. xx-xx.

ISBN Number

Conference Edition	1-55752-210-3 (softcover)
Postconference Edition	1-55752-211-1 (hardcover)
(Note: Postconference Edition includes postdeadline papers.)	
1991 Technical Digest Series	1-55752-192-1 (hardcover)

Library of Congress Catalog Card Number

Conference Edition	91-66977
Postconference Edition	91-66978

Copyright © 1991, Optical Society of America

Individual readers of this digest and libraries acting for them are permitted to make fair use of the material in it, such as to copy an article for use in teaching or research, without payment of fee, provided that such copies are not sold. Copying for sale is subject to payment of copying fees. The code 1-55752-192-1/91/$2.00 gives the per-article copying fee for each copy of the article made beyond the free copying permitted under Sections 107 and 108 of the U.S. Copyright Law. The fee should be paid through the Copyright Clearance Center, Inc., 21 Congress Street, Salem, MA 01970.

Permission is granted to quote excerpts from articles in this digest in scientific works with the customary acknowledgment of the source, including the author's name and the name of the digest, page, year, and name of the Society. Reproduction of figures and tables is likewise permitted in other articles and books provided that the same information is printed with them and notification is given to the Optical Society of America. Republication or systematic or multiple reproduction of any material in this digest is permitted only under license from the Optical Society of America; in addition, the Optical Society may require that permission also be obtained from one of the authors. Address inquiries and notices to Director of Publications, Optical Society of America, 2010 Massachusetts Avenue, NW, Washington, DC 20036. In the case of articles whose authors are employees of the United States Government or its contractors or grantees, the Optical Society of America recognizes the right of the United States Government to retain a nonexclusive, royalty-free license to use the author's copyrighted article for United States Government purposes.

P37

HEAVY-HOLE EFFECTIVE MASS IN InP - A CRITICAL EXAMINATION

Marek Osiński

Department of Electronic Engineering, University of Tokyo, 7-3-1 Hongo, Bunkyo-ku, Tokyo 113, Japan

Permanent address: *Center for High Technology Materials, University of New Mexico, Albuquerque, New Mexico 87131*

ABSTRACT

The abundance of grossly inconsistent estimates for the heavy-hole effective mass in InP, quoted throughout the literature, clearly demonstrates a pressing need for a comprehensive evaluation and for reaching a consensus on this issue. A critical survey of existing theoretical and experimental results is presented, and the most trustworthy data are selected.

1. INTRODUCTION

In spite of intensive studies of InP and related materials, prompted by a widening range of their applications, there remains a number of important parameters on which no consensus exists as to what should be their values. Such is the case of the heavy-hole effective mass m_{v1}, apparently one of the poorest established parameters in InP. Growing technological importance of InP is in the longer run irreconcilable with the confusion that reigns in the literature. A large amount of conflicting theoretical or rough experimental estimates stands in sharp contrast to the scarcity of reliable experimental data, and no conclusive evaluation seems to be agreed upon (see, for example, Refs. [1-4], where m_{v1} ranges from $0.39m_0$ to $0.85m_0$, with m_0 denoting the free-electron mass). The degree of difficulties encountered in attempting to make a rational choice is also illustrated in some compilations of InP properties whose authors would decide not to quote any value of the heavy-hole mass whatsoever (see, for example, Ref. [5]). At least partially, the continuing confusion can be attributed to rather arbitrary selection of an earlier result without a careful assessment of other available data. This is regrettably reflected in many recent books and monographs. To give but a few examples, in addition to Refs. [1-4]: (i) Harrison [6] quotes m_{v1}/m_0 in InP to be 0.85, the value obtained theoretically by Lawaetz [7] (and misquoted as an experimental result), while (ii) Wiley [8] believes that a reasonable value is 0.65, *i.e.* a middle value between theoretical estimates of [7] (0.85) and [9] (0.50), and (iii) Pearsall [10] gives preference to an experimental evaluation of m_{v1} by Leotin *et al.* [11] (0.56), in the same instance ascribing it mistakenly to experiments of Rochon and Fortin [12].

As the technology of InP-based optoelectronic devices matures, precise knowledge of m_{v1} becomes critical. Due to their large density of states, heavy holes play a dominant role in optical transitions. In addition, the effective masses in multi-component alloys, and notably in InGaAsP, are usually estimated from interpolation formulae which rely on the corresponding values in the constituent binary materials. It is the objective of this paper to present a systematic survey of existing data on m_{v1} in order to select its most plausible estimate.

2. HOLE-MASS DEFINITIONS

The valence bands in III-V compounds are warped from spherical symmetry and it has been shown that, depending on the method of measurement, heavy-hole mass values ranging from $0.17m_0$ to $0.87m_0$ are theoretically possible for InP [13,14]. It is therefore important to use either the same type of effective mass or the same set of band parameters when comparing different theoretical predictions and experimental evaluations. We choose the Dresselhaus valence band warping parameters A, B, C^2 [15] as a basis for comparison between various results.

The shape of the valence bands near the Γ point in III-V compounds is given by the following approximate formula [8]

$$E(\mathbf{k}) = (\hbar/2m_0)\{Ak^2 \mp [B^2k^4 + C^2(k_x^2k_y^2 + k_y^2k_z^2 + k_x^2k_z^2)]^{1/2}\} \quad . \qquad (1)$$

The upper (lower) sign refers to the heavy- (light-) hole band. Eq. (1) was derived for semicon-

ductors with a diamond structure [15]. The lack of inversion symmetry in the zinc-blende lattice introduces additional linear k terms, but it was shown that their effect is extremely small [16].

Eq. (1) can be used to express the effective masses $m_{vi}[100]$, $m_{vi}[111]$ along [100] and [111] directions, as well as the density-of-states and conductivity masses m_{dvi} and m_{cvi}, in terms of parameters A, B, and C^2 [17]. Note that $i = 1$ (2) indicates the heavy- (light-) hole band.

3. THEORETICAL EVALUATIONS

Table 1 contains a survey of theoretical and experimental evaluations of A, B, C^2, together with corresponding values of $m_{vi}[100]$, $m_{vi}[111]$, m_{dvi} and m_{cvi}. For the sake of conciseness, the reader is referred to [17] for details on how the values given in Table 1 were obtained when conversion from other parameters or corrections of published results were necessary.

Table 1

WARPING PARAMETERS A, B, C^2 AND VALENCE-BAND EFFECTIVE MASSES FOR InP ON THE BASIS OF PUBLISHED LITERATURE

Warping parameters			Heavy-hole mass		Light-hole mass		Density-of-states mass		Conductivity mass		
A	B	C^2	$m_{v1}[100]/m_0$	$m_{v1}[111]/m_0$	$m_{v2}[100]/m_0$	$m_{v2}[111]/m_0$	m_{dv1}/m_0	m_{dv2}/m_0	m_{cv1}/m_0	m_{cv2}/m_0	Ref.
(a) Theoretical evaluations											
7.54	4.76	35.10	0.36	0.60	0.081	0.075	0.49	0.077	0.45	0.077	9*
8.26	5.07	62.13	0.31	0.69	0.075	0.066	0.50	0.069	0.43	0.069	13*
8.13	5.81	26.13	0.43	0.62	0.072	0.068	0.54	0.070	0.51	0.070	20
5.75	2.78	27.4	0.34	0.61	0.117	0.101	0.49	0.107	0.44	0.106	21
6.28	4.16	39.49	0.47	1.32	0.096	0.085	0.85	0.089	0.67	0.088	7
6.61	4.50	25.44	0.47	0.80	0.090	0.084	0.65	0.086	0.60	0.086	18
6.34	4.38	33.44	0.51	1.20	0.093	0.084	0.84	0.088	0.70	0.087	19*
(b) Experimental determinations											
5.04	3.12	6.57	0.52	0.63	0.123	0.118	0.58	0.120	0.58	0.120	11
5.15	1.88	20.89	0.31	0.52	0.142	0.119	0.43	0.126	0.40	0.125	12

* Corrected values, see Ref. [17].

The theoretical estimates of the valence band parameters assembled in Table 1(a) are based on the k·p perturbation theory [7,9,13,18], the pseudopotential approach [19], or combinations of both [20,21]. The k·p method involves many parameters (energy gaps and momentum matrix elements) that could in principle be determined empirically [16]. In practice, however, some of these parameters are difficult to assess because of insufficient experimental data; consequently, additional assumptions cannot be avoided.

Cardona [9] circumvented the lack of complete data on the energy gaps in III-V compounds by estimating them from "equivalent" group IV materials. He assumed also that the covalent part of the matrix elements joining the Γ_{15v} levels with the Γ_{1c}, Γ_{15c} and Γ_{12} levels had the same value for all zinc-blende and diamond-type semiconductors. His approach was also embraced by Kołodziejczak *et al.* [13,14], who updated the values of the aforementioned covalent matrix elements. The arbitrary assumption of constant matrix elements seems to be too crude since more recent studies suggest a rather strong material dependence [7,22]. Moreover, an early estimate of the low-temperature principal energy gap $E_0 = 1.34$ eV adopted in [9,13,14] differs considerably from recent measurements where $E_0 = 1.42$ eV [12].

The approach of Pollak *et al.* [20] is somewhat similar to that of [9] except that the energies of states not experimentally available for group IV materials are estimated by solving pseudopotential matrices. Also, the homopolar matrix elements of "equivalent" group IV elements are no longer assumed to be constant, but are adjusted to obtain a good agreement of the calculated bands with the ultraviolet-reflection and electroreflectance data. The same procedure is then adopted to obtain the antisymmetric matrix elements for III-V compounds. However, it has been

indicated that while such a procedure may well fit the overall band structure, it can still give rather unsatisfactory values for the band-edge masses [7].

Lawaetz [7] developed a semi-empirical model to describe the variation of the matrix elements in different materials as functions of lattice constant and ionicity. There remains some uncertainty in the value of his matching parameter β accounting for ionicity, although his choice of $\beta = 0.5$ for InP appears to be a felicitous one, for his interaction energy E_p agrees well with a subsequent experimental determination [22]. However, the energy gap between the Γ_{15v} and Γ_{15c} levels at 0 K ($E_0' = 5.10$ eV), estimated by Lawaetz using a dielectric method of Van Vechten [23], is at variance with the result of Van Vechten himself, electroreflectance measurements, and pseudopotential calculations [19,24], which all fall between 4.44 and 4.78 eV. The adjustment of E_0' in Lawaetz's theory would increase the anisotropy of the heavy- and light-hole masses which already is much larger than reported in [11].

Recognizing that the anisotropy of calculated heavy-hole masses was larger than indicated by the then available cyclotron resonance data for GaSb, InSb and ZnTe, Lawaetz [7] suggested that his method may have given a wrong estimate for the magnitude of the G parameter which describes the interaction between the Γ_{15v} and Γ_{12} states. Therefore, in his subsequent work [18] Lawaetz treated G simply as fitting parameter, indeed obtaining a reduced valence-band anisotropy. However, although smaller than previously ($\gamma_3^L - \gamma_2^L = [B^2 + C^2/3)^{1/2} - B]/2 = 0.43$ instead of the former 0.68, where γ_2^L, γ_3^L are Luttinger parameters), it is still substantially larger than experimental value of 0.17 [11].

Bowers and Mahan [21] use the empirical pseudopotential method [24] to calculate the momentum matrix elements. The effective masses for holes are then found from the $\mathbf{k}\cdot\mathbf{p}$ theory of [15]. The reliability of their results seems to be rather doubtful since their approach fails to predict a correct value of the energy gap for InP (1.10 eV instead of 1.42 eV), possibly because effects of the atomic cores on the pseudowavefunctions were neglected.

The pseudopotential treatment of Chen and Sher [19] neglects the spin-orbit coupling that has an important bearing on the values of valence-band effective masses. Moreover, their masses deviate from a relation that follows from the $\mathbf{k}\cdot\mathbf{p}$ theory with no spin-orbit interaction (see [17]), which raises some uncertainty regarding our extraction of the warping parameters A, B, C^2 from these masses. Thus the corresponding masses given in Table 1(a) (corrected for the spin-orbit coupling) should be viewed with a degree of reservation.

4. EXPERIMENTAL DETERMINATIONS

None of the theoretical approaches discussed above emerges as clearly superior to the others, although our criticism of the results of Cardona [9], Kołodziejczak *et al.* [13,14] and Bowers and Mahan [21] is stronger than that of the remaining three models. It should also be noted that all averaged theoretical masses in Table 1(a) differ significantly from measurements of [11] and [12], especially in the case of light-hole masses. A large discrepancy between the experimental data themselves creates however an impression that the accuracy of the hole masses derived from measurements is perhaps not much better than that of theoretical methods.

Cyclotron resonance measurements of Leotin *et al.* [11] permit a relatively direct determination of hole effective masses, but the observed masses have to be corrected in order to obtain bare band-edge values. The largest correction (~12%) is due to nonparabolicity of the light-hole band which increases the observed light-hole mass. Another correction, which apparently was not made in [11], would eliminate the effect of electron-phonon interaction on the observed masses. However, since the magnitude of this correction (~3%) lies within the experimental uncertainty, one can argue that it can be neglected.

A weak point of the experimental study of Rochon and Fortin [12] is that it involves a theoretical model in order to deduce the valence-band masses from interband magneto-absorption data. In particular, an early value of the anisotropy factor [7] was assumed, hence the effective masses of [12] exhibit much stronger anisotropy than the results of [11]. Moreover, interband magneto-absorption measurements provide rather poor accuracy of deduced heavy-hole mass. For instance, variation of electron and light-hole masses by less than 3% in the analysis of interband magneto-transmission data changes the deduced m_{v1} by 25% [25].

Apart from [11] and [12], no other experimental data on the heavy-hole mass in InP seem to have been published since 1970. Early experiments prior to 1970 provided only very rough estimates of the averaged conductivity mass m_{cv}, derived from Hall mobility measurements. Analysis of mobility data requires a number of scattering mechanisms to be included, which in turn involves additional parameters of uncertain magnitude, such as the deformation potentials, ef-

fective charges, *etc.* The wide range of effective masses derived from mobility measurements (0.2 to $1.0m_0$) illustrates how poor is the accuracy of any such estimate.

5. CONCLUSIONS

A comprehensive survey of theoretical and experimental data on heavy-hole effective mass in InP is reported. The valence-band warping parameters A, B, C^2 are chosen as a basis for comparison between various results. Experimental evaluation by Leotin *et al.* (density-of-states heavy-hole mass of $0.58m_0$) is judged to be the most trustworthy among the existing data.

It is rather surprising that the only two experimental results on the heavy-hole mass in InP published since 1970, date back to 1975. Despite growing technological importance of InP, little effort seems to have been devoted to this particular issue. This paper illustrates that there is an urging need for new measurements. We are now preparing for such measurements at the Megagauss Laboratory of the University of Tokyo.

6. ACKNOWLEDGEMENT

Prof. Takeshi Kamiya is gratefully acknowledged for his hospitality and support during the author's visit at the University of Tokyo.

REFERENCES

1. G. Burns, Solid State Physics, Academic Press, Orlando 1985, p. 312.
2. G. P. Agrawal and N. K. Dutta, Long Wavelength Semiconductor Lasers, Van Nostrand Reinhold, New York 1986, p. 85.
3. M. Shur, GaAs Devices and Circuits, Plenum Press, New York 1987, p. 19.
4. M. L. Cohen and J. R. Chelikowsky, Electronic Structure and Optical Properties of Semiconductors, Springer Series in Solid-State Sciences Vol. 75, Springer-Verlag, Berlin 1988, p. 49.
5. B. R. Pamplin, "*Tables of Properties of Semiconductors*", CRC Handbook of Chemistry and Physics, 67th Edition, CRC Press, Boca Raton 1986, pp. E-104 - E-105.
6. W. A. Harrison, *Electronic Structures and the Properties of Solids*, W. H. Freeman, San Francisco 1980, p. 157.
7. P. Lawaetz, Phys. Rev. B 4, 3460 (1971).
8. J. D. Wiley, *Mobility of Holes in III-V Compounds*, in Semiconductors and Semimetals, Vol 10, R. K. Willardson and A. C. Beer (Eds.), Academic Press, New York 1975, Ch. 2, pp. 91-174.
9. M. Cardona, J. Phys. Chem. Solids 24, 1543 (1963), and Erratum, J. Phys. Chem. Solids 26, 1351 (1965).
10. T. P. Pearsall, *Some Physical Properties of GaInAsP Alloys* - $Ga_xIn_{1-x}As_yP_{1-y}$, in GaInAsP Alloy Semiconductors, T. P. Pearsall (Ed.), John Wiley & Sons, Chichester 1982, Appendix, pp. 456-458.
11. J. Leotin, R. Barbaste, S. Askenazy, M. S. Skolnick, R. A. Stradling, and J. Tuchendler, Solid State Comm. 15, 693 (1974).
12. P. Rochon and E. Fortin, Phys. Rev. B 12, 5803 (1975).
13. J. Kołodziejczak, S. Żukotyński, and H. Stramska, Phys. Stat. Sol. 14, 471 (1966).
14. J. Kołodziejczak and S. Żukotyński, Phys. Stat. Sol. 16, K55 (1966).
15. G. Dresselhaus, A. F. Kip, and C. Kittel, Phys. Rev. 98, 368 (1955).
16. E. O. Kane, *The* k·p *Method*, in Semiconductors and Semimetals, Vol. 1, R. K. Willardson and A. C. Beer (Eds.), Academic Press, New York 1966, Ch. 3, pp. 75-100.
17. M. Osiński, CRC Critical Rev. Solid State & Material Sciences 15, 327-343 (1989).
18. P. Lawaetz, The Influence of Holes on the Phonon Spectrum of Semiconductors, D.Sc. Thesis, Technical University of Denmark, Lyngby 1978.
19. A.-B. Chen and A. Sher, Phys. Rev. B 22, 3886 (1980).
20. F. H. Pollak, C. W. Higginbotham, and M. Cardona, Proc. 8th Int. Conf. Phys. Semiconductors, Kyoto 1966, J. Phys. Soc. Japan 21 (Suppl.), 20 (1966).
21. R. L. Bowers and G. D. Mahan, Phys. Rev. 185, 1073 (1969).
22. C. Hermann and C. Weisbuch, Phys. Rev. B 15, 823 (1977).
23. J. A. Van Vechten, Phys. Rev. 187, 1007 (1969).
24. M. L. Cohen and T. K. Bergstresser, Phys. Rev. 141, 789 (1966).
25. K. Alavi, R. L. Aggarwal, and S. H. Groves, J. Magn. & Magn. Mat. 11, 136 (1979).

CONFERENCE PROCEEDINGS

Second International
Conference on

Indium Phosphide and Related Materials

April 23-25, 1990

Radisson Hotel Denver
Denver, Colorado

Sponsored by the IEEE Lasers and Electro Optics Society
and the
IEEE Electron Devices Society
in cooperation
with SPIE

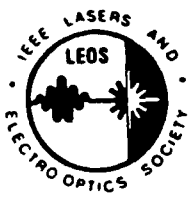

IEEE Catalog # 90CH2859-7
Library of Congress #90-80596

D
E
N
V
E
R

The as-grown wafers were optically excited using the 740 nm line of Ar-ion-pumped dye laser, with the pumping beam diameter of 10 μm. Even though no heat sink was used, the cw output power of 7 mW is considerably higher than that obtainable from single-quantum-well microlasers, while it is comparable to that of DBR-RPG devices.

BROAD-AREA MODE-COUPLING MODEL FOR CARRIER-GUIDED DIODE LASER ARRAYS

Marek Osinski and Chung-Pin Cherng, Center for High Technology Materials, University of New Mexico, Albuquerque, New Mexico 87131-6081.*

The objective of this paper is to demonstrate suitability of a broad-area mode-coupling approach to describe modal properties of carrier-guided semiconductor laser arrays. The supermode theory often adopted to explain modal behavior of phased array lasers is suitable only for index-guided arrays, since it requires a basis of individual waveguide modes. For carrier-guided arrays, with no built-in lateral variation of refractive index, such approach fails to predict correctly the number of system modes and their relative gains. It is more appropriate to treat the carrier-guided array as a perturbed broad-area laser, since the number of lateral modes is not limited in this case by the number of array elements. Recently, a simple model of carrier-guided arrays was proposed, based on the standard perturbation theory. It assumes an infinite loss outside the active region and ignores differences between modal gains of all the unperturbed (broad area) modes, claiming that these simplifications would not affect the results significantly. In this paper, we show that either of these assumptions has important consequences on the calculated modal gains for the array modes.

Rather than using the perturbation theory, we follow the coupled mode formulation, but with a basis of broad-area modes instead of individual waveguide modes. An active broad-area waveguide is considered, with the gain-index coupling as well as spatially averaged temperature effects included. The perturbation due to array structure is assumed in form a raised sinusoidal modulation of permittivity, with gain maxima at stripe centers. A smooth half-period cosine profile of temperature is also included in the perturbation.

As an example, we consider a 10-stripe GaAs/AlGaAs carrier-guided array similar to commercially available devices (SDL-2410C, 6-μm stripes on 10-μm centers, multiple-quantum-well active region). A comparison of the present theory with earlier simplified perturbation analysis corresponding to a limit of very high loss and constant reveals that the previous treatment is unreliable in predicting the modal gains of high-order array modes (mode number larger than the number of emitters). It should be emphasized that these high-order modes usually dominate in carrier-guided arrays, hence precise knowledge of their modal gains is very important in considerations of mode ordering and mode suppression schemes.

Our results reveal that earlier agreement between the simplified model and experimental observations was fortuitous. On the other hand, broad-area coupled-mode theory can contribute to improved understanding of array laser behavior and constitutes an important design and interpretation tool.

OPERATOR ORDERING IN EFFECTIVE-MASS HAMILTONIAN FOR SEMICONDUCTOR SUPERLATTICES AND QUANTUM WELLS

Mohammad Moiahedie and Marek Osinski, Center for High Technology Materials, University of New Mexico, Albuquerque, New Mexico 87131-6081.*

In recent years, effective-mass theory has been used extensively as a computational tool for determining electronic states and other properties of abrupt heterostructures, superlattices, and quantum wells. It has been recognized that application of the effective mass theory to abrupt interfaces between different materials suffers from ambiguity in kinetic energy operator ordering, caused by non-vanishing commutator of the momentum operator and the position-dependent effective mass $m(z)$. This leads to non-uniqueness of Hamiltonian, which in its general form can be written as

Meeting Program

Third Annual Symposium on Ceramics and Advanced Materials

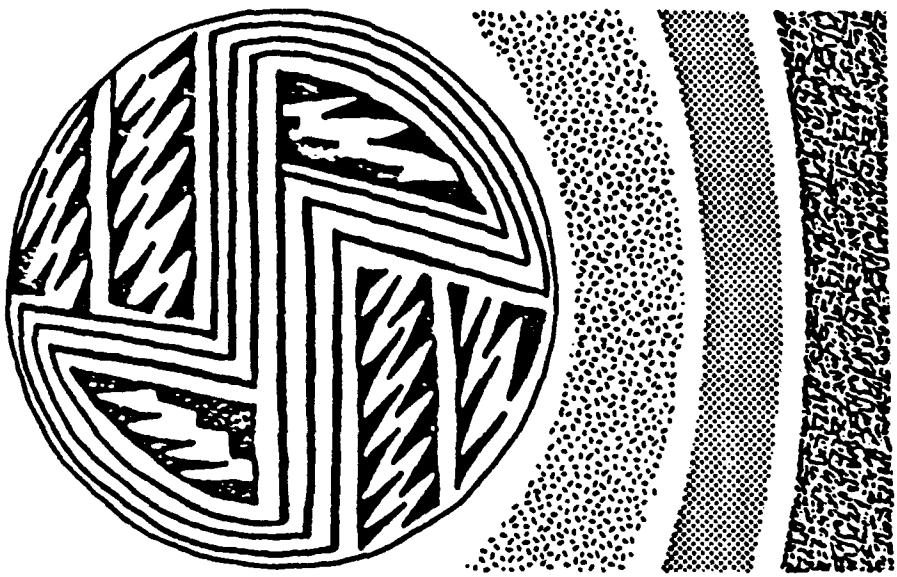

Hyatt Regency Hotel
Albuquerque, NM
October 24-25, 1991

Sponsored by:

The New Mexico Sections of the
American Ceramic Society and
the Materials Research Society

threshold for facet damage. The primary challenge has been to maintain a coherent single spatial mode at high power levels from a large aperture device. For this reason, multielement phase-locked arrays have been under development for over a decade as a means of obtaining a mode stabilized device that can operate reliably at power levels in the range 0.5–1.0 W.

Monolithic phase-locked arrays have been studied for many years. To date the best approach for stable phase-locking to high powers is resonant arrays of antiguides[1] (so called ROW arrays). ROW arrays have the unique property that full coherence and lateral-optical-mode stability coexist. Results to date are: 0.5-W cw diffraction-limited (DL) operation; 1.5-W DL pulsed operation; and 5 W in a beam 3 × DL. Reliable operation at 1-W cw power is expected in the near future. Particularly attractive is the fact that ROW devices do not need active phase control. In turn the devices' reliability is expected to be high. Beyond 1 W, ROW arrays can be scaled in two dimensions with the ultimate goal of >10-W coherent power.

As for emitting facet passivation the approach is nonabsorbing mirror. It has been implemented by etch-and-regrowth diffusion-induced lattice disordering and, more recently, using sulphur-based solutions prior to facet coating. Another recent development is the discovery that strained-layer quantum well InGaAs/GaAs/AlGaAs lasers have virtually no initial degradation, and that the emitting facet damage threshold is 3–4 times that of GaAs-active-layer devices. Passivating the emitting facets will increase the reliable power level by a factor of 3 to 4.

References

1. D. Botez, *et al.*, Appl. Phys. Lett. 54, 2183 (1989).

2:00pm

WS3 Recent advances in antiguided diode laser arrays

L. J. Mawst, D. Botez, M. Jansen, S. Peterson, S. S. Ou, M. Sergant, T. J. Roth, and C. Z. Mutz

TRW Research Center, 1 Space Park, Redondo Beach, California 90278

Resonant-optical-waveguide (ROW) arrays are monolithic devices capable of radiating in a diffraction-limited beam to high output power levels. These devices are attractive for many applications because they are one wire devices with no active phase control required, that is, the internal structure of the array both controls and locks the phase of each emitter. In effect, the ROW array operates as lateral DFB for spatial modes.

Modal discrimination in these structures is a complex process that involves several mechanisms: (1) edge radiation losses, (2) modal overlap with gain (gamma effect), and (3) interelement losses. As expected, there is a tradeoff between low threshold, high efficiency operation and strong modal discrimination. However, as demonstrated here, high performance cw operation can be obtained from optimized ROW-type devices. ROW arrays with optimized facet coatings operate in an in-phase mode with a diffraction-limited beam up to 500 mW in cw conditions. Threshold currents are 270 mA with efficiencies of 42% for a 1000-μm long cavity.

Since optimal performance in these devices is dependent on matching a lateral resonance condition, a new type of antiguided array based on the self-aligned stripe geometry has been pursued. In these structures, layers critical to obtaining the resonance condition (i.e., passive guide layer) are grown planar during a first phase growth. Design, fabrication, and device characteristics of these devices are discussed.

2:15pm

WS4 Thermal focusing effects in gain-guided diode laser arrays

Marek Osinski and Chung-Pin Cherng

University of New Mexico, Center for High Technology Materials, Albuquerque, New Mexico 87131-6081

Thermal effects in diode laser arrays are known to be important for the array mode selection.[1] Here, we examine in detail the role of active region heating, considering a uniform ten-strip GaAs/AlGaAs gain-guided array. The array is regarded as a perturbed broad-area laser whose modes are coupled via complex-permittivity perturbations induced by heating and injected carriers. Array modes are determined using the coupled-mode theory. The thermal perturbation is taken as a half-period cosine with center value of ΔT, vanishing at the lateral claddings. When heating-induced waveguide nonuniformity is small, the dominant array mode is $v = 10$. Calculated temperature dependence of modal gain spectra reveals that with raising temperature, the highest-gain mode shifts gradually from $v = 10$ to $v = 13$. Thus, thermal focusing results in sequential excitation of high-order modes with increasing pumping current. Calculated near- and far-field patterns for $\Delta T = 4°C$ are in excellent agreement with injection-seeding experiments,[2] while numerical simulations[2] with $\Delta T = 10°C$ give somewhat narrower near fields for $v > 10$. This indicates that the active region heating may not be as severe as previously thought. Sensitivity of the high-order modes to thermal focusing can be used to establish the actual temperature increase with good accuracy.

References

1. G. R. Hadley, J. P. Hohimer, and A. Owyoung, J. Appl. Phys. 61, 1697 (1987).
2. G. R. Hadley, J. P. Hohimer, and A. Owyoung, IEEE J. Quantum Electron. QE-23, 765 (1987).

2:30pm

WS5 Array-mode selection in nonabsorbing-mirror diode laser arrays

William E. Thompson, Chung-Pin Cherng, and Mark Osinski

University of New Mexico, Center for High Technology Materials, Albuquerque, New Mexico 87131-6081

Nonabsorbing mirror (NAM) GaAs/AlGaAs arrays have been shown to deliver thermally limited cw output power as high as 2.4 W from a 100-μm aperture.[1] Typically, these devices operate in high-order array modes with a double-lobe far field. In this paper, we show that with careful design, the NAM section can be utilized to favor single far-field lobe operation. We treat the NAM array as a composite cavity consisting of a waveguide region in which parallel single-mode waveguides are coupled through evanescent fields of guided modes and a uniform NAM section that provides further coupling between individual waveguide modes via diffraction. The eigenmodes of the waveguide section (supermodes) are calculated using the improved coupled-mode theory.[2] The supermode mixing coefficients, determining the eigenmodes of the composite cavity, are obtained by evaluating the reflected image at the interface between the waveguiding and uniform sections of the device using the 3-D diffraction integral. If the phase difference between light returning from the NAM section and injected back into any particular waveguide and its nearest neighbor is an integer multiple of 2π, the in-phase supermode is reinforced. On the other hand, a small variation in the NAM-section length and/or the waveguide spacing is sufficient to dramatically change the far-field. The performance of NAM arrays, is therefore, very sensitive to details of the waveguide structure.

References

1. D. F. Welch, W. Streifer, R. L. Thornton, and T. Paoli, Electron. Lett. 23, 525 (1987).
2. A. Hardy and W. Streifer, J. Lightwave Technol. LT-4, 90 (1986).

2:45pm

WS6 Phase-locked multidiode laser beam combining cavity optimized by asymmetrical design

Roger S. Putnam

Aerodyne Research, Inc., 45 Manning Road, Billerica, Massachusetts 01821

Phase-locked laser combining systems using intracavity holograms, spatial filters, or beam splitters are shown to be mathematically equivalent and to provide strong phase-locking by providing a minimum loss for in-phase cooperation. Our model accurately predicts the combinations of diode laser currents required by a multidiode laser system to achieve threshold. This model also correctly predicts the parabolic increase in optical power emitted at the phase canceled port as a function of the diode lasers' drive current imbalance. The automatic phase adjustments needed for efficient power collection, which are produced by small changes in the optical frequency, are shown to be greatly augmented by increasing the mismatch in cavity lengths among the various laser arms of the compound cavity. This cavity design guarantees efficient power collection independent of pathlength changes along the laser arms. A real-time measurement of the self-locked phase error is also shown to decrease for narrow spectral behavior and increase for broadband lasing.

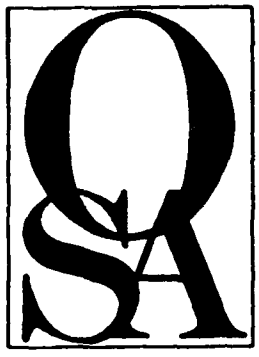

1991 Optical Society of America Annual Meeting

Summaries of papers presented at the Annual Meeting of the Optical Society of America

November 3–8, 1991
San Jose, California

1991 Technical Digest Series
Volume 17

CONFERENCE EDITION

Optical Society of America
2010 Massachusetts Avenue, NW
Washington, DC 20036

Articles in this publication may be cited in other publications. In order to facilitate access to the original publication source, the following form for the citation is suggested:

> Name of Author(s), "Title of Paper," in OSA Annual Meeting Technical Digest, 1991 (Optical Society of America, Washington, D.C., 1991), Vol. 17, pp. xx-xx.

ISBN Number

Conference Edition	1-55752-210-3 (softcover)
Postconference Edition	1-55752-211-1 (hardcover)
(Note: Postconference Edition includes postdeadline papers.)	
1991 Technical Digest Series	1-55752-192-1 (hardcover)

Library of Congress Catalog Card Number

Conference Edition	91-66977
Postconference Edition	91-66978

Copyright © 1991, Optical Society of America

Individual readers of this digest and libraries acting for them are permitted to make fair use of the material in it, such as to copy an article for use in teaching or research, without payment of fee, provided that such copies are not sold. Copying for sale is subject to payment of copying fees. The code 1-55752-192-1/91/$2.00 gives the per-article copying fee for each copy of the article made beyond the free copying permitted under Sections 107 and 108 of the U.S. Copyright Law. The fee should be paid through the Copyright Clearance Center, Inc., 21 Congress Street, Salem, MA 01970.

Permission is granted to quote excerpts from articles in this digest in scientific works with the customary acknowledgment of the source, including the author's name and the name of the digest, page, year, and name of the Society. Reproduction of figures and tables is likewise permitted in other articles and books provided that the same information is printed with them and notification is given to the Optical Society of America. Republication or systematic or multiple reproduction of any material in this digest is permitted only under license from the Optical Society of America; in addition, the Optical Society may require that permission also be obtained from one of the authors. Address inquiries and notices to Director of Publications, Optical Society of America, 2010 Massachusetts Avenue, NW, Washington, DC 20036. In the case of articles whose authors are employees of the United States Government or its contractors or grantees, the Optical Society of America recognizes the right of the United States Government to retain a nonexclusive, royalty-free license to use the author's copyrighted article for United States Government purposes.

In summary, a one-stripe antiguided array has operated in an output power in excess of 500 mW CW. The array has a 170 mA threshold and differential efficiency of 30%. The output spectra of the device at single mode to 330 mA, where a second longitudinal mode is observed. By spectrally resolving the FF, operation of two spatial modes has been verified.

The authors wish to thank W. B. Plano, T. Tully, and J. Baquerra for expert assistance and G. Ronald Hadley and C. P. Schaus for helpful discussions.

1. D. Ackley and R. Engelmann, Appl. Phys. Lett. 39, 27 (1981).
2. J. Moser, D. Botez, M. Jansen, T. J. Roth, J. Rosenberger, Electron. Lett. 27, 389 (1991).
3. P. Hohimer, G. R. Hadley, D. C. Craft, T. H. Shen, S. Sun, and C. P. Schaus, Appl. Phys. Lett. 58, 452. (1991).

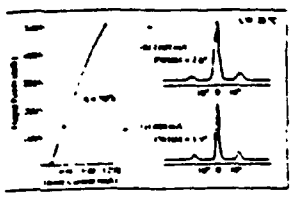

Figure 1

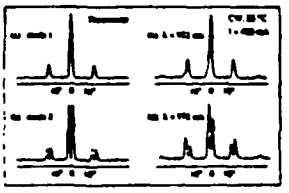

Figure 2

SDL1.5
2:15pm
INJECTION LOCKING OF ANTIGUIDED RESONANT OPTICAL WAVEGUIDE (ROW) ARRAYS*

M. Jansen, D. Botez, L. Mawst, T. Roth, J. Yang,
P. Hayashida, L. Dossi, and J. Rosenberger
TRW
Space and Technology Group
One Space Park
Redondo Beach, Ca. 90278

Resonant antiguided arrays[1] are very different from either broad area lasers or strongly index guided arrays since they combine a strong lateral coupling mechanism (leaky wave coupling), with a strong index-guided profile. This presents new opportunities for efficient injection locking (high injection ratios), and a way to minimize requirements on the master oscillator (MO) beam profile. In addition, since the far-field profiles are diffraction limited to begin with, it is not necessary to alter the far-field emission, but rather to reinforce the in-phase eigenmode to higher output powers.

20 element ROW antiguided arrays were locked to 2.6 times above the threshold level ($2.6 \times I_{th}$) by injecting light from a master oscillator in a direction normal to the diode facet and only in one element of the array (i.e. the MO beam was brought to a tight focus on the slave laser (SL) aperture at normal incidence, corresponding to an approximate incident beam diameter of 5 μm). The spectra and far-field output pattern of the SL were found to be independent of the MO beam position on the SL facet, and the far-field pattern was stable with wavelength detuning (i.e. no steering). Single frequency tuning was achieved over a > 30 Å spectral range, and the beam pattern was found to be stable and diffraction-limited for nearly resonant devices.

The injection-locking behavior of ROW arrays was found to be significantly different from that of weakly-guided arrays or broad area lasers, where locking is optimized for MO injection at an angle, the far-field pattern varies widely with injection conditions, locking can only be achieved close to and up to $2 \times I_{th}$, and wavelength tuning has been shown to result in beam steering[2-4].

To the best of our knowledge, this is the first demonstration of successful injection-locking of a monolithic index-guided array. Furthermore it is the first report of wavelength tuning with no impact on the beam shape or position in laser diode arrays.

* This work was funded by Phillips Laboratory.

1. L.J. Mawst, D. Botez, T.J. Roth, G. Peterson, and J. Rosenberger, Appl. Phys. Lett. 58 (1), 22 (1991)
2. M.E. Chun, L. Goldberg and J.F. Weller, Optics Lett. 14 (5), 272 (1989)
3. G.L. Abbas, S. Yang, V.O.S. Chan, and J.G. Fujimoto. IEEE J. Quantum Electron., QE (4), 609 (1988)
4. J.P. Hohimer, G.R. Hadley, and A. Owyoung, Appl. Phys. Lett. 49 (22), 1504 (1986)

SDL1.6
2:30pm
BROAD-AREA MODE COUPLING IN GAIN-GUIDED DIODE LASER ARRAYS

Marek Osiński and Chung-Pin Cheung

*Center for High Technology Materials, University of New Mexico
Albuquerque, New Mexico 87131-6081*

Diode laser arrays are very attractive for applications requiring high-power optical sources, such as solid-state laser pumping and laser printers. CW output power as high as 8 W has been reported[1] for single-quantum-well gain-guided arrays with 200-μm aperture. However, gain-guided arrays usually operate multimode with rather low degree of coherence. Many applications, for example fiber and free-space satellite communications, require a highly coherent light source, preferably consisting in a single lobe. From this perspective, it is very important to reach a good understanding of lateral mode properties in gain-guided arrays.

A standard method of investigating the modal behavior of phased-array lasers is the coupled-mode (supermode) theory, suitable only for index-guided arrays, as it utilizes a basis of individual waveguide modes. For gain-guided arrays, with no built-in lateral variations of refractive index, such treatment fails to predict correctly the number of array modes and their relative gains. It has been pointed out that a more appropriate approach should be to treat the gain-guided array as a perturbed broad-area laser[2], since the number of lateral modes is not limited in this case by the number of array elements. Such approach has been chosen recently as a simple model of gain-guided arrays, based on standard perturbation theory[3]. In order to simplify numerical calculations, an infinite loss was assumed outside the active region and all the unperturbed (broad area) modes were ascribed a constant modal gain.

Rather than using the perturbation theory, we apply the improved coupled mode formulation[4], but with a basis of broad-area modes instead of individual waveguide modes. An active dielectric-slab broad-area waveguide is considered, with the gain-index coupling as well as temperature effects included as a perturbation. Exact complex solutions of the broad-area problem are used, without relying on the aforementioned assumptions. The device under study is similar to commercially available GaAs/AlGaAs gain-guided arrays (SDL-2410C), with ten 6-μm stripes on 10-μm centers and with a multiple-quantum-well active region.

Our results demonstrate that the good agreement between the simplified perturbation model and experimental observations[3] was fortuitous. When a very high loss in the lateral claddings is assumed, the modal gains of broad-area modes are indeed nearly constant. However, as soon as a realistic value of loss in the lateral cladding is adopted, dramatic changes occur in the modal gain spectra. This is caused by increasing penetration of broad-area modes into claddings with decreasing loss. Calculated near- and far-field patterns are in excellent agreement with comprehensive numerical simulations[5] and experimental observations[3], which demonstrates that the broad-area coupled-mode theory provides fairly accurate description of array modes.

In conclusion, we report on an improved coupled-mode analysis of gain-guided arrays, treating the device as a perturbed broad-area laser. The broad-area mode coupling removes the constraints of supermode theory and leads to formation of high-order array modes. Excellent agreement with numerical simulations and experimental observations is achieved.

References

1. D. F. Welch, B. Chan, W. Streifer, and D. R. Scifres, Electron. Lett. 24, 113 (1988).
2. J. P. Hohimer, G. R. Hadley, and A. Owyoung, Appl. Phys. Lett. 48, 1504 (1987).
3. J.-M. Verdiell and R. Frey, IEEE J. Quantum Electron. 26, 270 (1990).
4. W. Streifer, M. Osiński, and A. Hardy, J. Lightwave Techn. LT-5, 1 (1987).
5. G. R. Hadley, J. P. Hohimer, and A. Owyoung, IEEE J. Quantum Electron. QE-23, 765 (1987).

SDL1.7
2:45pm
STRAINED LAYER QUANTUM WELL LASERS AT 1.06μm WITH UP TO 5.25W CW FROM A SINGLE 100μm STRIPE

Richard P. Morton, Nigel Holehouse, Shuyan R. Lee, Alan H. Moore,
EG&G Optoelectronics, 22001 Dumberry Road, Vaudreuil, Quebec J7V 8P7, Canada

T.M. Cockerill, J.J. Coleman,
University of Illinois at Urbana-Champaign, 137 Microelectronics Laboratory,
208 North Wright St., Urbana, IL 61801, USA

Various authors have reported direct generation of 1.06μm radiation from laser diodes [1-3] using different materials systems, of which the strained-layer quantum well approach [3,4] is the most promising. We present results showing high power 1.06μm emission at room temperature from strained layer quantum well laser diodes, reaching 5.25 Watts under continuous operation at room temperature from a single 100μm stripe before catastrophic facet damage.

The epitaxial structure is a InGaAs/GaAs/AlGaAs step-index separate confinement strained quantum well heterostructure [5] grown in an atmospheric pressure, vertical geometry, MOCVD reactor. The sources used for the epitaxial growth were trimethylgallium, trimethylaluminium, and ethyldimethylindium and 10% arsine in hydrogen, and the n- and p-type dopant sources were disilane and diethylzinc respectively. The active region comprises a single $In_{0.2}Ga_{0.8}As$ 70Å quantum well surrounded by 100Å GaAs barriers, with $Al_{0.3}Ga_{0.7}As$ confining layers 1.5μm thick. The growth temperature was 720°C, reduced to 625°C for the strained quantum well. The threshold current density was 100Acm^{-2} and the characteristic temperature T_0 was 160K.

The wafers were processed into 100μm broad area oxide stripes with the degenerately doped contact layer etched away outside the stripe. Devices were cleaved at 1000μm cavity length, and facet coatings were applied, giving front and rear facet reflectivities of around 5% and 95% respectively. They were then soldered onto metallised diamond heatsinks. The threshold current in this configuration was 185mA, and the differential quantum efficiency was measured to be 68% from the front facet.

The CW room temperature light-current characteristic is shown in Figure 1, reaching to 5.25W at 9A, at which point catastrophic facet damage (CFD) occurred. Pulsed measurements obtained at 200ns and 10kHz, continued to rise to 25W at 48A, also limited by CFD. Subsequent examination using an SEM confirmed CFD as the failure mechanism in both cases. The measured total power conversion efficiency at 1W output is 39%, falling to 28% at 3W. The spectrum at 20°C at 1W output is given in Figure 2.

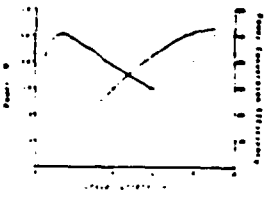

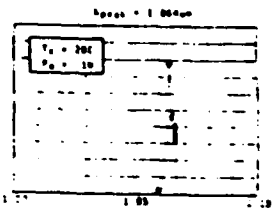

REFERENCES

[1] NUESE et al. *Appl. Phys. Lett.* 20 (12) P987
[2] VAN DONGEN et al. *Electron. Lett.*, 20, (19), p827
[3] MAJOR et al. *Appl. Phys. Lett.* 56 (7) p685
[4] YOUNG et al. *Appl. Phys. Lett.* 54, (6) p499
[5] BEERNINK et al. *Appl. Phys. Lett.* 55 (25) p2585

LEOS '91 Conference Digest

IEEE Lasers and
Electro-Optics Society
1991 Annual Meeting
November 4 - 7, 1991

San Jose Convention Center
San Jose, CA

In conjunction with OPTCON '91 and the following major conferences:

Optical Society of America Annual Meeting (OSA)
International Congress on Applications of Lasers and Electro-Optics (LIA)
and
SPIE's 1991 Symposium on Optical Science and Engineering

IEEE Catalog #: 91CH2949-6
Library of Congress #: 90-85246

Submitted to CLEO'92 Conf. on Lasers & Electro-Optics, Anaheim, CA, May 10-15, 1992

ARRAY MODE EVOLUTION IN GAIN-GUIDED DIODE LASER ARRAYS

by

MAREK OSIŃSKI and CHUNG-PIN CHERNG

Center for High Technology Materials, University of New Mexico,

Albuquerque, New Mexico 87131-6081

Corresponding author: Professor Marek Osiński,

Center for High Technology Materials,

University of New Mexico,

Albuquerque, New Mexico 87131-6081.

Tel. (505) 277-6031

Fax (505) 277-6433

Abstract

Array modes of gain-guided diode laser arrays are studied using broad-area coupled-mode theory incorporating thermal waveguiding. Calculated near- and far-fields are in excellent agreement with experimental and numerical data. Thermally driven high-order mode switching is predicted.

ARRAY MODE EVOLUTION IN GAIN-GUIDED DIODE LASER ARRAYS

by

MAREK OSIŃSKI and CHUNG-PIN CHERNG

Center for High Technology Materials, University of New Mexico,

Albuquerque, New Mexico 87131-6081

Corresponding author: Professor Marek Osiński,

Center for High Technology Materials,

University of New Mexico,

Albuquerque, New Mexico 87131-6081.

Tel. (505) 277-6031

Fax (505) 277-6433

In spite of a significant progress in increasing the output power of gain-guided diode laser arrays, their modal behavior remains poorly understood. This can be attributed to absence of adequate analytical treatment valid for these devices. On the other hand, it is difficult to gain insight into mechanisms determining modal properties of laser arrays by applying comprehensive numerical analysis[1].

Recently, we have developed a new analytical approach to gain-guided arrays[2]. The array modes are determined using coupled-mode theory with a broad-area mode basis. We have shown that earlier simple analytical treatment[3] relying on assumptions of infinite loss in the lateral claddings and equal modal gains for all broad-area modes led to

considerable errors in predicted array mode gains and was therefore unsuitable for gain-guided array analysis.

Incorporation of thermal waveguiding in the analysis is important for above-threshold operation of the array. As the pumping current increases, so does the active-region temperature and the lateral temperature profile becomes increasingly nonuniform. We approximate the thermally-induced perturbation of broad-area waveguide by a half-period of the raised cosine function, falling to zero at the edges of the array.

The device considered is a uniform 10-stripe GaAs/AlGaAs gain-guided array, similar to commercially available devices (SDL-2410C, 6-μm stripes on 10-μm centers, multiple-quantum-well active region). 40 broad-area modes are included in calculations.

Fig. 1 shows temperature dependence of modal gain spectra, with center value of temperature raise ΔT as a parameter. Note that with rising temperature, the highest-gain mode shifts gradually from $\nu = 10$ to $\nu = 13$. Incidentally, heating by only 1 °C suffices to neutralize the carrier-induced index antiguiding. Thus, we predict that due to thermal focusing the dominant array mode will be shifting towards higher-order modes with increasing pumping current.

A rather spectacular result of our analysis is an impressive sensitivity of modal intensity patterns to the active-region temperature. Fig. 2 shows near- and far-field patterns for the array mode $\nu = 10$ which dominates when heating-induced waveguide nonuniformity is small. $\Delta T = 0$ corresponds to index antiguiding, $\Delta T = 2$ °C to very weak index guiding, and $\Delta T = 4$ °C to index guiding. As illustrated by Fig. 3 (mode $\nu = 15$), near-field patterns of other high-order modes also experience significant transformation with increasing temperature.

By adjusting the value of ΔT to 4 °C we were able to obtain excellent agreement with injection-seeding experiments and extensive numerical simulations for all high-order modes for which published data were available[1]. Examination of results reveals that the confinement of high-order array modes improves with increasing temperature. However, once a given mode is well confined, its near-field pattern remains almost unchanged, while higher-order modes continue to narrow down. The high-order modes are more sensitive to thermal focusing and can be used to establish the actual temperature increase with greater accuracy.

In conclusion, incorporation of thermal effects in broad-area coupled-mode theory of gain-guided laser arrays leads to an excellent agreement with earlier experimental data and comprehensive numerical simulations. Sequential excitation of high-order modes with increasing temperature is predicted. Remarkable changes in calculated near-field patterns with increasing strength of thermal waveguide make it possible to utilize spectrally-resolved near-field measurements to determine temperature profile inside the active region.

References

1. G. R. Hadley, J. P. Hohimer, and A. Owyoung, IEEE J. Quantum Electron. QE-23, 765 (1987).
2. C.-P. Cherng and M. Osiński, J. Appl. Phys. 70, 4617 (1991).
3. J.-M. Verdiell and R. Frey, IEEE J. Quantum Electron. 26, 270 (1990).

Figure Captions

Fig. 1. Temperature dependence of modal gain spectra of first 20 array modes in a 10-stripe 100-μm aperture gain-guided array. The perturbation term has a form of a sinusoidal modulation of gain (and index through the linewidth broadening factor) with amplitude of 10 cm^{-1}, superimposed on a half-cosine thermal profile with amplitude ΔT.

Fig. 2. Near- and far-field patterns of the array mode $\nu = 10$ calculated for various amplitudes ΔT of lateral temperature profile.

Fig. 3. Near- and far-field patterns of the array mode $\nu = 15$ calculated for various amplitudes ΔT of lateral temperature profile.

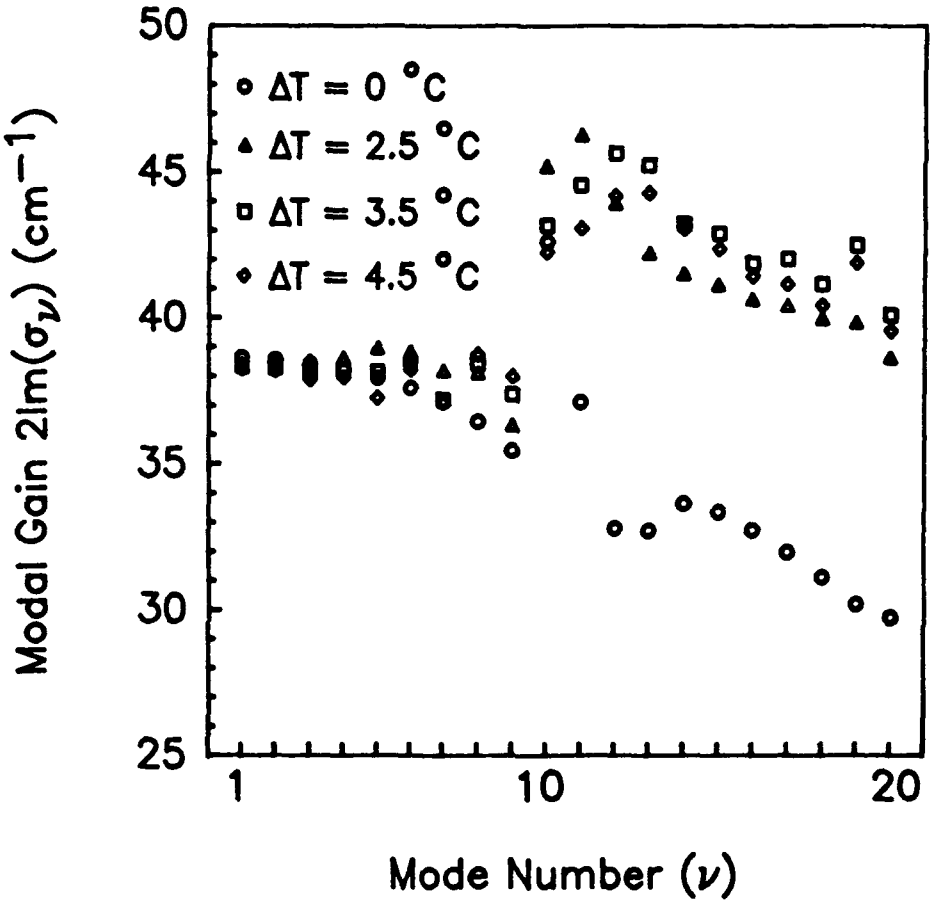
50
45
40
35
30
25
1
10
20
ΔT = 0 °C
ΔT = 2.5 °C
ΔT = 3.5 °C
ΔT = 4.5 °C
Modal Gain 2Im(σν) (cm⁻¹)
Mode Number (ν)

Figure 1

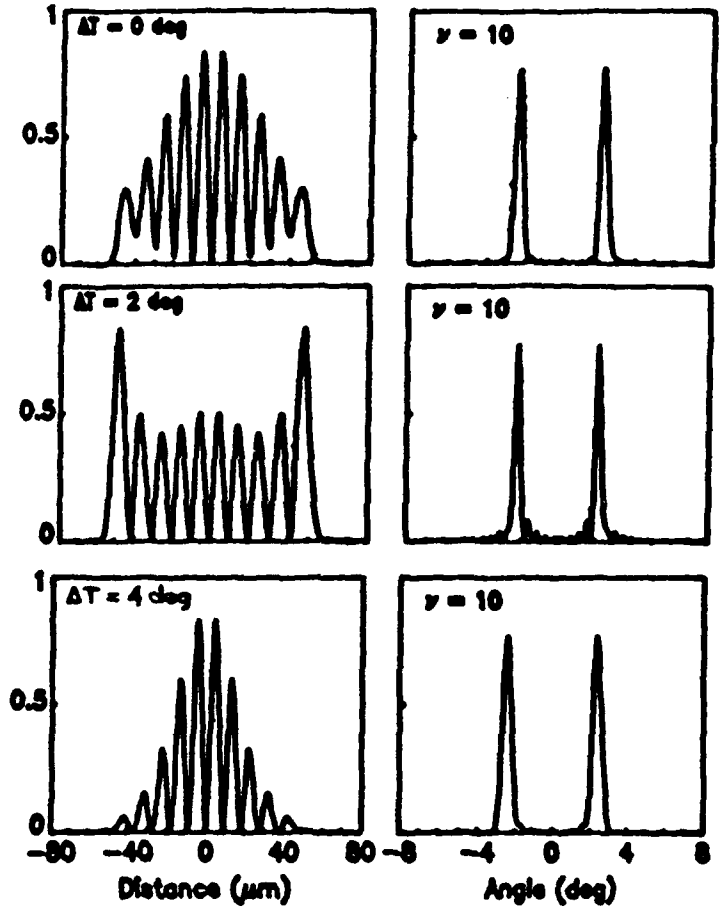
ΔT = 0 deg
γ = 10
ΔT = 2 deg
γ = 10
ΔT = 4 deg
γ = 10
1
0.5
0
−80 −40 0 40 80
Distance (μm)
−8 −4 0 4 8
Angle (deg)

Figure 2

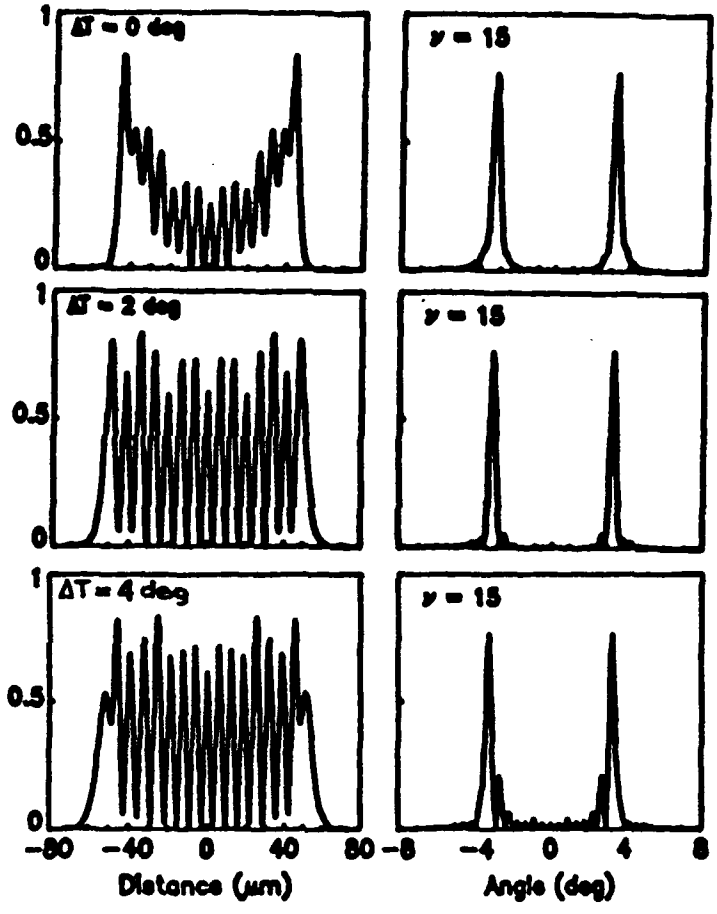
ΔT = 0 deg
γ = 15
ΔT = 2 deg
γ = 15
ΔT = 4 deg
γ = 15
1
0.5
0
−80 −40 0 40 80
Distance (μm)
−8 −4 0 4 8
Angle (deg)

Figure 3

Submission to CLEO '92 - Symposium on Semiconductor Lasers

HIGH POWER SINGLE-LATERAL-MODE UNSTABLE RESONATOR WIDE-STRIPE SEMICONDUCTOR LASERS

Swaminathan T. Srinivasan*, Christian F. Schaus, Eric A. Armour, John G. McInerney and Steve Hersee

Center for High Technology Materials (CHTM)
University of New Mexico, Albuquerque, NM 87131-6081

Alan H. Paxton

Mission Research Corporation, 1720, Randolph SE, Albuquerque, NM 87106

David J. Gallant, Michael L. Tilton

Rockwell Power Systems, 2511, Broadbent Parkway NE, Albuquerque, NM 87185

Gregory C. Dente

GCD Associates, 2100, Alvarado NE, Albuquerque, NM 87110

* Corresponding author. Tel. (505) 277-0239 / 277 -1427 ; Fax (505) 277-6433.

ABSTRACT

Single-lateral-mode, high power operation has been achieved in wide-stripe InGaAs/GaAs/AlGaAs semiconductor lasers using an unstable resonator configuration with diverging elements distributed along the stripe. Pulsed output powers of 490 mW have been demonstrated.

HIGH POWER SINGLE-LATERAL-MODE UNSTABLE RESONATOR WIDE-STRIPE SEMICONDUCTOR LASERS

Swaminathan T. Srinivasan, C.F. Schaus, E.A. Armour, J.G. McInerney and S. Hersee
Center for High Technology Materials
University of New Mexico, Albuquerque, NM 87131-6081

Alan H. Paxton
Mission Research Corporation, 1720, Randolph SE, Albuquerque, NM 87106

D. J. Gallant, M. L. Tilton
Rockwell Power Systems, 2511, Broadbent Parkway NE, Albuquerque, NM 87185

G. C. Dente
GCD Associates, 2100, Alvarado NE, Albuquerque, NM 87110

High-power semiconductor lasers are required for a broad range of applications. There are limitations on the peak output power that can be obtained from single-stripe lasers. Phase-locked arrays have been used to increase output powers with coupling between individual narrow-stripe emitters.

A novel solution is to implement an unstable resonator configuration. Higher order lateral modes encounter more loss and filament-formation is discouraged. Cylindrical etched facets have been used to induce single-lateral-mode operation in wide-stripe lasers [1]. Another way to form an unstable resonator is to introduce diverging lens-like optical elements along the stripe[2]. By modifying this geometry, we have achieved single-lateral-mode operation in broad area lasers more than 150 μm wide.

HIGH POWER SINGLE-LATERAL-MODE UNSTABLE RESONATOR WIDE-STRIPE SEMICONDUCTOR LASERS

Swaminathan T. Srinivasan, Alan H. Paxton, D. J. Gallant, C.F. Schaus, E.A. Armour, J.G. McInerney , S. Hersee, M. L. Tilton and G. C. Dente

Negative cylindrical lenses were incorporated into the laser above the active region by wet-chemical etching, with subsequent regrowth of the p-AlGaAs cladding layer. Detailed calculations were made to estimate the optical mode profile in the transverse direction, and an asymmetric Graded-Index Separate-Confinement-Heterostructure (AGRIN-SCH) active region was chosen to enhance the coupling with the diverging lens-train.

The structure was grown by Metal-Organic Chemical Vapor Deposition (MOCVD). The asymmetric GRIN-SCH active region contains an InGaAs Single Quantum Well (SQW). A GaAs layer (600 Å thick) was grown on top of a 0.1 μm AlGaAs spacer which is immediately above the active region, following which the growth was stopped. The lens-train pattern was formed using wet-chemical etching. The etch depth was 400 Å, corresponding to an effective index step of about 0.01. The top p-AlGaAs cladding and GaAs cap layers were re-grown subsequently. The gain-guided lasers were then fabricated using a standard process .

Single-lateral-mode operation at upto 3.5 times the threshold current (I_{th}) has been achieved in 1000 μm long, 100 μm wide lasers with a total output power of 490 mW for pulsed (1μs, 10 kHz) operation. Spatial coherence (measured using Young's double-slit in the near-field image plane) across 80 μm of the near- field is 65% at 3.5 x I_{th} and 80% at twice threshold. To the best of our knowledge, this is the highest single-lateral-mode power achieved

HIGH POWER SINGLE-LATERAL MODE UNSTABLE RESONATOR WIDE-STRIPE SEMICONDUCTOR LASERS

Swaminathan T. Srinivasan, Alan H. Paxton, D. J. Gallant, C.F. Schaus, E.A. Armour, J.G. McInerney, S. Hersee, M. L. Tilton and G. C. Dente

with a single wide-stripe semiconductor laser without external optical elements. The threshold current density was 400 A/cm^2 and external differential quantum efficiency was 36%. The nominal round-trip divergence factor is 2.53 for these devices. The far-field divergence angle is less than 1.4 times the diffraction limit.

Using a different design with a nominal round-trip divergence factor of 1.91, single-lateral-mode operation has been obtained in 170 μm wide laser stripes, with 175 mW total output power at 2.5 x I_{th}. Spatial coherence across 135 μm centered in the near field exceeds 60 %. For 1000 μm long devices, the threshold current density was 250 A/cm^2 with an external differential quantum efficiency of 27 %.

Results from several different designs are being analyzed to optimize the performance of these devices. New results will be also be presented.

HIGH POWER SINGLE-LATERAL-MODE UNSTABLE RESONATOR WIDE-STRIPE SEMICONDUCTOR LASERS

Swaminathan T. Srinivasan, Alan H. Paxton, D. J. Gallant, C.F. Schaus, E.A. Armour, J.G. McInerney , S. Hersee, M. L. Tilton and G. C. Dente

REFERENCES

1) "High Power, Nearly Diffraction-Limited Output from a Semiconductor laser with an Unstable Resonator", M.L. Tilton et al., *Journal of Quantum Electronics, Vol. 27, No. 9, September 1991.*

2) "Fundamental Lateral- Mode Operation in Wide-stripe Lasers Having Built-in Lenslike Refractive Index Distributions", S. Nakatsuka and K. Tatsuno, *Japanese Journal of Applied Physics, Vol. 28, No. 6, June 1989.*

HIGH POWER SINGLE-LATERAL-MODE UNSTABLE RESONATOR WIDE-STRIPE SEMICONDUCTOR LASERS

Swaminathan T. Srinivasan, Alan H. Paxton, D. J. Gallant, C.F. Schaus, E.A. Armour, J.G. McInerney , S. Hersee, M. L. Tilton and G. C. Dente

Fig. 1(a)

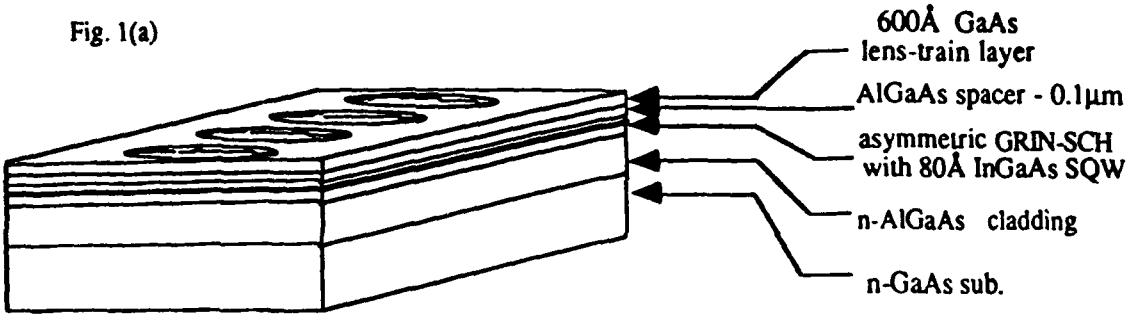

Fig. 1 (b)

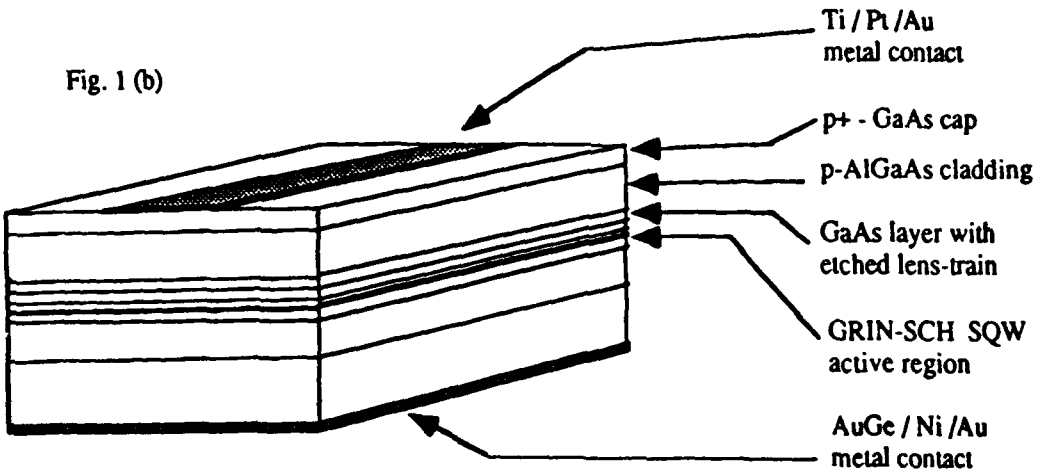

HIGH POWER SINGLE-LATERAL-MODE UNSTABLE RESONATOR WIDE-STRIPE SEMICONDUCTOR LASERS

Swaminathan T. Srinivasan, Alan H. Paxton, D. J. Gallant, C.F. Schaus, E.A. Armour, J.G. McInerney , S. Hersee, M. L. Tilton and G. C. Dente

FIGURE CAPTIONS

Fig. 1(a) - Structure after first MOCVD growth and etching of lens pattern

Fig. 1(b) - Structure after MOCVD regrowth of p-type cladding and cap layers, followed by a gain-guided laser fabrication process

Presented at SPIE/OE LASE 92.
Jan 19-25, LA.

Submitted to SPIE

Semiconductor laser with unstable resonator consisting of negative cylindrical lenses

Swaminathan T. Srinivasan, Christian F. Schaus, Shang-Zhu Sun and Eric. A. Armour
Center for High Technology Materials (CHTM)
University of New Mexico, Albuquerque, NM 87131-6081

Alan H. Paxton
Mission Research Corporation, 1720, Randolph SE, Albuquerque, NM 87106

David J. Gallant
Rockwell Power Systems, 2511, Broadbent Parkway NE, Albuquerque, NM 87185

Charles E. Moeller
Phillips Laboratory, Kirtland Air Force Base, Albuquerque, NM 87117-6008.

ABSTRACT

We have obtained high power single-lateral-mode operation in wide-stripe InGaAs/GaAs/AlGaAs semiconductor lasers using a monolithic unstable resonator (consisting of diverging elements incorporated above an asymmetric GRIN-SCH). The fabrication involves MOCVD regrowth after wet-chemical etching of lens-like patterns in a GaAs layer above the active region. Pulsed output powers of 175 mW and 490 mW have been obtained in 170 μm and 100 μm wide lasers respectively, with spatial coherence in the near-field exceeding 60%. We observe good lateral mode discrimination upto 3.5 times threshold in 100 μm stripes with a round-trip magnification of 6.4.

1. INTRODUCTION

High-power single-lateral-mode lasers are required for a wide range of applications where the beam has to be focussed tightly. Wide-stripe lasers have poor lateral beam profiles due to the presence of several higher-order modes and filamentation effects. Narrow stripe lasers have a fundamental limitation in that the peak power at the facet should not exceed about 10 MW/cm^2 - thus the peak powers obtainable are limited. Phase-locked arrays with different geometries are being developed to obtain a single high-power supermode in the far-field[1][2][3][4].

Wide stripes with unstable resonator geometries are very promising in this regard. In such a configuration, the higher order modes, especially the second, encounter significantly more loss than the fundamental one, thus providing a strong mode discrimination even at high current-injection levels. Besides, the divergence associated with the cavity prevents filamentation. Cylindrical ion-beam-milled facets have been used to obtain single-lateral-mode operation [5]. Also, diverging lens-like elements have been used along the stripe to induce fundamental mode operation [6]. We have implemented the latter design with several modifications to obtain single-lateral-mode operation in lasers with widths over 170 μm.

2. FABRICATION AND DESIGN CONSIDERATIONS

Theoretical calculations on optical mode profiles were done to determine an optimum structure in the transverse direction. The laser was grown in two steps using LP-MOCVD. Fig. 1(a) shows the structure after the first growth and incorporation of the lens-train. The structure is as follows : n^+ GaAs substrate; n-GaAs buffer layer; 1.5μm n-$Al_{0.4}Ga_{0.6}As$ cladding; 0.3μm $Al_xGa_{1-x}As$ (x_{Al}, 0.4 - 0.2) graded region; 100Å $In_{0.2}Ga_{0.8}As$ SQW; 0.1μm $Al_xGa_{1-x}As$ (x_{Al}, 0.2 - 0.4) graded region; 0.1μm $Al_{0.4}Ga_{0.6}As$ spacer layer, and a 600Å GaAs lens layer. Different lens patterns were then etched 400Å into the GaAs lens layer using a 1:1:800 $NH_4OH : H_2O_2 : H_2O$ solution. Subsequent MOCVD regrowth included a 1.5μm p-$Al_{0.4}Ga_{0.6}As$ cladding, 500Å $Al_xGa_{1-x}As$ (x_{Al}, 0.4 - 0.0) graded layer and a p^+ GaAs cap layer. The interfaces on either side of the lens layer were graded over 100Å to minimize series resistance. Tellurium was used as the n-type dopant ($1x10^{18}/cm^3$) while Carbon and Zinc were used as dopants in the p-cladding ($1x10^{18}/cm^3$) and cap layer ($1x10^{20}/cm^3$), respectively. Fig. 1(b) shows the final structure after the regrowth of the cladding and cap layers followed by a standard wide-stripe fabrication process.

Since the convex-shaped lens patterns are etched into GaAs with subsequent lower index AlGaAs regrowth, these are effectively diverging elements. Several different designs were implemented by changing the curvatures and number of lenses.

Some significant design features are the asymmetric GRIN-SCH, the use of GaAs for the lens layer and the etch depth for the pattern. The asymmetric GRIN-SCH (AGRIN-SCH) was chosen to shift the peak of the optical mode over towards the lens layer. This increases the effective index step at the etch boundaries, thereby allowing us to reduce the thickness of the lens layer and the etch depth. For the lasers reported in this letter, the etch depth was 400 Å into a layer 600 Å thick. The nominal effective index step in the transverse direction is 0.01. GaAs was chosen for the lens layer instead of AlGaAs since MOCVD regrowth on AlGaAs with significant x_{Al} is affected by oxide formation on the surface. This could have an adverse effect on the reliability of the lasers. Regrowing on GaAs by modification of the basic design results in good materials growth and is reflected in laser characteristics.

3. POWER AND SPATIAL COHERENCE MEASUREMENTS

We measured power vs. current characteristics and spatial coherence across the near-field of the lasers in pulsed operation. The setup for the latter is shown in Fig. 2. A magnified image of the near-field of the laser is formed in a plane containing a double-slit[7]. The resulting Young's interference fringes in the far-field are recorded on a CCD camera. We obtain the spatial coherence as the visibility calculated from a plot of the fringes. The spacing between the slits can be varied and their position in the near-field image can be shifted to investigate the degree of spatial coherence across the beam. All coherence figures quoted here are obtained from visibility measurements with a slit spacing of 80% of the magnified near-field width. The far-field of the lasers was obtained with an imaging lens since there is a natural divergence associated with the unstable resonator.

4. MATERIALS GROWTH QUALITY (Laser Results)

For a control laser diode without any lenses (Fabry Perot) with a cavity length of 500 μm, threshold current density (J_{th}) was 320 A/cm^2 and double-facet differential quantum efficiency (η_d) was over 85%. The series resistance was 0.8Ω. The lasing wavelength was about 0.95 μm. For a similar 1000 μm long laser, J_{th} was 200 A/cm^2 with an η_d of 75%. These results indicate good materials growth, especially the regrowth on GaAs.

5. PERFORMANCE OF UNSTABLE RESONATOR LASERS

For a 170μm wide, 1000 μm long laser, the spatial coherence was over 60% at 175 mW total output power (from both facets) at approximately twice threshold. The threshold current density was about 250 A/cm^2 with an external differential quantum efficiency of 27% (both facets) at a lasing wavelength around 955 nm. The nominal magnification for this lasers was 3.65.

For a 100μm wide, 1000 μm long laser, 490mW total output power was obtained at 3.5 times threshold with a spatial coherence of 65%. At twice threshold, the spatial coherence is 80%. The threshold current density was about 400 A/cm^2 with a differential quantum efficiency of 36%. The nominal magnification for this laser was 6.4. The far-field for currents upto 3 x I_{th} is shown in Fig. 3.

The data from different stripe widths, magnifications and laser cavity lengths are being analyzed to optimize design parameters. The theoretical calculations leading to the design will be published elsewhere.

6. CONCLUSIONS

In conclusion, we have demonstrated single-lateral-mode, high-power pulsed operation of semiconductor lasers using an unstable resonator configuration, with diverging lens-like elements incorporated along the laser stripe. Results from Fabry Perot lasers without lenses indicate excellent MOCVD regrowth over GaAs. With optimization of design parameters we expect to be able to improve the characteristics of these lasers further.

7. ACKNOWLEDGEMENTS

We would like to acknowledge G. Dente and C. Largent for discussions regarding the design and characterization, and Alfonso Torres and Morris Snipes for helpful suggestions regarding the processing. We would also like to thank Microphase Labs, Albuquerque for the fabrication of the unconventional masks involved in this work.

8. REFERENCES

1) T. H. Shiau, S. Sun, C. F. Schaus, K. Zheng and G. R. Hadley, Photonics Technology Letters, Vol. 2, Aug. 1990 (pp. 534);

2) D. Botez, M. Jansen, L. J. Mawst, G. Peterson and T. J. Roth, Applied Physics Letters, Vol. 58 (19), May 1991;

3) M. Jansen, D. Botez, L. J. Mawst, T. J. Roth, J. J. Yang, P. Hayashida, L. Dozal and J. Rozenbergs, Applied Physics Letters, Vol. 60 (1), Jan. 1992;

4) D. Mehuys, William Streifer, Robert G. Waarts, and David F. Welch, Optics Letters, Vol. 16 (11), June 1991;

5) M. L. Tilton, G. C. Dente, A. H. Paxton, J. Caer, R. K. Defreez, C. Moeller and D. Depatie, IEEE Journal of Quantum Electronics, Vol. 27, Sept. 1991 (pp. 2098);

6) S. Nakatsuka and K. Tatsuno, Japanese Journal of Applied Physics, Vol. 28 (6), June 1989;

7) G. C. Dente, K. A. Wilson, T. C. Salvi and D. Depatie, Applied Physics Letters, Vol 51 (1), July 1987;

8) A. H. Paxton and G. C. Dente, Journal of Applied Physics, Vol. 70 (6), Sept. 1991;

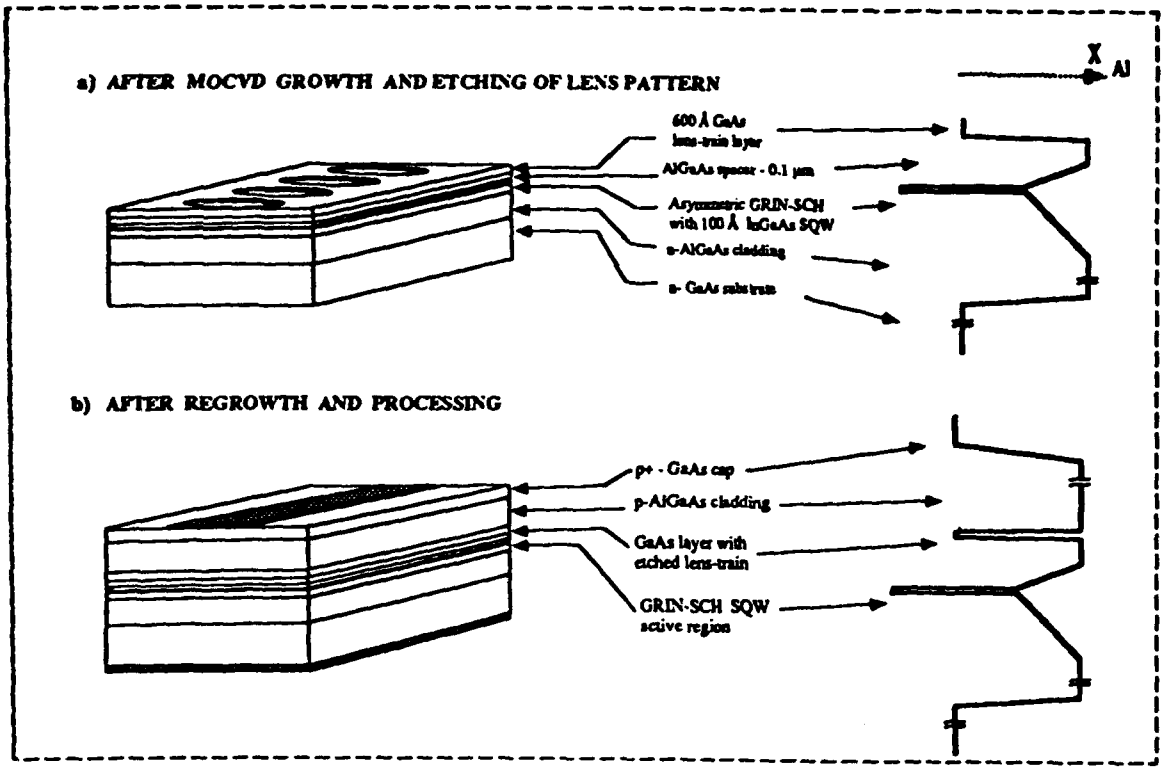

Fig. 1 - Structure of Unstable Resonator Semiconductor lasers

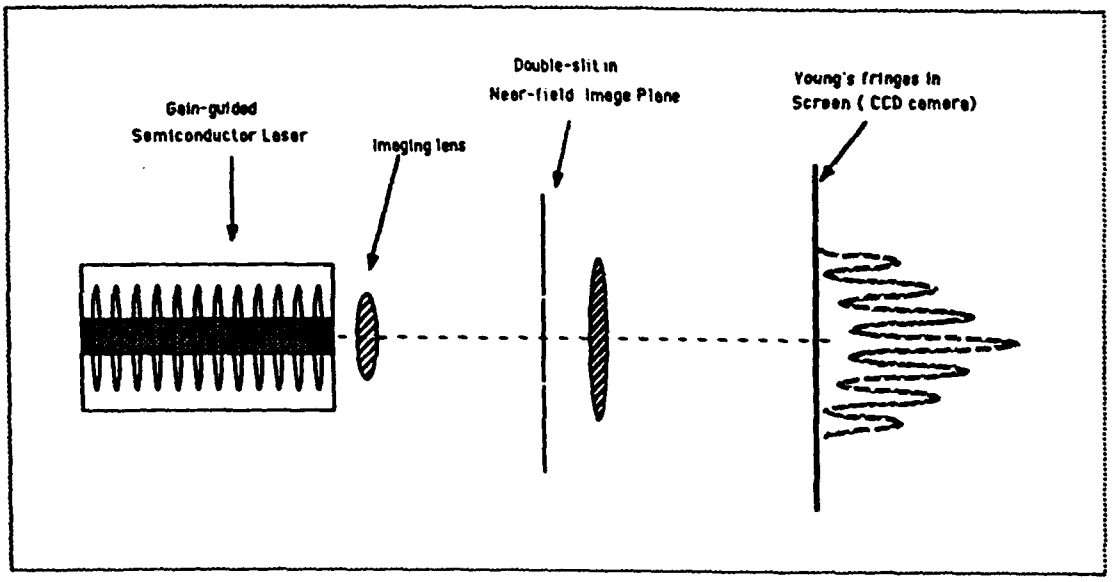

Fig. 2 - Setup for measuring spatial coherence in the near-field

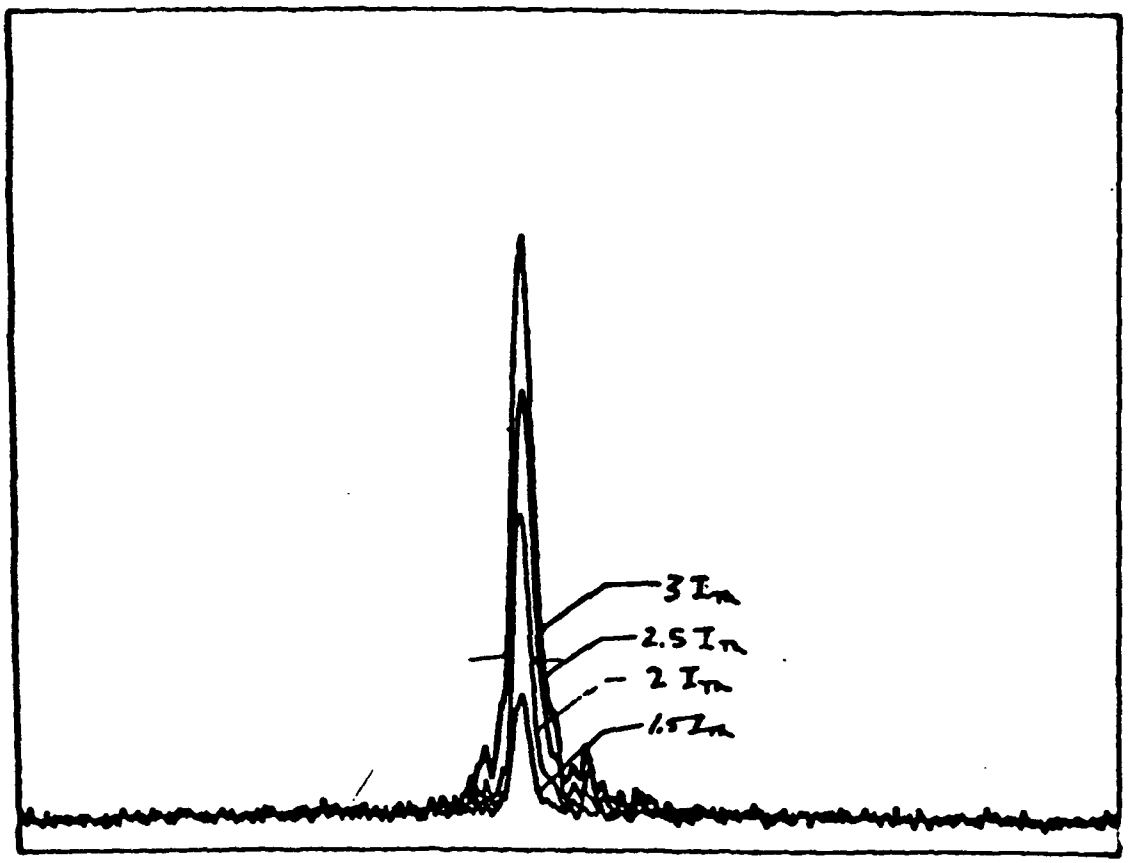

Fig. 3 - Far-field of 170 μm x 1000 μm wide stripe laser with a magnification of 3.65, for different currents upto 3 x I_{th}.

threshold for facet damage. The primary challenge has been to maintain a coherent single spatial mode at high power levels from a large aperture device. For this reason, multielement phase-locked arrays have been under development for over a decade as a means of obtaining a mode stabilized device that can operate reliably at power levels in the range 0.5–1.0 W.

Monolithic phase-locked arrays have been studied for many years. To date the best approach for stable phase-locking to high powers is resonant arrays of antiguides[1] (so called ROW arrays). ROW arrays have the unique property that full coherence and lateral-optical-mode stability coexist. Results to date are: 0.5-W cw diffraction-limited (DL) operation; 1.5-W DL pulsed operation; and 5 W in a beam 3 × DL. Reliable operation at 1-W cw power is expected in the near future. Particularly attractive is the fact that ROW devices do not need active phase control. In turn the devices' reliability is expected to be high. Beyond 1 W, ROW arrays can be scaled in two dimensions with the ultimate goal of >10-W coherent power.

As for emitting facet passivation the approach is nonabsorbing mirror. It has been implemented by etch-and-regrowth diffusion-induced lattice disordering and, more recently, using sulphur-based solutions prior to facet coating. Another recent development is the discovery that strained-layer quantum well InGaAs/GaAs/AlGaAs lasers have virtually no initial degradation, and that the emitting facet damage threshold is 3–4 times that of GaAs-active-layer devices. Passivating the emitting facets will increase the reliable power level by a factor of 3 to 4.

Reference

1. D. Botez, *et al.*, Appl. Phys. Lett. 54, 2183 (1989).

2:00pm

WS3 Recent advances in antiguided diode laser arrays

L. J. Mawst, D. Botez, M. Jansen, S. Peterson, S. S. Ou, M. Sergant, T. J. Roth, and C. Z. Mutz

TRW Research Center, 1 Space Park, Redondo Beach, California 90278

Resonant-optical-waveguide (ROW) arrays are monolithic devices capable of radiating in a diffraction-limited beam to high output power levels. These devices are attractive for many applications because they are one wire devices with no active phase control required, that is, the internal structure of the array both controls and locks the phase of each emitter. In effect, the ROW array operates as lateral DFB for spatial modes.

Modal discrimination in these structures is a complex process that involves several mechanisms: (1) edge radiation losses, (2) modal overlap with gain (gamma effect), and (3) interelement losses. As expected, there is a tradeoff between low threshold, high efficiency operation and strong modal discrimination. However, as demonstrated here, high performance cw operation can be obtained from optimized ROW-type devices. ROW arrays with optimized facet coatings operate in an in-phase mode with a diffraction-limited beam up to 500 mW in cw conditions. Threshold currents are 270 mA with efficiencies of 42% for a 1000-μm long cavity.

Since optimal performance in these devices is dependent on matching a lateral resonance condition, a new type of antiguided array based on the self-aligned stripe geometry has been pursued. In these structures, layers critical to obtaining the resonance condition (i.e., passive guide layer) are grown planar during a first phase growth. Design, fabrication, and device characteristics of these devices are discussed.

2:15pm

WS4 Thermal focusing effects in gain-guided diode laser arrays

Marek Osinski and Chung-Pin Cherng

University of New Mexico, Center for High Technology Materials, Albuquerque, New Mexico 87131-6081

Thermal effects in diode laser arrays are known to be important for the array mode selection.[1] Here, we examine in detail the role of active region heating, considering a uniform ten-strip GaAs/AlGaAs gain-guided array. The array is regarded as a perturbed broad-area laser whose modes are coupled via complex-permittivity perturbations induced by heating and injected carriers. Array modes are determined using the coupled-mode theory. The thermal perturbation is taken as a half-period cosine with center value of ΔT, vanishing at the lateral claddings. When heating-induced waveguide nonuniformity is small, the dominant array mode is $v = 10$. Calculated temperature dependence of modal gain spectra reveals that with raising temperature, the highest-gain mode shifts gradually from $v = 10$ to $v = 13$. Thus, thermal focusing results in sequential excitation of high-order modes with increasing pumping current. Calculated near- and far-field patterns for $\Delta T = 4°C$ are in excellent agreement with injection-seeding experiments,[2] while numerical simulations[2] with $\Delta T = 10°C$ give somewhat narrower near fields for $v > 10$. This indicates that the active region heating may not be as severe as previously thought. Sensitivity of the high-order modes to thermal focusing can be used to establish the actual temperature increase with good accuracy.

References

1. G. R. Hadley, J. P. Hohimer, and A. Owyoung, J. Appl. Phys. 61, 1697 (1987).
2. G. R. Hadley, J. P. Hohimer, and A. Owyoung, IEEE J. Quantum Electron. QE-23, 765 (1987).

2:30pm

WS5 Array-mode selection in nonabsorbing-mirror diode laser arrays

William E. Thompson, Chung-Pin Cherng, and Mark Osinski

University of New Mexico, Center for High Technology Materials, Albuquerque, New Mexico 87131-6081

Nonabsorbing mirror (NAM) GaAs/AlGaAs arrays have been shown to deliver thermally limited cw output power as high as 2.4 W from a 100-μm aperture.[1] Typically, these devices operate in high-order array modes with a double-lobe far field. In this paper, we show that with careful design, the NAM section can be utilized to favor single far-field lobe operation. We treat the NAM array as a composite cavity consisting of a waveguide region in which parallel single-mode waveguides are coupled through evanescent fields of guided modes and a uniform NAM section that provides further coupling between individual waveguide modes via diffraction. The eigenmodes of the waveguide section (supermodes) are calculated using the improved coupled-mode theory.[2] The supermode mixing coefficients, determining the eigenmodes of the composite cavity, are obtained by evaluating the reflected image at the interface between the waveguiding and uniform sections of the device using the 3-D diffraction integral. If the phase difference between light returning from the NAM section and injected back into any particular waveguide and its nearest neighbor is an integer multiple of 2π, the in-phase supermode is reinforced. On the other hand, a small variation in the NAM-section length and/or the waveguide spacing is sufficient to dramatically change the far-field. The performance of NAM arrays, is therefore, very sensitive to details of the waveguide structure.

References

1. D. F. Welch, W. Streifer, R. L. Thornton, and T. Paoli, Electron. Lett. 23, 525 (1987).
2. A. Hardy and W. Streifer, J. Lightwave Technol. LT-4, 90 (1986).

2:45pm

WS6 Phase-locked multidiode laser beam combining cavity optimized by asymmetrical design

Roger S. Putnam

Aerodyne Research, Inc., 45 Manning Road, Billerica, Massachusetts 01821

Phase-locked laser combining systems using intracavity holograms, spatial filters, or beam splitters are shown to be mathematically equivalent and to provide strong phase-locking by providing a minimum loss for in-phase cooperation. Our model accurately predicts the combinations of diode laser currents required by a multidiode laser system to achieve threshold. This model also correctly predicts the parabolic increase in optical power emitted at the phase canceled port as a function of the diode lasers' drive current imbalance. The automatic phase adjustments needed for efficient power collection, which are produced by small changes in the optical frequency, are shown to be greatly augmented by increasing the mismatch in cavity lengths among the various laser arms of the compound cavity. This cavity design guarantees efficient power collection independent of pathlength changes along the laser arms. A real-time measurement of the self-locked phase error is also shown to decrease for narrow spectral behavior and increase for broadband lasing.

1991 Optical Society of America Annual Meeting

Summaries of papers presented at the Annual Meeting of the Optical Society of America

November 3–8, 1991
San Jose, California

1991 Technical Digest Series
Volume 17

CONFERENCE EDITION

Optical Society of America
2010 Massachusetts Avenue, NW
Washington, DC 20036

Articles in this publication may be cited in other publications. In order to facilitate access to the original publication source, the following form for the citation is suggested:

> Name of Author(s), "Title of Paper," in OSA Annual Meeting Technical Digest, 1991 (Optical Society of America, Washington, D.C., 1991), Vol. 17, pp. xx-xx.

ISBN Number

Conference Edition	1-55752-210-3 (softcover)
Postconference Edition	1-55752-211-1 (hardcover)
(Note: Postconference Edition includes postdeadline papers.)	
1991 Technical Digest Series	1-55752-192-1 (hardcover)

Library of Congress Catalog Card Number

Conference Edition	91-66977
Postconference Edition	91-66978

Copyright © 1991, Optical Society of America

Individual readers of this digest and libraries acting for them are permitted to make fair use of the material in it, such as to copy an article for use in teaching or research, without payment of fee, provided that such copies are not sold. Copying for sale is subject to payment of copying fees. The code 1-55752-192-1/91/$2.00 gives the per-article copying fee for each copy of the article made beyond the free copying permitted under Sections 107 and 108 of the U.S. Copyright Law. The fee should be paid through the Copyright Clearance Center, Inc., 21 Congress Street, Salem, MA 01970.

Permission is granted to quote excerpts from articles in this digest in scientific works with the customary acknowledgment of the source, including the author's name and the name of the digest, page, year, and name of the Society. Reproduction of figures and tables is likewise permitted in other articles and books provided that the same information is printed with them and notification is given to the Optical Society of America. Republication or systematic or multiple reproduction of any material in this digest is permitted only under license from the Optical Society of America; in addition, the Optical Society may require that permission also be obtained from one of the authors. Address inquiries and notices to Director of Publications, Optical Society of America, 2010 Massachusetts Avenue, NW, Washington, DC 20036. In the case of articles whose authors are employees of the United States Government or its contractors or grantees, the Optical Society of America recognizes the right of the United States Government to retain a nonexclusive, royalty-free license to use the author's copyrighted article for United States Government purposes.

Submission to CLEO '92

Classification: Applications of Nonlinear Optics and Laser Spectroscopy

(Nonlinear dynamics in devices)

PERIOD-DOUBLING ROUTE TO CHAOS IN A COHERENCE-COLLAPSED SEMICONDUCTOR LASER

Jun Ye, Hua Li and John G. McInerney*

Optoelectronic Device Physics Group

Center for High Technology Materials

University of New Mexico

Albuquerque, NM 87131-6081

ABSTRACT

We report the first experimental and theoretical observations of a period-doubling route to chaos in a semiconductor laser undergoing coherence collapse, occurring when the external cavity mode spacing is an integer sub-multiple of the relaxation oscillation frequency.

* Corresponding author: Professor John G. McInerney. Tel. (505) 277-0768, -3317; Fax (505) 277-6433.

PERIOD-DOUBLING ROUTE TO CHAOS
IN A COHERENCE-COLLAPSED SEMICONDUCTOR LASER

Jun Ye, Hua Li and John G. McInerney*

Optoelectronic Device Physics Group
Center for High Technology Materials
University of New Mexico
Albuquerque, NM 87131-6081

SUMMARY

Semiconductor injection lasers are frequently operated in external cavities for spectral narrowing and mode stabilization. However, the external cavity laser can exhibit coherence collapse, a catastrophic broadening of the spectral linewidth to tens of gigahertz under moderate external feedback [1]. For fundamental and practical reasons, one needs to know whether this behavior is stochastic (noise-driven) or deterministic, and how the final coherence-collapsed state is attained.

Here we describe experimental and theoretical studies of the coherence-collapsed semiconductor laser. Our experiments have used GaAs/GaAlAs index-guided lasers (Hitachi HLP-1400), operated from 1.5-1.7 times threshold and coupled to long (10-60 cm), weakly coupled ($\sim 10^{-3}$-10^{-4} in intensity) linear external cavities. The theoretical analyses of these experiments are based on rate equations for the carrier density and complex optical field; phase-amplitude coupling, gain saturation and coherent feedback terms are included. These equations are integrated for the free-running laser and the coherence-collapsed laser with and without noise terms: the time series, return map, autocorrelation function, power spectrum and correlation dimension are calculated in each case.

The results provide the first clear evidence, following the suggestions of Dente *et al.* [2], that the coherence-collapsed state is formally chaotic, with a correlation dimension of ~ 2.5, and occurs due to mixing between external cavity mode partition fluctuations and feedback-induced relaxation oscillations. When the relaxation oscillation frequency is an integer multiple of the external cavity mode spacing, a period-doubling sequence is observed, while otherwise the coherence-collapsed state is attained via quasiperiodicity [3]. This is the first

observation of period-doubling in a semiconductor laser with optical feedback. In each case, the addition of noise tends to obscure the finer features of the chaotic attractor and makes the correlation dimension more difficult to determine.

We acknowledge financial support from the USAF Office of Scientific Research and the USAF Phillips Laboratory.

References

[1] D. Lenstra, B. H. Verbeek and A. J. DenBoef, *IEEE J. Quantum Electron.* QE-21, 674 (1985).

[2] G. C. Dente, P. S. Durkin, K. A. Wilson and C. E. Moeller, *IEEE J. Quantum Electron.* QE-24, 2441 (1988).

[3] J. Mork, J. Mark and B. Tromborg, *Phys. Rev. Lett.* 65, 1999 (1990).

For Office Use

category #

For Office Use

paper #

CLEO® '92

CONTRIBUTED PAPER CATEGORIZATION FORM (Attach to Original)

Paper Title: Phase-conjugate External Cavity Semiconductor Lasers

Corresponding Author: John G. McInerney

Address: CHTM, Univ. of New Mexico Albuquerque NM 87131-6081

Phone: 505-277-0718

Fax: 505-277-6433

Mode of Presentation

The program committee will schedule both oral and poster sessins. For poster sessions each author is provided a 4-foot-high x 8 foot-wide bulletin board on which to display a summary of the paper. Authors remain in the vicinity of the bulletin board for the duration of the session to answer the questions of attendees. The abstract and summary of both oral and poster papers are published in the same fashion, both in the advance program and in the digest.

Check one

- ☐ To be scheduled for poster presentation only.
- ☐ To be scheduled for oral presentation only.
- ☒ To be scheduled for poster presentation only if oral presentation is not possible or desirable.
- ☐ To be scheduled for oral presentation only if poster presentation is not possible or desirable.
- ☐ To be scheduled only for demonstration presentation.

THE FINAL DECISION WILL BE MADE BY THE PROGRAM COMMITTEE. IN CASES WHEN NO PREFERENCE IS STATED SCHEDULING WILL BE AT THE OPTION OF THE PROGRAM COMMITTEE.

- ☐ **To be scheduled only for the CLEO® '92 Conference.**

CLEO® '92 TOPICS TO BE CONSIDERED

- ☐ **1. Gas and Free-Electron Lasers**
  Gas laser technology and engineering • Gas laser science including kinetics spectroscopy chemistry materials, pulse power and novel applications • VUV and XUV gas laser sources • Free-electron lasers
- ☐ **2. Solid-State and Liquid Lasers**
  Advances in solid-state laser media • Advances in liquid lasers including dye lasers • Novel pump sources including high-power laser diodes • Novel resonator geometries, fiber lasers • Modeling of solid-state and liquid lasers resonators
- ☐ **3. Semiconductor Lasers**
  High-power semiconductor lasers and arrays • Short and long wavelength lasers • Coherent diode arrays • Surface-emitting lasers • Semiconductor laser applications • Narrow linewidth and tunable lasers • Quantum well wire and dot structures • Superlattice devices, novel materials and processes
- ☐ **4. Applications of Nonlinear Optics and Laser Spectroscopy**
  Nonlinear-optical probing of surfaces • Cooperative phenomena and up-conversion lasers • Nonlinear dynamics in devices solitons, instabilities and chaos • Nonlinear optics in fibers • Frequency conversion and optical parametric oscillators • Nonlinear spectroscopy for materials and device studies • Multiwave mixing processes
- ☒ **5. Phase Conjugation and Photorefractive Devices**
  Mechanisms and applications of phase conjugation • Phase conjugation by SRS and SBS • Phase-conjugate lasers • Photorefractive materials and mechanisms • Photorefractive devices and applications
- ☐ **6. Optical Materials and Fabrication**
  Crystal growth • Microfabrication techniques • Quantum well wire and dot fabrication techniques • Microprogrammable materials • Materials with enhanced nonlinear optical response • Materials for high-power and nonlinear propagation
- ☐ **7. Lasers for Fusion and Strong-Field Physics**
  Laser fusion technology • Laser plasma interactions • Picosecond and femtosecond lasers for strong-field physics • Applications of laser-produced plasmas • Laser-driven accelerators
- ☐ **8. Ultrafast Optics and Electronics**
  Generation of ultrashort pulses • Measurement of ultrafast optical and electronic properties of materials and devices • Ultrahigh-speed optoelectronic devices and switching techniques
- ☐ **9. Atmospheric, Space, and Ocean Optics**
  Lidar and laser radar systems • Ranging tracking and navigation • Free-space optical communications • Media effects on optical propagation and system performance • Optical remote sensing • Atmospheric space and underwater optical systems • Optical devices for use in atmospheric space and ocean systems
- ☐ **10. Optical Switching, Logic, and Storage Systems**
  Optical storage components and systems • Optical switching and logic devices • Optical computing and neural networks • Integrated optics • Quantum well and superlattice devices • Bistability and bistable devices • Optical signal processing
- ☐ **11. Electro-Optical Device and Infrared Sensor Technologies**
  Electro-optical devices and instruments for metrology • Beam conditioning isolation, modulation switching, sensing and pulse power applications • Electro-optical displays • Passive and active infrared sensors • Focal plane arrays and imaging systems • Innovative detector technology
- ☐ **12. Diagnostic, Analytical, and Industrial Applications**
  Flow combustion and plasma diagnostics • Chemical analysis • Sensors and detectors • Visualization and imaging • Process monitoring • Robotic sensing and control • Materials processing and surface treatment
- ☐ **13. Medical and Biological Applications**
  Laser angioplasty • Lasers in ophthalmology • Laser surgery • Laser phototherapy • Fiber optic delivery systems for surgery diagnostics and phototherapy • Laser design and engineering for the medical environment • Laser photobiology • Optoelectronic medical sensors and devices
- ☐ **14. Lasers in Electronic and Optical Device Processing**
  Laser modification of materials including etching deposition doping and mixing • Laser ablation and recrystallization of solids • Laser induced chemistry • Projection printing and lithography by lasers • Lasers in process diagnostics and materials characterization
- ☐ **15. Lightwave Communications**
  Fiber optics • Sources detectors optical amplifiers and integrated components • Transmitters receivers and performance considerations • System applications

Dev. Res. Conf.

Low Series Resistance Continuously-Graded-Mirror GRIN-SCH-MQW Vertical-Cavity Surface-Emitting Lasers Grown by MOCVD

Ping Zhou, JulianCheng*, C. F. Schaus, S. Z. Sun,
D. Kopchik, C. Hains, Wei Hsin, Chien-hua Chen
University of New Mexico, Center for High Technology Materials
Albuquerque, NM 87131 *(505)277-5605

D. R. Myers, and G. A. Vawter
Sandia National Laboratories, Albuquerque, NM 87185

We report the first demonstration of room-temperature, cw operation of GaAs/AlGaAs graded-index separate-confinement-heterostructure (GRINSCH) vertical-cavity surface-emitting lasers (VCSELs) with continuously-graded mirror layers grown by MOCVD. Continuous grading of the heterojunction interfaces in the heavily-doped p-type distributed Bragg reflector (DBR) layers significantly reduced the diode resistance and self heating, thus leading to higher power efficiencies, a wider cw current range, and a light output that is comparable to the MBE results [1]. Reduction of the series resistance of the DBR layers has previously been achieved by the insertion of an intermediate layer or a superlattice at each heterointerface of the DBR [2], and by implantation techniques [1, 3]. However, MOCVD allows the continuous grading of these heterointerfaces, which virtually eliminates the energy barriers to hole conduction, thus producing the lowest series resistance yet reported.

The VCSEL epilayer structure, grown by a low-pressure MOCVD system, is comprised of an undoped four quantum-well GRINSCH active layer structure bounded by Te-doped and C-doped DBR mirrors, containing 38.5 and 27 pairs of quarter-wave AlAs and AlGaAs layers, respectively. The AlGaAs/AlAs interfaces are continuously graded. The GRINSCH [4] structure is incorporated to improve the optical confinement and to lower the threshold current, while lateral current confinement in the VCSELs is achieved by proton-implantation [1].

The room-temperature, cw electrical (V-I) and optical (L-I) characteristics of two unpackaged VCSELs, with active areas of 11 μm and 20 μm diameters, respectively, are shown in Fig. 1. Their threshold currents and voltages are 3.85 mA/3.5 V and 5.0/mA/2.6 V, respectively, with corresponding threshold current densities of 4KA/cm^2 and 1.6KA/cm^2, respectively, and differential quantum efficiencies of about 80%. The output optical power levels of 1 mW and 0.9 mW are limited by self-heating effects in these unsoldered devices. A higher optical power of 2 mW is obtained with an active area diameter of 32 μm device, whose threshold current density is 1.2KA/cm^2. The series resistances of 11 μm and 20 μm devices are 80 ohms and 30 ohms, respectively, which are three times lower than the values reported for comparably-sized MBE-grown devices [1]. The overall power efficiency is 2.8% for the 11 μm device, and is 3.7% for the 32 μm device. The spectrum in Fig. 2, for an 11 μm device, shows a very low level of spontaneous emission and a resolution-limited spectral width of 0.7 A. These data, representing the best MOCVD results to date, are comparable to the state-of-the-art MBE results.

[1] B. Tell, Y. H. Lee, K. F. Brown-Goebeler, J. L. Jewell, R. E. Leibenguth, M. T. Asom, G. Livescu, L. Luther, and V. D. Materra, Appl. Phys. Lett. 57, 1855(1990).
[2] K. Tai, L. Yang, Y. H. Wang, J. D. Wynn, and A. Y. Cho, Appl. Phys. Lett. 56, 2496(1990).
[3] H. J. Yoo, J. R. Hayes, N. Andreadakis, E. G. Paek, G. K. Chang, and Y. S. Kwon, Appl. Phys. Lett. 56, 1942(1990).
[4] Y. H. Wang, K. Tai, J. D. Wynn, M. Hong, R. J. Fischer, J. P. Mannaerts, and A. Y. Cho, IEEE Photonic Technol. Lett. 2, 456(1990).

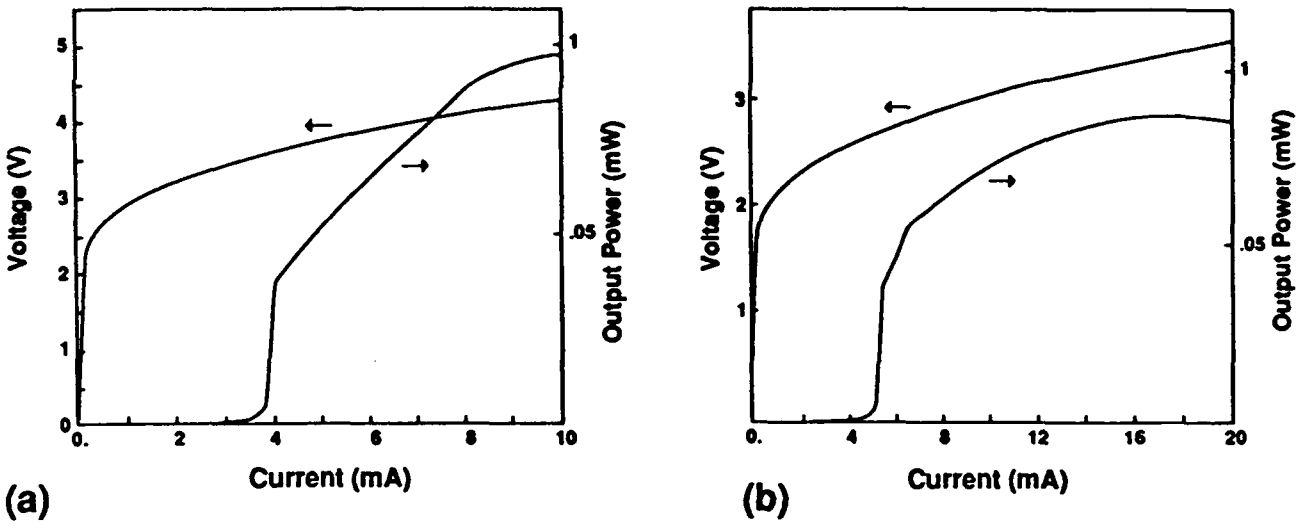

Fig. 1. L-I and I-V characteristics of the GRINSCH VCSEL for (a) 11 μm diameter active area and (b) 20 μm diameter active area.

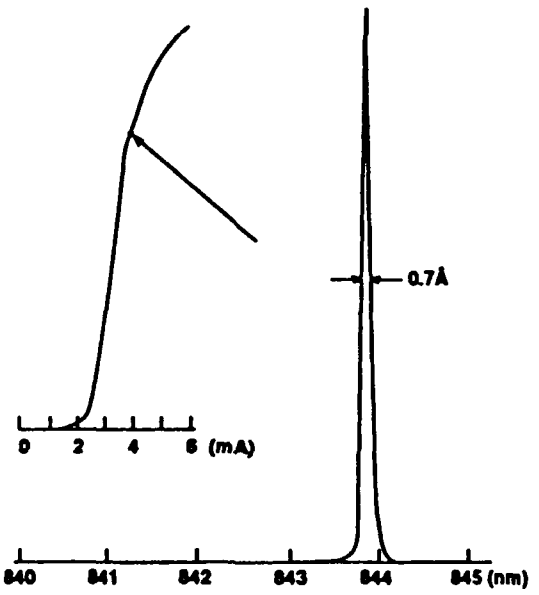

Fig. 2. Spectrum of the GRINSCH VCSEL with 11 μm diameter active area.

The as-grown wafers were optically excited using the 740 nm line of Ar-ion-pumped dye laser, with the pumping beam diameter of 10 μm. Even though no heat sink was used, the cw output power of 7 mW is considerably higher than that obtainable from single-quantum-well microlasers, while it is comparable to that of DBR-RPG devices.

BROAD-AREA MODE-COUPLING MODEL FOR CARRIER-GUIDED DIODE LASER ARRAYS

Marek Osinski and Chung-Pin Cherng, Center for High Technology Materials, University of New Mexico, Albuquerque, New Mexico 87131-6081.*

The objective of this paper is to demonstrate suitability of a broad-area mode-coupling approach to describe modal properties of carrier-guided semiconductor laser arrays. The supermode theory often adopted to explain modal behavior of phased array lasers is suitable only for index-guided arrays, since it requires a basis of individual waveguide modes. For carrier-guided arrays, with no built-in lateral variation of refractive index, such approach fails to predict correctly the number of system modes and their relative gains. It is more appropriate to treat the carrier-guided array as a perturbed broad-area laser, since the number of lateral modes is not limited in this case by the number of array elements. Recently, a simple model of carrier-guided arrays was proposed, based on the standard perturbation theory. It assumes an infinite loss outside the active region and ignores differences between modal gains of all the unperturbed (broad area) modes, claiming that these simplifications would not affect the results significantly. In this paper, we show that either of these assumptions has important consequences on the calculated modal gains for the array modes.

Rather than using the perturbation theory, we follow the coupled mode formulation, but with a basis of broad-area modes instead of individual waveguide modes. An active broad-area waveguide is considered, with the gain-index coupling as well as spatially averaged temperature effects included. The perturbation due to array structure is assumed in form a raised sinusoidal modulation of permittivity, with gain maxima at stripe centers. A smooth half-period cosine profile of temperature is also included in the perturbation.

As an example, we consider a 10-stripe GaAs/AlGaAs carrier-guided array similar to commercially available devices (SDL-2410C, 6-μm stripes on 10-μm centers, multiple-quantum-well active region). A comparison of the present theory with earlier simplified perturbation analysis corresponding to a limit of very high loss and constant reveals that the previous treatment is unreliable in predicting the modal gains of high-order array modes (mode number larger than the number of emitters). It should be emphasized that these high-order modes usually dominate in carrier-guided arrays, hence precise knowledge of their modal gains is very important in considerations of mode ordering and mode suppression schemes.

Our results reveal that earlier agreement between the simplified model and experimental observations was fortuitous. On the other hand, broad-area coupled-mode theory can contribute to improved understanding of array laser behavior and constitutes an important design and interpretation tool.

OPERATOR ORDERING IN EFFECTIVE-MASS HAMILTONIAN FOR SEMICONDUCTOR SUPERLATTICES AND QUANTUM WELLS

Mohammad Moiahedie and Marek Osinski, Center for High Technology Materials, University of New Mexico, Albuquerque, New Mexico 87131-6081.*

In recent years, effective-mass theory has been used extensively as a computational tool for determining electronic states and other properties of abrupt heterostructures, superlattices, and quantum wells. It has been recognized that application of the effective mass theory to abrupt interfaces between different materials suffers from ambiguity in kinetic energy operator ordering, caused by non-vanishing commutator of the momentum operator and the position-dependent effective mass $m(z)$. This leads to non-uniqueness of Hamiltonian, which in its general form can be written as

$$H = -\frac{1}{2}\hbar^2 [m(z)]^{\alpha}\nabla[m(z)]^{\beta}\nabla[m(z)]^{\alpha} + V(z),$$

with $2\alpha + \beta = -1$. Corresponding with this one-parameter family of operators, the matching conditions for the envelope wave function $\psi(z)$ and its derivative $\psi'(z)$ are also parametized, with continuity of $[m(z)]^{\alpha}\psi(z)$ and $[m(z)]^{\beta}d([m(z)]^{\alpha}\psi(z))/dz$ at the interfaces.

The values of α and β can in principle be determined by comparison with microscopic theory or experiment. Yet, while theoretical considerations indicate that only $\beta = -1$ ($\alpha = 0$) is consistent with microscopic treatment, there have been reports that experimentally observable interband transition energies are not sensitive to the choice of β. In this paper, we resolve this apparent controversy by demonstrating that, contrary to earlier claims, the interband transition energies do vary substantially with β. Comparison with available data confirms that the choice of $\beta = -1$ provides the best fit with experiment.

Specifically, we have analyzed GaAs/$Al_xGa_{1-x}As$ superlattice and quantum well systems using the transfer matrix technique. The results show that within the conduction band a subband-edge energy shifts approximately linearly with β ($-1 \leq \beta \leq 0$). We have also investigated the effects of superlattice parameters, such as subband index, thicknesses of both constituent materials, and barrier height (composition) on the shifts of subband-edge energy, between the two extreme cases of $\beta = -1$ and $\beta = 0$. Calculated energy levels are more sensitive to the choice of β for higher subbands and for decreasing well thickness. Increasing the barrier height or thickness also results in larger shift of subband-edge energies.

SURFACE NORMAL SECOND HARMONIC GENERATION IN PLZT AND GaAs THIN-FILM WAVEGUIDES

L C. Zou, K. J. Malloy and A. Y. Wu, Center for High Technology Materials (CHTM), EECE Building, The University of New Mexico, Albuquerque, New Mexico 87131-6081.

We compare SHG in P:LZT and GaAs thin-film waveguides. PLZT should offer higher conversion efficiencies and interaction with other optoelectronic devices. However, the difficulties presented by the polycrystalline structure of PLZT films need be examined for PLZT based devices.

Our waveguide structure requires the interaction of two counterpropagating laser beams to emit the second harmonic from the surface. The single crystal $LiNbO_3$- and GaAs-based structures have been studied previously. It is possible to deposit PLZT thin films with c axis (001) normal to the surface and with the a (and b) axes of the polycrystallites randomly oriented in the plane. Assuming such a microstructural model, our calculations show the second order nonlinear polarization for emission from the surface is present only when one of the incident laser beams is TE and the other is TM. $P^{2\omega}$, the source of the nonlinear output is independent of the orientation of the grains in the waveguide plane,

$$P^{2\omega} = d_{15}E_1^{\omega}E_2^{\omega}Y.$$

This result implies that, except for scattering losses at grain boundaries, a polycrystalline PLZT waveguide will have identical properties to a single crystal structure.

We report on these considerations for PLZT and compare them with our experimental results on single crystal GaAs-based structures. The technological advantages of GaAs and the difficulties encountered with PLZT will be discussed.

MICROSTRUCTURE AND ELECTRICAL PROPERTIES OF R.F. SPUTTERED BARIUM TITANATE FILM ON SILICON

Bi-Shiou Chiou and Jenq-I Jiang Institute of Electronics, National Chiao Tung University, Hsinchu, Taiwan.*

Meeting Program

Third Annual Symposium on Ceramics and Advanced Materials

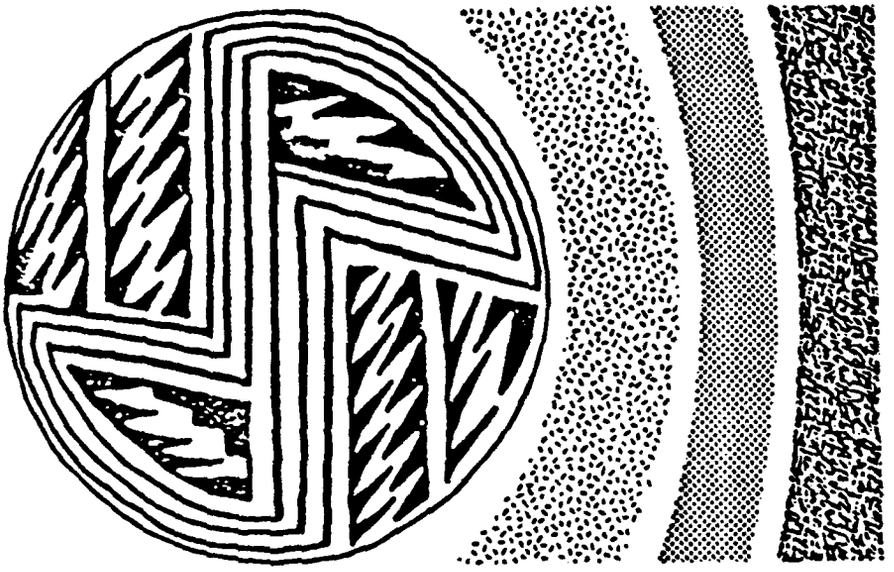

Hyatt Regency Hotel
Albuquerque, NM
October 24-25, 1991

Sponsored by:

The New Mexico Sections of the
American Ceramic Society and
the Materials Research Society